The Pennsylvania State University

The Graduate School

ADVANCING THE SUSTAINABLE AND ACOUSTIC DESIGN OF CONCRETE STRUCTURES

A Dissertation in

Architectural Engineering

by

Jonathan Michael Broyles

Submitted in Partial Fulfillment
of the Requirements
for the Degree of

Doctor of Philosophy

May 2024

The dissertation of Jonathan Michael Broyles was reviewed and approved by the following:

Nathan C. Brown
Assistant Professor of Architectural Engineering
Dissertation Advisor
Chair of Committee

Andrew R. Barnard
Professor and Director of the Graduate Program in Acoustics

Rebecca K. Napolitano
Assistant Professor of Architectural Engineering

Ryan L. Solnosky
Associate Teaching Professor of Architectural Engineering

Michelle C. Vigeant-Haas
Associate Professor of Acoustics and Architectural Engineering

James D. Freihaut
Professor of Architectural Engineering
Interim Department Head of Architectural Engineering

ABSTRACT

The building and construction sector contributes 35-40% of global carbon emissions, with concrete attributed to around 7% of global carbon emissions. With the substantial volume of concrete used in building floor systems, design practitioners and engineers are increasingly tasked to identify concrete floor systems with the least amount of embodied carbon (EC) emissions. A prominent EC reduction pathway is through the removal of structurally unnecessary concrete material in floors. This low-carbon pathway is directly applicable in the selection of more material-efficient concrete floor systems in buildings, as several concrete systems exist that are more material-efficient than conventional concrete slabs. Further concrete material reductions can be realized at the component scale when optimization frameworks are employed to determine non-traditional floor forms that improve upon the material efficiency of conventional systems. While existing concrete floor systems can reduce the EC emissions by up to 50%, greater EC savings can be achieved through the design of optimized components. However, challenges have hindered both the selection of low-carbon conventional concrete floor systems and the realization of optimized components.

Material-efficient concrete floor systems have been designed, engineered, and constructed for many years; however, identifying the floor system with the lowest EC emissions has been restricted due to the variety of floor system types, the bevy of possible design scenarios, and the uncertainty of the carbon footprint of concrete mixtures. Additionally, the selection of a low-carbon floor system can happen in early-stage design phases, potentially restricting the consideration of alternative systems, especially when design parameters are loosely defined. Furthermore, the design of a concrete floor system may be controlled by non-structural objectives. Secondary objectives such as fire-resistance, acoustic insulation, and vibrations may influence the design of a concrete floor structure, further complicating the selection of a low-carbon concrete system. These limitations currently impede how designers can identify which concrete floor system has the largest EC savings when considering various design scenarios and performance goals.

While optimized concrete components have been found to achieve material savings up to 70% when compared to conventional concrete slabs, their implementation has been restricted because floors

influence additional design performance goals. Several researchers have evaluated how secondary considerations, like walking vibrations, can be influenced by the design of optimized components, yet air- and structure-borne insulation performance has been less studied. Although air-borne sound insulation of optimized concrete floors can be adequately estimated using analytical expressions, a high-resolution numerical model is necessary to quantify impact sound insulation. However, computational resource restrictions limit simulating the full-frequency radiated sound power needed to evaluate impact insulation. An additional challenge when evaluating optimized floors for acoustic insulation is that the existing sound transmission metrics have known functional limitations that can inflate or penalize the true acoustic performance of a concrete component. As a result of these challenges, little research has evaluated the performance of optimized concrete components for acoustic performance and other design goals.

This dissertation responds to these research gaps by deriving equations and design tools to aid in the selection of a low-carbon concrete floor system, developing a new simulation method to quantify impact sound insulation, and proposing new sound transmission metrics to improve the acoustic assessment of optimized concrete components. At the building system scale, multivariate polynomial regression models, which encompass many design scenarios, were trained to estimate EC for ten conventional concrete systems tailored to the two early design phases to better inform the selection of a low-carbon floor system. A subset of the concrete floors was then evaluated for fire resistance, air-borne sound insulation, and walking vibrations to evaluate how the inclusion of additional design objectives affected which floor system had the lowest EC for six unique design scenarios. To improve the assessment of structure-borne sound insulation of optimized components, experimental results were used to validate a numerical model used to quantify impact sound insulation performance, with new acoustic transmission metrics proposed to improve the performance rating and customizability of optimized structural components. Finally, the simulation method to quantify impact sound and proposed transmission metrics were applied to a case study of shaped one-way slabs to demonstrate how comprehensive assessments of optimized concrete components can inform building practitioners on complex floor design trade-offs, and to evaluate the design benefits of optimized components when compared to an equivalent conventional floor system.

TABLE OF CONTENTS

LIST OF FIGURES

LIST OF TABLES

LIST OF SYMBOLS

a	Depth of the equivalent rectangular stress block in a concrete structure
A_c	Area of concrete
A_{cf}	Greater gross cross-sectional area of the two orthogonal slab-beam strips intersecting at a column of a two-way prestressed slab
A_i	Area of each element (i)
A_{Mod}	Modified area of concrete
A_{ps}	Area of prestressed longitudinal tension reinforcement
A_s	Provided area of non-prestressed longitudinal tension reinforcement
$A_{s,min}$	Minimum required area of non-prestressed longitudinal tension reinforcement
$A_{s,reqd}$	Required area of non-prestressed longitudinal tension reinforcement
A_t	Tributary floor area
ACI	American Concrete Institute
ASCE	American Society of Civil Engineers
ASTM	American Society for Testing and Materials
b	Width of a concrete slab column or middle strip
b_o	Width of the critical section for punching shear in a concrete slab
b_{op}	Perimeter of critical section for two-way shear in a concrete slab
b_1	Dimension of the critical section in a concrete floor measured in the direction of the span for which moments are determined
b_2	Dimension of the critical section measured in the direction perpendicular to b_1
c	Distance from extreme compression fiber to neutral axis in a concrete structure
c_0	The speed of sound of air
col_{width}	Width of a square concrete column
col_{width_in}	Initial estimated width of a square concrete column
CM	Categorical Method
COBYLA	Constrained optimization by linear approximation

CRSI	Concrete Reinforcing Steel Institute
CTF	Composite Transmission Function
d	Distance from extreme compression fiber to centroid of longitudinal tension reinforcement in a concrete structure
d_b	Diameter of a steel reinforcement bar
d_p	Distance from extreme compression fiber to centroid of prestressed reinforcement in a concrete structure
$depth_{beam}$	Depth of the concrete beam below the bottom of the slab
$depth_{DropPanel}$	Depth of the drop panel below the bottom of the slab
D	Bending stiffness
D_c	Diameter of a concrete cylinder
DL	Dead load
e	Eccentricity of prestressing force parallel to axis measured from the centroid of a section
E_c	Modulus of elasticity of concrete
EC	Embodied carbon
EE	Embodied energy
EPD	Environmental Product Declaration
f	Frequency
f_c	Coincidence frequency
f'_c	Compressive strength of the concrete
f'_r	Modulus of rupture of concrete
f_{ps}	Stress in prestressed reinforcement at nominal flexural strength
f_{py}	Specified yield strength of prestressing reinforcement
f_{se}	Effective stress in prestressed reinforcement, after allowance for all prestress losses
f_y	Yield strength of the non-prestressed steel reinforcement bars
F	Inputted force

FEA	Finite element analysis
FEM	Finite element model
FRF	Frequency response function
GHG	Greenhouse gasses
GP	Gaussian process
GWP	Global warming potential
h	Concrete slab thickness
h_{in}	Initial estimated concrete slab thickness
h_{void}	Height of the void former in a concrete slab
HW	Heavyweight (e.g., a concrete structure)
I	Moment of inertia of gross section about centroidal axis
I_{cr}	Moment of inertia of cracked section transformed to concrete
I_e, I_{e1}, I_{em}	Effective moment of inertia for calculation of deflection
I_g	Moment of inertia of gross concrete section about centroidal axis, neglecting reinforcement
IBC	International Building Code
IEQ	Indoor environment quality
IIC	Impact Insulation Class
IIC-Like	Impact Insulation Class-Like
*IIC**	Modified Impact Insulation Class
k_0	Wavenumber
l	Centerline-to-centerline span length
l_n	Clear span length measured face-to-face of supports
l_{nin}	Initial clear span length estimate
LCA	Life Cycle Assessment
LHS	Latin Hypercube Sampling
LL	Live load
LW	Lightweight (e.g., timber structure)

m	Mass density of structure
M_a	Maximum moment in concrete structure due to service loads at stage deflection is calculated
M_{cr}	Cracking moment
M_{serv}	Service moment at section
M_u	Factored moment at section
M_{uNeg}	Negative factored moment at end sections
M_{uPos}	Positive factored moment at mid sections
M_0	Total factored static moment
MDO	Multi-disciplinary design optimization
MOO	Multi-objective optimization
N_c	Resultant tensile force acting on the portion of the concrete cross section that is subjected to tensile stresses due to the combined effects of service loads and effective prestress
$NRCC$	National Research Council of Canada
$NRMCA$	National Ready Mixed Concrete Association
$NSGA\text{-}II$	Non-dominated sorting genetic algorithm II
OC	Operational carbon
p_i	Sound pressure at each element (i)
P_{eff}	Effective prestress force in prestressed steel tendons after all losses
$P_{effprov}$	Provided prestress force in prestressed steel tendons after all losses
P_i	Injected power
P_{max}	Maximum rupture load of a concrete cylinder
P_n	Nominal axial strength of the concrete column
P_{Rad}	The full frequency (low to high frequencies) radiated sound power
$P_{Rad_{Low}}$	The low frequency radiated sound power
PT	Post-tensioned
q_u	Factored load per unit area
q_{uin}	Estimate of the factored load per unit area

R_n	Resistance coefficient used in the estimation of non-prestressed steel reinforcement (as defined by Setareh and Darvas, 2017)
R^2	Coefficient of determination
RC	Reinforced Concrete
$RSME$	Root mean square error
S	Elastic section modulus
S_{max}	Maximum spacing of non-prestressed longitudinal steel reinforcement bars
S_{Mod}	Modified elastic section modulus
SCM	Supplementary cementitious material
SDL	Superimposed dead load
SNQ	Single number quantity
STC	Sound Transmission Class
$STC*$	Modified Sound Transmission Class
TL	Transmission loss calculated from the analytical transmission model
u_i	Particle velocity at each element (i)
U_{CLim}	Compression stress limit (for Class U)
U_{Tlim}	Tensile stress limit (for Class U)
$\langle \lvert v \rvert^2 \rangle$	Surface-averaged velocity
V_c	Nominal shear strength provided by concrete
V_u	Factored shear force at section
w_{Dlconc}	Weight from concrete dead load
w_{LL}	Weight from live load
w_{SDL}	Weight from superimposed dead load
w_{serv}	Service load per unit length
WP	Walking path (referring to the six walking paths used in the IIC-Like method in Ch. 6)
$width_{beam}$	Width of the concrete beam
$width_{DropPanel}$	Width of the square concrete drop panel
y	Drape distance of PT tendon

α_T	Weighting coefficient used in the calculation of the CTF rating
β_1	Factor relating depth of the equivalent rectangular compressive stress block to depth of neutral axis in a concrete structure
β_n	Analytically derived coefficients corresponding to the EC equations in Ch. 3
η	Transformed area coefficient (related to structural analysis equations)
η	Damping coefficient of concrete (related to acoustic analysis equations)
Δ_{DL}	Deflection contribution from concrete dead load
Δ_{DL+SDL}	Deflection contributions from concrete dead load and superimposed dead load
$\Delta_{DL+SDL+LL}$	Deflection contributions from concrete dead load, superimposed dead load, and live load
$\Delta_{LT_{lim}}$	Long-term deflection limit
Δ_{LT}	Long-term deflection
ξ	Time-dependent factor for sustaining load
ρ_0	The density of air
ρ_p	Ratio of A_{ps} to bd_p
σ_{Rad}	Radiation efficiency
τ	Transmission coefficient
φ	Angle of sound incidence
ϕ	Strength reduction factor
ω	Angular frequency

LIST OF EQUATIONS

ACKNOWLEDGEMENTS

First, and most importantly, I want to thank my Lord and Savior Jesus Christ for the incredible journey I've had since I came to Penn State. I have experienced the highest highs and toughest challenges, but I am so grateful for all of it. Few people are given the opportunity to obtain a PhD and conduct research on topics that they are truly passionate about. Fewer people have that opportunity while experiencing significant personal milestones (i.e., marriage and the birth of your first child). Furthermore, I have had so many deep relationships here at Penn State and in the State College area. It is because of the help from this incredible community of people that my wife completed her PhD last year, even after the birth of our son, and how I have completed mine. We could not have succeeded without the community that God has provided during our time here.

Second, I am deeply grateful to my advisor, Dr. Nathan Brown, for giving me an opportunity to learn and grow as a researcher while exploring my scientific interests. I would not be in the position that I am today, nor would have had as many fantastic collaborations and future career pathways, without him. Over the last four years, it is very evident that I've learned so much during my time working with him. Even through the challenge of advising me through all the extracurricular activities that I participated in, Dr. Brown consistently held me to a high standard which has shaped me into the researcher that I am today.

I'd also like to thank my doctoral committee for their incredible support of my research and endeavors. Thank you, Dr. Michelle Vigeant-Haas, for first introducing me to academic research at Penn State, for the six years of working with me, and for always having a positive personality. Thank you, Dr. Ryan Solnosky, for your willingness to talk with me, even on a whim, and for sharing your wealth of structural engineering knowledge. Thank you, Dr. Rebecca Napolitano, for always being encouraging and supportive. Lastly, thank you, Dr. Andrew Barnard, for joining this committee and providing helpful structural-acoustic insight on this work. I am genuinely thankful for all of you and value our friendships.

Additionally, I would like to thank three others who have worked closely with me on this dissertation and related research efforts. Dr. Micah Shepherd has been an excellent friend and mentor to me

on the structural-acoustic topics of this dissertation. Dr. Juan Pablo Gevaudan has also been a great friend and has taught me a lot about sustainability in the built environment. Also, I have really enjoyed working alongside Michael Hopper, whose structural engineering insights greatly improved the contributions of this dissertation. Moreso, thank you to the other faculty and staff at Penn State, including Dr. Thomas Boothby, Dr. Gregorgy Pavlak, Professor Moses Ling, Dr. Catherine Berdanier, Dr. Jessica Menold, and Dr. John Messner. Thank you, Scarlet Tobin, for being an excellent graduate student coordinator for the AE department and responding to my many emails. Thank you, Dr. Anand Swaminathan, for all your help with moving the concrete floor slabs. And lastly, thank you Scott Landes for always fixing Karamba (or any other misbehaving software) on our research computers.

In addition to the faculty at Penn State, I've had the privilege to work with many other researchers, including Mohamed Ismail, Eduardo Gascón Alvarez, Ashley Hartwell, Demi Fang, Samantha Leonard, Zane Rusk, Mohamad Bader Eddin, Kristen Murphy, and Morgan Prichard. A special thank you to Dr. Caitlin Mueller for inviting me to present my research to Digital Structures, and for inspiring many of my research interests. I'd also like to thank Ian Self and Skylar Farrow for their help with my research efforts: it's been very exciting to see you both grow as researchers. I'd like to thank the Building Design Group for their support and comradery over the years; especially Stephanie Bunt, Hossein Zargar, and Laura Hinkle, who are all equally intellectually and personally bright people.

I want to thank the SEI sustainability committee and SE2050 subgroup team members for their inspiration and collaboration on efforts to reduce carbon emissions in the built environment. I am especially grateful to have had the opportunity to work with Demi Fang, Martin Torres, Mel Chafart, Eric Borchers, and Lauren Wingo on the SE2050 Data Science Team. I would also like to recognize Mike Gryniuk, Mark Webster, Emily Lorenz, Jay Arehart, and many others for encouraging me to participate in the sustainability and SE2050 committees and for their support of my doctoral research.

I cannot fully express my appreciation for the community I've had during my years at Penn State. To my friends at Park Forest Baptist Church, the Architectural Engineering department, the Graduate Program in Acoustics, Penn State Christian Grads, and beyond: I have cherished these years together. I

would like to give a special recognition to several people, as I would not have been able to succeed without their help: Josh Kerr, Jason Sammut, Jake Sorber, Zane Rusk, Jude and Yawen Anderson, Caleb Frantz, Brian Habas, Pat Simoneta, Connor and Rachel Gaffney, Alex An, Mary Ogidigben, the Cetnar family, and the Sharkey family. Two more shout outs to my good friends Dennis DiMaggio and Jonathan Kadan who are both finishing or have graduated with their PhDs. Thank you to everyone who has participated in the small groups that I've helped lead, as I have thoroughly enjoyed diving into scripture together.

Lastly, I would not be here without the love and support of my family. My parents have been nothing short of incredible over these years, especially helping care for Noah during busy times. Thank you to Rachel and Ben for your continued support. A special thank you to my grandparents for all of your prayers and encouragement throughout my collegiate journey. And thank you to my new family (the Trepaniers) for your support and encouragement. Especially, thank you to Mike Trepanier, who I've really enjoyed getting to know over the last four years. Finally, thank you to Lauren for your continuous love, prayers, silliness, and encouragement. I would not have been able to do this without you.

DEDICATION

To Lauren and Noah, for your endless love and support.

And

In loving memory of Haskell Leroy Broyles,

whose dedication to family and education will continue for generations.

Part I:

INTRODUCTION

Chapter 1

Background

1.1 Global climate change and carbon emissions in the built environment

Addressing climate change is one of the most pressing global grand challenges today (Grand Challenges, 2024; Vardoulakis & Kinney, 2019). Within the last century, the global temperature has increased by 1.1°C due to the substantial amount of global carbon emissions produced (McKay et al., 2022; Yoro & Daramola, 2020). With the expectation that the global temperature will continue to increase, catalyzing other climate change tipping points (e.g., rising sea levels, increased risk of severe weather), researchers anticipate widespread negative effects on human health and well-being (Ebi et al., 2021; Frederikse et al., 2020; Kotcher et al., 2021). Therefore, immediate strategies to curb global carbon emissions are of paramount importance. Because the Architectural-Engineering-Construction (AEC) is responsible for 35-40% of global carbon emissions, there is a big role the AEC can play in reducing global carbon emissions (WBCSD and ARUP, 2021). Considering this, building engineers, architects, manufacturers, and other building stakeholders all must participate in curbing carbon emissions to mitigate the effects of global climate change and its widespread effects on the global population.

The carbon emissions associated with the AEC sector are categorized as operational carbon and embodied carbon emissions. Operational carbon (OC) is defined as the carbon emissions associated with the daily functional operations that occur during daily use of a building (Lu & Lai, 2020), including lighting and mechanical loads (Costa et al., 2013). Embodied carbon (EC), in the context of the AEC sector, refers to the carbon emissions produced from the manufacturing, transportation, construction, maintenance, and end-of-life disposal of building materials (Pomponi & Moncaster, 2018). Both OC and EC emissions are measured by a life cycle assessment (LCA) which is a method that systematically tracks the carbon emissions (amongst other LCA midpoint indicators, like acidification and freshwater consumption) of a product through different stages (ISO, 2006a, 2006b). The carbon emissions are quantified in kilograms of carbon dioxide equivalent ($kgCO_2e$) and reflect the carbon footprint of a material, component, system, or whole building (Carlisle et al., 2021). Although the sustainable performance of a building product can be assessed using other greenhouse gas (GHG) metrics, carbon dioxide is the most prevalent GHG and is the most attributed to global climate change (Solomon et al., 2009). Hence, EC emissions are often labeled as EC, or as the Global Warming Potential (GWP) of a product in $kgCO_2e$, which is also the common nomenclature used in Environmental Product Declarations.

The United Nations Environment Programme reported that building OC and EC emissions account for approximately 28% and 11% of the global carbon emissions attributed to buildings (see Fig. **1-1**) (UNEP, 2020). Although OC emissions more than double the reported EC emissions, many studies have theoretically demonstrated that net-zero OC emissions are possible as urban areas transition towards renewable energy sources (Deng et al., 2014; D'Oca et al., 2018). These studies highlighted improvement technologies such as low-carbon energy grids and improvements in building operation technologies. Yet while there has been several studies on the reduction of OC emissions, there is a need for more research on effective low-carbon EC pathways, as the impact that EC emissions has on the total carbon footprint of a building has only been realized within the last two decades (De Wolf et al., 2017; Dixit et al., 2012; Pomponi & Moncaster, 2016; Röck et al., 2020). Because EC emissions are produced across different stages of a building material's life span, careful consideration must be given to how building materials are extracted, manufactured, constructed in a building, and are disposed of at the end-of-life phase.

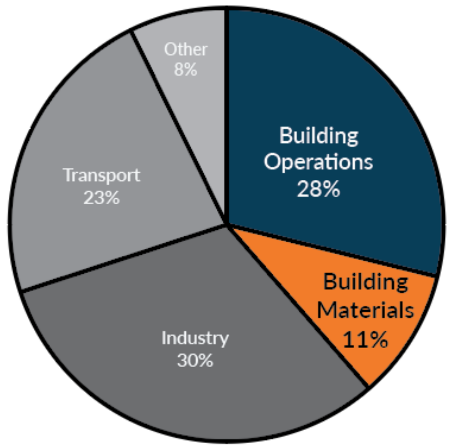

Figure **1-1**: Distribution of global carbon emissions by sector (image after CLF, 2020).

As building operations continue to improve and more efficient energy grids are implemented, EC emissions are expected to surpass OC emissions and must be accounted for in reducing the carbon footprint of a building (Kovacic et al., 2018). Unlike OC emissions that occur during the use of a building, the majority of EC emissions occur in the production stage of a building (Asdrubali et al., 2013; Dixit et al., 2012). This means the amount of material required for the construction of a building directly affects the EC emissions. Since the largest contribution of EC comes from the structural system of a building (Cabeza et al., 2013; Foraboschi et al., 2014; Li et al., 2014), structural engineers, architects, and other building designers have to consider how design decisions, including the selection of structural material and system type, can influence the carbon footprint of a building.

1.2 Concrete: The world's most consumed man-made material

Three of the most common structural materials used in the design of buildings in the U.S. include concrete, steel, and lumber / mass timber (Arehart et al., 2022; Reyna & Chester; 2015). Of these structural materials, concrete is the most commonly used because it is widely accessible across global markets, economical, can be easily constructible depending on the structural form, and has inherent benefits for other design considerations including high fire-resistance, because concrete is a non-flammable material (Khoury, 2000), favorable acoustic sound insulation, because of the large mass density and stiffness (Dupree, 1980), and has thermal insulation benefit because of the slow rate of heat transfer (Thomas &

Rees, 1999). Not coincidentally, concrete structures have existed for many centuries including famous built wonders like the Colosseum in Rome, Italy, in part because of the implementation of high strength (i.e., hydraulic cement) concrete mixture (Gagg, 2014). More recently, concrete structures are often an integral part of Passive House design, which is a modern net-zero energy building design concept (Schnieder et al., 2020).

Despite the longevity, durability, and inherent benefits to the interior environment of a building, concrete structures are often criticized as having high EC emissions (Moncaster et al., 2022). On the surface it appears that concrete structures are at a clear disadvantage when being compared to other structural systems for EC emissions, as shown in Fig. **1-2** (image results are from Fig. 5, pg. 139 using the Athena results from Stringer & Comber, 2015). However, concrete as a material has a low carbon footprint. Indeed, concrete has lower carbon emissions per weight or volume (i.e., one cubic meter), when equivalently compared to other structural materials (see Fig. **1-3**, which is after Fig. 3 on pg. 1058 in Barcelo et al., 2014). This prompts the question: *why does a concrete structure have high EC emissions when the concrete material has a low carbon footprint?* The answer is that there is typically more concrete used in concrete systems compared to the amount of structural material used in other kinds of systems (e.g. steel and wood structural elements), resulting in high EC emissions.

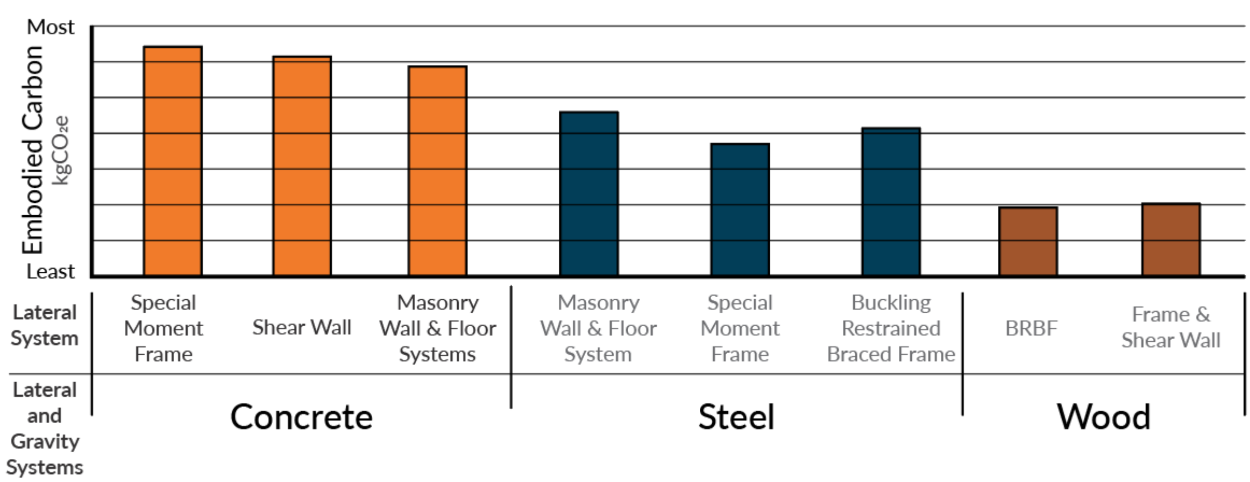

Figure **1-2**: EC emissions affiliated with common structural lateral systems (image adapted from Stringer & Comber, 2015).

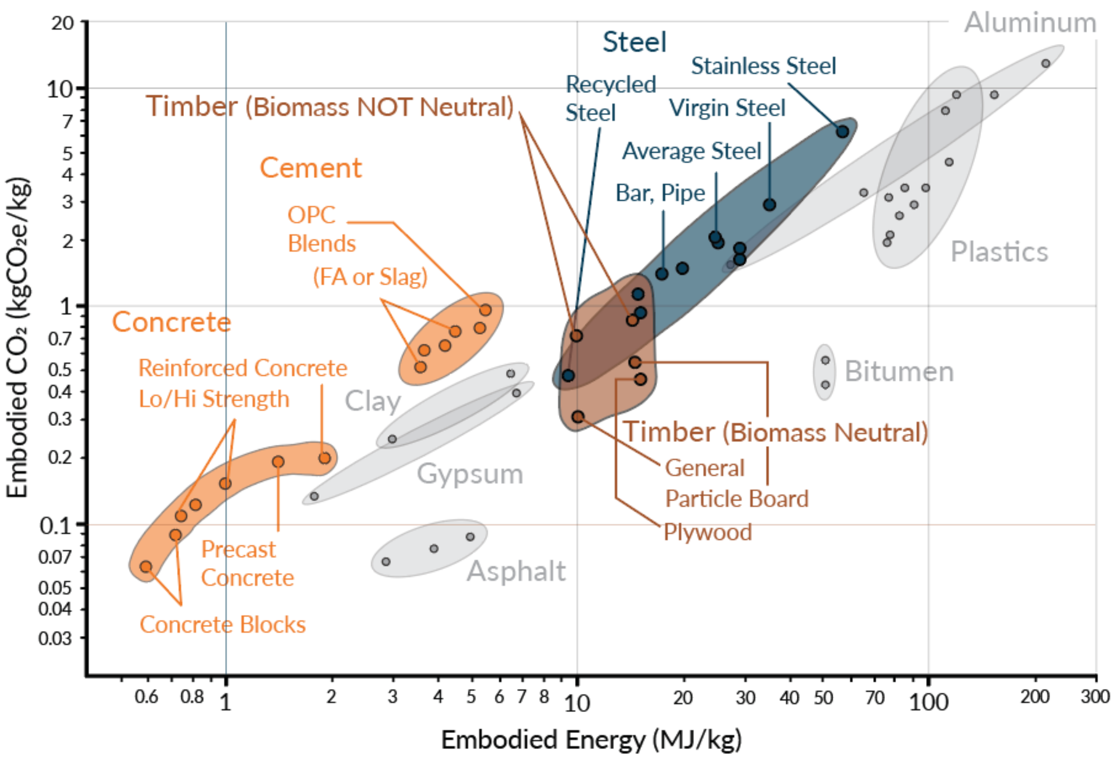

Figure **1-3**: Normalized EC and embodied energy for common structural materials (image adapted from Barcelo et al., 2014).

Outside of water, concrete is the most consumed material in the world (Gagg, 2014). Within the built environment, concrete is used more than twice as much as any other construction material (steel). In the U.S. alone, over 400 million cubic yards (over 700 million metric tons) of concrete is produced per year (NRMCA, 2022). These facts underscore that the high EC emissions of concrete structures are due to the large amount of concrete material that comprise a concrete structure. Undoubtedly, it is because of the large-scale production of concrete material in the world that concrete is responsible for up to 8% of global carbon dioxide emissions (Barcelo et al., 2014; Griffiths et al., 2023). Yet despite the amount of carbon emissions attributed to concrete manufacturing, the production of concrete has continued to increase in recent years because of other decision-based drivers, including material cost (Watari et al., 2023). Moncaster et al. (2022) summarizes this well by saying, "concrete is cheap, readily available and extremely versatile, and there is always likely to be a market for its use. But its continued use is also contributing significantly to climate change."

When prioritizing the reduction of carbon emissions in the selection of a structural system, there are design scenarios in which concrete structures are preferred. For example, public assembly buildings (e.g., libraries) are known to experience high structural loads while prioritizing long span lengths. Ribbed concrete floors are advantageous in these design scenarios as the concrete material is efficiently used in the ribs to account for the high structural load. While ribbed concrete floors are known to be more material-efficient than concrete flat plates, concrete flat plates are still designed in many building types because they are easily constructible and have inherent benefits for secondary design objectives. Because there are design scenarios in which concrete floors are advantageous, there has been an increase in researchers investigating low-carbon pathways to reduce the EC emissions of concrete structures. The engineering and optimization of low-carbon concrete mixes has been the focus of many studies (Chen et al., 2023; DeRousseau et al., 2020; Habert & Roussel, 2009; Helsel et al., 2022; Purnell & Black, 2012; Shah et al., 2022; UN Environment et al., 2018), but currently only small-scale production of low carbon mixtures is possible. Reduction of carbon emissions at the source of concrete production (i.e., at the factory) by using carbon sequestration techniques, such as precure carbonate reactions, is a second pathway, but carbon sequestration technology is costly and not widespread (Hanifa et al., 2023; Nehdi et al., 2024; Stefaniuk, 2023). Its effectiveness is also uncertain due to many variables such as the factory’s manufacturing processes and the strength of the concrete (Ravikumar et al., 2021). A third, more viable and immediate low-carbon pathway is to reduce structurally unnecessary material in a concrete structure (Dong et al., 2015), thereby reducing the quantity of concrete produced (Watari et al., 2023).

1.3 A low-carbon pathway: Reducing concrete material in floor structures

One popular academic and industry low-carbon strategy is to ensure the integrity of a building structure while using less structural material (Danatzko & Sezen, 2011; De Wolf et al., 2017; Evins et al., 2012; Fang et al., 2023b). This strategy is especially relevant for conventional concrete floors, as concrete slabs are known to be materially inefficient. To aid the demanding construction schedules of building projects, concrete flat plates are often poured at the building site, resulting in thick concrete floors, even though not all the concrete material is needed to maintain structural integrity. This material inefficiency is demonstrated by Huberman et al (2015) in which concrete floors and similar horizontal spanning elements were found to contribute as much as half of the carbon emissions in a multi-story concrete frame (Huberman et al., 2015).

Conventional concrete slabs are primary contributors to the carbon footprint of a multi-story building, yet there are several alternative and more material-efficient concrete floor systems that can be designed to replace a conventional slab. Ribbed systems, such as one-way and two-way modular pan joist floors, and voided systems, like hollow-core planks and bubbledeck slabs, are known to be material-efficient compared to conventional concrete slabs (Aouf, 2019; Ferreiro-cabello et al., 2017; Fraile-Garcia et al., 2016; Jayasinghe et al., 2021; Oh et al., 2019). Post-tensioned concrete floors are another existing floor system that reduces the thickness of conventional reinforced systems through the implementation of high-strength steel tendons, thereby reducing significant concrete material (Broyles & Hopper, 2023; Zelickman & Amir, 2022). Optimization strategies can also be applied to conventional structural systems to realize highly material-efficient floor spans and geometries (Jayasinghe et al., 2022; Miller et al., 2015; Zelickman & Guest, 2023). These existing floor systems have been shown to reduce EC emissions up to 50%, emphasizing how the implementation of low-carbon concrete floors can meaningfully curb building carbon emissions in the present (see Fig. **1-4**).

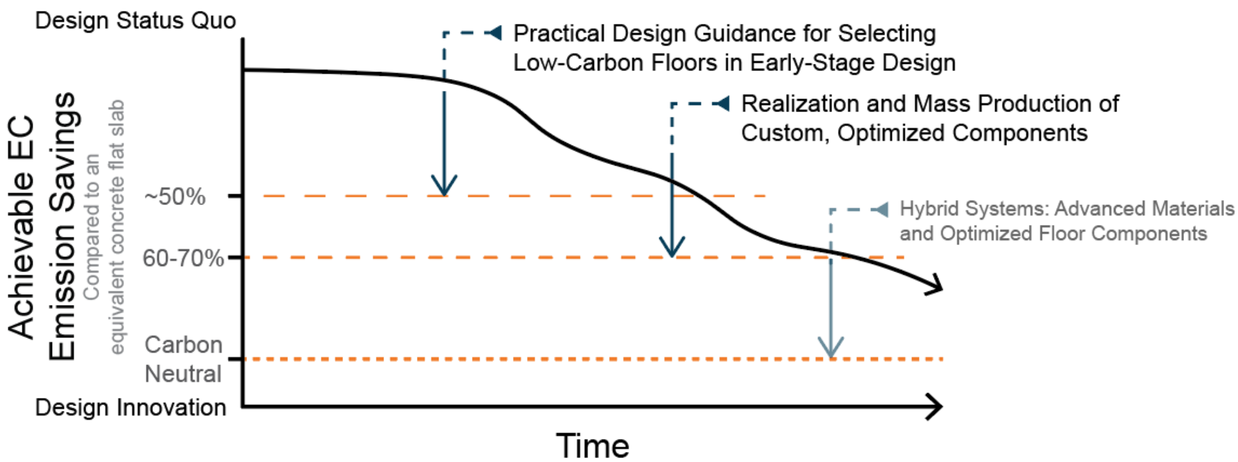

Figure **1-4**: Theoretical progression of reducing EC emissions of concrete floors in relation to the advancements needed to achieve carbon neutrality in concrete floor systems.

Construction technology advancements, such as digital fabrication and 3-D printed formwork, help to further reduce material consumption in optimized and customizable structural concrete floor components. Application of advanced computational frameworks to realize more efficient floor forms (Ismail & Mueller, 2021; Leschok et al., 2018) have been the focus of recent research as EC reductions of over 58% are possible when compared to a conventional, and functionally equivalent, concrete slab (Hawkins et al., 2020). Meibodi et al. (2018) used digital fabrication approaches to realize concrete material savings up to 70%, confirming that significant EC emissions can be reduced by optimizing concrete components. Yet unlike the material-efficient conventional concrete floor systems, optimized concrete components are not widespread in the design community. Although it is anticipated that the digital fabrication technology to mass produce optimized concrete components will be available in the future, the exact timeline is uncertain. The combination of low-carbon concrete mixtures and sustainable structural materials with material-efficient geometric forms of concrete structures has the highest potential to reduce EC, yet this topic has only recently been subject to research studies.

Another major limitation of optimized concrete components is that many research studies have solely focused on structural performance. While ensuring structural integrity of concrete components is essential, more research is needed to better understand the performance of optimized concrete floor components for other building objectives before they can be broadly implemented in building design. Specifically, advanced methodologies and comprehensive assessments of the design trade-offs of optimized concrete components are necessary before optimized concrete components can be widely implemented in buildings.

1.4 Consideration of additional building design goals

Although there are direct benefits of structural optimization for reducing the carbon footprint, building cost, and structural weight, such optimization interacts with other important secondary design considerations (Abbaszadeh et al., 2006; Shafigh et al., 2018). On a building scale, designers have to balance many competing design objectives (e.g., structural, mechanical, daylighting) to ensure the safety and functionality of building occupants. On a smaller scale, building components, like floors, have other different functions and performance goals. In addition to structural integrity, engineers have to consider the cost, EC, fire-resistance, serviceability, acoustic insulation, thermal insulation, and aesthetics of floor structures as the design of a floor structure, especially the geometry and material characteristics, can inadvertently affect the performance of secondary design considerations when not considered.

The reduction of structurally unnecessary concrete materials in a floor slab is a proven strategy to reduce EC; however, the reduction of structural mass may result in the failure to meet performance criteria for secondary design goals. For example, Wu et al. (2020) assessed an optimized funicular concrete floor for vibration performance and found that 70% of the funicular floor designs did not satisfy vibration requirements despite being a low-carbon, structurally viable design. Therefore, an optimization framework would be useful to help engineers carefully consider both structural optimization and secondary design concerns. Related, the air- and structure-borne sound insulation of a concrete floor are secondary design objectives that should be considered in tandem with efforts to minimize EC. This is because neglect of acoustic phenomena in multi-story buildings could potentially contribute to harmful health consequences for building occupants (Ajayi et al., 2016). Concrete structures have high sound insulation performance because of the inherent mass density of the floor structure. Yet, there is a trade-off between reducing concrete material and corresponding EC and achieving high acoustic attenuation performance (Broyles et al., 2022c). Furthermore, the inclusion of acoustic insulation as an additional design goal may influence what the best performing concrete floor design is.

While structural optimization of building components has been a rapidly growing research field, the direct effect on acoustic insulation has largely been unexplored. Previous work by Broyles et al. (2022c) demonstrated how the inclusion of air-borne acoustic insulation as a design objective does influence the best performing concrete floor designs; however, the optimal solutions were not compared to the performance of conventional concrete systems. The study did not consider impact sound performance, which is known to be a significant source of acoustic complaints in buildings (Vardaxis et al., 2018c). A study by Mendez Echenagucia et al. (2016). demonstrated how the form of a funicular concrete component influenced impact sound insulation performance but limited the number of floor shapes investigated and only considered low frequencies (10 to 200 Hz). Moreso, the metrics that quantify acoustic insulation specified in building code have known functional limitations that can be exploited in evaluating and optimizing concrete floor components (Broyles et al., 2021; LoVerde & Dong, 2017).

1.5 Overarching research motivation

This dissertation is motivated by the need to reduce EC emissions while considering multiple design goals for concrete floor systems at the building system and component scales. Specifically, this dissertation responds to the broad question: *How can building engineers realize low-carbon concrete floor structures while achieving high performance for design objectives (e.g., air-borne acoustic insulation, fire rating) that compete with reducing carbon emissions?* While one dissertation cannot fully respond to this question, this dissertation comprehensively evaluates performance trade-offs in structural concrete floor systems at the building scale and proposes and validates a new simulation methodology and acoustic metrics for designing optimal concrete floors at the component scale. Therefore, the work presented directly contributes to the conversation of minimizing EC emissions in the built environment without inadvertent negative effects on secondary performance goals.

1.6 Dissertation organization

The chapters in this dissertation are grouped into Parts I to IV, to demonstrate the overall hierarchy of the work presented. Part I (Introduction) includes Chs. 1 and 2 which provide important background information on why the EC emissions of concrete floor systems are being evaluated. Ch. 2 details related research work at the building system and component scales to help identify research gaps and formulate research questions addressed in the following chapters. Part II describes two studies (Chs. 3 and 4) at the building system scale to help inform building designers on the selection of low-carbon conventional concrete floor systems while considering various structural design parameters and additional performance goals. Ch. 3 derives polynomial regression equations appropriate at the two early design phases to estimate the EC emissions of concrete floor systems designed for different structural parameters. Additionally, the aleatoric uncertainty regarding the carbon emissions of concrete mixtures was considered in the obtained equations, enabling a more precise EC estimate. These results are expanded in Ch. 4 to evaluate eight concrete floor systems for fire-resistance, air-borne acoustic insulation, and walking vibrations in relation to EC. Although conventional concrete plates perform well for these secondary design objectives, other systems, especially ribbed floors, are more susceptible to varying objective performance goals. The results from these two studies at the building system scale help contextualize the results of the shaped one-way slab designs found in Ch. 8.

Part III includes four studies (Chs. 5 to 8) conducted at the component scale. Furthering the work of Broyles et al. (2022c), four shaped concrete slabs were experimentally tested to ascertain the dynamic performance of the shaped floors (see Ch. 5). A 1:1 numerical model was validated using the experimental results, which helped validate a computational method to obtain the impact sound insulation performance of non-traditional concrete floor forms. The IIC-Like method in Ch. 6 is a hybrid air-hemisphere method, which uses the acoustic concept of radiation efficiency to determine the structure-borne sound insulation performance at frequencies above coincidence and the conventional air-hemisphere method used to determine the low-frequency impact sound performance. Related, Ch. 7 proposes alternative acoustic transmission metrics without the functional limitations of the existing North American sound transmission metrics and assessing how the different metrics influence the identification of preferred design in a small case study of three shaped concrete components and one flat plate. Ch. 8 demonstrates the IIC-Like method and new transmission metrics on a case study of shaped concrete floors to explore the design trade-offs between minimizing EC emissions and maximizing acoustic insulation.

Part IV presents the results and takeaways of the work presented in this dissertation. A summary of the conclusions, contributions, limitations, and opportunities for future research are provided in Ch. 9. Three appendices provide additional information on the methods used and results obtained from Ch. 3.

Chapter 2

Literature Review

This chapter summarizes existing literature that evaluates and determines engineering solutions that achieve low-carbon (EC) emissions of conventional and innovative concrete floor structures in buildings, and how the inclusion of additional building objectives influences the EC emissions of concrete structures. Relevant literature that responds to the overarching research motivation of this dissertation is organized as research of low-carbon concrete floor structures at the building system scale and the component scale. Although there is a clear relationship between the two scales, studies at the building system scale commonly focus on existing concrete floor systems and have a larger scope boundary (e.g., columns, beams, foundations) while studies at the component scale demonstrate how innovative construction technologies and practices realized through novel computational strategies can be used to achieve greater EC savings of the floor itself (i.e., smaller scope boundary). It is imperative to motivate research at both scales because low-carbon conventional concrete floor solutions can immediately curb carbon emissions in design practice today as advanced construction methods are not widely available in many global markets. However, it is reasonable to believe that these technologies will become more widespread over the coming years as the AEC sector continues to strive towards low- and net-zero carbon emission structural systems. Furthermore, performance baselines of existing concrete floor systems are needed to contextualize the design benefits of optimized concrete structural components in buildings.

The selection of a concrete floor system is often based on the performance of multiple design objectives. The design of concrete floor structures is commonly controlled by structural limit states (i.e., flexure, shear, ductility, cracking, and deflection) to ensure structural integrity, yet concrete floor systems participate in the performance of multiple indoor environmental quality (IEQ) domains including floor vibrations, sound attenuation, and thermal insulation. This chapter reviews how the consideration of multiple design objectives can influence the aim to reduce EC emissions of concrete floor structures at both the building system and component scales and motivates why the consideration of multiple design objectives is more necessary at the component scale of concrete floors than the building system scale. Of the many IEQ domains that floors contribute to, this dissertation focuses on the implications of building acoustic performance, specifically air- and structure-borne sound insulation, as a critical secondary design objective that must be considered alongside the goal of minimizing EC emissions. One reason is that the structural-acoustic characteristics that can improve sound insulation, such as mass density and stiffness, can be inadvertently affected by material reduction and geometric shaping, worsening the IEQ in a building. This chapter concludes by identifying specific research gaps with corresponding research questions that are addressed in the subsequent chapters of this dissertation.

2.1 Low-carbon concrete floor structures at the building system scale

2.1.1 Embodied carbon emissions of conventional concrete floor systems

At the beginning of the modern age of concrete structures in the early 20th century, concrete was among the more expensive construction materials because of the lack of large-scale production around the world. But because of the versatility of concrete as a material, efficient concrete floor forms could be designed and fabricated to minimize the cost of the concrete material while ensuring structural integrity (Jayasinghe et al., 2022). The isostatic ribbed concrete floors of Pier Luigi Nervi, as shown in Fig. **2-1**, serve as an example that concrete floor systems can be engineered to reduce material consumption (Halpern et al., 2013). However, with increased cost of construction labor and formwork, hastened construction schedules, and the growth of large-scale production of concrete in the late 20th century, material efficiency in concrete floors was prioritized less giving way to concrete systems with an excess of structurally unnecessary concrete material. Because of this trend, many researchers have shown that common concrete floor structures have unfavorable EC emissions (Gan et al., 2017; Hart et al., 2021; Miller et al., 2015).

Fig. **2-1**: An example isostatic concrete floor system designed by Pier Luigi Nervi (taken from Fig. 4 in Halpern et al., 2013).

The worst performing EC structural floor system, regardless of building geometry and structural design parameters, is reinforced concrete (RC) flat plates (D'Amico & Pomponi, 2020; Ferreiro-Cabello et al., 2016; Jayasinghe et al., 2021a). Although RC flat plates can be efficiently designed to reduce material consumption (and corresponding cost implications) (Sahab et al., 2005) and continue to be designed and constructed in buildings today, there are several alternative concrete floor systems that have been engineered to further reduce material consumption, and corresponding EC emissions, and are widespread in many global markets. RC two-way slabs with drop panels (referred to as RC flat slabs) and RC two-way slabs with beams are examples of how slight geometric changes to the floor system can result in a thinner slab and reduce concrete material (Miller et al., 2015). Modular ribbed concrete floor systems, specifically RC one-way pan joist floors and RC two-way waffle slabs, have existed for many decades with various thicknesses and sizes to accommodate for different floor geometries, structural loads, and floor-to-floor depth requirements while using less concrete material than a conventional RC flat plate (D'Amico &

Pomponi, 2020). Voided RC plates utilize void formers to reduce concrete material in locations along the floor that experience lower structural load demands thereby needing less material (Fanella et al., 2017). Related, hollow-core floor systems are typically precast components that have high material efficiency (Prakashan et al., 2016; Xu et al., 2014). Lastly, post-tensioning (PT) of high-strength steel tendons in a concrete floor system can be implemented to realize thin concrete floor slabs while maintaining structural integrity (Aalami & Jurgens, 2003).

The abundance of alternative material-efficient concrete floor systems demonstrates how the concrete design community has progressed towards both the cost reduction of concrete material and minimization of carbon emissions. Yet as the sustainable metric of EC formulated in recent years, research was needed to identify which concrete floor system is preferable with the goal of reducing carbon emissions. Indeed, many studies have been conducted to evaluate the EC (and cost) of different concrete floor systems, as is summarized in Table **2-1**. Yet Table **2-1** reveals that the majority of existing literature limits the EC assessment of concrete floor systems to conventional RC flat plates. Although these studies have varying differences in system boundary, life cycle assessment (LCA) scope, design objective(s), and may have evaluated the EC emissions of floor systems comprised of other structural materials (i.e., steel and mass timber), only four research studies investigated more than two different types of concrete floor systems limiting the identification of the preferred low-carbon concrete floor system.

Table **2-1**: Summary of the studies that evaluated the EC and EE of conventional concrete floor systems.

Source	**Concrete Floor Structure(s) Investigated**	**System Boundary and LCA Scope**	**Primary Design Objectives**	**Secondary Design Objectives**
Miller et al. (2015)	Conventional RC and PT Systems (Flat Plate, Flat Slab, and One-Way Slab)	Building Scale; A1-A3	Minimize[1] EE for Structural Limit States[2]	N/A
Ferreiro-Cabello et al. (2016)	Conventional RC System (Flat Plate)	Building Scale; A1-A5	Minimize EC and Cost for Structural Limit States	N/A
Lotteau et al. (2017)	Conventional RC System (Flat Plate)	Building Scale; A1-A3, B2-B4, C1-C4	Minimize EC for Structural Limit States	Thermal Insulation
Gan et al. (2017)	Conventional RC System (Flat Plate)	Building Scale; A1-A4	Minimize EC for Structural Limit States	N/A
Eleftheriadis et al. (2018)	Conventional RC System (Flat Plate)	Building Scale; A1-A3	Minimize EC and Cost for Structural Limit States	N/A
Oh et al. (2019)	Conventional RC System (Flat Plate)	System Scale (Floor and Column); A1-A3	Minimize EC and Cost for Structural Limit States	Human-Induced Floor Vibrations
Gan et al. (2019)	Conventional RC System (Flat Plate)	Building Scale; A1-A4	Minimize EC for Structural Limit States	N/A
D'Amico and Pomponi (2020)	Conventional RC Systems (Flat Plate, One-Way Slab)	Building Scale; A1-A3	Minimize weight (EC) for Structural Limit States	N/A
Hart et al. (2021)	Conventional RC Systems (Flat Plate, One-Way Slab)	Building Scale; A1-A5, B1, C1-C4, D	Minimize EC for Structural Limit States	N/A
Jayasinghe et al. (2021a)	Conventional RC and PT Systems (RC and PT Flat Plates, RC One-Way Slab, RC One-Way Slab – Wide Beam, RC Troughed Slab, RC Two-Way Slab, RC Waffle Slab, RC Hollow-core Slab)	Building Scale; A1-A3	Minimize EC and Cost for Structural Limit States	Fire-Resistance Rating (1-hr only)
Zhang and Zhang (2021)	Conventional RC System (Flat Plate)	Building Scale; A1-A4	Minimize EC and Cost for Structural Limit States	N/A
Trinh et al. (2021)	Conventional RC and PT Systems (RC and PT Flat Plates)	Building Scale; A1-A3	Minimize EC for Structural Limit States	Fire-Resistance Rating (1.5-hr only)

Source	Concrete Floor Structure(s) Investigated	System Boundary and LCA Scope	Primary Design Objectives	Secondary Design Objectives
Jayasinghe et al. (2022a)	Conventional RC System (Flat Plate)	System Scale (Floor and Column); A1-A3	Minimize EC for Structural Limit States	Fire-Resistance Rating (1.5-hr only)
Jayasinghe et al. (2022b)	Conventional RC and PT Systems (RC and PT Flat Plates, RC One-Way Slab, RC One-Way Slab – Wide Beam, RC Troughed Slab, RC Two-Way Slab, RC Waffle Slab, RC Hollow-core Slab) and Optimized Vaulted Floor (Thin Shell)	System Scale (Floor and Column); A1-A3	Minimize EC for Structural Limit States	Fire-Resistance Rating (1.5-hr only)
Broyles and Hopper (2023)	Conventional RC and PT Systems (RC and PT Flat and Voided Plates) and Non-Traditional PT Voided Plates (Diagonal and Curved PT Tendon Layouts)	System Scale (Floor and Column); A1-A3	Minimize EC for Structural Limit States	Fire-Resistance Rating (2-hr only)

[1] Minimizing in this context refers to the optimization of the structural design, floor layout, or column grid. Shape and topology optimization strategies are not considered in these studies, aside from the vaulted floor in Jayasinghe et al. (2022b).
[2] Structural limit states differed study to study and typically consisted of only one to two structural load combinations.

Miller et al. (2015) evaluated RC and PT flat plates, flat slabs, and one-way slabs and found that the three concrete floor systems constructed using PT had EE savings up to 49.1% compared to their RC floor system counterpart. Additionally, the authors evaluated an RC and PT flat plate for 16 different design scenarios - 4 different square span lengths (6.67 m, 8 m, 10 m, and 13.33 m) and 4 different concrete strengths (32 MPa, 40 MPa, 50 MPa, and 65 MPa) with one structural load condition (a uniform live load of 3.0 kN/m^2 and a superimposed dead load of 1 kN/m^2) - to demonstrate that structural weight savings in a building can be reduced by over 34% by manipulating the design parameters, indicating that different design scenarios can meaningfully influence the carbon footprint of a building. Jayasinghe et al. (2021a) assessed the EC and cost for eight concrete floor structures for 17 different span lengths (4 m to 12 m at 0.5 m increments or ~13 ft to ~40 ft at ~1.6 ft increments), two concrete strengths (30 MPa for RC systems and 32 MPa for PT systems), and one structural load condition (a uniform live load of 2.5 kN/m^2 and a superimposed dead load of 0.85 kN/m^2) and found that RC two-way slabs on beams and hollow-core slabs were optimal for both objectives. It was noted that PT flat slabs had similar EC savings as the optimal concrete systems at spans from 9 m to 12 m yet had larger construction costs. This study was extended to contextualize the EC performance of an optimized vaulted thin shell floor system and found that EC savings of up to 65% are achievable using a vaulted thin shell compared to ~36% EC savings for RC two-way slabs on beams and hollow-core slabs (Jayasinghe et al., 2022b). The floor systems were evaluated for the same structural design scenarios as the earlier study, except that the superimposed dead load was increased to 1.5 kN/m^2. Despite the potential of large EC savings, Jayasinghe et al. (2022b) noted that the technology to construct thin shell vaulted floors is not widespread and that further research is needed to determine the performance for other design considerations including fire-resistance, floor vibrations, and acoustics.

Of the conventional concrete floor systems and construction technologies available in global markets, the combination of PT and void formers has been demonstrated to be an existing sustainable alternative to conventional RC flat plates. In a study by Broyles and Hopper (2023), six concrete floor systems (RC and PT flat plates and RC and PT voided plates, with three different PT tendon layouts as shown in Fig. **2-2**) were evaluated for 41 different span lengths (3 m to 15 m at an 0.333 m increment, or 10 ft to 50 ft at a 1 ft increment) for five concrete strengths (27.6 MPa, 34.5 MPa, 41.4 MPa, 48.3 MPa, and 55.2 MPa), four uniform live loads (1.92 kN/m^2, 2.87 kN/m^2, 3.83 kN/m^2, and 4.79 kN/m^2), and four superimposed dead loads (0.239 kN/m^2, 0.718 kN/m^2, 1.44 kN/m^2, 2.39 kN/m^2), for a total of 3,280 different structural design scenarios per concrete floor system. The results showed that PT voided plates can achieve 50% EC savings at a span of 9 m (~30 ft) compared to RC flat plates and indicated that larger EC savings are possible at longer spans. The authors mentioned that construction and cost limitations, in addition to the performance of secondary design objectives, could hinder the selection of PT voided plates in the design of a multi-story concrete building. Furthermore, the study did not compare these floor systems to other low-carbon concrete floors identified in literature (RC two-way slab with beams and hollow-core slabs), again limiting the identification of the optimal low-carbon concrete floor system.

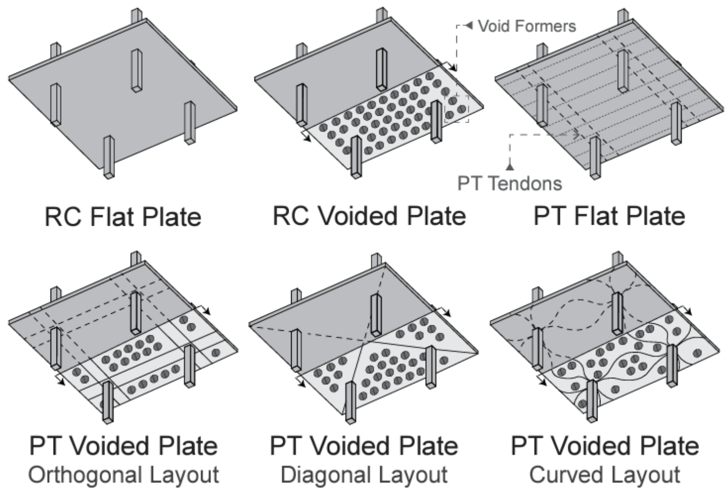

Fig. **2-2**: The six floor systems, including the three PT voided plates considered by Broyles & Hopper (taken from Fig. 4 in Broyles & Hopper, 2023).

A subtle, yet important observation is that many of the aforementioned studies evaluated the concrete floor systems for a limited sampling of floor geometries and structural design scenarios. This is an important point because the floor geometry (i.e., span length) and structural design scenarios (applied structural loads and concrete strengths) can result in a range of potential EC emissions for a single concrete floor system. Fig. **2-3** illustrates this point by showing how the structural design scenarios explored by Broyles and Hopper (2023) can vary the EC emissions from a range of 25 $kgCO_2e/m^2$ at a span of 6 m to over 75 $kgCO_2e/m^2$ at spans above 13.5 m for an RC flat plate. While the 3,280 different design scenarios assessed by Broyles and Hopper are a better sampling of design scenarios compared to other published studies, it pales in comparison to the nearly limitless amount of design scenarios possible in building design.

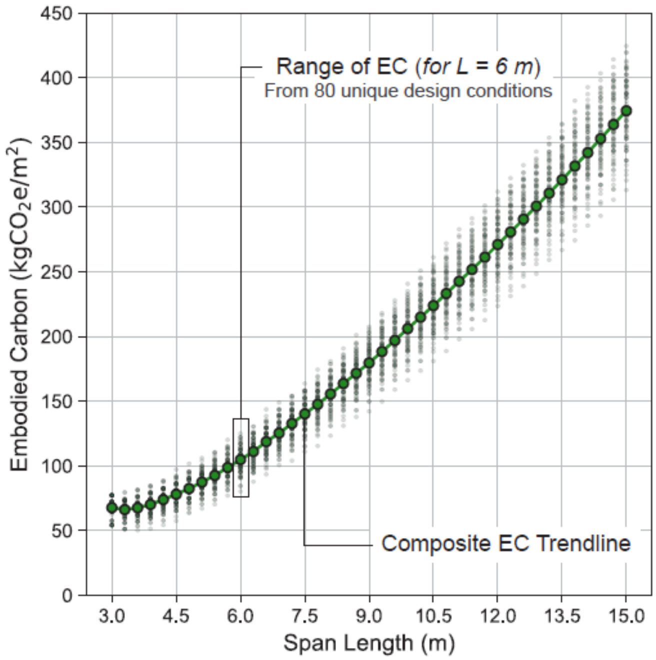

Figure **2-3**: The range of EC emissions for an RC flat plate (adapted from Fig. 7 in Broyles and Hopper, 2023).

A study by D'Amico and Pomponi (2020) also parametrically sampled possible structural design scenarios for RC, steel, and timber structural frames, including parameters such as span length (5.0 m to 8.5 m), floor height (3.5 to 4.0 m), uniform live load (1.5 kN/m^2 to 5.0 kN/m^2), and superimposed dead load (0.0 kN/m^2 to 0.6 kN/m^2) for a total of 10,460 design scenarios. One clear distinction between this work and the previous studies is that the primary objective is to find the structural systems with the least amount of structural weight (or mass quantities), which can serve as a proxy to EC. Yet an advantage of ascertaining the distribution of structural mass quantities (SMQs) is that these results are not subject to the same uncertainty that is inherent in the corresponding GWP of different concrete mixes. Therefore, as low-carbon concrete mixes become more widely manufactured, lower GWP values can be multiplied to the SMQs for a concrete system to obtain a more accurate EC estimate. The determination of a distribution of SMQs is certainly an effective method for evaluating the EC performance of concrete floor structures and consequent selection of a low-carbon system because it circumvents the complex distribution of environmental performance of concrete mixes. Yet as D'Amico and Pomponi mention as a limitation of their work, the distributions of concrete floor system SMQs found in the study are limited to only two systems: RC flat plates and RC ribbed (one-way) slabs.

Another aspect in the determination and selection of a low-carbon concrete floor system is that the amount of design knowledge of a structure changes across different phases of the design process. Furthermore, fixing design decisions early in the design process such as floor plan layout, structural material type, and building use (corresponding to structural loads) can restrict opportunities for the structural engineer to explore low-carbon design alternatives. On the other hand, architects and building designers may not know how early-stage design decisions influence the structural design of concrete floor systems and consequent EC emissions. While simulating thousands of different design scenarios can help inform the distribution of EC emissions for different concrete floor systems, training regression models, as was done by D'Amico and Pomponi (2020), can be used to derive equations to estimate the SMQs and EC performance of different concrete floor systems. However, more robust analytical models are needed to account for the subtle differences in SMQs influenced by different structural design parameters, as the linear and exponential regression models used by D'Amico and Pomponi may limit accurate estimates of SMQs. As mentioned previously, more concrete floor systems beyond an RC flat plate and RC one-way ribbed slab should be evaluated using this approach. Lastly, while analytical equations and robust models can be a strategy to better estimate the SMQs and EC of a concrete system, the employment of trained models as an interactive design tool can enable building practitioners to better understand how different design parameters influence the EC emissions of a concrete system – which is especially important when design parameters are not fixed. These analytical methods and tools can therefore inform designers on the selection of a low-carbon concrete floor system while evaluating many different systems and considering the bevy of possible design scenarios.

2.1.2 Consideration of additional floor design performance goals

Concrete floor systems are typically designed to satisfy structural design limit states as determined by building design codes (Seyedabadi et al., 2024). But structural performance is not the only building consideration that influences the design of a concrete floor. Indeed, secondary design performance goals including resistance to fire-resistance, vibration requirements, acoustic insulation, thermal insulation, construction scheduling considerations, the experience of the construction team, and the aesthetics can influence the geometric design of a concrete floor system (Orr et al., 2019). Although concrete floor systems typically perform well for objectives such as fire-resistance and vibrations, the need to meet secondary design goals may require geometric modifications to the concrete system, potentially influencing the EC emissions of the system, and further nuancing the selection of low-carbon concrete floor systems.

Referring back to Table **2-1**, seven studies explicitly mentioned if a secondary design objective was considered in the design of the concrete floor system and the corresponding assessment of carbon emissions. Of the seven studies, five (Broyles & Hopper, 2023; Jayasinghe et al., 2021a; Jayasinghe, et al., 2022a; Jayasinghe, et al., 2022b; Trinh et al., 2021) mentioned that fire-resistance performance was considered as a constraint in the design of the concrete floor structures, with three different fire ratings (1-hr, 1.5-hr, and 2-hr) evaluated across the five studies. These five studies used a prescriptive fire resistance rating method based on the floor thickness to satisfy the fire rating criterion. The remaining studies investigated how low-carbon structural design influenced thermal insulation (Lotteau et al., 2017) and human-induced walking vibration performance (Oh et al., 2019).

Concrete floor systems have favorable fire-resistance performance because concrete is inherently a non-flammable material, with a slow rate of heat transfer (Khoury, 2000). The results of experimental fire tests informed the prescriptive fire-resistance ratings defined in the International Building Code (IBC) which are a function of thickness and concrete mixture type (International Code Council, 2018). For example, a normal weight (i.e., silicious) concrete floor system will achieve a 2-hr fire rating if the floor system has a minimum thickness of ~125 mm (5 in). As a result, concrete floor systems designed for long span lengths and large structural loads are not typically governed by fire-resistance rating because the structural limit states control the thickness of the concrete floor design. However, both Jayasinghe et al. (2021, 2022a, 2022b) and Broyles and Hopper (2023) mention that the minimum slab thickness is governed by fire-resistance rating at short spans, suggesting that fire-resistance performance can vary the material-efficiency, and EC, of a concrete floor system.

Related to fire-resistance performance, concrete floors can aid heating and cooling load demands in a building because of their resistance to change temperature. Although heating and cooling loads are associated with OC emissions, the work by Lotteau et al. (2017) demonstrates how building engineers and designers can influence thermal performance through the efficient design of concrete systems in buildings. However, the ability to accurately evaluate the relationship between conventional concrete systems and thermal insulation is highly dependent on the geographical location and IEQ conditions (i.e., indoor temperature, moisture content) of the building (Shafigh et al., 2018), nuancing how the geometric design and material selection of a concrete floor improves thermal performance.

Due to their inherent mass density and stiffness, conventional concrete floor systems are not typically susceptible to human-induced vibration issues (Pavic, 2002). However, Oh et al. (2019) found that depending on the design scenario, and subsequent serviceability requirements, floor vibration criteria can affect the design of concrete floor systems. The authors evaluated optimal RC flat plate designs for minimized EC emissions and cost while subject to structural loads and walking vibration requirements typical of an office and residential building. In the case of the office building, an RC flat plate can be efficiently designed through the combination of different RC floor geometries and material properties to realize EC savings over 15% while satisfying vibration requirements. However, the consideration of walking vibrations in the residential building case resulted in an 8.9% EC increase compared to the same scenario without the vibration condition due to increased floor thickness to satisfy the vibration design criteria. This study contributes to the narrative that secondary design objectives can govern the design of concrete floor systems, restricting the identification of low-carbon solutions.

Air-borne acoustic insulation performance (e.g., speech, music), is similarly viewed as a favorable performance objective in the design of concrete floor systems (Ward & Randall, 1966; A. C. C. Warnock, 1985). Although a multi-objective study of air-borne sound insulation and EC has not been performed for conventional concrete floor systems, experimental reports provided by the National Research Council of Canada (A. C. C. Warnock & Birta, 2000), Concrete Reinforcing Steel Institute (2016), and the National Ready Mix Concrete Association (NRMCA, 2022) reveal that bare conventional concrete floor systems (namely RC flat plates) typically meet or exceed building code requirements for air-borne sound insulation. However, experimental studies addressing the air-borne acoustic insulation performance of more modern conventional concrete floor systems, like PT and voided plates, is a glaring research gap as few experimental findings have been published. It is worth noting that while bare concrete floor systems have favorable air-borne sound insulation, the systems perform poorly for structure-borne, or impact, sound insulation often requiring additional floor layers and acoustic treatments (Jeon et al., 2004; Kylliäinen et al., 2017; Stewart & Craik, 2000; A. Warnock, 1999).

As demonstrated by these studies, secondary objectives can control the design of a concrete floor and result in increased EC for a concrete system; however, the number of studies that include a secondary design objective in assessing the EC performance of a concrete floor system is limited. Furthermore, no study evaluated how the combination of multiple secondary design considerations influenced the EC of concrete systems. While design objectives such as cost, construction considerations, and thermal insulation are directly affected by the location and interior environment of a building, objectives including prescribed fire-resistance rating, floor vibrations, and acoustic performance can be more accurately estimated with knowing only the geometry and material characteristics of the concrete floor implying that a holistic multi-objective assessment of concrete floor systems is possible. Yet the exclusion of secondary design objectives complicates the estimation of EC and selection of a low-carbon concrete floor system, especially in the context that different design scenarios require different building performance criteria.

2.2 Low-carbon concrete floor structures at the component scale

2.2.1 Realization of high carbon reductions in novel concrete components

Over the last decade, advancements in construction technology, such as digital fabrication, and the application of optimization frameworks in the digital design of concrete structures, have enabled the realization of unconventional concrete floor forms and the potential for significant concrete material reduction. Certainly, the construction of unconventional concrete floor systems, like the isostatic floors of Pier Luigi Nervi, have been possible for many decades (Billington & Garlock, 2004); however, the economical limitations of the concrete material, shaped formwork, and labor costs limited the capability to mass produce optimized floor components until more recent advances in digital fabrication technologies (Menna et al., 2020; Mata-Falcón et al., 2022) enable the ability to mass produce custom components. This new capability, coupled with the urgency to determine low-carbon concrete systems, has inspired many innovative research studies focused on optimizing concrete floors at the component scale (i.e., single bay floor system). Table **2-2** summarizes recent research studies on optimizing the form of concrete floor components to minimize concrete material and EC emissions while withstanding structural loads and any secondary design objectives. Many conducted a computational design analysis before selecting a low-carbon concrete component which could be validated through fabrication and experimentation, indicating how mathematical optimization frameworks and other numerical design strategies can empower building designers and engineers to determine novel, material-efficient concrete floor forms (Turrin et al., 2011). Another observation is that all the studies evaluated the optimized floors at the A1 to A3 LCA stages, which considers the carbon emissions from material extraction, transportation to the production plant, and the manufacturing of the structural material. These stages have been to be the most carbon-intensive stages for concrete (Anderson & Moncaster, 2020).

Table **2-2**: Summary of the studies that evaluated the EC and EE of novel concrete floor components.

Source	**Concrete Floor Structure(s) Investigates**	**System Boundary and LCA Scope**	**Primary Design Objectives**	**Secondary Design Objectives**
López López et al. (2014)	Optimized[1] Funicular Floor	Component Scale; N/A	Minimize Material for Structural Limit States	N/A
Méndez Echenagucia et al. (2016)	Optimized Funicular Floor	Component Scale; N/A	Structure-borne Sound Insulation	N/A
Block et al. (2017)	Optimized Funicular Floor	Component Scale; N/A	Minimize Material for Structural Limit States	N/A
Roozen et al. (2018)	Optimized Funicular Floor	Component Scale; N/A	Air-borne Sound Insulation	N/A
Hawkins et al. (2020a)	Optimized Vaulted Floor and Conventional RC System (Flat Plate)	Component Scale; A1-A3	Minimize EE for Structural Limit States	N/A
Wu et al. (2020)	Optimized Funicular Floor	Component Scale; N/A	Human-Induced Floor Vibrations	N/A
Ismail and Mueller (2021)	Optimized (Shaped) RC One-Way Slabs and Conventional RC System (Flat Plate)	Component Scale; A1-A3	Minimize EE and Cost for Structural Limit States	N/A
Ranaudo et al. (2021)	Optimized Funicular Floor	Component Scale; A1-A3	Minimize EC for Structural Limit States	Fire-resistance Rating (not specified) and Acoustics (not specific)
Broyles et al. (2022c)	Optimized (Shaped) RC One-Way Slabs and Conventional RC System (Flat Plate)	Component Scale; A1-A3	Minimize EC for Structural Limit States	Air-borne Sound Insulation
Gascón Alvarez et al. (2022)	Optimized (Shaped) RC One-Way Slabs and Conventional RC System (Flat Plate)	Component Scale; A1-A3	Minimize EC for Structural Limit States	Thermal Performance / Building Operations
Broyles et al. (2022a)	Optimized (Shaped) RC One-Way Slabs and Conventional RC System (Flat Plate)	Component Scale; A1-A3	Minimize EC for Structural Limit States	Air-borne and Structure-borne Sound Insulation, Thermal Mass, and Thermal Transmittance
Mata Falcón et al. (2022)	Optimized Funicular Floor and Conventional RC Systems (Flat Plate,	Component Scale; A1-A3	Minimize EC for Structural Limit States	Fire-resistance Rating (0.5-hr only)

Source	Concrete Floor Structure(s) Investigates	System Boundary and LCA Scope	Primary Design Objectives	Secondary Design Objectives
	One-Way Slab, Two-Way Slab)			
Oval et al. (2023)	Optimized Valuated Floor and Conventional RC Systems (Flat Plate, Waffle Slab)	Component Scale; A1-A3	Minimize EC for Structural Limit States	N/A

[1] Optimization in this context refers to the shape and/or topology optimization of a concrete component and is not directly associated with conventional strategies that influence material efficiency (e.g., optimizing column grid).

Research on optimizing concrete floor components has primarily focused on three geometric forms: vaulted floors, funicular floors, and shaped-ribbed floors. With inspiration from historical masonry tile vaults such as the Guastavino tile floor system (Ochsendorf, 2010), vaulted concrete floors are materially-efficient because the concrete material acts almost entirely in compression with edge beams or tension rods applied at the supports of the floor. Funicular floors are an extension of vaulted floors. With a similar vaulted shape, funicular floors are stiffened with ribs to realize more material reduction despite increases in span length and structural load (Block, et al., 2017b). The underlying structural principle of these two systems is that the structural load is carried to the floor supports resulting in a thrust force that necessitates the inclusion of an edge beam or tension rod to maintain structural equilibrium. Vaulted and funicular concrete component forms can thus be realized through the mathematical optimization of the thrust force given specific geometric, material, and structural constraints (Block & Ochsendorf, 2007).

The studies conducted by the Block Research Group and associated researchers specifically apply this concept to funicular floors given various design scenarios to realize structural weight savings exceeding 70% compared to a conventional RC flat plate (Block, et al., 2017a; López López et al., 2014; Mata-Falcón et al., 2022; Ranaudo et al., 2021). Furthermore, their work has been constructed using digital fabrication technologies and implemented in the design of buildings resulting in large EC savings (Block, et al., 2017a; Meibodi et al., 2018). With the intention of incorporating optimized funicular concrete components in buildings to curb building related carbon emissions, more targeted studies were conducted to assess the performance of acoustic insulation, human-induced walking vibrations, and fire-resistance (Mata-Falcón et al., 2022; Mendez Echenagucia et al., 2016; Ranaudo et al., 2021; Roozen et al., 2018; Wu et al., 2020).

Achieving thin-shell, vaulted concrete forms with the intention of reducing concrete material has been well studied by Hawkins et al. (Hawkins, 2017; Hawkins et al., 2019, 2020). Enabled by the advancements in flexible formwork technologies and similar practices, low-carbon concrete vaulted forms can be fabricated (Curth et al., 2022; Hawkins et al., 2016), achieving EC emissions savings up to 58% compared to an equivalent RC flat plate (Hawkins et al., 2020). The ACORN project, which extends the work by Hawkins et al., demonstrates how greater carbon emission savings are possible through the design and fabrication of a vaulted concrete floor designed for disassembly (Oval et al., 2023). Vaulted concrete components can therefore be a low-carbon concrete floor solution; however, the corresponding implications of secondary design objectives have not been thoroughly evaluated.

A different strategy to realizing material-efficient concrete floor components is through the geometric manipulation of a ribbed concrete floor, specifically a one-way system. With the context that developing countries have less access to advanced digital fabrication technologies, alternative low-carbon floor system solutions are needed as developing countries are expected to experience larger population increases over the coming decades, resulting in increased building construction and urban environment growth (M. Ismail, 2019). Unlike vaulted and funicular forms, shaped ribbed floors can be designed assuming simple boundary conditions, without the need for tension rods, and are less limited by floor plans and column layouts. Ismail et al. (2021) demonstrated how the shaping of a ribbed beam can be optimized for material efficiency, resulting in shaped one-way floor systems with up to 64% EE savings compared to conventional RC flat plates (Ismail & Mueller, 2021). This work has served as an inspiration to the work conducted by Gascón Alvarez et al. (2022) and Broyles et al. (2022a; 2022c) to understand how optimized ribbed concrete components can be shaped to consider additional design objectives.

2.2.2 Balancing competing objectives in the design of concrete components

As discussed in Sec. 2.1.2, concrete floor systems actively participate in many secondary design performance objectives that influence the IEQ of a building, with conventional RC flat plates regarded as having favorable performance in many of these domains. But because of the reduction of concrete material and the novelty of nonconventional concrete floor components in building, further research on how these components fare when considering additional design objectives (i.e., acoustic insulation, floor vibrations, and thermal insulation) was required.

In the evaluation of optimal funicular concrete forms for secondary design considerations, Méndez Echenagucia et al. (2016) studied structure-borne sound transmission, Roozen et al. (2018) assessed air-borne sound transmission performance, and Wu et al. (2020) investigated the dynamic performance of the systems due to walking vibrations. In the paper by Méndez Echenagucia et al. (2016), the authors created a finite element model (FEM) for various concrete funicular floor forms with a single impact point to evaluate radiated structure-borne sound to find that optimizing the shape of the floor has the largest potential to influence impact sound radiation at low frequencies. Yet, the study limited the structure-borne acoustic assessment to frequencies below 200 Hz and noted that high frequency structure-borne sound performance could result in different optimal funicular concrete forms. Further, the exclusion of frequencies above 200 Hz prevented the funicular floors from being evaluated for a broad frequency impact sound insulation metric like Impact Insulation Class. Related, Roozen et al., (2018) experimentally evaluated the air-borne sound transmission of a fabricated funicular concrete floor using a mobility-based approach using a shaker. The authors used the experimental findings to obtain the transmission loss over a broad frequency range to ascertain an acoustic rating using the European metric, Sound Reduction Index. Yet unlike the study by Méndez Echenagucia et al. (2016), no numerical or optimization study was conducted, therefore limiting the knowledge on if the tested funicular floor form was the most favorable for air-borne acoustic insulation.

The study by Wu et al. (2020) presented a clearer design trade-off with the intention to minimize concrete material through optimizing the form of a concrete funicular floor. The researchers created a FEM of multiple concrete funicular floor forms to ascertain their dynamic response subject to walking vibrations. Then the FEM results were used to train a surrogate model to evaluate the dynamic performance of funicular forms that were not evaluated, thereby reducing computation time. Wu et al. found that approximately 70% of the funicular floor forms failed the walking vibration criteria when optimizing the floor shape for material efficiency; yet a 10% increase of concrete material improved the dynamic response up to 50%. More interesting, relocating the structural material of a funicular floor, or manipulating the form of a concrete floor component, can improve dynamic performance by 30-40%. This finding emphasizes how secondary design objectives have to be balanced with the primary goal of reducing concrete material in optimized concrete floors, but that the consideration of additional design objectives can result in floor designs with improved objective performance while minimizing material consumption.

On the assessment of shaped ribbed one-way concrete components, Gascón Alvarez et al. (2022) evaluated how manipulating the form of the ribbed floors improved thermal insulation to reduce OC emissions and material efficiency to reduce EC emissions. The researchers explored how geometrically shaping the concrete component alone could dramatically improve the thermal factor of the floor by a factor of 8 while achieving over 50% EC emissions savings compared to a conventional RC flat plate. Yet when optimizing for both objectives, the authors noted a design trade-off, as 52.5% EC savings were achievable with OC savings up to 14% while OC savings up to 32% were realized when EC savings were reduced to 30%. Broyles et al. (2022c) also noted a design trade-off when reducing concrete material in a floor component and achieving high air-borne sound transmission. Although the study limited the acoustic analytical model to a 45° angle of incidence, the results demonstrated that shaped ribbed concrete floor components can be optimized for improved air-borne sound insulation but at the expense of increasing concrete material. This was confirmed by the sensitivity analysis of optimizing for structural mass and air-borne sound insulation for different angles of incidence (Broyles, App. C, 2020). When considering the breadth of acoustic angles of incidence, Broyles et al. (2022a) showed that shaped ribbed floors can achieve code-minimum to high-performing air-borne sound insulation ratings by strategically shaping ribbed concrete floors. However, the authors noted that a direct trade-off exists between reducing EC and achieving high acoustic and thermal insulation, as both design considerations can be improved but at the expense of increasing material consumption and EC. Furthermore, the optimal design for each acoustic and thermal insulation differed in structural form, indicating the complexities of considering many building objectives in the design of an optimized concrete component.

These research studies demonstrate that while concrete floor components can be optimized to reduce substantial material reductions and EC savings, the loss of material can have adverse effects on other design objectives. Indeed, depending on the building design scenario, the secondary design goals can govern the shaping of a structural concrete component. However, the studies by Wu et al. (2020) and Broyles et al. (2022a) indicate that synergies between minimizing EC and considering the performance of secondary design goals are feasible. However, a comprehensive evaluation of multiple secondary design considerations with the primary goal of reducing EC through the shaping of a concrete component has been limited to Broyles et al. (2022c), and the authors noted that the work was a first step towards understanding how to balance the complex relationships. It is also noteworthy that although fire-resistance rating was considered in many studies of conventional concrete floor systems in Sec. 2.1.2, only two studies (Ranaudo et al., 2021, Mata Falcón et al., 2022) applied fire rating considerations as a constraint when assessing a funicular concrete floor. Therefore, there are many research opportunities when studying the complex building design trade-offs of concrete floor components, especially when progressing towards unconventional low-carbon concrete floor solutions in the built environment.

2.2.3 Acoustic insulation implications when reducing concrete material in floors

Of the many secondary design objectives that both conventional and nontraditional concrete systems affect, air-borne and structure-borne acoustic insulation is of particular interest because optimizing concrete floors can directly influence structural-acoustic characteristics including mass density, stiffness, and damping. For example, the acoustic principal Mass Law can reasonably predict the air-borne acoustic performance of a conventional floor component at a given frequency by simply knowing the mass density

(Long, 2005). However, Broyles et al. (2022c) demonstrated why mass density, stiffness, and damping must be considered because Mass Law severely overrated the air-borne acoustic insulation performance for certain floor shapes, especially those with low mass densities. Furthermore, a lack of sufficient sound isolation can worsen the IEQ in multi-story buildings, which is well-studied in literature showing the inadvertent health effects on occupants from neighbor noise (Jensen et al., 2018, 2019; Maschke, 2016; Mohamed et al., 2020; Rasmussen & Ekholm, 2019; Rindel, 2015). The ability to block unwanted noise from an adjacent floor is an important yet overlooked design consideration. Acoustic treatments applied after a building has been constructed often requires costly retrofits (Alonso et al., 2020). These reasons motivate why the inclusion of sound insulation as a design consideration is necessary in the selection of low-carbon concrete floor components and systems.

Sound transmission in buildings can be categorized by the acoustic medium in which the sound originates from: air- and structure-borne sound (Asakura et al., 2018). In the context of a building, air-borne sound is created from talking and music and is evaluated in the frequency range of speech, while structure-borne sound is generated from an impact on a structure, such as footfall and is evaluated in low and high frequency ranges (LoVerde & Dong, 2017a). Because floor systems attenuate both acoustic phenomena, the design of concrete floors must consider both air-borne and structure-borne sound to provide adequate acoustic insulation. In response to the need to consider air- and structure-borne sound transmission in the design of a building, building design codes are needed to define transmission loss performances of different structures. Specifically, the International Building Code (IBC) specifies minimum Sound Transmission Class and Impact Insulation Class ratings to quantify air-borne and structure-borne sound (Kihlman, 1970). Sound Transmission Class (STC) is a metric that provides a single scalar value for the air-borne sound transmission performance from the 125 Hz one-third octave (OTO) band to the 4 kHz OTO band. Similarly, Impact Insulation Class (IIC) is a metric that provides a single scalar value for the impact sound transmission performance from the 100 Hz OTO band to the 3.15 kHz OTO band. Knowledge of both STC and IIC ratings allows a designer to fully assess the acoustic insulation performance of a floor system and prevent any inadvertent consequences from poor building acoustics.

To determine the STC and IIC ratings of different structural components, the acoustic performance can be experimentally obtained or numerically estimated. Historically, the determination of acoustic transmission performance has been on the experimental side, especially when investigating the air-borne transmission performance of walls (Beranek, 1959; Sharp, 1978), but less experimental results have been published on the STC and IIC performance of floors (Dupree, 1980). One of the major limitations to experimentally determining the acoustic insulation performance of different building elements is that the experimental methods to ascertain acoustic insulation performance have been debated for decades, especially regarding the testing for impact sound (Girdhar et al., 2021; Girdhar & Barnard, 2020; Pereira et al., 2014; Zeitler et al., 2013). A second important limitation is that significant lab-to-lab differences in STC and IIC ratings have been observed, complicating the certainty of acoustic performance of different building elements (Dijckmans & Vermeir, 2013; Pedro Carvalho, 2006; Yadav et al., 2019). While improvements have been made on the reproducibility of experimental methods (Dong et al., 2021; Girdhar et al., 2023b), the STC and IIC ratings can still vary significantly, as suggested in a recent acoustic report by the NRMCA (2022) that provided ranges of ratings for STC and IIC for each floor structure. Because of the uncertainties in experimentation methodologies and laboratory environment, in addition to the cost to fabricate different floor systems and perform the experiment, numerical models are an alternative strategy to estimate acoustic insulation.

Numerical methods for determining the sound transmission of structures have been derived from the classic mathematical wave equation. For example, the infinite panel theory can be simplified to approximate the air-borne sound transmission of structural elements to obtain an STC rating. The use of FEMs is another numerical strategy to determine sound insulation. The air-hemisphere and Raleigh integral methods are among the most common acoustic methods for modeling impact sound performance using an FEM (Conta et al., 2020), which can simulate the radiated sound performance caused by impacts acting on a structure. An analytical IIC rating can be obtained using these methods, yet one important limitation is that the computational resources required to simulate a broad frequency range for impact sound is significant (Howard & Cazzolato, 2014). Depending on the capabilities of the computer, a single acoustic simulation can require over 100 GB of RAM and last for many hours, potentially multiple days (Howard & Cazzolato, 2014). As a result, many studies that have numerically assessed impact sound insulation of concrete floors only consider a few low-frequency OTO bands (Cho, 2013; Mendez Echenagucia et al., 2016). Yet this limits the holistic assessment of floor systems, especially innovative concrete floor components, because concrete floors commonly have impact sound deficiencies at both low and high frequencies, indicating the need for other simulation methods to better estimate impact sound performance.

An additional challenge when considering the acoustic insulation performance of floor components are the acoustic metrics used to rate them. Both STC and IIC provide a single integer rating that enables easy comparisons of structural systems side-by-side. Yet researchers have questioned if STC and IIC are sufficient for accurately quantifying the acoustic transmission performance of a structure (LoVerde & Dong, 2017a). For example, a designer may mistakenly assume that a structure that meets minimum STC and IIC rating requirements is acoustically satisfactory, yet due to the functional limitations of STC and IIC, the structure may prove to be acoustically insufficient once constructed, resulting in a poor design. The functional limitations, including the low frequency limit of STC and IIC (Langfeldt et al., 2020; LoVerde & Dong, 2018; LoVerde & Dong, 2017b; Maluski & Gibbs, 2016; Müller-Trapet et al., 2020) and the 8-dB rule (Dong, 2020), have been demonstrated to influence the acoustic rating of concrete floor components when STC was applied in an optimization framework (Broyles et al., 2021). The authors noted that the functional limitations of STC complicates the knowledge of the ground truth acoustic insulation performance of optimized concrete components, with inflated STC ratings awarded to floor components with a coincidence dip below the STC low frequency threshold. This result further complicates the consideration of acoustic insulation in the design of progressive, low-carbon concrete floor systems (as well as conventional building elements), prompting the development of modified metrics.

2.3 Synergizing literature to identify research gaps and formulate questions

The findings of the studies in Sec. 2.1.1 provide some clarity on which concrete floor systems are sustainable for certain structural scenarios. However, the bevy of possible structural design scenarios coupled with the limited research that evaluated the nuances of balancing secondary design objectives with the goal of reducing EC emissions presented in Sec. 2.1.2, indicates that more research is needed to better inform building engineers and designers towards the selection of low-carbon concrete floor systems. Significant concrete material reduction is achievable for structurally optimized concrete components, potentially making them a more sustainable concrete floor solution compared to existing concrete systems. Yet a common thread in the studies discussed in Sec. 2.2.1 is that the material reduction and carbon emission savings can influence the secondary design objectives of a floor. Sec. 2.2.2 details how air-borne and structure-borne sound insulation, human-induced floor vibrations, and thermal insulation can all be adversely affected when neglected in the design of an optimized concrete component. Although many secondary design goals can affect life-safety and the comfortability of building tenants, Sec. 2.2.3 discusses why the acoustic insulation of floors cannot be overlooked in the realization of material-efficient concrete floors as the structural-acoustic characteristics that influence sound transmission can be significantly influenced by the geometric gorm of a concrete floor. Furthermore, the complexities of accurately modeling structure-borne sound transmission and the inherent limitations of existing acoustic metrics to quantify sound transmission into a single objective suggest that there are many opportunities to further the knowledge in the building acoustic domain, especially when evaluating unconventional concrete floor shapes.

Table **2-3** provides a summary of the motivations, relevant findings, and existing gaps to the research discussed in this literature review. Research questions are formulated to directly respond to the gaps identified.

Table **2-3**: Research motivations, relevant results, gaps, and questions addressed in this dissertation.

Motivation	**Literature Review**	**Gap**	**Question(s)**
- The selection of a low-carbon concrete floor system can vary based on the structural design scenario. - There are a wide variety of material-efficient (low-carbon) conventional concrete floor systems. - There is a broad distribution of GWPs for concrete mixtures at different strength classes. - The largest potential to reduce EC is in the earliest design phases.	- Broyles and Hopper (2023) found ranges of EC when varying design parameters, which was also found by D'Amico and Pomponi (2020) for SMQs. - Jayasinghe et al. (2021a) found that RC two-way slabs with beams and hollow-core slabs have the least EC. PT voided plates are also a viable low-carbon solution (Broyles & Hopper, 2023). - D'Amico and Pomponi (2020) derived SMQ equations knowing that concrete mixtures have GWP uncertainty. - The SMQ equations enable quick EC estimates for concrete floors (D'Amico & Pomponi, 2020).	-A design strategy to better inform the selection of a (low-carbon concrete floor system considering the bevy of possible structural design scenarios… - …that investigates many conventional concrete floor systems… - …while considering the uncertainty of the GWP of concrete mixtures at various strengths… - …with the knowledge applicable to aid floor system selection in early-design phases.	What are the EC emissions of concrete floor systems when varying structural design parameters, such as span length, concrete compressive strength, applied loads, and deflection limits? …and… How can building designers identify the most material-efficient (low-carbon) concrete floor system at the early design stages given the breadth of possible design scenarios, variety of concrete floor systems, and the uncertainty of carbon emissions associated with different concrete mixtures?
- The selection of a material-efficient (low-carbon) concrete floor system can be influenced by secondary design objectives. - Optimal conventional concrete floor systems may require additional material (EC) to satisfy other building requirements.	- Walking vibrations (Oh et al., 2019) and fire-resistance rating (Jayasinghe et al., 2021a, 2022a, 2022b; Broyles & Hopper, 2023) have been shown to influence the EC of floor systems. - Oh et al. (2019) found that additional concrete material (EC) was needed to satisfy vibration requirements.	- Design knowledge on how secondary design considerations influence the EC of conventional concrete systems… - …such as if additional concrete material is needed to meet the secondary design goals…	What concrete floor system(s) is the most material-efficient (lowest EC emissions) when considering both structural performance and secondary design requirements for floors, including fire-resistance, air-borne sound insulation, and walking vibrations?

Motivation	Literature Review	Gap	Question(s)
- Conventional RC flat plates perform favorably for secondary design objectives, yet the performance of other conventional systems has been less studied.	- RC flat plates have high fire-resistance ratings, acoustic insulation, or less susceptible to vibration problems (Warnock, 1985; Khoury, 2000).	- …is needed to determine the optimal conventional concrete floor systems.	
- Shape ribbed concrete components can achieve higher material reductions than conventional concrete floors. - Experimental testing of shaped ribbed concrete components has been limited to the structural and thermal domains. - The dynamic response of concrete floor components can be adversely affected by the shape (form) of the component.	- Ismail & Mueller (2021) demonstrate EE savings up to 64% compared to RC flat plates. Ismail & Mueller (2021) and extended through Gascón Alvarez et al. (2022) fabricated and tested scaled shaped ribbed concrete components. Wu et al. (2020) found that 70% of funicular concrete forms had unacceptable dynamic response performance.	- Research on shaped ribbed concrete floor components… - …that are fabricated and tested for design objectives such as dynamic response… - …is needed to validate numerical models to determine if the shapes (forms) can have adverse effects on building design objectives.	What is the experimentally-obtained dynamic response of fabricated, quarter-scaled shaped ribbed concrete slabs, and can these results be used to tune numerical models for each slab?
- Structure-borne sound insulation can be influenced by the shape (form) of a concrete floor component. - Concrete floors without any material layers can have poor structure-borne performances at low and high frequencies.	- Méndez Echenagucia et al. (2016) found that optimizing the form of a funicular concrete floor improved low frequency impact sound insulation. - Bare concrete floors have deficiencies at low and high frequencies (CRSI, 2016). Yet simulating low and high frequencies using conventional methods is computationally expensive.	- A method that investigates the structure-borne sound insulation of shaped ribbed concrete floors… - …while adequately simulating impact sound insulation performance at both low and high frequencies…	How can a numerical method adequately estimate the full frequency (including both low and high frequencies) impact sound insulation performance of non-traditional concrete slabs while reducing the required computational resources?

Motivation	Literature Review	Gap	Question(s)
- The computational resources to numerically approximate the radiated sound power using conventional methods (i.e., air-hemisphere method) is extensive.	- Simulating large FEMs require significant computer memory and can have long CPU time, limiting the exploration of many design forms (Wu et al., 2020).	- …while minimizing computational resources to enable adequate design space exploration of different forms and implementation in optimization frameworks.	
- North American sound transmission metrics have existing methodological limitations. - The application of North American sound transmission metrics can be taken advantage of in optimization frameworks.	- The inclusion of the 8-dB rule (Dong, 2020) and the exclusion of low frequency OTO bands limits the rating of acoustic insulation of floors (LoVerde & Dong, 2018). - Broyles et al. (2020) found that the shaped floors with a coincidence frequency outside of the 125 Hz OTO band inflated the STC rating.	- Alternative sound transmission metrics without the limitations of the existing North American metrics are needed to accurately rate floor structures… - …and prevent inflated acoustic ratings when incorporated in design space exploration and optimization frameworks.	How can modifications to the existing acoustic transmission metrics correct the functional limitations of the metrics to improve the acoustic rating of floors in computational design frameworks?
- Research on the optimization of multiple secondary design objectives (especially acoustic insulation) with the intent to minimize material (or EC) of optimized concrete components is in its infancy. - The optimal concrete component form may be influenced by the geometric, structural, and design objectives specified.	- The consideration of multiple secondary design objectives and minimizing EC has only been preliminary explored by Broyles et al. (2022c) and did not include objectives such as fire-resistance rating. - The structural design scenario may influence the optimal form of a concrete component and corresponding carbon emission savings (Ismail & Mueller, 2021).	- Research on the knowledge of how multiple secondary design considerations and minimizing EC can be balanced in the design of optimal concrete components… - …when varying the structural design parameters such as span length, structural loads, and concrete strength.	How does the implementation of a computationally-efficient method to simulate impact sound insulation and the incorporation of modified acoustic transmission metrics influence the selection of a low-carbon concrete slab, and how do the best performing shaped concrete slabs compare to an equivalent conventional system?

Table **2-3** provides seven research questions which are listed below for readability:

A) What are the EC emissions of concrete floor systems when varying structural design parameters, such as span length, concrete compressive strength, applied loads, and deflection limits?

B) How can building designers identify the most material-efficient (low-carbon) concrete floor system at the early design stages given the breadth of possible design scenarios, variety of concrete floor systems, and the uncertainty of carbon emissions associated with different concrete mixtures?

C) What concrete floor system(s) is the most material-efficient (lowest EC emissions) when considering both structural performance and secondary design requirements for floors, including fire-resistance, air-borne sound insulation, and walking vibrations?

D) What is the experimentally-obtained dynamic response of fabricated, quarter-scaled shaped ribbed concrete slabs, and can these results be used to tune numerical models for each slab?

E) How can a numerical method adequately estimate the full frequency (including both low and high frequencies) impact sound insulation performance of non-traditional concrete slabs while reducing the required computational resources?

F) How can modifications to the existing acoustic transmission metrics correct the functional limitations of the metrics to improve the acoustic rating of floors in computational design frameworks?

G) How does the implementation of a computationally-efficient method to simulate impact sound insulation and the incorporation of modified acoustic transmission metrics influence the selection of a low-carbon concrete slab, and how do the best performing shaped concrete slabs compare to an equivalent conventional system?

Questions A, B, and C focus on the need to derive new analytical models and further the design knowledge to better inform the selection of the most material-efficient (low-carbon) concrete floor at the building system scale while considering structural and other building design objectives (see Fig. **2-4**). Questions D and E concentrate on the need to determine the dynamic response and impact sound performance of shaped ribbed concrete floors through experimentation and the need to determine a computationally-efficient numerical method for approximating structure-borne sound insulation (see Fig. **2-5**). Question F proposes three alternative acoustic transmission metrics that addresses the methodological limitations of the existing metrics to improve the rating and application of acoustic insulation metrics in design space exploration and optimization frameworks. Lastly, Question G incorporates the methodologies, metrics, and results from the studies corresponding to Questions A, C, E, and F to thoroughly evaluate the shaped ribbed concrete floor design space for minimizing EC and maximizing sound insulation given different structural design scenarios. The remaining chapters of this dissertation are as follows: Ch. 3 addresses Questions A and B while the remaining chapters (Ch. 4 to Ch. 8) address Questions C to G, followed by a summary of conclusions in Ch. 9.

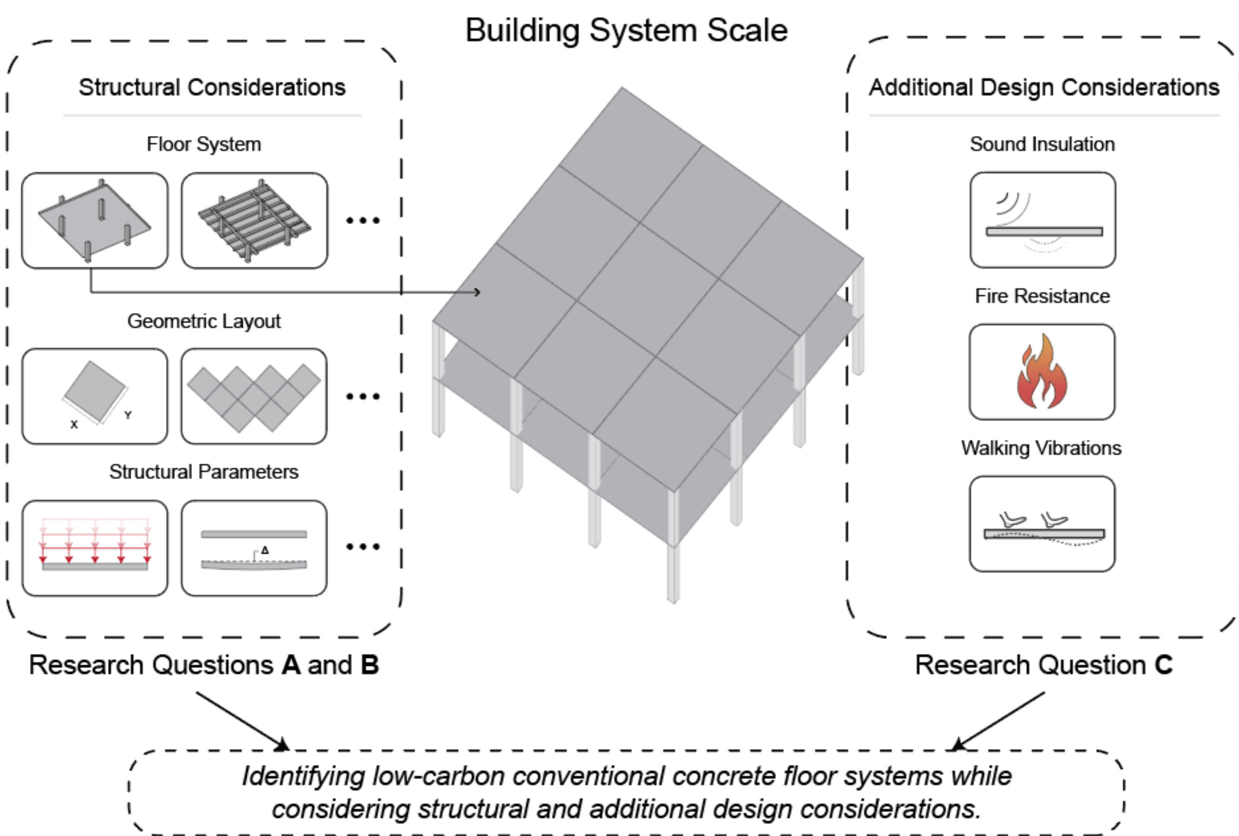

Figure **2-4**: Relationship between research questions A to C to guide designers towards low-carbon concrete floors.

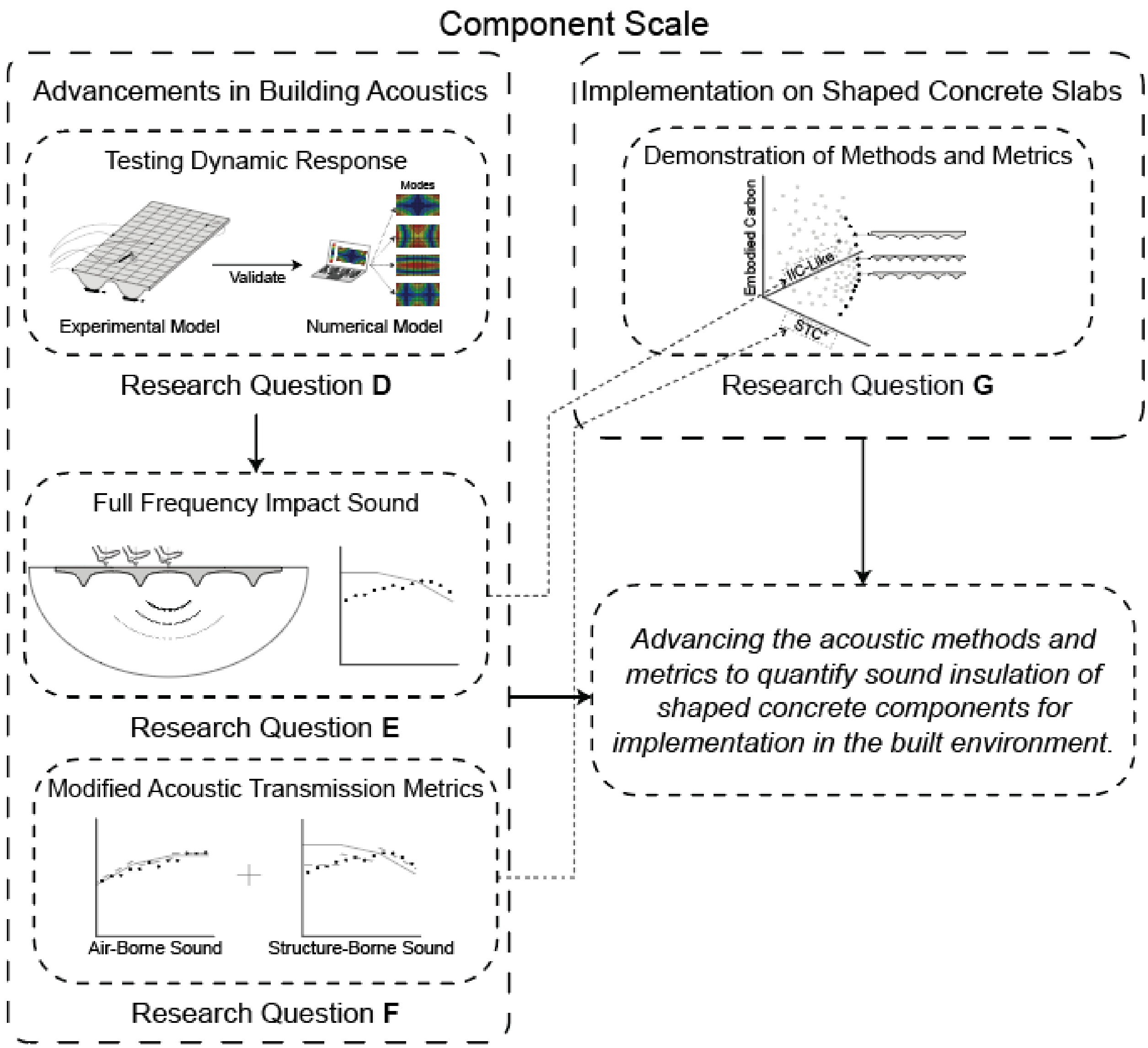

Figure **2-5**: Relationship between research questions D to G to advance the acoustic design of shaped concrete slabs.

The methodologies, metrics, and findings of these studies contribute to three broad research directions: 1) design guidance for selecting low-carbon concrete floor systems to further the efforts of reducing EC in buildings, 2) simulating impact sound and enhancing the metrics to quantify sound insulation to better understand the acoustic performance of non-traditional concrete floor components, and 3) demonstrate that optimized concrete components (e.g., shaped ribbed slabs) can be designed with less EC with favorable acoustic insulation in comparison to conventional systems.

Part II:

BUILDING SYSTEM SCALE

Chapter 3

Early-stage EC equations for concrete floor systems[1]

3.1 Introduction

The Architectural-Engineering-Construction sector contributes between 35% to 40% of global carbon emissions (De Wolf et al., 2017; WBCSD and ARUP, 2021). To mitigate the effects of climate change, reducing the carbon footprint of the built environment is essential (United Nations, 2015). While the carbon emissions related to building operations have seen notable reductions over several decades, research on embodied carbon (EC) reduction has only been more recently studied (Chen & Ng, 2016), with national and international organizations setting targets of 40% EC reductions by 2030 (WBCSD and ARUP, 2021) and net-zero EC buildings by 2050 (WGBC, 2019).

Due to the significant amount of concrete material used in buildings in comparison to the consumption of other construction materials, concrete structures are amongst the worst performing building systems regarding their global warming potential (GWP). Horizontal spanning concrete elements (i.e., floors) contribute approximately half of the EC to those project types (Huberman et al., 2015), more than any other common concrete structures in multi-story buildings. The high EC contribution is primarily resulting from concrete production, in relation to greenhouse gas emissions (Barcelo et al., 2014; Hasanbeigi et al., 2012), and the large quantity of concrete material used in the design of concrete structures. This corresponds to the cradle-to-gate (A1-A3) life cycle assessment (LCA) stages, which are the most carbon-influential stages for concrete structures (Anderson & Moncaster, 2021; Davies et al., 2015). Eq. **3-1** is used to calculate the EC for the A1-A3 stages, where GWP is a multiplier relating the GWP (in $kgCO_2e$ per declared unit) for a structural material, i, and MQ, which is the quantity for a given structural material;

---

[1] Chapter 3 is adapted from the published work by Broyles et al. "Equations for early-stage design embodied carbon estimation for concrete floors of varying loading and strength." (2024). *Engineering Structures*, 301, 117369.

$$EC_{A1-A3} = \sum_i GWP_i \times MQ_i. \qquad \text{(Equation } \mathbf{3\text{-}1}\text{)}$$

Equation **3-1** shows that there are two ways to reduce the EC of a structure: improving material quality (low-carbon) and reducing material quantity. Recent research has shown that these two strategies, with different variations, can meaningfully reduce EC (Danatzko & Sezen, 2011; Fang et al., 2023b; Malmqvist et al., 2018; Minunno et al., 2021). Strategies to improve material quality include computational frameworks to optimize the material design of concrete mixtures to minimize carbon emissions (DeRousseau et al., 2018; Helsel et al., 2022; Imbabi et al., 2012; Knight, 2023; Nukah et al., 2022; Tošić et al., 2015). Structural design optimization strategies implemented to reduce material demand have successfully reduced unneeded concrete material in structures (Hawkins et al., 2020; Ismail & Mueller, 2021; Leschok et al., 2018; Oval et al., 2023).

3.1.1 Engineering strategies to reduce embodied carbon emissions

Several approaches have been effective at reducing the carbon footprint of concrete mixtures, including the substitution of portland cement clinker with clinker-based cement alternatives and including supplementary cementitious materials (SCMs) that have lower carbon footprints (Althoey et al., 2023; Miller et al., 2018; Shah et al., 2022). Other researchers have employed statistical models, machine learning algorithms, and similar strategies to identify sustainable concrete mixtures using different SCMs while achieving different strength classes (DeRousseau et al., 2018, 2021; Hafez et al., 2023; Liu et al., 2023; Miller et al., 2016). Low strength concrete mixtures, which have smaller quantities of clinker compared to high strength mixtures, is another approach to improve the EC footprint of concrete (Thilakarathna et al., 2020; Wu et al., 2022), suggesting that a building designer must consider if the concrete MQ savings is worth the higher GWP when using a high strength concrete mix.

Optimizing the structural design of concrete structures is another well-researched strategy as case studies on reinforced concrete (RC) beams (Ismail et al., 2021; Jayasinghe et al., 2021b; Yeo & Gabbai, 2011), floors (Hawkins et al., 2020; Ismail & Mueller, 2021; Leschok et al., 2018; Oval et al., 2023), and structural frames (Foraboschi et al., 2014), suggested EC savings upwards of 70% compared to conventional RC structures. Optimized floors have been the topic of many studies, as Foraboschi et al. (2014) found that the floor system was the most critical component in reducing the EC of a building, which was validated by a study of multi-story RC buildings (Huberman et al., 2015). Although geometric optimization of a floor system can result in significant concrete MQ savings, conventional concrete systems can often be efficiently designed to reduce structural material quantities (SMQs) compared to alternatives and are more immediately constructable (Gan et al., 2017; Jayasinghe et al., 2021a; Lee et al., 2020), including post-tensioned (PT) voided plates, which were found to have EC savings up to 51% compared to conventional flat slabs (Broyles & Hopper, 2023). Furthermore, the reduction of concrete material in the floor system has a compounding effect on the dead load of the superstructure, which can consequently reduce the SMQs and EC of the columns and foundations (Feickert & Mueller, 2023).

3.1.2 Challenges when reducing embodied carbon emissions

These two pathways to reducing the EC are promising, yet there are several key challenges which make it difficult to widely utilize them across structural engineering practice. These include:

1. A lack of specification of "low-CO_2" concrete mixtures. Historically, "low-CO_2" concrete mixtures are not widely manufactured, have higher costs, and are consequently less desired by building clients (World Economic Forum, 2023; Imbabi et al., 2012; Liew et al., 2017; Roy, 1999). Also, an engineer may not know the variety of concrete mixtures available, potentially missing opportunities to reduce EC without sacrificing strength.
2. Design and construction limitations (e.g., material challenges, knowledge of novel concrete forms) with structurally-optimized concrete floors (Erdogan et al., 2019; Menna et al., 2020; Wangler et al., 2019). Contractors and manufacturers have to significantly invest in construction technology to fabricate optimized systems (Caulfield, 2022).
3. The greatest design flexibility (and largest EC reduction potential) is early in the design process (Dunant et al., 2021; Fang et al., 2023b). Yet because of the many thousands of design scenarios,

comprehensive early-stage design exploration aimed at reducing carbon emissions is limited for engineers.

4. A comprehensive study that establishes EC benchmarks for various concrete floor systems under different design scenarios has not been conducted, making it difficult to fairly compare different concrete systems, and to compare with optimized concrete systems.

The first two issues may be resolved over time with advances in the production of alternative concrete mixtures with "low-CO_2" footprints and progressive construction techniques, with structural concrete code adaptations also catalyzing some advancements. However, solutions to the latter two issues can be better addressed with a comprehensive study of EC relationships to derive EC equations suited for early-stage design. Specifically, this study addresses the following two research questions:

1) What are the EC emissions of concrete floor systems when varying structural design parameters, such as span length, concrete compressive strength, applied loads, and deflection limits?
2) How can building designers identify the most material-efficient (low-carbon) concrete floor system at the early design stages given the breadth of possible design scenarios, variety of concrete floor systems, and the uncertainty of carbon emissions associated with different concrete mixtures?

This chapter responds to these questions by first evaluating ten different concrete floor systems for a bevy of different design parameters and then deriving analytical models for materially-efficient concrete floors using polynomial regression models tailored to the decisions known at the two early design phases. These models can equip structural engineers to make more sustainable design decisions. The scope of this chapter is thus to simulate structural analyses appropriate at the early design phases to show how design decisions influence both the EC and structural performance of concrete floors.

3.2 Background

3.2.1 Early-stage design decisions and their influence on embodied carbon

While minimizing the EC of a building, the conceptual and schematic design phases provide the most design flexibility to modify building geometry, material selection, and structural system. As Fig. **3-1** shows, the limited design knowledge (D'Amico & Pomponi, 2020) of the structure restricts opportunities for large EC reductions in the early design stages (Kanyilmaz et al., 2023). Moreover, as global building decisions may not be defined, strategies to pursue EC reductions can be fraught with uncertainty. For example, design parameters such as applied loads and material strength may not be known until later in the design process, potentially preventing meaningful EC reduction (Hawkins et al., 2021). Additionally, as the design process evolves from the conceptual to the schematic phase, decisions made in the conceptual phase can directly influence (or limit) decisions made during schematic design. Furthermore, the plethora of design scenarios each encompasses assumptions that may not be uniform across all scenarios, restricting comprehensive design exploration and comparison. Different structural systems have varying amounts of SMQs and assumptions, further complicating early-stage design exploration (Eleftheriadis et al., 2018; Jayasinghe et al., 2022; Kanyilmaz et al., 2023; Trinh et al., 2021). For concrete structures, the GWP of different strength classes varies significantly depending on the mix design, implying uncertainty even if the SMQs are known (DeRousseau et al., 2020).

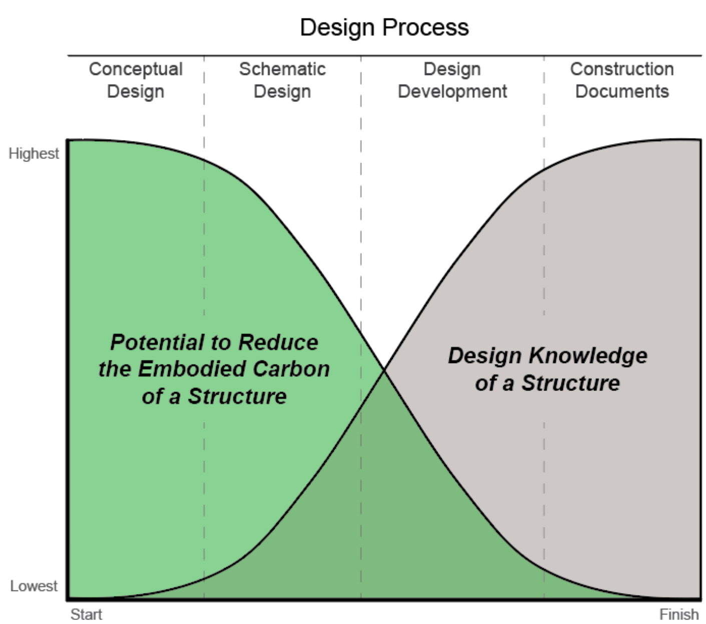

Figure **3-1**: Relationship between reducing the EC of a structure to the design knowledge of a structure during the design process. Image adapted and modified from Mueller (2014) and Paulson (1976).

3.2.2 Embodied carbon uncertainty due to variability of design parameters

Given the importance of early design decisions, several researchers have successfully employed conceptual frameworks for early-stage design exploration with the aim of reducing EC for concrete systems (Hawkins et al., 2020; Ismail & Mueller, 2021), steel structures (D'Amico & Pomponi, 2018; He et al., 2022), tall buildings composed of conventional construction materials (Helal et al., 2020, 2023) and mass timber (Hens et al., 2021). An important limitation across the studies is that only a limited number of design scenarios (one to three) are considered, yet there are a multitude of design scenarios in practice. Table **3-1** summarizes design decisions typically made in the conceptual and schematic design phases and how they could affect the design of a building structural system. While these variables can also affect other building systems, the emphasis here is on structural implications.

Table **3-1**: Early-stage design decisions and their corresponding influence on a structural concrete system.

Conceptual Design Phase		**Schematic Design Phase**	
Design Decision	**Corresponding Structural Design Variable**	**Design Decision**	**Corresponding Structural Design Variable**
Building Type	Live Load (range), Deflection	Superimposed Loads (e.g., mechanical equipment, additional floor layers)	Dead Load
Global Building Geometry (i.e., floor area, bay lengths, number of stories)	Area, Span Length, Building Height	Secondary Floor Considerations	Fire Rating
Structural System	Floor System, Main Structural Material	Structural Material Strength / Mix	Specified Concrete Strength, Mix Design, Cement Manufacturer

The structural design of concrete floors is directly affected by the structural parameters specified in a design scenario (Orr et al., 2019). For example, larger applied loads equate to higher design forces, resulting in thicker concrete slabs, greater concrete MQ, and larger EC. Because of the breadth of design scenarios, a single structural system may have a wide EC range based on the structural design parameters (Hawkins et al., 2021). The structural design parameters are often determined based on the use of the building. Table **3-2** summarizes live load ranges for five common building types, which are similarly labeled in a study by Simonen et al. (2017). While all building types must consider secondary design requirements such as minimum fire rating, certain building types have more stringent requirements. In some cases, the secondary design condition may control the structural design, however those considerations are beyond the scope of this study.

Table **3-2**: Common building types and their affiliated live loads as specified by ASCE 7-16 Table 4.3-1 (American Society of Civil Engineers, 2016).

Building Type	**L_0[1] Range in kN/m^2 (psf)**	**Additional Building Type Considerations**
Hospital / Health Care	1.92 – 3.83 (40 – 80)	Deflection, Vibrations
Office	2.40 – 4.79 (50 – 100)	Fire Rating
Public Assembly[2]	2.87 – 7.18 (60 – 150)	Fire Rating, Vibrations
Residential[3]	1.92 – 4.79 (40 – 100)	Sound Insulation
Educational / School	1.92 – 4.79 (40 – 100)	Fire Rating

[1] L_0: Unreduced uniform live load, as specified in ASCE 7 Sec. 4. Note that live load reductions are permitted for some building types but are not considered in the present study.

[2] Examples of public assemblies include stadiums, libraries, lobbies, and stage floors.

[3] Attics were not considered in the provided L_0 range. Considers both single- and multi-family residences.

Due to the range of structural parameters, a fair LCA comparison between structures requires functional equivalence, meaning that the design scenario must be the same, not just that the structures satisfy all strength and serviceability checks (Lützkendorf, 2020). Aside from the inherent epistemic uncertainty of structural design parameters, there is significant variability in the GWP of a concrete mix, suggesting that there is a probabilistic distribution of EC for a concrete structure (DeRousseau et al., 2020). These challenges have limited the understanding of EC savings when comparing conventional structural systems (Pan & Teng, 2021; Pomponi & Moncaster, 2018).

3.2.3 Analytical models for estimating embodied carbon during early design

If trained with data from many fully engineered designed scenarios, analytical regression models can help practitioners obtain an accurate prediction of EC while accounting for the variability in building design. Several researchers have derived analytical models to predict the carbon footprint of buildings (Fenton et al., 2023). This has been done for the residential housing sector (Cang et al., 2020; Gardezi et al., 2016; Teng & Pan, 2020) using simulated EC data, and for commercial buildings (Victoria & Perera, 2018) using existing office building data in the UK. Similar studies (Gan et al., 2017; Helal et al., 2023) also employed regression analyses to better understand how design decisions affect EC for high-rise buildings, with Helal et al. (2023) developing a tool based on their regression models. While these studies guide practitioners towards more sustainable designs at the building scale, they do not yet incorporate structural parameters including the strength of materials and applied structural loads, which are a source of variability and can affect the results.

Fewer studies have evaluated the variability at the building element and material scales. In a study that investigated wall constructions, Božiček et al. (2021), developed an analytical method for interpreting potential environmental impacts, while considering alternative wall designs in order to enable sustainable design decision making. Kang et al. (2015) used statistical models to find distributions of GWPs for various building construction materials to better inform environmental design decisions. D'Amico and Pomponi (2020) derived analytical models based on simulated structural mass quantities corresponding to the structural design of gravity systems composed of RC, steel, and mass timber. Span and applied loads were parametrically varied; however, concrete strengths and deflection limits were not. This significant study provided analytical equations to predict the EC of the structural systems that could be immediately incorporated in design practice. However, the assessment of concrete structures was limited to an RC flat plate and an RC one-way slab, noting that other concrete floor systems exist that have lower SMQs.

3.2.4 Chapter scope

Motivated by the challenges to reduce EC in early-stage design, this chapter elucidates key relationships in the structural design and environmental impact of ten conventional concrete floor systems (six RC floor systems and four PT floor systems) for use in the conceptual and schematic design phases. In the conceptual design phase, a univariate polynomial regression model fits averaged EC trendlines for each floor system, using the median GWP value corresponding to specific concrete compressive strengths (20.7 MPa to 41.4 MPa). This straightforward model enables building practitioners to quickly estimate and compare the EC of concrete floor systems. For the schematic design phase, an estimate of floor MQ (concrete slab volume) is calculated using a multivariable polynomial regression model based on span length and structural design parameters (concrete strength, live load, dead load, and deflection limit). The estimated concrete MQ is multiplied by the range of concrete mix GWPs and added to the estimated EC contribution of the other structural materials comprising the floor system, demonstrating that there is a probabilistic distribution of total EC. This method enables practitioners to tune the EC estimate of a floor system based on the design scenario and structural parameters known in the schematic design phase. To help designers apply the equations and visualize the results, a website application was developed.

3.3 Methods

This study analyzed ten concrete floor systems under many design scenarios to ascertain their SMQs and EC. The structural design was conducted to determine the floor design with the least amount of concrete MQ, while adhering to the American Concrete Institute (ACI) 318 structural code (ACI Committee 318, 2019). Then a database of Environmental Product Declarations (EPDs) was used to provide average values, median values, and distributions of GWPs corresponding to commonly specified concrete strength classes. After obtaining the SMQs for every unique design scenario for each floor system, EC equations were derived for the conceptual and schematic design phases.

3.3.1 Concrete floor systems

The floor systems considered are (as shown in Fig. **3-2**):

1. RC flat plate,
2. RC flat slab (i.e., a flat plate with drop panels),
3. RC one-way pan joist slab with beams,
4. RC two-way slab with beams,
5. RC two-way module joist waffle slab,
6. RC voided plate,
7. PT flat plate with banded-uniform tendons,
8. Precast PT hollow core slab sitting on RC beams in one direction (one-way),
9. PT voided plate with orthogonal banded-banded tendons, and
10. PT voided plate with diagonal banded-banded tendons.

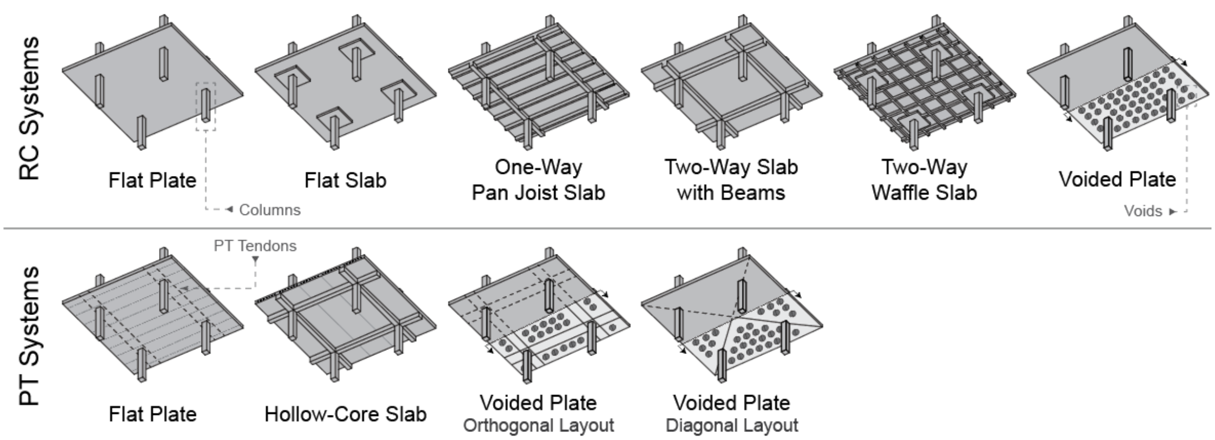

Figure **3-2**: The ten concrete floor systems investigated in this study.

These ten concrete systems are used across several building applications and are available in many global markets. The systems include conventional floors that have been designed for centuries (e.g., RC flat plates and RC one-way slabs), to modern systems (e.g., PT hollow core slabs and PT voided plates). The breadth of concrete floor structures is reflective of the different options available to a designer, each with unique advantages depending on the design scenario; however, this is not an exhaustive list. All concrete floor systems are designed and analyzed as a square 3 bay by 3 bay system, which is the minimum number of bays to design the floor using the Direct Design Method (DDM) according to ACI 318, with the EC normalized to the floor area to provide a fair comparison. All concrete floor systems are evaluated for two different span length ranges: a span length range of 3 m to 15 m (at a 0.33 m interval) and a subset of the full range (called the economic range) that is specific to each concrete floor system based on formwork and current construction practices (Wright, 2016). Table **3-3** reports the different economical span ranges for each floor system.

Table **3-3**: Economical span length ranges for each concrete floor system.

Concrete System	**Economical Span Length Range in m (ft)**
RC Flat Plate	3 to 9 (~10 to ~30)
RC Flat Slab	6 to 12 (~20 to ~40)
RC One-Way Pan Joist Slab	3 to (~10 to ~30)
RC Two-Way Slab with Beams	6to 12 (~20 to ~40)
RC Two-Way Waffle Slab	9 to 15 (~30 to ~50)
RC Voided Plate	6 to 12 (~20 to ~40)
PT Flat Plate	6 to 15 (~20 to ~50)
PT Hollow Core Slab	6 to 15 (~20 to ~50)
PT Voided Plate – Orthogonal Layout	6 to 15 (~20 to ~50)
PT Voided Plate – Diagonal Layout	6 to 15 (~20 to ~50)

This study considers six concrete compressive strength classes, seven live loads, eight superimposed dead loads, and three long-term deflection limits, with the values reported in Table **3-4**. The six strength classes represent a range of low to high concrete strengths commonly specified in the design of concrete floors. The seven live loads are uniform loads for various building applications, based on ASCE 7-16 (American Society of Civil Engineers, 2016) (refer to Table **3-2**). Live load reductions and pattern live loads are not considered, since non-reduced loads result in conservative structural floor designs. The eight dead loads range from small to large loads, reflective of design practice. The three long-term deflection limits were selected as different building applications have varying serviceability requirements. The deflection limit of L/480 was considered as a worst-case deflection scenario in the design of the concrete floor systems and reduces the chance of being susceptible to vibrations. This deflection limit is specified in ACI 318 Table 24.2.2 (ACI Committee 318, 2019) to prevent damage to non-structural elements that are likely to be damaged by large deflections. Furthermore, this deflection limit is required in certain local design codes (e.g., the New York State Residential Code, 2015). It should be noted that short-term deflections were considered as part of the calculation of long-term deflection (refer to Appendix B); however, only the long-term deflection limits were varied. Advanced strategies to determine deflections are appropriate in later design stages (Aalami, 2011; Scanlon & Suprenant, 2011) and are beyond the scope of this work. The concrete floor systems are designed for 2-hr fire rating per the International Building Code (International Code Council, 2018), which requires a minimum slab thickness of ~125 mm (5 in). Although the load values used in the present study may be comparable to building codes in other geographic regions (Seyedabadi et al., 2024), including Eurocode 2 (British Standards Institution, 2008), this study focuses on North American building codes to obtain an accurate EC estimation.

Table **3-4**: The design scenarios evaluated for the concrete floor systems.

Concrete Compressive Strength in MPa (psi)		**Applied Live Load in kN/m^2 (psf)**		**Applied Dead Load in kN/m^2 (psf)**		**Long-term Deflection Limit**
20.7 (3,000)	31.0 (4,500)	1.915 (40)	4.788 (100)	0.239 (5)	1.197 (25)	$\Delta < L/240$
24.1 (3,500)	34.5 (5,000)	2.394 (50)	5.985 (125)	0.479 (10)	1.436 (30)	$\Delta < L/360$
27.6 (4,000)	41.4 (6,000)	2.873 (60)	7.182 (150)	0.718 (15)	1.676 (35)	$\Delta < L/480$
		3.830 (80)		0.958 (20)	1.915 (40)	

Using the geometric (span length) and structural design parameters, this study simulated 41,328 design scenarios for each of the six RC concrete systems and 27,552 design scenarios for each of the four PT concrete systems. The RC systems were designed for all strengths, but the PT systems were not designed for strengths lower than 27.6 MPa, reflective of PT design practices. The SMQs that satisfied the strength and serviceability limit states according to the appropriate ACI 318 (ACI Committee 318, 2019) provisions were obtained for each design scenario. The steel reinforcement was designed according to the distributed design moments at different locations in the floor (Foraboschi, 2019). The number of bars that satisfied the bending moment was obtained for every nominal U.S. rebar size between a #4 bar to a #10 bar, after which the lowest total area of steel was selected and used in the EC calculation. The steel rebar was arranged at locations of maximum positive and negative bending moments, following typical U.S. design practices. The geometric information of the floor and SMQs including concrete volume, steel rebar mass, void former volume, and PT tendon mass are provided in a dataset available at https://doi.org/10.1016/j.engstruct.2023.117369, with the structural equations provided in Appendix B.

3.3.2 GWPs for various concrete mixtures and other structural materials

This study considers the EC contributions from the A1-A3 (cradle-to-gate) LCA stages, following the ISO standards 14040 (ISO, 2006a) and 14044 (ISO, 2006b), as is used in design practice. The EC has a declared unit of m^2 to account for floor area differences based on varying span lengths. This study made use of EPDs of concrete mixtures to improve the accuracy of the EC estimates and to demonstrate the large variability of GWPs corresponding to different strengths. This study used a compiled dataset (version 1) of ready-mix concrete EPDs from U.S. concrete manufacturers (see Appendix A), and considered 32,440 EPDs for six different strength classes in the database. All strength classes are well represented, with many thousands of EPDs for each class. As Fig. **3-3** shows, the median GWP generally increases as the concrete strength increases; however, the GWP range also increases as the strength increases, implying that the carbon impacts of concrete and cement are complex and highly variable. This finding has also been observed in preceding works that evaluated EPDs (Anderson, 2023; Anderson & Moncaster, 2020).

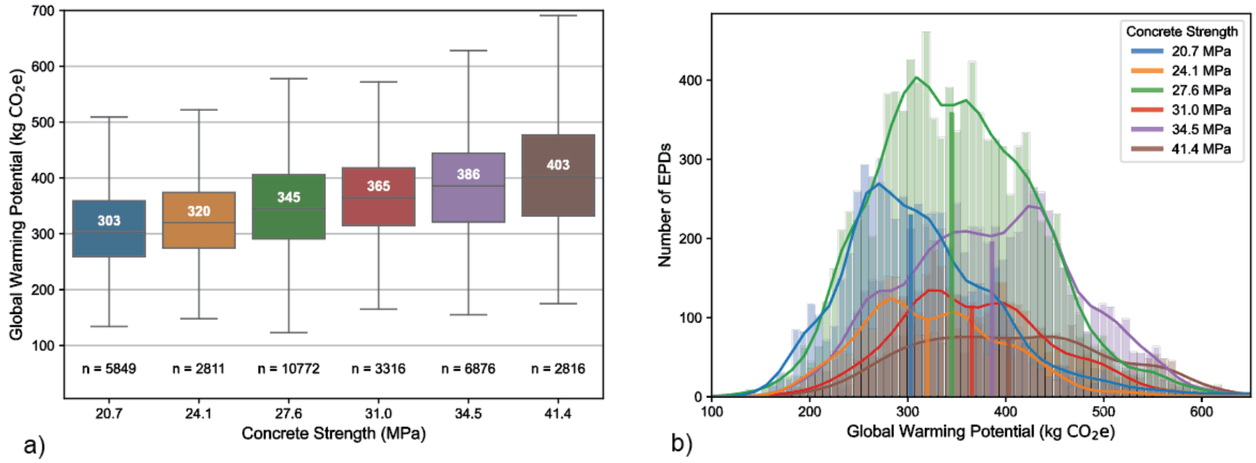

Figure **3-3**: (a) GWP variability for six concrete strength classes, with the number of EPDs corresponding to each strength class reported below the whiskers. (b) Density plot for each concrete strength class.

The EPDs in the database were filtered to have a uniform strength unit (i.e., MPa / psi at 28 days) and a declared unit of 1 m^3. The collection of EPDs for the six strength classes was primarily composed of portland cement (94.3%), which is the main ingredient that drives the GWP intensity of a concrete mix. This study excludes the strength classes of 37.9 MPa and above 48.3 MPa as 57.0% of the mixtures in those classes used alternates to portland cement (e.g., Type 1L cement) and had fewer EPDs represented in the database (n = 393 and n = 1,560, respectively).

To validate the median GWPs from the independent EPD database, the GWPs are compared to published national averages from the Carbon Leadership Forum (CLF) (2021) material baseline values and the NRMCA (2022). Table **3-5** shows that the GWP median values found from the EPD database were lower than the published averages, especially for high strength concrete mixtures. Yet there are multiple limitations in this comparison. First, the GWP intensities provided by the CLF and NRMCA are reported at a grainer resolution. Second, 30.3% and 10.6% of the EPDs in the database were published in 2022 and 2023, which were after the CLF and NRMCA baseline studies were conducted. Third, although the NRMCA published national GWP benchmarks, no specific GWPs for compressive strengths, such as 24.1 MPa and 31.0 MPa, were provided. Because of these limitations, the EPD database detailed in Appendix A potentially provides a more realistic representation of the concrete mixtures currently available to practitioners, including low-CO_2 mixtures. Due to these improvements, the median GWP intensities from the EPD database were selected.

Table **3-5**: A comparison of the concrete strengths and their corresponding GWPs.

Concrete Compressive Strength	Median GWP Intensities	CLF Baseline	NRMCA Baseline	Selected GWP Intensities
20.7 MPa (3,000 psi)	303 kg CO_2e/m^3	291 kg CO_2e/m^3	268 kg CO_2e/m^3	303 kg CO_2e/m^3
24.1 MPa (3,500 psi)	320 kg CO_2e/m^3	359 kg CO_2e/m^3	329 kg CO_2e/m^3	320 kg CO_2e/m^3
27.6 MPa (4,000 psi)	345 kg CO_2e/m^3	359 kg CO_2e/m^3	329 kg CO_2e/m^3	345 kg CO_2e/m^3
31.0 MPa (4,500 psi)	365 kg CO_2e/m^3	443 kg CO_2e/m^3	401 kg CO_2e/m^3	365 kg CO_2e/m^3
34.5 MPa (5,000 psi)	386 kg CO_2e/m^3	443 kg CO_2e/m^3	401 kg CO_2e/m^3	386 kg CO_2e/m^3
41.4 MPa (6,000 psi)	403 kg CO_2e/m^3	543 kg CO_2e/m^3	422 kg CO_2e/m^3	403 kg CO_2e/m^3

The GWPs for the additional structural materials (aside from concrete) used in the study are reported in Table **3-6**, which are typical industry values. The values are obtained from U.S. EPDs, though similar values from EPDs in other geographic regions around the world can be obtained. An important note is that there is not a U.S. industry standard EPD for PT tendons; therefore, this study conservatively estimated the EC of PT tendons based on a 100% increase of the GWP reported for non-prestressed steel reinforcement, as was similarly done by Miller et al. (2015).

Table **3-6**: Embodied carbon coefficients for non-concrete structural materials.

Structural Material	GWP	Declared Unit	Source
Non-Prestressed Steel Reinforcement	0.854 kgCO_2e	Per kg	CRSI EPD (2022)
Steel Post-Tension Tendons	1.708 kgCO_2e	Per kg	Based on CRSI EPD (2022)
Recycled Void Formers (Plastic Bubbles)	10.5 kgCO_2e	Per m^3	Cobiax EPD (2018)

3.3.3 Deriving EC equations

Following the structural analyses and evaluation of the concrete EPD database, polynomial regression models were trained to derive analytical equations for the conceptual and schematic design phases. Fig. **3-4** illustrates the methodology for deriving both sets of equations. The concrete MQs were used to calculate the cradle-to-gate EC for the floor systems for all design scenarios. The average EC for each span length was found and defined as the EC trendline for each system, which was fitted using a univariate second order polynomial regression model. For the schematic design phase, a second order multivariate polynomial regression model was used to derive an equation to predict the concrete slab volume, which was then used to obtain the EC of a slab and total EC. Although higher order polynomial models can be used in the conceptual and schematic design equations, a second order model was selected to provide a simple expression to quickly estimate the EC and to minimize the number of interaction terms between structural parameters.

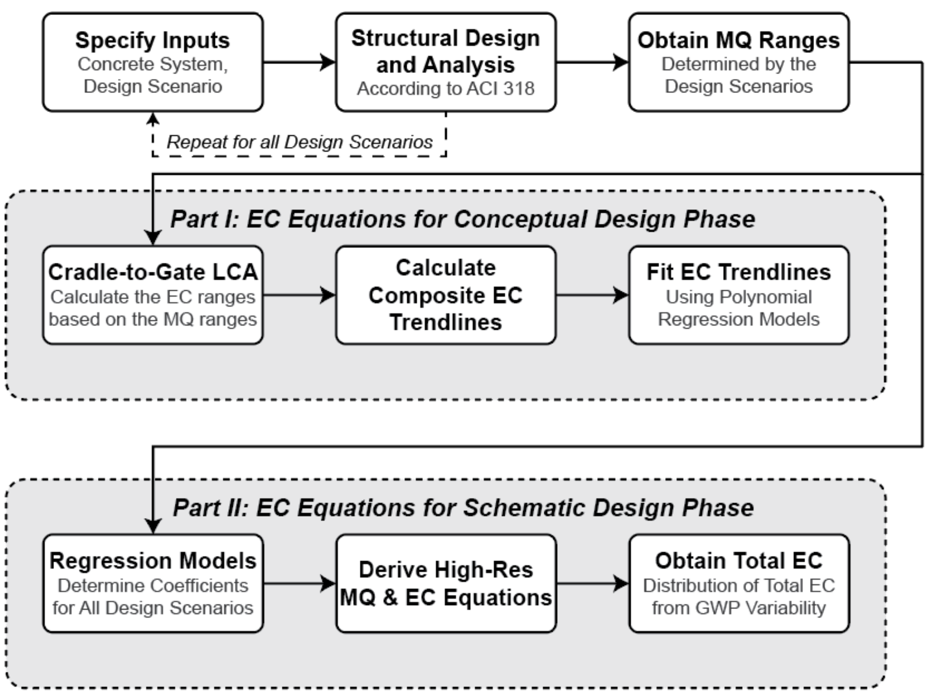

Figure **3-4**: The method for deriving the analytical models for the conceptual and schematic design phases.

3.3.3.1 Conceptual design phase: Curve-fitting based on composite EC

Equation **3-2** was used to fit the composite, averaged cradle-to-gate EC trendlines for each concrete floor system across span length by tuning the β coefficients. The single variable used in the model is the span length, L, because of its large influence on the MQ of a concrete floor. The estimated EC, EC^*, considers the EC for all structural materials that compose a given concrete floor system—the concrete slab, steel rebar, void formers, and PT tendons.

$$EC^* = \beta_0 + \beta_1 L + \beta_2 L^2 \qquad \text{(Equation } \mathbf{3\text{-}2}\text{)}$$

There are two main advantages of using this expression. First, to determine a rough EC estimate for a concrete floor system, a designer only needs to know the span length and the system type. The second advantage is that there is only one EC equation that considers all structural materials corresponding to a floor system, therefore providing an efficient way to compare floor systems to each other. The equations derived in the conceptual design phase use both full and economic span length ranges to provide a means of comparison at extreme span lengths and more accurate EC estimates at spans that are more economical for certain floor systems. Yet a more rigorous model is needed to help tailor the EC estimate when more design information is known.

3.3.3.2 Schematic design phase: Curve-fitting based on concrete MQ and GWP variability

A more accurate EC prediction requires an accurate estimation of MQ; therefore, Equation **3-3** was used to fit the concrete slab volume for each floor system. This model accounts for the span length, L, in addition to the four structural design parameters parametrically evaluated: the specified design concrete strength, $f'c$, the uniform live load, LL, the superimposed dead load, DL, and the long-term deflection limit, Δ_{Lim}. The coefficients, β_n, help tune the MQ estimate of the slab, MQ^*, and each β_n is associated with the listed variable(s).

$$MQ^* = \beta_0 + \beta_1 L + \beta_2 f'c + \beta_3 LL + \beta_4 DL + \beta_5 \Delta_{Lim} + \beta_6 L^2 + \beta_7 Lf'c + \beta_8 L * LL + \beta_9 L * DL + \beta_{10} L\Delta_{Lim} + \beta_{11} f'c^2 + \beta_{12} f'cLL + \beta_{13} f'cDL + \beta_{14} f'c\Delta_{Lim} + \beta_{15} LL^2 + \beta_{16} LL * DL + \beta_{17} LL\Delta_{Lim} + \beta_{18} DL^2 + \beta_{19} DL\Delta_{Lim} + \beta_{20} {\Delta_{Lim}}^2 \quad \text{(Equation 3-3)}$$

After obtaining the MQ^* of a concrete floor system from Eq. **3-3**, it can be multiplied with a single GWP value or a set of GWPs, $\boldsymbol{GWP}$, related to a concrete strength class to approximate a set of estimated EC contributions from the concrete slab, $\boldsymbol{EC_{slab}}^*$, as shown in Eq. **3-4**. Because there is less variation with the GWP compared to concrete, the EC contribution of the steel rebar, $EC_{Rebar}{}^*$, void formers, $EC_{Voids}{}^*$, and PT tendons, $EC_{PT}{}^*$, were estimated as a single EC value instead of as a set of values using Equation **3-5**. Depending on the system, a set of total ECs, $\boldsymbol{EC_{Total}}^*$, can then be obtained by summing the EC contributions from every structural material (Equation **3-6**).

$$\boldsymbol{EC_{slab}}^* \sim \boldsymbol{GWP} \times MQ^* \quad \text{(Equation 3-4)}$$

$$EC_{Rebar}{}^*, EC_{Voids}{}^*, EC_{PT}{}^* = \beta_0 + \beta_1 L + \beta_2 f'c + \beta_3 LL + \beta_4 DL + \beta_5 \Delta_{Lim} + \beta_6 L^2 + \beta_7 Lf'c + \beta_8 L * LL + \beta_9 L * DL + \beta_{10} L\Delta_{Lim} + \beta_{11} f'c^2 + \beta_{12} f'cLL + \beta_{13} f'cDL + \beta_{14} f'c\Delta_{Lim} + \beta_{15} LL^2 + \beta_{16} LL * DL + \beta_{17} LL\Delta_{Lim} + \beta_{18} DL^2 + \beta_{19} DL\Delta_{Lim} + \beta_{20} {\Delta_{Lim}}^2 \quad \text{(Equation 3-5)}$$

$$\boldsymbol{EC_{total}}^* \sim \boldsymbol{EC_{slab}}^* + EC_{Rebar}{}^* + EC_{Voids}{}^* + EC_{PT}{}^* \quad \text{(Equation 3-6)}$$

The primary advantage of this model is that the MQ^* (and corresponding $\boldsymbol{EC_{slab}}^*$) of a floor system can be tuned to a specific design scenario, resulting in a more accurate total EC estimate. A second advantage is that a breadth of concrete mix GWPs can be considered in the model, aiding designers to help evaluate how much a mix can influence the EC. A third advantage of this model MQ^* can be used to estimate other design objectives that are a function of concrete slab volume, such as the cost of concrete material. Despite these advantages, this analytical model is more complex compared to the conceptual design equations, requiring more design information (i.e., strength, loads, and deflection limit) to obtain an estimate for the total EC of a floor system.

3.4 Results and discussion

3.4.1 Conceptual design phase: EC equations

After conducting all structural analyses and corresponding design procedures, the SMQs were obtained. The EC results were then compiled across the 41 unique span lengths (average EC results from every design scenario for each span length) to obtain composite EC trendlines. An example is shown in Fig. **3-5**, with the dark line representing the composite EC trendline, while the gray dots represent the range of EC used to obtain this trendline.

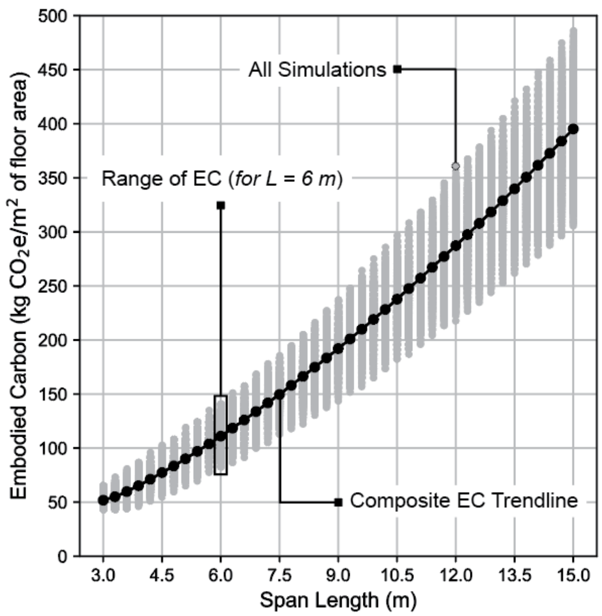

Figure **3-5**: Possible EC values for an RC flat plate for all simulated design scenarios.

The composite EC trendlines for each system are shown in Fig. **3-6**. Intuitively, as the span length of each floor system increases, the EC increases due to added concrete material (thicker slab) needed to satisfy larger structural force demands. This is especially noticeable at larger spans, due to the non-linear increase in EC. The floors have varying ranges of total EC across different span lengths. Some floor systems

(RC flat plate, RC flat slab, and RC voided plate) have gradual increases in the range of total EC for a given span length, but this relationship is not seen across all floors. Other systems (the RC one-way slab, PT flat plate, and PT voided plates) have smaller EC variability at short span lengths (below 9 m), but significant variability at high span lengths (above 12 m). This variability suggests that engineers may need to know additional structural information to better assess which floor system has the lowest EC for a given design scenario.

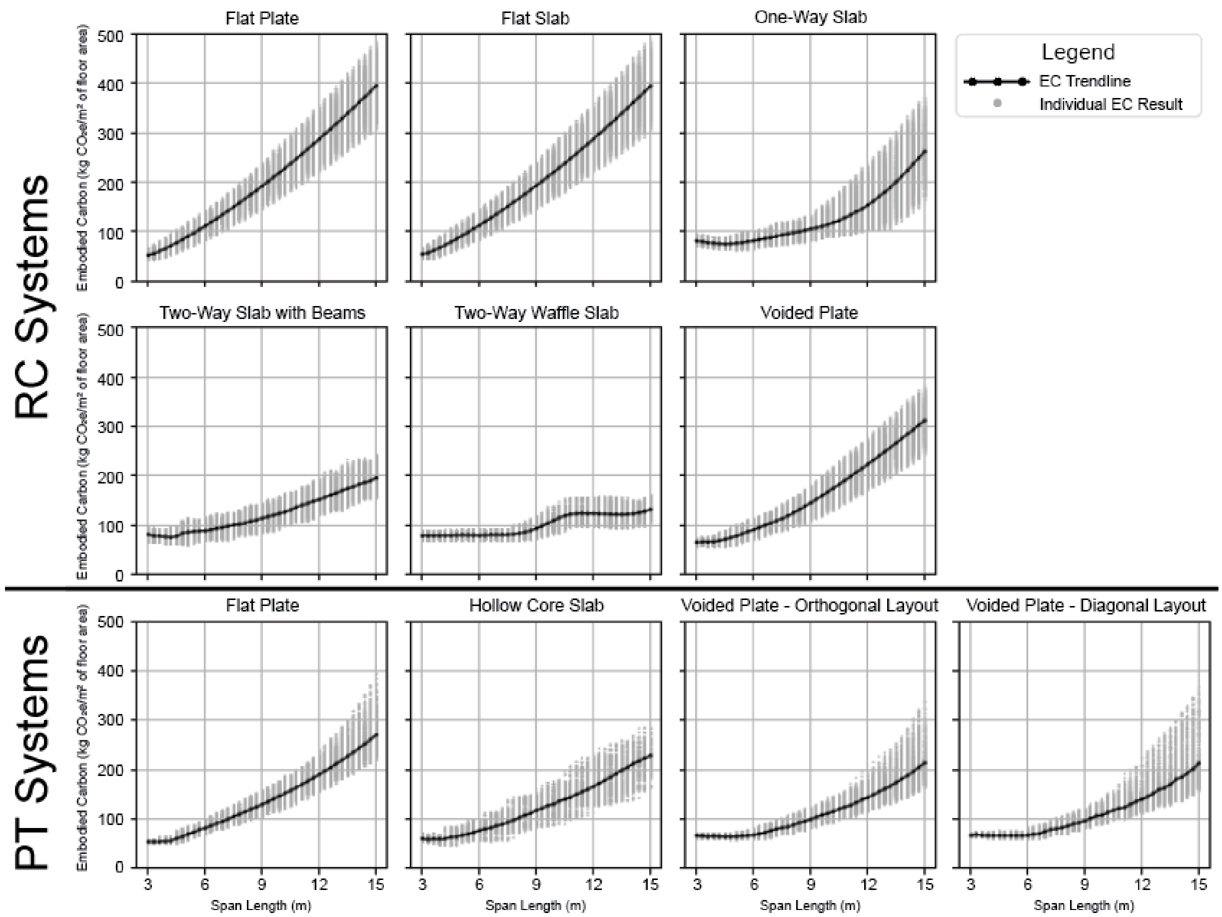

Figure **3-6**: The composite EC trendlines superimposed over all simulated results for each concrete floor system.

Fig. **3-7** compares the EC trendlines for each system to one another. The comparison further cements that floor system selection is complex, as the floor with the least amount of EC varies across the span range. For very short spans (below 4.5 m), favorable solutions include an RC flat plate, an RC flat slab, a PT flat plate, and a PT hollow core slab. From a span length of 4.5 m to 7.5 m, all PT systems have low EC, in addition to an RC one-way slab and RC waffle slab. An RC waffle slab is the optimal system from a span length from 7.5 m to 9.5, while the PT floor systems and an RC one-way slab are also viable options. Notably, Fig. **3-7** reveals that many concrete floor systems could be selected when minimizing EC at a span length from 9.5 m to 11 m, suggesting that a higher fidelity model (the schematic design equations) are needed to refine the comparison. Beyond a span length of 11 m, an RC waffle slab was found to be the best floor system for reducing EC, which is in line with practical design knowledge of the system.

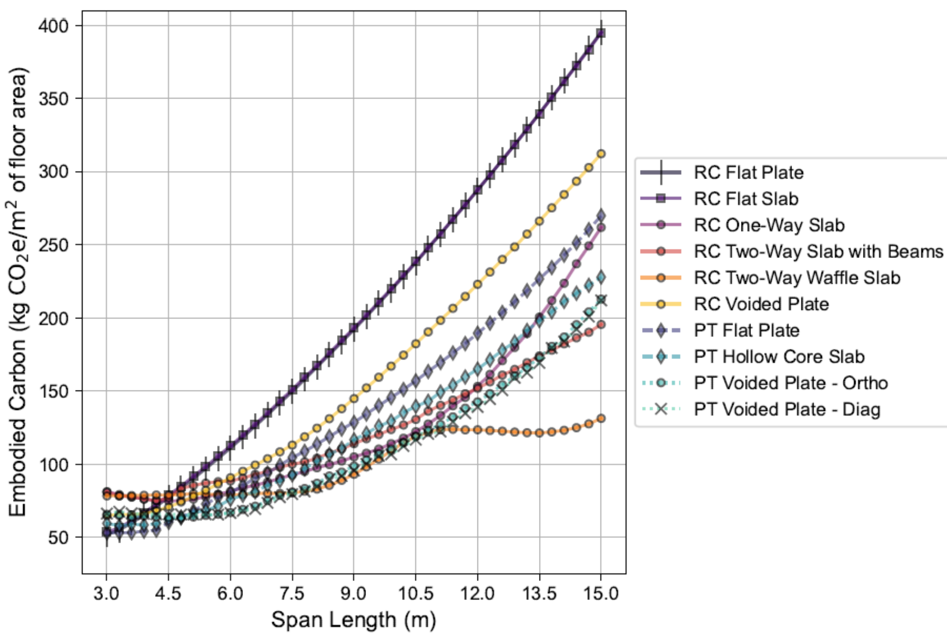

Figure **3-7**: Comparison of the composite EC trendlines for the ten concrete floor systems.

As mentioned in Sec. 3.3.3.1., different floor systems are more economical for specific span ranges (Wright, 2016), which is supported by Figs. **3-6** and **3-7**. Fig. **3-8** compares the analytically fitted EC trendlines for the whole span range and the economical span ranges in Table **3-3**, with the derived equations presented in Table **3-7** (see Sec. C.1 in Appendix C for the equations in imperial units). The fitted lines were in high agreement with the EC trendlines (R^2 values for all fitted lines are above 0.99 for all systems, except for the RC waffle slab which had an R^2 value of 0.88), suggesting that these equations can adequately serve as a very-early EC estimate for concrete floor systems. It should be noted that the RC waffle slab EC trendline has the form of a third order polynomial, suggesting that higher order polynomial regression models could have better statistical agreement.

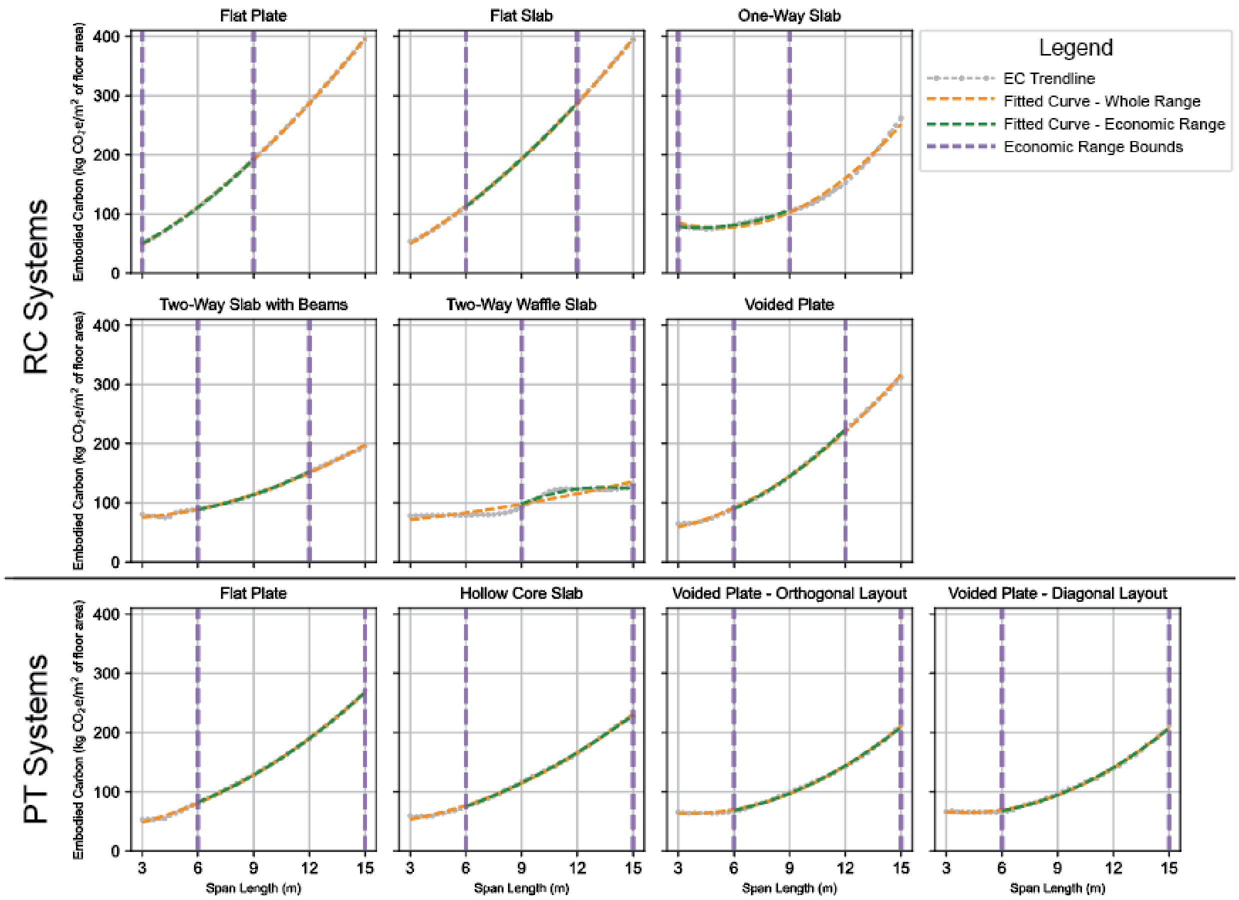

Figure **3-8**: The fitted composite EC trendlines for the ten concrete systems for the full span range investigated and a more economical span range.

Table **3-7**: The analytically derived EC equations for use in the conceptual design phase.

Concrete System	**Full Span Range Equations** (3 m to 15 m)	**Economical Spans Equations**	**Economical Span Ranges in m**
RC Flat Plate	$EC_{est} = 0.85\ L^2 + 13.81\ L - 1.1$	$EC_{est} = 1.16\ L^2 + 9.90\ L + 9.8$	3 to 9
RC Flat Slab	$EC_{est} = 0.84\ L^2 + 13.84\ L + 0.49$	$EC_{est} = 0.76\ L^2 + 15.4\ L - 7.7$	6 to 12
RC One-Way Pan Joist Slab	$EC_{est} = 1.83\ L^2 - 19.08\ L + 126$	$EC_{est} = 1.32\ L^2 - 11.1\ L + 100$	3 to 9

Concrete System	Full Span Range Equations (3 m to 15 m)	Economical Spans Equations	Economical Span Ranges in m
RC Two-Way Slab with Beams	$EC_{est} = 0.62\ L^2 - 1.00\ L + 73$	$EC_{est} = 0.78\ L^2 - 3.38\ L + 81$	6 to 12
RC Two-Way Waffle Slab	$EC_{est} = 0.17\ L^2 + 2.34\ L + 63$	$EC_{est} = -1.40\ L^2 + 37.8\ L - 128$	9 to 15
RC Voided Plate	$EC_{est} = 1.18\ L^2 + 0.22\ L + 48$	$EC_{est} = 1.37\ L^2 - 2.27\ L + 54$	6 to 12
PT Flat Plate	$EC_{est} = 0.83\ L^2 + 3.37\ L + 31$	$EC_{est} = 0.89\ L^2 + 1.91\ L + 39$	6 to 15
PT Hollow Core Slab	$EC_{est} = 0.78\ L^2 + 0.74\ L + 44$	$EC_{est} = 0.64\ L^2 + 3.68\ L + 30$	6 to 15
PT Voided Plate – Ortho.	$EC_{est} = 1.11\ L^2 - 7.79\ L + 77$	$EC_{est} = 1.01\ L^2 - 5.50\ L + 65$	6 to 15
PT Voided Plate – Diag.	$EC_{est} = 1.19\ L^2 - 9.68\ L + 85$	$EC_{est} = 1.09\ L^2 - 7.52\ L + 74$	6 to 15

Note: L: Length in m. EC_{est}: Embodied carbon in $kgCO_2e/m^2$.

3.4.2 Schematic design phase EC equations

More accurate EC estimates can be made when accounting for structural design parameters that are more likely to be known in the schematic design phase. Yet one challenge is that the ten concrete systems have various combinations of additional structural materials, including steel rebar, void formers, and PT tendons. Fig. **3-9** shows the breakdown of the structural materials' contribution to the composite EC for each concrete system, revealing that the concrete in the slab contributes the most EC for each system, with a contribution of around 80%. Because concrete is the primary contributor to the total EC of a concrete floor system, it is important to accurately predict the concrete slab MQ before considering the GWP variability of concrete mixtures.

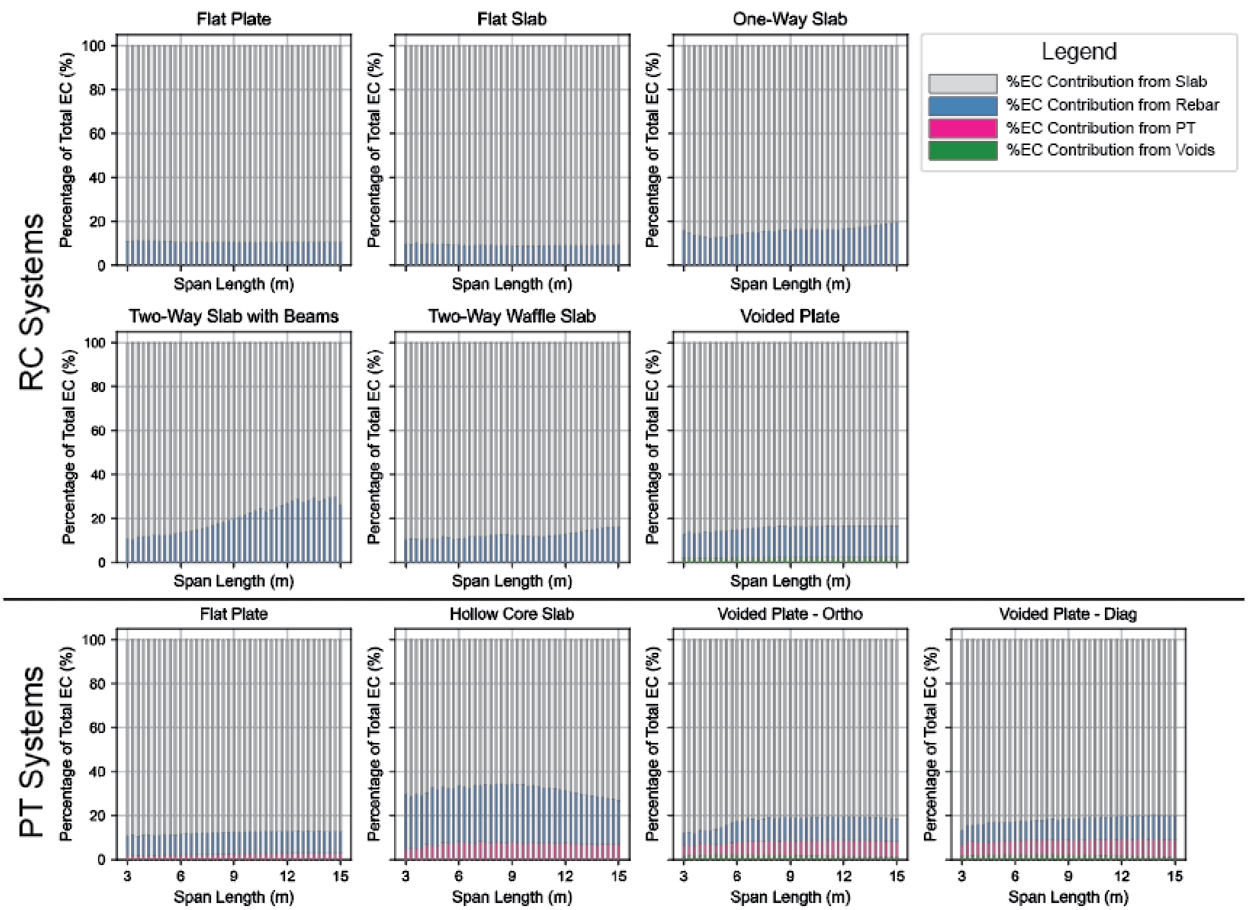

Figure **3-9**: Breakdown of the contribution to the floor's EC for each structural material.

Like the EC variability shown in Fig. **3-5**, there is significant variability in the concrete slab MQ due to variations in structural design parameters. This is illustrated in Fig. **3-10**, as the lowest bound of concrete slab MQ is generally obtained with the combination of the highest concrete strength, the lowest applied loads, and the lowest specified deflection limit. The inverse is true for the upper bound. As a result, all four structural design parameters need to be accounted for in the equation to better estimate the concrete MQ, and corresponding EC, of a concrete floor.

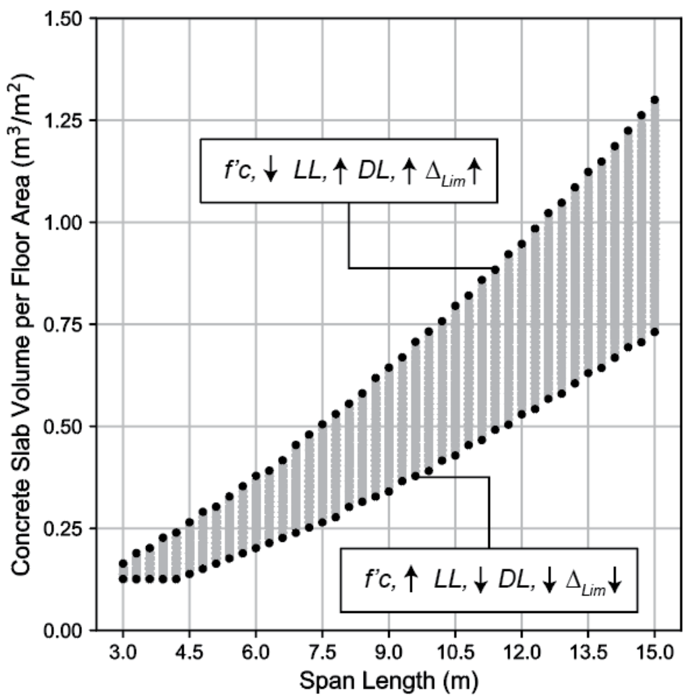

Figure **3-10**: Range of concrete slab MQ for an RC flat plate.

After obtaining the range of concrete slab MQ for the ten systems, the multivariable polynomial regression model was used to derive the $MQ*$ equations. The analytical model tuned the coefficients for the analytical equations based on Eq. **3-3**. To assess how the coefficient terms in the analytical equations influence the prediction of the concrete MQ for each system, Fig. **3-11** compares the magnitudes for every term. The coefficient magnitudes are normalized for each term and compared across all ten systems. The coefficient values are reported in Sec. C.2 in Appendix C, including the coefficients of determination (R^2). Aside from the RC waffle slab ($R^2 = 0.74$), the multivariate polynomial regression models had an R^2 above 0.95 implying that the models provide an accurate estimate of the MQ in a concrete floor. Future work should evaluate the RC waffle slab results obtained in this study using higher order polynomial models.

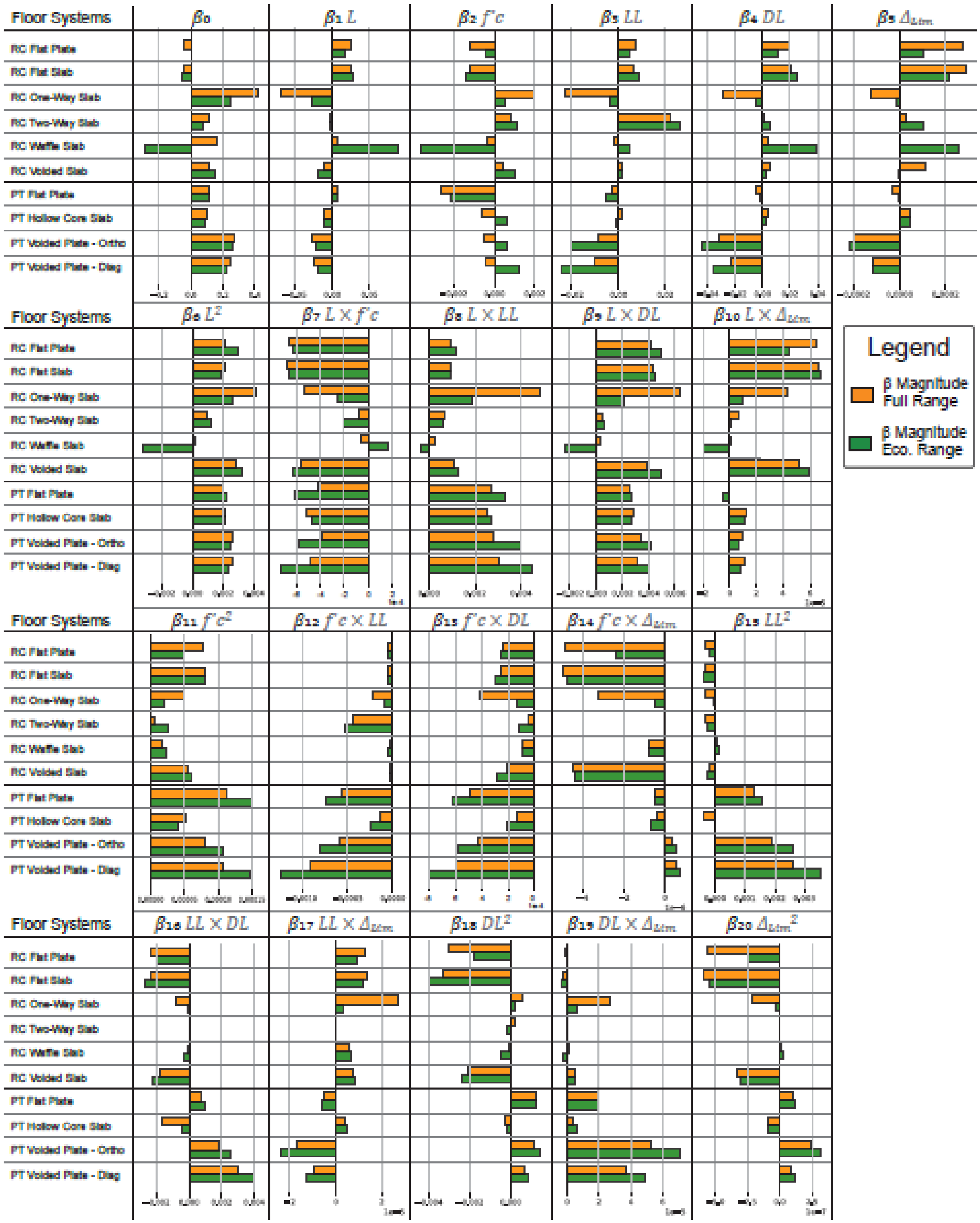

Figure **3-11**: Comparing the Beta coefficient magnitudes for the concrete *MQ** equations.

The coefficient magnitudes in the MQ^* equations illustrate the influence of each structural design parameter and the influence of the interaction between the parameters. For example, the applied live load meaningfully influenced the prediction of the concrete slab MQ for the RC one-way slab, the RC two-way slab with beams, and the PT voided plates, while the deflection limit significantly influenced the RC flat plate, the RC flat slab, and the RC waffle slab. While certain floor systems have similar coefficient magnitudes (e.g., RC flat plate and RC flat slab, and the PT voided plates), no coefficient magnitudes are identical for any floor system. Fig. **3-11** can thus be used to help designers select a floor system if a structural parameter is an extreme (high or low) design value, or when identifying a floor system that is less influenced by specific structural design parameters.

After deriving the MQ^* equations, the GWP variability for the six concrete compressive strengths was considered. Fig. **3-12** shows the distribution of GWP for each concrete strength class. The GWPs follow normal distributions for each strength class, suggesting that the median GWP value could be an under- or over-estimate. Another insight from Fig. **3-12** is that the GWP values for the median and the standard deviations increase as the concrete strength classes increase; however, there are low-CO_2 (<200 kgCO_2e) concrete mixtures in every strength class. The spreads (or a specific value) of GWP can then be multiplied to the MQ^* to obtain a range of concrete slab EC (refer to Eq. **3-4**). To account for the additional structural materials, the EC equations for the structural materials were derived, using Eq. **3-5**. Finally, the total EC can be predicted, summing the range of EC from the concrete slab and the structural materials that comprise the floor system. This procedure, using an example of a spread of GWPs for a concrete strength class of 27.6 MPa, is illustrated in Fig. **3-13**.

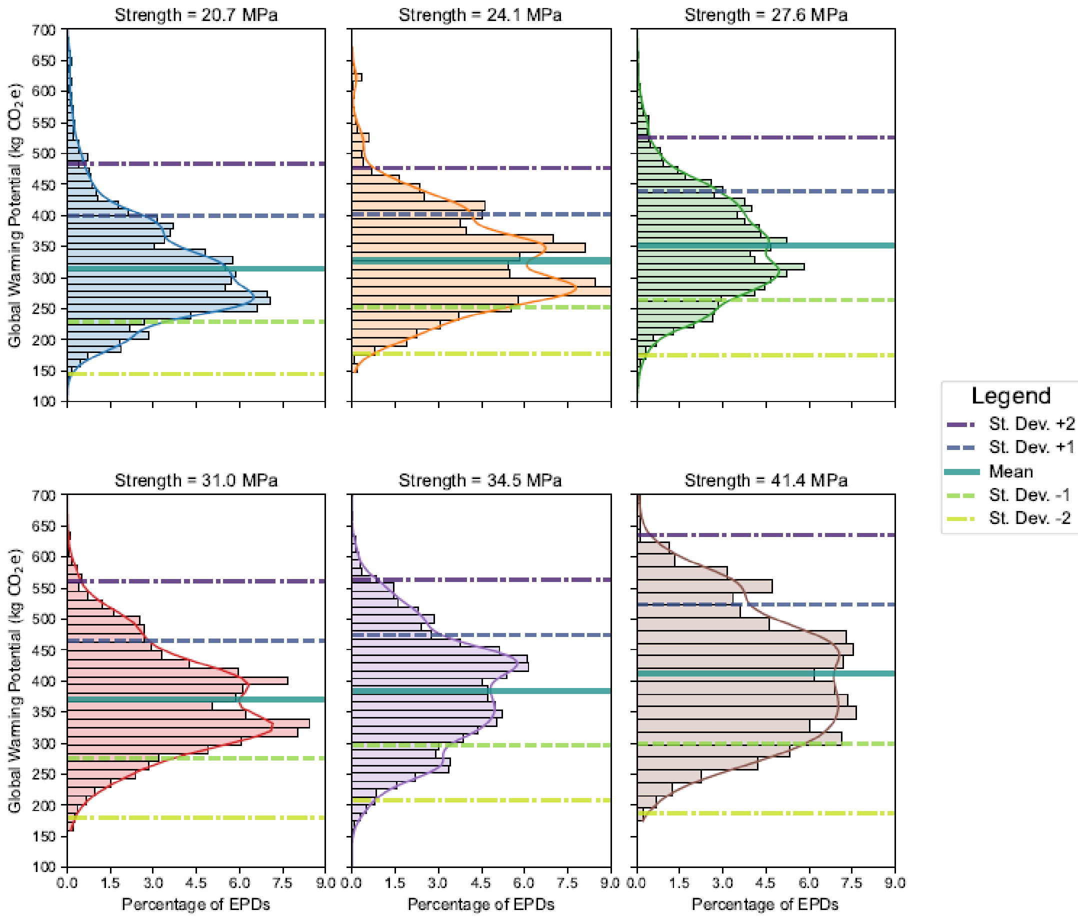

Figure **3-12**: GWP distributions for the six concrete strengths evaluated in the study.

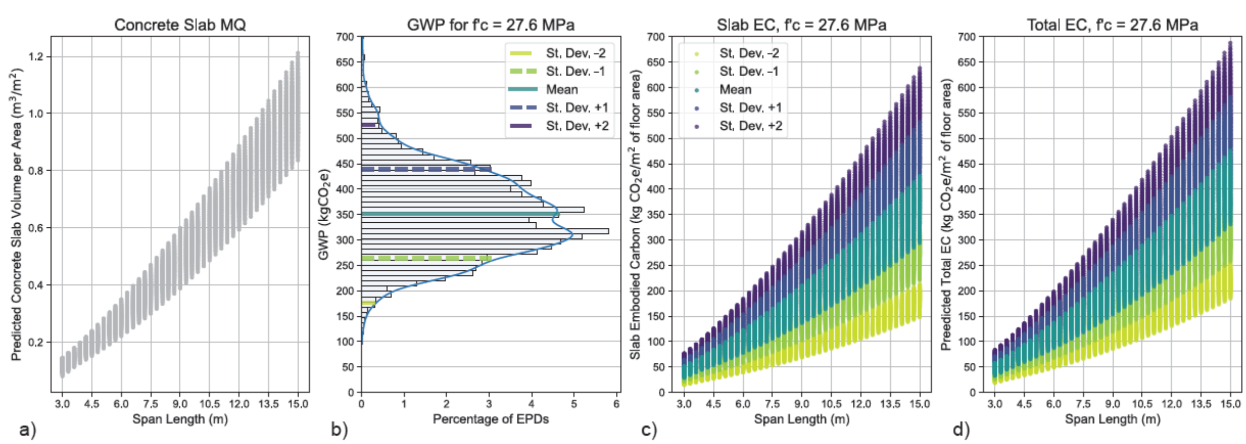

Figure **3-13**: Implementation of the schematic design phase equations. Progression from a) estimating *MQ**, b) accounting for concrete GWP variability, c) obtaining the range of $\boldsymbol{EC_{slab}}^*$, and d) adding the EC contribution from the other structural materials (i.e., steel rebar) to obtain a range of $\boldsymbol{EC_{total}}^*$.

The ranges of total EC can thus be obtained for each floor system for different concrete strengths. Figs. **3-14**, **3-15**, and **3-16** show the ranges of total EC for each floor system at a concrete strength of 27.6 MPa, 34.5 MPa, and 41.4 MPa. These figures show wider ranges of EC spread compared to Fig. **3-6** because of the GWP variability from the concrete mixtures, leading to a probabilistic distribution for the total EC (EC_{Total}^*) of a concrete floor system. Figs. **3-14** to **3-16** also reveal which floor systems have the least / greatest amount of total EC variability. Specifically, systems including the RC two-way slab with beams, the RC waffle slab, and the PT systems have less total EC variability when compared to an RC flat plate.

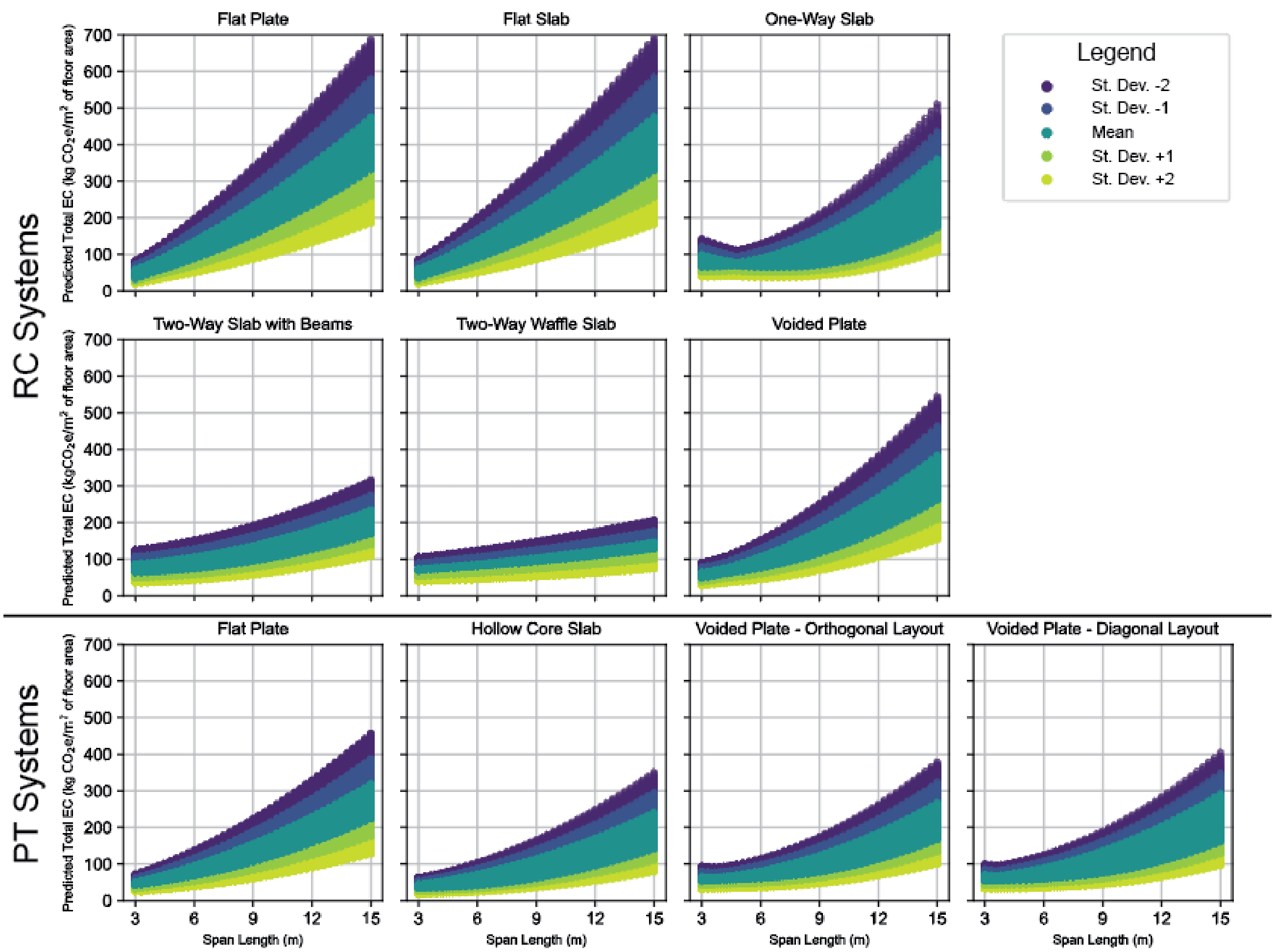

Figure **3-14**: The EC_{Total}^* for each floor system across all span lengths with a strength of 27.6 MPa (4 ksi).

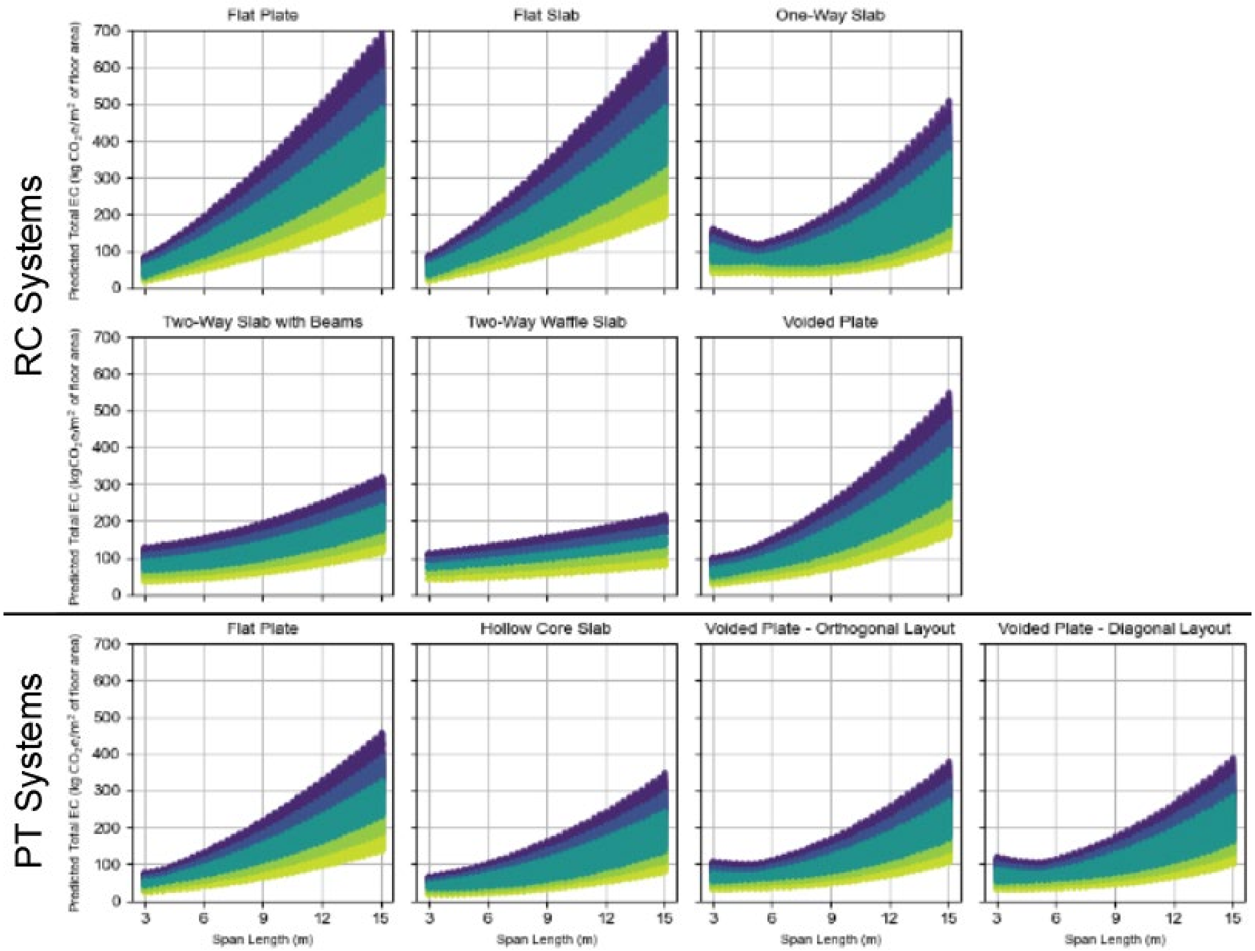

Figure **3-15**: The $\boldsymbol{EC_{Total}}^{*}$ for each floor system across all span lengths with a strength of 34.5 MPa (5 ksi).

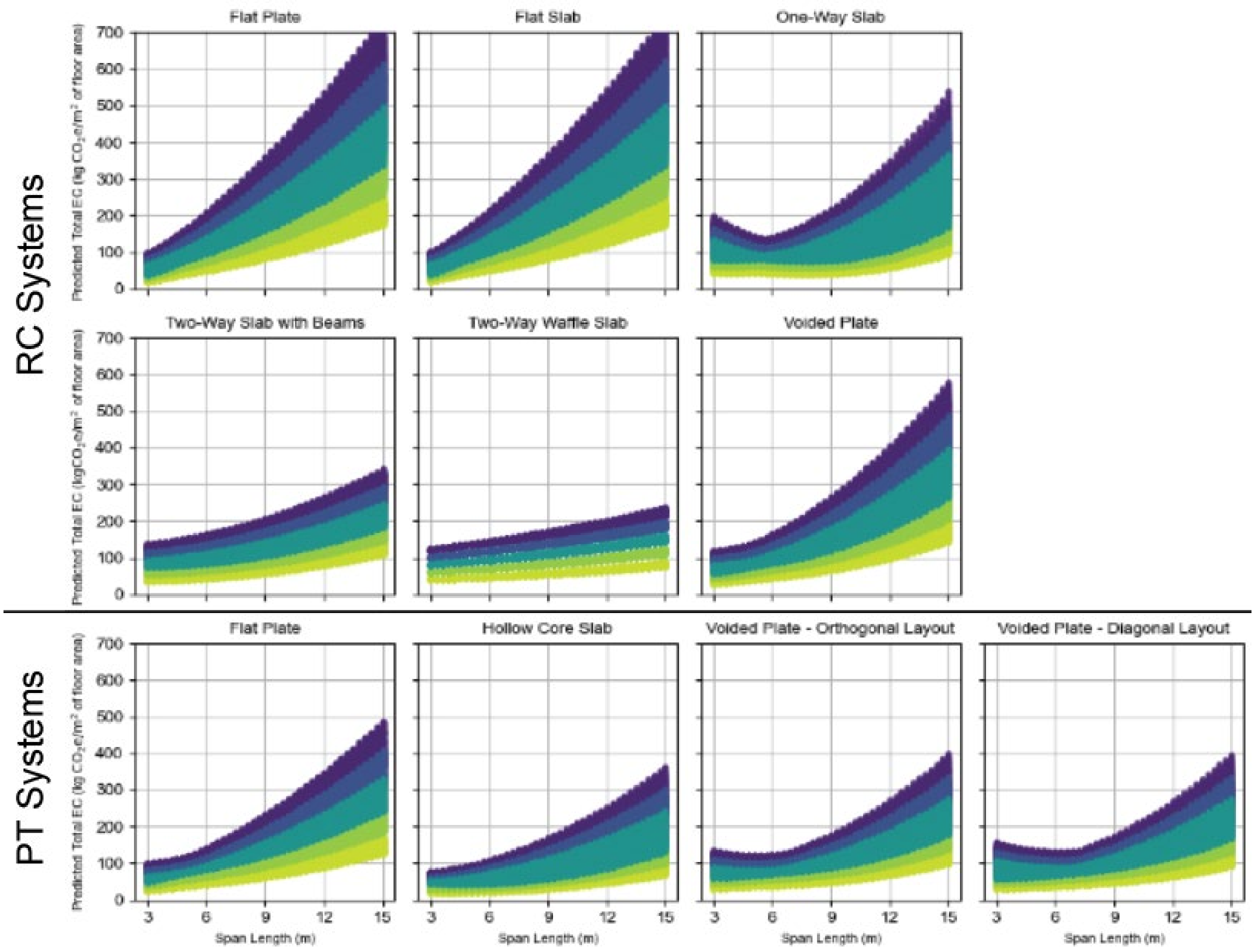

Figure **3-16**: The $\boldsymbol{EC_{Total}}^{*}$ for each floor system across all span lengths with a strength of 41.4 MPa (6 ksi).

The distributions of total EC shown in Figs. **3-14** to **3-16** illustrate that a more accurate estimate of EC is possible in schematic design than in conceptual design, since additional parameters are incorporated in the regression model to refine the prediction. However, the trends between span length and embodied carbon remain similar across the two phases. Together, these results demonstrate how early design decisions can directly influence the EC of a concrete floor system. For example, fixing a decision such as the floor system type and typical floor span length early in the design, before even getting to schematic design, can significantly limit later opportunities to reduce the EC, once additional parameters are being decided that could be potentially adjusted to lower the EC. Similar limitations created by rigid early decisions were also noted by D'Amico and Pomponi (2020). Finally, these results indicate that the combination of SMQ reduction through the selection of more efficient concrete floor systems, floor spans, and strategic structural design parameters in parallel with low-carbon concrete mixtures provide the best solution to reduce the EC footprint of concrete floor structures.

3.4.3 Applying the EC equations in a design tool

Given the inherent difficulties in visualizing such data and interpreting the results, an open-access website application was developed to help structural engineers and building consultants better engage with the analytical models derived in this study. The interactive tool, accessible with the link: https://embodied-carbon-equations-for-concrete-6f8t.onrender.com/, employs both sets of equations for the conceptual and schematic design phases to aid in design decision making with the intent of lowering building EC. Designers can therefore make environmentally informed design decisions tailored to the knowledge of the design in early-stage design phases to reduce building carbon emissions. Fig. **3-17** shows the interface for the conceptual design phase equations, where a designer can select which concrete floor systems to consider and toggle the range slider to consider specific span length ranges. The right-side plots update for every change made by the user, and allows a user to quickly identify a low EC concrete floor system.

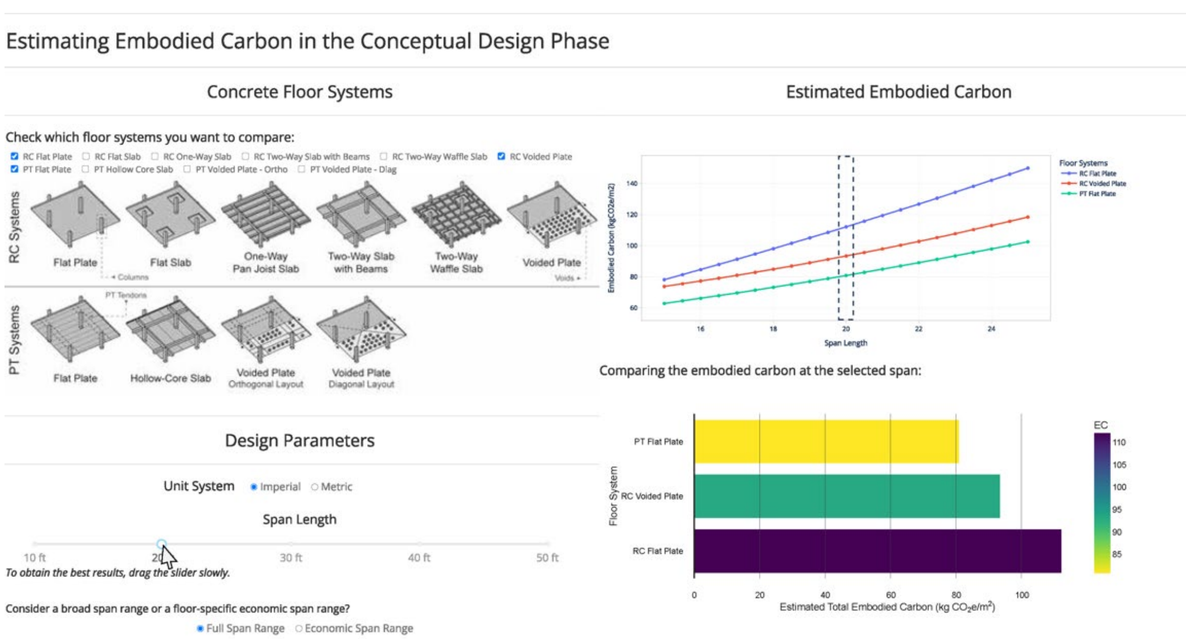

Figure **3-17**: Interactive web app interface using the derived *EC** equations for the conceptual design phase.

A separate interface (see Fig. **3-18**) can be created using analytical models for the schematic design phase. To provide the user with options for design exploration, toggles for exploring different combinations of structural design parameters and concrete systems are included to ascertain an accurate concrete MQ estimation per the selected design scenario. Additionally, the selected concrete strength enables the user to engage with a second slider that displays the GWP variability, showing the median and other statistical GWP values, for a specific concrete strength. A user can then tailor the EC calculation for a different GWP value to obtain a more accurate EC estimate. The tool also provides a plot showing the EC contributions for each structural material, which refreshes with each input change. This interface is especially insightful for building engineers and designers who want to compare baseline SMQ and EC values for different floor systems, as the values provided can serve as early-stage design benchmarks to help inform sustainable design decisions.

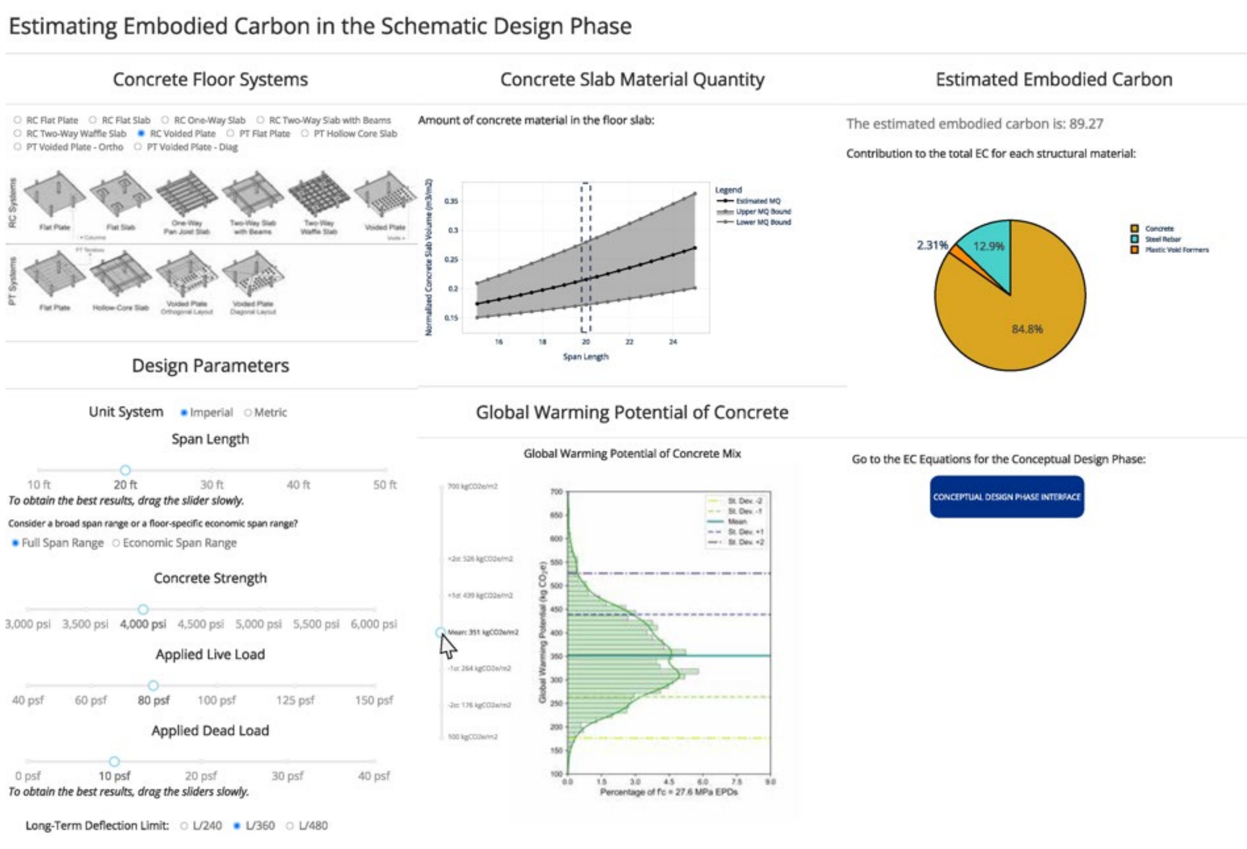

Figure **3-18**: Interactive web app interface using the derived $MQ*$ and EC equations for the schematic design phase.

3.5 Limitations and opportunities for future work

To ensure that the analytical models and corresponding EC estimates are fair across all ten systems, several assumptions were made in the structural design and analysis (see Appendix B for the comprehensive methodologies and equations used for each concrete floor system):

- All concrete floors are designed as 3 bays by 3 bay systems, with an equivalent span length in both orthogonal directions. Alternative geometries would have slightly different EC values based on how the forces and corresponding moments are distributed across the floor.
- The ten concrete floors were designed and analyzed following DDM. Since PT systems cannot be effectively designed using DDM due to variability of stiffness and secondary effects from the PT, a modified DDM approach was used (Broyles & Hopper, 2023), though the modified coefficients are conservative compared to the DDM coefficients.
- The sizing of the concrete column may be conservative for lighter weight systems under certain design scenarios. Though the columns are not accounted for, the column size can affect the structural analysis and design of a system, potentially resulting in conservative slab depths, beam cross-sections (especially for the PT hollow core slabs), and EC results.
- A minimum slab thickness of ~125 mm (5 in) was used to obtain a 2-hr fire rating. This assumption governs the EC of floors with low spans and lighter loading scenarios, as other fire ratings (i.e., 1-hr, 3-hr) have alternative slab thickness requirements. No maximum thickness requirement was specified; however, depth limits could also influence the selection of a low EC concrete floor system (Broyles et al., 2020).
- A maximum pre-compression limit of 2.07 MPa (300 psi) was set for the PT systems, which is a common design limit used in industry. However, there may be certain cases where more PT could be used, further reducing the amount of concrete material needed.

These assumptions emphasize the complexity of the structural design and analysis of concrete floors and their corresponding SMQs and EC. However, the assumptions used in this study provide a conservative bound for estimating and comparing the EC of concrete floors in early design and could serve as EC and SMQ benchmarks for concrete floor systems. Benchmarking of EC and SMQs for concrete systems has been similarly done by Belizario-Silva et al. (2024) for flat RC plates in Brazil, and benchmarking of structural systems can help guide designers balancing carbon budgets (Habert et al., 2020). Whole-Building LCA studies that evaluate the ten concrete floors studied in this work would reveal further EC benefits for different structural systems.

A limitation with the LCA conducted in this study is the exclusion of concrete waste and GWP manufacturing uncertainty. A crude but simple solution is to introduce waste and uncertainty multipliers in the EC equation. A less trivial limitation is that there are inherent uncertainties in the calculation of SMQs in the floor systems. Yet proper accounting for material-specific uncertainty and design-specific uncertainty in an LCA is complex (Huijbregts, 1998; Marsh et al., 2023), potentially requiring further analyses in case-by-case studies, which is beyond the scope of this present work. Another opportunity for future research is to build Bayesian models to account for LCA uncertainty from all parameters. Although Bayesian analyses could provide probabilistic EC ranges in a more robust way, it has limitations in design practice applications, as designers may be unfamiliar with implementing this method and interpreting the results. Instead, regression equations are easily transferable and programmable into typical engineering tools.

Though out of the scope of this work, there are other design objectives that could control the design and selection of a concrete floor system. Constructability is an important design consideration in practice (Orr et al., 2019) that was not considered, except implicitly due to the inclusion of economical ranges. The constructability of a concrete floor system affects the timeline of a building and EC when considering the LCA construction phase. Local availability, transportation distances, and regional differences in manufacturing of concrete products can meaningfully influence the environmental performance of concrete systems (Biswas et al., 2017; Sandanayake et al., 2018). Similarly, accurate cost estimates of structural materials, construction, and labor can influence the selection of a concrete system (Gauch et al., 2023; Kanyilmaz et al., 2023; Jayasinghe et al., 2021a). Furthermore, vibrations (Wu et al., 2020), thermal insulation (Gascon et al., 2022), heating and cooling loads (Duan, 2023), acoustics (Broyles et al. 2022c;

Roozen et al., 2018) and fire rating (Khoury, 2000) can all be inadvertently affected by reducing concrete MQ. The consideration of multiple objectives can compete with aims of minimizing EC, complicating how designers consider multiple objectives in the design of sustainable buildings (Broyles, et al., 2022a). Therefore, comprehensive understanding of multi-objective design trade-offs is a critical research field as decarbonization efforts continue in the building sector.

3.6 Conclusion

EC equations for ten concrete floor systems were derived at the conceptual and schematic design stages using polynomial regression models to aid building practitioners towards more sustainable building design decisions. Variations of the EC equations were derived because as the design process progresses, more design information about the geometry and structural parameters is known. The univariate polynomial regression equations for the conceptual design phase enable quick EC estimates of a specific concrete floor system for different spans. Schematic design phase equations were developed to provide a more tailored prediction of the EC of a concrete slab given the variability of concrete mix GWPs and the structural design parameters of concrete strength, live load, dead load, and deflection limit. The predicted range of EC from the slab is then added to the predicted EC contribution of the other structural materials that comprise the concrete floor system to obtain an estimate of the total EC of a concrete floor system. Last, a website application was developed that employs the derived equations, enabling designers to evaluate how early-stage design decisions influence the EC of concrete floors. In summary, the primary contributions of this chapter are easy-to-use equations to estimate the EC of ten concrete floor systems for a broad sampling of potential design scenarios while accounting for the variability of GWP in concrete mixtures for use in the conceptual and schematic design phases. These equations can thus be easily accessed and visualized through an open-source web app and the regression equation coefficients provided in Appendix C.

Chapter 4

EC trade-offs with secondary design objectives for concrete floor systems[1]

4.1 Introduction

To meet national and international initiatives to reduce carbon emissions in the built environment (United Nations, 2015), building engineers and designers are increasingly tasked to find sustainable design strategies (Dixit et al., 2012; Jusselme et al., 2018; Lützkendorf, 2020). As strategies to reduce the carbon emissions of building operations have improved, the reduction of embodied carbon emissions (EC) has been the focus of significant academic and industry research (De Wolf et al., 2017; Kang et al., 2015). Since the structural system of a building is the primary contributor to the EC of a building, the selection of the type of structural load-bearing system is important (Fang et al., 2023b; Li et al., 2014) as structural load-bearing systems comprised of concrete, steel, and wood all have significant and varying EC performance (Cole, 1998; Hart et al., 2021; Lenzen & Treloar, 2002; Venkatarama Reddy & Jagadish, 2003). Concrete structures have been well studied because of the large volume of concrete used in buildings, despite the low energy and carbon footprint of concrete as a construction material (Ashby, 2012; Hammond and Jones, 2008). Outside of water consumption, concrete is the most used construction material and is widely accessible around the world but contributes up to 7% of global carbon emissions (Barcelo et al., 2014). To curb the carbon emissions corresponding to concrete systems, two solutions have been identified: the use of low-carbon concrete mixtures (Long et al., 2015; Marinković et al., 2017; Müller et al., 2014; Van Den Heede & De Belie, 2012) and the implementation of concrete systems that use less concrete material while ensuring structural integrity (Broyles & Hopper, 2023; Huberman et al., 2015; Jayasinghe, et al., 2022a; Jayasinghe et al., 2022b; Olsson et al., 2023). Although the production of low-carbon concrete mixtures

---

[1] Chapter 4 is in preparation for submission to a peer-reviewed journal.

has been progressing in some global markets, this strategy is not widespread and universally implemented today (Liew et al., 2017; Roy D M, 1999). However, the selection of concrete floor systems that use less structural material is a strategy that building designers can employ today.

The strategy of reducing structural material quantity (SMQ) of concrete floor systems without sacrificing the integrity of the structure has existed for many decades. Historical precedents, including the ribbed concrete floors by Pier Luigi Nervi, demonstrate that unconventional floor systems are a solution to reduce concrete material (Halpern et al., 2013). More recently, researchers have explored ways to optimize concrete floor systems, including topology optimized floors (Leschok et al., 2018), shape optimized floors (Ismail & Mueller, 2021), and optimized vaulted floors (Hawkins et al., 2019; Oval et al., 2023). Conventional concrete floor systems can also be designed efficiently to reduce SMQs, by means of strategic column and floor plan layouts (Gauch et al., 2022) and applying additional structural technologies, such as post-tensioning and void formers to reduce concrete material (Broyles & Hopper, 2023). While these studies indicate the potential for large EC savings, the functional equivalence, or the quantitated functional or technical requirements between systems for a basis of comparison (ISO, 2006a, 2006b), has often been restricted to only satisfying structural design considerations. Structures, especially floor systems, not only support structural loads but also contribute to the interior environment and performance within a building (Mata-Falcón et al., 2022). Yet despite the quantity of literature that explored the reduction of SMQ in concrete systems, few studies have expanded the definition of functional equivalence when identifying sustainable conventional and modern concrete floor solutions. Additionally, the inclusion of secondary design objectives may reveal advantages that concrete structures have over structural systems composed of other materials.

Furthermore, it is imperative to select low-carbon design solutions in the early stages of the design process (Häkkinen et al., 2015). As the design process continues, decisions made in the early stages can enable or limit pathways to reduce the EC of a structure (Dunant et al., 2021; Kanyilmaz et al., 2023). This is especially true for concrete structures, as floor system selection can influence EC-related design characteristics including the architectural layout and column grid of a building (Eleftheriadis et al., 2017, 2018; Trinh et al., 2021). Because of the complexity of building design, the bevy of structural design decisions, and the need to consider secondary design objectives, early-stage design guidance for selecting low-carbon concrete floor systems has been limited. These challenges motivate the question: “what concrete floor system(s) is the most material-efficient (lowest EC emissions) when considering both structural performance and secondary design requirements for floors, including fire-resistance, air-borne sound insulation, and walking vibrations?”

In response, this study evaluates how the inclusion of three secondary design objectives (fire-resistance rating, air-borne acoustic insulation, and walking vibration) influence the EC for eight conventional concrete floor systems for different building design scenarios. This study expands the work presented in Ch. 3 with an emphasis on how varying secondary design goals influence the EC and selection of low-carbon concrete floors. Furthermore, six design charts for use in early design stages were developed to aid building designers towards low-carbon concrete floor systems for five building types (office, multi-family residential, hospital, school, and public assembly). This work demonstrates the importance of including secondary design objectives in the definition of functional equivalence when comparing different concrete floor systems to meet sustainable design goals.

4.2 Background

Reinforced concrete (RC) and post-tensioned (PT) concrete floor systems are among the most designed systems because of their structural performance. Because of the importance of minimizing environmental impact, many researchers have evaluated conventional RC and PT concrete structures to determine the most material-efficient, or low-carbon, concrete system. Several researchers have engineered non-traditional, or geometrically optimized, concrete floor systems that improve upon the environmental performance of conventional systems. However, few researchers have fully examined how the influence of additional design objectives affects the EC of concrete structures (Salomao & Pinheiro, 2023).

4.2.1 The influence of secondary design objectives on EC

Reinforced concrete (RC) and post-tensioned (PT) concrete floor systems are among the most designed systems because of their structural performance. Yet, there are inherent benefits to normal-weight concrete floor systems such as fire-resistance (Khoury, 2000), sound attenuation (Hongisto et al., 2015), and vibration performance (Pavic, 2002). Additionally, several concrete floor systems have flat soffits, which enables architectural flexibility for column placement. Furthermore, certain concrete floor systems can have a low floor-to-floor depth compared to other floor systems, providing another architectural benefit in the design of multi-story buildings. Lastly, RC and PT floors can be constructed as cast-in-place slabs to aid demanding construction schedules; however, a construction-related objective is not considered in this study. Concrete floors have a slow heat transfer rate, helping concrete floors contribute to the thermal performance in a building. However, thermal performance is excluded from this study because the interior environmental quality (IEQ) of a building and the climate that the building is geographically located in directly influence the thermal performance of a building.

4.2.1.1 Consideration of fire-resistance in the design of concrete floors

Since the Great Chicago fire in 1871, the fire-resistance performance of a building structure in the U.S. has been a necessary design aspect due to life-safety and property damage implications when not adequately considered (Pauly, 1984). The tragedy motivated many experimental fire tests to ascertain the fire-resistance performance of common structural systems (Babrauskas & Williamson, 1978). The results of the experimental fire tests were then used to inform empirical formulas to estimate fire-resistance performance of a structure without requiring experimentation, ultimately culminating in the development of prescriptive fire-resistance rating guidelines adapted in building codes (Khoury, 2000). Building structural systems composed of concrete and steel were found to have favorable fire-resistance performance (Cowlard et al., 2013; Maraveas et al., 2014). Then in 2001, the attack on the World Trade Center and subsequent fires prompted further assessment of how fire-resistance in buildings is quantified. The development of high-resolution performance-based fire resistance numerical models followed, which account for factors including how the fire is fueled, ventilation in a building, building geometry, and thermal properties of the structural elements and surface finishes (Cowlard et al., 2013; Gross et al., 2010). To accurately ascertain the performance-based fire-resistance performance in multi-story concrete structures, building engineers have to consider additional structural parameters including the depth of the steel reinforcement clear cover, if the steel is corroded, and the type of concrete floor system (e.g., ribbed geometry, hollow-core) (Ba et al., 2019; Fanella et al., 2017; Khoury, 2000; Kovalov et al., 2018).

In sustainable-driven design, the fire-resistance performance should not be neglected in the selection of the optimal concrete floor system. Although Ch. 3 demonstrated that material-efficient concrete floor systems such as ribbed and voided systems are low-carbon concrete floor alternatives compared to a conventional RC flat plate, the loss of concrete material in a floor system causes it to be more susceptible to lower fire-resistance performance. For example, Kovalov et al. (2018) demonstrated the need for a fire-retardant coating on a voided concrete floor to obtain a 4-hr fire rating through experimentation and numerical calculations. While experimental tests are one strategy to validate numerical models that estimate fire-resistance performance of concrete floor systems, there are a variety of concrete floor systems which have varying geometric characteristics and material quantities due to the bevy of different structural design parameters (refer to Ch. 3). Therefore, it is difficult to test each unique floor system design through experimentation. A second strategy are numerical performance-based models, which can accurately estimate fire-resistance performance but require several building-specific assumptions in the calculation of fire rating (Cowlard et al., 2013; Gross et al., 2010).

A third strategy is to find the prescribed fire-resistance rating based on empirical guidelines. Although the determination of fire-resistance rating of a structure using prescribed methods is the least accurate, this method is also the least computationally expensive (Khoury, 2000). Therefore, prescribed fire-resistance ratings can be roughly approximated for a large quantity of different structural systems, as has been investigated for tall mass-timber buildings (Hens et al., 2023; Leonard, 2023; Leonard et al., 2023; Leonard et al., 2024). Obtaining the prescribed fire-resistance rating for different concrete floor systems is more straightforward compared to timber systems as the fire-resistance is primarily a function of the concrete material type and the thickness of the concrete floor system (International Code Council, 2018) and is well-suited for evaluating fire-resistance performance in the early design stages. This strategy can hence be used to quickly obtain the prescribed fire rating for many concrete floor designs.

4.2.1.2 Air-borne sound insulation of conventional concrete floors

Interest in air-borne acoustic insulation grew during the postwar population growth in the U.S. (Mankiw & Weil, 1989). As lightweight residential buildings were constructed to meet the housing demands, acoustic insulation complaints were prominent (Northwood, 1964). Because of the connection between the acoustic IEQ in a building and potential health consequence to tenants (Andargie et al., 2023; Rasmussen, 2010), studies explored how well different structural assemblies fared for minimizing acoustic transmission and consistently found that conventional concrete flat plates were among the most favorable for sound insulation (Clark, 1970; Dupree, 1980; Northwood, 1962; Warnock, 2005). Furthermore, as structures composed of wood and steel required additional material layers to meet air-borne acoustic building code requirements, concrete floors with a depth of ~150 mm (6 in) were satisfactory without any additional treatments (Dupree, 1980).

While conventional concrete plates (i.e., RC flat plates) have known air-borne acoustic insulation performance, the performance of alternative concrete floor systems is less known. Experimental studies of conventional concrete floor systems typically limited the evaluation to RC flat plates and did not consider alternative floor systems. While the experimental findings can help inform similar rectilinear geometries, the tested acoustic performance of floor systems with large ribs and void formers is less known (Fanella et al., 2017). Therefore, the effects of different geometric configurations and varying concrete material properties on the air-borne acoustic insulation of conventional concrete floor systems are similarly not well known (Fediuk et al., 2021). However, it is well known that structural-acoustic characteristics such as the mass density and flexural rigidity can directly influences acoustic insulation (Concrete Reinforcing Steel Institute, 2016; Rindel, 2018), as such, the sound transmission loss of a structure, and subsequent air-borne sound insulation performance, can be reasonably obtained using analytical models (Mak & Wang, 2015). Broyles et al. (2022c) used an analytical expression to quantify air-borne sound insulation of shaped ribbed floors to find that different floor geometries can meaningfully affect the air-borne acoustic insulation rating. However, little design guidance exists when considering the breadth of different concrete floor systems in selecting a low-carbon concrete floor system while ensuring favorable air-borne acoustic insulation.

4.2.1.3 Walking vibration requirements for conventional concrete floors

Similar to air-borne acoustic insulation, conventional concrete floors perform well when designed to satisfy walking vibration requirements in buildings because of the inherent mass density and flexural rigidity of conventional concrete floors (Concrete Reinforcing Steel Institute, 2016). However, a study by Oh et al. (2019), found that human-induced floor vibrations can result in an increase of 8.9% EC emissions depending on the building design scenario. Furthermore, concrete floor systems with less weight (e.g., voided slabs) can be more susceptible to floor vibrations compared to conventional RC flat plates (Caballero-Garatachea et al., 2021; Liu et al., 2020). Although U.S. building codes do not specify walking vibration requirements, floor vibration problems can worsen the IEQ and potentially lead to failure (Concrete Reinforcing Steel Institute, 2016; Mouring & Ellingwood, 1994).

While the dynamic response of a concrete floor system can be ascertained experimentally, numerical models are more commonly implemented. Finite element models (FEMs) are one numerical strategy to determine if a concrete floor system can satisfy walking vibrations (Liu et al., 2020; Pavic et al., 2001). The dynamic response obtained from an FEM can be compared against the criteria set by Design Guide 11, which quantifies vibration requirements based on different building types and dynamic response conditions (Murray et al., 2016). Another approach is to analytically obtain the dynamic response from a human walking on a floor. The Concrete Reinforcing Steel Institute (CRSI) published a design guide to determine the vibrations for multiple concrete floor systems (Fanella & Mota, 2014) and found that the analytical equations were within a 10% difference from the responses obtained by an equivalent FEM. Therefore, different concrete floor systems can be roughly assessed for walking vibration performance, even when considering various geometries and structural design parameters to evaluate how walking vibrations can influence the selection of the low-carbon concrete floor system.

4.2.2 Chapter scope

This chapter investigates how the inclusion of fire-resistance, air-borne sound transmission, and walking vibrations influences the selection of low-carbon concrete floor systems. Eight conventional concrete floor systems are evaluated for structural performance (using the same structural parameters as was used in Ch. 3), with the SMQs obtained for each design to calculate the cradle-to-gate EC emissions of the floor system. This study evaluates the objectives for different design scenario cases, with varying design performance goals corresponding to the building use type. The results of this study inform the development of multi-objective design charts for identifying low-carbon and material-efficient concrete floor systems for various building design scenarios, with application in early design stages. This study ultimately contributes to the growing amount of literature aimed at reducing carbon emissions in the built environment with the novelty of this work focused on how building engineers should balance secondary design objectives that compete with intentions of reducing EC in a concrete floor system.

4.3 Methods

4.3.1 Concrete floor systems, structural design, and analysis

This study focused on eight different concrete floor systems, as illustrated in Fig. **4-1**:

1. RC flat plate;
2. RC one-way pan joist slab with beams;
3. RC two-way slab with beams;
4. RC two-way module joist waffle slab;
5. RC voided plate;
6. PT flat plate with banded-uniform tendons;
7. PT voided plate with orthogonal banded-banded tendons; and
8. PT voided with diagonal banded-banded tendons.

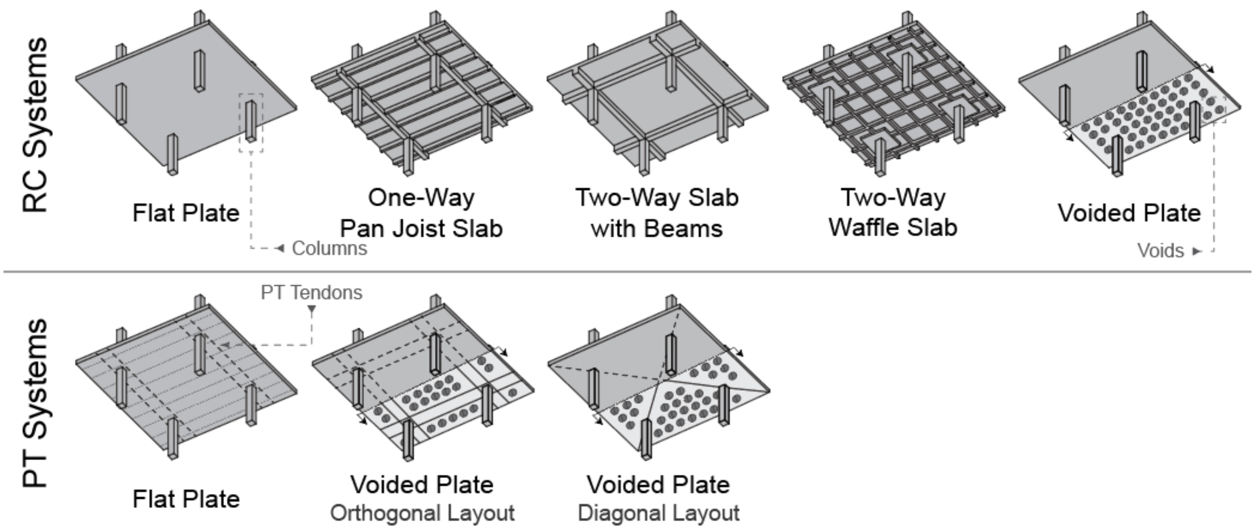

Figure **4-1**: The eight concrete floor systems evaluated in this study.

The eight concrete floor systems considered is not a comprehensive list of all possible floor types but is representative of existing floor systems that have been designed for many centuries (e.g., RC flat plates) to more modern systems (PT voided plates). The variety of floor systems also shows variation in concrete SMQs due to geometric differences (e.g., ribbed), and the addition of other structural materials (e.g., void formers and PT tendons) used to construct the concrete floor system.

The structural design and analysis of each system follows the same structural methodologies and equations as Ch. 3, which are provided in Appendix B. Likewise, the same structural design parameters were evaluated in this study (see Table **4-1**). All concrete floor systems were evaluated as 3 bay by 3 bay floors with an equivalent span length in the x- and y-directions (i.e., square bays). The span length ranged from 3 m to 15 m (approximately 10 ft to 50 ft).

Table **4-1**: The design scenarios evaluated for the concrete floor systems.

Concrete Compressive Strength in MPa (psi)		**Applied Live Load in kN/m² (psf)**		**Applied Dead Load in kN/m² (psf)**		**Long-term Deflection Limit**
20.7 (3,000)	31.0 (4,500)	1.915 (40)	4.788 (100)	0.239 (5)	1.197 (25)	$\Delta < L/240$
24.1 (3,500)	34.5 (5,000)	2.394 (50)	5.985 (125)	0.479 (10)	1.436 (30)	$\Delta < L/360$
27.6 (4,000)	41.4 (6,000)	2.873 (60)	7.182 (150)	0.718 (15)	1.676 (35)	$\Delta < L/480$
		3.830 (80)		0.958 (20)	1.915 (40)	

Using the geometric (span length) and structural design parameters, this study simulated 41,328 different design scenarios for each of the five RC concrete systems and 27,552 different design scenarios for each of the three PT concrete systems. The RC systems were designed for all strengths, but the PT systems were not designed for strengths lower than 27.6 MPa, reflective of PT design practices. The SMQs that satisfied the strength and serviceability limit states according to the appropriate ACI 318 (ACI Committee 318, 2019a) provisions were obtained for each design scenario. The steel reinforcement was designed according to the distributed design moments at different locations in the floor (Foraboschi, 2019). The number of bars that satisfied the bending moment was obtained for every nominal U.S. rebar size between a #4 bar (with a diameter of 12.7 mm, or 0.5 in) to a #10 bar (with a diameter of 32.3 mm, or 1.27 in, after which the lowest total area of steel was selected and used in the EC calculation. The steel rebar was arranged at locations of maximum positive and negative bending moments, following typical U.S. design practices.

4.3.2 Determination of the prescribed fire-resistance rating

The prescriptive fire-resistance method was used to determine the corresponding fire-resistance rating for each unique concrete floor system design. The prescriptive fire-resistance is based on the guidelines provided in Sec. 722.2 in the International Building Code (IBC) (2018). As shown in Table 4-2, knowledge of the concrete material type and floor thickness gives a fire-resistance rating. Five code-specified fire-resistance ratings are considered: 1-hr, 1.5-hr, 2-hr, 3-hr, and 4-hr. Although thicker slabs may have longer fire-resistance performance, only the five prescribed fire ratings specified were considered. This study conservatively assumed that the concrete aggregate type is siliceous because it is the most common type and has the most stringent thickness requirements, however, it should be noted that alternative concrete types can be designed as thinner slabs while satisfying fire-resistant design (see Sec. 4.4.1).

Table **4-2**: Minimum slab thicknesses for prescribed fire resistance for concrete floors according to the IBC, Table 722.2.2.1 (2018).

Concrete Type	Minimum Slab Thickness for Prescribed Fire-Resistance Rating				
	Required Thickness in mm (in) for 1-hr	Required Thickness in mm (in) for 1.5-hr	Required Thickness in mm (in) for 2-hr	Required Thickness in mm (in) for 3-hr	Required Thickness in mm (in) for 4-hr
Siliceous	88.9 (3.5)	109.2 (4.3)	127 (5)	157.5 (6.2)	177.8 (7)
Carbonate	81.3 (3.2)	101.6 (4)	116.8 (4.6)	144.8(5.7)	167.6 (6.6)
Sand-lightweight	68.6 (2.7)	83.8 (3.3)	96.5 (3.8)	116.8 (4.6)	137.2 (5.4)
Lightweight	63.5 (2.5)	78.7 (3.1)	91.4 (3.6)	111.8 (4.4)	129.5 (5.1)

The thickness used in the determination of the prescribed fire-resistance ratings varies for each type of concrete floor system. The thickness used to determine the fire-resistance rating for the RC and PT flat plates is only the depth of the slab. The thickness used to determine the fire-resistance rating for the RC and PT voided plates is based on the equivalent thickness of the floor to account for the void formers in the slab. Eq. **4-1** shows the simple calculation to determine the equivalent thickness, h_{eq}, based on the normalized concrete volume displacement, h_{cx}, for a voided concrete floor system (Fanella et al., 2018).

$$h_{eq} = h - h_{cx} \quad \text{(Equation 4-1)}$$

For the floor systems with ribbed soffits (RC one-way pan joist slab and the RC two-way waffle slab) and the RC two-way slab with beams, the thickness is determined in accordance to the equations provided in IBC 722.2.2.1.3. Based on the schematic shown in Fig. **4-2**, the thickness of the slabs is determined by one of the following expressions which considers the spacing of the ribs, s, and the minimum thickness of the slab, t. If $s > 4t$, then the thickness used to obtain the fire rating is the minimum thickness of the slab. If $s \leq 2t$, then the thickness used to obtain the fire rating is the equivalent thickness of the slab, calculated as the net area of the slab divided by the width, in which the maximum thickness does not exceed $2t$ (see Fig. **4-2**). Lastly, if $4t > s > 2t$, the thickness shall be obtained using the equation:

$$t + \left(\frac{4t}{s} - 1\right)(t_e - t) \qquad \text{(Equation 4-2)}$$

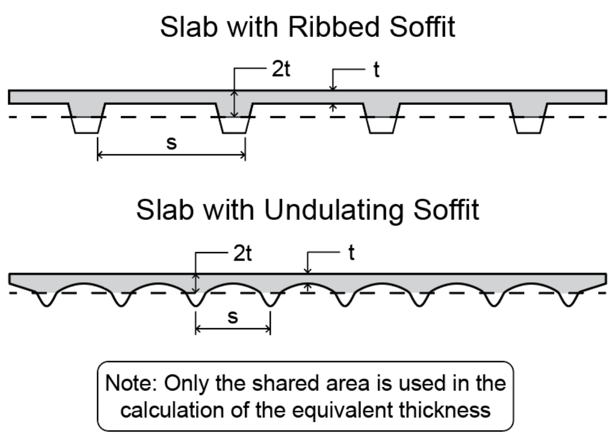

Figure **4-2**: Method for calculating the equivalent thickness of slabs with ribbed and undulating soffits following IBC 722.2.2.1.3 (2018).

The steel reinforcement must meet a minimum clear cover. In this study, it is assumed that the clear cover is at least 38 mm (1.5 in) for RC floor systems and at least 51 mm (2 in) for PT floor systems. Note that the clear covers may fluctuate for each unique design as higher fire-resistance ratings require slightly larger covers. Of note, concrete columns were considered out of the scope of this work and were not considered in the design of the prescribed fire-resistance of the floor system.

4.3.3 Approximation of air-borne sound transmission performance

An analytical approximation was used in determining the air-borne sound insulation of each unique concrete floor design. The air-borne acoustic insulation metric of Sound Transmission Class (STC), which is a North American metric that truncates the transmission loss (TL) performance across 16 one-third octave bands into a single integer value (ASTM E413, 2016; Northwood, 1962) was used in this study. The calculation of the acoustic performance assumed normal room conditions (i.e., c_0 = 343 m/s, ρ_0 = 1.29 kg/m^3). The density of the non-stressed and the pre-stressed steel reinforcement was assumed to be 7,850 kg/m^3. The density of the concrete, ρ_c, was assumed to be 2,400 kg/m^3 with a Poisson's ratio, ν, of 0.20. Because of the different concrete strengths considered in the study, the Modulus of Elasticity of the concrete, E_c, varied, and was determined using:

$$E_c = 4700\sqrt{f_c'} \qquad \text{(Equation 4-3)}$$

The flexural rigidity, D, of the concrete floors varied due to the geometric changes of each system. Table **4-3** reports the equations to calculate the flexural rigidity for each system, which are a function of the geometric and material characteristics. The modulus of elasticity of the floor system, E, was taken as the weighted average of the moduli for each structural material (e.g., E_c, E_s) based on their corresponding volume within the floor system. For the floor systems with a ribbed soffit, the moment of inertia (I) and the spacing of the rib (Δ_{Rib}) are determined by the rib geometry while the top slab height (h) is determined by the slab depth. Similar to the prescriptive fire rating method, the equivalent thickness is used to find the flexural rigidity of the voided floor systems.

Table **4-3**: The bending stiffness equations for the concrete floor systems.

Concrete Floor System(s)	**Flexural Rigidity Equation**
RC Flat Plate, PT Flat Plate	$D = \dfrac{Eh^3}{12(1-\nu^2)}$
RC One-Way Slab	$D = \dfrac{Eh^3}{12(1-\nu^2)} + \dfrac{EI}{\Delta_{Rib}} + \dfrac{EI}{\Delta_{Girder}}$
RC Two-Way Slab (Waffle slab and slab with beams)	$D = \dfrac{Eh^3}{12(1-\nu^2)} + \dfrac{EI}{\Delta_{Rib_x}} + \dfrac{EI}{\Delta_{Rib_y}}$
RC Voided Plate, PT Voided Plate (Orthogonal and Diagonal PT tendon layouts)	$D = \dfrac{E{h_{eq}}^3}{12(1-\nu^2)}$

Equations **4-4** and **4-5** describe how the TL data was obtained by calculating the transmission coefficient (τ). The frequency range evaluated was from 100 Hz to 5 kHz at a 1 Hz interval, which was used to determine the angular frequency (ω) and the wavenumbers (k_0). It should be noted an angle of incidence (φ) range was considered from 0° to 78° (Leppington et al., 1987), at 1° intervals. The area density (m) was determined by dividing the total mass of the floor by the area.

$$\tau(\varphi,\omega) = \frac{\left(\frac{2\rho_0 c_0}{sin\varphi}\right)^2}{\left(\frac{2\rho_0 c_0}{sin\varphi}+\eta\left(\frac{D}{\omega}\right)(k_0 sin\varphi)^4\right)^2+\left(\omega m-\left(\frac{D}{\omega}\right)(k_0 sin\varphi)^4\right)^2} \quad \text{(Equation 4-4)}$$

$$TL = 10\log_{10}\left(\frac{1}{\tau}\right) \quad \text{(Equation 4-5)}$$

The TL was calculated for each one-third octave (OTO) band from 125 Hz to 4 kHz to approximate the STC rating of the concrete floor. Table **4-4** relates different STC rating levels to the air-borne acoustic insulation of the concrete floor system. Although the TL at different frequencies can be compared, only the STC rating is assessed in comparison to the other design objectives in this study.

Table **4-4**: Various air-borne acoustic insulation performance goals based on IBC (2018) and Long (2005).

Performance Criterion	Sound Transmission Class (STC) Rating
Meets Minimum IBC Code Requirement	STC-50
Good Acoustic Performance	STC-55
Great Acoustic Performance	STC-60

4.3.4 Analytical calculation to assess walking vibration criteria

In this study, the walking vibration criteria were analytically evaluated in accordance with the CRSI vibration design guide (2014) and considered the following assumptions. The mass of the person walking on the floor is 71.2 kg (157 lbs). A vibration live load of 0.527 kN/m^2 (11 psf) was also assumed, as is recommended when assessing concrete floors for walking vibration criteria (Fanella & Mota, 2014). The damping ratio, β, was 0.03, which is a conservative assumption (Fanella & Mota, 2014), however, specific building scenarios could have different damping ratios.

The analytical vibration analysis for all the concrete floor systems had followed a similar procedure, as shown in Fig. **4-3**. First, the structural design parameters were defined, including the material properties of the concrete (refer to Sec. 4.3.1). Second, a structural design and analysis was performed (see Sec. 4.3.1 and Appendix B), followed by the calculation of the effective moments of inertia (see Appendix B). Next the deflection contributions from the joists and girders were found for the RC one-way pan joist floor, and the crack coefficients, k_1 and k_2, were determined for all other floor systems. Then the natural frequency, f_n, and effective floor weight, W, was found for the design, using the equations provided in Table **4-5**. Lastly, the walking acceptance criterion, a_p/g, for walking excitation of floor systems was checked using Equation **4-6**. It should be noted that although other floor harmonics will cause additional steady-state vibrations at their forcing frequencies, their contribution to the total dynamic response (vibration performance) is considered to be negligible in this study. Additionally, cracking was not considered, thereby the assessment of walking vibrations in RC and PT systems is the same.

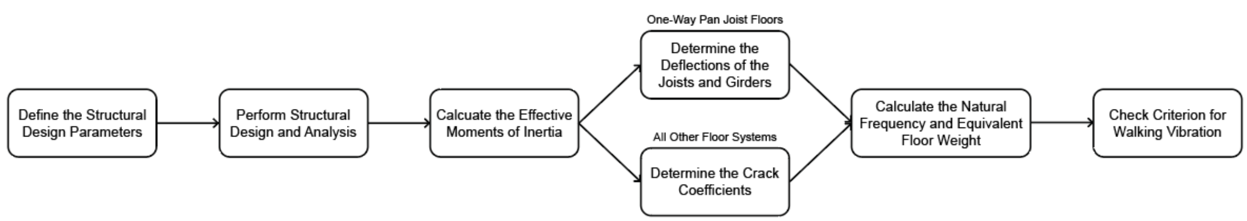

Figure **4-3**: Design process for evaluating the walking vibration performance of a concrete floor system.

Table **4-5**: The analytical natural frequency equations for the concrete floor systems.

Concrete Floor System(s)	**Fundamental Frequency Equation**
RC Flat Plate, RC Two-Way Slab with Beams, RC Two-Way Waffle Slab, RC Voided Plate, PT Flat Plate, PT Voided Plate (Orthogonal and Diagonal PT tendon layouts)	$f_n = \frac{k_2 \lambda_1^2}{2\pi L^2}\left[\frac{k_1 E_c h^3}{12\gamma(1-\nu^2)}\right]^{1/2}$
RC One-Way Slab	$f_n = 0.18\sqrt{\frac{g}{\Delta_j + \Delta_g}} = \frac{3.54}{\sqrt{\Delta_j + \Delta_g}}$

Notes: γ is the mass density of the floor system. The constant λ_1^2 equals 7.12 since the span length is equivalent in the orthogonal directions. The constant k_2 is 1.9 for floors with a column width less than or equal to ~600 mm (24 in), or 2.1 for floors with a column width greater than ~600 mm (24 in). Δ_j and Δ_g are the instantaneous mid-span deflections of the joists (or beams) and girders relative to their supports.

$$\frac{a_p}{g} = \frac{65e^{-0.35fn}}{\beta W} \leq \frac{a_0}{g} \quad \text{(Equation 4-6)}$$

The perception of floor vibrations differs across the natural frequency of the floor system, therefore the fundamental frequency of each floor system design must be found and plotted against the peak acceleration experienced from on the system (see Fig. **4-4**). If the acceleration to gravity of the floor system is found to be below the threshold corresponding to the building use type, then the floor system is sufficiently designed for walking vibrations.

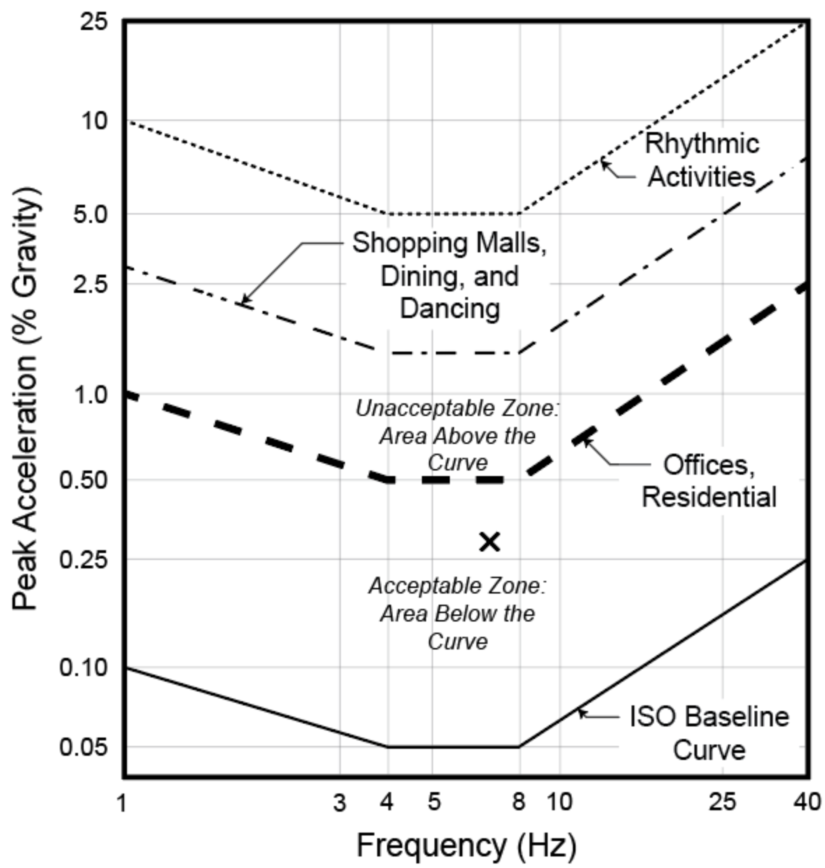

Figure **4-4**: Peak acceleration curves for various building use types and vibration criteria, after the floor vibration design guide (Fanella & Mota, 2014).

4.3.5 Cradle-to-gate life cycle assessment

A cradle-to-gate (i.e., A1-A3) life cycle assessment (LCA) was performed for each design based on the geometric and material characteristics to determine the EC for each floor system, as was similarly done in Ch. 3. The LCA was conducted according to ISO standards 14040 (2006) and 14044 (2006). The declared unit was set as 1 m^2, so that the floor systems can be compared fairly despite differences in span length. The purpose of this study considers how the addition of prescribed fire-resistance, air-borne acoustic insulation, and walking vibrations influence the definition of functional equivalence for a concrete floor system designed to satisfy structural design code (ACI Committee 318, 2019), as shown in Fig. **4-5**. Different combinations of design objectives are considered to explore the nuances of minimizing concrete material while meeting additional performance goals.

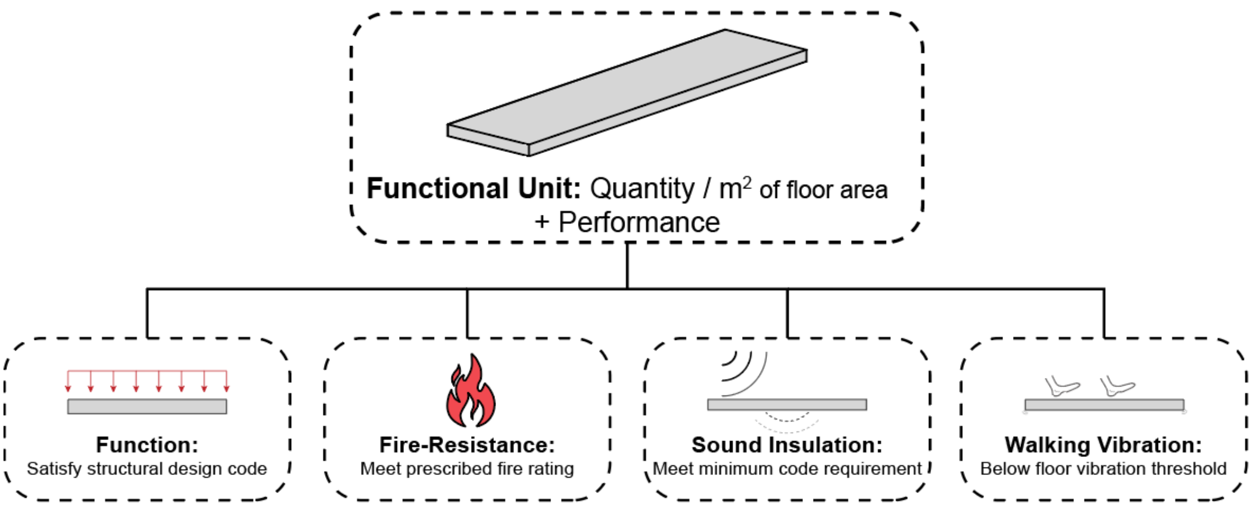

Figure **4-5**: The functional unit of the concrete floor systems.

Table **4-6** reports the GWP intensities for the six concrete strength classes used in this study, which follows the values used in Ch. 3 and were obtained from U.S. Environmental Product Declarations of ready-mixed concrete mixtures (for details, see Appendix A). Table **4-6** provides the GWP intensities for the three additional structural materials (steel rebar, PT tendons, and void formers), which are typical industry values (Cobiax, 2018; Concrete Reinforcing Steel Institute, 2022). The values are obtained from U.S. EPDs, though similar values from EPDs in other geographic regions around the world can be obtained. An important note is that there is not a U.S. industry standard EPD for PT tendons; therefore, this study conservatively estimated the EC of PT tendons based on a 100% increase of the GWP reported for non-prestressed steel reinforcement, as was similarly done by Miller et al. (2015).

Table **4-6**: The GWPs for different concrete strength classes and other structural materials.

Structural Material		GWP Intensity
Concrete	Concrete Compressive Strength in MPa (psi)	
	20.7 (3,000)	303 kg CO_2e/m^3
	24.1 (3,500)	320 kg CO_2e/m^3
	27.6 (4,000)	345 kg CO_2e/m^3
	31.0 (4,500)	365 kg CO_2e/m^3
	34.5 (5,000)	386 kg CO_2e/m^3
	41.4 (6,000)	403 kg CO_2e/m^3
Non-Prestressed Steel Reinforcement		0.854 kg CO_2e/kg
Steel Post-Tension Tendons		1.708 kg CO_2e/kg
Recycled Void Formers (Plastic Bubbles)		10.5 kg CO_2e/m^3

4.4 Results and discussion

4.4.1 EC and fire-resistance rating

The relationship between minimizing EC emissions while achieving high fire-resistance ratings lies at the intersection of the floor thickness and concrete mixture type. Fig. **4-6** demonstrates this relationship for the four concrete mixture types in Table **4-2**. When comparing the four concrete mixture types for an equivalent GWP intensity of concrete (345 kgCO_2e), it is clear that the siliceous concrete which has the largest thickness requirements, is the worst performing. Yet when accounting for how GWP intensities can vary for the four concrete mixture types (Siliceous: 345 kgCO_2e, Carbonate: 376 kgCO_2e, Sand: 362 kgCO_2e, Lightweight: 690 kgCO_2e), the lightweight concrete is the worst due to the much larger corresponding GWP. This figure reveals the complications when considering alternative concrete mixture types and implies that the combination of a low GWP intensity and minimum slab thickness requirement provides the optimal strategy for reducing EC emissions and achieving different fire ratings. However, this study conservatively concentrates on siliceous concrete as it is the most used mixture type, with the following graphics reflective of the slab thickness requirements for siliceous concrete.

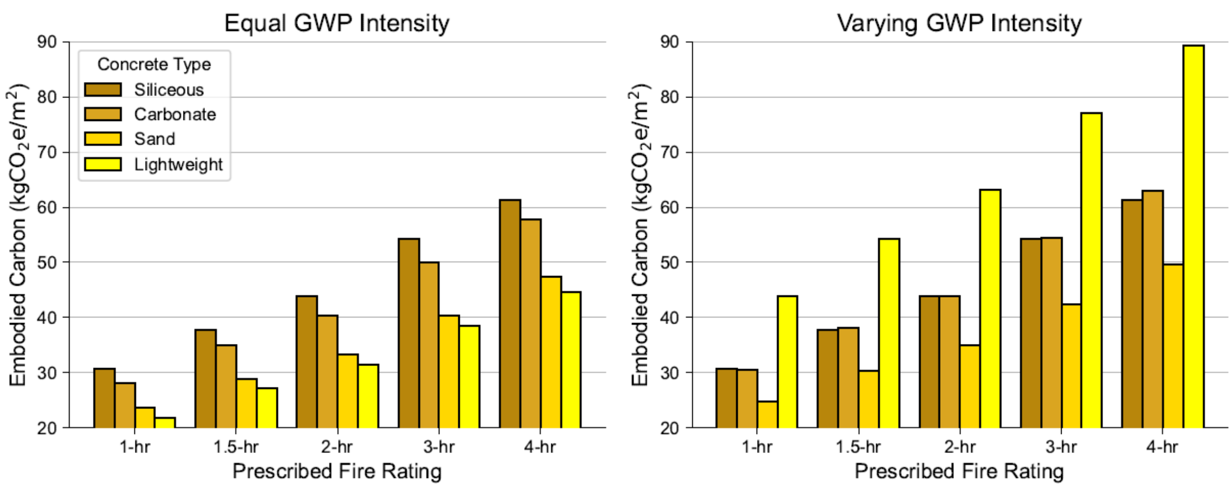

Figure **4-6**: Difference in EC emissions for the four different concrete mixture types for the five prescribed fire ratings given their prescribed minimum concrete floor thicknesses.

In the assessment of prescriptive fire-resistance rating, all structural design scenarios were first simulated to identify how the structural limit states controlled the thickness and corresponding fire resistance. Because the slabs are designed to minimize EC emissions, the structural design and analysis consisted of finding the thinnest floor depth possible while satisfying the structural limit states and was then rated for fire-resistance performance. The percentage and number of floor designs that could satisfy the structural limit states by minimizing floor thickness and corresponding prescribed fire-resistance rating is presented in Table **4-7**. Table **4-7** reveals that the floor systems with the ribbed soffits and the RC two-way slab with beams, could achieve all five fire ratings for the majority of the possible structural design scenarios. This is because these floor systems can be designed for thin floor depths for many structural design parameters because the ribs take the structural design loads. Additionally, the ribs are spaced too far apart for these systems to get any thickness benefits when determining the fire-rating. This directly affected the RC two-way slab with beams, as almost every design scenario could be designed for each fire rating, indicating that the fire-rating can significantly influence the selection of these floor systems. On the other hand, RC and PT flat plates had a low percentage of design scenarios that could meet the worst fire ratings, as satisfying structural limit states were found to control the structural design, requiring thicker floor depths. Due to the minimum thickness requirements of voided concrete plates, the RC and PT voided plates could not be designed for a fire-resistance rating below 2-hrs. A final observation is that of the floor systems with a flat soffit, PT voided plates had the most design scenarios influenced by prescriptive fire rating, indicating that stringent fire rating requirements can influence the thickness and corresponding EC of these systems.

Table **4-7**: Percentage (top) and number (bottom) of structural design scenarios that could achieve each fire rating.

	Prescribed Fire-Resistance Rating				
Floor System	**≥1-hr**	**≥1.5-hr**	**≥2-hr**	**≥3-hr**	**≥4-hr**
RC Flat Plate	100% *50,017*	99.4% *49,722*	97.0% *48,497*	90.6% *45,337*	82.6% *41,328*
RC One-Way Slab	100% *152,913*	82.9% *126,716*	65.2% *99,766*	46.3% *70,826*	27.0% *41,328*
RC Two-Way Waffle Slab	100% *199,775*	81.0% *161,788*	61.5% *122,854*	41.2% *82,251*	20.7% *41,328*
RC Two-Way Slab with Beams	100% *135,202*	92.3% *124,802*	77.3% *104,506*	54.1% *73,163*	30.6% *41,328*
RC Voided Plate	100% *58,062*	100% *58,062*	100% *58,062*	86.7% *50,359*	71.2% *41,328*
PT Flat Plate	100% *48,429*	96.6% *46,774*	88.6% *42,889*	73.7% *35,686*	56.9% *27,552*
PT Voided Plate – Orthogonal Layout	100% *50,010*	100% *50,010*	100% *50,010*	79.4% *39,688*	55.1% *27,552*
PT Voided Plate – Diagonal Layout	100% *51,299*	100% *51,299*	100% *51,299*	79.8% *40,911*	53.7% *27,552*

Since the eight concrete floor systems had different amounts of design scenarios that achieved each of the five prescribed fire-resistance ratings, the influence that fire rating had on the EC of the floor system differed significantly. For example, the RC one-way slab had at least 41,328 designs that satisfied each of the five fire ratings, resulting in a distribution of EC values (see Fig. **4-7**). The EC trendlines, which are the average EC at a specific span length for the different fire ratings, more clearly shows that the defined fire-resistance rating can influence the EC up until a span length near 12 m, at which the structural limit states dictate the design of the floor system (i.e., the slab has to be thick to satisfy the structural limit states, thereby having a favorable fire rating). The distributions of EC for the five fire-resistance ratings and the corresponding EC trendlines are shown for all eight floors in Figs. **4-8** and **4-9**, with the general relationship between EC and different fire ratings shown in Fig. **4-8** and the composite EC fire-rating trendlines shown in Fig. **4-9**.

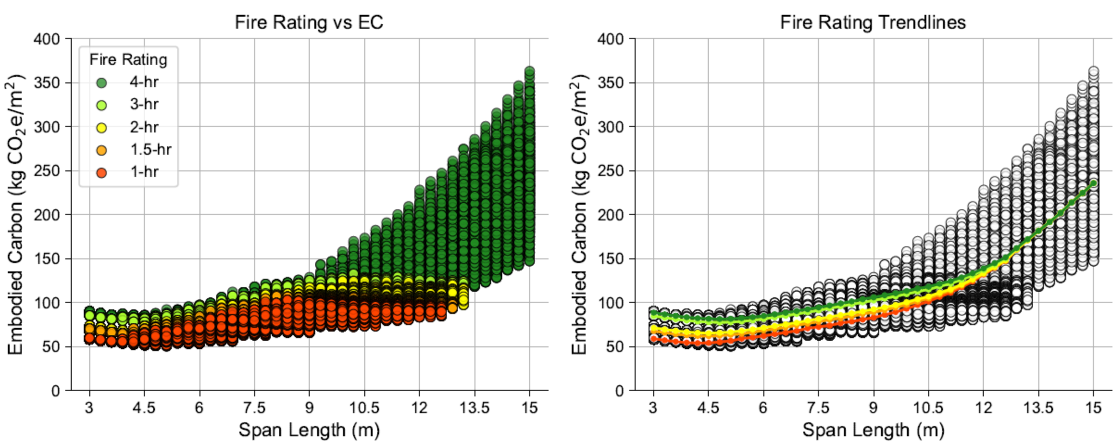

Figure **4-7**: The influence of the prescribed fire-resistance rating on the EC for an RC one-way slab.

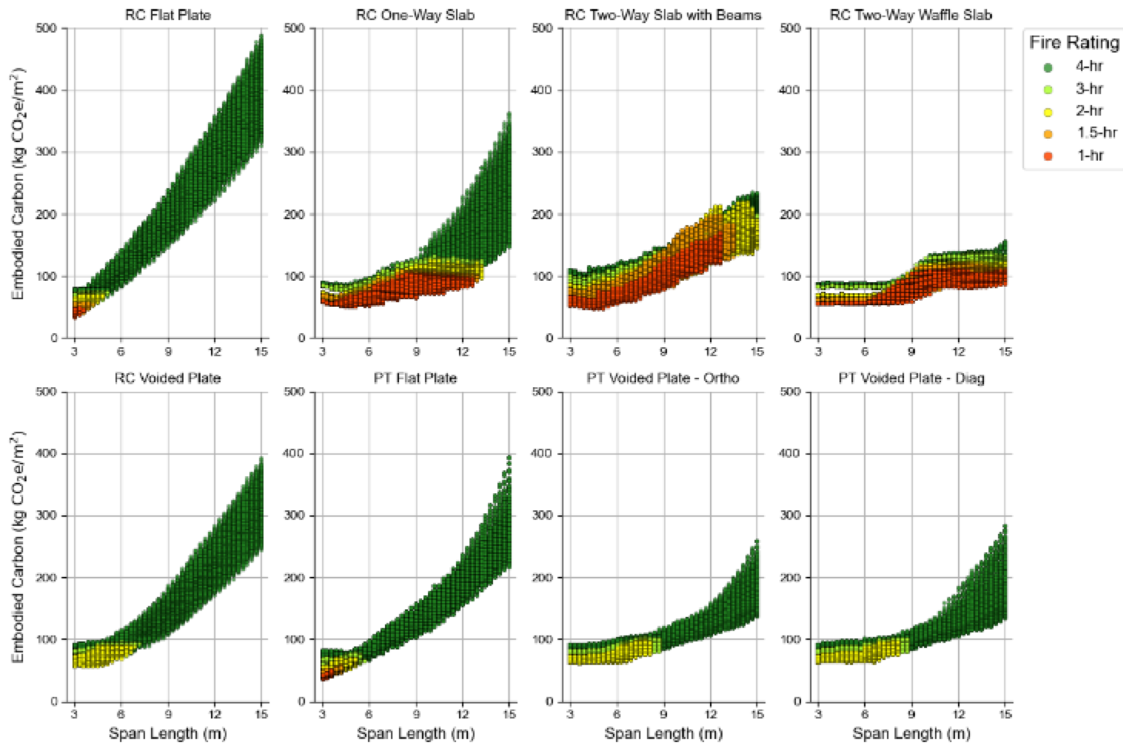

Figure **4-8**: The distribution of EC emissions for the five fire ratings for all eight concrete floor systems.

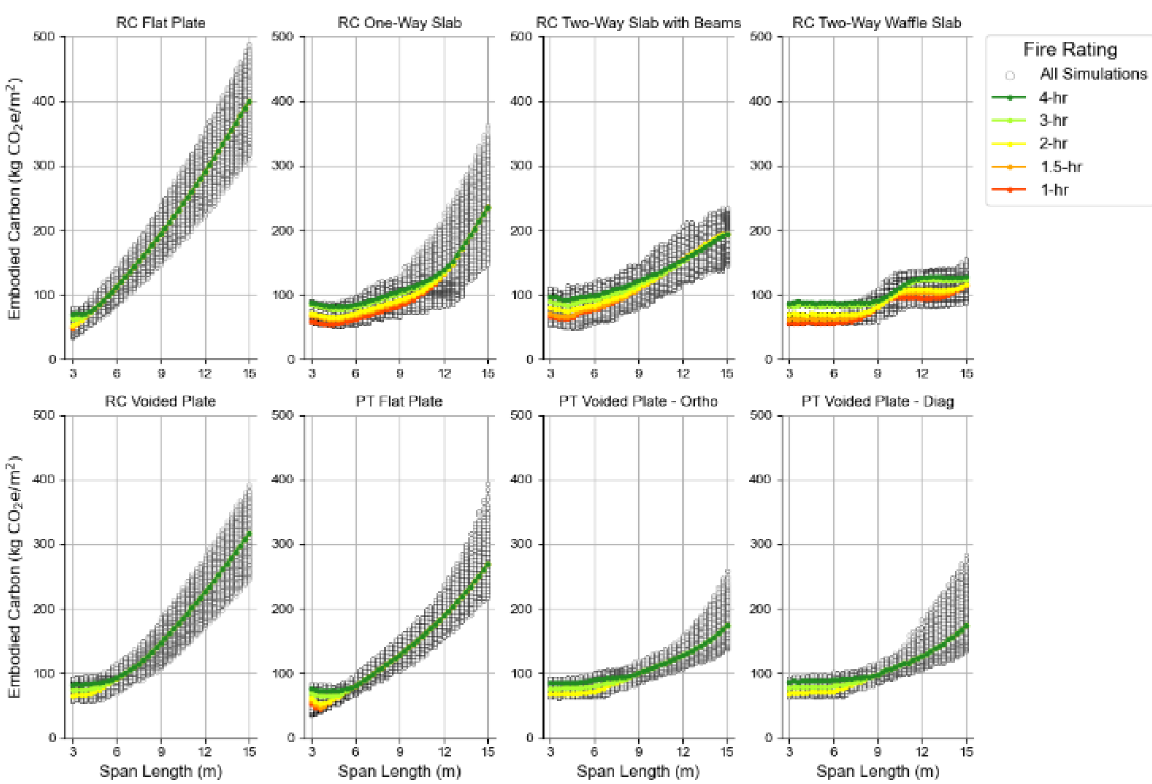

Figure **4-9**: The EC trendlines for the five fire ratings for the eight concrete floor systems.

Figs. **4-8** and **4-9** reinforce the finding of Table **4-7** that concrete floor systems with ribbed soffits are the most influenced by the prescribed fire rating, with the RC two-way waffle slab as the most affected system. The RC flat plate, RC voided plate, and PT flat plate are only affected by varying fire-resistance ratings below a span length of 6 m, while both PT voided plates are influenced by the prescribed fire rating up to a span length of 9 m. This reveals the intuitive trade-off that at low span lengths, when structural limit states are less likely to control, the design of a floor system and consequent EC is more susceptible to fire rating requirements. Yet as the span length increases, causing the structural demand on the floor system to increase, fewer design scenarios are influenced by the slab thickness requirements to meet different fire-ratings. Table **4-8** confirms this by quantifying how the EC is influenced at different spans. The prescribed fire-resistance ratings are shown to influence the EC emissions up to 54.5% for a span length at or below 9 m. However, only the ribbed floor systems and the RC two-way slab with beams are affected by fire rating for span lengths greater than 9 m with decreasing percentage differences as the span length increases.

Table **4-8**: The EC emissions and percentage difference for each fire-resistance rating trendline for all concrete systems. The percentage differences are taken between the lowest and highest fire rating observed for each floor system.

Concrete Floor System	**Fire Rating (hr)**	**Span Length (m)**								
		3	**4.5**	**6**	**7.5**	**9**	**10.5**	**12**	**13.5**	**15**
RC Flat Plate	1	48.7	78.3	112.7	151.9	194.6	240.7	290.4	343.9	400.0
	1.5	49.6 *+1.71%*	78.3 *+0%*	112.7 *+0%*	151.9 *+0%*	194.6 *+0%*	240.7 *+0%*	290.4 *+0%*	343.9 *+0%*	400.0 *+0%*
	2	52.4 *+7.61%*	78.3 *+0%*	112.7 *+0%*	151.9 *+0%*	194.6 *+0%*	240.7 *+0%*	290.4 *+0%*	343.9 *+0%*	400.0 *+0%*
	3	62.8 *+28.9%*	78.4 *+0.22%*	112.7 *+0%*	151.9 *+0%*	194.6 *+0%*	240.7 *+0%*	290.4 *+0%*	343.9 *+0%*	400.0 *+0%*
	4	69.5 *+42.6%*	79.2 *+1.21%*	112.7 *+0%*	151.9 *+0%*	194.6 *+0%*	240.7 *+0%*	290.4 *+0%*	343.9 *+0%*	400.0 *+0%*
RC One-Way Slab	1	59.1	54.4	62.2	72.5	83.2	101.6	132.0	181.7	235.9
	1.5	67.8 *+14.8%*	61.9 *+13.9%*	68.7 *+10.4%*	78.4 *+8.21%*	89.2 *+7.32%*	104.9 *+3.22%*	132.8 *+0.61%*	181.7 *+0%*	235.9 *+0%*
	2	71.4 *+20.9%*	65.4 *+20.3%*	71.6 *+15.1%*	81.7 *+12.7%*	92.6 *+11.4%*	107.1 *+5.33%*	133.6 *+1.22%*	181.7 *+0%*	235.9 *+0%*
	3	85.0 *+43.7%*	77.9 *+43.3%*	81.6 *+31.2%*	91.3 *+25.9%*	102.6 *+23.4%*	115.2 *+13.3%*	137.1 *+3.91%*	181.7 *+0%*	235.9 *+0%*

Concrete Floor System	Fire Rating (hr)	Span Length (m)								
		3	4.5	6	7.5	9	10.5	12	13.5	15
	4	88.8 *+50.2%*	81.7 *+50.3%*	85.1 *+36.8%*	94.6 *+30.5%*	106.1 *+27.6%*	118.1 *+16.2%*	139.0 *+5.31%*	181.7 *+0%*	235.9 *+0%*
RC Two-Way Slab with Beams	1	66.9	64.4	76.9	91.4	110.0	130.3	132.0	173.6	193.2
	1.5	71.2 *+6.42%*	67.8 *+5.34%*	78.9 *+2.66%*	92.5 *+1.14%*	111.5 *+1.28%*	130.4 *+0.28%*	150.9 *+0.10%*	173.6 *+0%*	193.2 *+0%*
	2	80.3 *+20.1%*	77.3 *+20.1%*	84.2 *+9.51%*	96.5 *+5.54%*	111.8 *+1.65%*	130.5 *+0.86%*	151.0 *+0.23%*	173.6 *+0%*	193.2 *+0%*
	3	89.8 *+34.3%*	86.0 *+33.5%*	92.4 *+20.1%*	103.5 *+13.2%*	116.8 *+6.21%*	132.3 *+2.50%*	151.8 *+1.80%*	174.3 +1.6%	193.4 *+0.4%*
	4	97.0 *+45.0%*	93.6 *+45.4%*	98.9 *+28.6%*	109.4 *+19.7%*	121.9 *+10.8%*	136.3 *+3.49%*	153.9 *+2.45%*	174.5 +1.8%	193.5 *+0.5%*
RC Two-Way Waffle Slab	1	56.2	56.9	56.7	61.3	81.3	96.4	94.8	97.8	114.6
	1.5	62.4 *+11.0%*	63.0 *+10.8%*	63.5 *+12.1%*	66.0 *+7.65%*	81.0 *+0.28%*	102.4 *+6.19%*	103.5 *+9.19%*	103.1 *+5.%*	115.2 *+0.%*
	2	69.3 *+23.2%*	71.2 *+25.1%*	68.8 *+21.5%*	70.2 *+14.5%*	81.8 *+0.59%*	104.2 *+8.13%*	108.0 *+13.9%*	106.5 *+8.%*	116.1 *+1.%*
	3	82.8 *+47.3%*	83.5 *+46.8%*	83.7 *+47.7%*	84.2 *+37.3%*	89.2 *+9.75%*	109.6 *+13.7%*	122.9 *+29.6%*	122.6 *+25%*	124.0 *+8.1%*
	4	86.7 *+54.1%*	87.3 *+53.6%*	87.5 *+54.5%*	88.0 *+43.5%*	91.9 *+13.1%*	110.7 *+14.8%*	126.3 *+33.2%*	127.2 *+30%*	127.5 *+11.%*
RC Voided Plate	2	65.7	71.8	92.0	114.6	146.9	184.9	226.1	169.9	316.6
	3	74.0 *+12.6%*	77.6 *+8.10%*	92.4 *+0.43%*	114.6 *+0%*	146.9 *+0%*	184.9 *+0%*	226.1 *+0%*	269.9 *+0%*	316.6 *+0%*
	4	82.2 *+25.1%*	84.9 *+18.4%*	93.4 *+1.48%*	114.6 *+0%*	146.9 *+0%*	184.9 *+0%*	226.1 *+0%*	269.9 *+0%*	316.6 *+0%*
PT Flat Plate	1	53.9	60.3	80.7	104.6	128.7	157.1	189.6	226.7	269.9
	1.5	57.8 *+7.41%*	60.3 *+0%*	80.7 *+0%*	104.6 *+0%*	128.7 *+0%*	157.1 *+0%*	189.6 *+0%*	226.7 *+0%*	269.9 *+0%*
	2	62.0 *+15.1%*	60.3 *+0%*	80.7 *+0%*	104.6 *+0%*	128.7 *+0%*	157.1 *+0%*	189.6 *+0%*	226.7 *+0%*	269.9 *+0%*
	3	69.3 *+28.7%*	65.7 *+8.95%*	80.7 *+0%*	104.6 *+0%*	128.7 *+0%*	157.1 *+0%*	189.6 *+0%*	226.7 *+0%*	269.9 *+0%*
	4	75.7 *+40.6%*	72.8 *+20.7%*	80.7 *+0%*	104.6 *+0%*	128.7 *+0%*	157.1 *+0%*	189.6 *+0%*	226.7 *+0%*	269.9 *+0%*
PT Voided Plate (Ortho.)	2	68.0	68.7	72.2	86.0	100.1	113.7	128.0	146.7	173.7
	3	76.6 *+12.7%*	77.3 *+12.5%*	80.7 *+11.6%*	88.1 *+2.42%*	100.1 *+0%*	113.7 *+0%*	128.0 *+0%*	146.7 *+0%*	173.7 *+0%*
	4	85.2 *+25.3%*	85.9 *+25.1%*	89.2 *+23.5%*	93.1 *+8.26%*	100.1 *+0%*	113.7 *+0%*	128.0 *+0%*	146.7 *+0%*	173.7 *+0%*
PT Voided	2	68.9	71.0	72.2	85.2	98.3	113.0	127.0	145.7	174.9
	3	77.5 *+12.5%*	79.6 *+12.1%*	80.6 *+11.6%*	87.2 *+2.31%*	98.3 *+0%*	113.0 *+0%*	127.0 *+0%*	145.7 *+0%*	174.9 *+0%*

Concrete Floor System	Fire Rating (hr)	Span Length (m)								
		3	4.5	6	7.5	9	10.5	12	13.5	15
Plate (Diag.)	4	86.1 *+25.0%*	88.2 *+24.3%*	89.2 *+23.5%*	92.3 *+8.37%*	98.3 *+0%*	113.0 *+0%*	127.0 *+0%*	145.7 *+0%*	174.9 *+0%*

4.4.2 EC and air-borne sound insulation

The relationship between EC emissions and the analytically obtained air-borne sound insulation performance is slightly more nuanced than the trade-off between prescribed fire rating and EC. Sound attenuation is directly influenced by the mass density and the flexural rigidity of the concrete floor systems. Therefore, the various geometric characteristics (e.g., top slab, ribs) and material properties (e.g., concrete strength class which effects the modulus of elasticity) result in wide distributions of sound transmission performance, quantified by the STC rating, for the concrete systems as shown in Fig. **4-10**. These results indicate that the RC flat plate is the preferred floor system above a span length of 6 m when high air-borne sound insulation (a high STC rating) is desired. The ribbed floor systems had the greatest STC distribution across the span lengths, indicating how the rib dimensions can meaningfully benefit or worsen air-borne acoustic performance. The PT floor systems have the smallest distribution of STC rating likely due to the smaller range of thicknesses needed to satisfy the structural limit states.

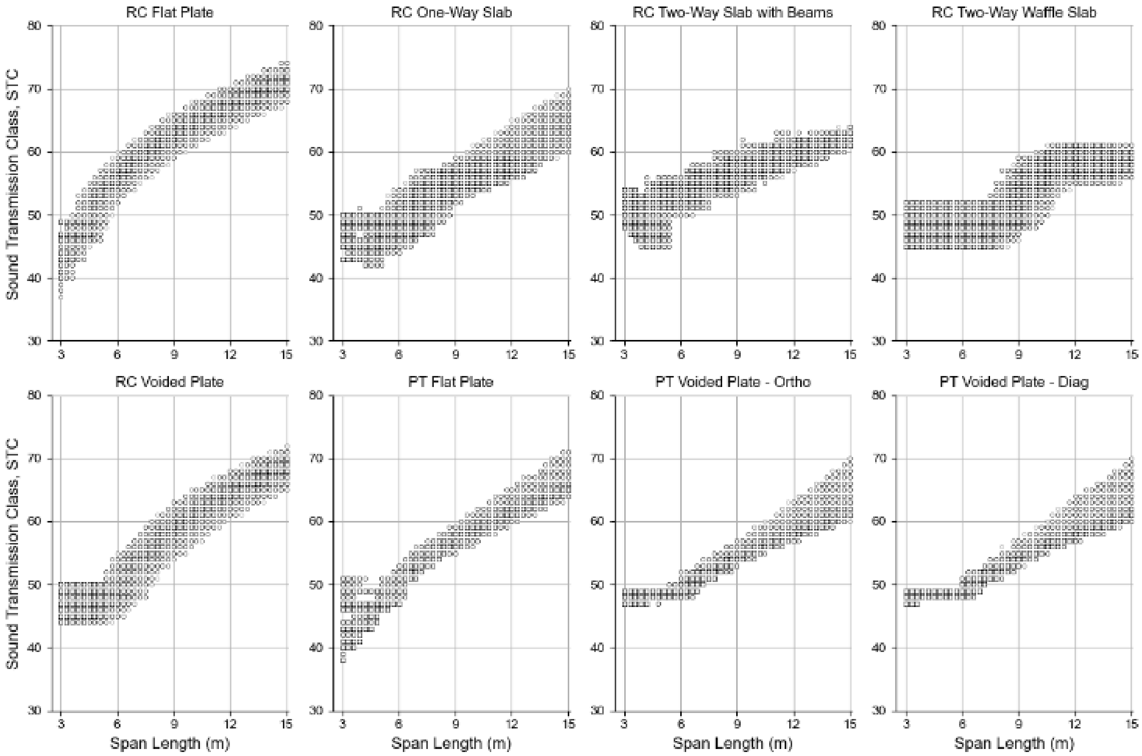

Figure **4-10**: The relationship between STC ratings and span length, showing that as the span increases, the STC rating increases.

As shown in Fig. 4-**10**, the spread of STC ratings is influenced by the span length; however, Fig. **4-11** reveals the trade-off between EC emissions and the STC rating for the eight concrete floor systems. While the relationship between span length and STC rating is more linear, the relationship between EC and STC rating is more quadratic, emphasizing that there is a balancing relationship between EC and STC. The findings of Fig. **4-11** can help reveal the concrete floor designs that perform well for both EC and STC, as several different designs are observed as non-dominated for both objectives in all eight floor systems. Furthermore, there are noticeable "knee" points, where increases to the STC rating require more EC emissions, except for the RC two-way slab with beams and the RC two-way waffle slab. The RC two-way waffle slab does not have a clear knee point, but also has the smallest spread of STC ratings. On the other hand, the RC one-way slab has a range of STC ratings from STC-42 to STC-70 with many different geometries having low EC emissions and STC ratings up to STC-57, with higher STC ratings possible at the expense of increasing the corresponding EC emissions of the floor.

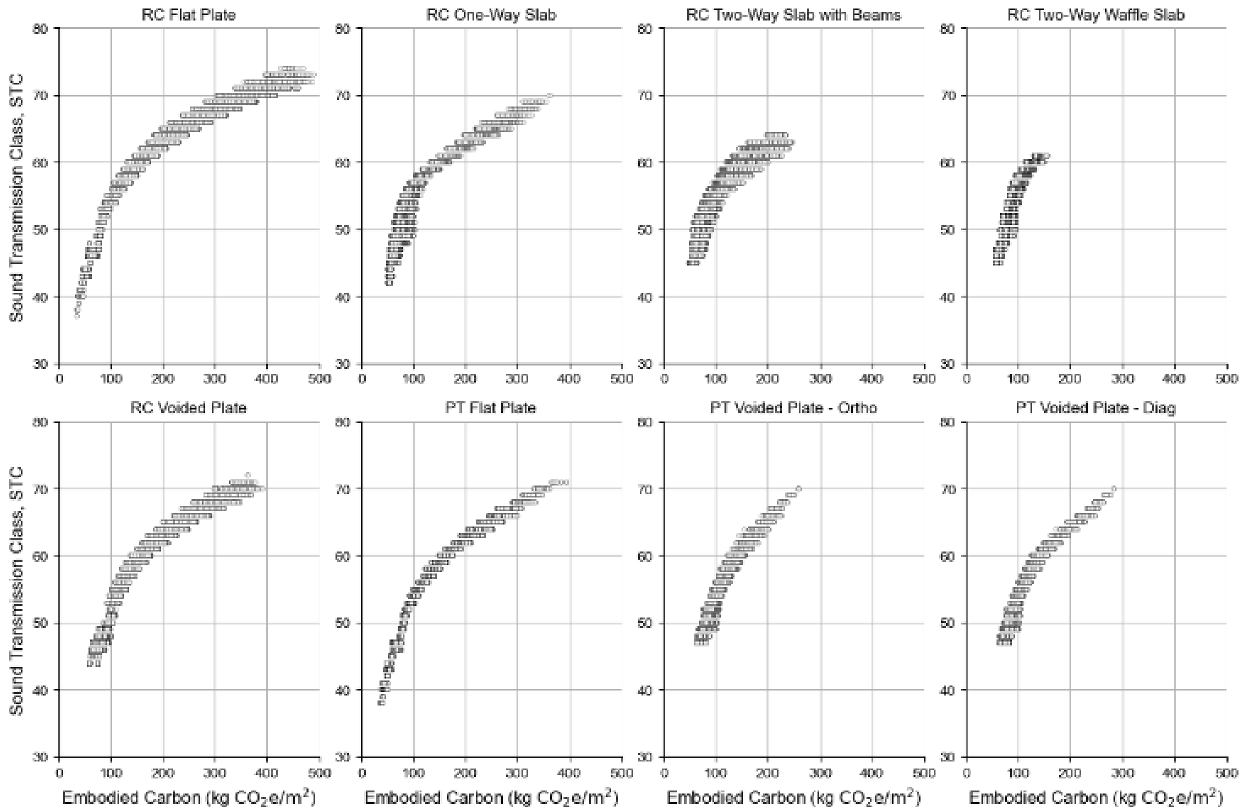

Figure **4-11**: The trade-off between minimizing EC emissions and achieving high air-borne acoustic insulation for the eight concrete floor systems.

4.4.3 EC and floor vibrations

In the assessment of walking vibrations, only the RC two-way slab with beams had designs that failed the vibration criterion. Specifically, the RC two-way slab with beams geometries with a slab thickness between 89 mm (3.5 in) to 127 mm (5 in) at long span lengths (above 9 m) were susceptible to vibration problems. Notably, these designs can only achieve low fire-resistance ratings (1-hr and 1.5-hr) and do not meet the minimum IBC requirement of an STC rating of 50. Although the ribbed one-way and two-way slabs also have thin slabs, those floor systems have ribs that provide additional flexural rigidity to stiffen the floor against walking vibrations.

While the assessment of walking vibrations found that most concrete floor systems do not need geometric alterations to satisfy vibration criteria (i.e., the structural limit states control and thereby satisfy vibration requirements), the analytically obtained natural frequency of the floors was found to be directly correlated to the span length and mass density of the concrete floor system as seen in Fig. **4-12**. Aside from the RC two-way slab with beams, all concrete floor systems have a natural frequency above 4 Hz, further indicating that they are less susceptible to vibration problems as below 4 Hz (and especially below 2 Hz) are frequencies that can cause vibration problems. This can help inform building engineers and designers when considering other vibration issues, such as rhythmic vibrations, as these results reveal what floor systems inherently have higher natural frequencies by satisfying the structural limit states.

A clear relationship exists between the span length and natural frequency of a floor system; however, the trade-off between EC emissions and natural frequency is less clear (see Fig. **4-13)** as the natural frequency generally decreases with more EC. This effect is likely caused by the wider distributions of EC at longer span lengths, which coincides with lower natural frequencies. The results from the walking vibration analysis demonstrate that longer span lengths can be more susceptible to walking vibration, yet the concrete floor thicknesses required to satisfy the structural limit states typically prevents the structure from failing vibration criteria. In design scenarios that have stringent vibration requirements, the results presented indicate that prioritizing short span lengths or designing thicker concrete floor systems reduces the risk of vibration problems.

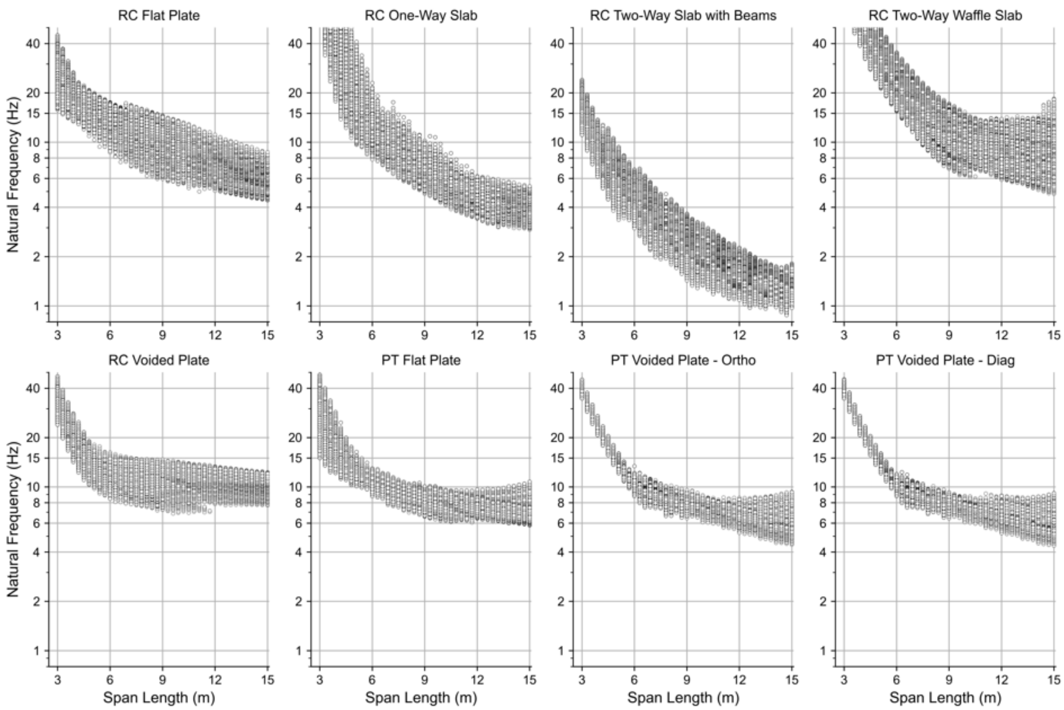

Figure **4-12**: The relationship between the span length and the natural frequency of the floor systems.

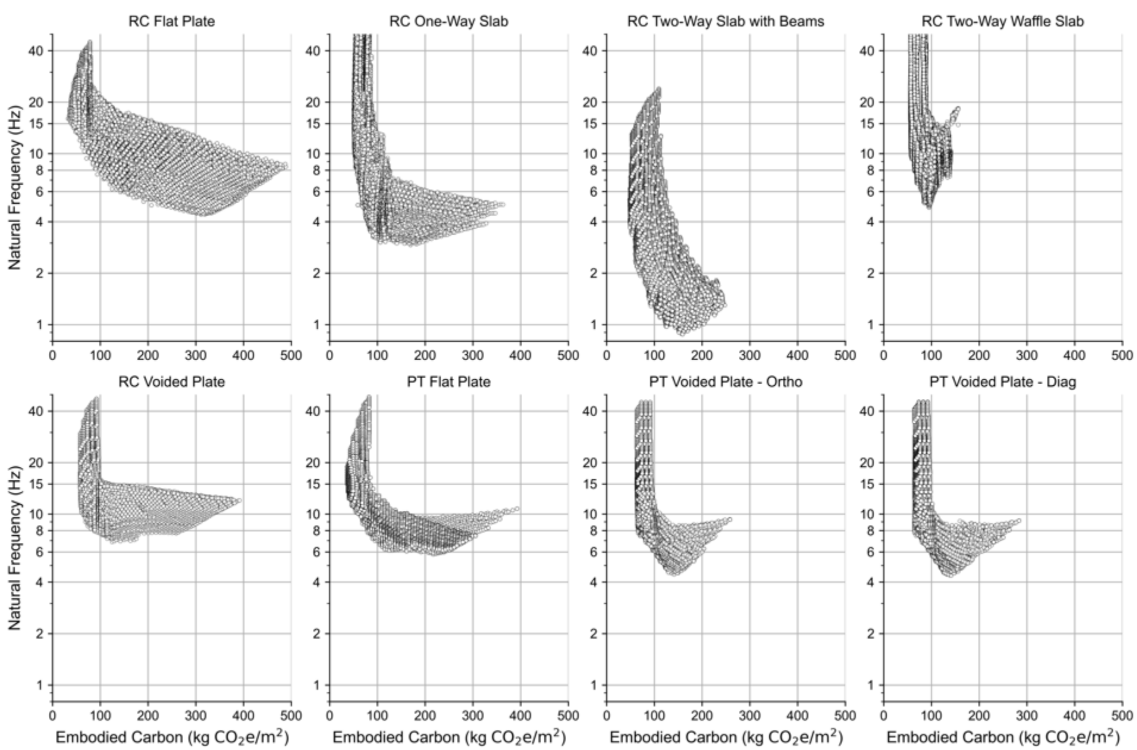

Figure **4-13**: The relationship between the EC emissions and the natural frequency of the floor systems.

4.4.4 EC and all secondary objectives

The figures in the proceeding subsections help illustrate how prescribed fire-resistance rating, air-borne acoustic attenuation, and walking vibrations, can each individually influence the EC emissions for the eight concrete floors. However, it is often necessary to consider multiple design objectives in the selection of a low-carbon concrete floor system. Fig. **4-14** shows a parallelaxis plot when evaluating all eight floor systems against EC and the three secondary objectives, in addition to the total floor depth and the natural frequency of the floor. It is evident that the relationship between reducing EC emissions and achieving favorable performance for secondary objectives is complex. Despite the complexities, one important observation is that the floor designs with the lowest EC emissions (below 50 kgCO_2e/m^2) have lower fire-resistance ratings (1-hr to 2-hr ratings) and STC ratings (STC-37 to STC-63) compared to floor systems with slightly higher EC. However, further design guidance is needed to provide more clarity on which floor system is preferable when balancing these design objectives.

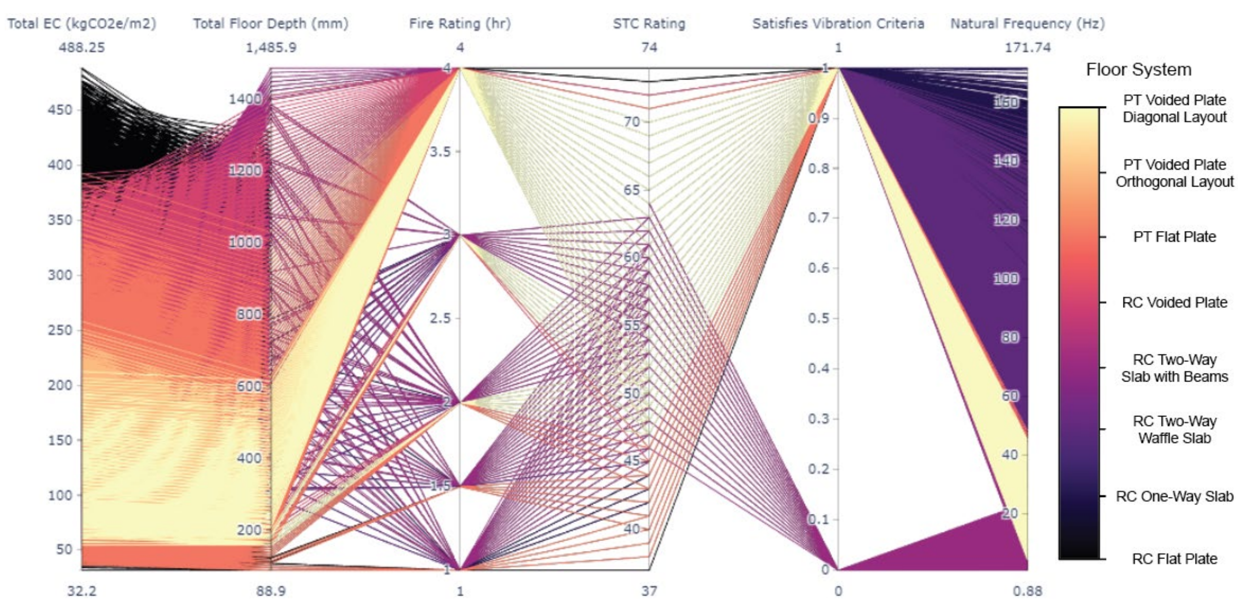

Figure **4-14**: The relationship between EC emissions and the secondary design objectives.

4.4.5 Early-stage design charts to inform low-carbon selection of concrete floors

As illustrated in Fig. **4-14**, it is difficult to determine which concrete floor system(s) are the best performing for different design scenarios. Like Ch. 3, design guidance appropriate in early design stages can improve the selection of a low-carbon concrete floor system while considering different floor systems and design parameters. However, including the performance of secondary design objectives in multivariate regression models can significantly complicate the regression models used in Ch. 3, limiting their accuracy and implementation in design practice. Therefore, this chapter proposes the creation of design charts based on the simulated results to identify low-carbon concrete floor systems given six different design scenarios. These design charts are intended to act as a complement to the multivariate polynomial regression equations in Ch. 3, especially when considering the fire-resistance, air-borne acoustic insulation, and walking vibrations performance of bare concrete floors. For example, building designers and engineers can use these charts first to search for a low-carbon concrete floor system(s) given multiple design performance criteria and then refine the EC estimate using the schematic design equations derived in Ch. 3.

Six different design scenarios (cases) are investigated, with the specific structural and building design scenarios provided in Table **4-9**. The six cases broadly represent different building requirements that floor systems need to be designed to. The live loads specified are representative of the design loads corresponding to the building use type, as specified in ASCE 7-16 Table 4.3-1. The superimposed dead loads are typical to the building use types, as residential and office buildings would have lower dead load compared to medical, educational and public assembly buildings which would likely support larger mechanical ducts and floor toppings. All of the design scenarios are designed for a long-term deflection limit of $L/360$ except for the medical building, which would likely have a more stringent requirement because of sensitive medical equipment susceptible to floor deflections. The prescribed minimum fire rating and air-borne sound insulation ratings for the six cases can vary, but the defined ratings align with higher performance requirements expected for those building types (refer to Table **3-2** in Ch. 3 for more details).

Table **4-9**: The building and structural design parameters for each design scenario case.

Design Scenario	Structural Live Load in kN/m^2 (psf)	Superimposed Dead Load in kN/m^2 (psf)	Deflection Limit	Minimum Fire Rating	Minimum STC Rating	Corresponding Figure
Case A: Typical Multi-Unit Residential Building	1.915 (40)	0.479 (10)	Δ < L/360	≥ 2-hr	≥ STC-50	Fig. **4-15**
Case B: High-End Multi-Unit Residential Building	1.915 (40)	0.718 (15)	Δ < L/360	≥2-hr	≥ STC-60	Fig. **4-16**
Case C: Office Building	4.788 (100)	0.718 (15)	Δ < L/360	≥2-hr	≥ STC-50	Fig. **4-17**
Case D: Medical Building	3.830 (80)	0.958 (20)	Δ < L/480	≥3-hr	≥ STC-55	Fig. **4-18**
Case E: Educational Building	4.788 (100)	0.958 (20)	Δ < L/360	≥2-hr	≥ STC-55	Fig. **4-19**
Case F: Public Assembly Building	7.182 (150)	1.436 (30)	Δ < L/360	≥4-hr	≥ STC-50	Fig. **4-20**

The following figures (Figs. **4-15** to **4-20**) identify the low-carbon concrete floor system for each of the six cases defined above. These design chart identify the concrete floor system that has the lowest EC or concrete SMQ at each span length for the given design scenario defined in Table **4-9**. The design charts are provided in both the total EC of a floor system (i.e., includes the EC contributions from the concrete, steel rebar, void formers, and PT tendons as applicable) and in the volume (SMQ) of concrete in the floor system. The EC design charts represent the average EC value at each span length that satisfies the design requirements for the given design scenario. The SMQ charts similarly find the average concrete volume in the floor system, but do not consider the EC contributions of the additional structural materials in the system. This is because the SMQ design charts are intended to be multiplied by a GWP value specific to a concrete mix (refer to Equation **3-1**): this enables a more accurate EC estimate of the concrete floor system. A designer can refer to Fig. **3-9** in Ch. 3 to estimate the percent contribution to the total EC from the other structural materials to obtain a more tailored estimate of the total EC of a floor system. Note that the "Mix" label in the design charts means that multiple floor systems (or a mix of systems) are viable low-carbon design solutions. Error bars that represent the standard deviation for each combination of floor system and design scenario are also provided to help visualize the variability of EC emissions and concrete SMQs for each design scenario. Therefore, small error bars communicate a smaller distribution of EC emissions and concrete SMQs while large error bars communicate a larger distribution.

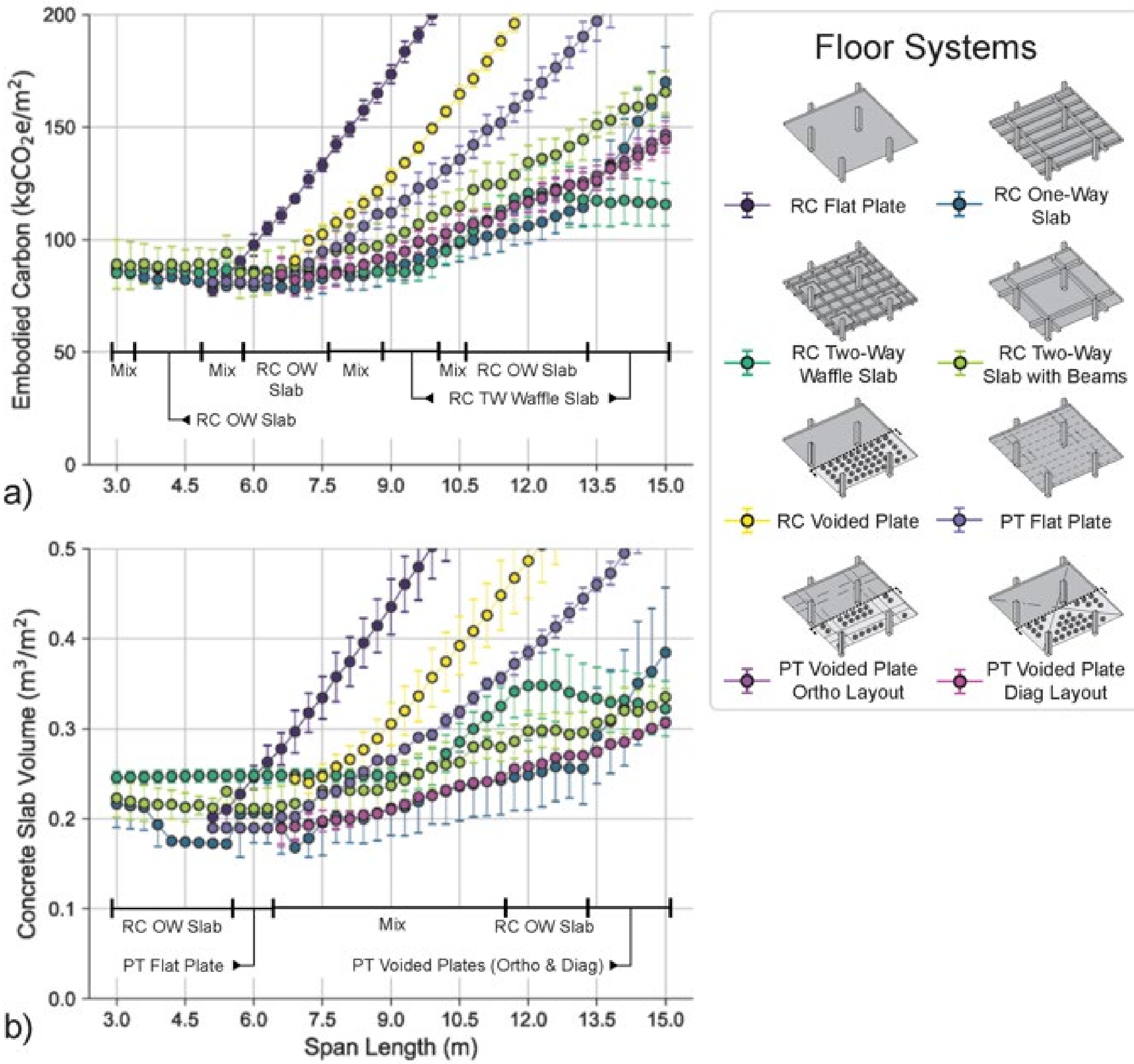

Figure **4-15**: Design charts for a typical multi-unit residential building displaying the concrete floor system(s) with the lowest a) EC and b) concrete SMQs across different spans.

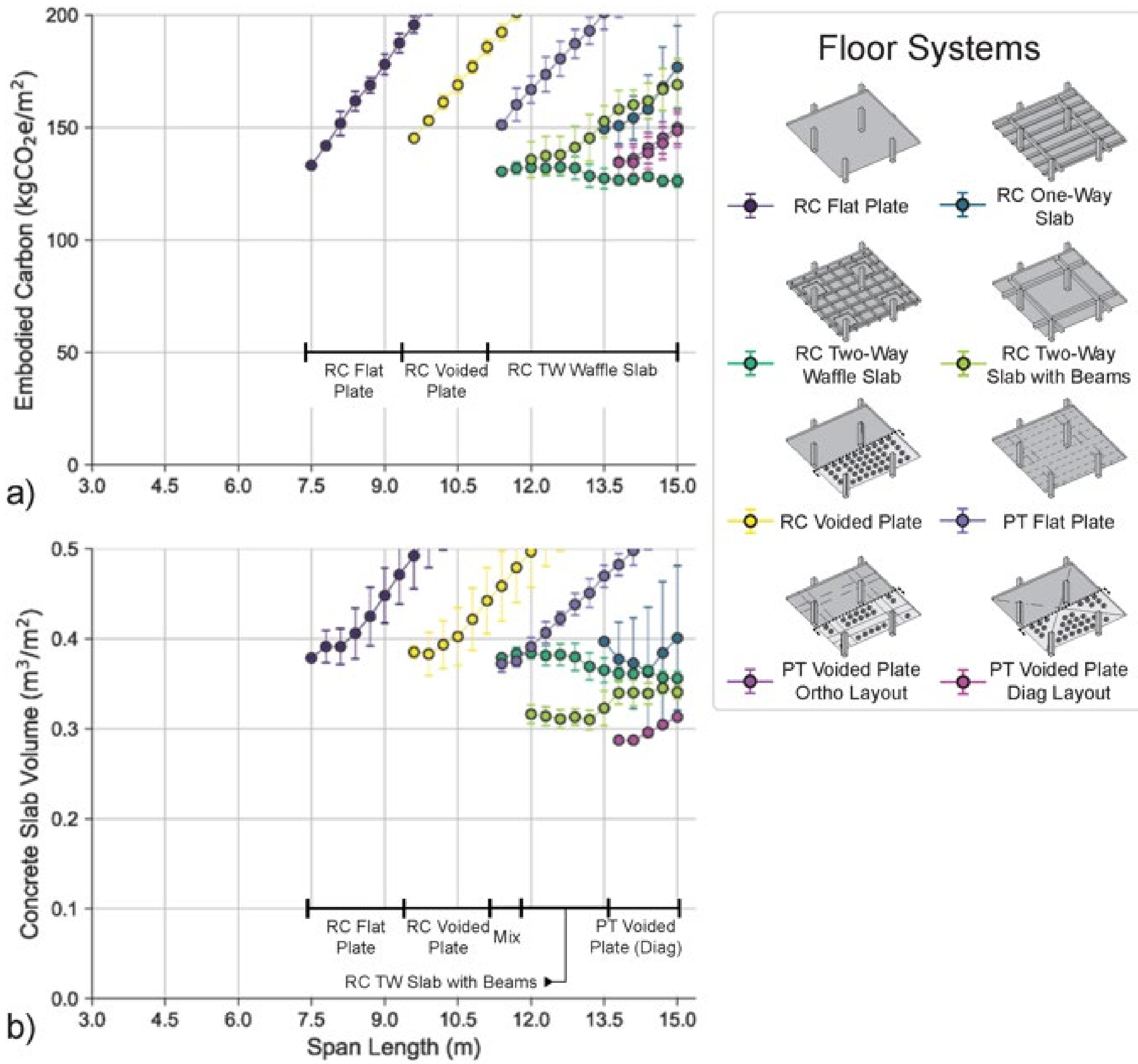

Figure **4-16**: Design charts for a high-end multi-unit residential building displaying the concrete floor system(s) with the lowest a) EC and b) concrete SMQs across different spans.

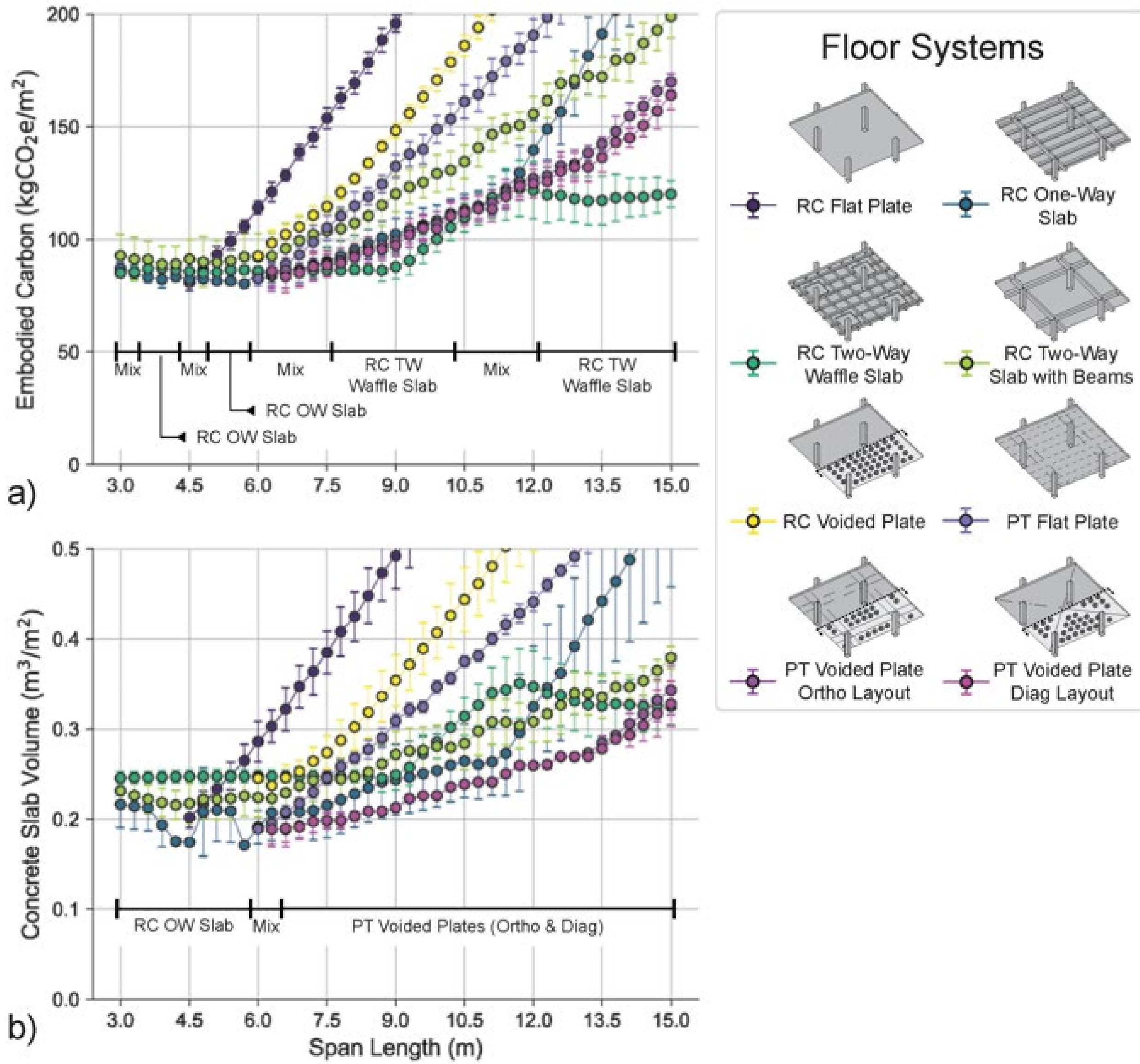

Figure **4-17**: Design charts for a multi-story office building displaying the concrete floor system(s) with the lowest a) EC and b) concrete SMQs across different spans.

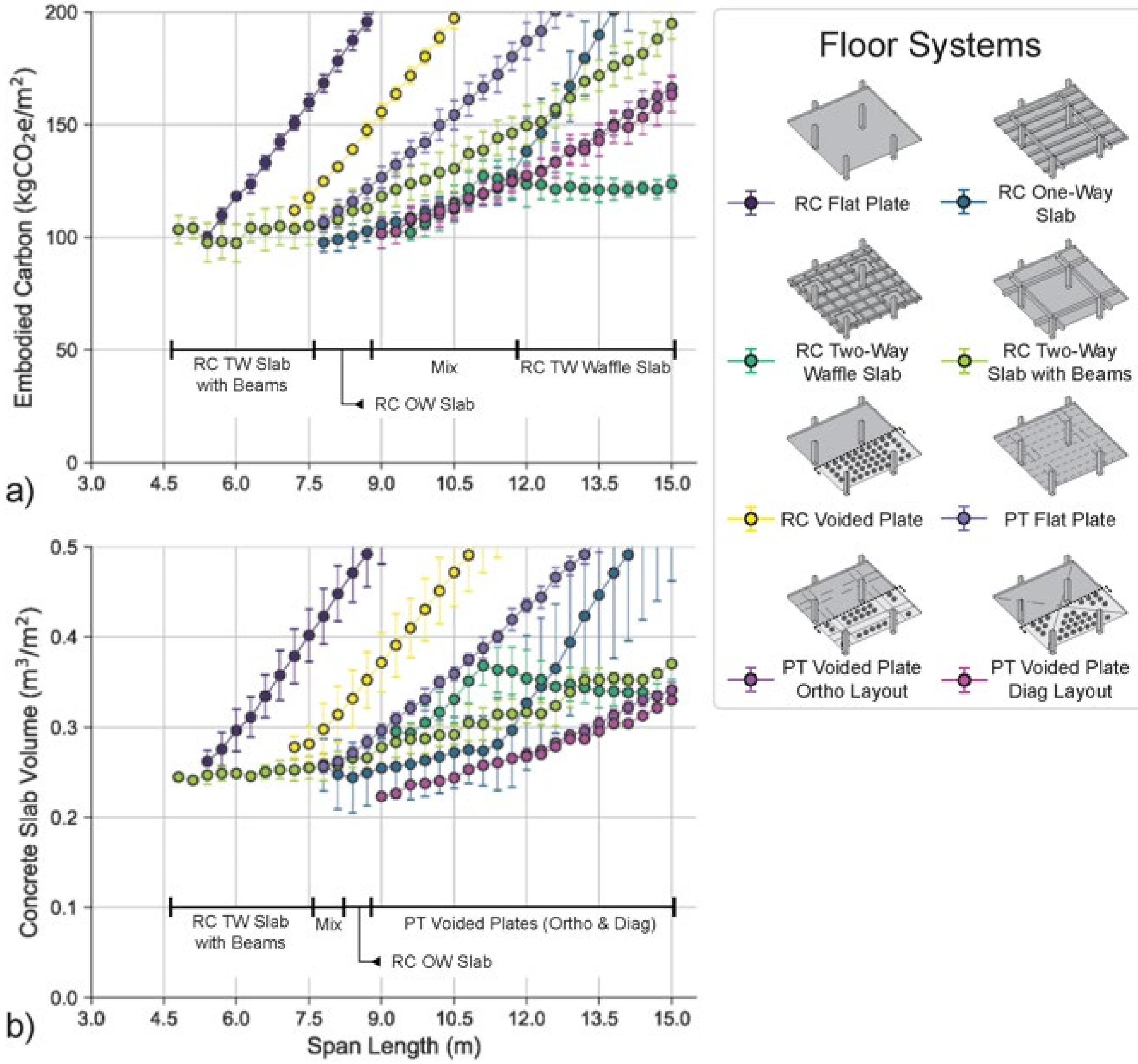

Figure **4-18**: Design charts for a medical building displaying the concrete floor system(s) with the lowest a) EC and b) concrete SMQs across different spans.

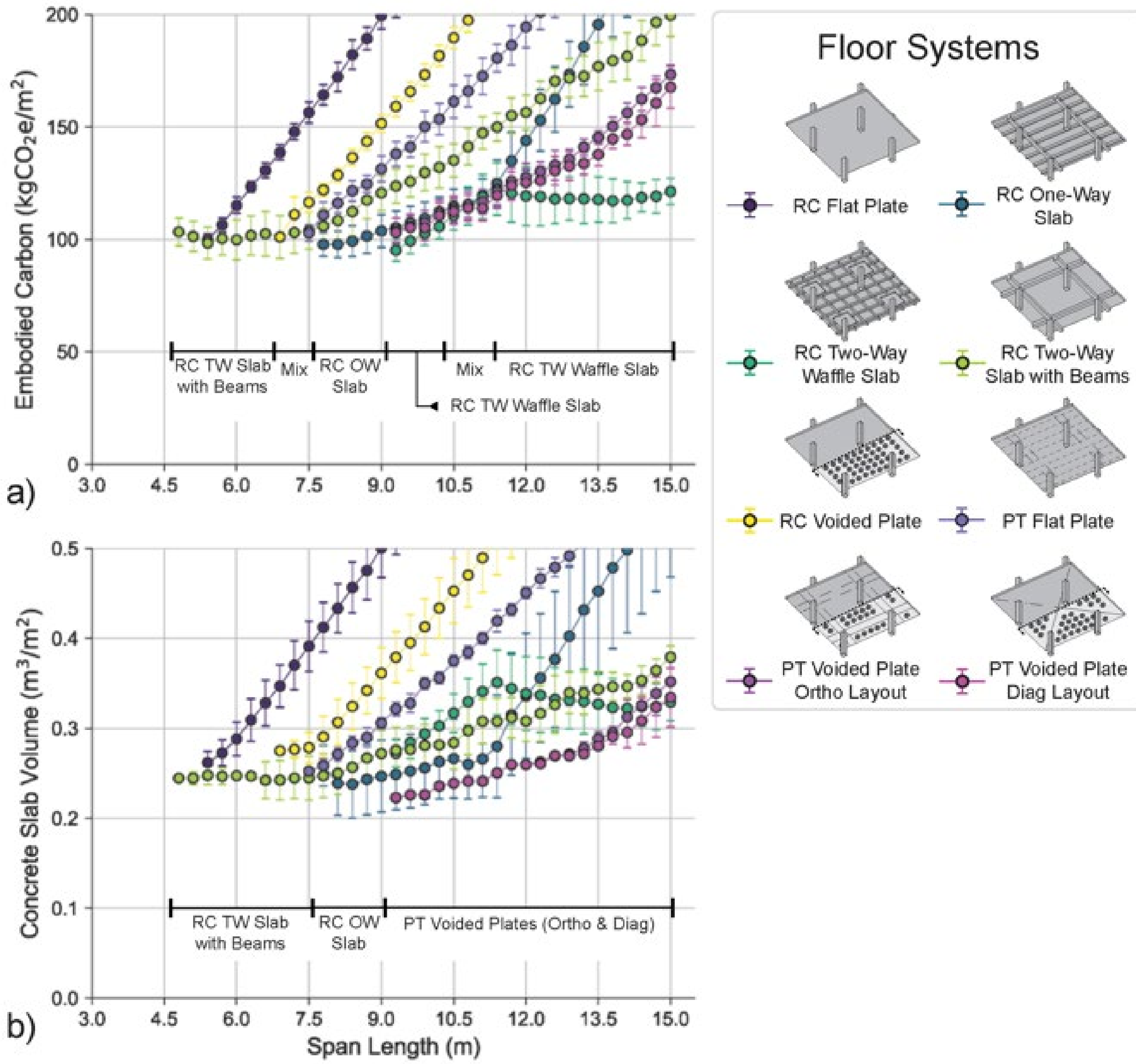

Figure **4-19**: Design charts for an educational building displaying the concrete floor system(s) with the lowest a) EC and b) concrete SMQs across different spans.

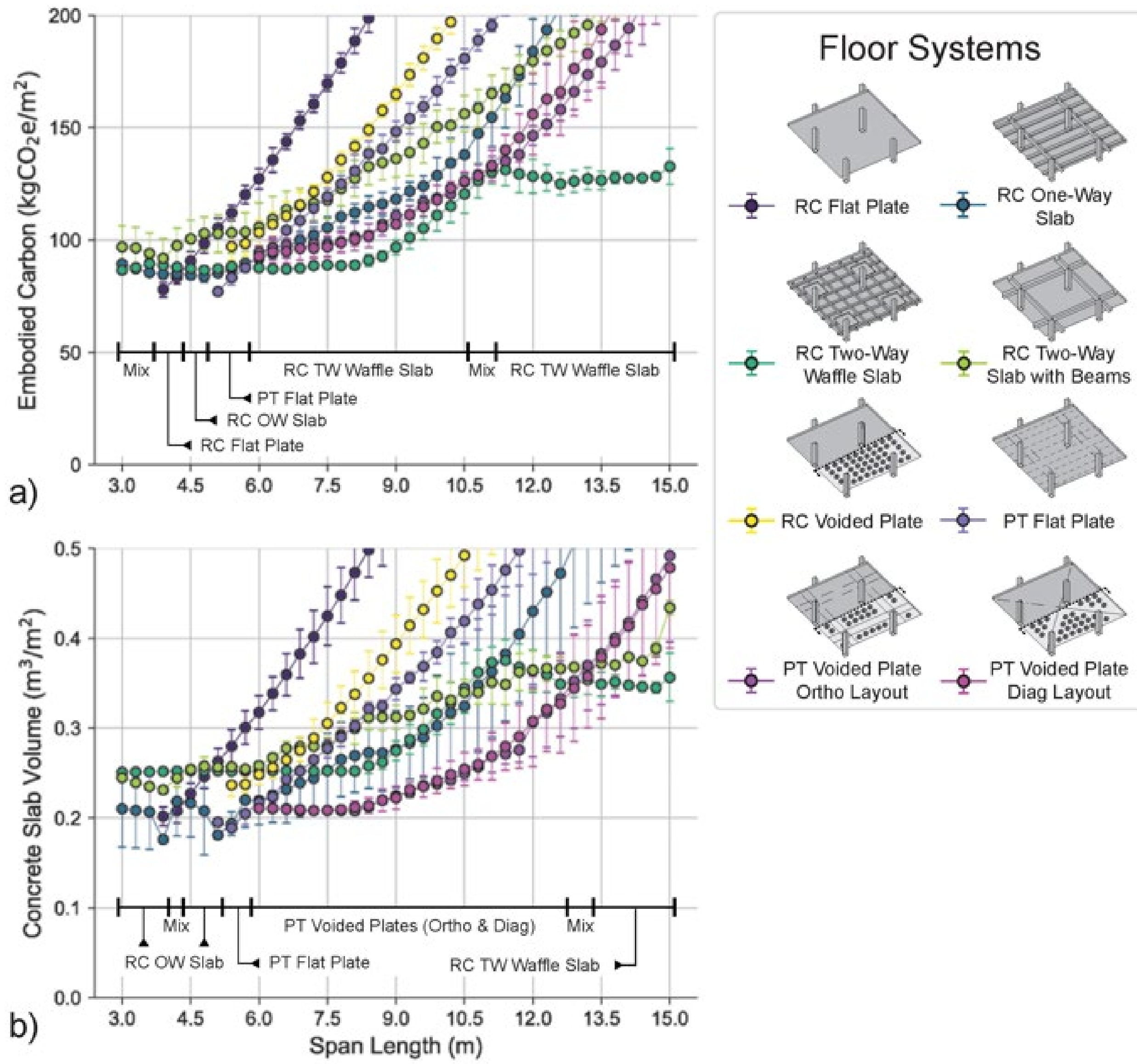

Figure **4-20**: Design charts for a public assembly building displaying the concrete floor system(s) with the lowest a) EC and b) concrete SMQs across different spans.

The design charts reveal that for certain design scenarios and span lengths, the most preferred floor system can vary significantly. In fact, when assessing across all six cases, each of the eight floor systems is found to be preferred at a specific span length and design scenario. This finding underscores how the inclusion of fire-resistance, air-borne sound insulation, and floor vibrations does indeed influence the selection of a low-carbon concrete floor system. Despite the nuances across the six design charts, there are three important observations:

1. The preferred concrete floor systems at short span lengths are typically RC one-way slabs and RC two-way slabs with beams. This is largely because these floor systems can be designed with thin top slabs and small rib / beam cross sections thereby reducing concrete material and EC.
2. However, when an STC rating above 50 is desired (i.e., Cases B, D, and E), no concrete floor system can satisfy all design requirements at short span lengths. Specifically, a requirement of STC-55+ (Cases D and E) disqualifies all floor systems at or below a span length of 4.5 m and a requirement of STC-60+ (Case B) disqualifies all floor systems below a span length of 7.5 m. This indicates that material layers (or other acoustic treatments) may be necessary to achieve high sound insulation performance for shorter spans as designing for structural limit states alone does not meet higher acoustic performance goals.
3. Regardless of the design scenario (including structural loads and secondary design requirements), the preferred concrete floor systems at long span lengths are typically RC two-way waffle slabs and the PT voided plates. This result is intuitive if only considering structural performance as both types of concrete systems are known to be economical at longer span lengths (refer to Sec. 3.3.1). Yet it is surprising that both floor systems (especially for two systems with different soffits) are found to be non-dominated even when the secondary design goals vary; however, the span length in which these systems begin to govern does appear to be influenced by the performance goals.

Overall, these results reveal that building designers and engineers have to be aware that high performance design goals can influence the EC and selection of a low-carbon concrete floor system, especially at short span lengths where concrete floor systems can be designed as thin floors while maintaining structural integrity. Concrete floor systems commonly satisfy all structural and design code requirements at long span lengths; however, long spans have higher EC emissions and SMQs than shorter spans, including larger distributions of EC and SMQs as indicated by the increasing length of the error bars.

4.5 Design implications, limitations, and future work

The EC emissions of RC and PT concrete floors can be influenced by the inclusion of fire-resistance rating, air-borne sound transmission, and floor vibrations in the definition of functional equivalence. The results indicate that different concrete floor systems are advantageous when considering secondary design objectives and that fire-resistance rating was the most influential objective when minimizing EC emissions. While out of the scope of this work, these results can help inform the selection of a low-carbon floor system when concrete floors are compared to structures composed of alternative structural materials (i.e., steel and mass timber). Depending on the design scenario, a concrete floor system can be designed without additional treatments for fire-resistance, air-borne acoustic attenuation, and vibrations to satisfy building code requirements. This is not the case for all structural floor systems. For example, long-spanning mass timber floors commonly need acoustic treatments and may have vibration concerns (Bazli et al., 2022; Kurent et al., 2024). Similarly, steel composite floor systems are more susceptible to floor vibrations than concrete systems (Gaspar et al., 2016; Tahmasebinia et al., 2022). Because secondary design considerations can control the design of the floor when using alternative structural materials to concrete, it is therefore important to expand the functional equivalence when comparing the EC emissions of different structural floor systems.

Conventional RC and PT concrete floor systems have other building design benefits that are not considered in this study. The cost of the floor system can significantly influence the selection of a low-carbon floor system (Jayasinghe et al., 2021), but a cost analysis is highly dependent on the cost indexes in a given location (Idrus, 2002). The SMQ design charts in this study can serve as a proxy on the cost of the structural materials, but formwork and labor costs would also need to be considered. Related, constructability is another important design consideration (Idrus, 2002; Orr et al., 2019). The LCA scope was limited to the A1-A3 stages and excludes the EC contribution of concrete columns and foundations. Further work can extend the EC results present study by evaluating these floor systems using whole-building LCA and dynamic LCA methods.

Regarding the three secondary design objectives considered, an important limitation in the fire-resistance analysis is that only a siliceous concrete mixture type was considered, although other concrete types can vary the minimum thickness needed to achieve different fire-resistance ratings, potentially implying lower EC emissions (refer to Fig. **4-6**). Acoustically, single integer building acoustic objectives, like STC, may not appropriately capture the perceived acoustic insulation performance in a building (Park et al., 2009). Structure-borne sound insulation was not considered in this study because 1) accurate estimations require advanced computational models or experimentation and 2) bare concrete floor systems are typically unfavorable for impact sound insulation, often requiring additional material layers to satisfy IBC requirements (Arenas & Sepulveda, 2022; Jeon et al., 2004; Kylliäinen et al., 2017; Neves E Sousa & Gibbs, 2011). This study focused on bare concrete floor systems, but future work could evaluate low-carbon concrete floor systems for different material layers to expand the findings presented in this chapter. Other room acoustic phenomena such as sound reflection and absorption were not considered, but researchers could explore low-carbon synergies to improve acoustics through the geometric shaping and optimization of material properties of the concrete floor (Broyles et al., 2022c; Butko, 2021; Cottone et al., 2023). Another limitation is that only walking vibrations were considered in this study. Vibrations caused by rhythmic excitations can influence the design of a floor system, potentially requiring additional mass (concrete material). Adjusting the assumptions made in this study could alter some of the designs to pass/fail vibration criteria, as could the use of a FEM to ascertain the dynamic response of the floor system.

Lastly, different permutations of design charts can be generated for other building types and design scenarios. A helpful alternative is to expand the web app created in Ch. 3 with the inclusion of fire-resistance ratings, STC ratings, and to check if the design can satisfy human-induced walking vibration requirements.

4.6 Conclusion

This study investigated how the inclusion of the prescribed fire-resistance rating, air-borne sound insulation, and floor vibration performance can influence the selection of a low-carbon concrete floor system. Eight conventional concrete floor systems were investigated for varying structural design parameters, floor span lengths, and required performances for additional design objectives. Of the three additional design objectives, it was found that the prescribed fire-resistance rating had the largest influence on the EC emissions of a concrete floor system, with a percentage difference as high as 54.5% between the 1-hr and 4-hr fire ratings for the RC waffle slab.

The EC emissions of all concrete floor systems was influenced by the prescribed fire rating at span lengths below 6 m, while the EC emissions for floors with ribbed soffits and for the RC two-way slab with beams were affected for span lengths up to and exceeding 12 m. Air-borne acoustic insulation was shown to be heavily influenced by the span length of the concrete floor system, with the RC flat plate having the most favorable acoustic attenuation despite being the worst performing for EC. However, when balancing the reduction of EC emissions with high air-borne acoustic insulation, the RC two-way waffle slab and RC one-way slab were the most favorable floor systems. Regarding walking vibrations, all floor systems met the vibration requirement except for the RC two-way slab with beams. However, the distribution of natural frequencies for a concrete floor system is greatest at short span lengths suggesting that other vibration issues could arise (e.g., susceptible to rhythmic vibrations) with more material-efficient concrete floor systems (i.e., ribbed, and voided floor systems) designed for short spans.

Because of the nuances and complexities of balancing multiple, competing design objectives, this study developed six design charts to aid building practitioners in the selection of a low-carbon concrete floor system. The six design charts correspond to six unique design scenarios common representative of different building types, including two multi-family residential building scenarios, an office building scenario, a hospital scenario, an educational building scenario, and a public assembly building scenario. The design charts displayed the results in EC emissions (assuming averages found from concrete EPDs) and in SMQs so that building designers can obtain a more tailored EC estimate if the GWP of a concrete mixture is known, as was similarly done in the schematic design equations in Ch. 3. The findings of this study and corresponding design charts directly respond to the urgent need to reduce carbon emissions in the built environment by informing the building design community on how three secondary design objectives influence the sustainability-driven design of concrete floor systems in buildings.

Part III:

COMPONENT SCALE

Chapter 5

Experimental testing and model validation of shaped concrete slabs[1]

5.1 Introduction

The dynamic response of structural elements, especially floors, is an important consideration in building design since it relates to sound insulation and vibration performance (Caniato et al., 2022; Ebrahimpour & Sack, 2005; Rasmussen, 2010; Reinhold & Hopkins, 2021; Varela & Battista, 2011). Humans spend upwards of 90% of their time in buildings (Evans & McCoy, 1998), and poor sound insulation has short-term health consequences such as annoyance (Jeon & Sato, 2008), sleep loss (J.T. Weissenburger, 2004; Northwood, 1964), and fatigue (Monteiro et al., 2016; Rasmussen, 2021). Worse, failure to have proper sound attenuation can cause occupants to develop long-term health consequences including hypertension and depression (Maschke, 2016). To prevent potential health concerns, building designers need to consider both the air- and structure-borne transmission performance of structural elements. Although air-borne transmission is an essential component of the indoor acoustic environment (Ward & Randall, 1966), structure-borne transmission from activities such as walking have been found to be the "most disturbing noise source" (Vardaxis & Bard, 2018), emphasizing the need to strive for satisfactory impact sound insulation in building design (Cho, 2013; Yoo & Jeon, 2014).

Vibrations, a common design concern for building elements, are often created by a rhythmic force caused by footfall, or machinery, and other transient excitations. If vibrations are not accounted for in the design of a floor system, it could be susceptible to amplified displacements, depending on its natural frequency (Longinow et al., 2009; Varela & Battista, 2011). If a force excites the natural frequency of the

[1] Chapter 5 is adapted from the published work by Broyles et al. "Evaluation of the dynamic response for scaled models of shaped concrete floor slabs." (2023). *Building Acoustics*, *30*(2), 143-163.

floor, a resonance can occur that could cause human discomfort, and in extreme cases, cause structural damage leading to failure (Longinow et al., 2009; Svinkin, 2004).

While favorable dynamic performance of floors is critical to a safe and satisfactory design, building design is increasingly driven by environmental objectives. The construction and operation of buildings accounts for 35- 40% of global energy consumption (De Wolf et al., 2017), and floors made of concrete significantly contribute to embodied carbon emissions when compared to other common structural elements (Ismail & Mueller, 2021; Meibodi et al., 2018). One potential solution to reduce the carbon footprint of concrete floors is through reducing material by geometric optimization, since typical floors are designed for ease of construction and thus often overuse material (Hawkins et al., 2020; Ismail et al., 2021). Optimized structures can ensure structural integrity while reducing material consumption and corresponding carbon emissions, with possible material savings up to 70% (Meibodi et al., 2018). Yet lighter, geometrically optimized floors may have adverse effects on the dynamic performance of the structure when they are not properly considered (Nandy & Jog, 2012), potentially inadvertently affecting the natural frequency and the sound attenuation.

Previous studies have demonstrated that simulated dynamic results of rectilinear concrete structures can be validated with experimental testing (Asakura et al., 2018; Gollob & Kocur, 2021; Neves E Sousa & Gibbs, 2011; Reinhold & Hopkins, 2021). A study by Roozen et al. (2018) showed how computational models (e.g., finite element models) can provide accurate simulations of dynamic performance, including phenomena such as sound insulation, of an optimized funicular concrete slab. Yet the numerical findings were trusted only after the model and results were experimentally validated. A later computational study by Wu et al. (2020) evaluated the vibration performance of the same optimized funicular slab system, indicating that the computational dynamic study was trusted only after experimental validation. Although optimized concrete slabs are a solution to reduce material consumption in a floor, there are alternative non-traditional concrete floor systems including shaped, ribbed slabs. Further, optimizing the ribbed soffit of a concrete floor can reduce material consumption but may significantly influence the dynamic response of the structure; yet this behavior has not been researched.

Although optimized structures have a direct environmental benefit, determining their acoustical performance is a challenge. Unlike simple constructions, optimized structural elements cannot presume the same theoretical assumptions when predicting acoustic performance. As mentioned previously, a known strategy to model the dynamic performance of optimized floors is finite element analysis (FEA) (Maluski & Gibbs, 2016; Reinhold & Hopkins, 2021; Reynders et al., 2014; Roozen et al., 2018; Wu et al., 2020). Unlike many theoretical approximations, FEA is not restricted to rectilinear structures, since unique geometries can easily be approximated using a mesh composed of hexahedral, pentahedral, or tetrahedral elements (refer to Sec. 6.1). FEA can also account for structures with complicated material properties, such as steel-reinforced concrete elements (Badiger, 2014). These advantages make FEA an appealing option for estimating the dynamics of complex, optimized structures. However, before the results from numerical analyses of shape-optimized structures can be more widely utilized, experimental measurements should be used to validate the dynamic response. This prompts the research question: what is the experimentally-obtained dynamic response of fabricated, quarter-scaled shaped ribbed concrete slabs, and can these results be used to tune numerical models for each slab?

This chapter addresses this question by evaluating the dynamic performance of four unique, quarter-scaled shape-optimized reinforced concrete slabs. First, the shaped slab specimens were designed using nominal reinforced concrete properties. Next, experimental modal analysis using the roving force hammer method was performed on the fabricated slabs. Then, FEA models of the concrete slabs were created using nominal reinforced concrete material properties to estimate the mode shapes and eigenfrequencies. The natural frequencies and mode shapes were then compared to establish the validity of the modeling approach. Modal damping of the slabs, which cannot be easily modeled using FEA, was also determined from the experiments. Finally, the nominal concrete material properties, which naturally exhibit variability, were uniformly updated in the four models to achieve better agreement with experimental results. The following sections include background information on the shaped slabs, the experimental set-up and post-processing, the numerical FEA model, and lastly comparisons of the dynamic results.

5.2 Floor selection, geometry, and design

5.2.1 Floor Selection

Four unique, quarter-scaled shape-optimized concrete slabs were evaluated in this study. The shapes (shown in Figure **5-1**) were selected to assess the dynamic performance of specimens with known differences in mass density (corresponding to material savings) and simulated air-borne sound insulation calculated for the full-scale specimens. Additional information regarding the air-borne sound insulation methodology can be found in Broyles et al. (2022c). The Sound Transmission Class (STC) ratings were found to be STC-51, STC-55, STC-60, and an STC-50 for slabs 1 – 4, when using an angle of incidence of 45° as was done by Broyles et al. (2022c) However, when considering a range of sound incident angles from 0° to 78°, the STC ratings are STC-52, STC-56, STC-60, and STC-46. It should be noted that the STC only describes the air-borne sound transmission directly through the building element and ignores flanking sound transmission. Although a numerical model approximating STC was used for the slab selection, it was anticipated that the four slabs would have differing dynamic results due to differences in mass density and stiffness. This study focuses on the evaluation of dynamic performance rather than air-borne sound transmission.

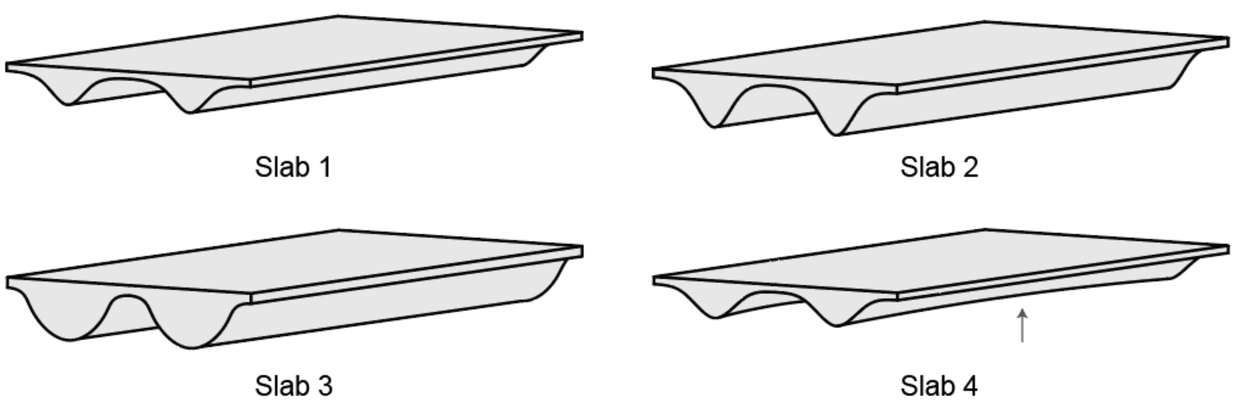

Figure **5-1**: The shapes of the four concrete slabs. An arrow is shown underneath Slab 4 to highlight the difference from Slab 1 (i.e., variation of cross-sectional area along span length compared to uniform cross-sectional area).

5.2.2 Specimen geometry and design

After the four shapes were chosen, computational models for each slab shape were generated using NURBS curves in Rhinoceros3D v. 6. To experimentally obtain the dynamic performance of the specimens, fabrication plans (see Figure **5-2**) were developed for each specimen. Due to scaling, the temperature and shrinkage steel in the top slab was specified as a steel wire grid to limit concrete cracking. Steel-reinforcement was designed at 13 mm (0.5 in) from the bottom of both ribs. The placement of the steel reinforcement and wire was the same for slabs 1-3, but the reinforcement for slab 4 was located about 26 mm (1.0 in) from the bottom of the rib ends to accommodate the curvature across the length of the rib.

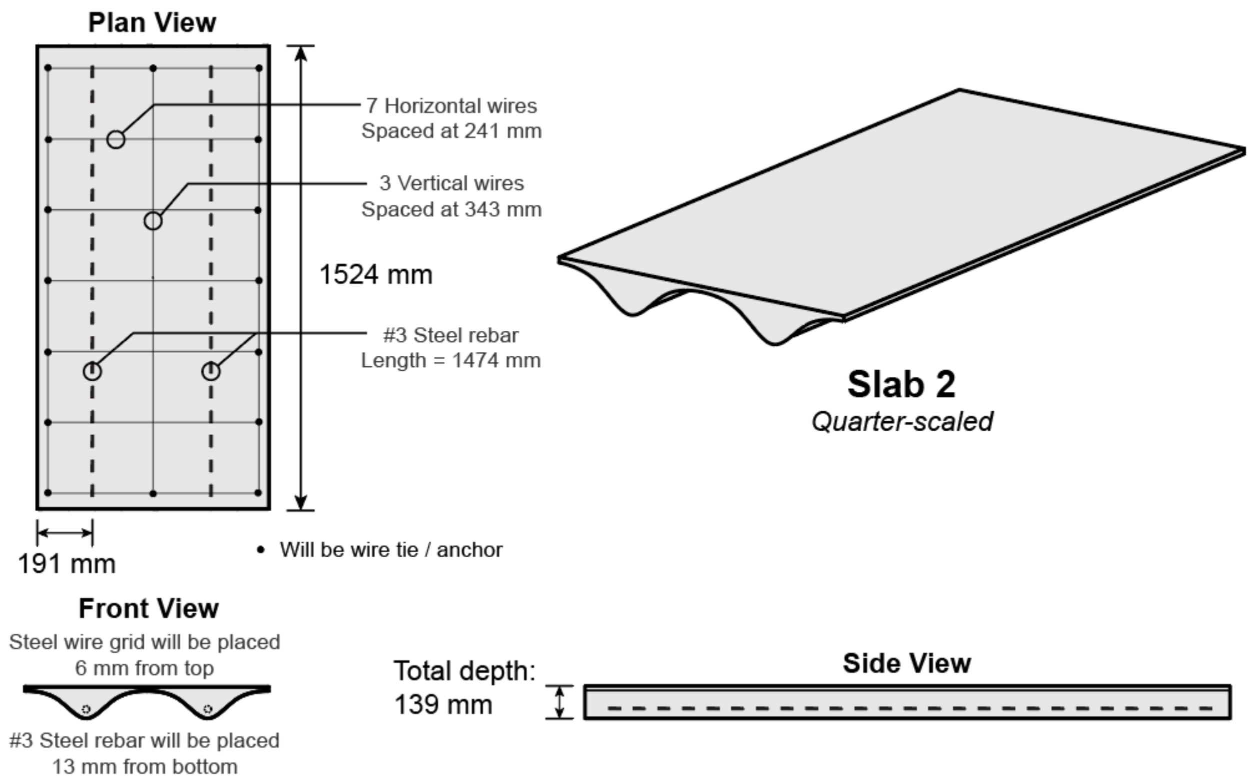

Figure **5-2**: Fabrication plans for a representative shaped steel-reinforced concrete slab.

The floor slabs are essentially a one-way slab with the ribs "shaped" to improve acoustical and sustainable performance. Since they are unconventional geometries within a parametric design space of possibilities, several can begin to look like a Double "T" shape. However, they would be analyzed structurally as one-way slabs as long as they maintain the dimensional requirements for this analysis. Each design had top slab dimensions of 762 mm x 1524 mm (2.5 ft x 5 ft), with varying top slab and rib depths, as noted in Table **5-1**. Each slab contained two ribs, which would span the narrow side of a building, with multiple slabs placed next to each other. Slabs 1, 2, and 3 had a uniform rib cross section across the length of the slab. Slab 4 had rib curvature that varied across the slab length, but the ends of the ribs had the same cross section profile as slab 1. The mass and mass densities of the quarter-scaled specimens are also provided.

Table **5-1**: Geometric properties of the four quarter-scaled slabs.

Shaped Slab	**Top Slab Depth in mm (in)**	**Rib Depth in mm (in)**	**Rib Cross Section Area in mm^2 (in^2)**	**Total Mass in kg (lb)**	**Mass Density in kg/m^2 (lb/ft^2)**
1	19 (0.75)	77 (3.03)	38236 (59.27)	120 (263)	103.3 (21.0)
2	22 (0.87)	117 (4.61)	58558 (90.77)	163 (359)	140.4 (28.7)
3	26 (1.02)	124 (4.88)	99939 (154.91)	251 (553)	216.1 (44.2)
4 (Ends)	19 (0.75)	77 (3.03)	38236 (59.27)	115 (253)	99.0 (20.2)
4 (Middle)	19 (0.75)	64 (2.52)	31391 (48.66)		

Normal strength concrete was specified for the slab models, with a modulus of elasticity, E_c, of 29,721 MPa (f'_c of 5.8 ksi), and a steel reinforcement strength of 210,000 MPa (30,450 ksi). The concrete floor models presented in this work are designed to resist the same structural load, corresponding to typical ASCE 7-16 (American Society of Civil Engineers, 2016) floor requirements scaled to the experiment. Further details of the structural design and performance can be found in the thesis by Broyles (2020).

Although a flat slab specimen was not fabricated nor experimentally tested in this study, the flat slab that would be designed according to the structural conditions specified would have a uniform thickness of 230 mm (9 in). A quarter-scale specimen would thus have a uniform thickness of 57.5 mm (2.25 in), with a total mass of 163 kg (360 lb). Slabs 1 and 4 would have a mass savings (which corresponds to a more sustainable design) compared to the flat slab of 26.3% and 29.4%, respectively. Slab 2 would have marginal mass savings, while Slab 3 would have an increase of mass of 54.0%. However, Slabs 2 and 3 would likely have better air-borne sound transmission performance compared to the flat slab. Experimental modal analysis and numerical validation has been previously conducted on RC flat slabs (Ahmed & Mohammad, 2014, 2015), however, a direct comparison to the slab specimens in this study would require maintaining the same specimen scale, concrete mixture, specimen fabrication, and experimental procedure. Such a comparison could be performed in future work.

5.3 Experimental procedure

5.3.1 Specimen fabrication

Following numerical modeling, the four shaped slabs were fabricated using a normal concrete mixture with cement, water, sand, and pebble-sized aggregate. The surface of the formwork was created by bending sheet metal to follow the curvature of the ribs. The sheet metal was held in place by plywood supports cut into the cross-section shape at increments along the slab length. Steel reinforcement was then placed inside the form. After the wet concrete was poured, the specimens remained in place until curing finished (i.e., after 28 days). Since the shaped concrete specimens were poured explicitly for testing (i.e., no structural load other than the slab self-weight was applied), it is assumed that the specimens had not cracked, which was confirmed by inspection. One of the scaled specimens is shown in Figure **5-3**.

Figure **5-3**: The fabricated slab 2 specimen.

5.3.2 Testing of structural properties

To validate the material properties of the four concrete specimens, the concrete strength was verified by breaking concrete cylinders with a diameter (D_c) of 102 mm (4 in) and a height of 203 mm (8 in) from the same mixture used for the slab specimens. A uniaxial compressive test following ASTM C39 (ASTM, 2021b) was conducted on three concrete cylinders on the 28th day from the concrete pour. The rupture load (P_{max}) was found for each cylinder, as shown in Table **5-2**. The rupture load (reported in kN) is then used to approximate the compressive strength of concrete (f'_c) in MPa,

$$f'_c = \frac{4000\, P_{max}}{\pi D_c^2}, \qquad \text{(Equation 5-1)}$$

which is used to determine an initial static modulus of elasticity of the concrete (E_c) in MPa:

$$E_c = 4700\sqrt{f'_c}\,. \qquad \text{(Equation 5-2)}$$

Table **5-2**: The rupture load for three concrete cylinders with the corresponding material properties.

Cylinder	Rupture Load in kN (kips)	Compressive Strength in MPa (ksi)	Modulus of Elasticity in MPa (ksi)
A	274.4 (61.7)	33.9 (4.909)	27,365 (3,969)
B	243.3 (54.7)	30.0 (4.353)	25,743 (3,734)
C	217.9 (49.0)	26.9 (3.898)	24,377 (3,536)

After testing, the three concrete cylinder compression test results were found to have an average compressive strength of 30.3 MPa and a standard deviation of 3.5 MPa. The initial material properties used in the numerical FEA models were an E_c, of 25,871 MPa (f'_c of 30.3 MPa) with a Poisson's ratio of 0.15, and a steel modulus of elasticity, E_s, of 210,000 MPa with a Poisson's ratio of 0.30; however, due to the variability found in the concrete cylinder tests, it was deemed necessary to evaluate the FEA models for other structural material property combinations.

5.3.3 Modal test set-up

For each specimen, four accelerometers were attached to the top surface using wax. The surface was then excited using the roving force hammer approach at the points shown in Figure **5-4** (a, b). Four Winbags (see Figure **5-4**, c) were used to create a "free-free" boundary condition. The Winbags were inflated with air and placed under the ends of both ribs. Although the Winbags rested on the ground, the air created a free-free condition to isolate the slabs under a force load without significantly influencing the recorded modal response.

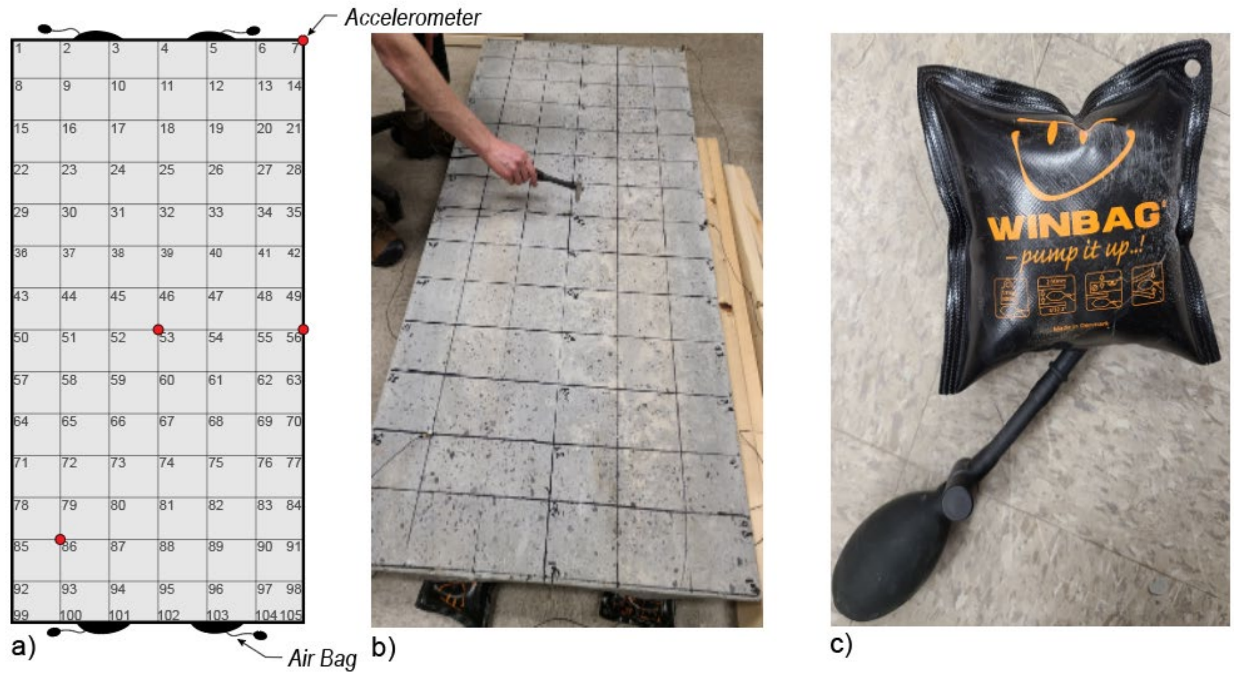

Figure **5-4**: Experimental set-up for the roving hammer method. a) The grid showing the locations of the hammer impacts on the top slab of each concrete specimen. b) A picture during the experimental testing. c) Four Winbag supports were positioned on the ends of both ribs to replicate free-free boundary conditions.

Each grid point was excited three times and averaged to reduce noise in the frequency response functions (FRF) measurements (Schwarz & Richardson, 1999). The FRFs (acceleration over force) were acquired with a National Instruments PXI system sampling at 10,240 Hz with a blocksize of 16,384. Due to the anti-aliasing filter within the system, the usable bandwidth was 0 – 4 kHz, with a frequency resolution of 0.625 Hz. Reciprocity was conducted to test the validity of the structure, and coherence was checked during testing to partially consider linearity.

5.3.4 Experimental data post-processing

Experimental modal analysis was performed on the four slabs to obtain its mode shapes, natural frequencies, and modal loss factors. This analysis was based on the roving hammer exciting the structure at regular grid points, with the response captured by the accelerometers. The accelerometers were attached in the normal direction to the flat side of the slab to obtain acceleration to force frequency response functions (FRFs) for each excitation point (see Figure **5-5**).

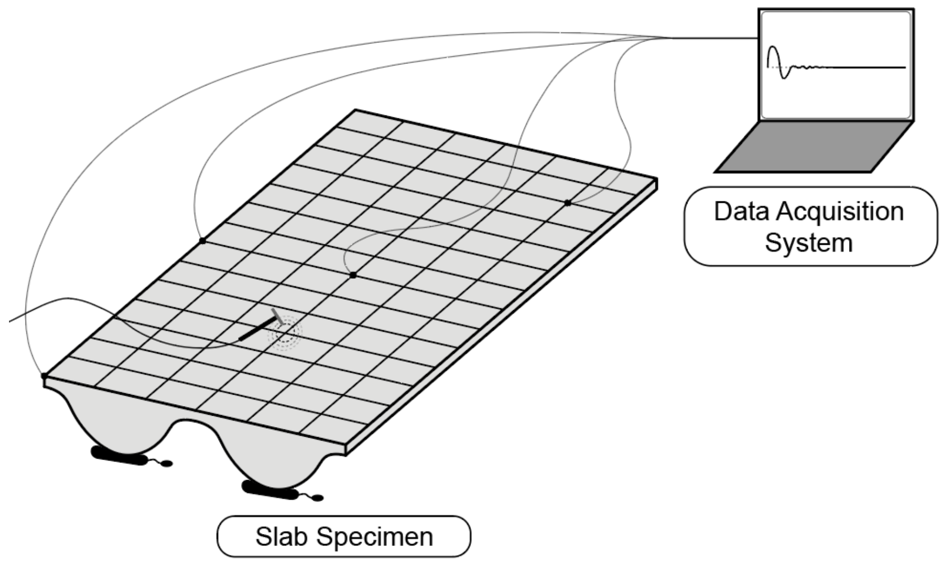

Figure **5-5**: Experimental data obtained through the roving force hammer method was post-processed.

The matrix of FRFs, referred to as $\mathbf{H}(\omega)$, was then decomposed to extract modal parameters using a poly-reference technique (Peeters et al., 2004). To summarize the poly-reference technique, each FRF matrix was decomposed into a numerator matrix polynomial and a denominator matrix polynomial,

$$[\mathbf{H}(\omega)] = [\boldsymbol{B}(\omega)][\boldsymbol{D}(\omega)]^{-1}\,, \qquad \text{(Equation 5-3)}$$

with the matrices $\boldsymbol{B}$ and $\boldsymbol{D}$ being expanded with pth-order polynomial basis functions. To find the model coefficients of the expansions, the error between the model and the measured matrix was minimized using a nonlinear least squares scheme. Stabilization diagrams were then used to determine the appropriate order of the basis functions. Once the modal parameters were determined, the measured acceleration was synthesized to ensure that all relevant modal parameters were accurately estimated.

5.4 Numerical FEA model

5.4.1 Geometric model and meshing

The slab geometry files were imported into ANSYS (v. 2021 R1) to conduct the finite element analysis, with a unique mesh generated for each slab. The top slab was modeled using solid hexahedral elements with an average width, depth, and height of 25 mm, and the ribs were modeled using a combination of hexahedral and tetrahedral elements with a base of 25 mm, due to the curved geometry. For more information on the types of finite elements and how they influence the model accuracy and computational time, refer to Sec. 6.1. To ensure that the slab models had an adequate mesh, the skewness, which is a unitless measure that accounts for the mesh quality (Knupp, 1999), was assessed for each shaped slab. Table **5-3** presents the range, average, and standard deviation of the mesh skewness for each slab model. Skewness ranges from 0 to 1, with a smaller number corresponding to a better mesh quality. The meshes were deemed satisfactory based on 84% of the finite elements having a skewness value at or below 0.630 for each slab, which is below the maximum skewness of 0.95 recommended by ANSYS.

Table **5-3**: FEM mesh properties for each slab.

Model	Number of Elements	Skewness Range	Skewness Average	Skewness Standard Deviation
Slab 1	3,021 elements	1.306×10^{-10} to 0.998	0.264	0.331
Slab 2	4,389 elements	1.306×10^{-10} to 0.992	0.273	0.357
Slab 3	7,875 elements	1.306×10^{-10} to 0.997	0.195	0.309
Slab 4	2,709 elements	1.306×10^{-10} to 0.992	0.274	0.332

5.4.2 Steel reinforcement and model pre-processing

Since steel reinforcement was placed near the bottom of both ribs for each slab design (Figure **5-6**), two strips of elements were selected within each mesh to have steel reinforcement properties after the shaped slab was meshed. These steel elements were centered in each rib at a height above 25 mm. Although the exact steel reinforcement geometry can be incorporated in an FEA model, this approach simplified the numerical model by reducing the number of solids that needed meshing, reducing computational cost. This approach enables the concrete and steel elements to have element nodes and faces aligned.

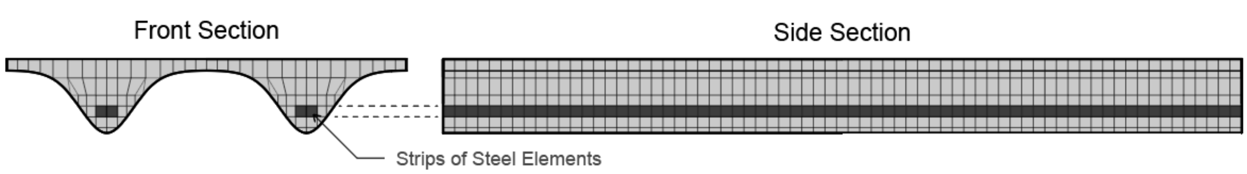

Figure **5-6**: Two strips of elements were selected for steel reinforcement, as shown in the model of slab 2.

After specifying the steel reinforcement elements, the first 40 modes and eigenfrequencies were found for each slab. The boundary conditions were modeled as free-free to match the experimental set-up described previously.

5.5 Results and discussion

5.5.1 Initial result comparison

Figure **5-7** shows the mode shapes and eigenfrequencies obtained for each slab after post-processing the experimental data. The first four mode shapes are characterized as (1,1), (2,0), (0,2) and (2,1) and are seen across all slabs. The eigenfrequency order switches for slabs 2 and 3, which is expected since the different slab and rib depths (See Table **5-1**) create different ratios of bending to torsional stiffnesses. The natural frequencies of the modes, except for the (0,2) mode, still increase with weight as seen by slab 4 (the lightest panel) having the lowest frequency and slab 3 (the heaviest panel) having the highest eigenfrequencies.

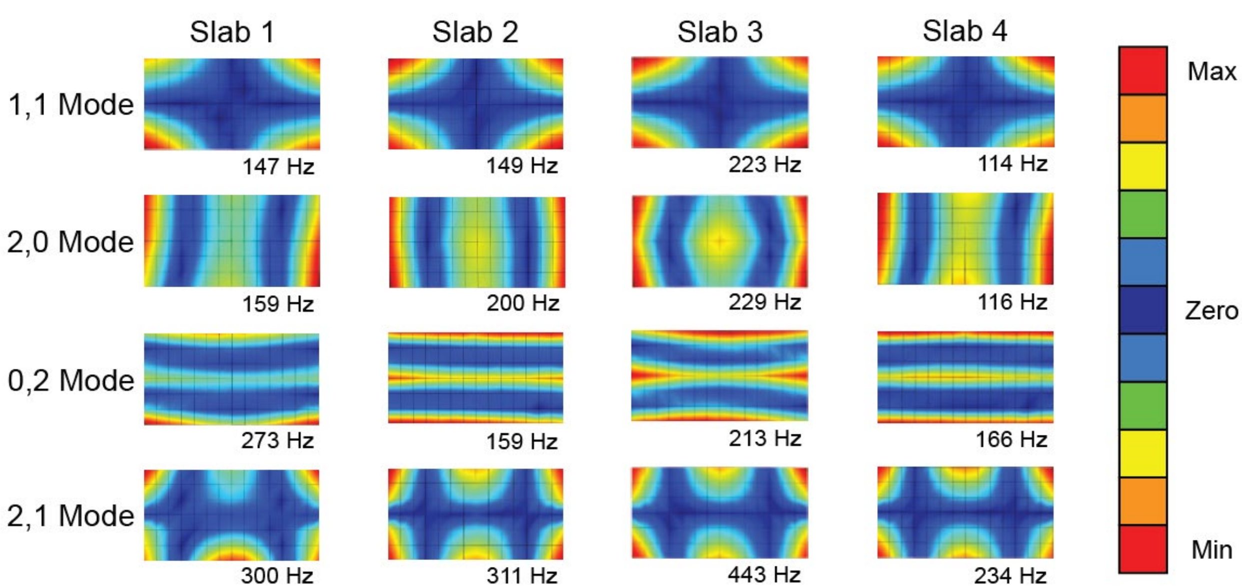

Figure **5-7**: The first four experimentally obtained mode shapes for each slab specimen. Red represents both the maximum positive and maximum negative displacement of each mode while blue represents zero displacement.

The modal damping for the four slabs is compared in Figure **5-8**. Damping loss factors were estimated using the poly-reference technique previously discussed. The values fall roughly around 0.01 and are mostly consistent between the slabs. The variation increases slightly above 1 kHz and is mostly pronounced in slab 1. This suggests that the damping of the concrete slabs at lower frequencies is not strongly influenced by the rib shape, but damping may have some influence at higher frequencies.

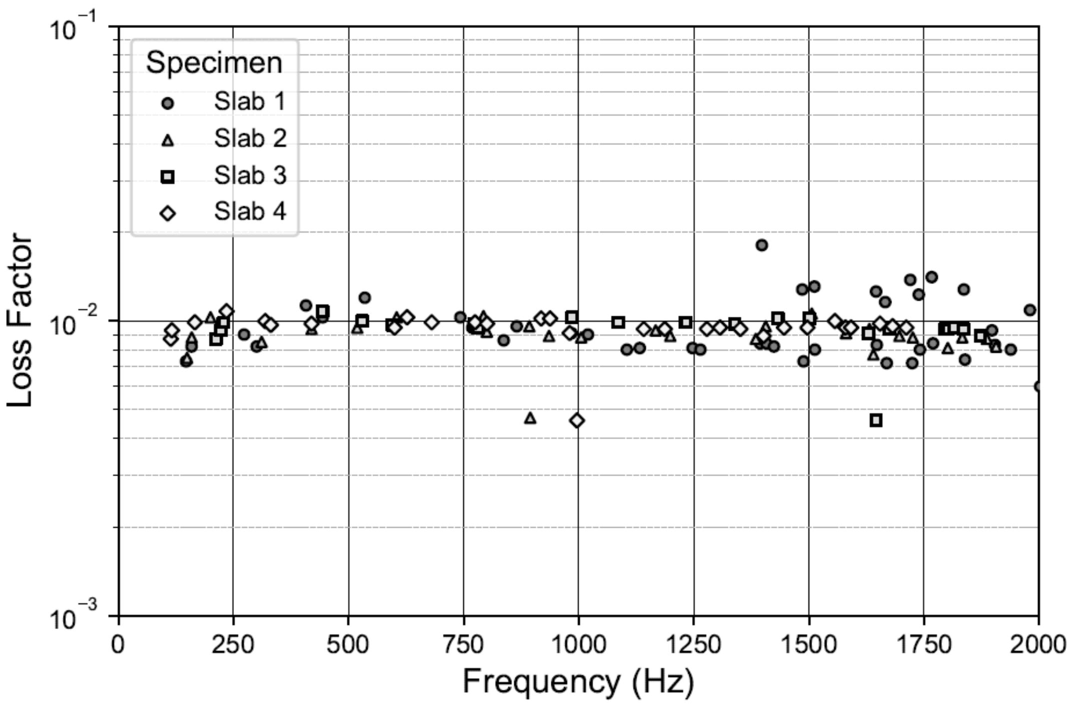

Figure **5-8**: Modal loss factors for the four slabs.

The experimental results are compared to the initial numerical results using the specified material properties in the design of the four shaped slabs as seen in Figure **5-9**. The mode shapes match well overall, suggesting that the numerical model reasonably agrees with the experimental results, but the measured natural frequencies are higher than what was obtained experimentally. Because the numerical and experimental masses are nearly identical (see Figure **5-10**), the initial comparison suggests that the concrete modulus in the numerical models is too low. Therefore, a systematic sensitivity analysis that varied the material properties was performed to identify the properties that best matched the experimental results.

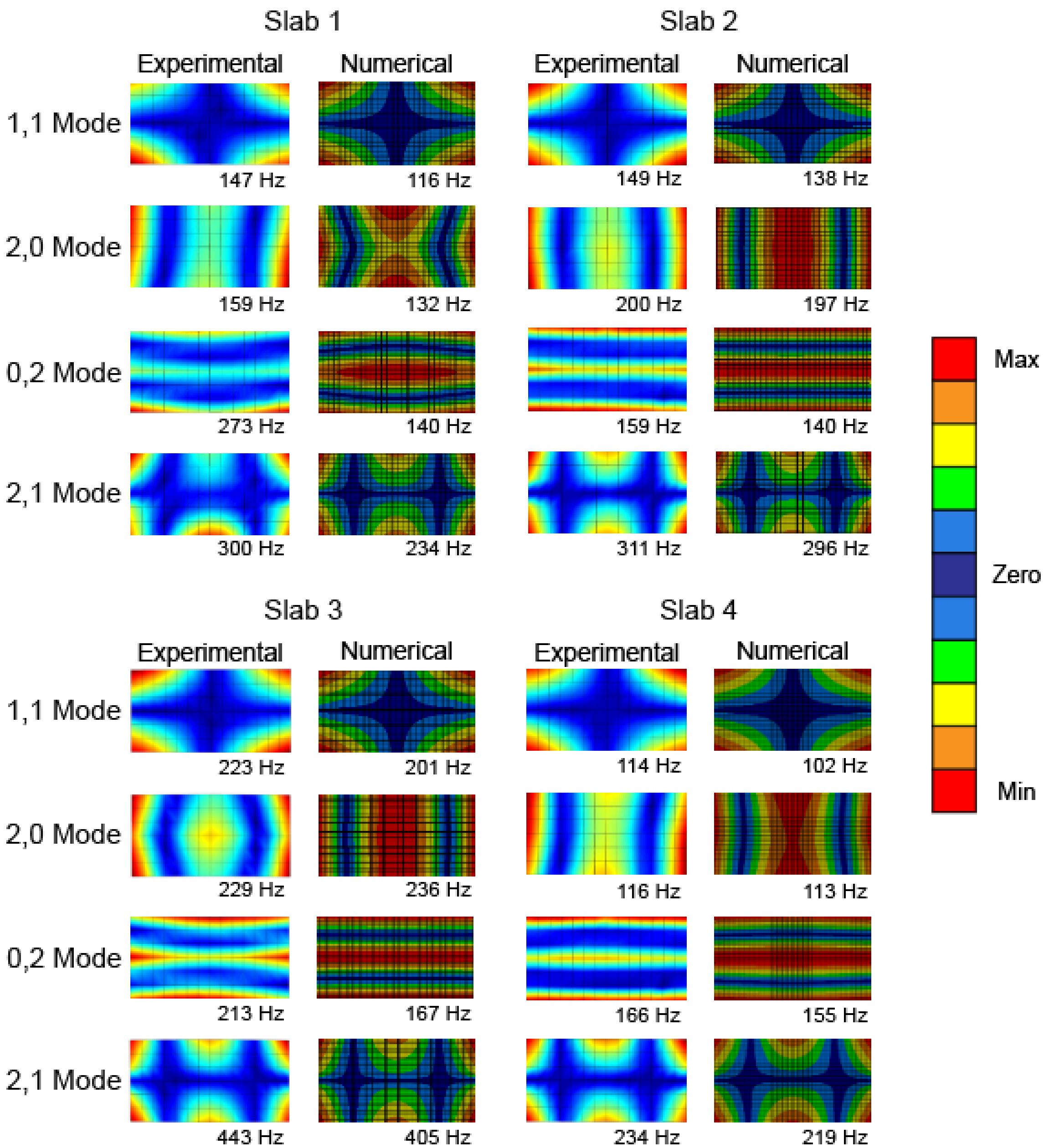

Figure **5-9**: The initial mode shape comparison of the experimental and numerical results.

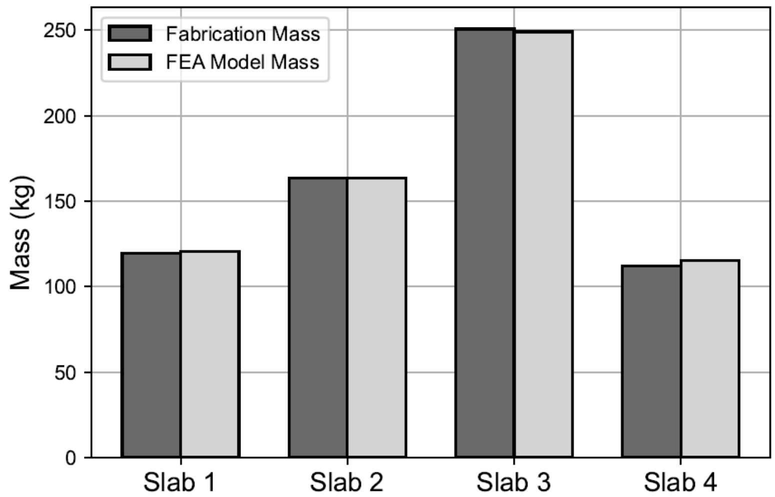

Figure **5-10**: Comparison between the fabricated and modeled mass of the four slabs.

5.5.2 Material property exploration

After the experimental results were obtained, the material properties in the FEA models were systematically explored to minimize the error with the experimental results. The material properties that were varied included the concrete compressive strength from a range of 37.92 MPa to 48.26 MPa (5.5 ksi to 7 ksi), which corresponds to a modulus of elasticity of 28,943 MPa to 32,652 MPa, and a Poisson's ratio from a range of 0.10 to 0.20. In sampling to find the smallest percent error, the numerical modes were matched to the first 16 experimental modes for each grouping of material properties. The percentage error between the natural frequency of each mode shape pairing was taken and then averaged across the 16 mode shape pairings. The composite percent error for each material property combination is shown in Figure **5-11**. In the contour plot, the light color corresponds to low percent error while the dark color corresponds to high percent error. When assessing Fig. **5-11**, it is obvious that slab 1 has a higher percentage error compared to the other three slabs. This difference is hypothesized to be caused by the fabrication difference between the slabs. Specifically, slab 1 was poured at an earlier time than slabs 2 to 4, which were poured at the same time / day. As a result, slab 1 had a longer curation time before the experimental modal test, potentially resulting in different concrete material properties from the other three slabs and resulting in the percentage differences seen in Fig. **5-11**.

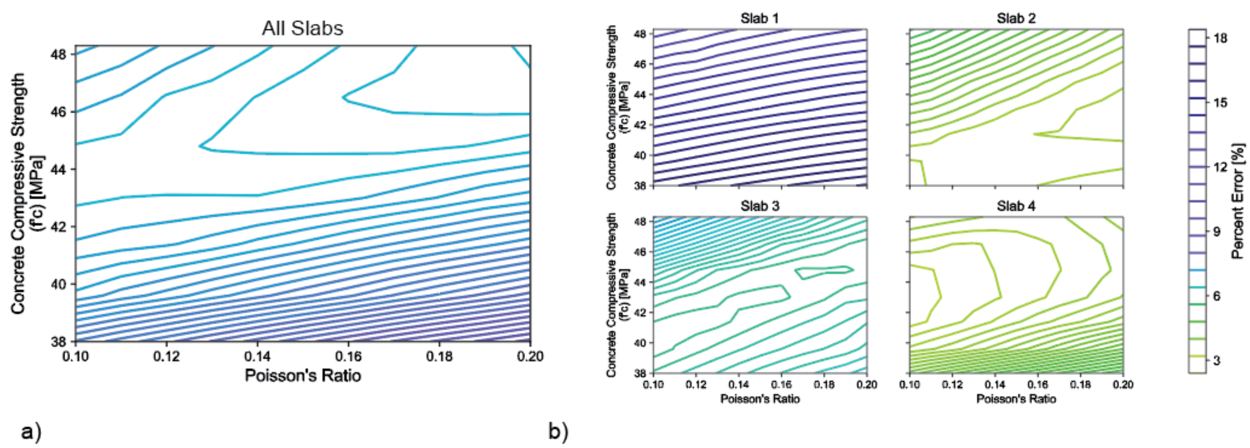

Figure **5-11**. a) A contour plot showing the averaged percent errors for the four slabs to ascertain the material properties, and b) contour plots for each slab.

The composite percentage errors were averaged across the four slabs to identify the material properties that work best for all slabs. The lowest composite percent error was 6.75% using the material property combination of a modulus of elasticity of 32,064 MPa (f'_c of 46.54 MPa) and a Poisson's ratio of 0.18. This grouping of materials was selected to obtain the final modal performance. After the material properties were determined, the first sixteen mode shapes were found (Table **5-4**), including the percentage errors calculated between the experimental and numerical eigenfrequencies (Table **5-5**). Although the first four numerical modes were in a similar order as the first four experimental modes, the numerical mode order varied greatly for the latter 11 experimental mode shapes. This point is better observed in Figures **5-12**, **5-13**, **5-14**, and **5-15**, which compare the 16 experimental and numerical mode shapes for shaped slabs 1 to 4, respectively.

Table 5-4: The order of the first 16 experimentally obtained mode shapes.

Mode Shape	Order of Modes for Slab 1	Order of Modes for Slab 2	Order of Modes for Slab 3	Order of Modes for Slab 4
(1, 1)	1	1	2	1
(2, 0)	2	3	3	2
(0, 2)	3	2	1	3
(2, 1)	4	4	4	4
(3, 0)	5	6	6	6
(1, 2)	6	5	5	5
(3, 1)	7	7	7, 8	7
(0, 3)	-	9	12	11
(4, 0)	8	11	10	8
(2, 2)	9	8	9	9
(4, 1)	10, 11	12	11	10
(1, 3)	12, 13	10	13	12
(2, 3)	-	13	-	15
(3, 2)	14	14	14	13
(5, 0)	15	15	15, 16	14
(5, 1)	16	16	-	16

Table 5-5: Eigenfrequencies and numerical-to-experimental percent errors.

Mode Number	Slab	Experimental Eigenfrequency (Hz)	Numerical Eigenfrequency (Hz)	Percent Error (%)
1	Slab 1	147	127	13.6
	Slab 2	149	152	2.0
	Slab 3	213	187	12.2
	Slab 4	114	112	1.8
2	Slab 1	159	146	8.2
	Slab 2	159	157	1.3
	Slab 3	223	222	0.4
	Slab 4	116	124	6.0
3	Slab 1	273	156	42.9

Mode Number	Slab	Experimental Eigenfrequency (Hz)	Numerical Eigenfrequency (Hz)	Percent Error (%)
	Slab 2	200	215	7.5
	Slab 3	229	256	11.8
	Slab 4	166	173	4.2
4	Slab 1	300	258	14
	Slab 2	311	326	4.8
	Slab 3	443	446	0.7
	Slab 4	234	241	3.0
5	Slab 1	407	384	5.7
	Slab 2	420	425	1.2
	Slab 3	529	533	0.8
	Slab 4	319	334	4.7
6	Slab 1	444	361	18.7
	Slab 2	519	554	6.7
	Slab 3	595	657	10.4
	Slab 4	331	318	3.9
7	Slab 1	535	477	10.8
	Slab 2	604	642	6.3
	Slab 3	773	813	5.2
	Slab 4	420	433	3.1
8	Slab 1	743	773	4.0
	Slab 2	793	798	0.6
	Slab 3	781	813	4.1
	Slab 4	600	620	3.3
9	Slab 1	769	664	13.7
	Slab 2	800	769	3.9
	Slab 3	985	997	1.2
	Slab 4	627	590	5.9
10	Slab 1	837	773	7.6
	Slab 2	893	879	1.6

Mode Number	Slab	Experimental Eigenfrequency (Hz)	Numerical Eigenfrequency (Hz)	Percent Error (%)
	Slab 3	1086	1173	8.0
	Slab 4	680	693	1.9
11	Slab 1	865	773	10.6
	Slab 2	935	985	5.3
	Slab 3	1232	1309	6.3
	Slab 4	775	732	5.5
12	Slab 1	984	777	21.0
	Slab 2	1000	1051	5.1
	Slab 3	1339	1176	12.2
	Slab 4	801	798	0.4
13	Slab 1	1020	777	23.8
	Slab 2	1167	1151	1.4
	Slab 3	1432	1309	8.6
	Slab 4	918	871	5.1
14	Slab 1	1104	972	12.0
	Slab 2	1199	1193	0.5
	Slab 3	1501	1496	0.3
	Slab 4	937	949	1.3
15	Slab 1	1132	1062	6.2
	Slab 2	1384	1430	3.3
	Slab 3	1629	1544	5.2
	Slab 4	980	950	3.1
16	Slab 1	1247	1099	11.9
	Slab 2	1410	1520	7.8
	Slab 3	1646	1771	7.6
	Slab 4	996	986	1.0

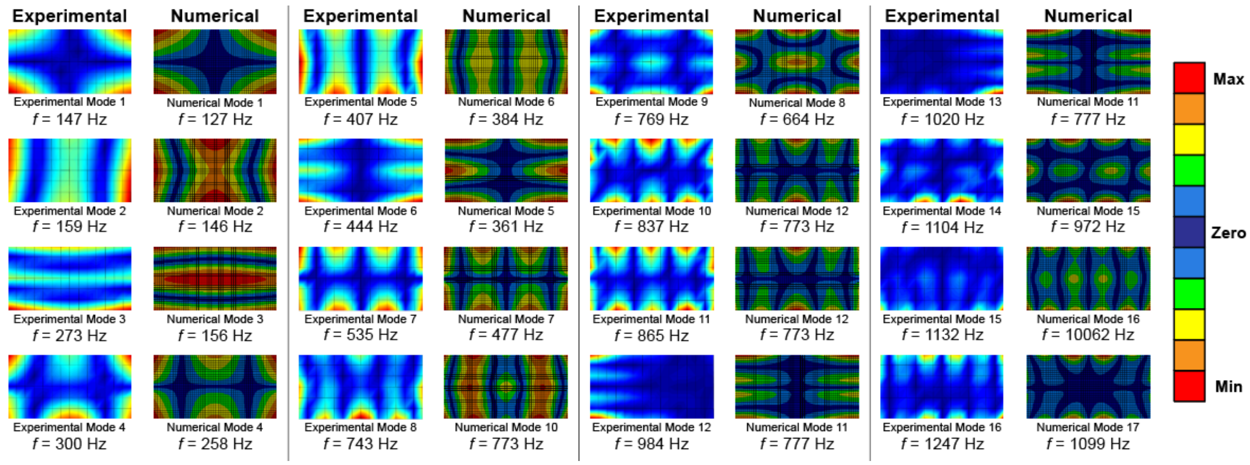

Figure **5-12**: Comparison between the experimental and numerical mode shapes and eigenfrequencies for slab 1.

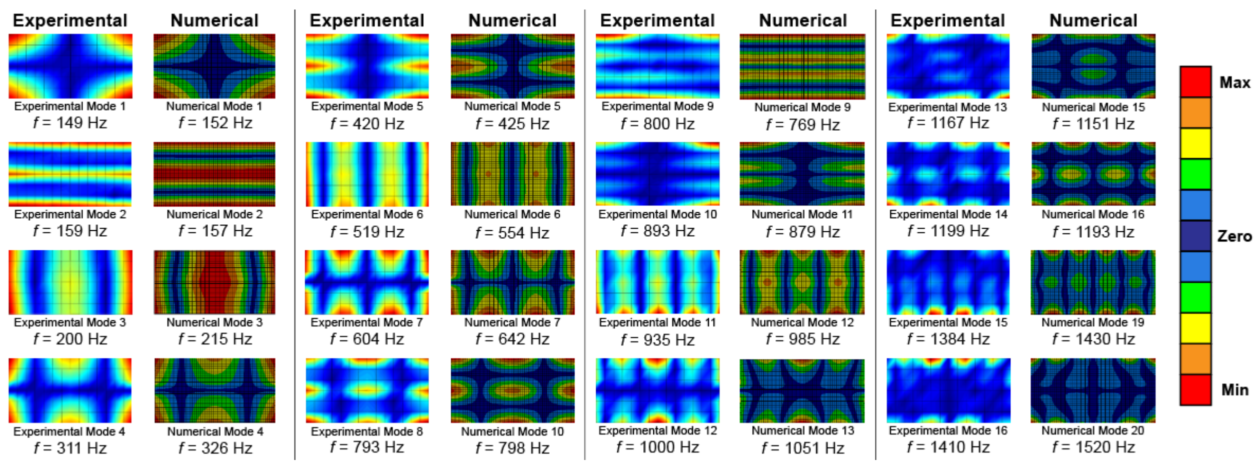

Figure **5-13**: Comparison between the experimental and numerical mode shapes and eigenfrequencies for slab 2.

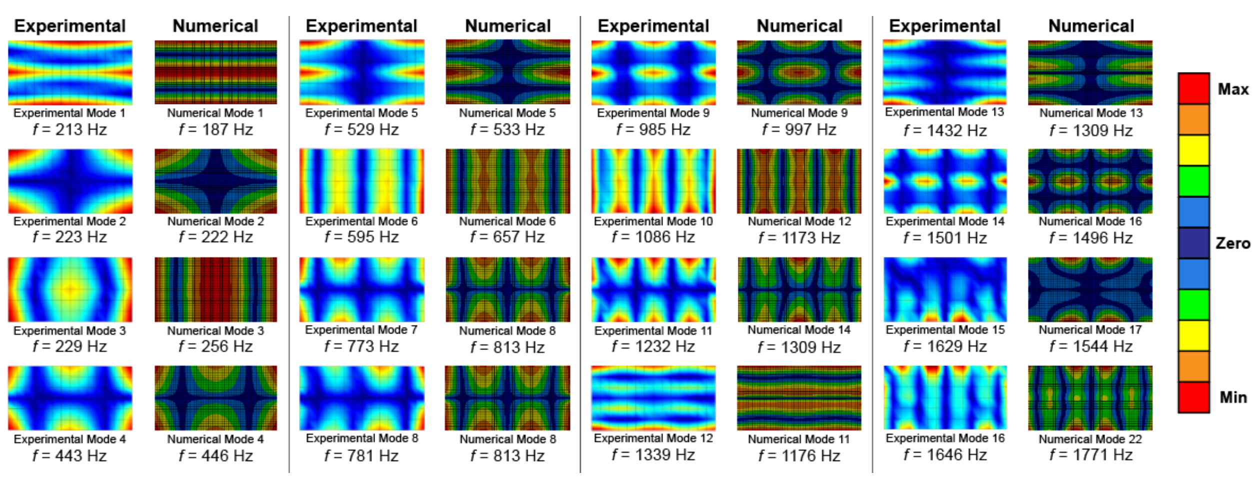

Figure **5-14**: Comparison between the experimental and numerical mode shapes and eigenfrequencies for slab 3.

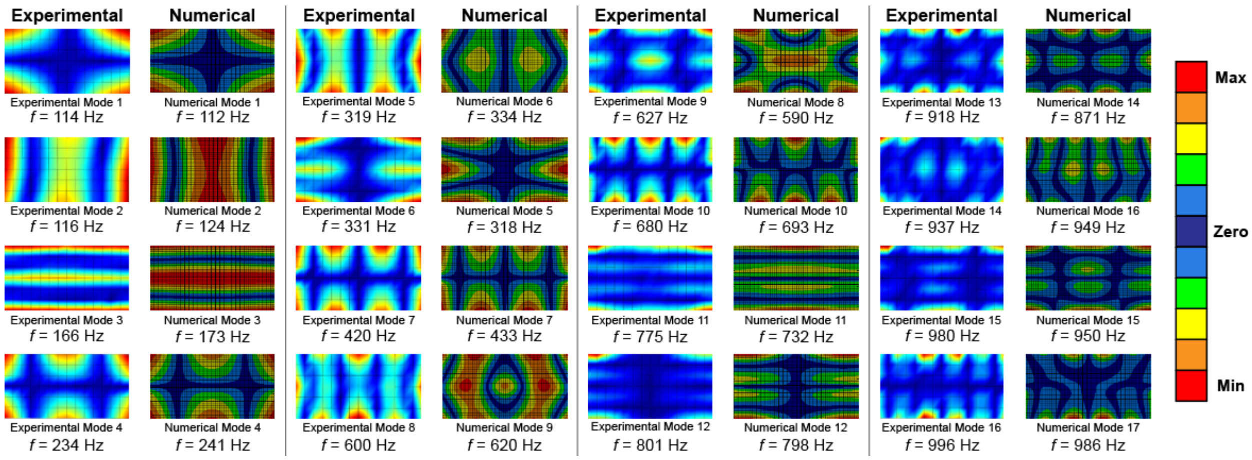

Figure **5-15**: Comparison between the experimental and numerical mode shapes and eigenfrequencies for slab 4.

5.5.3 Final validation

Figure **5-16** displays the contrast between the experimental and numerical natural frequencies for each slab using the material properties that best matched the experimental results. Slab 1 has the worst correlation of numerical to experimental eigenfrequencies, with lower numerical frequencies at frequencies at, and above, 1 kHz. As previously mentioned, this is likely due to the difference in fabrication time between slab 1 and the other three slabs. Slab 3 had poor correlation above 1 kHz but had good correlation below 1 kHz. Slabs 2 and 4 match very well with little percentage error across all 16 mode shapes.

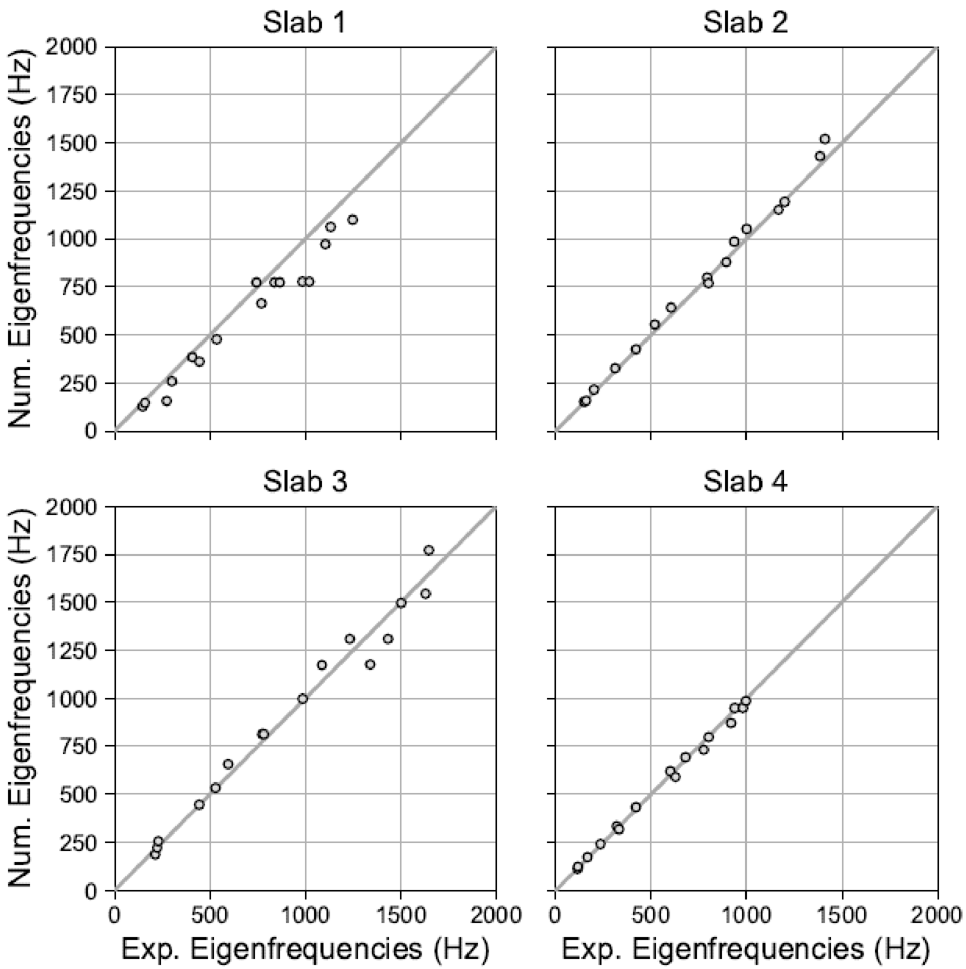

Figure **5-16**: Comparison of the experimental and numerical eigenfrequencies.

To further validate the results of the numerical model to the experimental results, a Modal Assurance Criterion or MAC calculation was used. The MAC calculation is used in modal analyses to indicate the correlation of a pair of mode shapes which can help validate a numerical model using experimental results. The MAC calculation is defined as,

$$MAC = \frac{\left|\{\boldsymbol{\varphi_A}\}^T\{\boldsymbol{\varphi_X}\}\right|^2}{(\{\boldsymbol{\varphi_A}\}^T\{\boldsymbol{\varphi_A}\})(\{\boldsymbol{\varphi_X}\}^T\{\boldsymbol{\varphi_X}\})}, \qquad \text{(Equation 5-4)}$$

where $\{\boldsymbol{\varphi_A}\}$ and $\{\boldsymbol{\varphi_X}\}$ represent the displacement vectors for the experimental and numerical methods respectively. The MAC provides a scalar number from 0 (no correlation) to 1 (perfect correlation) indicating the quality of the correlation of each pair of mode shapes (Allemang, 2003; Pastor et al., 2012). The results of the MAC for the first 16 experimentally obtained mode shapes for each quarter-scaled slab in comparison to the corresponding numerical mode shapes are shown in Figure **5-17**. The results show that mode shape pairs have high correlation for each slab. Of note, some of the experimentally obtained modes (e.g., modes 12 and 13 for slab 1) were practically identical. As a result, the MAC calculation for some of the pairs of modes shows a weak correlation to the numerical results, but this is due to experimental error. The primary takeaway from the MAC calculation is that the numerical model correlates well to the experimentally obtained results, indicating that the numerical FEA models for the four slabs can be trusted.

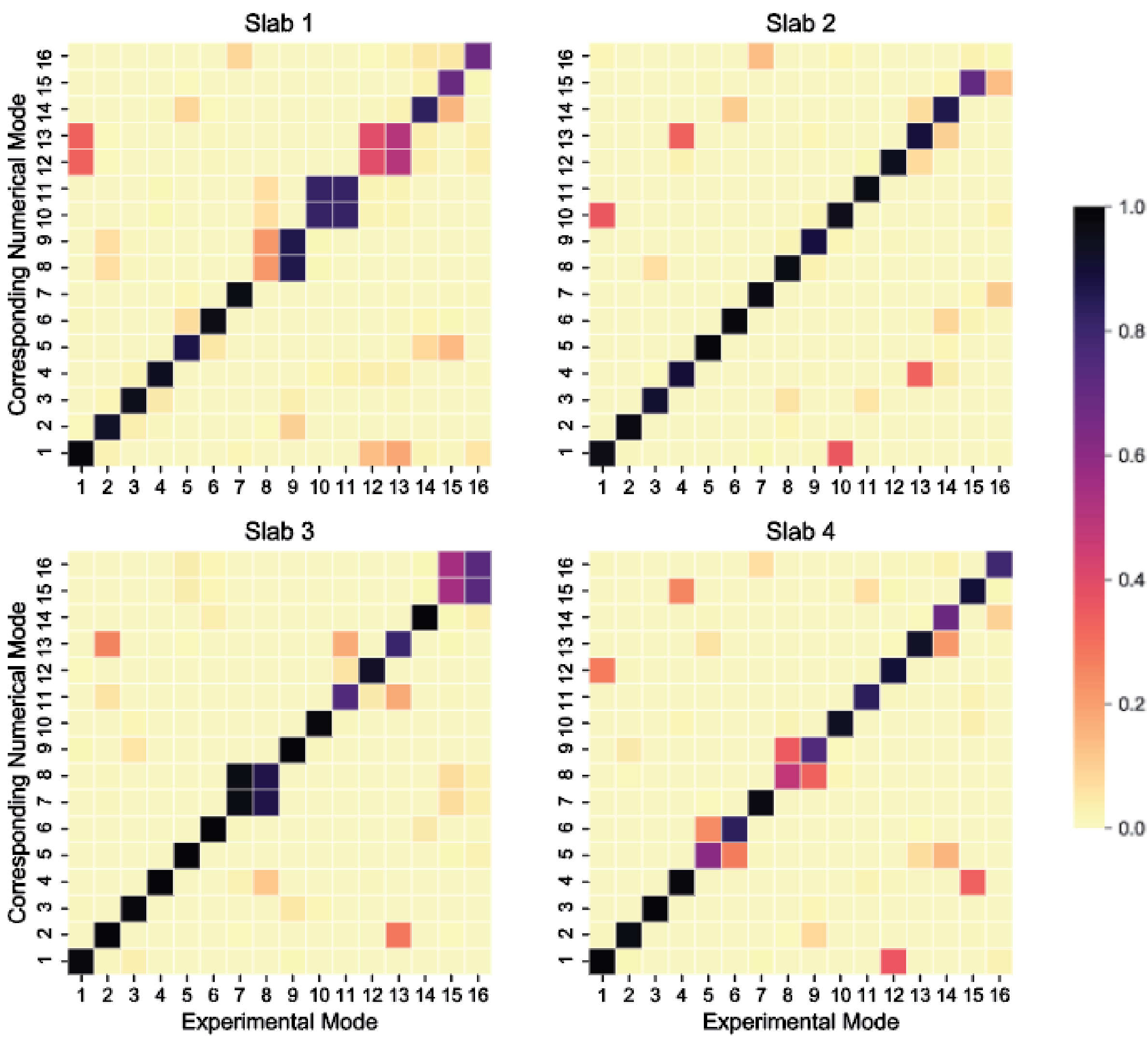

Figure **5-17**: The MAC for each quarter-scaled slab for the first 16 experimentally obtained mode shapes.

The modal damping factors that were experimentally obtained were used in the numerical model to determine the dynamic response, as seen in Figure **5-18**. The mobilities were obtained with an excitation point at grid point 1 (for reference, see Figure **5-4** a) and a reception point at grid point 7. It should be noted that the anti-resonances shown below correspond to minimal dynamic responses in between modes. In the numerical model, the equivalent viscous damping is applied as a constant value. Experimental values for the damping were needed due to the lack of a predictive damping model for shaped concrete specimens.

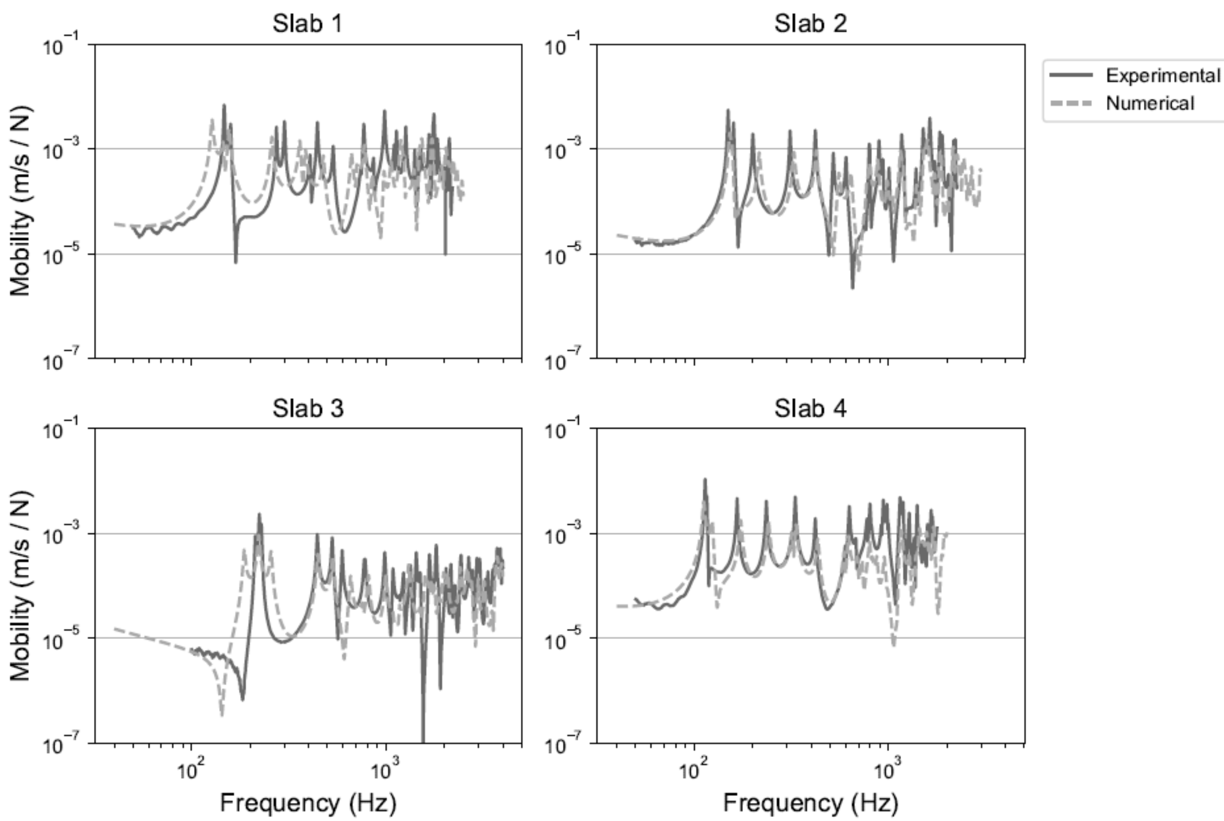

Figure **5-18**: The mobilities of each floor given an impact force at the corner of the slab.

5.5.4 Discussion

The previous figures show good agreement between experimental and numerical results. However, there are multiple factors of uncertainty that should be noted. First, concrete material can vary from pour to pour even when using the same concrete mixture. Although the ASTM C39 (ASTM, 2021b) standard was followed, previous research has reported significant variations in concrete material properties (Aït-Mokhtar et al., 2013; Pacheco et al., 2019). Second, while the placement of the steel rebar was located near the center of each rib, slight imperfections can create uncertainty in the numerical results. Finally, human error is a factor in fabricating specimens and conducting experimental measurements, leading to small uncertainties. The accuracy of the comparison between measurement and model is not entirely consistent between the four slabs, likely due to the differences in fabrication time. Nevertheless, the results from this study provide helpful insight on the dynamic performance of shaped floors, validating the numerical FEA approach used.

5.6 Implications in building acoustics

Validating the modeling procedure of shaped concrete specimens promotes many research opportunities in the field of building acoustics. Primarily, future researchers can implement the method demonstrated here to explore the dynamic performance of other uniquely shaped building elements. The structural geometry can be coupled to optimization frameworks aimed at increasing the sound insulation or improving the fundamental frequency. Furthermore, FEA models could be implemented as a decision-making tool to determine if optimized structures are acoustically advantageous compared to traditional building elements. Wall elements, which have been shown to have favorable acoustical performance when optimized (Hoban & Peters, 2022), can also be assessed using the proposed method.

Further experimental research should be conducted on shaped structural elements. For instance, a study determining the dynamic modulus of elasticity of different shaped specimens would be valuable for further dynamic analysis. A structural four-point bending test would also help validate the expected structural performance of these specimens. Experimental studies encompassing other building disciplines would give insight on the holistic performance of optimized floors.

This study also encourages the expansion of full-scale shaped slab specimen models (Filippou, 1990). The eigenfrequencies of the full-scale models could be compared to the experimentally obtained eigenfrequencies. A ratio of four-to-one would be expected from the quarter-scaled specimens. Although full-scale numerical FEA models have high computational costs, full-scale models could aid designers in finding the fundamental frequency of an entire floor or building (Pérez Caldentey et al., 2021). Full-scale models are also necessary to further understand the behavior of optimized structures (Burger et al., 2022). For example, the vibration performance caused by rhythmic loads, such as those experienced from a machine or human activity (i.e., walking), can be assessed to determine if vibration control measures are required (Wu et al., 2020). The computational results could be compared to a conventional flat slab to further study the influence of the shaped slabs.

Related, another research application is to determine the sound insulation performance of the bare shaped slabs. Using a simplified injected force of 1 N normal to the top (flat) side of the slabs, the modal frequency response can be found. A single impulse that excites a broad frequency range would be preferable as simulating rhythmic forces at many locations using FEA is computationally costly. The drive point impedance can be generated from the force and used to calculate the input power. The transmitted radiated sound power can then be calculated by determining the pressure at the boundary of a free-field air hemisphere (Conta et al., 2020). This strategy can help designers consider the impact sound insulation performance of different shaped structural elements in the conceptual design stage and is addressed in Ch. 6. A related subject to sound insulation is the coincidence frequency of a structure. Previous work by Broyles et al. (2021) found that the shape of concrete specimens can influence the frequency that the coincidence dip occurs in simulated transmission loss. Further, optimization techniques can improve air-borne performance of slabs by shaping the rib to have a coincidence frequency below the 125 Hz one-third-octave band, suggesting the need for alternative acoustic metrics in optimization frameworks. Later studies that optimize structural elements in buildings, like walls, should similarly study the coincidence frequency.

Additional areas of future research include the incorporation of room acoustic modeling techniques, such as ray-tracing, to determine the holistic acoustical performance in the building. Shaped ceilings have shown that geometric alterations can improve the acoustics in a room (Broyles et al., 2022b); however, sound insulation was neglected from this study. Incorporation of floating floors or hung ceilings is another avenue for future research. Similarly, assessment of the absorptive performance of non-traditional structures may be valuable for designers to explore alternatives for improving room acoustics (Butko, 2021). Lastly, incorporating accurate acoustic objectives can aid in multi-disciplinary studies aimed at determining the overall best performing designs (Broyles et al., 2022a).

5.7 Conclusion

This chapter presents the results of an experimental modal hammer test on four quarter-scaled shaped ribbed concrete slabs to help validate the results of a numerical FEA model. The numerical models were adjusted to minimize the percentage error between the eigenfrequencies obtained in the numerical modal analysis with the experimental modal response. Such validation is crucial before evaluating shape-optimized structures in larger numerical building analyses, especially for further optimization that incorporates acoustical objectives such as impact sound insulation and vibration control.

Chapter 6

Computationally efficient method for estimating impact sound insulation[1]

6.1 Introduction

Concrete floor structures have been the subject of significant research because they are among the leading contributors of the embodied carbon footprint in a multi-story building (Foraboschi et al., 2014; Huberman et al., 2015). To mitigate carbon emissions, building designers and engineers have employed optimization strategies to design non-conventional concrete floor geometries by removing unnecessary concrete material that is not contributing to the structural integrity of the floor (Ismail & Mueller, 2021). These strategies enable the potential for significant carbon emission savings, yet the reduction of concrete material can inadvertently affect the performance of other building objectives. Acoustic insulation is especially susceptible to the removal of concrete material as structural-acoustic characteristics, like mass density and bending stiffness, rely on dense structural material to achieve favorable acoustic insulation performance (Hambric & Fahnline, 2007). Poor acoustic insulation in buildings could result in costly building retrofits post-construction (Longinow et al., 2009), or serious health concerns to occupants, including increased annoyance (Jeon & Sato, 2008), stress (Jensen et al., 2018), and sleep disorders (Nivison & Endresen, 1993; Rasmussen & Ekholm, 2019). Impact sound insulation has been found to be a leading cause of acoustic complaints in buildings (Vardaxis et al., 2018), indicating the need to assess structure-borne sound insulation of material-optimized floor components.

To prevent the consequences of poor sound insulation in buildings, it is necessary to consider acoustic design goals when optimizing floor components. Roozen et al. (2018) tested a funicular concrete

[1] Chapter 6 is in preparation for submission to a peer-reviewed journal.

floor to help validate a numerical model in estimating the air-borne sound insulation performance. Similarly, Broyles et al. (2022c) explored how shaping one-way concrete floors could improve the air-borne acoustic insulation with the intent of minimizing concrete material and corresponding carbon emissions. Both studies demonstrated that air-borne acoustic insulation could be adequately estimated using experimentally validated finite element models and analytical expressions. However, the assessment of impact sound transmission performance for optimized concrete floors has been less studied.

Méndez Echenagucia et al. (2016) evaluated different funicular forms (i.e., different heights and rib geometries) for radiated sound power, but only considered frequencies below 200 Hz. While low frequency sound insulation should be evaluated, the full frequency impact sound performance was not considered, preventing the knowledge of how well the funicular floors can attenuate high frequency impact sounds. Furthermore, the rating of bare concrete floors using the North American acoustic transmission metric, Impact Insulation Class (IIC), is often controlled by the impact performance at high frequencies (ASTM E989, 2006). The analytical expressions that quantified air-borne sound insulation for shaped slabs are less precise for determining impact sound insulation. Broyles et al. (2022a) used a simple analytical expression by approximating the force of the hammers in an ISO tapping machine, however this approach could only estimate an impact sound rating, bypassing the determination of the normalized sound pressure levels across a broad frequency range. A more robust numerical method is therefore needed to evaluate the impact sound insulation performance of non-traditional floor structures.

Conventional methods to adequately simulate the impact sound insulation performance of concrete floors include wave-based methods, such as the finite element method (FEM) and the boundary element method (BEM). These methods have been widely implemented in research to evaluate rectilinear concrete floors. Neves e Sousa and Gibbs (2011) used analytical FEMs to assess the structure-borne sound insulation of homogeneous concrete plates. Asakura et al. (2018) validated the structure-borne sound insulation results of a 5-story concrete building using a computational FEM. Additionally, Reinhold and Hopkins (2021) experimentally assessed a concrete reception plate for structure-borne sound to tune a numerical model to better assess structural-borne sound insulation. Despite the popularity of wave-based methods to obtain the sound insulation performance of concrete floor structures, a major drawback is the computational (CP) time (Kim et al., 2019). Indeed, the large CP time and expertise to create an accurate FEM or BEM have limited the number of studies evaluating concrete floor structures for impact sound.

Another drawback to current numerical methods is that a very fine mesh resolution is needed to appropriately consider the acoustic performance at high frequencies (Howard & Cazzolato, 2014). Popular FEM software programs (i.e., Ansys, Abaqus) recommend a minimum of six finite elements per wavelength (Marburg, 2002), which can significantly increase the CP time from a few hours to many hours or days. The type of finite element can also further increase CP time. As seen in Fig. **6-1**, higher order element types result in accurate results, but extensive computational costs, suggesting a trade-off between accuracy and CP time. The substantial computational cost hinders the ability to simulate many different concrete floor forms for impact sound insulation, especially in design exploration frameworks. These limitations motivate the question: how can a numerical method adequately estimate the full frequency (including both low and high frequencies) impact sound insulation performance of non-traditional concrete slabs while reducing the required computational resources?

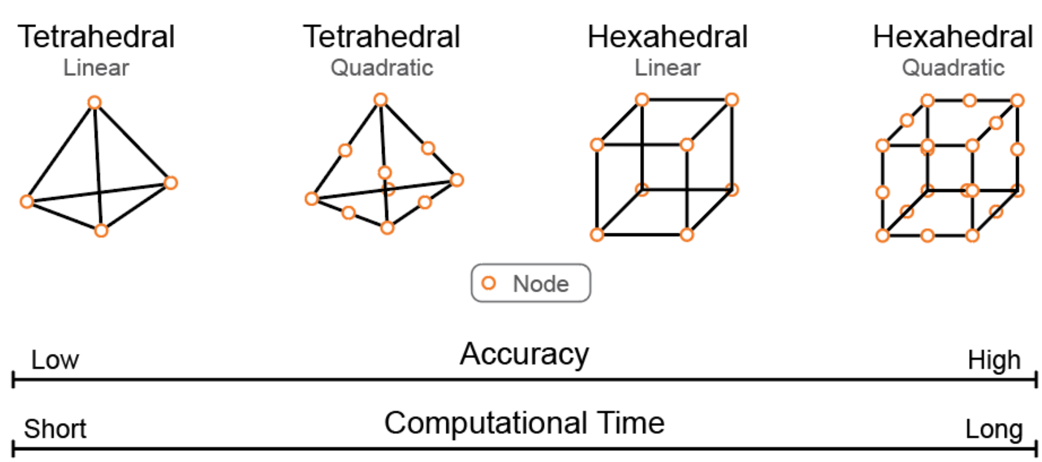

Figure **6-1**: Comparison between the common FEM element types and associated accuracy and computational time.

This chapter responds to this question by describing a numerical method to approximate the full frequency impact sound insulation performance of shaped concrete floors. A hybrid air-hemisphere and radiation efficiency method is proposed to estimate the broad frequency range required to impact sound insulation for concrete floors. Specifically, the conventional air-hemisphere method can be applied at a subset of low frequencies, while the radiation efficiency can be calculated and used to approximate the radiated sound power at frequencies above the coincidence frequency. This approach is especially suited for concrete floors because the coincidence frequency is relatively low, thereby allowing mid- and high-frequencies to be approximated. As a result, the required meshing in the FEM model and consequent computational time are reduced to enable quicker evaluations. This method, which in this dissertation is referred to as the IIC-Like method, is validated for three rectilinear concrete plates and four shaped concrete floors that were experimentally tested for dynamic performance. This method also makes use of six different walking paths to determine the worst-case impact sound insulation scenario. After validating this method for the flat and shaped concrete floor case studies, additional methodological considerations are addressed including the inclusion of low frequency impact sound below 100 Hz and to determine if modeling walking paths is needed. A discussion of the application of this method, including estimated computational resource savings, concludes this chapter. Overall, this chapter details a numerical approach to more efficiently approximate impact sound insulation performance for conventional and non-traditional concrete floors.

6.2 Background

6.2.1 Conventional methods to simulate impact sound insulation

The air-hemisphere method is an existing numerical method to quantify the radiated sound power of a structure. To evaluate the impact sound insulation performance of a structure, force(s) that act normal to a floor structure are modeled to obtain the input power. The dynamic response of the structure is then used to determine the radiated sound power at the boundary of a hypothetical air hemisphere that represents the far-field condition. Fig. **6-2** illustrates this conventional methodology for a rectilinear plate.

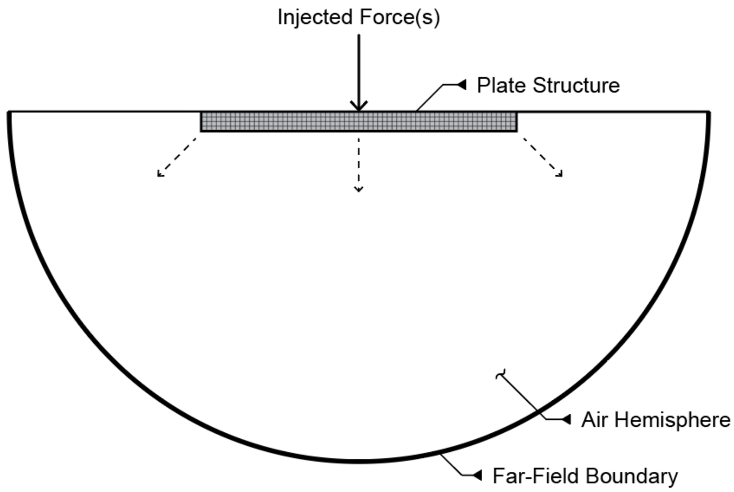

Figure **6-2**: Illustration of the far-field air-hemisphere method for a conventional plate.

The radiated sound power, P_{rad}, can be obtained at the boundary of the far-field air hemisphere and compared to the injected sound power, P_i, acting on the structure to determine the transmission coefficient, τ, performance across a broad frequency range. The surface-averaged velocity, $\langle|v|\rangle$, which is caused by an input force(s), F, can be used to calculate the input power, P_i,:

$$P_i = \frac{1}{2}\mathrm{Re}(F\langle|v|\rangle^*) \qquad \text{(Equation 6-1)}$$

The radiated sound power, P_{rad}, is calculated by taking the summation of the complex conjugate between the pressure, p, and particle velocity, u, for each element, i, multiplied by the corresponding area of the element, A_i, along the boundary of the far-field air hemisphere:

$$P_{rad} = \frac{1}{2}\sum_i \mathrm{Re}\,\{p_i u_i^*\}A_i \qquad \text{(Equation 6-2)}$$

The ratio of input power to radiated power is calculated to obtain the transmission coefficient, τ, for a given frequency range,

$$\tau = \left(\frac{P_i}{P_{Rad}}\right), \qquad \text{(Equation 6-3)}$$

and can be used to obtain normalized sound pressure levels (L_N), which can be used to obtain a numerical impact insulation rating.

6.2.2 Challenges to simulating impact sound insulation performance

Impact sound is a growing concern in the design of the built environment, as poor impact sound insulation has been found to be one of the primary sources of complaints in residential buildings (Vardaxis & Bard, 2018). In North America, impact sound transmission in buildings is often quantified as an Impact Insulation Class (IIC) rating (ASTM E989, 2006), which provides a single scalar value for the structure-borne transmission performance of a structure. Impact sound performance is commonly obtained experimentally using a tapping machine in North America, as follows ASTM E492 (2022). Yet the procedure to extract an IIC rating from the tapping machine has many limitations at lower frequencies due to the 2 Hz / 10 Hz harmonic dropout in the frequency domain. Indeed, the lower frequency bound to calculate IIC has been well studied, but not agreed on, as researchers have proposed various lower-bound limits down to 50 Hz (Loverde & Dong, 2018). Researchers have also questioned whether the laboratory measurements for impact sound are reliable, especially at low frequencies, complicating the assessment of structure-borne sound insulation (Girdhar et al., 2023a; 2023b). Further, alternative impact sound metrics have been developed to complement the existing IIC rating to provide a more comprehensive understanding of the impact sound insulation performance of a floor (LoVerde & Dong, 2017).

Conventional FEM methods for determining the radiated sound power of a structure have been available for many decades, yet the large computational cost of running a single FEM simulation has limited its utility in many engineering applications. This is because the conventional IIC rating evaluates the impact sound transmission loss of a structure from the 100 Hz OTO band to the 3.15 kHz OTO band, requiring both a large enough air hemisphere to account for low frequencies and a very fine mesh resolution to accommodate the high frequencies, resulting in a very large FEM. Additionally, concrete floor systems commonly have impact sound deficiencies at both low and high frequencies, indicating why little studies have evaluated the full frequency impact sound performance of concrete floor systems. These challenges provide helpful context to why many related studies investigating the impact sound of structures look at a subset of the frequencies needed to evaluate IIC (Mendez Echenagucia et al., 2016), indicating a need for an alternative approach to existing conventional numerical methods to evaluating impact sound.

6.2.3 Chapter scope

Motivated by the challenge of estimating impact sound insulation performance across a broad frequency range for concrete floors while minimizing computational resources, this study details a computationally-efficient method to determine the impact sound insulation performance of conventional and non-traditional concrete systems. The procedure for this method is outlined in the next section, followed by validation and a discussion on the applications, estimated computational resources that are saved when using this method, and the limitations of this work. Overall, this study extends existing research on the numerical quantification of impact sound insulation of floors in buildings by detailing a hybrid air-hemisphere that uses the acoustical concept of radiation efficiency to evaluate the broad frequency impact sound insulation performance of different floor shapes (forms) without expending significant computational resources.

6.3 Methods

This section describes the method for simulating an impact sound objective (IIC-Like) for concrete floor components. The general procedure for the IIC-Like method is as follows:

1. Conduct a modal analysis of the slab,
2. Simulate the low frequency response function (FRF) for each walking path,
3. Obtain the low frequency radiated sound power using the far-field air-hemisphere method,
4. Calculate the radiation efficiency,
5. Simulate the broad (low to high) FRF for each walking path,
6. Check that the low and broad FRFs match, otherwise apply a correction to the radiation efficiency,
7. Compute the injected and radiated power, and
8. Determine the L_N curve to find the simulated IIC-Like objective.

While neither the conventional air-hemisphere method and the concept of radiation efficiency are by themselves novel, the strategic combination by simulating only a subset of frequencies which can be used to calculate the radiation efficiency of a structure to determine the full frequency impact sound performance is novel. The following subsections provide the necessary details to replicate this method and how this method was validated to ensure that the results obtained from this method can be trusted in future design exploration and optimization frameworks of optimized concrete components.

6.3.1 A hybrid air-hemisphere and radiation efficiency method

This study used the FEM program Ansys (version 2023, R1) to obtain the FRFs, sound pressures, and velocities needed to calculate the injected and radiated sound powers which can be used to obtain the L_N data and subsequent IIC-Like rating. Three rectilinear concrete flat plates and four shaped floor components were used in the validation of the method. The three concrete flat plates had varying thicknesses of 101.6 mm (4 in), 152.4 mm (6 in), and 203.2 mm (8 in), with a width of 3 m and a length of 6 m to match the dimensions of the shaped specimens, which are the full-scaled equivalent slabs tested in Ch. 5. The thicknesses were selected to align with the reported experimental results from the NRCC (Warnock, 2005) and the National Ready Mixed Concrete Association (NRMCA) (2022). The normalized sound pressure levels (L_N) and experimentally obtained IIC ratings were used in the validation of the IIC-Like method in Sec. 6.4.1. Normal material properties of the flat concrete plates were assumed; therefore, the concrete density was defined as 2,400 kg/m^3, (150 pcf), with a strength of 28.2 MPa (~4,000 psi), a modulus of elasticity of 25,000 MPa, and a Poisson's ratio of 0.18. The shaped slabs were modeled with slightly modified properties than the flat concrete plates, so to match the material properties used to tune the quarter-scaled numerical model in Ch. 5; therefore, a concrete density of 2,400 kg/m^3, a strength of 46.54 MPa (~6,500 psi), a modulus of elasticity of 32,064 MPa, and a Poisson's ratio of 0.18 were specified.

To adequately compute the acoustic performance of the shaped concrete components using a FEM, a multizone mesh method was applied. This mesh method consisted of linear hexahedral elements with an element size no larger than 0.03 m. Steel reinforcement was modeled as a strip of elements, as was similarly done in Ch. 5. After specifying the material properties and defining the mesh, a modal analysis of the slab was conducted. The number of modes to adequately obtain the dynamic performance is recommended to be at least twice the frequency of what is desired to be investigated. Due to the high upper frequency bound of 3548 Hz to simulate impact sound, the highest eigenfrequency was set to 8 kHz to ensure that enough modes are considered in determining the dynamic response.

The low FRF was found following the modal analysis. As described previously, a single impact can be used to approximate the impact sound performance of a homogeneous structure. Yet this study modeled average walking paths in six patterns to determine the walking path pattern that controlled the IIC-Like rating. To provide an accurate representation of a walking path, the dimensions of the footfall impacts are based on an anthropometric schematic (see Fig. **6-3**), with the centroids of the feet modeled as idealized forces in the FEM.

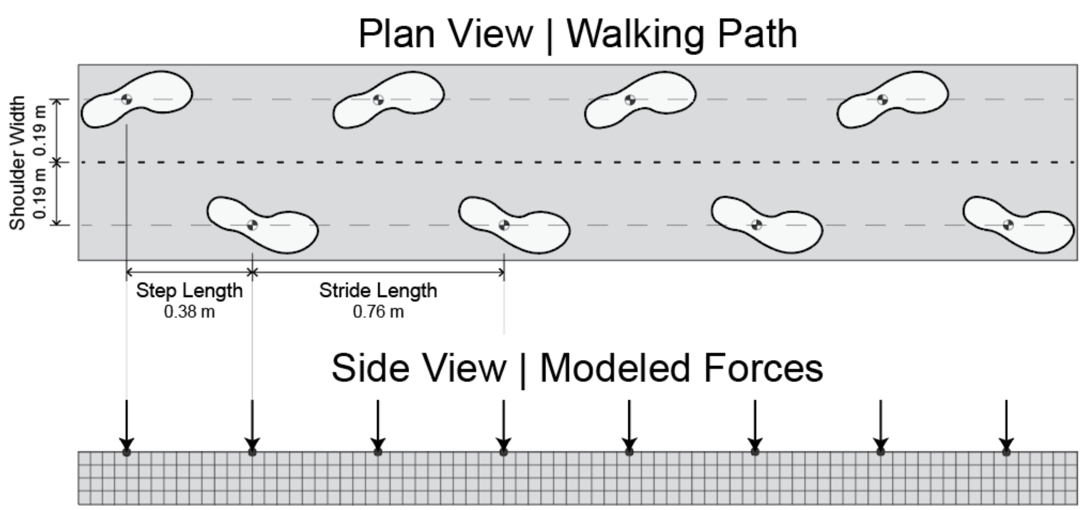

Figure **6-3**: Anthropometric walking path schematic and idealized forces in the computational model.

Six unique walking paths (WPs) were defined (see Fig. **6-4**) to represent distinct scenarios that could result in varying impact sound insulation ratings, especially given the different rib forms. In this study each WP was modeled in the FEM, with the results from the worst-case WP used to quantify the IIC-Like.

Yet to further reduce the computational time needed to ascertain the dynamic response, only half of the slab was modeled because the floor is symmetric as shown in Fig. **6-5**. The impacts on each WP (shown as the red circles in Fig. **6-4**) represent footfall, with the summation of the forces modeled as a 1 N force applied normal to the slab in the negative z-direction. To account for the differences in the number of nodes across the six WPs, the impact force was divided by the number of impact forces. The forces were simulated in steady state, acting in phase to excite a broad frequency range. Although the modeling of in-phase forces along a WP is not representative of real footfall, it is a computationally-conservative estimate for determining the impact sound insulation. The frequency range of the low FRF corresponded to the first four OTO bands needed to obtain an IIC rating (100 Hz, 125 Hz, 160 Hz, and 200 Hz) were simulated. To ensure that a high fidelity FRF was obtained, the dynamic response was found between a frequency range of 89 Hz (the lower bound of the 100 Hz OTO band) to 224 Hz (the upper bound of the 200 Hz OTO band) with 144 logarithmic spaces, or 36 logarithmic spaces per OTO band.

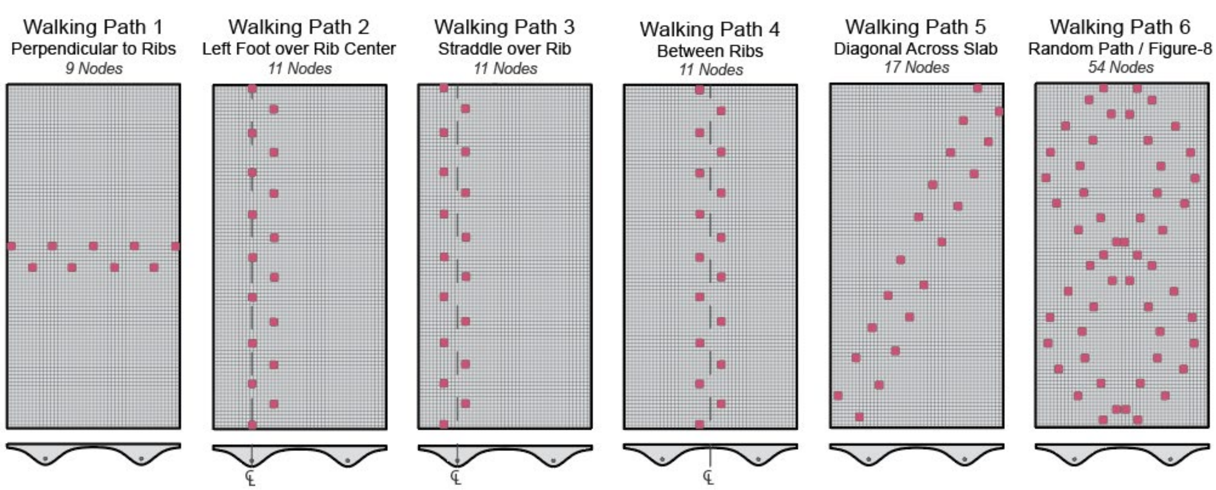

Figure **6-4**: The six WPs modeled for every slab to determine the worst-case impact sound insulation scenario.

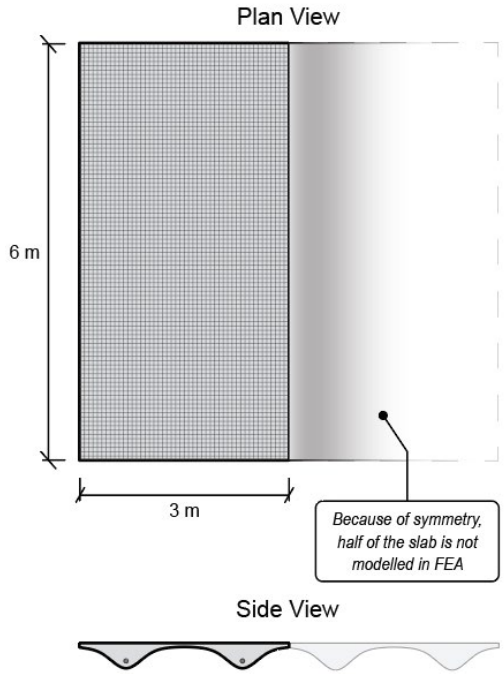

Figure **6-5**: Only half of the concrete slab was modeled due to symmetry to reduce the size of the FEM.

The low frequency, surface-averaged velocities normal to the slab caused by the input forces from each WP were then used to obtain the low frequency radiated sound power by using the far-field air-hemisphere method (Kirkup, 1994). In this study, the interior of the air-hemisphere was modeled as Fluid30 acoustic elements, and the exterior of the hemisphere modeled as Fluid130 acoustic elements, as shown in Fig. **6-6**. The radius of the hemisphere to obtain the low frequency radiated sound power was determined to be 4.12 m, using the equation:

$$r \geq r_{panel} + 0.2\lambda_{max} \quad \text{(Equation 6-4)}$$

The radius of all panels was 3.35 m and the contribution from the largest wavelength (at 89 Hz) was 0.771 m. Therefore, the radius of the air hemisphere for all slabs evaluated in this study was set at 4.12 m.

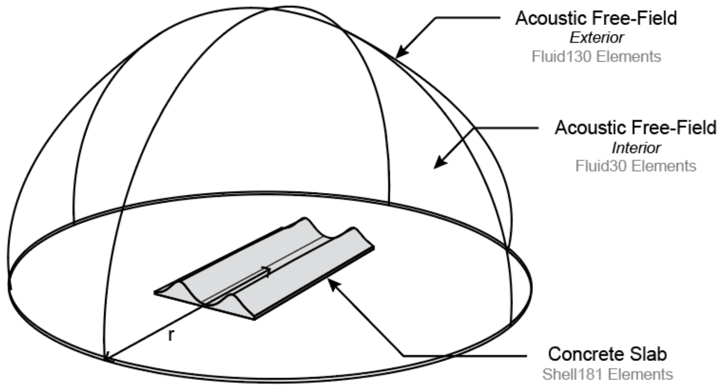

Figure **6-6**: A representative far-field air-hemisphere model to determine the radiated sound power.

After the simulating the frequency response in the air-hemisphere, the low frequency radiated sound power, $P_{Rad_{Low}}$, is calculated by taking the summation of the complex conjugate between the pressure, p, and particle velocity, u, for each element, i, multiplied by the corresponding area of the element, A_i, along the boundary of the far-field air hemisphere:

$$P_{Rad_{Low}} = \frac{1}{2}\sum_i \mathrm{Re}\,\{p_i u_i^*\} A_i \qquad \text{(Equation 6-5)}$$

The low frequency radiated sound power was then used to obtain the radiation efficiency, σ_{rad}, using the equation,

$$\sigma_{rad} = \frac{P_{Rad_{Low}}}{\rho_0 c_0 A \langle |v|^2 \rangle}, \qquad \text{(Equation 6-6)}$$

where the density of the air, ρ_0, is assumed to be 1.29 kg/m^3, A is the area of the underside of the slab, and $\langle |v|^2 \rangle$ is the surface-averaged velocity.

Following the calculation of the radiation efficiency, the dynamic frequency response is calculated for the full frequency range needed to determine an impact sound objective. The dynamic response is assessed from 89 Hz, the lower bound of the 100 Hz OTO band, to 3.548 kHz, the upper bound of the 3.15 kHz with 684 logarithmic spaces, or 36 logarithmic spaces per OTO band. The broad frequency response is then compared to the low frequency response to evaluate if a correction factor needs to be applied to the radiation efficiency to correctly obtain the radiated sound power for the full frequency range. The correction factor is applied by shifting the full frequency dynamic response based on the difference from to the low frequency dynamic response. The corrected full frequency response is then used to determine the radiated sound power:

$$P_{Rad} = \sigma_{rad}\rho_0 c_0 A\langle|v|^2\rangle. \qquad \text{(Equation } \mathbf{6\text{-}7}\text{)}$$

The injected power, P_i, is calculated by the input force from each walking path, F, and the surface-averaged velocity,

$$P_i = \frac{1}{2}\mathrm{Re}(F\langle|v|\rangle^*), \qquad \text{(Equation } \mathbf{6\text{-}8}\text{)}$$

which is then used in the ratio of input to radiated sound power to obtain the transmission coefficients, τ, for the full frequency impact performance, using the equation:

$$\tau = \left(\frac{P_i}{P_{Rad}}\right). \qquad \text{(Equation } \mathbf{6\text{-}9}\text{)}$$

The transmission coefficients at each of the 684 logarithmic spaces are used to find the normalized sound pressure levels, L_N, using Eq. **6-10**. The L_N values are binned according to the OTO bands to be used in determining the IIC-Like rating.

$$L_N = 10\log\left(\frac{1}{\tau}\right) \qquad \text{(Equation } \mathbf{6\text{-}10}\text{)}$$

The structure-borne sound insulation objective, IIC-Like, is determined following ASTM E989 (ASTM, 2004). As mentioned previously, IIC considers 16 OTO bands, from 100 Hz to 3.15 Hz. The IIC contour defined in ASTM E989 is the same, the only difference is that the L_N values used to obtain the impact rating are simulated, hence the use of the "-Like" tag in this study.

6.3.2 The relationship between radiation efficiency and the coincidence frequency

As motivated previously, the conventional air-hemisphere method requires significant computer memory and CP time when evaluating a broad frequency range; therefore, a computationally-efficient method is needed to be able to explore many floor shapes for impact sound performance. To this end, the concept of radiation efficiency was used to determine the radiated sound power, and consequent L_N, at frequencies above the coincidence frequency of a concrete structure. As Fig. **6-7** illustrates, the radiation efficiency stabilizes above the coincidence frequency of a structure; therefore, the full frequency radiated sound power can be based on the low frequency radiated sound power found above the coincidence frequency. Because of this, it is necessary to calculate the coincidence frequency of the concrete slabs to check that the IIC-Like method is applicable.

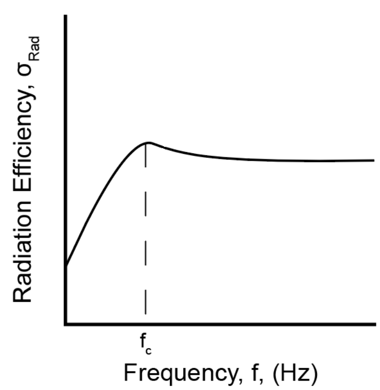

Figure **6-7**: The relationship between frequency and the radiation efficiency of a radiating structure.

The coincidence frequency (see Eq. **6-11**) is a function of the speed of sound of the air, c_0, and the density, ρ, thickness, h, and bending stiffness, D, of a structure. This work assumes normal room temperature conditions, so the speed of sound and density of the air is 343 m/s and 1.29 kg/m^3 respectively.

$$f_c = \left(\frac{1}{2\pi}\right) {c_0}^2 \sqrt{\frac{\rho h}{D}} \qquad \text{(Equation 6-11)}$$

The bending stiffness of the shaped ribbed slabs can be approximated using Eq. **6-12**, where E_c is the modulus of elasticity of the concrete, ν is the Poisson's ratio, I is the moment of inertia, and Δ_{Rib} is the rib spacing. Both terms are used to find the bending stiffness of the shaped slabs with ribs in one direction, while only the left term is used to calculate the bending stiffness of flat plates.

$$D = \frac{Eh^3}{12(1-\nu^2)} + \frac{EI}{\Delta_{Rib}} \qquad \text{(Equation } \mathbf{6\text{-}12}\text{)}$$

As seen in Eq. **6-12**, larger mass increases the coincidence frequency, while larger bending stiffness decreases the coincidence frequency. For concrete plates, thickening the slab results in a larger stiffness than mass increases, resulting in a low coincidence frequency. Determining the coincidence frequency for ribbed concrete floors is more nuanced than flat plates, because the rib geometry can meaningfully influence its contribution to the bending stiffness. Yet as found through experimentation and analytical calculations, concrete flat plates and ribbed slabs have low coincidence frequencies (Dupree, 1980; Warnock, 2005).

6.4 Validation and results

Validating the impact sound performance obtained by the IIC-Like method is a necessary step before the method can be broadly implemented and the results can be trusted. To validate novel acoustic methodologies, researchers have previously:

1) validated the numerical findings obtained through the novel method through experimental validation (Asakura et al., 2018; Kim et al., 2019; Kohrmann, 2016; Kuo et al., 2016; LoVerde & Dong, 2017);

2) compared the simulated results to simplified numerical case studies with the expected, or ground truth, performance known (Chevillotte & Panneton, 2011; Christen et al., 2016; Dostart et al., 2017; Yang et al., 2018); and

3) compared the numerical results obtained from the new method to the numerical results from a well-vetted and trusted numerical method or model (Dostart et al., 2017; Prasetiyo, 2012; Qian et al., 2019; Yang et al., 2018).

This work used the first two validation strategies to assess if the IIC-Like method is appropriate for quantifying impact sound of concrete structures. First, the simulated L_N values and corresponding IIC-Like ratings were compared to experimental findings for three concrete flat plates. Second, the modal performances and FRFs of the quarter-scaled slabs that were experimentally tested in Ch. 5 were compared to the numerical results of the same four shapes but at full scale.

6.4.1 Validation A: Flat concrete plates

The first validation strategy was to compare the simulated results of three flat concrete plates to reported experimental findings. The three concrete flat plates had thicknesses of 0.102 m (4 in), 0.152 m (6 in), and 0.203 m (8 in), as illustrated in Fig. **6-8**. The slabs had a length and width of 6 m by 3 m to be comparable to the IIC-Like results for the full-scaled shaped ribbed slabs. The steel reinforcement elements were specified at a spacing of 0.5 m (~20 in) with a minimum clear cover of 0.038 m (1.5 in).

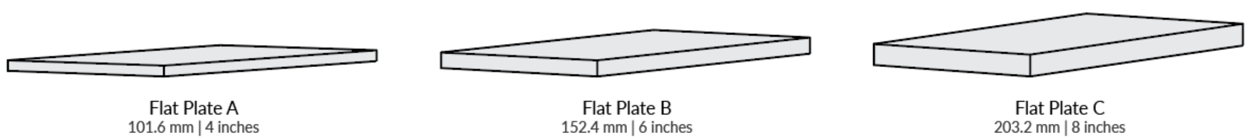

Figure **6-8**: The three concrete plates used in the validation of the IIC-Like method.

To ensure that the IIC-Like method can be applied to the three flat plates, the coincidence frequency for each plate was calculated, as reported in Table **6-1**. Flat plate A was found to have a meaningfully higher coincidence frequency compared to Flat plates B and C; however, the radiated sound power was calculated at frequencies above 194.6 Hz. Additionally, the comparison of low-to-full FRFs matched, requiring no correction to the calculation of the radiation efficiency, implying that the IIC-Like method was still appropriate.

Table **6-1**: Structural-acoustic characteristics of the three flat plates.

Slab	**Mass Density, (kg/m^2)**	**Bending Stiffness (N*m)**	**Coincidence Frequency, f_c, (Hz)**
Flat Plate A	243.8	2.258 x 10^6	194.6
Flat Plate B	365.8	7.621 x 10^6	129.7
Flat Plate C	487.7	1.806 x 10^7	97.3

Figure **6-9** compares the simulated L_N values for flat plate A and flat plate B to the experimentally obtained data reported by the NRCC (Warnock & Birta, 2000). Note that these were the only flat concrete plates described in the NRCC report. The experimental *TL* data provided in the NRCC report was obtained in accordance with ASTM E90 (2009), with the STC rating determined following ASTM E413 (2016). Similarly, the experimental L_N data was measured in accordance with ASTM E492 (2022), with the IIC rating obtained based on ASTM E989 (2006). Although the comparison of L_N values is not uniform across all OTO bands, it is observed that the simulated and experimental values are in better agreement in the mid- and high-frequencies compared to the low-frequencies. Although impact sound performance must be appropriately considered at low frequencies, the upper frequencies control the impact rating of bare concrete floors, suggesting that the IIC-Like method is viable to provide an estimate of impact sound. Another aspect of this comparison is that only the worst-case L_N data (WP 6 for both flat plates) was used in the comparison, as this would be the controlling IIC-Like rating given to a specific structural element (see Fig. **6-10**).

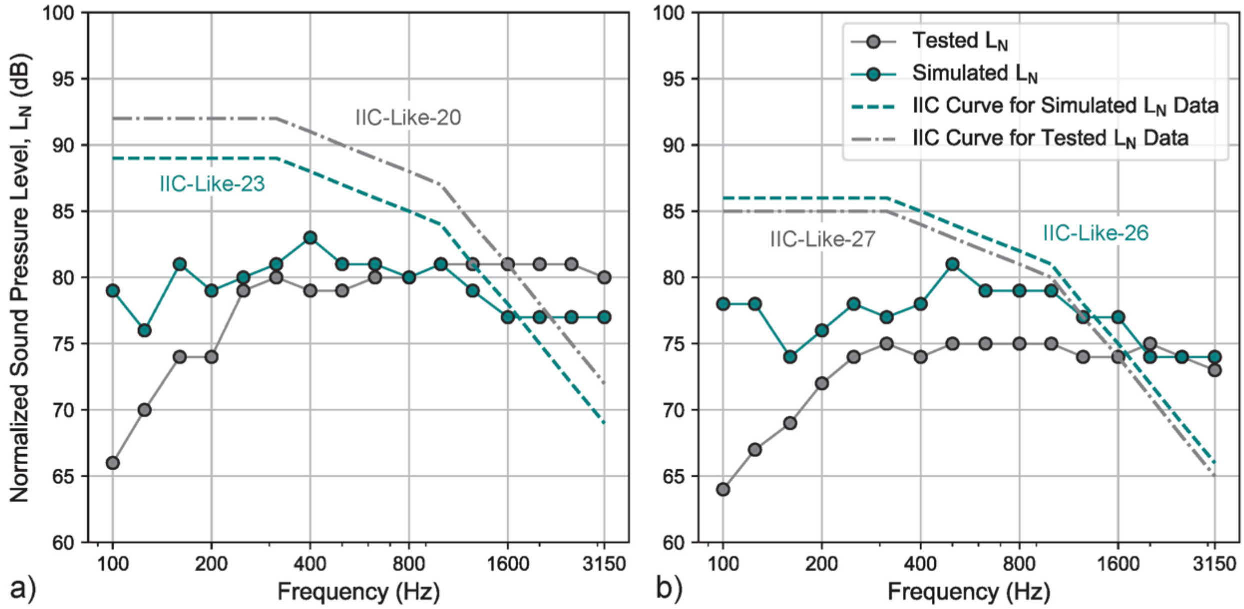

Figure **6-9**: Comparison of the experimentally tested L_N data for a) flat plate A and b) flat plate B to the simulated L_N values obtained using the IIC-Like method.

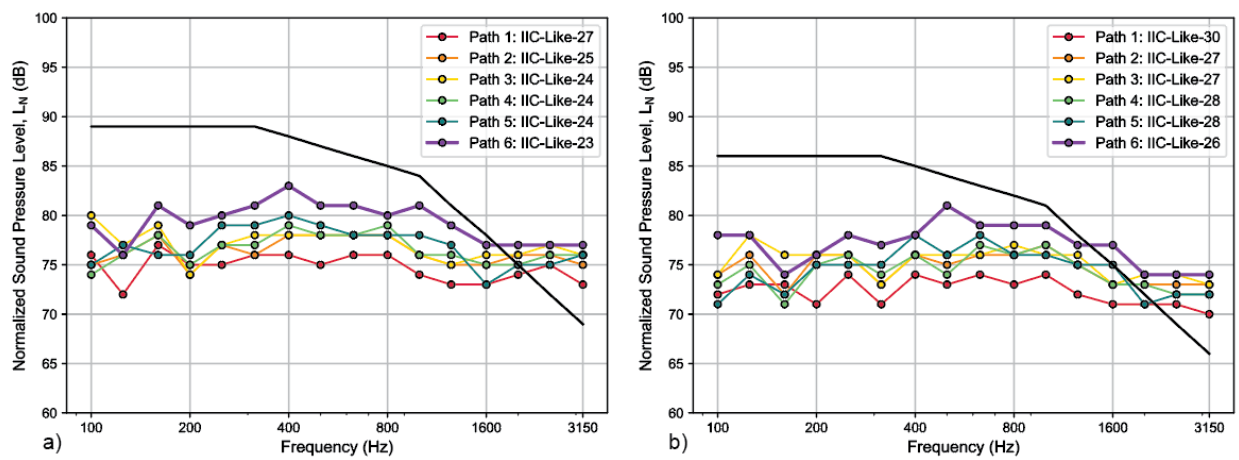

Figure **6-10**: The L_N data for all six WPs for a) flat plate A and b) flat plate B with the controlling WP used to determine the IIC-Like rating.

The simulated IIC-Like ratings were also compared to the experimentally obtained values for the three flat plates. A recent NRMCA report (2022) provided ranges of IIC ratings for the three flat plates, as shown in Fig. **6-11**. The simulated IIC-Like ratings are within the ranges in the report but are on the lower end of the IIC rating ranges obtained for flat plates B and C. Intuitively, both the experimental ratings and the simulated ratings show the same trend that as the mass density of the slab increases, the impact sound insulation also increases. Since mass density acts as a proxy for EC, it is expected that higher impact sound insulation is achieved with high EC. One final observation is that the IIC and IIC-Like ratings fall between a rating of 20 to 32. These ratings are well short of the International Building Code (IBC) requirement of an IIC rating of 50.

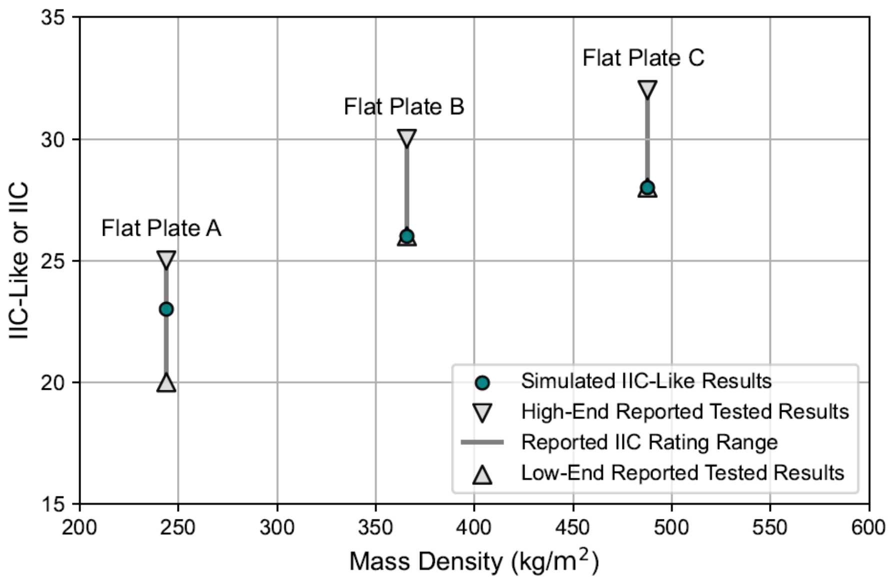

Figure **6-11**: Comparison between the experimentally obtained IIC ratings to the simulated IIC-Like ratings for the three flat plates.

6.4.2 Validation B: Quarter-scaled shaped concrete slabs

The second validation strategy was to ensure that the dynamic response for the full-scaled shaped slabs matched the tested dynamic response of four quarter-scaled shaped slabs (refer to Ch. 5). Fig. **6-12** shows the shaped slabs and Table **6-2** provides the structural-acoustic characteristics. In comparison to the three flat plates, the four shaped slabs have higher mass densities and bending stiffnesses, resulting in lower coincidence frequencies.

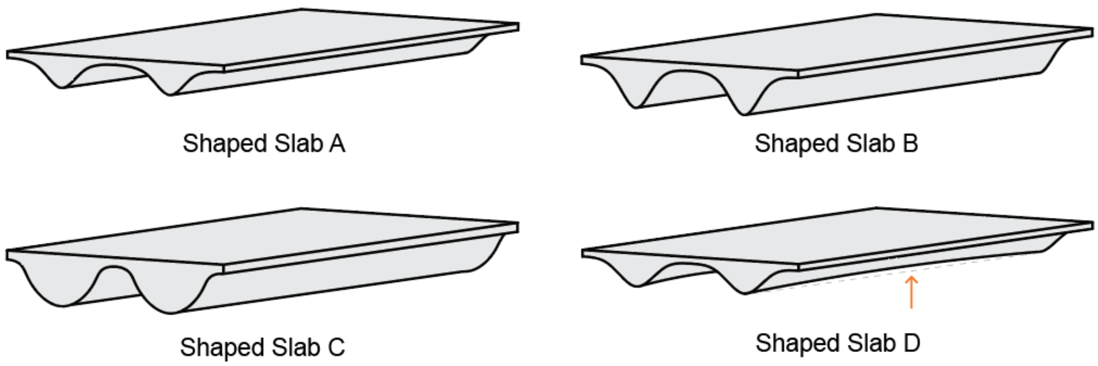

Figure **6-12**: The four slab shapes were used to validate the dynamic response for the full-scaled shaped slabs.

Table **6-2**: Structural-acoustic characteristics for the four full-scaled shaped slabs.

Slab	Mass Density (kg/m^2)	Bending Stiffness (N*m)	Coincidence Frequency, f_c, (Hz)
Shaped Slab A	459.1	2.228 x 10^7	85
Shaped Slab B	586.7	6.800 x 10^7	55
Shaped Slab C	896.8	1.423 x 10^8	47
Shaped Slab D	413.0	1.219 x 10^7	109

First, the numerical eigenfrequencies for the first 16 mode shapes were compared to the experimentally obtained eigenfrequencies (see Fig. **6-13**). Because the tested slabs were at quarter scale, a 1:4 ratio of the experimental to the numerical eigenfrequencies is expected. Aside from shaped slab A, which had an earlier fabrication time than shaped slabs B, C, and D (refer to Sec. 5.5.2 for more information), the comparison of eigenfrequencies shows that the numerical eigenfrequencies are true to the 1:4 ratio. This implies that the full-scaled shaped slab FEMs agree with the experimental findings of the quarter-scaled specimens. Second, Fig. **6-14** shows a Modal Assurance Criterion (MAC) analysis. The MAC analysis was conducted between the experimental quarter-scaled slabs and the numerical full-scaled slabs and also shows good agreement for the first 16 modes for the four shaped slabs. Lastly, the mobilities between the numerical full-scaled slabs to the experimental quarter-scaled slabs were compared as shown in Fig. **6-15**. The numerical frequencies were scaled by a factor of 4 and the mobility magnitude was scaled by a factor of the angular frequency. Similar to the comparison of the eigenfrequencies, the numerical mobility for shaped slab A differs slightly from the experimental results; yet the scaled numerical results largely agree with the experimental findings. Figs. **6-13**, **6-14**, and **6-15** confirm that the full-scaled slabs agree with the experimental results found in Ch. 5, thereby trusting the numerical FRFs. However, because the L_N data was not experimentally obtained, the numerical results could only be validated up to the comparison of the FRFs.

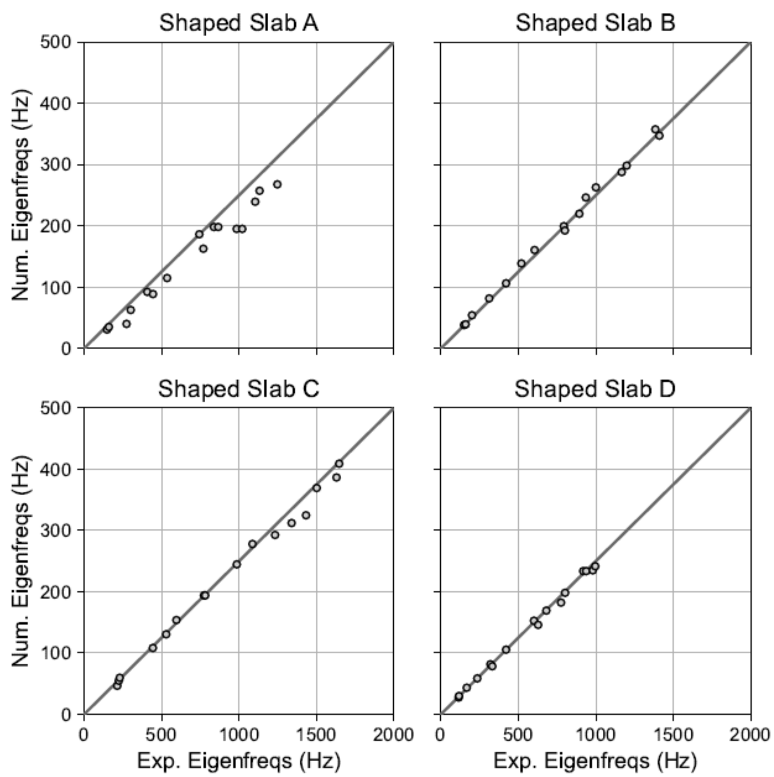

Figure **6-13**: Comparison of the experimentally obtained eigenfrequencies of the quarter-scaled specimens to the numerically obtained eigenfrequencies of the full-scaled specimens.

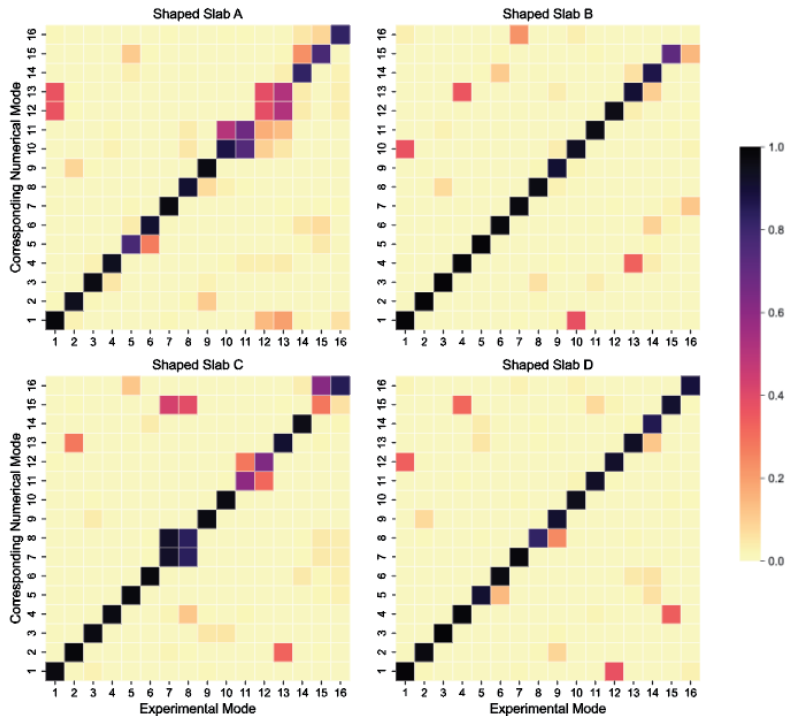

Figure **6-14**: The MAC between the quarter-scaled specimens and full-scaled models.

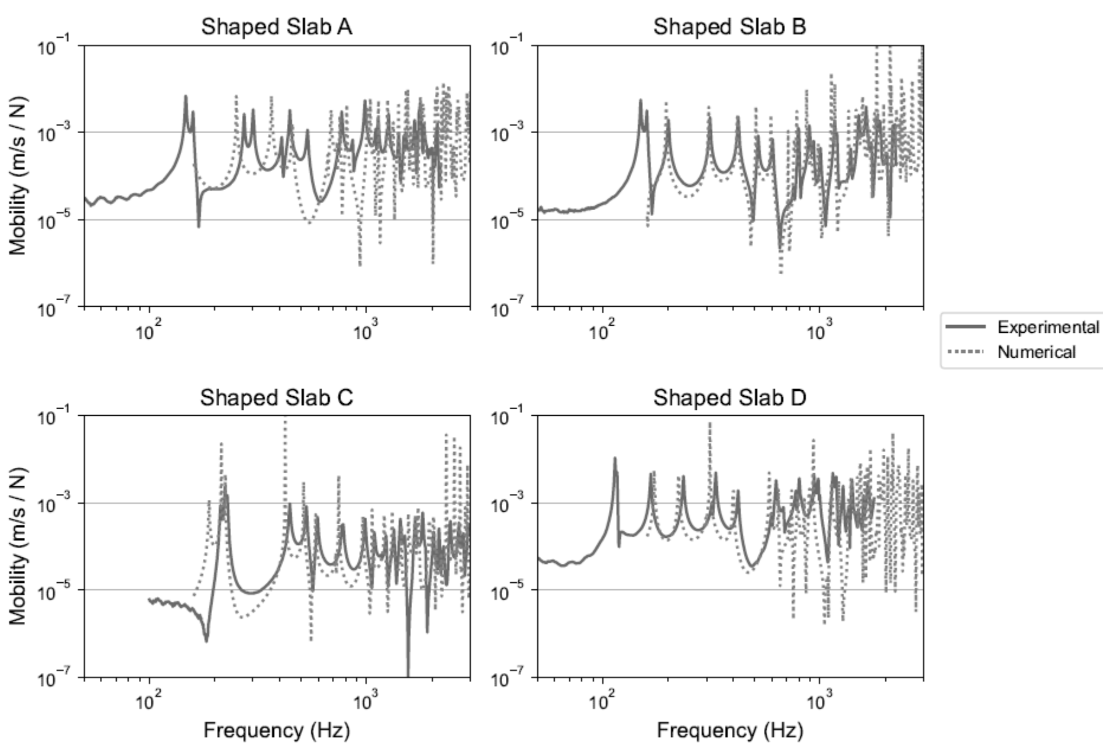

Figure **6-15**: Comparing the experimentally obtained mobilities of the quarter-scaled specimens to the numerical mobilities of the full-scaled models.

After validating that the FRFs obtained for the full-scaled shaped slabs could be trusted, the IIC-Like ratings were obtained following the IIC-Like method. Figs. **6-16** to **6-19** show the low to full FRF comparison to check if a correction needed to be applied to the calculation of the radiation efficiency for each shaped slab. As stated before, if the low FRF differed from the FRF obtained for the full frequency range needed to determine an IIC-Like rating, then the magnitude needed to shift (match) the low FRF was multiplied to the radiation efficiency. However, the FRFs matched for the four shaped slabs, therefore no correction factor was necessary to determine the radiated efficiency. Although the low-to-full FRFs matched, it can also be observed that each WP produced a unique FRF, indicating different impact sound insulation performance, which is confirmed when evaluating the L_N data for each slab.

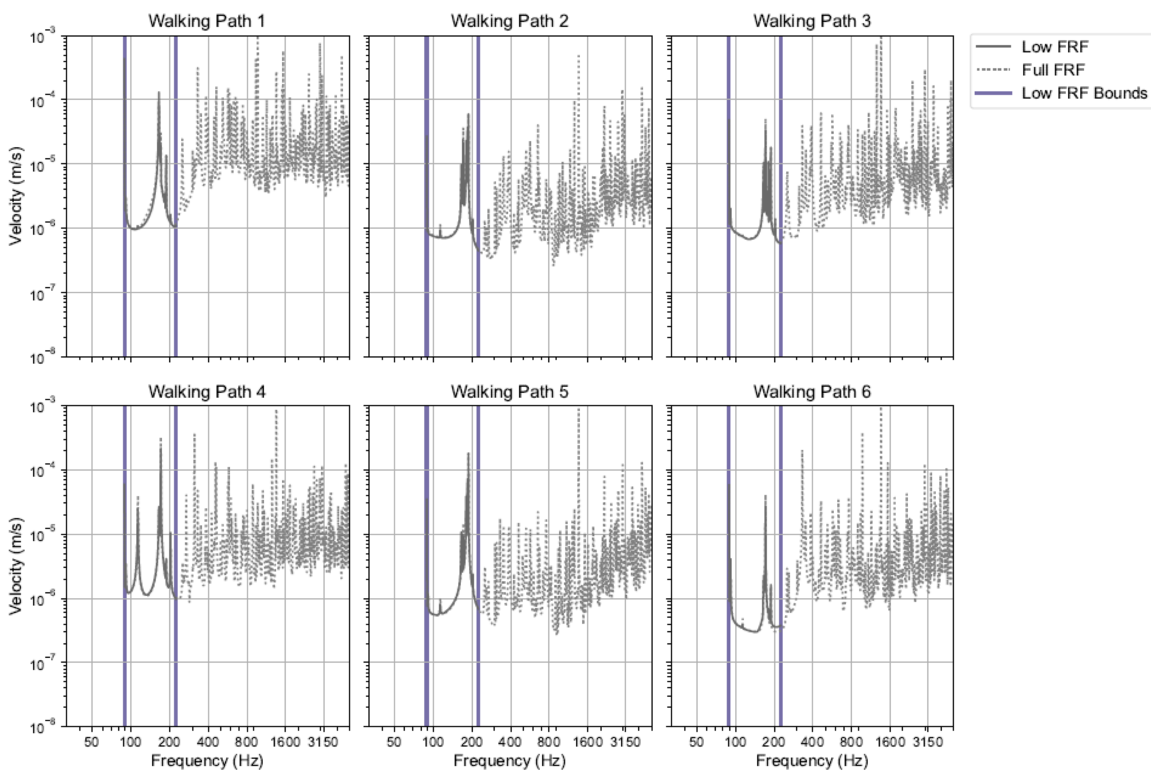

Figure **6-16**: Comparison of the low to full FRFs for all six WPs acting on shaped slab A.

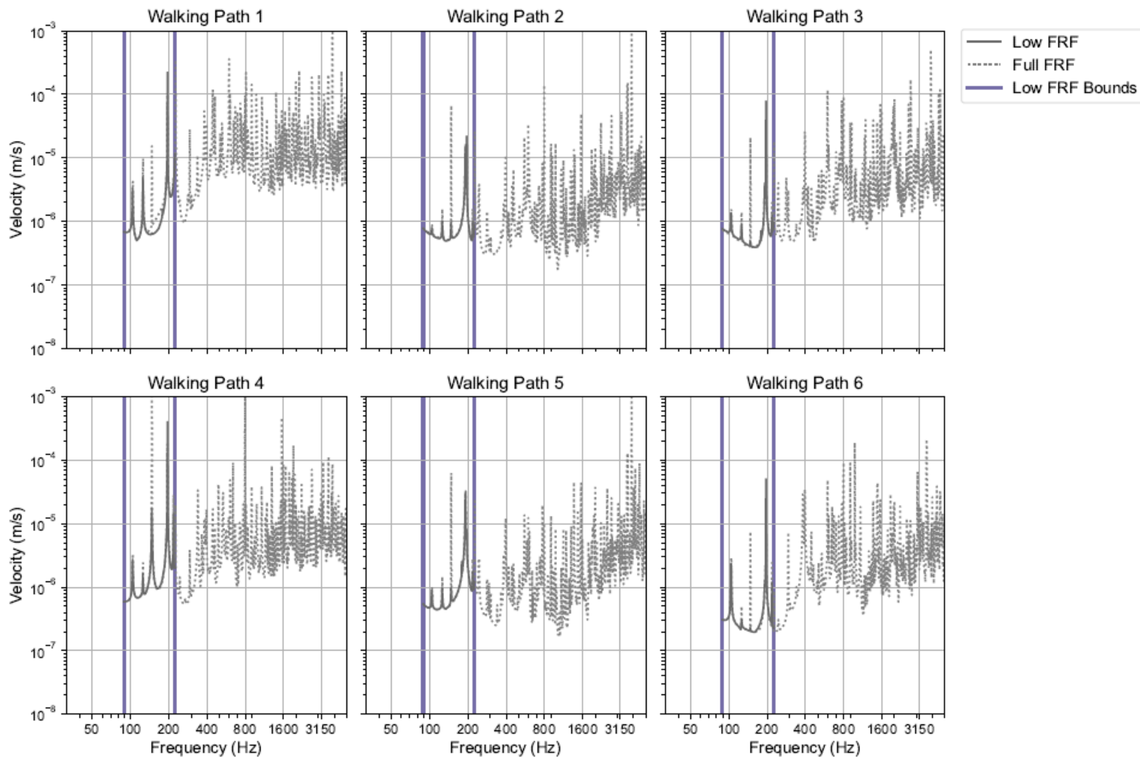

Figure **6-17**: Comparison of the low- to full FRFs for all six WPs acting on shaped slab B.

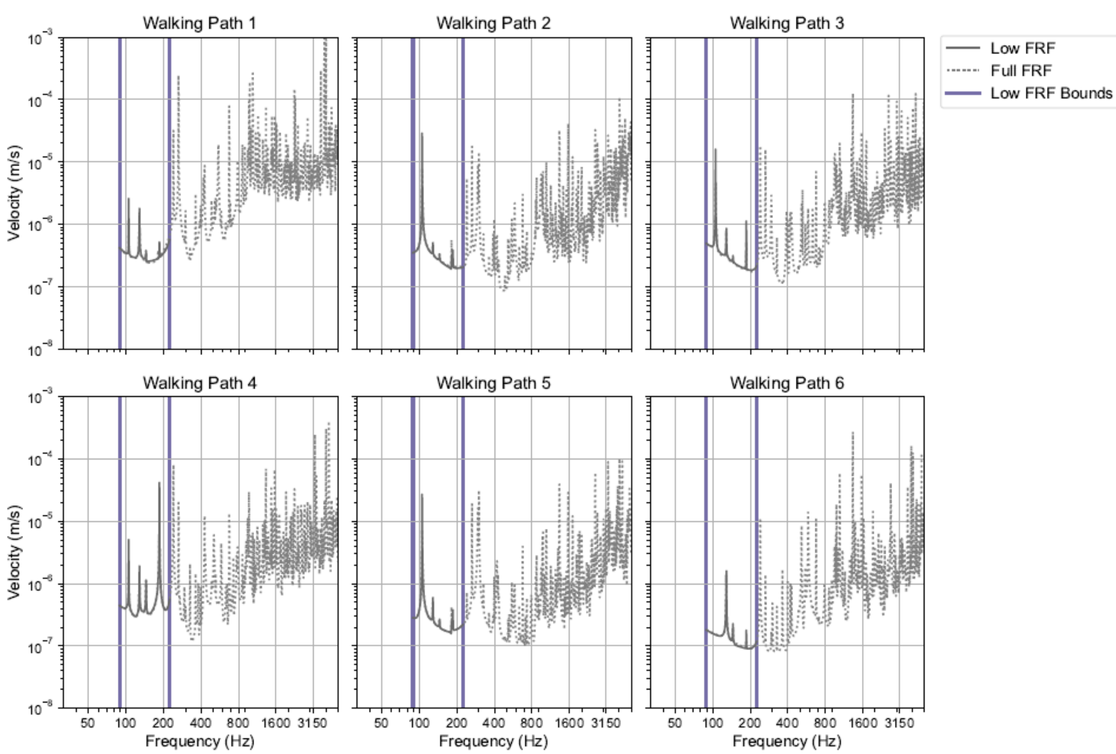

Figure **6-18**: Comparison of the low- to full FRFs for all six WPs acting on shaped slab C.

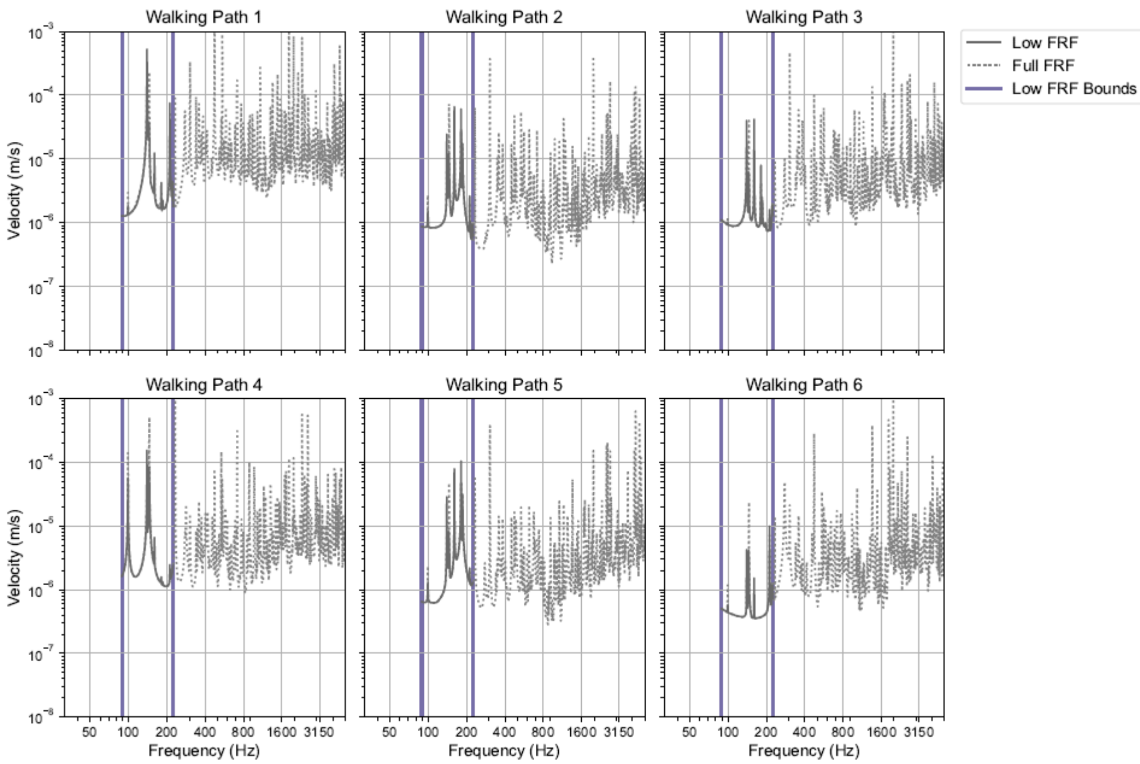

Figure **6-19**: Comparison of the low- to full FRFs for all six WPs acting on shaped slab D.

All L_N data for each of the shaped slabs is shown in Fig. **6-20**, with the controlling WP L_N data bolded. Several takeaways are observed in the comparison of L_N data. First, none of the WPs had identical L_N data; however, some of the WPs had equivalent IIC-Like ratings. This emphasizes the challenge of comparing floors for impact sound because the method for obtaining an IIC and IIC-Like rating truncates potentially useful acoustic data into a single integer value. A second observation is that WPs 2, 3, and 6 had the lowest IIC-Like rating and controlled the rating for each floor system, while WP 1 had the best performance for impact sound insulation across all slabs. This observation indicates that it is important to model at least WPs 2, 3 and 6 to determine the worst-case WP, but not all six WPs may need to be simulated to determine the IIC-Like rating for a concrete floor. The IIC-Like ratings that controlled for the four shaped slabs were then compared to the mass densities of the full-scaled shaped slabs as seen in Fig. **6-21**.

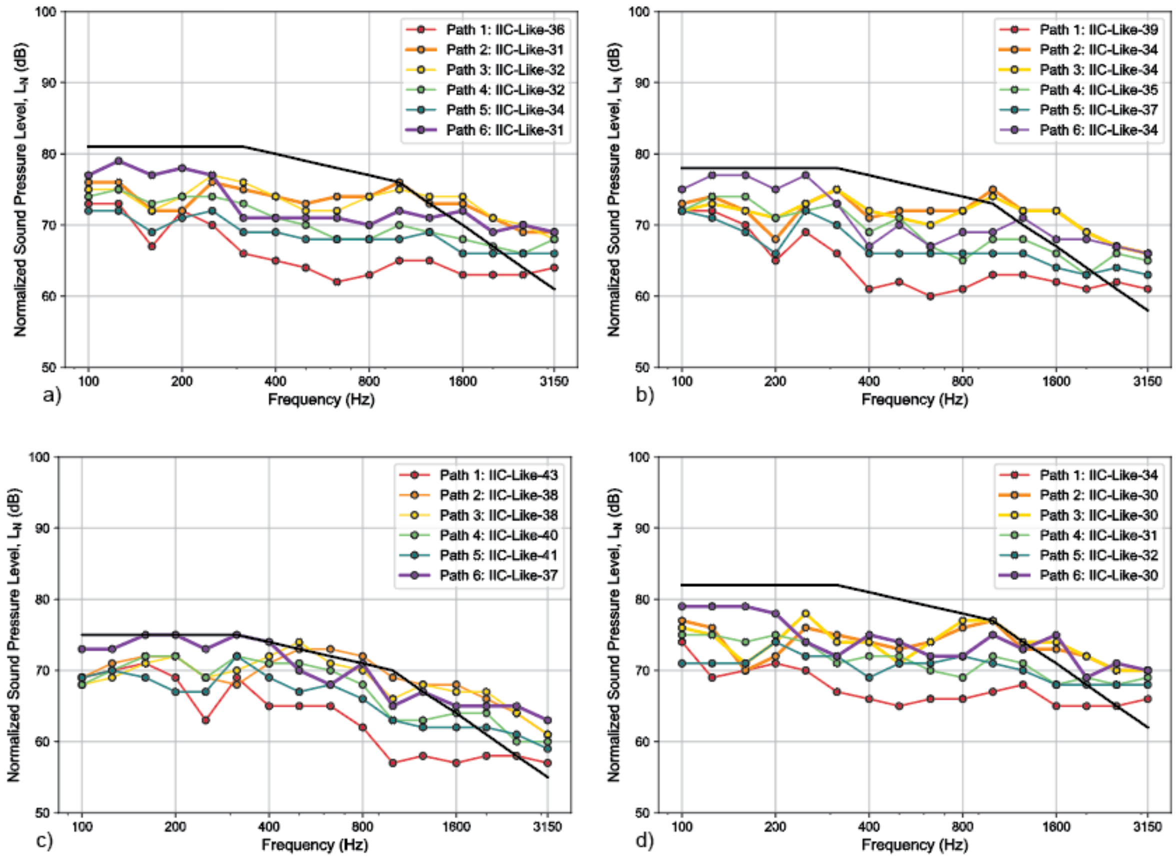

Figure **6-20**: The L_N data for the six WPs for each slab: a) shaped slab A, b) shaped slab B, c) shaped slab C, and d) shaped slab D.

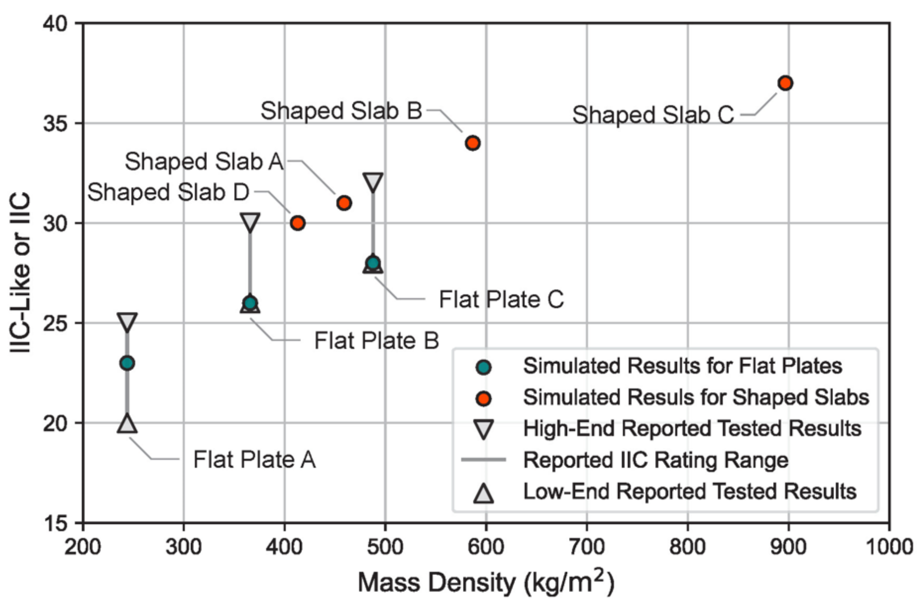

Figure **6-21**: The IIC-Like ratings and mass densities for the three flat plates and four shaped slabs.

As can be seen in Fig. **6-21**, as the mass density of the concrete floors increases, the IIC-Like rating increases. The IIC-Like ratings of the four shaped slabs are also put in context to the ratings of the flat slabs, revealing that the shaped slabs A and D have higher simulated IIC-Like ratings compared to the simulated flat slabs. Yet, the IIC-Like ratings fall within the region of experimentally obtained values, which helps validate the obtained results, even though the structural system type differs. Another observation is that all flat and shaped slabs are still below the minimum building code requirement of IIC-50, indicating that substantial mass density would be required to achieve that performance goal when additional material layers on top of the concrete surface (e.g., a carpet and pad) are not considered.

The two validation strategies ensure that the computationally-obtained results are in tune to the experimental findings of flat plates and the dynamic performance of shaped concrete slabs, indicating that the IIC-Like method can be widely applicable to more shaped one-way slab designs and similar concrete topologies. However, two additional aspects of the IIC-Like method should be considered before widespread implementation.

6.4.3 Additional consideration A: Frequencies below 100 Hz

While much of the focus of the IIC-Like method has been on validating the performance of high-frequency impact sound, as this is the frequency range that controls the impact sound rating of bare concrete slabs, consideration should also be given to frequencies below 100 Hz (LoVerde & Dong, 2017). One of the limitations of using the IIC-Like method is that the radiated sound power of frequencies at or below coincidence cannot be adequately obtained. However, the conventional air-hemisphere method can be applied because the upper frequency limit of the 80 Hz OTO band is 89.1 Hz, equating to a minimum mesh resolution of 0.641 m, despite the increased air-hemisphere radius and subsequent increase in finite elements. The large mesh resolution enables researchers and acousticians to employ this method on standard computers with the expectation that the computational time won't be extensive.

6.4.4 Additional consideration B: Single impact vs. multi-point walking paths

A second consideration, specifically related to the modeling of the six WPs, is to determine if all of the impact points along the WP need to be modeled. If a single impact point had similar performance, then the modeling of the IIC-Like method could be simplified. A sensitivity analysis was thus conducted to compare the L_N data obtained when modeling a single impact point that acts at the center of the WP to the L_N data obtained when modeling the WPs as defined in the IIC-Like method. Three shaped one-way slabs, different than the four shaped slabs used in the second validation strategy, were used as case studies for this method (see Fig. **6-22**). Following the procedure of the IIC-Like method, the L_N data from the single point and multi-point WPs were compared, as shown in Figs. **6-23** to **6-25**.

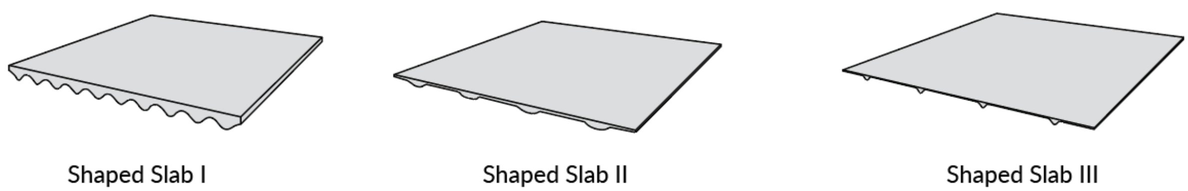

Figure **6-22**: The three shaped slabs considered in the L_N comparison from a single vs multi-point impact.

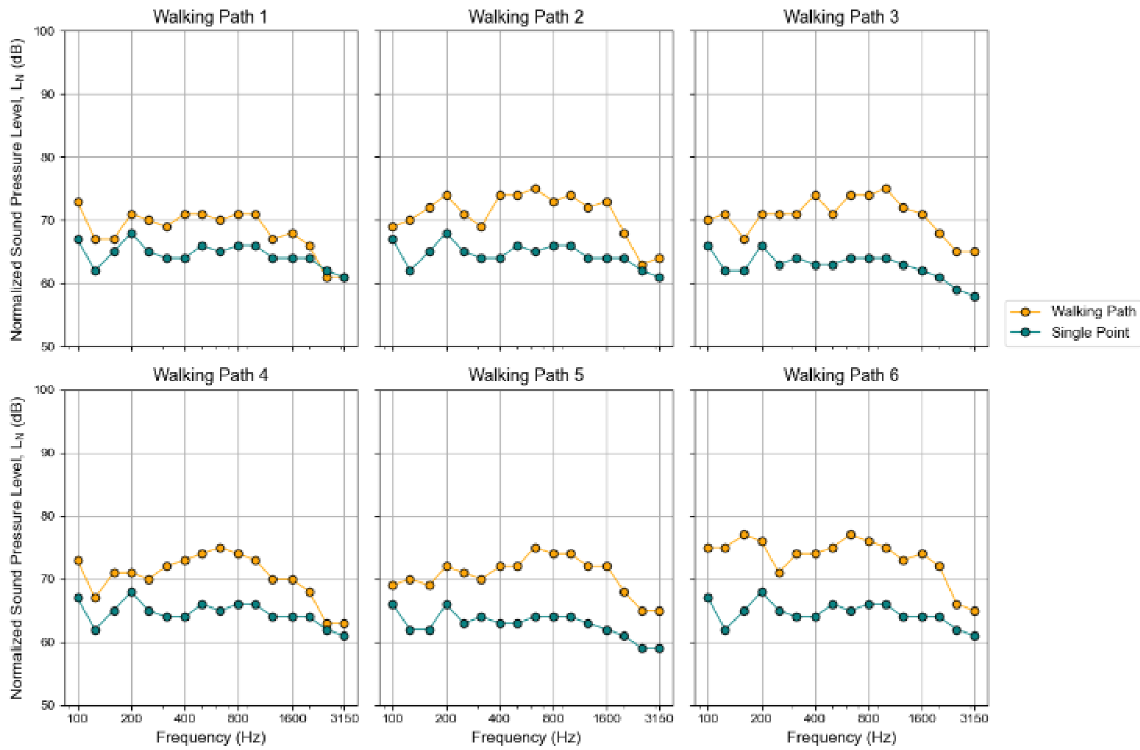

Figure **6-23**: Comparison of the single vs multi-point L_N data for shaped slab I.

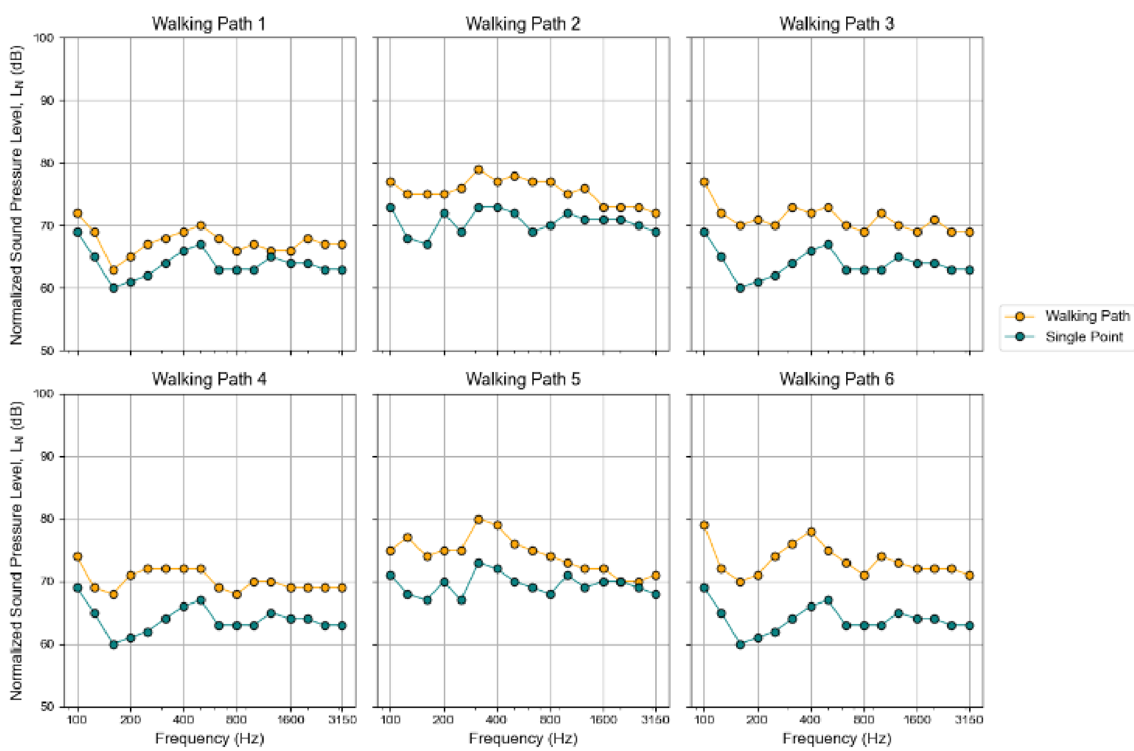

Figure **6-24**: Comparison of the single vs multi-point L_N data for shaped slab II.

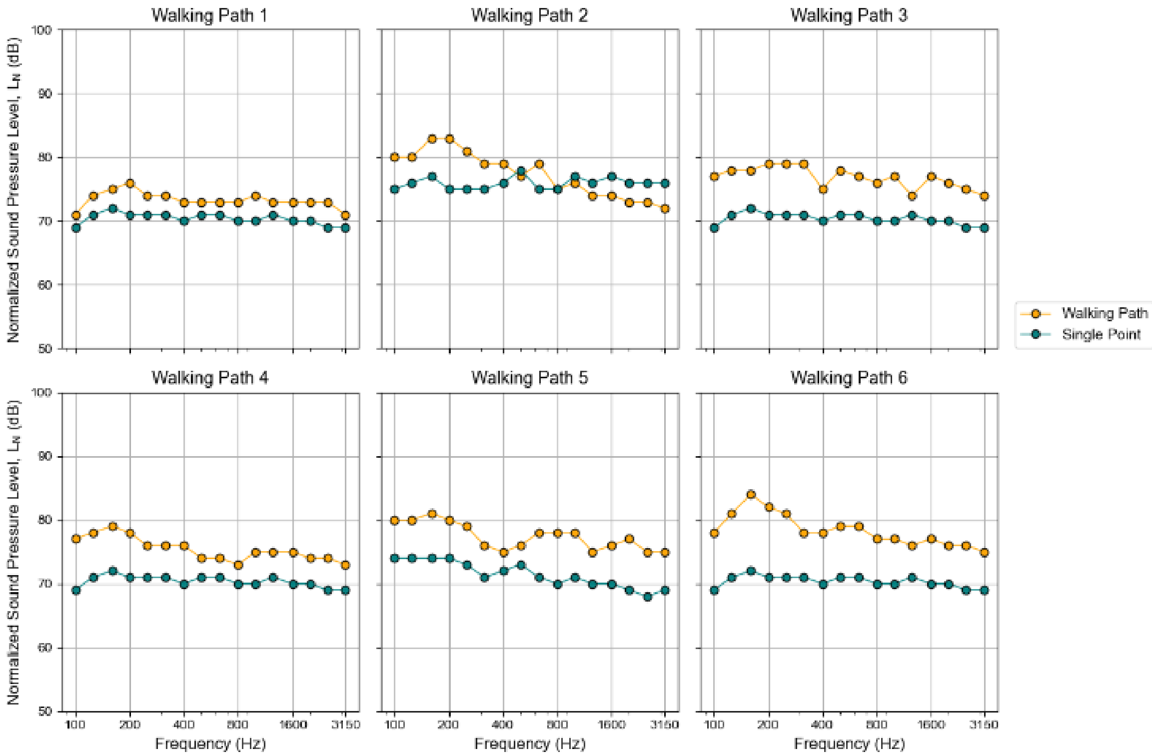

Figure **6-25**: Comparison of the single vs multi-point L_N data for shaped slab III.

The comparison of a single impact to the multi-point WPs reveals that the two impact cases vary significantly from each other. While the general shape of the L_N data typically matched well, the WP L_N data was typically 5 dB worse for attenuating impact sound. The single impact point only controlled for WP 1 acting on shaped slab I; yet the multi-point WPs controlled for all other cases. While this does potentially suggest that the IIC-Like method may penalize the actual impact sound insulation performance, at the same time, the WPs provide a more realistic impact scenario that must be accounted for in the design of optimized concrete floors.

6.5 Applications, estimated computational resource savings, and limitations

The proposed IIC-Like method has been demonstrated to adequately rate impact sound insulation performance of flat and shaped one-way concrete slabs. The application of this method can be directly applied to other optimized concrete floors and components to estimate the structure-borne sound transmission. For example, the funicular concrete floors investigated by Méndez Echenagucia et al. (2016)

could be further evaluated for high frequency impact sounds by using the IIC-Like method. However, correct specification of boundary conditions is necessary to employ the IIC-Like method on different concrete forms, like funicular floors. For example, simple support boundary conditions were used by Méndez Echenagucia et al. (2016) to properly evaluate the low-frequency radiated sound power. Therefore, similar boundary conditions can be used to explore the impact sound insulation of other optimized concrete floors, including vaulted concrete floors and shells.

The computational resource savings for this study are best realized by comparing the number of finite elements and nodes for the custom air-hemispheres used in the IIC-Like method to the number of elements and nodes for the air-hemisphere when considering a frequency range of 100 Hz to 3.15 kHz. Table **6-3** shows the comparison of finite elements and nodes needed to evaluate impact sound insulation for each method. It should be noted that this comparison assumes that quadratic tetrahedral elements are used, and that the minimum mesh resolution for the 200 Hz and 3.15 kHz OTO bands is 0.255 m and 0.016 m, respectively. The comparison shows that the required number of nodes and elements for the conventional air-hemisphere method is significantly higher, as less than 1% of the number of finite elements and less than 3% of the nodes are required to obtain an IIC-Like rating when using the IIC-Like method. To compare the computational time (CP time) between the two methods, an FEM simulation was conducted using the shaped slab B case study using a Windows computer with an AMD Ryzen 5 3600X 6-Core Processor. The CP time to simulate the radiated sound power using the IIC-Like method was 2.93 hours. However, because of licensing restrictions, the CP time using the conventional air-hemisphere method could not be computed. Yet using the number of finite elements provided in Table **6-3** as a reference, the CP time is estimated to be 903.9 hours, or 37.7 days, highlighting that significant computational resources are saved using the IIC-Like method.

Table **6-3**: Comparison of the number of elements and nodes needed to evaluate impact sound insulation performance.

Total Number of:	**Air-Hemisphere Corresponding to:**	**Conventional Air-Hemisphere Method**	**IIC-Like Method**	**Percentage Savings**
Finite Elements	Flat Plate A	105,025,998	72,066	>99.9%
	Flat Plate B	105,154,923	71,124	>99.9%
	Flat Plate C	105,101,577	71,578	>99.9%
	Shaped Slab A	86,315,408	123,228	99.9%
	Shaped Slab B	85,527,531	277,250	99.7%
	Shaped Slab C	86,106,986	159,415	99.8%
	Shaped Slab D	86,450,327	211,773	99.8%
Model Nodes	Flat Plate A	17,989,516	103,486	99.4%
	Flat Plate B	18,012,484	102,263	99.4%
	Flat Plate C	18,005,517	102,881	99.4%
	Shaped Slab A	14,814,524	173,739	98.8%
	Shaped Slab B	14,690,706	384,887	97.4%
	Shaped Slab C	14,788,702	226,646	98.5%
	Shaped Slab D	14,836,940	296,931	98.0%

The IIC-Like method is not without limitations. First, concrete structures are prone to cracking during their lifespan. Although cracking can influence the dynamic performance of concrete floors (Gollob & Kocur, 2021), crack propagation can be influenced by many environmental factors including constructability and building type and was therefore not in the scope of this work. However, the incorporation of crack propagation can be considered in more advanced models, especially when evaluating the impact sound insulation performance of one specific floor design. Another limitation is that the walking path impacts all act in phase. A more realistic walking path would include a time domain model of the walking paths. Lastly, the IIC-Like method may not be applicable to very lightweight floor structures (e.g., mass timber floors), as the accuracy of the IIC-Like rating is dependent on the coincidence frequency. The IIC-Like method may not be appropriate for mass timber floors in particular, unless additional material layers or acoustic metamaterials lowered the coincidence frequency of the floor assembly (Gibson et al., 2022).

6.6 Conclusion

This chapter proposed a hybrid computational method that used the air-hemisphere method to simulate the radiated sound power at the four lowest OTO bands required to obtain an IIC rating, which was used to determine the radiation efficiency of the floor system to estimate the high frequencies necessary to determine a simulated IIC (IIC-Like) rating. To validate that the IIC-Like method could adequately estimate the impact sound insulation performance of concrete structures, the method was validated based on the comparison of experimental lab results of three flat concrete plates and to the experimentally obtained dynamic responses of four shaped concrete slabs, which were tested in Ch. 5. This method is specifically advantageous for acousticians and building designers who aim to evaluate the structure-borne sound insulation performance of many different concrete floor forms, as the computational resources required are significantly less (<1% of the finite elements and <3% of the model nodes) compared to the computational resources required to ascertain the broad frequency impact insulation performance using conventional acoustic methods. Future work will implement the IIC-Like method to the design exploration of shaped concrete components, with the IIC-Like rating employed as a design objective in multi-objective frameworks.

Chapter 7

New sound transmission metrics for computational design frameworks[1]

7.1 Study context

In the 1950's, significant population growth in the United States led to an increased demand for affordable housing in suburban communities (Mankiw & Weil, 1989). Lightweight structures, built out of wood, were used to expedite the construction process of multi-unit residential buildings while minimizing construction costs. A consequence of such lightweight structures was high sound transmission because of decreased structural mass, choice of material, and poor construction practices (Clark, 1970; Northwood, 1964). The need for reduced acoustic transmission in multi-unit dwellings sparked research into sound transmission within buildings (Brandt, 1965; Schultz, 1964; Zwicker, 1961; Zwicker et al., 1957), leading to the publication of standardized metrics (ASTM, 2004; ASTM, 2016; Northwood, 1962).

Yet while acoustic and other performance requirements still exist, contemporary building design is increasingly driven by the concern for sustainability and environmental impacts (Attia et al., 2012; De Wolf et al., 2017; Jensen et al., 2020; Thormark, 2001, 2002). In parallel with the growing emphasis on sustainable design, advances in construction technology (Costa et al., 2020; Valente et al., 2019) and construction practices (Müller et al., 2014) have given designers the freedom to envision unique building structures (Hens et al., 2021; Jipa, Andrei; Meibodi, Mania Aghaei; Bernhard, Mathias; Dillenburger et al., 2016) and components (Hawkins et al., 2019; Ismail & Mueller, 2021) that satisfy building code requirements while reducing material consumption (Attia et al., 2012, 2019). Simulation-based computational tools have also increased opportunities for designers to reduce material in the early-stage

[1] Chapter 7 is adapted from the published work by Broyles et al. "Modified acoustic transmission metrics for early-stage design exploration using a computational case study of heavyweight floors." (2023). *Applied Acoustics*, *196*, 108865.

design of structures, specifically using optimization methods (N. Brown et al., 2016; N. C. Brown et al., 2020). These numerical strategies have enabled the rapid evaluation of novel structures, fabricated with traditional structural materials such as concrete (Costa et al., 2020; Ismail & Mueller, 2021; Jipa et al., 2016), in order to rank them according to various objectives such as decarbonization goals by minimizing structural weight (Broyles et al., 2021).

While the potential benefits of reducing structural materials have been demonstrated, the consequences for sound transmission have not been adequately considered. Acoustic performance should be evaluated during design conceptualization and exploration of optimized designs since poor sound insulation can reduce the overall quality of life of building tenants, potentially leading to sleep problems (Rasmussen & Ekholm, 2019), physical impairments (Jensen et al., 2018), annoyance (Rasmussen, 2010), and mental health concerns (Jensen et al., 2019). In order to address sound insulation within a rapid evaluation design strategy, sound transmission metrics need to accurately account for the full physics-based transmission loss performance of building structures and how increasing sound insulation performance might enhance the quality of life. The existing American acoustic transmission metrics were originally developed for experimental measurements and are acceptable for sound insulation assessment at final design stages and post-construction. However, the metrics have deficiencies that limit their ability to capture the full physics-based and perceptual performance when implemented within early building design exploration and rapid evaluation using computational frameworks (Dong, 2020; LoVerde & Dong, 2018; LoVerde & Dong, 2017). These limitations prompt the question: how can modifications to the existing acoustic transmission metrics correct the functional limitations of the metrics to improve the acoustic rating of floors in computational design frameworks?

In response, this chapter explores the existing American standards for quantifying sound insulation of building structures, notes the functional and perceptual limitations of current metrics, and proposes alternative approaches that may better fit the context of early-stage design. First, a brief history of the development and use of Sound Transmission Class (STC) and Impact Insulation Class (IIC) metrics is provided, including discussions on their shortcomings. Alternative rating methods for early-stage design simulations are then proposed which help overcome the shortcomings of STC and IIC for early-stage design. The new and existing metrics are then applied to a computational case study of shape-optimized concrete floors. Last, suggestions for implementing the new metrics within an optimization framework for early-stage design exploration are provided.

7.2 STC and IIC: History, implementation limitations, and perception shortcomings

7.2.1 History of STC and IIC

American acoustic standards first grew out of an international context. Following WWII, many multi-unit residential buildings in Europe required significant repairs, and several countries introduced standardized acoustic considerations in building code (Brandt, 1965). A range of practices were used, including the arithmetic average of transmission loss values at several frequencies (Blaeser & Struck, 2019) and the energy average method (Waterhouse, 1957), resulting in different sound transmission standards and requirements across European countries.

American acoustic standards followed these developments and were consequently influenced by existing European methods. Although lightweight wood construction was popular in the post-war United States, the acoustic transmission metrics were adopted from the European approaches originally developed for heavyweight concrete and masonry, which have distinctly different transmission loss performances (Northwood, 1962). Despite being applied to different structures and materials, the American Standards for Materials and Testing (ASTM) based standard E413, Classification for Rating Sound Insulation (ASTM, 2016), on the European acoustic metrics. In 1961, ASTM E90-61T was introduced as the primary method for obtaining the sound transmission loss (TL) of structures in buildings, with Sound Transmission Class (STC) used to rate air-borne sound transmission. Structural-borne sound transmission classification was recommended later in the 1960's (Waterhouse, 1957).

Subjective human hearing studies were conducted to assess how well STC ratings correlated with the perceived sound transmission performance. Studies by Northwood (1962) and Clark (1970) found that STC ratings were appropriate for quantifying sound insulation, which then propelled the incorporation of

STC into design and construction practice beyond residential buildings. Although air-borne sound insulation was quickly incorporated into design and construction practice, adequate metrics for impact sound insulation was not considered until the 1980's. Despite the positive results found for the rating method STC, Schultz (1964) described the rating method for impact noise in the 1960's as "primitive" and "inadequate," suggesting a need for more stringent methods for multi-unit buildings. Schultz's findings influenced the development of ASTM E989, which introduced the Impact Insulation Class (IIC) rating method (ASTM, 2006).

7.2.2 Limitations of STC and IIC when implemented in early-stage design

STC and IIC were formulated with defined frequency ranges and rules based on a standardized contour (see Figure **7-1**). The first rule is the summation of deficiency rule, which includes 16 one-third octave (OTO) bands and allows for a 2 dB float; therefore, the STC and IIC deficiency total cannot exceed 32 dB. The second rule is the 8 dB rule, which limits the STC and IIC rating from including any OTO deficiency greater than 8 dB. Both the deficiency rule and 8 dB rule control how much the reference contour for STC and IIC are shifted. To obtain the STC rating, the reference contour shifts up until the summation of deficiency total is met, or a single OTO band contains a deficiency that exceeds 8 dB. This approach is similar for IIC; however, the reference contour shifts down. Figure **7-1** provides examples of calculating the sound insulation performance for a lightweight (LW) timber wall and a heavyweight (HW) concrete masonry unit wall, while Figure **7-2** demonstrates the air-borne and impact sound insulation performance for a LW timber floor, and a HW concrete floor, using previously published laboratory values (Gatland II, 2003; Litvin & Belliston, 1978; Mehta et al., 1999; Warnock, 1990, 2005).

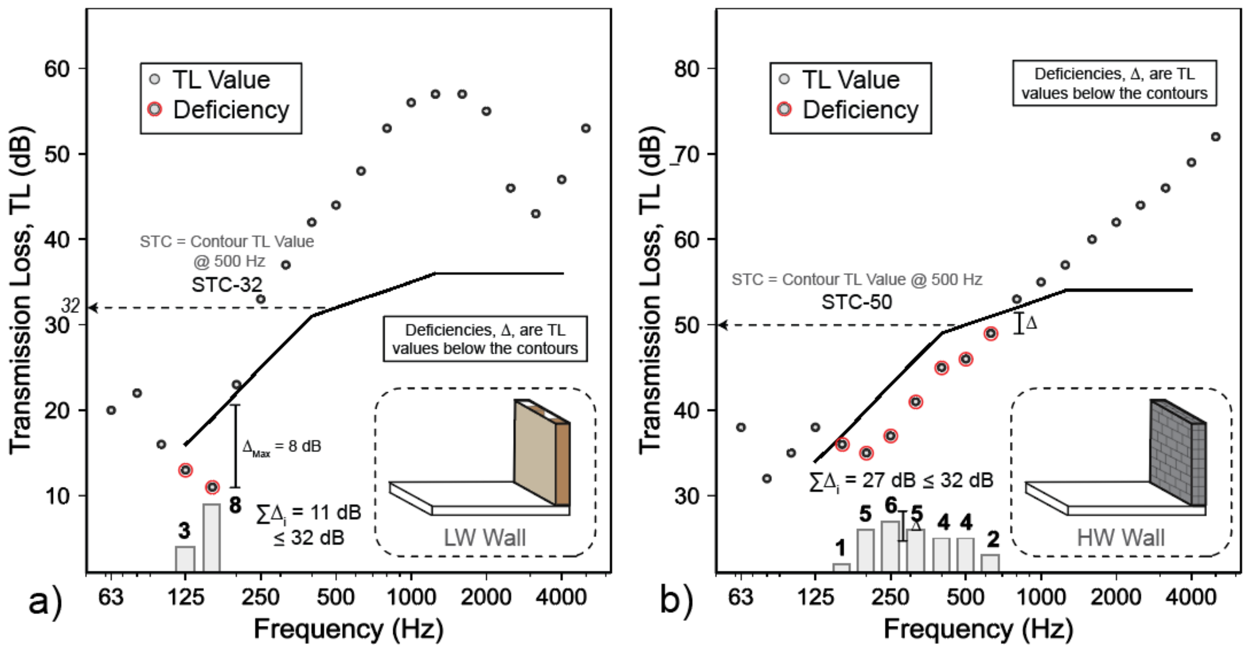

Figure **7-1**: STC calculations for a) a LW wall and b) a HW wall, with TL data shown as the gray dots. The histograms at the bottom of the plots represent the deficiency values for each rating method. The STC contour, shown as a solid line, is moved up until both deficiency rules are met.

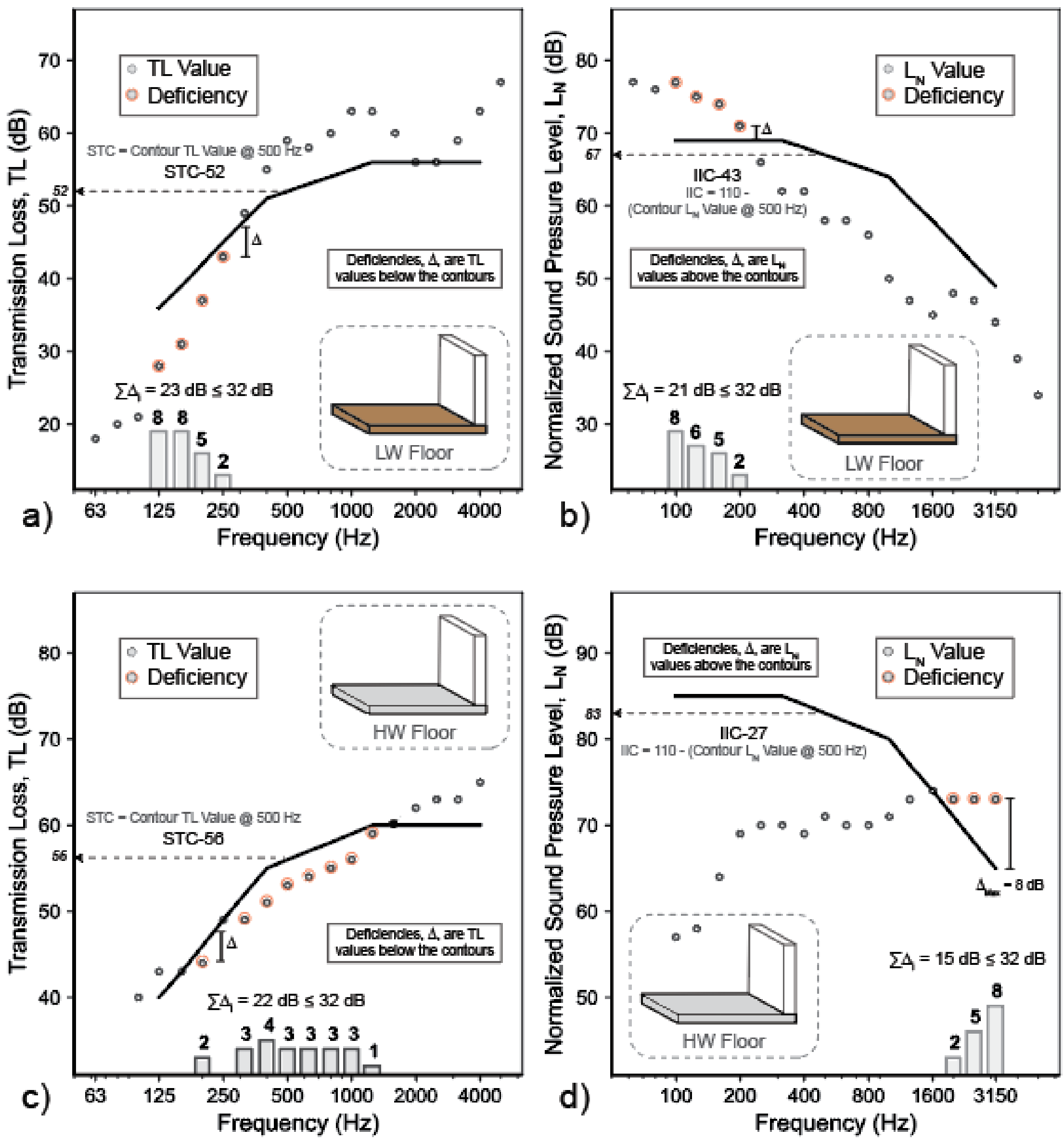

Figure **7-2**: STC calculations for a) a LW floor and c) a HW floor, and IIC calculations for a b) LW floor and d) a HW floor. TL (a, c) and L_N (b, d) data are shown as the gray dots. The histograms at the bottom of the plots represent the deficiency values for each rating method. The STC / IIC contours, shown as solid lines, are moved up / down until one or both deficiency rules are met.

The data found in Figs. **7-1** and **7-2** followed ASTM E90 to obtain the TL data for all assemblies, with ASTM E413 used to determine the STC rating. Similarly, ASTM E492 was used to obtain the L_N data, which implies that a tapping machine was used in the tests, with ASTM E989 used to determine the IIC rating. The LW wall in Fig. **7-1** is a timber wall composed of a two gypsum boards (one on each end) with thicknesses of 13 mm (0.5 in) each, 90 mm (3.5 in) wood studs spaced at 406 mm (16 in), and 90 mm (3.5

in) of blown cellulose fiber insulation within the wall cavity (Halliwell et al., 1998). The HW wall shown in Fig. **7-1**, is a 140 mm (5.5 in), 100% solid concrete block with a mass density of 300.7 kg/m^2 (Warnock, 1990). The LW floor in Fig. **7-2** is a timber floor composed of two plywood boards with thicknesses of 16 mm (0.63 in) each, 235 mm (9.25 in) thick wood joists spaced at 406 mm (16 in), 13 mm (0.5 in) thick resilient metal channels spaced at 406 mm (16 in), rock fiber batt insulation with a thickness of 178 mm (7 in) in the cavity, and a single, 16 mm (0.63 in) thick gypsum board (Warnock, 2005). Last, the HW floor in Fig. **7-2** is a 153 mm (6 in) concrete floor. PCA conducted air-borne experimental tests for the concrete floor (Litvin & Belliston, 1978; Mehta et al., 1999), yet impact measurements were not taken. CertainTeed Corporation conducted an in-house impact sound insulation test of a 153 mm (6 in) concrete slab to calculate the IIC rating (Gatland II, 2003).

Although the deficiency rules had historical significance, they have been shown to bias the interpretation of the air-borne transmission loss and impact sound insulation performance in design exploration and therefore are considered limitations of the metrics (Broyles et al. 2021). The 8 dB rule can bias interpretation of these metrics since it relates to only the level at a single OTO band. This is particularly relevant for structures with deep coincidence dips, which will likely have a large deficiency at the coincidence frequency. When a deep coincidence dip leads to a deficiency larger than 8 dB with an OTO band, the sound insulation performance, which may be favorable at other OTO bands, does not factor into the metric. The example of the LW wall in Fig. **7-1** shows that the STC rating is controlled by the 8 dB deficiency at the 160 Hz OTO band. However, no deficiencies are found above the 160 Hz OTO band, suggesting that the LW wall may have better sound transmission loss performance at mid and high frequencies. Removal of the 8 dB rule, which has been recommended for both sound transmission loss and impact sound insulation (Dong, 2020), could reduce severe rating penalties for structures with a narrow but deep coincidence dip and would be a better representation of the sound insulation performance in the entire frequency range. Although the removal of the 8 dB rule could increase the STC and IIC rating of structural assemblies that do not meet current building codes, keeping the rule would limit computational design exploration by giving preference only to designs with high integer ratings. It should be noted that the ISO metrics of Sound Reduction Index (*R'*) (ISO, 2014) and Standardized Impact Sound Pressure Level (L'_{nT}) (ISO, 2020) do not include the 8 dB rule.

Unlike the 8 dB rule, the 2 dB float per OTO band that formulates the summation of deficiency rule is scientifically backed (Rademacher, 1955). This rule controlled the STC rating for the HW wall and HW floor in Figs. **7-1** and **7-2**. A limitation associated with this rule is the frequency ranges affiliated with STC (125 Hz to 4k Hz) and IIC (100 Hz to 3.15k Hz). The coincidence frequencies of concrete and masonry structures are known to be around 100 Hz or lower, as shown by the example of the HW wall in Fig. **7-1**; indicating that STC does not fully capture the broadband air-borne transmission performance of HW structures. While IIC considers frequencies down to 100 Hz (ASTM. 2006), studies have found that impact sound insulation should be considered down to 50 Hz (LoVerde & Dong, 2018; Vardaxis & Bard, 2018a) or 20 Hz (Ljunggren et al., 2014) to account for the impact sound insulation for LW construction, such as the LW floor in Fig. **7-2**. These recommendations also have perceptual relevance, as discussed in Sec. 7.2.3.

A third limitation with STC and IIC is the utilization of a single, dependent contour to quantify the sound insulation performance over low, mid, and high frequencies. Since the contour truncates the performance over a broad frequency range into a single number, any information at specific frequency ranges is lost. For example, the HW floor in Fig. **7-2** has a low IIC rating because of the poor impact sound insulation in the high frequency range, however, the structure has better insulation at low and mid frequencies. Additionally, two different TL or L_N curves with different perceptions and corresponding psycho-effects could give the same STC / IIC rating. For example, the TL performance of the HW wall and LW floor in Fig. **7-2** contrast significantly, yet the STC ratings only differ by 2. Independent contours at frequency subranges could provide clearer insight on the sound insulation performance of the structure. A similar approach was previously proposed by LoVerde and Dong (2017) for impact sound ratings, which has recently been introduced as ASTM standards (ASTM), 2020, 2021) which provide low frequency and high frequency impact integer ratings that complement the broader IIC rating.

Regarding early-stage design exploration and numerical optimization, a fourth challenge is that separate single number quantities (SNQs) are used to quantify air and impact sound insulation. Two SNQs are useful in quantifying transmission performance in design as exemplified by the stark contrast in air-borne and impact ratings of the HW floor in Fig. **7-2**, yet STC and IIC may complicate multi-parameter optimization strategies. Many design optimization simulations converge towards a single maximum or minimum scalar objective, but interpreting the simulation results becomes more complex with additional objectives. Acoustics is also known to be influenced by a competing objective in another discipline such as structural, daylight, and thermal (Agirbas, 2021; Mendez Echenagucia et al., 2014; Schweiker et al., 2020), further complicating multi-objective studies. For example, Brown et al. (2016) optimized the structural, shelter, acoustic, and daylighting performance of a cantilevered stadium roof. To understand each discipline's performance, an SNQ was applied to explore and compare the performance of simulated designs. A SNQ incorporating air-borne and impact sound applied as an objective or constraint could be preferable in similar multi-objective optimization studies. Heckl and Rathe (1963) introduced a method for combining air and impact sound insulation performance, yet their proposed integer did not scale to the performance of the existing metrics (i.e., STC-50 corresponds to acceptable sound isolation performance). A SNQ that is scaled to the performance of STC and IIC ratings could be advantageous in early-stage design exploration and optimization frameworks to consider both sound and impact simultaneously.

7.2.3 Perceptual shortcomings of STC and IIC

In addition to the challenges associated with quantifying the complete physical performance of building structures in early design, STC and IIC have related perceptual shortcomings. Although mid-20th century subjective studies validated the implementation of metrics like STC, these studies occurred before the widespread commercialization of home theater systems (Frost, 1996), which introduced very low frequency sound within residential communities. A study by Grimwood (1997) found that the most common noise complaints within multi-tenant residential buildings were music and speech for air-borne sound, and footfall and door slams for impact sound. In addition to the noise source, the construction and structure type directly influence the perception of sound insulation performance and which frequencies and coincidence dips are likely to be relevant (Chmelík et al., 2020; Hongisto et al., 2014; Monteiro et al., 2016; Rychtarikova et al., 2020; Vardaxis et al., 2018; Vardaxis & Bard, 2018a, 2018b).

Park and Bradley (2009) found that the inclusion of the 100 Hz OTO band and the summation of deficiencies rule were good predictors of perceived ratings. However, the 8 dB rule had varying effects based on the type of air-borne sound. For attenuating speech sounds, removing the 8 dB rule leads to better predictions of perceived ratings, which was also found by Hongisto et al. (2014). Rindel (2015) explored the perception of impact noise, recommending that a structure-borne sound insulation metric expands the frequency range considered down to 50 Hz, which was supported by a subjective study from Ryu et al. (2010). The results of the perceptual studies correspond to the first and second limitations presented in Section 2.2. Although the recommendation of removing the 8 dB rule varies based on noise source, expanding the frequencies for STC and IIC has been strongly recommended for perceptual accuracy.

It is imperative that revised acoustic transmission metrics address both the physical and perceptual limitations affiliated with STC and IIC. In early-stage design, more accurate sound insulation metrics can provide designers with the needed information to improve the interior acoustic environment without needing acoustical treatments post-construction. Further, designers can use different metrics depending on the structure type and noise source that needs attenuating. Therefore, modifying the current metrics is necessary to address the physical and perceptual limitations previously outlined. New sound insulation metrics are defined in Section 3 and compared against the existing metrics of STC and IIC for several computational shaped concrete floors.

7.3 Definition of new sound transmission metrics for early-stage design

The new acoustic transmission metrics proposed are:

1. modified STC (STC*) and modified IIC (IIC*),

2. categorical method (CM), and

3. composite air- and impact sound insulation metric (CTF, CTF*),

which are described in the following sections.

7.3.1 Modified STC and modified IIC (STC and IIC*)*

The modified STC and IIC rating methods (which are denoted for the remainder of this chapter as STC* and IIC*, respectively), remove the 8 dB rule (STC_{No_8}, IIC_{No_8}) and expand the low frequency range (STC_{Low}, IIC_{Low}) from the standard definitions. Although STC* and IIC* include both modifications, each change is isolated to evaluate its influence, as shown in Sec. 7.4.2.1.

STC* drops the lower limit of the frequency range to 100 Hz because of the need to consider low-frequency coincidence dips common in concrete and masonry structures. It should be noted that R'also has a lower bound at 100 Hz (ISO, 2014). Similarly, the lower limit of the frequency range for IIC* was dropped to 50 Hz to capture low-frequency impact sounds that are perceivable (LoVerde & Dong, 2017). The summation of deficiency rule is the only rule for defining the STC* and IIC* ratings. The deficiency total is adjusted from the original STC and IIC totals by adding 2 dB per additional one-third octave band: STC* has a summation of deficiency total of 34 dB and IIC* has a summation of deficiency total of 38 dB. The contour shape extends the slopes of the existing contours for STC and IIC. Like STC and IIC, higher STC* and IIC* ratings equate to better transmission loss performance.

7.3.2 Categorical Method (CM)

The second approach is a categorical method, referred to as CM. It differs from the previous metric since the TL / L_N data are subdivided into three frequency ranges to obtain a total of six integer ratings for a single design. CM is a progressive rating method which can provide a designer more insight on the transmission performance at different frequency ranges. The CM also expands the air- and structure-borne frequency ranges and excludes the 8 dB rule, the subdivision of frequency ranges enables each contour shape to behave independently.

The division of air-borne and impact sound insulation performance into low, mid, and high frequencies (Air_{Low}, Air_{Mid}, Air_{High}, $Impact_{Low}$, $Impact_{Mid}$, and $Impact_{High}$) could be advantageous for evaluating complex structures. To determine the air-borne transmission performance, the OTO frequencies are subdivided into bands from 100 Hz to 315 Hz to quantify Air_{Low}, 400 Hz to 1 kHz to quantify Air_{Mid}, and 1.25 kHz to 4 kHz to quantify Air_{High}. In a similar manner, the OTO band ranges of 50 Hz to 315 Hz, 400 Hz to 800 Hz, and 1 kHz to 3.15 kHz to quantify $Impact_{Low}$, $Impact_{Mid}$, and $Impact_{High}$ respectively. The low frequency upper limit of 315 Hz was chosen based on previous air- and structure-borne sound insulation research by LoVerde and Dong (2017). While LW structures are known to have less deficiencies in the mid and high frequencies, HW structures are susceptible to deficiencies in these ranges. Because deficiencies are common at high frequencies for HW structures, six OTO bands were deemed necessary to properly capture the high frequency sound insulation, resulting in the 1 kHz and 1.25 kHz high frequency lower limit. The remaining OTO bands created the limits for the mid-frequency range.

The contours for the subdivided frequency ranges were derived from existing STC and IIC rating methods because of their familiarity as established American standards. Therefore, the contours have the same slopes but shift independently at each frequency subset, as demonstrated in the example of a HW floor shown in Fig. **7-3**. Because of the varied number of OTO bands in each frequency range, the deficiency total was calculated using a 2 dB float per OTO band as noted in Table **7-1**. To provide easier comparisons between frequency ranges, equations were developed according to the contour value at designated OTO bands. In the mid frequency range, the 500 Hz contour value is used as the integer rating for both air- and structure-borne transmission performance. The low and high frequency ranges incorporate different OTO bands and equations to scale the ratings so that an integer rating of 50 in the low and high frequencies corresponds to the transmission performance of STC-50 and IIC-50, enabling easier comparisons.

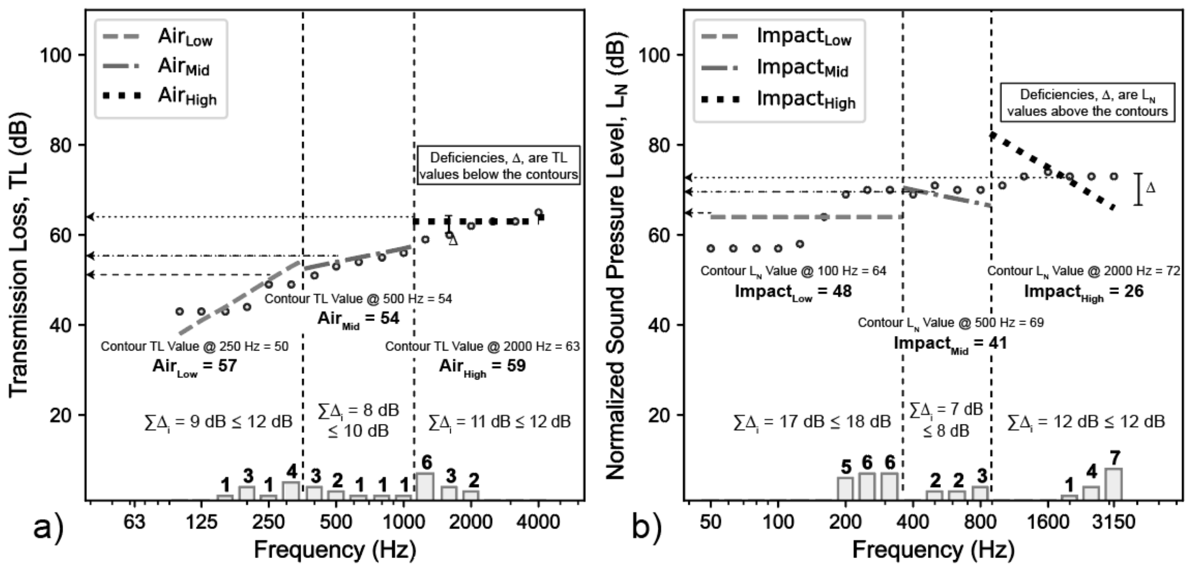

Figure **7-3**: Derivation of the six integers using CM. The a) TL and b) L_N data shown is for the HW floor from Figure **7-2**. In the calculation of the air-borne sound transmission, the frequency ranges had similar transmission loss performance; however, when assessing impact sound, the high frequency range had a poorer performance compared to the low and mid frequency ranges.

Table **7-1**: Max summation of deficiencies allowed and equations for CM rating values.

		Low Frequencies	***Mid Frequencies***	***High Frequencies***
Air-borne Sound	***OTO Frequencies***	100 – 315 Hz	400 – 1,000 Hz	1,250 – 4,000 Hz
	Max Σ Deficiencies Allowed	12 dB	10 dB	12 dB
	Rating Value	$Air_{Low} = TL_{Contour@250} + 7$	$Air_{Mid} = TL_{Contour@500}$	$Air_{High} = TL_{Contour@2000} - 4$
Structure-borne Sound	***OTO Frequencies***	50 – 315 Hz	400 – 800 Hz	1,000 – 3,150 Hz
	Max Σ Deficiencies Allowed	18 dB	8 dB	12 dB
	Rating Value	$Impact_{Low} = ((110 - L_{N, Contour@100}) + 2)$	$Impact_{Mid} = (110 - L_{N, Contour@500})$	$Impact_{High} = ((110 - L_{N, Contour@2000}) - 12)$

Conceptually, CM gives designers more sound insulation performance information to better address building needs. CM rating values can be adjusted based on the predominant noise source needing attenuation. The breakdown of TL and L_N data enables designers to target more specific frequencies without overwhelming the analysis with transmission data at every OTO band. While CM adds more scalar integers in a design exploration framework, it can provide a more holistic understanding of the transmission loss performance of in conceptual design exploration; however, it should be noted that multi-number objectives may be harder to incorporate in architectural acoustic practice.

7.3.3 Composite Transmission Function (CTF)

Although STC and IIC describe two fundamentally different acoustic transmission phenomena, their separation can complicate their inclusion in design exploration and optimization. CTF resolves this problem by combining the STC and IIC ratings into an SNQ. In design practice, it can be convenient to tune priorities between air- and structure-borne sound insulation performance to the needs of a specific building or space. To accommodate this, the formulation of CTF (Eq. **7-1**) includes a weighting coefficient, α_T, to vary how much air- to structure-borne sound insulation should be considered. The weighting coefficient varies from 0 to 1. An α_T value below 0.5 corresponds with a structural element that favors higher structure-borne sound insulation, while an α_T value above 0.5 favors air-borne transmission loss.

$$\mathrm{CTF} = \alpha_\mathrm{T}\,\mathrm{STC} + (1 - \alpha_\mathrm{T})\,\mathrm{IIC} \qquad \text{(Equation 7-1)}$$

A modified CTF rating, denoted as CTF*, is also considered by replacing STC and IIC with STC* and IIC* and thus addressing limitations inherited from both metrics. The CTF* approach includes the expanded frequency ranges described above, excludes the 8 dB rule, and provides an SNQ for quantifying sound insulation.

An important aspect of the CTF / CTF* is selecting an appropriate α_T value. Unlike existing sound transmission metrics, the α_T value is chosen before obtaining the integer rating and is selected according to building needs. Fig. **7-4** illustrates possible ranges of α_T values for initial CTF and CTF* transmission ratings of floor and wall structures, and how it could be adapted for five common building spaces:

residential dwellings, offices, lecture halls, gymnasiums, and shopping malls. It is widely known that residential spaces are susceptible to both air- and structure-borne sound insulation problems (S. H. Park & Lee, 2019), hence the recommendation of α_T around 0.5. The recommendation is similar for offices, but there are generally more complaints about speech, corresponding to a higher recommended α_T value (Navai & Veitch, 2003). A high α_T range is proposed for lecture halls as they are mostly concerned with air-borne sound insulation problems (Jaramillo & Ermann, 2017). Gymnasiums, on the other hand, are more concerned with impact sound insulation, resulting in the lowest recommended α_T range (Carels et al., 2019). Last, shopping malls are concerned with air- and structure-borne sound insulation due to the large amount of open space (Carvalho & Pereira, 2016) and proximity to urban centers (Wang et al., 2017).

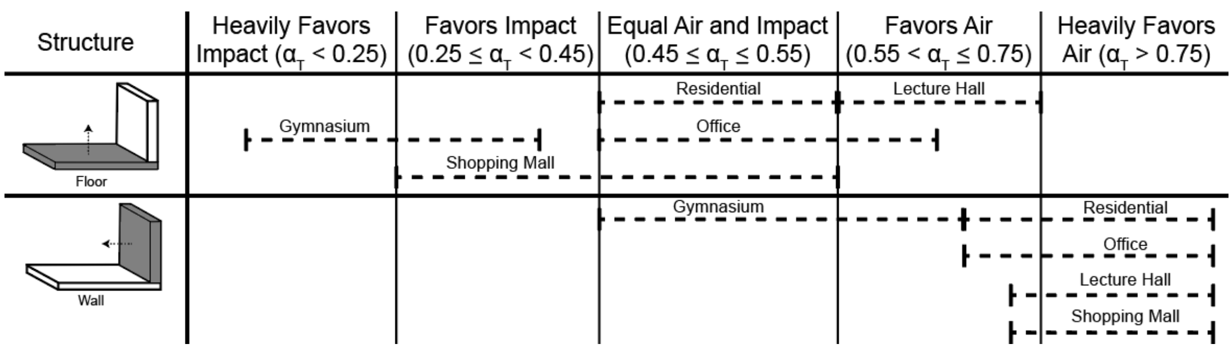

Figure **7-4**: Proposed α_T ranges for floors and walls in five building applications.

Floor structures have wider α_T ranges as they significantly attenuate both air- and structure-borne sounds. While wall structures commonly attenuate air-borne sounds, impact sound insulation could be explored, as door slams have been found to be a common structural-borne noise complaint (Grimwood, 1997). In any case, designers should be cognizant of the expected acoustic needs of the building, potentially at a room-to-room scale, even when first laying out the spaces or developing custom structural elements in early-stage design. Additionally, although the presented α_T ranges can be used as a starting point in the acoustical design of building components, future research should determine more precise α_T values.

7.4 Application: A case study of shape-optimized concrete slabs

In this section, the proposed rating methods are compared and evaluated in a computational case study of shape-optimized one-way concrete floors. Structural concrete floors were selected because their performance in terms of acoustic insulation, structural integrity, and embodied energy can all interact and should be accounted for in optimization problems (Broyles et al., 2022c). While the other aspects of the optimization are mentioned briefly, the focus is on the sound insulation metrics.

7.4.1 Geometry generation

A parametric model of concrete floors was developed using seven geometric variables, shown in Fig. **7-5**. The optimized slabs are designed to minimize the mass of a rectilinear floor, therefore reducing corresponding carbon emissions, and maximize the acoustic insulation performance. The seven variables include: rib number, top slab depth, rib depth, and four curvature control points that shape the ribs. Although many other designs are possible, four slabs with varying geometric features were selected to assess the performance of the proposed metrics. The four slabs will be referred to as the Tee slab, Wavy slab, Sawtooth slab, and Flat slab. The geometric properties of the slabs are provided in Table **7-2**.

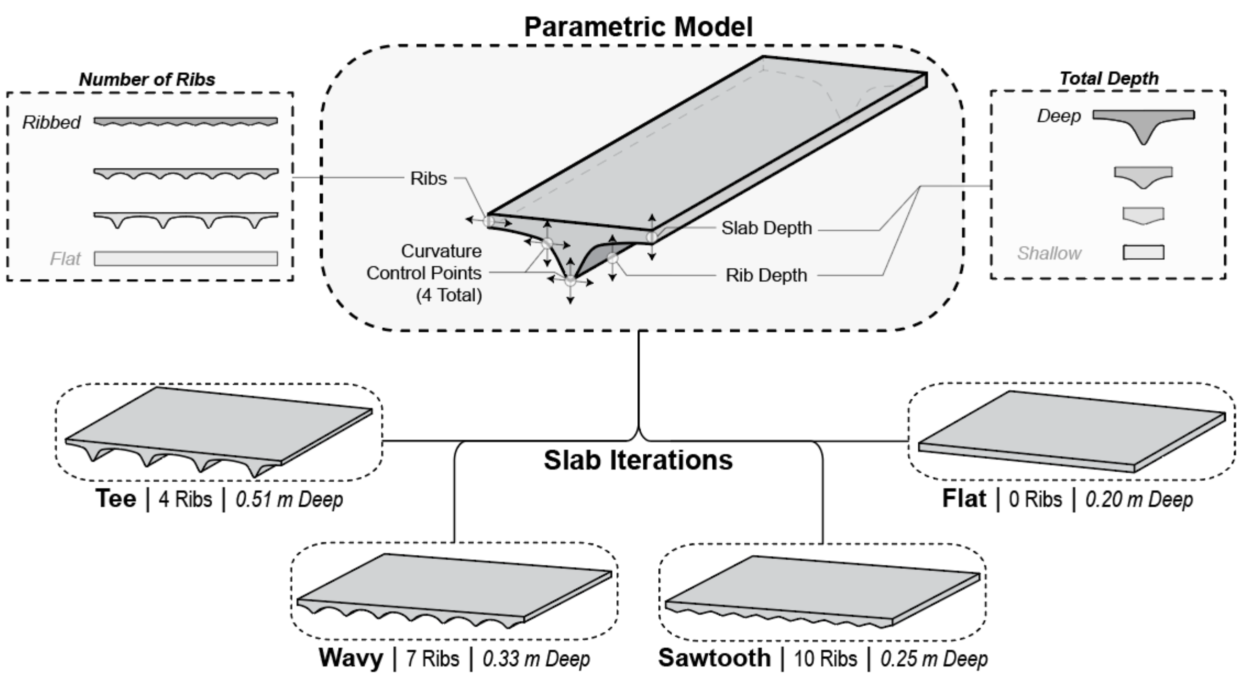

Figure **7-5**: Parametric model of shaped concrete slab components with seven different geometric variables.

Table **7-2**: Geometric properties of the four case study slabs.

Slab	Top Slab Thickness	Rib Depth	Rib Spacing
Tee	0.120 m	0.392 m	1.500 m
Wavy	0.140 m	0.184 m	0.857 m
Sawtooth	0.165 m	0.083 m	0.600 m
Flat	0.203 m	-	-

Despite the geometric differences, the four slabs have the same mass of 17,650 kg and floor area of 36 m^2 to provide a fair acoustic transmission comparison, as seen in Fig. **7-6**. In the context of a multi-objective framework for reducing material, constraining the floors' mass and area is like taking an isoperforming slice of the objective space in the structural material dimension. The contributions of longitudinal and shrinkage steel were neglected in the calculations. While a full explanation of the structural assessment is outside the scope of this chapter, the four concrete slabs satisfied all checks required by ACI 318 building design code (ACI Committee 318, 2019), ensuring that the slabs are structurally valid. Prior work by Broyles (2020) provides more information about structural-acoustic trade-offs of shape optimized concrete slabs.

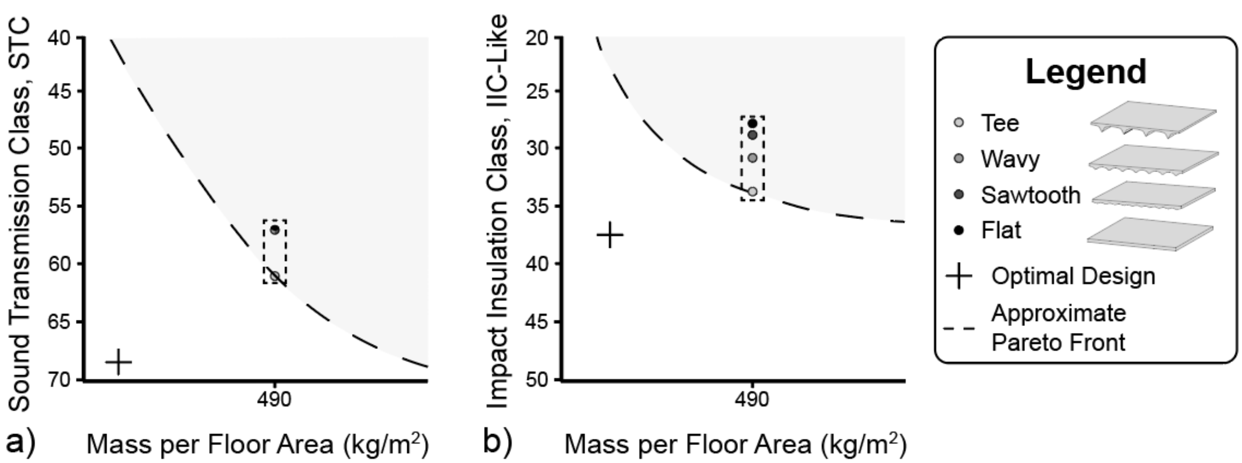

Figure **7-6**: a) Sound transmission class and b) impact insulation class-like integer ratings of the four shape-optimized concrete slabs. The dots represent the mass density and sound insulation performance for the four slabs, and the dashed lines are hypothetical Pareto front approximations based on the findings by Broyles et al. (2021).

7.4.2 Simulating air-borne and structure-borne sound insulation

Due to a lack of acoustic laboratory testing on shaped concrete slabs, the TL data was estimated using an analytical approach, and the IIC-Like method described in Ch. 6 was used to obtain the L_N for the four slabs. The air- and structure-borne transmission performances of the four slabs are displayed in Fig. **7-7**. The TL data for the four slabs is similar above the 250 Hz OTO band, with the TL data approaching (and matching) the TL obtained by mass law, using the simple equation: $TL = 20\log(mf) - 45$, where m is the mass density of the slab and f is the frequency. However, the slabs have differing coincidence dips, resulting in varying low frequency air-borne sound insulation. The L_N data has a similar pattern above the 100 Hz OTO band for all slabs, but similarly has varying performance at low frequencies. Tables **7-3** and **7-4** provide the TL and L_N data used to compare the rating methods in the case study. While the remainder of this section details the method for obtaining the TL data, it should be noted that the data was generated numerically for application in early-stage design, and experimental verification will be pursued in future work. The emphasis in this chapter is comparing the different sound insulation ratings based on the proposed methods.

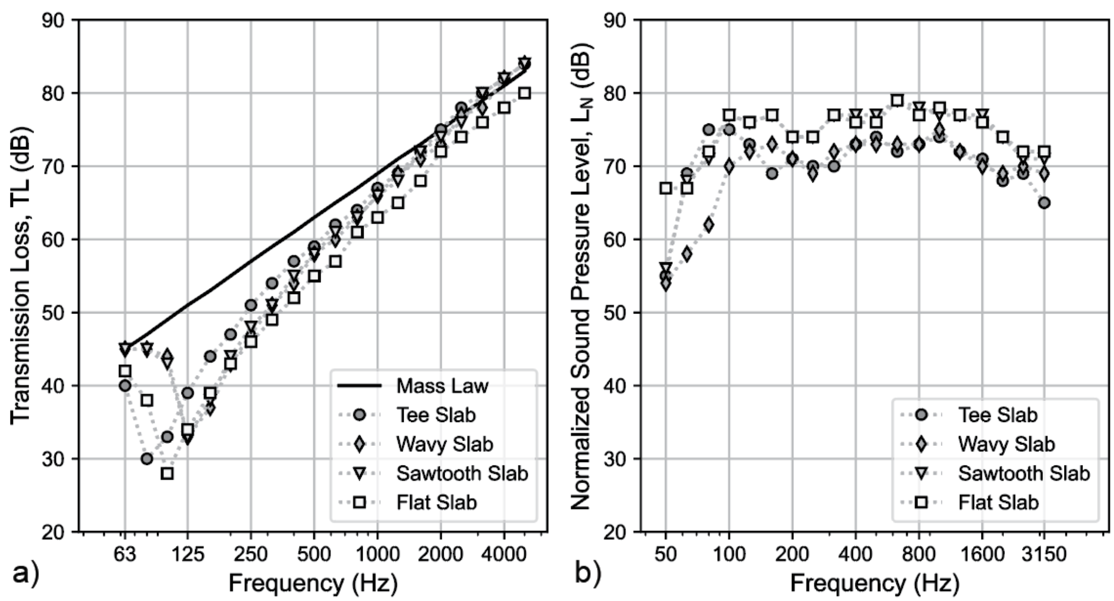

Figure **7-7**: a) TL and b) L_N data for the four slabs.

Table **7-3**: Simulated TL data for the four slabs from 63 Hz to 5 kHz in OTO bands.

Slab	**63 Hz**	**80 Hz**	**100 Hz**	**125 Hz**	**160 Hz**	**200 Hz**	**250 Hz**	**315 Hz**	**400 Hz**	**500 Hz**
Tee	40	30	33	39	44	47	51	54	57	59
Wavy	45	45	44	33	37	43	47	51	54	58
Sawtooth	45	45	43	33	38	44	48	51	55	58
Flat	42	38	28	34	39	43	46	49	52	55
Slab	**630 Hz**	**800 Hz**	**1 kHz**	**1.25 kHz**	**1.6 kHz**	**2 kHz**	**2.5 kHz**	**3.15 kHz**	**4 kHz**	**5 kHz**
Tee	62	64	67	69	72	75	78	80	82	84
Wavy	60	63	66	69	71	73	77	78	82	84
Sawtooth	61	63	66	68	72	74	76	80	82	84
Flat	57	61	63	65	68	72	74	76	78	80

Table **7-4**: Simulated L_N data for the four slabs from 50 Hz to 3.15 kHz in OTO bands.

Slab	**50 Hz**	**63 Hz**	**80 Hz**	**100 Hz**	**125 Hz**	**160 Hz**	**200 Hz**	**250 Hz**	**315 Hz**	**400 Hz**
Tee	55	69	75	75	73	69	71	70	70	73
Wavy	54	58	62	70	72	73	71	69	72	73
Sawtooth	56	68	71	77	76	77	74	74	77	77
Flat	67	67	72	77	76	77	74	74	77	76
Slab	**500 Hz**	**630 Hz**	**800 kHz**	**1 kHz**	**1.25 kHz**	**1.6 kHz**	**2 kHz**	**2.5 kHz**	**3.15 kHz**	
Tee	74	72	73	74	72	71	68	69	65	
Wavy	73	73	73	75	72	70	69	70	69	
Sawtooth	77	79	78	77	77	77	74	71	71	
Flat	76	79	77	78	77	76	74	72	72	

In the calculation of the floors' transmission performance, normal room conditions were assumed (i.e., $c_0 = 343$ m/s, $\rho_0 = 1.29$ kg/m^3), along with normal weight concrete properties ($\rho = 2{,}400$ kg/m^3, $E = 29.73$ GPa) with a Poisson's ratio (ν) of 0.18 and a damping coefficient (η) of 0.025 based on the recommended range (Khajeh Hesameddin et al., 2015). The flexural rigidity (D) of the concrete slab was determined by Eq. **7-2**, where the first term represents the stiffness supplied by the top slab and the second term represents the stiffness contributed by the rib. Moment of inertia (I) and the spacing of the rib (Δ_{Rib}) are determined by the rib geometry while the top slab height (h) is determined by the slab depth. The area density (m) was determined from the mass and area of the floors.

$$D = \frac{Eh^3}{12(1-\nu^2)} + \frac{EI}{\Delta_{Rib}} \qquad \text{(Equation 7-2)}$$

Eqs. **7-3** and **7-4** describe how the TL data was obtained by calculating the transmission coefficient (τ), as was similarly done in Ch. 4 (see Sec. 4.3.3). The frequency range evaluated was from 40 Hz to 6.3 kHz at a 1 Hz interval, which was used to determine the angular frequency (ω) and the wavenumbers (k_0). It should be noted an angle of incidence (φ) range was considered from 0° to 78° (Leppington et al., 1987), at 1° intervals.

$$\tau(\varphi,\omega) = \frac{(\frac{2\rho_0 c_0}{sin\varphi})^2}{(\frac{2\rho_0 c_0}{sin\varphi}+\eta(\frac{D}{\omega})(k_0 sin\varphi)^4)^2+(\omega m-(\frac{D}{\omega})(k_0 sin\varphi)^4)^2} \qquad \text{(Equation 7-3)}$$

$$\mathrm{TL} = \log_{10}\left(\frac{1}{\tau}\right) \qquad \text{(Equation 7-4)}$$

This analytical method is a homogenization approach that takes the effects of the shaped ribs parallel to their orientation. The contribution perpendicular to the ribs is assumed to be negligible. It should be noted that the modes of the slab in between ribs are not considered, and the size and type of boundary conditions are ignored. However, this approach to obtain TL is useful in estimating the air-borne sound insulation in conceptual design. A more accurate approach that considers the full modal response with accurate boundary conditions would be appropriate in later design stages.

The L_N data was obtained by employing the numerical IIC-Like method discussed in Ch. 6. All four slabs were modeled for each of the six walking paths (WPs), but only the L_N curve produced by the worse-case (controlling) walking path is shown, which was WP 6 for all four slabs. Note that the low frequency impact sound (i.e., the 50 Hz, 63 Hz, and 80 Hz OTO bands) were obtained using the air-hemisphere method for these three OTO bands. With the estimated TL and L_N data, the rating methods defined in this chapter were applied to rate the four concrete floor slabs. The following rating results, comparisons, and discussion explore the utility of the proposed methods for quantifying sound insulation in conceptual design and similar computational studies.

7.4.3 Comparison of rating methods

Existing STC and IIC rating methods are used as a basis for comparison, since they are specified by North American building codes such as the International Building Code (IBC) (International Code Council, 2018) and the United States Department of Housing and Urban Department (HUD) (2009). When applied to the computationally defined floor slabs, standard STC ratings varied from STC-57 to STC-61 while the standard IIC ratings ranged from IIC-28 to IIC-34, which are compared to the STC* and IIC* ratings as well as the CM and CTF methods. For reference, a summary of the limitations addressed by each new rating method is shown in Table **7-5**.

Table **7-5**: Proposed rating methods and the limitations of STC and IIC addressed by each approach.

Proposed Metrics	Sound Medium	Removal of 8 dB Rule	Modified Frequency Range	Independent Contours	Single Number Quantity
STC_{Low}	Air-borne		X		
$STC_{No\ 8}$	Air-borne	X			
STC*	Air-borne	X	X		
IIC_{Low}	Structure-borne		X		
$IIC_{No\ 8}$	Structure-borne	X			
IIC*	Structure-borne	X	X		
CM	Air- & Structure-borne	X	X	X	
CTF	Air- & Structure-borne				X
CTF*	Air- & Structure-borne	X	X		X

7.4.3.1 Modified STC and modified IIC results

The STC* and IIC* methods produced different air- and structure-borne integer ratings as noted in Table **7-6** and demonstrated for the flat slab in Fig. **7-8**. The most significant rating alteration was due to the removal of the 8 dB rule from the STC and IIC metrics, which increased the air- and structure-borne sound transmission ratings for all four slabs. The IIC ratings were especially constrained by the high deficiencies in the 3.15 kHz OTO band, so the IIC_{No_8} ratings were controlled by the summation of deficiencies rule in the high frequency range. However, the IIC_{Low} ratings were not influenced by the inclusion of the 50 Hz, 63 Hz, and 80 Hz OTO bands because the 8 dB rule was still applied. Yet the STC_{Low} ratings changed for all four slabs due to the inclusion of the 100 Hz OTO band. Overall, the sound transmission ratings for all concrete slabs (except for the Tee slab for air-borne sound) were modified by a rating of -1 to +4. While The change in rating may appear minor, it is important to note that in optimization frameworks, a rating change could influence the selection of the best performing designs, potentially favoring different floors than when the conventional STC and IIC metrics are applied.

Table **7-6**: The integer ratings obtained using standard STC, IIC derivations, and proposed variations for the four concrete slabs. The original STC and IIC ratings differ from the STC* and IIC* ratings with the changes emphasized in bold.

Acoustic Rating Metric	**Concrete Slab**			
	Tee Slab	**Wavy Slab**	**Sawtooth Slab**	**Flat Slab**
STC	STC-61	STC-57	STC-57	STC-57
STC_{Low}	STC_{Low}-64 (+**3**)	STC_{Low}-60 (+**3**)	STC_{Low}-60 (+**3**)	STC_{Low}-59 (+**2**)
STC_{No_8}	STC_{No_8}-64 (+**3**)	STC_{No_8}-60 (+**3**)	STC_{No_8}-61 (+**4**)	STC_{No_8}-59 (+**2**)
STC*	STC*-61	STC*-58 (+**1**)	STC*-58 (+**1**)	STC*-56 (**-1**)
IIC	IIC-34	IIC-31	IIC-29	IIC-28
IIC_{Low}	IIC_{Low}-34	IIC_{Low}-31	IIC_{Low}-29	IIC_{Low}-28
IIC_{No_8}	IIC_{No_8}-35 (+**1**)	IIC_{No_8}-34 (+**3**)	IIC_{No_8}-30 (+**1**)	IIC_{No_8}-30 (+**2**)
IIC*	IIC*-35 (+**1**)	IIC*-35 (+**4**)	IIC*-31 (+**2**)	IIC*-30 (+**2**)

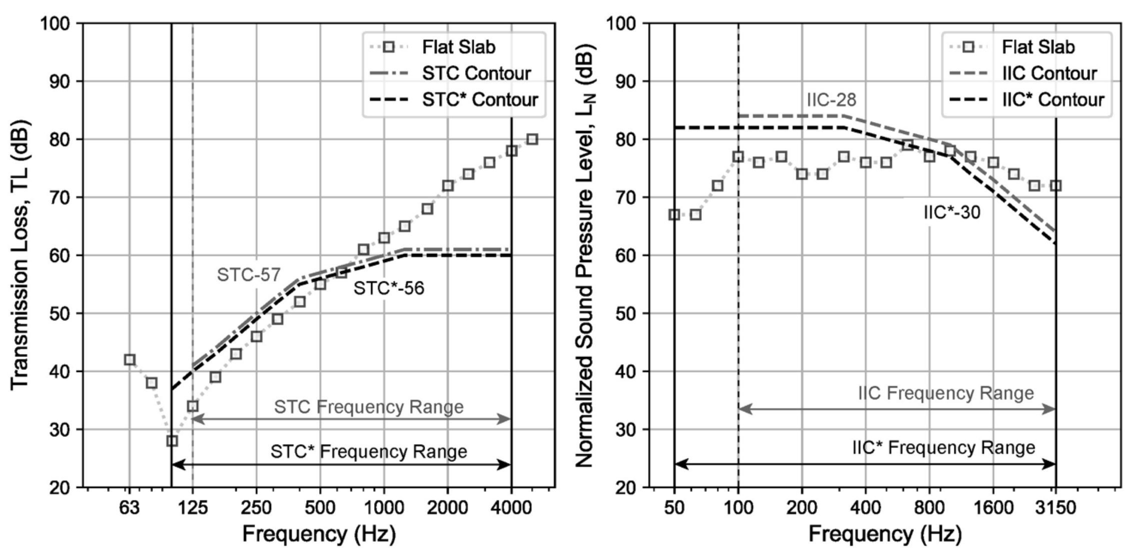

Figure **7-8**: a) Comparison of the STC and STC* and b) the IIC and IIC* rating methods for the flat slab.

7.4.3.2 Categorical Method results

Since the CM approach gives a designer an integer summary for low, mid, and high frequencies for air- and structure-borne transmission loss, Fig. **7-9** and Table **7-7** provide scalar ratings for each frequency range for the four slabs. The CM results reveal that all slabs have high air-borne sound transmission loss, especially the Tee slab. The lowest air-borne sound insulation ratings were in the low frequency range, with the highest acoustic ratings observed in the high frequency range. A key observation of the air-borne sound insulation ratings is that the Tee slab had the highest CM ratings across all three frequency ranges. However, when assessing the performance of the impact CM ratings, no slab had the highest ratings across all three frequency ranges. The Tee and Wavy slabs were the best performing, especially at the low and mid frequency ranges. Yet a takeaway is that the CM rates all four slabs as having very poor structure-borne sound insulation performance at the high frequency range, which further affirms that bare concrete floors have impact sound deficiencies at high frequencies.

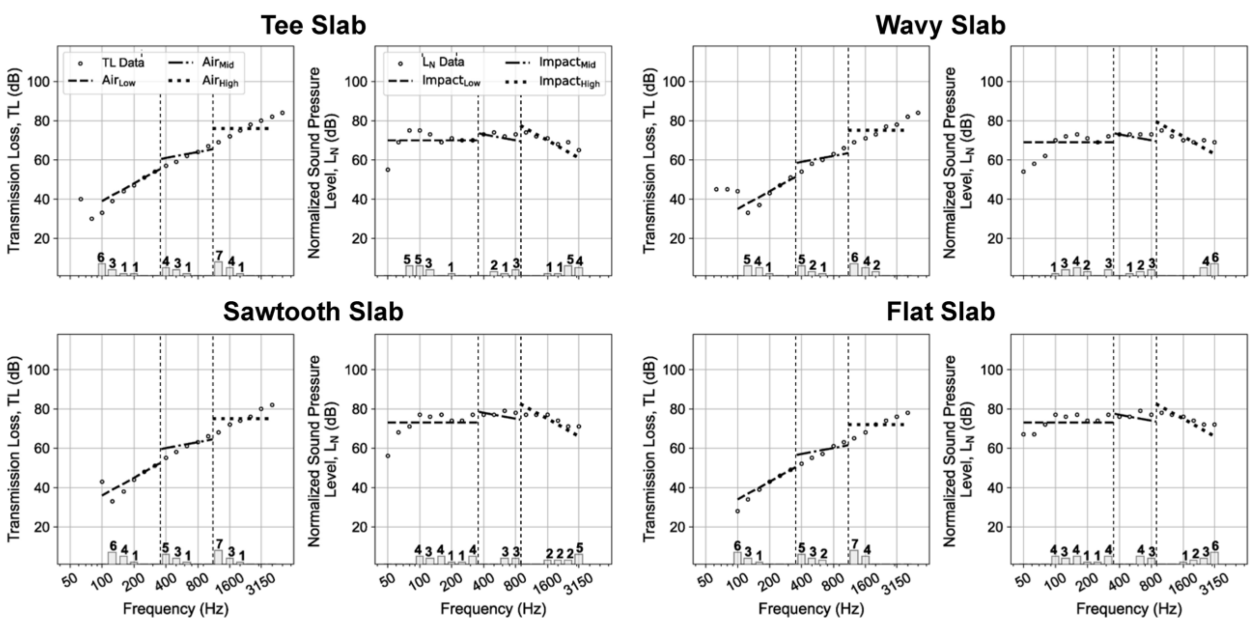

Figure **7-9**: Assessing the air- and structure-borne performance of the four floor slabs using the CM approach. The histograms at the bottom of each individual chart feature the deficiency values in each OTO band.

Table **7-7**: Rating values for the four slabs using the CM rating method. Air_{Low}, Air_{Mid}, and Air_{High} quantify the air-borne transmission loss, while $Impact_{Low}$, $Impact_{Mid}$, and $Impact_{High}$ quantify the structure-borne transmission loss.

Slab	**Air_{Low}**	**Air_{Mid}**	**Air_{High}**	**$Impact_{Low}$**	**$Impact_{Mid}$**	**$Impact_{High}$**
Tee	58	62	72	42	38	31
Wavy	54	60	71	43	38	29
Sawtooth	55	61	71	39	33	26
Flat	53	58	68	39	34	26

7.4.3.3 Composite Transmission Function results

Lastly, the CTF approach was evaluated using both traditional STC and IIC ratings and STC* and IIC* ratings, as shown in Fig. **7-10**. The left plots (a and c) show the air-borne, structure-borne, and equally weighted composite (CTF) ratings for all four slabs; right-hand plots (b and d) show the influence of the weighting coefficient, α_T, for the Wavy slab and Flat slab. Averaging (i.e., setting $\alpha_T = 0.5$) the air- and structure-borne integer ratings causes the CTF rating to be equally influenced by very high or low STC and/or IIC integer ratings. Specifying a proper α_T value in accordance with design goals is therefore critical to the utility of the CTF/CTF* integer rating. Because the slabs that have high higher air-borne sound insulation also have higher structure-borne sound insulation ratings, there are not design scenarios that would influence whether the Flat slab would be preferred over the Wavy slab (i.e., the Wavy slab controls for every different α_T value). However, this is likely not the case for other concrete slab shapes and different floor assemblies. Therefore, future design exploration studies using the CTF/CTF* method should consider what sound insulation ratio should be specified and how a very low or high rating for air- or structure-borne sound insulation could skew the resulting acoustic insulation rating.

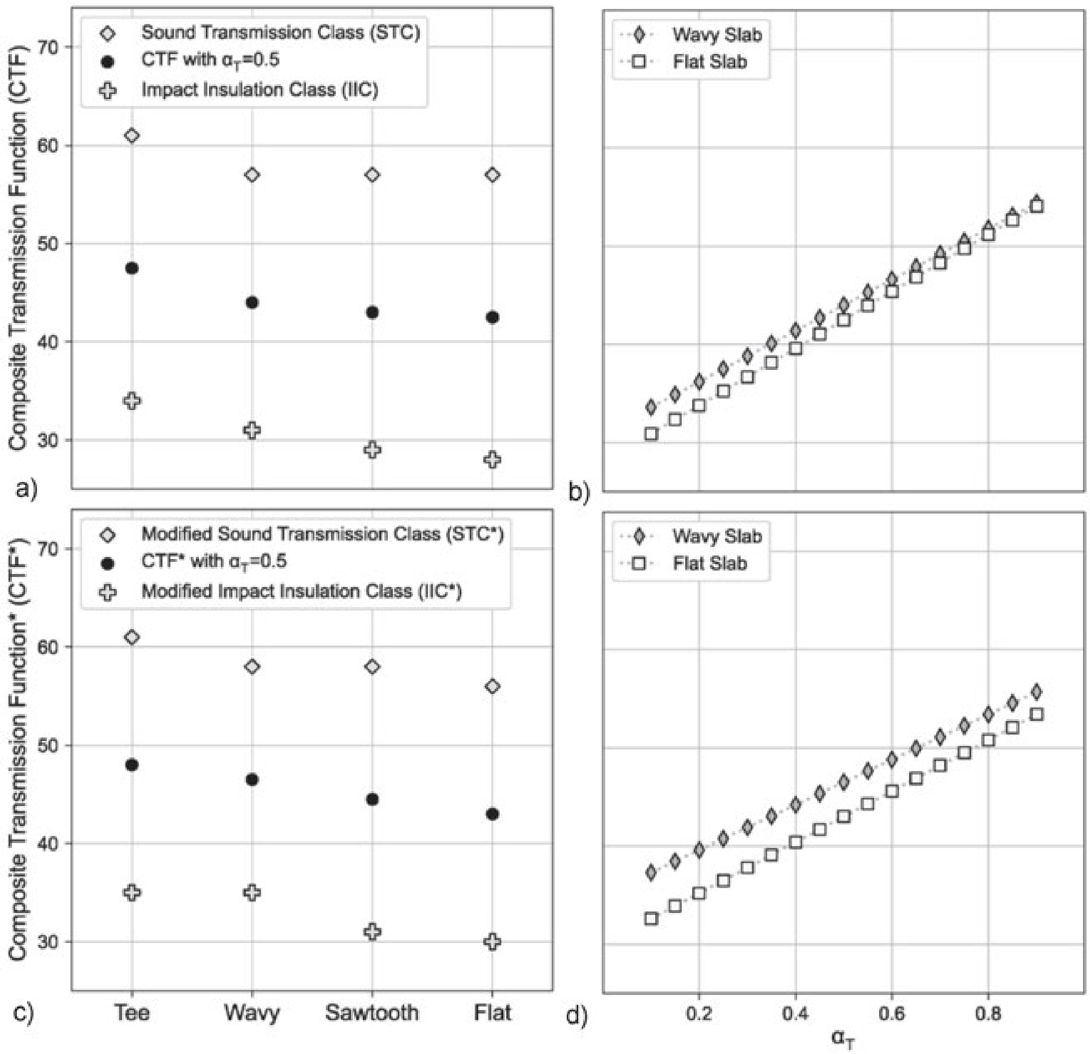

Figure **7-10**: Evaluation of the CTF and CTF*. a) STC, IIC and CTF (with $\alpha_T = 0.5$) ratings for the four slabs. b) Consequences of varying α_T in CTF for the Wavy and Flat slabs. c) Average STC*, IIC* and CTF* (with $\alpha_T = 0.5$) ratings for the four slabs. d) Consequences of varying α_T in CTF* for the Wavy and Flat slabs.

7.4.3.4 Summary and discussion of results

To summarize, Fig. **7-11** compares the rating integers provided by each approach. It is noteworthy that the traditional STC and IIC ratings differ in some cases significantly from the other number ratings, even when comparing them to their modified counterparts. The CM approach provides the most acoustic transmission information but could be difficult to incorporate into an optimization framework. While the CTF ratings provide seemingly less information, appropriate α_T values make this approach worthwhile in complex multi-objective studies involving other building disciplines.

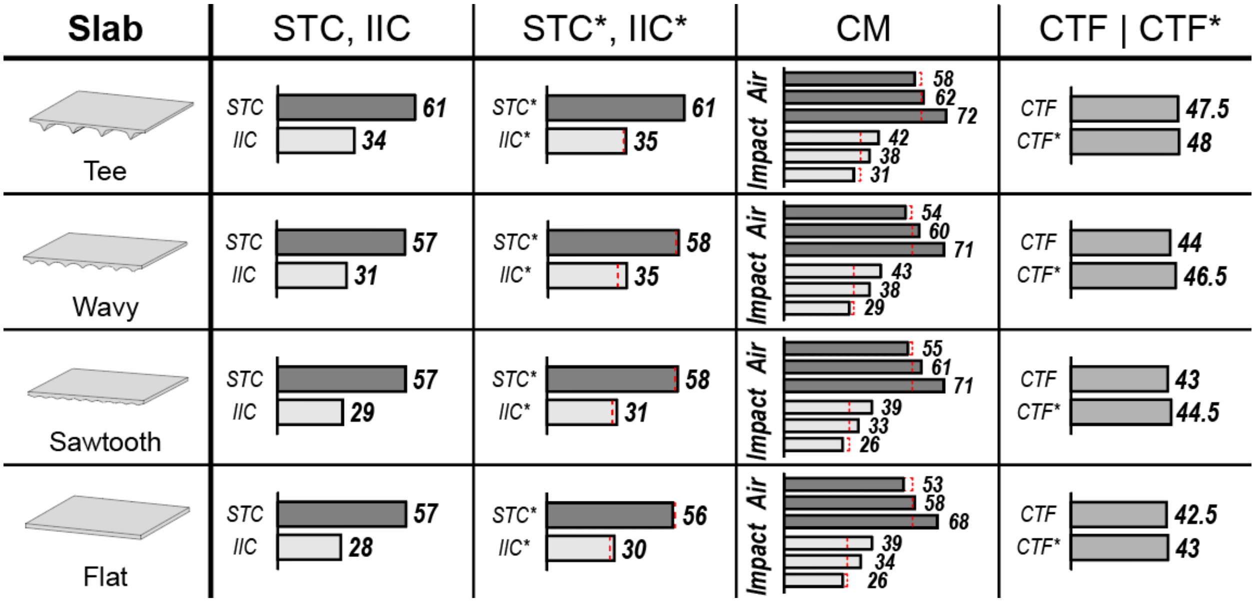

Figure **7-11**: Summary of the ratings obtained from STC and IIC, STC* and IIC*, CM, and CTF, CTF* metrics. The red dashed lines in STC*, IIC* and the CM refers to the original STC and IIC ratings. The CTF values in this table assume the α_T value to be 0.5.

To further analyze the integer rating results, parallel axis plots of each rating are provided in Fig. **7-12**, which can be compared to Fig. **7-6** For air-borne sound transmission, the objective space could be slightly condensed when specifying STC* and CM as an objective, potentially indicating that the four slabs have more similar sound transmission performance than can be seen with STC as the objective. It is noteworthy that across STC, STC* and CM for air-borne sound the same order for best air-borne sound transmission performance is generally kept, with the Tee slab having the best performance and the Flat slab having the worst performance. Yet the order does change slightly when considering impact sound insulation. A final observation is that there is a broad range of ratings across the air- and structure-borne sound insulation ratings. This ultimately factors into the CTF / CTF* ratings, as the slabs are rated below the minimum building code requirement of an acoustic insulation rating of 50.

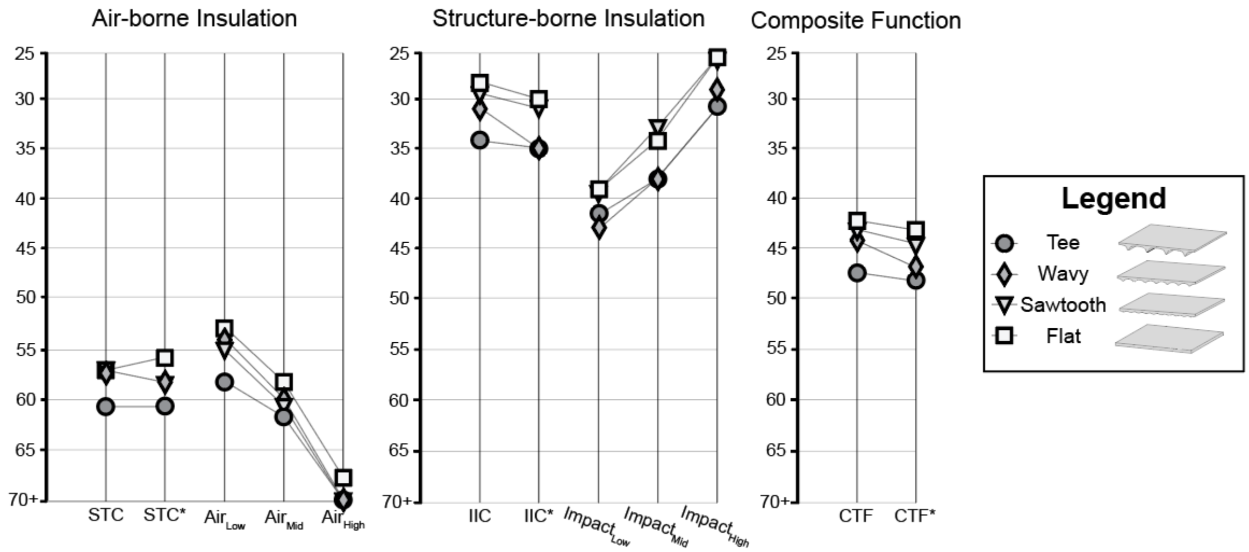

Figure **7-12**: Parallel axis plots for the integer ratings obtained, grouped by air-, structure-borne, or a composite medium for determining sound insulation performance.

7.4.4 Effect on early-stage optimization strategies

In addition to providing more robust ratings for structures in early design exploration, the four methods can be useful additions to optimization frameworks for structural components. Table **7-8** details the objectives, constraints, potential bounds, and practical optimization methods (single objective, multi-objective, and constrained optimization) applicable for each approach. Bounds for CTF can be targeted to air-borne or structure-borne sound insulation using applicable weighting coefficients, while the CM approach may require bounds on specific frequency ranges while maximizing the performance in other frequency ranges. The CM method is potentially advantageous when customizing a structural element to specific building needs.

Table **7-8**: Proposed optimization strategies for the four acoustic metrics. Although the constraints below reflect IBC requirements, higher ratings can be employed as constraints.

Method	**Possible use as Objective Function**	**Possible use as Constraints**	**Bounds**	**Possible Methods**
STC IIC	Max (STC) Max (IIC)	Subject to STC > 50 Subject to IIC > 50	-	Single, Multi, Constrained
STC* IIC*	Max (STC*) Max (IIC*)	Subject to STC* > 50 Subject to IIC* > 50	-	Single, Multi, Constrained
CM	Max ($Air_{Low, Mid, High}$) Max ($Impact_{Low, Mid, High}$)	Design Dependent	Design Dependent	Multi, Constrained, Bracket
CTF, CTF*	Max (CTF, CTF*)	Subject to STC > 50 Subject to IIC > 50	Lower Bound $\geq$ $\alpha_T \geq$ Upper Bound	Single, Constrained, Bracket

7.5 Conclusions

This chapter proposed new rating metrics that have the potential to improve on the limitations of STC and IIC, while addressing the challenge of incorporating sound transmission in computational design exploration or optimization. The methods included a modified STC and IIC, a rating that subdivides the frequency for independent evaluation of low, mid, and high frequency, and a composite air- and structure-borne transmission function. The new methods were compared to STC and IIC in a computational case study using simulated concrete floor structures generated from an early-design framework. Recommendations on which alternative method to use depend on the noise source needing attenuation, construction, and structure type, and how much sound insulation information is needed.

To further assess the rating methods, future work will integrate and test the strategies within optimization frameworks. Procedures will be varied to isolate how the different rating strategies influence the geometries of the best performing structural components, while also comparing the Pareto front approximations of the best performing designs in multi-objective optimization studies. Although HW concrete floors were the focus of the case study, structures composed of different materials such as wood can be considered using the general guidance provided.

Further experimental studies of optimized structures are also needed to validate simulated results for structural and acoustic performance. An important consideration in the development of novel acoustic methods is their correlation to the perceived performance, especially regarding acoustic transmission.

Finally, a perceptual study should be conducted to correlate the perceived sound insulation performance with the integer rating determined by the STC* and IIC*, CM CTF, and CTF*, metrics. A perceptual study validating the proposed metrics is crucial before the metrics are implemented within future revisions of building standards. Following a perceptual study, an additional metric without the use of a contour (potentially based on a weighted energetic summation, like Rw + C and similar ISO metrics), could be developed to have better correlations to the perceived performance. While the demonstrated case study is a first step, these combined efforts can improve how sound insulation performance is quantified in building design codes, leading to more livable, high-performance buildings.

Chapter 8

Assessing the air- and structure-borne sound insulation of shaped slabs[1]

8.1 Introduction

To curb global carbon emissions associated with the built environment, the building industry is progressing towards low-carbon structural systems (Ismail, 2023; Oval et al., 2023; Ranaudo et al., 2021). Significant reductions in the carbon emissions attributed to concrete are necessary, as concrete alone is responsible for 7-8% of global carbon emissions (Barcelo et al., 2014). Because concrete is the most used construction material (Gagg, 2014), many researchers have studied how concrete can be reduced in buildings, specifically concrete floor systems (Huberman et al., 2015; Li et al., 2014; Lupíšek et al., 2017). Reducing concrete material in a concrete floor system directly reduces the embodied carbon (EC) emissions associated with concrete and is recognized as a low-carbon pathway in the built environment (Akbarnezhad & Xiao, 2017; Feickert & Mueller, 2023; Ismail, 2023; Venkatarama Reddy & Jagadish, 2003). As demonstrated in Ch. 3, material-efficient conventional concrete floor systems, such as ribbed, post-tensioned, and voided floor systems, can reduce EC emissions over 50% compared to conventional concrete slabs, with similar results found in related studies (Broyles & Hopper, 2023; D'Amico & Pomponi, 2020; Fanella et al., 2017; Zelickman & Amir, 2021). The findings of these studies imply that concrete floor system EC emissions can be meaningfully reduced using existing construction technologies and design practices. Yet, structural optimization strategies applied to concrete floor components can further reduce EC emissions, as unconventional structural forms can shape or remove concrete material to realize EC savings of up to 58% when compared to an equivalent concrete slab (Hawkins et al., 2020; Ismail & Mueller, 2021; Mata-Falcón et al., 2022; Zelickman & Guest, 2023). While digital fabrication technology

[1] Chapter 8 is in preparation for submission to a peer-reviewed journal.

and other advanced construction practices are currently not widespread, it is anticipated that the technology will become more available over the next decade, suggesting that optimal concrete floor forms could be mass produced and implemented in building design (Lloret et al., 2015; Menna et al., 2020; Wangler et al., 2016).

While structural optimization frameworks applied to concrete floor components is a necessary step to achieve low-carbon structural systems in buildings, it is well known that structural limit states do not always control the design of a floor system (Gross et al., 2010; Longinow et al., 2009; Oh et al., 2019). Ch. 4 revealed how secondary design objectives, especially the combination of high fire-resistance and air-borne acoustic insulation rating requirements, can influence the design of a concrete floor system, potentially requiring more concrete material, and subsequent EC emissions, to achieve multiple performance goals. To strategically consider many different building design objectives, Multidisciplinary Design Optimization (MDO) is an computational strategy to ascertain the best design candidates for several, potentially competing, design objectives (Brown, 2019; Geyer, 2009). MDO frameworks have been applied to the case study of optimized concrete floor components, revealing that optimization strategies aimed at reducing material consumption, and subsequent EC emissions, can influence secondary design objectives, specifically air-borne sound insulation (Roozen et al., 2018; Broyles et al., 2022c), structure-borne sound insulation (Mendez Echenagucia et al., 2016), human-induced vibrations (Wu et al., 2020), thermal insulation (Gascón Alvarez et al., 2022), and a combination of these objectives (Broyles et al., 2022a). The results of these studies indicate that computational frameworks aimed at optimizing the shape of a concrete floor component may inadvertently affect the performance of these secondary objectives. Therefore, optimization frameworks intended to optimize concrete floor shapes must holistically consider the design of a floor by incorporating EC-influencing design objectives.

While all of these objectives all have important health and safety concerns if not properly accounted for, sound insulation is particularly important because of the long-term health concerns to building tenants (Babisch et al., 2013; Mohamed et al., 2020; Rasmussen & Ekholm, 2019) and costly retrofits to correct acoustic-related issues (Alonso et al., 2020). Indeed, sustainable buildings have been cited as having acoustic insulation complaints (Abbaszadeh et al., 2006; Ahmad Zawawi et al., 2018; Ajayi et al., 2016), emphasizing the need to consider acoustic insulation in optimization frameworks aimed to reduce concrete material and carbon emissions; however, acoustic design goals are often overlooked in the design of sustainable (low-carbon) buildings (Broyles, 2023b). Broyles et al. (2022c) explored how the inclusion of air-borne sound insulation in an optimization framework of shaped concrete components affected the geometric form of the floor and corresponding mass density. The study revealed that a concrete component can be shaped to improve air-borne sound attenuation, but high acoustic performance ratings were achieved by increasing the mass density of the floor. For structure-borne sound insulation, the study by Méndez Echenaguica et al. (2016) suggested that the form of a structural concrete component influenced the radiated sound power caused by a single impact force at low frequencies, but impact sound at high frequencies was not considered. A second study by Broyles et al. (2022a) compared shaped concrete floors for air- and structure-borne sound insulation but noted that the analytical expression used to quantify impact sound was a low-resolution model. These two studies helped motivate Ch. 6, which described a computational method to better estimate the impact sound insulation performance of a concrete floor component. However, Ch. 6 limited the IIC-Like assessment to three flat plates and four shaped slabs, acknowledging that other forms would have different impact insulation ratings. And aside from the study by Broyles et al. (2022a), the relationship between EC, air-, and structure-borne sound insulation ratings is not well known for shaped concrete floors. Furthermore, the effect that geometric characteristics (the span length) and structural design parameters (applied loads and concrete strength) have on the shaping of the optimized concrete floor component have not been deeply studied.

In response, this chapter addresses how shaped one-way concrete floors perform for both air- and structure-borne acoustic insulation in relation to the aim of reducing EC emissions. First, 100 different shaped concrete slab forms are evaluated for structure-borne sound insulation using the IIC-Like method defined in Ch. 6. The IIC-Like ratings are compared against the analytically obtained air-borne sound insulation rating and EC emissions to understand the shapes of the best performing designs. Second, the shaped one-way slab design space is further assessed, by applying an MDO framework for 16 unique structural design scenarios with various span lengths, structural loads, and concrete strengths. The non-dominated shaped concrete floors are identified and are used to create a design catalog with the performance of EC, acoustic insulation, and fire rating. Lastly, a sensitivity analysis is conducted to understand how the application of alternative acoustic transmission metrics (specifically STC*) influenced the form and performance of shape optimized concrete floors.

8.2 Background

The use of optimization frameworks, especially when coupled with a parametric model and evolutionary optimization algorithm, has been well known to find optimal building design solutions (Deb, 2011; Geyer, 2009; Turrin et al., 2011). Exploring the design space of possible designs using optimization frameworks has been well studied for applications in building and urban topologies, building structures, and other building components (Dadabai, 2022; Doraiswamy et al., 2015; Hinkle et al., 2022; Lopez & Astudillo, 2006; Mueller, 2014; Mueller & Ochsendorf, 2015) to optimize for a single objective (Ismail & Mueller, 2021; Sahab et al., 2005), or for multiple objectives (Brown, 2019; Marler & Arora, 2004; Yang et al., 2018). Exploration of the structural design space can therefore help inform the selection of the best performing design solution and inform designers on decisions to reduce the carbon footprint of a building (Brown & Mueller, 2019; Hens et al., 2021).

While MDO and similar optimization frameworks converge to a single optimal design, or a series of the best performing designs for multiple objectives (also referred to as a Pareto front of non-dominated designs), building designers and engineers may want to evaluate a larger sampling of high-performing (but not optimal) design candidates. This collection of high-performing design candidates is referred to as the design catalog in this chapter and can be useful in situations where hard-to-quantify objectives (e.g., aesthetics), are valued, or when comparing the performances for multiple design objectives (Balling, 1999).

Previously, design catalogs have been generated for different urban communities (Cardin et al., 2013), building forms (Bianconi et al., 2019; Brown & Mueller, 2017; Doraiswamy et al., 2015; Hens et al., 2021), and building components (Costa & Madrazo, 2015; Dadabai, 2022; Geyer, 2009; Lopez & Astudillo, 2006).

Concrete floor components can similarly inform the development of design catalogs depending on the design goals of a specific building. Costa and Madrazo (2015) coupled a design catalog of precast concrete components in a building information modeling (BIM) model to inform designers on how the precast product can be constructed and implemented in the design of a building. Related, Dadabai (2022) determined a catalog of low-carbon concrete structures that can help reduce the carbon footprint of buildings. These studies, in addition to the potential of mass production of optimized concrete floor components through digital fabrication, suggest that a design catalog of optimized concrete forms can better help designers and engineers assess when certain concrete components are advantageous, especially when considering multiple design objectives. Additionally, the design catalog can include a variety of different geometries, structural parameters, and secondary design considerations (as motivated by Chs. 3 and 4) to better inform designers on specific cases that the concrete components are best suited for. For example, the design space exploration and optimization studies investigating shaped concrete floors limited the assessment to one structural load case: 1.92 kN/m^2 to 2.00 kN/m^2, or 40 psf (Broyles et al., 2022a; Broyles et al., 2022c; Ismail & Mueller, 2021). Ismail and Mueller (2021) did consider five different span lengths (3 m, 5 m, 10 m, 15 m, and 20 m) showing that different span lengths have different embodied energy savings, yet the studies by Broyles et al. (2022a; 2022c) investigated only one span length. A comprehensive design catalog of shaped concrete floors can expand the work of these studies to reveal optimized concrete floor forms for various design scenarios which is needed to help in the implementation of optimized floors beyond single use cases.

The design catalog of shape optimized concrete floors can also show the performances for objectives in addition to EC emissions, including air- and structure-borne sound insulation. While the previous examples of design catalogs represent computationally-determined building systems, acoustic building catalogs were created in the late 20th century to help building designers choose different floor assemblies for their acoustic insulation performance. For example, the "Catalog of STC and IIC Ratings for Wall and Floor/Ceiling Assemblies" (Dupree, 1980) provides experimentally obtained Sound Transmission Class (STC) and Impact Insulation Class (IIC) ratings for various building components. Similar acoustic design catalogs exist that provide additional acoustic information (like the transmission loss values) for different building components, yet the variety of floor and wall assemblies are limited to what was tested in the laboratory (Warnock, 2005). Therefore, the inclusion of STC, IIC, alternative acoustic transmission metrics (refer to Ch. 7), and other secondary design objectives (i.e., fire rating, vibration performance, and floor depth) in the design catalog of numerically-determined shaped concrete floors can help inform building designers select the floor form that satisfies multiple design objectives while balancing the intent to reduce the carbon footprint of a building.

8.2.1 Chapter scope

This chapter makes use of the methodological contributions from Chs. 6 and 7 to evaluate the impact sound insulation performance of shaped concrete floors while putting the simulated results into context with the results found in Chs. 3 and 4. Specifically, this chapter responds to the question: How does the implementation of a computationally-efficient method to simulate impact sound insulation and the incorporation of modified acoustic transmission metrics influence the selection of a low-carbon concrete slab, and how do the best performing shaped concrete slabs compare to an equivalent conventional system? In response, this work employs the IIC-Like method described in Ch. 6 to rate the impact sound insulation performance of shaped one-way slabs, building off of the work by Broyles et al. (2022c). Sampled shaped slabs are rated for air- and structure-borne sound insulation against EC emissions to determine the design trade-offs between minimizing EC and maximizing acoustic insulation.

The results of the impact sound assessment will be used to inform what design objectives should be considered in the optimization framework. The design space will be evaluated using a multi-objective genetic algorithm to obtain the approximate Pareto fronts for 16 different design scenarios; 4 different span lengths, 2 load cases, and 2 concrete strength classes. The best performing designs from each design scenario will be used to create the design catalog of shaped concrete components, in which the form of the component in addition to its performance for sustainability (EC emissions), acoustic insulation, and fire-resistance will be displayed. These best performing designs will then be compared to a functionally equivalent conventional one-way slab to determine how much better shaped slabs perform for multiple building design objectives.

8.3 Methods

8.3.1 Parametric model of a shaped one-way concrete floor

The shaped concrete slabs evaluated in this work is an extension of the work by Broyles et al. (2021, 2022c) in which a parametric model was made to generate different structural forms of a one-way concrete floor. As shown in Fig. **8-1**, the parametric model used in this study consists of seven different geometric variables, each with an upper and lower numerical bound, that manipulate the shaping of the slab and rib. The span and width of the floor are equivalent for the four different span lengths considered, which are defined in Sec. 8.3.2. It should be noted that this parametric model differs slightly from earlier versions developed by Broyles et al. (2021, 2022c) to evaluate more construction-viable, yet geometrically-diverse design candidates. The parametric model and the design objectives, outside of structure-borne sound insulation, were evaluated in the Grasshopper environment of Rhino 7, with custom code used to ascertain the objective performances of EC emissions, air-borne sound insulation, fire-resistance, and walking vibrations.

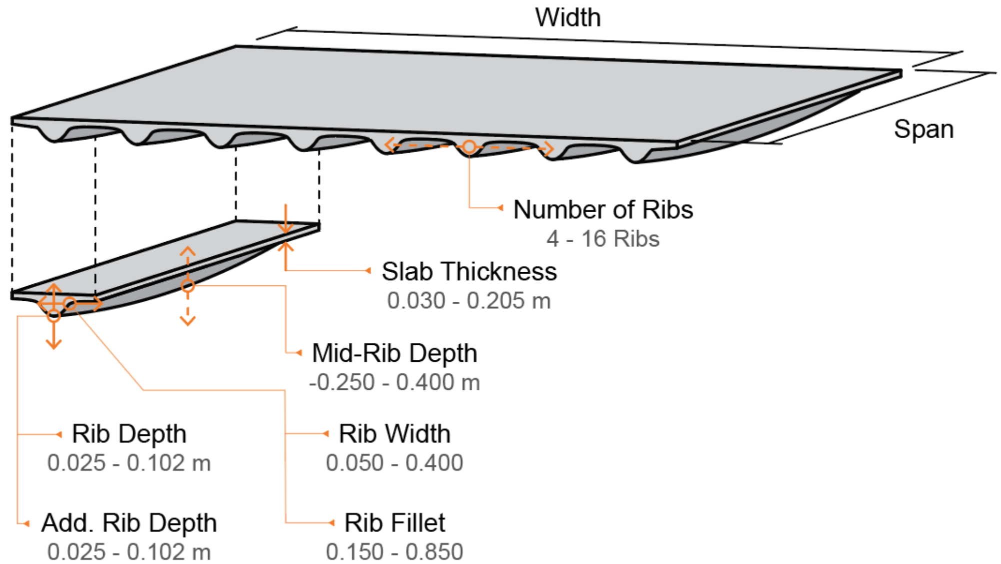

Figure **8-1**: Parametric model of a shaped concrete slab.

8.3.2 Structural design scenarios and structural material properties

The shaped concrete slabs were evaluated for structural performance according to ACI 318 concrete design code (American Concrete Institute, 2018). This study explored a subset of the breadth of structural design scenarios considered in Chs. 3 and 4, but with the intention of assessing how varying the geometry, concrete strength, and applied loads influenced the forms of the best-performing concrete slabs. Table **8-1** provides the different structural design parameters considered, including 4 span lengths, 2 concrete strength classes, and 2 uniform live loads (LLs) corresponding with 2 superimposed dead loads (DLs), for a total of 16 different design scenarios. The 1.915 kN/m^2 LL is only designed with the 0.239 kN/m^2 DL case, and the 4.788 kN/m^2 LL is only designed with the 0.958 kN/m^2 DL case, but both load cases are designed for each concrete strength class. Although different combinations of LLs and DLs could be considered, the two load cases are representative of loads experienced in a residential and office building. The long-term deflection limit is defined as $L/360$ for both cases. The shaped concrete slabs that did not satisfy the structural limit states (flexure, shear, deflection, and ductility) as defined in the ACI 318 design code were not considered in the assessment of impact sound performance and were excluded from the design catalog of shaped concrete slabs since these designs would not be implemented in the design of a building.

Table **8-1**: The various structural design parameters used in this study.

Span Length in m (ft)	**Concrete Strength Classes in MPa (ksi)**	**Applied Live and Dead Loads in kN/m^2 (psf)**	
6 (~ 20)	27.6 (4)	1.915 (40)	0.239 (5)
7.5 (~ 25)	34.5 (5)	4.788 (100)	0.958 (20)
9 (~ 30)	-		
10.5 (~ 35)			

All shaped slabs in the assessment of impact sound insulation were designed assuming normal weight concrete (i.e., density is 2,400 kg/m^3, or 150 pcf) with a strength of 28.2 MPa (~4,000 psi), a modulus of elasticity of 25,000 MPa, and a Poisson's ratio of 0.18. Note that the shaped slabs in the design catalog with a concrete strength of 34.5 MPa (~5,000 psi) had a corresponding modulus of elasticity of 27,600 MPa and a Poisson's ratio of 0.18. Longitudinal steel reinforcement was also considered in the structural design. The modulus of elasticity of the steel reinforcement was defined as 200 GPa with a density of 7,850 kg/m^3 and a yield strength of 420 MPa. All shaped slabs were designed for every steel rebar case, with the steel reinforcement case that satisfied the structural limit states with the least amount of mass was selected in the design of the shaped concrete slab. The steel reinforcement bars, sizes, mass per unit length, and areas considered in this study are presented in Table **8-2**. All steel reinforcement had a minimum clear cover of 38 mm (1.5 in).

Table **8-2**: The steel reinforcement sizes, bars, and material characteristics considered in the study.

Case #	**Rebar Size**	**Number of Bars**	**Mass per Unit Length in kg/m (lb/ft)**	**Rebar Area in mm^2 (in^2)**
Case 1	#6	1	2.240 (1.502)	284 (0.44)
Case 2	#7	1	3.049 (2.044)	387 (0.60)
Case 3	#8	1	3.982 (2.670)	509 (0.79)
Case 4	#9	1	5.071 (3.400)	645 (1.00)
Case 5	#7	2	6.098 (4.088)	774 (1.20)
Case 6	#10	1	6.418 (4.303)	819 (1.27)
Case 7	#11	1	7.924 (5.313)	1006 (1.56)
Case 8	#8	2	7.964 (5.340)	1018 (1.58)
Case 9	#9	2	10.142 (6.800)	1290 (2.00)
Case 10	#8	3	11.946 (8.010)	1527 (2.37)

8.3.3 Design objectives

8.3.3.1 Life cycle assessment and EC calculation

The calculation of the sustainable performance of the floors is quantified by EC emissions. EC is calculated as a function of the structural material quantity of a structure multiplied by the Global Warming Potential intensity (GWP) corresponding to each structural material (refer to Equation **3-1**). A cradle-to-gate LCA (only A1-A3 stages) was performed to quantify EC, as was done in Chs. 3 and 4 (for more information, see Secs. 3.3.2 and 4.3.5), which is considered the most influential for determining the carbon emissions of structures (Anderson & Moncaster, 2021; Davies et al., 2015). The GWPs considered in this study correspond to the values used in Ch. 3 (see Table **3-5**); therefore, GWPs of 345 $kgCO_2e/m^2$ and 365 $kgCO_2e/m^2$ were specified for the concrete strength classes of 27.6 MPa (4 ksi) and 34.5 MPa (5 ksi), respectively, with a GWP of 0.854 $kgCO_2e/kg$ defined for the steel reinforcement. The EC emissions are normalized by the total area of the shaped slab component (in $kgCO_2e/m^2$) to fairly compare slab designs with different span lengths. Note that the functional equivalence of the shaped concrete slabs in this study is only to satisfy the structural limit states; however, the design performance for additional objectives is used to further assess the concrete components.

8.3.3.2 Air- and structure-borne acoustic insulation

This study evaluated the shaped slabs for both air- and structure-borne sound insulation. The calculation of the air-borne sound insulation is the same analytical approach as was defined in Sec. 4.3.3. This analytical method can estimate the transmission loss (TL) across a broad frequency range while accounting for the mass density, bending stiffness, and damping of the shaped slab. It is important to note that this study considers a range of acoustic incident angles (0° to 78° at 1° intervals, as recommended by Leppington et al., 1987), which is different than the results found in Broyles et al. (2022c), which only looked at a single angle of incidence (45°). The determination of the structural-borne sound insulation follows the IIC-Like method detailed in Ch. 6. The IIC-Like method can be used to obtain the normalized sound pressure levels (L_N) across a broad frequency range, similar to the calculation of air-borne sound insulation. Although the six walking paths (WPs) defined in Ch. 6 may not be needed to determine the worst-case impact sound insulation scenario, this study modeled and assessed all six WPs for impact insulation performance to determine if only a subset needs to be modeled when evaluating across the shaped slab design space in future studies.

The calculated TL and L_N values across a broad frequency range can be used to obtain a single number quantity (SNQ) representative of the air- and structure-borne sound insulation performance. Although the resolution of sound insulation at the one-third octave (OTO) frequency bands is lost, truncating the TL and L_N values into an SNQ is advantageous for multi-objective optimization frameworks to better assess design trade-offs with acoustics (Broyles et al., 2022c). However, as detailed in Ch. 7, the conventional North American sound insulation metrics of Sound Transmission Class (STC) and Impact Insulation Class (IIC) have known functional limitations that can be taken advantage of in an optimization framework. Ch. 7 then proposed alternative acoustic transmission metrics including a modified STC (STC*), which includes the 100 Hz OTO band and removes the 8-dB rule.

8.3.3.3 Additional design considerations

Two additional secondary design objectives were considered in this chapter: fire-resistance rating and walking vibrations. Fire resistance and vibrations are only considered for the sampled shaped slabs when assessing impact sound insulation and in the design catalogs of the best performing optimized shaped slabs for the 16 different design scenarios. Future work will consider the addition of these design objectives in larger multi-objective studies.

The fire-resistance rating is determined using the prescribed International Building Code (IBC) code-based method (2018) defined previously in Sec. 4.3.2. Because of the geometry of the shaped slabs in this study, the floors were evaluated based on the "slab with undulating soffit" case which is defined in IBC 722.2.2.1.3 (refer to Fig. **4-2** in Ch. 4). While conventional pan joist one-way floor systems can have wide rib spacings, the rib spacing of the shaped one-way slabs can be optimized to improve the prescribed fire-resistance rating. Similarly, the assessment of walking floor vibrations follows the procedure outlined in Sec. 4.3.4. Although satisfying walking vibration requirements can be applied like a structural limit state, identifying which shaped concrete floor forms are/are not susceptible to vibrations can help inform designers on what geometric characteristics can influence floor vibration performance. Because the two structural load cases are representative of a residential and office building, only the walking vibration threshold corresponding to these building types was considered.

8.3.4 Design space exploration and optimization

The evaluation of the shaped concrete slab design space was conducted using two different frameworks. First, a Latin hypercube sampling (LHS) of 100 samples (n = 100) was obtained to assess the impact sound insulation performance of shaped concrete floors. The number of samples was limited by the computational cost of evaluating the impact insulation performance using the IIC-Like method but can still be helpful in discovering broad trade-offs with impact sound insulation. While high-performing shaped slab designs were identified, these designs were not included in the design catalogs determined from the second computational strategy.

The second framework used in the study to evaluate sound insulation performance is an MDO framework. To determine the best performing shaped concrete slabs across all design scenarios, an MDO framework using the genetic algorithm, Non-Dominated Sorting Genetic Algorithm-II (Deb et al., 2002), was employed. Sec. 8.4.1 shows that the shaped slabs have low impact sound insulation performance, failing to satisfy the IBC code-minimum rating of IIC-50 (2018); therefore, only the objectives of EC and STC / STC* (refer to Sec. 7.3.1) were considered. The optimization framework was repeated for all 16 design scenarios, with the best shaped slab designs taken at different acoustic insulation ratings, for incorporation in the design catalog. Note that not all of the best performing designs were included in the design catalog, as the shaped concrete slab with the least amount of EC and an STC rating between 50 to 54, 55 to 59, and above 60 which corresponds to different perceptual levels of sound insulation in buildings (refer to Table **4-4** in Sec. 4.3.3).

8.4 Results and discussion

8.4.1 Assessment of EC and sound insulation

An LHS of 100 unique shaped concrete slab designs was obtained to first evaluate shaped one-way slabs for impact insulation performance, using the IIC-Like method described in Ch. 6. Fig. **8-2** shows roughly half of the shaped slab profiles evaluated for impact sound insulation performance. The 100 shaped slabs were first evaluated for IIC-Like rating and EC emissions as shown in Fig. **8-3**. Similar to the assessment of the IIC-Like ratings for flat and shaped concrete floors against mass density in Ch. 6, there is a clear trade-off between reducing EC and maximizing IIC-Like. An important observation is that the shaped concrete floors with the least amount of EC have very poor IIC-Like ratings (a rating of IIC-Like-25) and had thin top slabs. The opposite is true for IIC-Like, as the best performing IIC-Like slabs had an EC near 100 $kgCO_2e/m^2$ and are characterized with many ribs and thick top slabs. Worse, the highest observed IIC-Like rating was an IIC-Like-37 for tested slab 3 (in Ch. 5), which is considerably lower than the minimum IBC requirement for impact sound insulation (a rating of IIC-50 or more) (2018). Yet an exciting observation is that shaped slabs outperformed the flat slabs for both reducing EC and maximizing impact sound insulation.

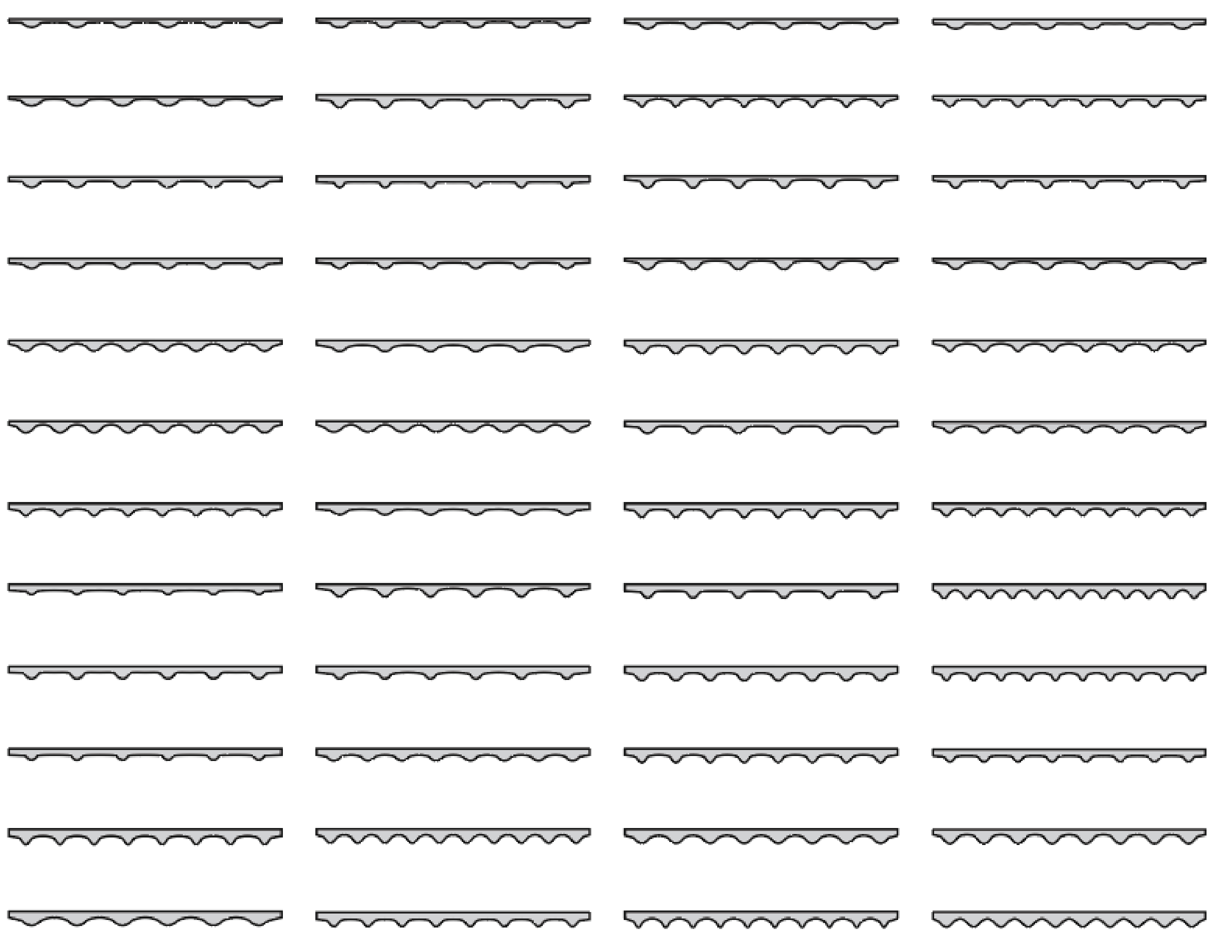

Figure **8-2**: Approximately half (48) of the 100 LHS shaped one-way slabs.

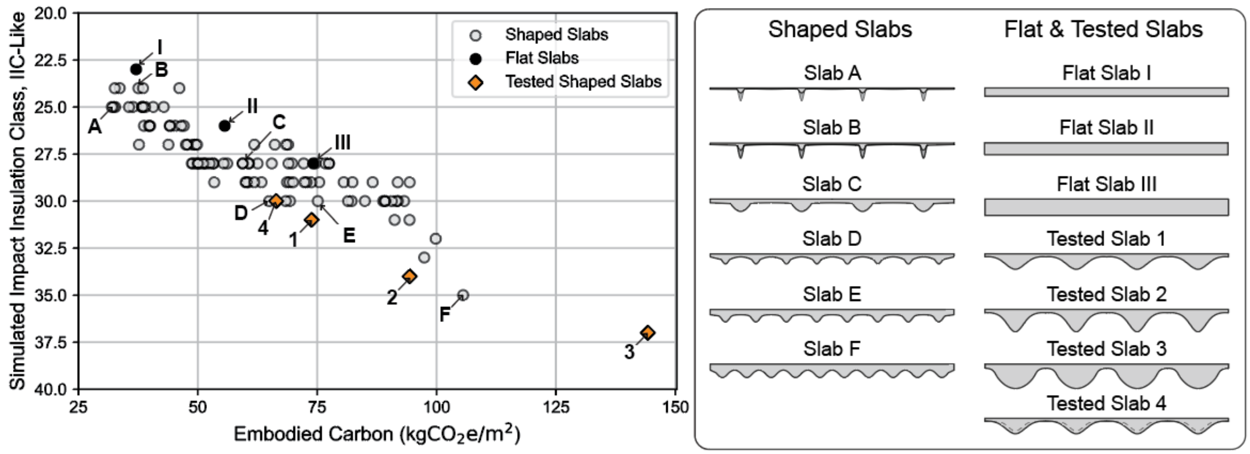

Figure **8-3**: Bi-objective plot showing EC vs IIC-Like. The approximate Pareto front is highlighted.

The sampled designs were then assessed to determine what was the controlling walking path (WP) to obtain the IIC-Like rating. As was suggested in the results of Ch. 6, not all WPs were found to control the IIC-Like rating. Fig. **8-4** shows that four different WPs controlled the IIC-Like rating, with many of the slabs controlled by WP 3 and WP 6. This implies that additional computational resource savings can be realized since WP 1 and WP 5 did not have the controlling IIC-Like rating for any of the shaped concrete slabs evaluated in this study.

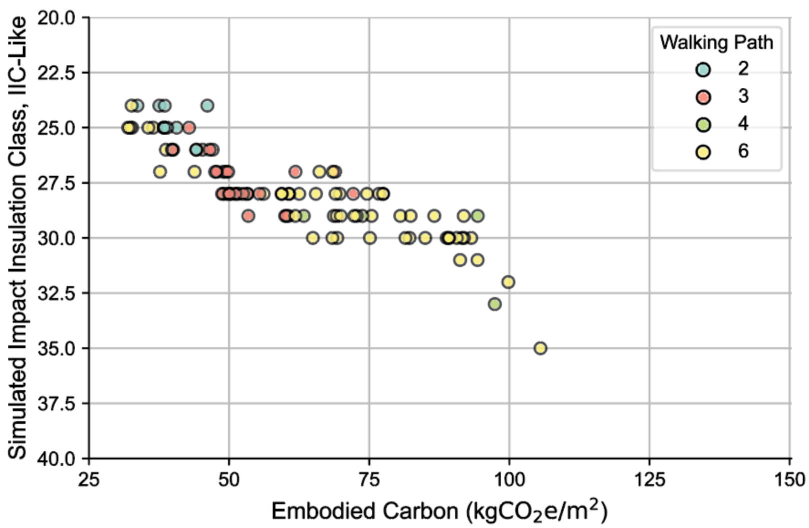

Figure **8-4**: Bi-objective plot showing EC vs IIC-Like and which walking path controlled.

Next, the concrete floors were evaluated for air-borne sound insulation, using the objective, STC, as seen in Fig. **8-5**. Unlike the assessment of impact sound insulation, the majority of the slabs were able to meet a minimum STC rating of STC-50. Interestingly, the spread of STC ratings is much larger than the spread of IIC-Like ratings, yet the band of the designs is thinner for STC than IIC-Like, suggesting that geometric shaping of the floor system can meaningfully influence both air- and structure-borne sound insulation. This relationship was further explored by comparing the STC and IIC-Like ratings of the sampled slabs against each other. Fig. **8-6** shows that as the STC rating generally increases, the IIC-Like rating increases, yet even when constraining for a single STC or IIC-Like rating, there are a variety of performance for the companion acoustic objective. While a similar finding was realized with mass timber floors (Leonard et al., 2022), the evaluation in this study exclusively evaluates how geometric shaping of a concrete component can create a wide distribution of acoustic insulation performances. Lastly, Fig. **8-7** shows a parallel-axis plot comparing the performance of the shaped slabs for EC, STC, STC*, IIC-Like, prescribed fire-resistance, and vibrations against a structurally-equivalent conventional one-way slab.

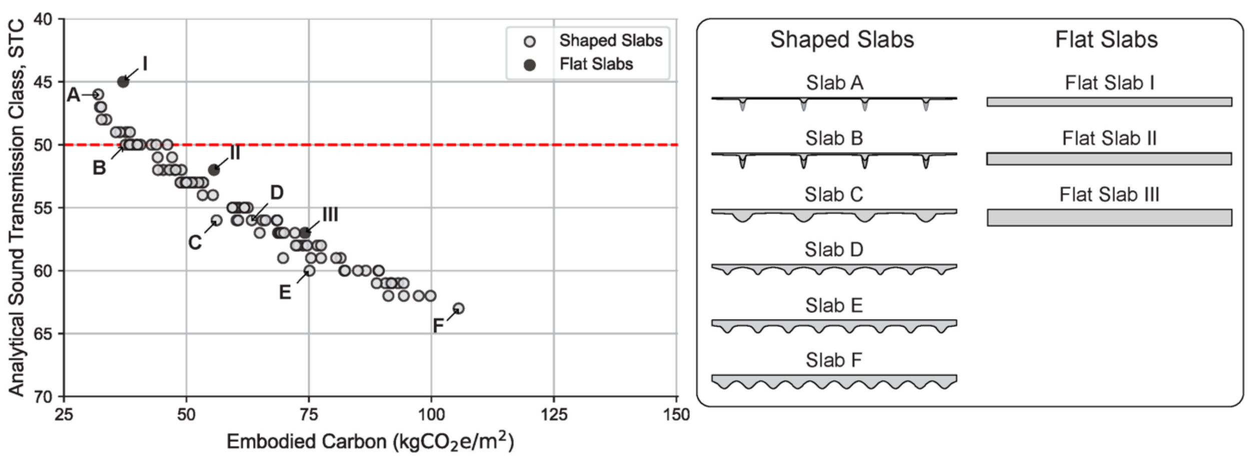

Figure **8-5**: Bi-objective plot showing EC vs STC. The approximate Pareto front is highlighted.

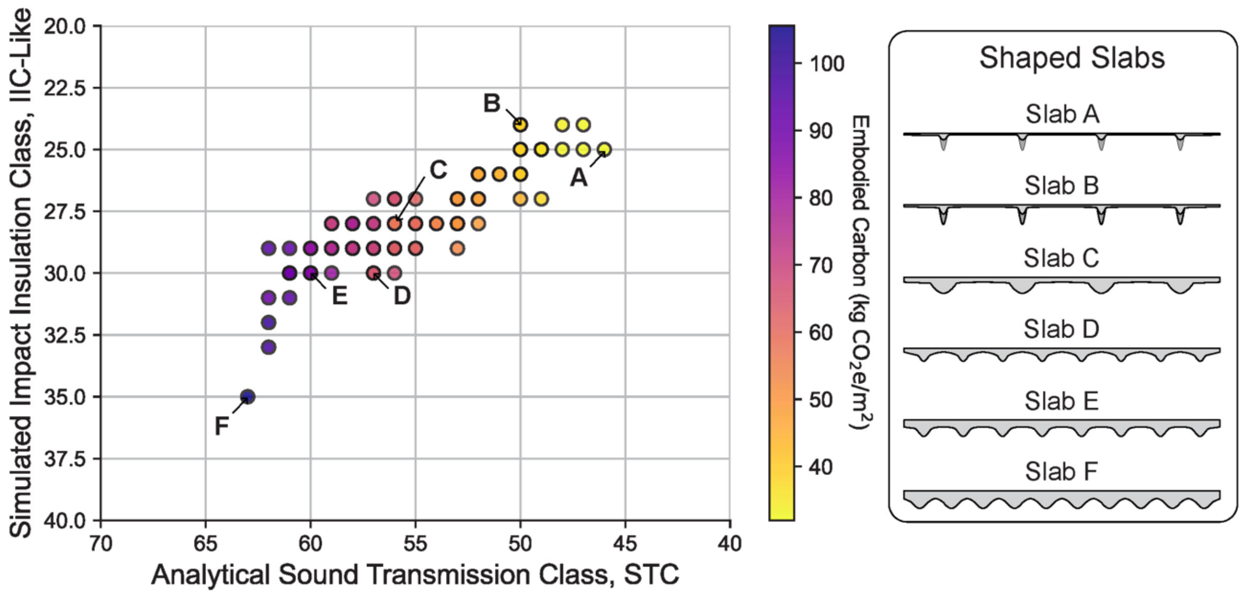

Figure **8-6**: Bi-objective plot showing STC vs. IIC-Like colored based on EC performance.

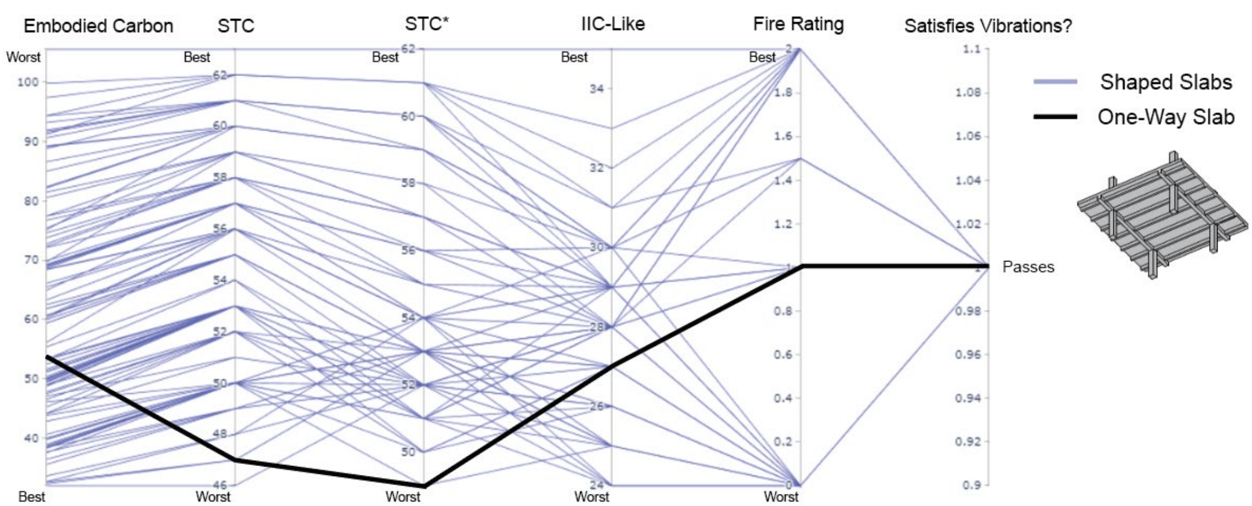

Figure **8-7**: Parallel axis plot comparing the performance of the shaped slabs for EC, acoustic insulation, and secondary design objectives against an equivalent conventional one-way slab.

To summarize, the assessment of shaped one-way concrete slabs for air- and structure-borne sound insulation revealed that different structural shapes can influence both the STC and IIC-Like rating of the floor systems. While high STC ratings can be obtained, lower IIC-Like ratings were found for shaped one-way slabs. As a result, additional floor layers would be needed to satisfy minimum design requirements for impact insulation performance. Therefore, the combination of EC and STC can be employed as design objectives in MDO strategies with the expectation that floor layers can be added to the optimized shaped floors to achieve favorable impact sound insulation performance. When comparing the shaped concrete slabs to conventional flat and one-way slabs, it was found that certain shaped slab forms outperformed the conventional systems. Specifically, the shaped slabs could outperform the flat slabs by an EC of about 51%, or near 37 $kgCO_2e/m^2$ (when comparing shaped slab B to flat slab III), with an increased STC rating up to 5 (when comparing shaped slab B to flat slab I). Similarly, shaped concrete slabs could achieve EC savings near 33% (about 19 $kgCO_2e/m^2$) with equivalent, or better acoustic insulation. However, Fig. **8-7** reveals that many of the low EC shaped slabs fail to have a fire-resistance rating of 1-hr or higher, indicating that the inclusion of fire-resistance should be explored in future studies.

8.4.2 A sensitivity analysis of varying structural design scenarios

Based on the assessment of acoustic insulation for shaped one-way concrete floors, the air-borne sound insulation objective of STC and EC were employed in an MDO framework for the 16 different design scenarios. Figs. **8-8** to **8-11** show four unique design scenarios for each of the four span lengths (6 m, 7.5 m, 9 m, and 10.5 m). The approximate Pareto front was identified for each optimization iteration. Additionally, non-dominated shaped floor designs were selected to be included in future design catalogs of high performing shaped concrete slabs. It should be noted that no shaped concrete floor designs could sustain high structural design loads at a span length of 10.5 m. This procedure was repeated when substituting STC with the modified STC metric proposed in Ch. 7, with the results presented in Figs. **8-12** to **8-15**.

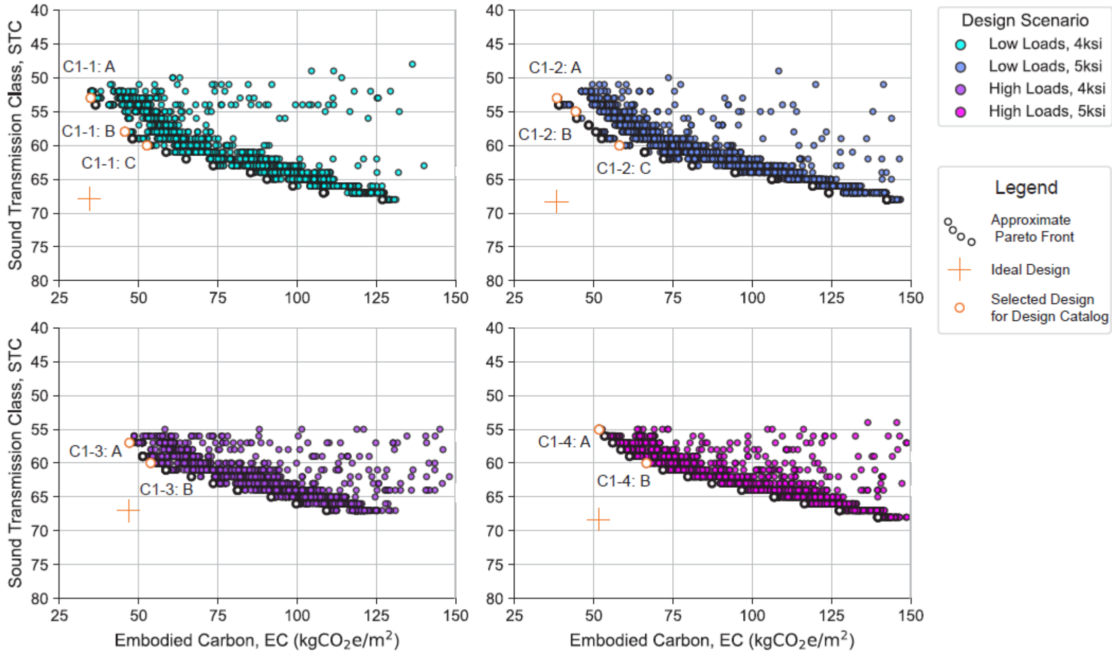

Figure **8-8**: Bi-objective plots showing EC vs. STC with a span length of 6 m for the two concrete strength classes and load conditions.

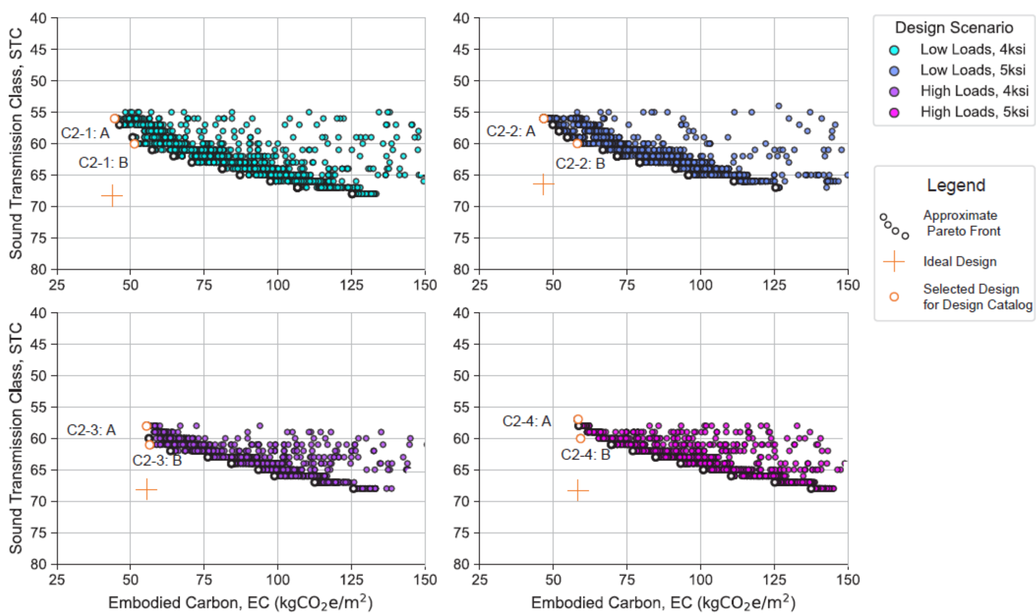

Figure **8-9**: Bi-objective plots showing EC vs. STC with a span length of 7.5 m for the two concrete strength classes and load conditions.

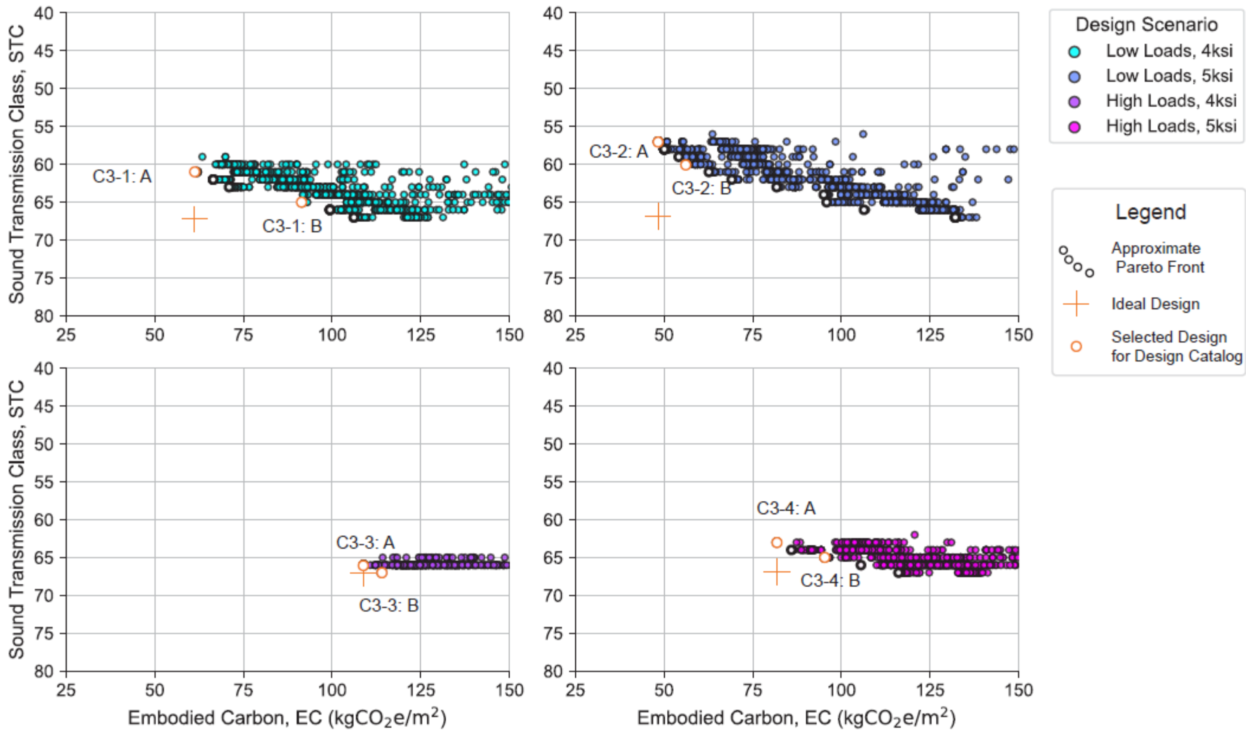

Figure **8-10**: Bi-objective plots showing EC vs. STC with a span length of 9 m for the two concrete strength classes and load conditions.

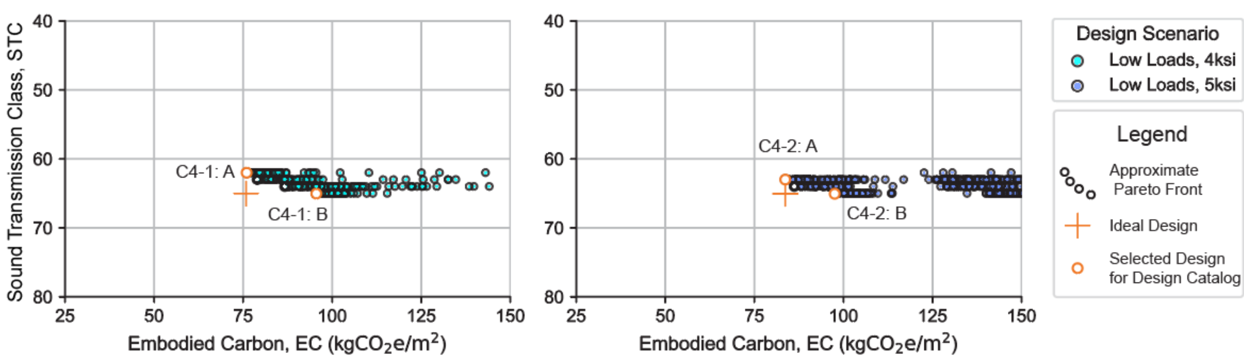

Figure **8-11**: Bi-objective plots showing EC vs. STC with a span length of 10.5 m for the two concrete strength classes and load conditions.

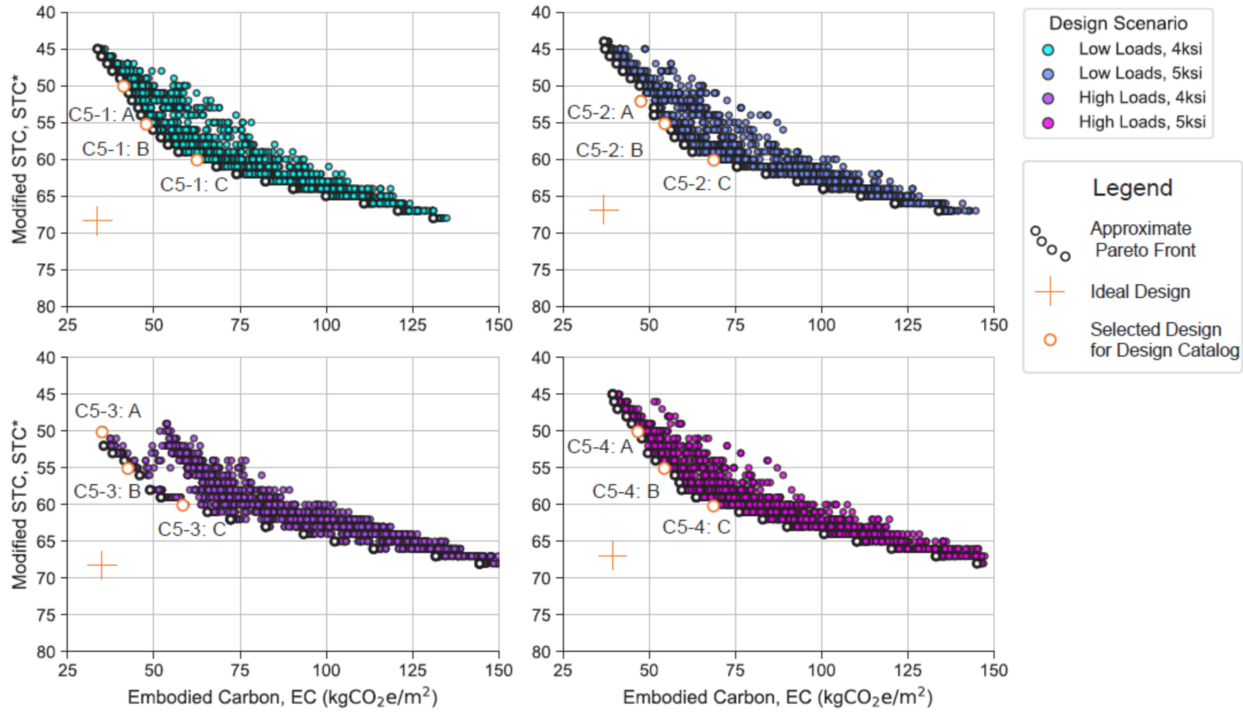

Figure **8-12**: Bi-objective plot showing EC vs. STC* with a span length of 6 m.

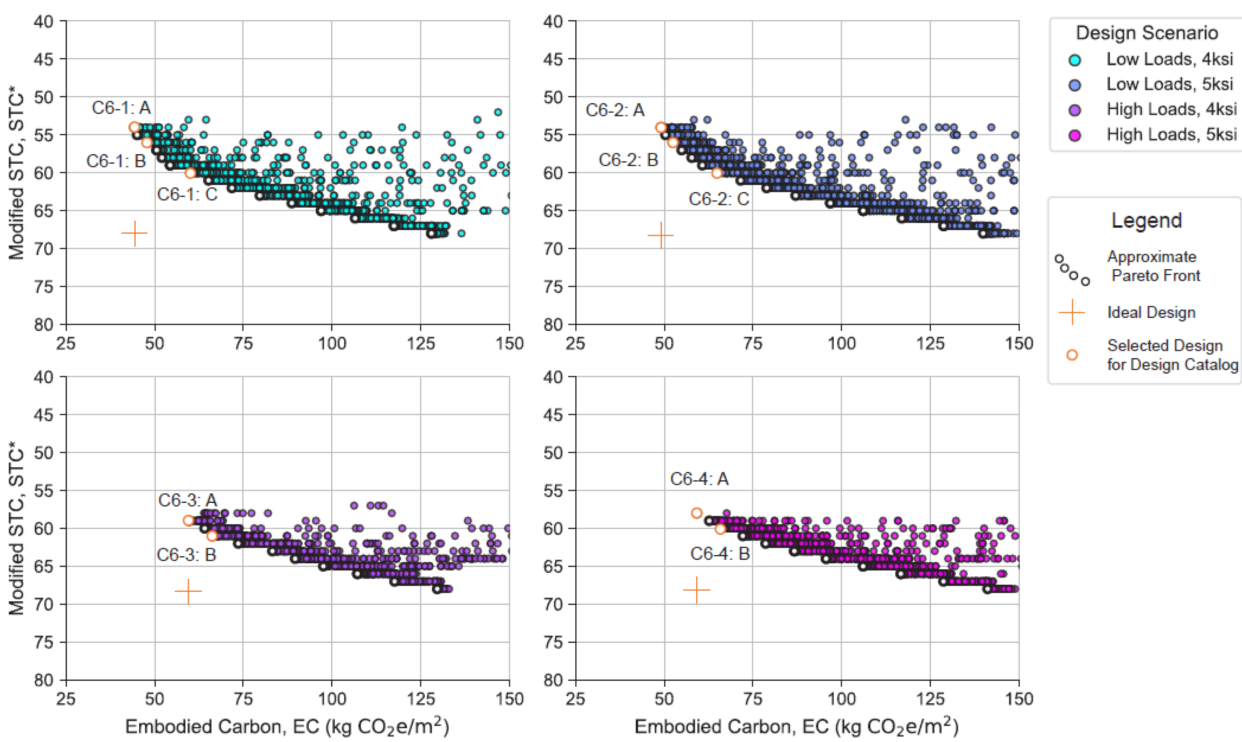

Figure **8-13**: Bi-objective plot showing EC vs. STC* with a span length of 7.5 m.

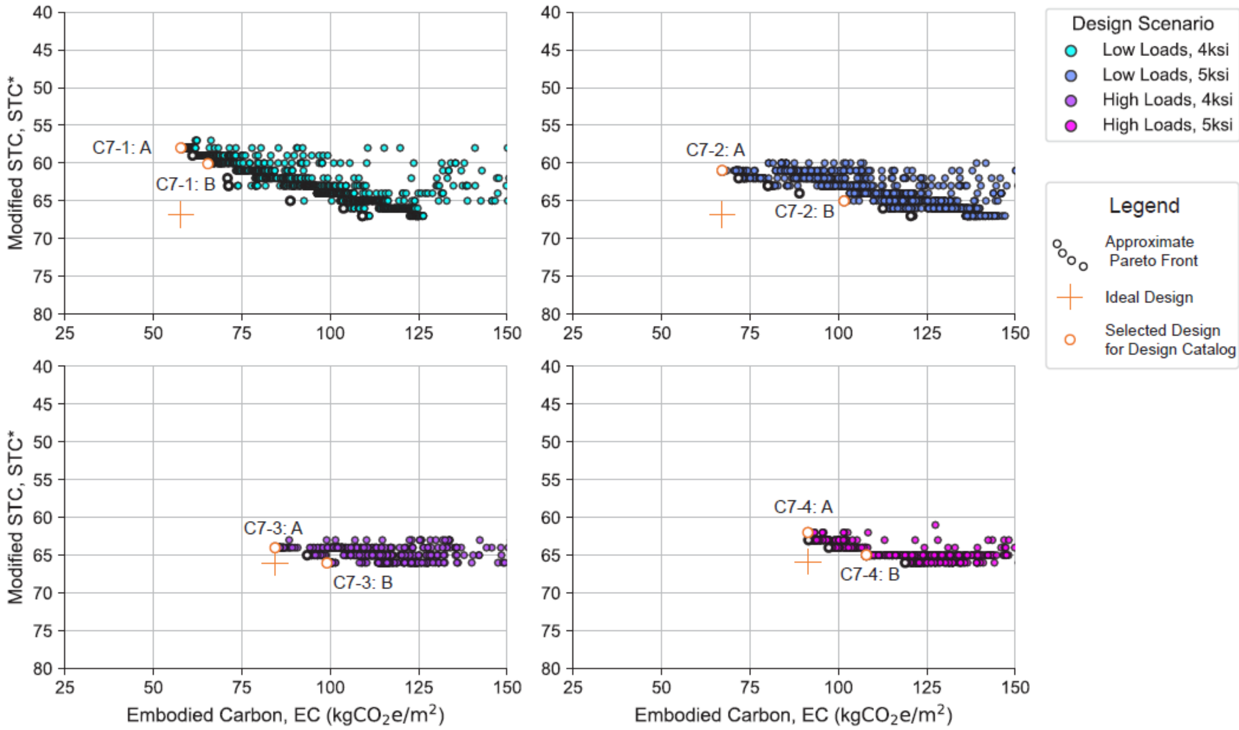

Figure **8-14**: Bi-objective plot showing EC vs. STC* with a span length of 9 m.

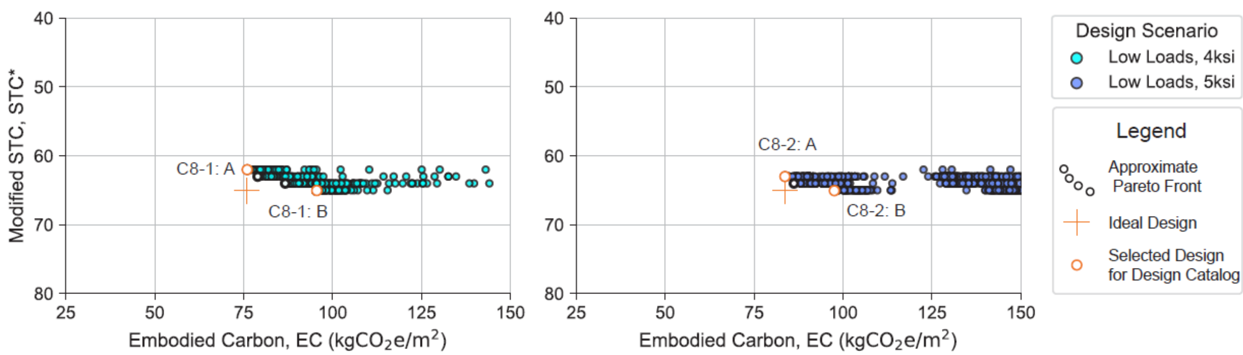

Figure **8-15**: Bi-objective plot showing EC vs. STC* with a span length of 10.5 m.

Several observations can be made when comparing the different bi-objective plots for EC vs STC and EC vs modified STC. First, higher structural loads and longer span lengths limit the number of shaped one-way slabs that are structurally viable. The structural limit states directly limit the amount of EC that can be reduced and restrict the trade-off between air-borne sound insulation and EC. Additionally, the shape of the approximate Pareto fronts differs when employing the modified STC metric in place of the conventional STC metric. Fig. **8-16** more clearly compares the approximate Pareto fronts obtained when STC and STC* were employed. Although it is clear that the approximate Pareto fronts converge for higher EC emissions, the selection of air-borne acoustic insulation metric can meaningfully influence the rating of shaped one-way slabs at lower EC emissions. The comparison of approximate Pareto fronts with a span length of 6 m most clearly shows this relationship.

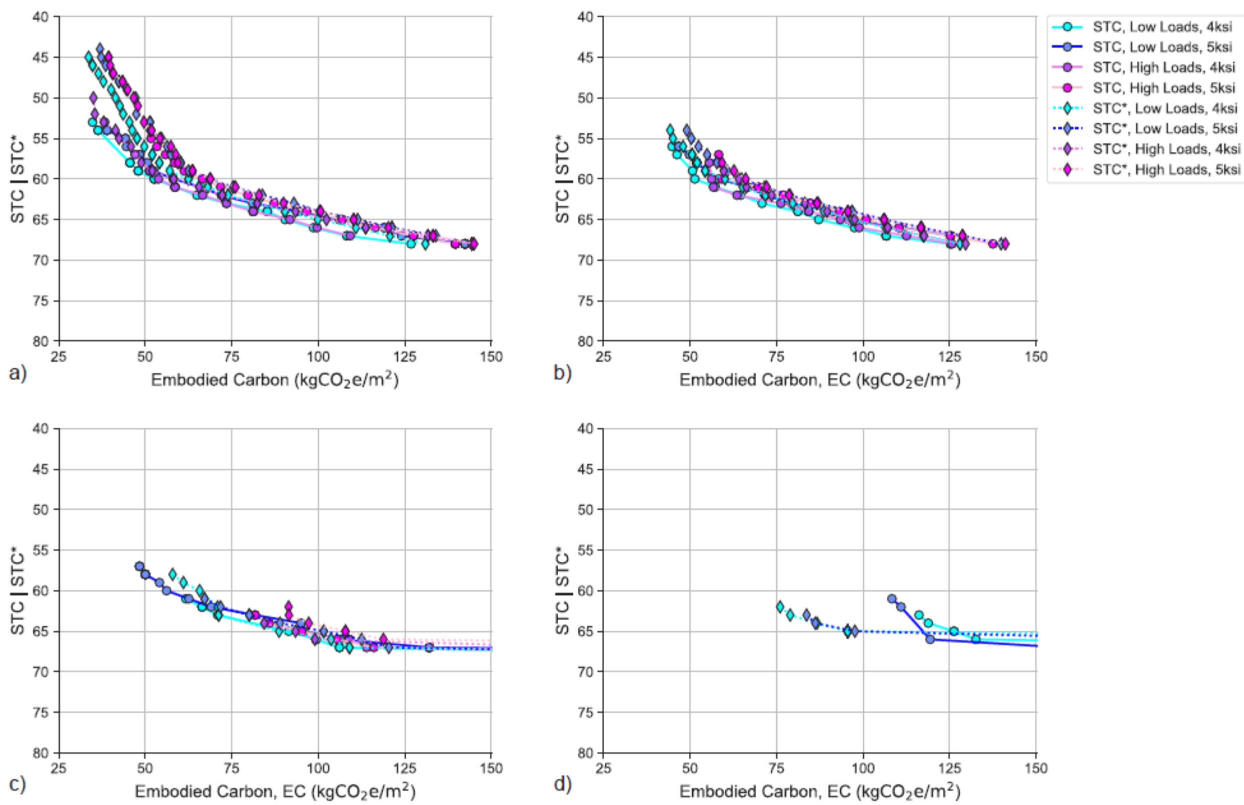

Figure **8-16**: Comparison of the EC vs STC and EC vs STC* approximate Pareto fronts for a) the design scenario with a span length of 6 m, b) the design scenario with a span length of 7.5 m, c) the design scenario with a span length of 9 m, and d) the design scenario with a span length of 10.5 m.

The best performing (non-dominated) shaped slabs labeled in Figs. **8-8** to **8-15** are evaluated for additional design objectives STC / STC* (whichever was not optimized), fire-resistance rating, and walking vibrations. The design scenario, objective performances, and the shaped slab are shown in Figs. **8-17** to **8-24**. These design guides provide an example of how optimized floor components can be selected in the design of low-carbon and high-performing buildings.

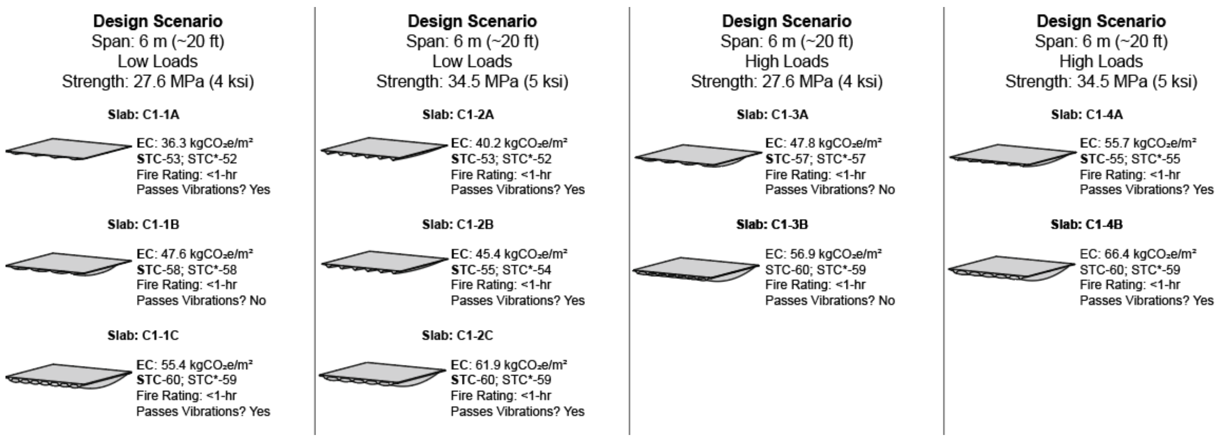

Figure **8-17**: Design guide when optimizing EC and STC for a span length of 6 m.

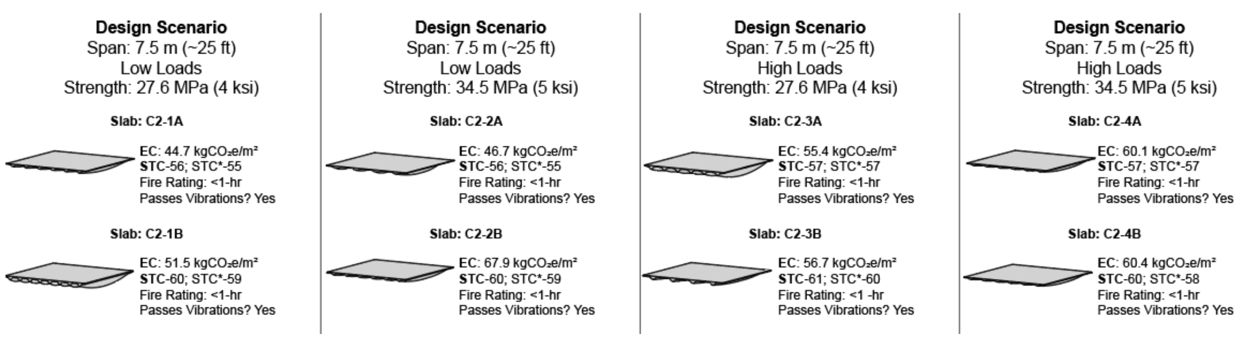

Figure **8-18**: Design guide when optimizing EC and STC for a span length of 7.5 m.

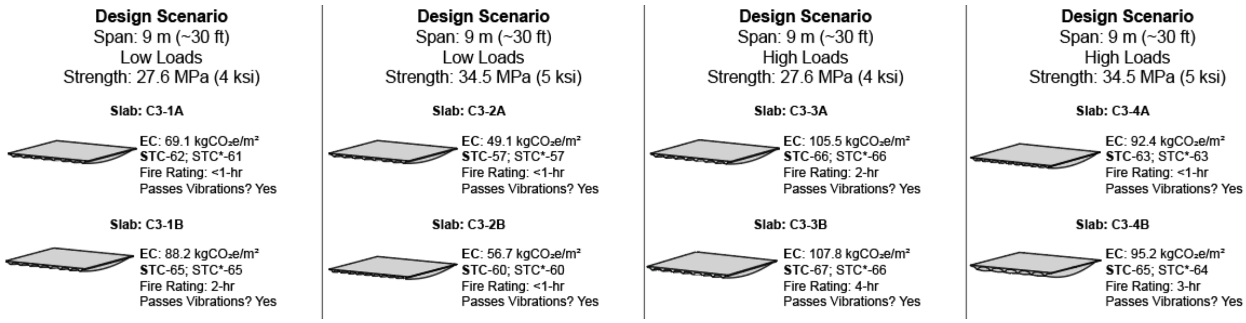

Figure **8-19**: Design guide when optimizing EC and STC for a span length of 9 m.

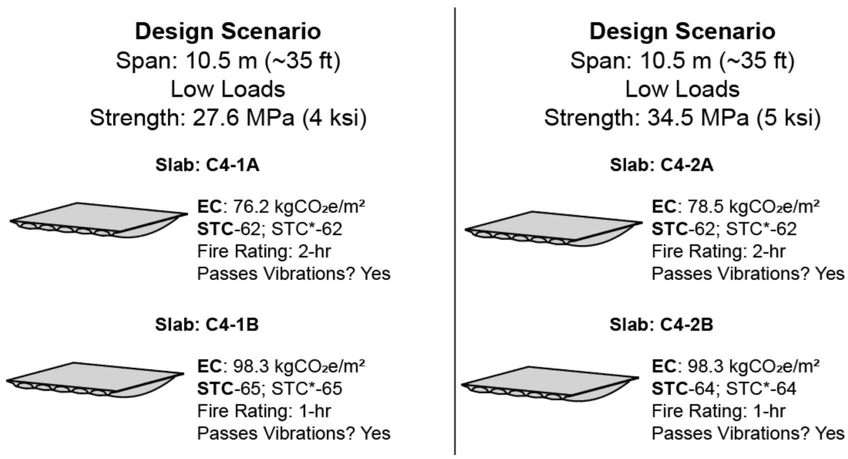

Figure **8-20**: Design guide when optimizing EC and STC for a span length of 10.5 m.

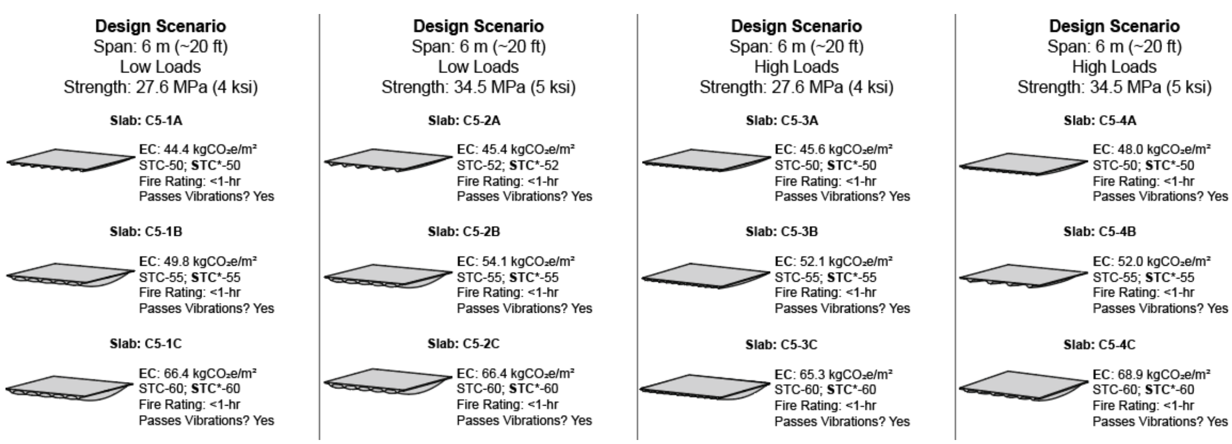

Figure **8-21**: Design guide when optimizing EC and STC* for a span length of 6 m.

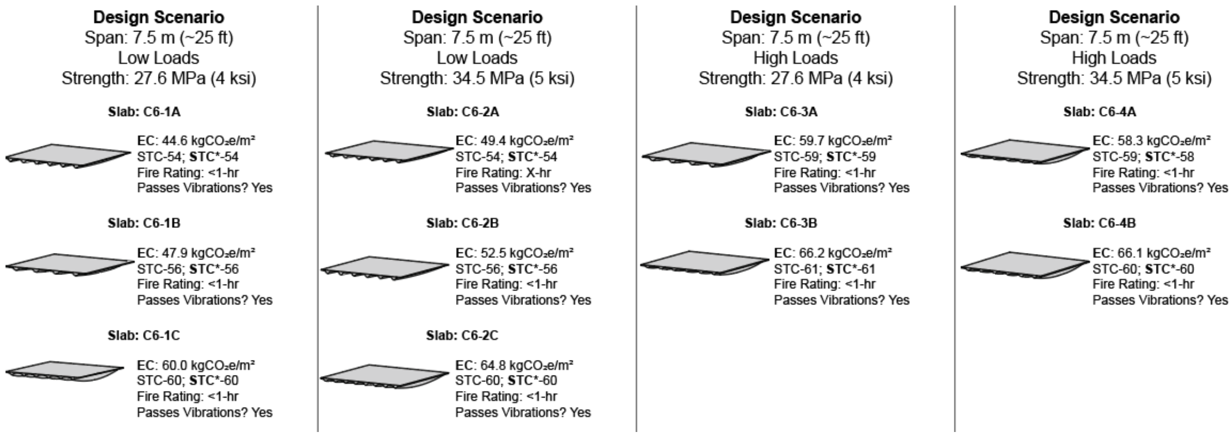

Figure **8-22**: Design guide when optimizing EC and STC* for a span length of 7.5 m.

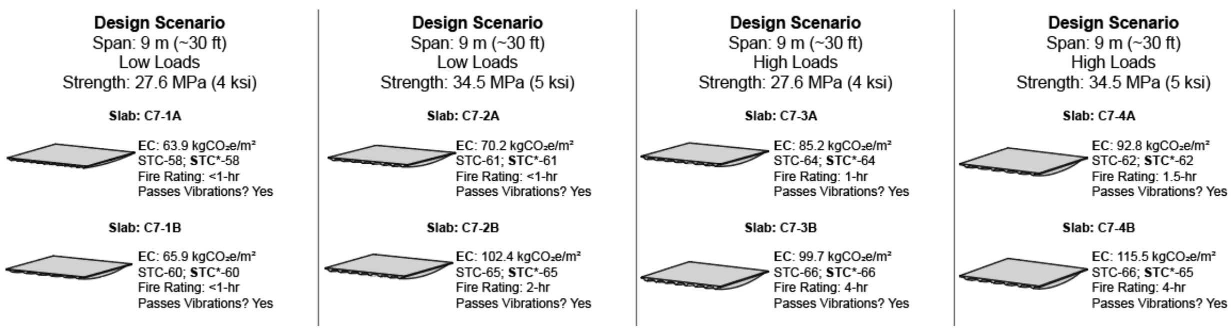

Figure **8-23**: Design guide when optimizing EC and STC* for a span length of 9 m.

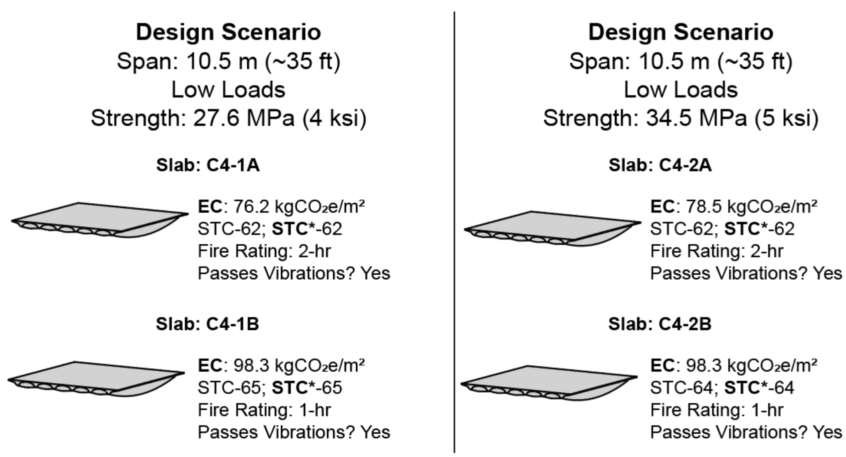

Figure **8-24**: Design guide when optimizing EC and STC* for a span length of 10.5 m.

There are several takeaways when evaluating the non-dominated shaped slabs across the 16 different design scenarios. The first is that low loads and small spans generally equated to thinner floors with low EC, but fair STC ratings. However, the thin top slab resulted in a poor fire resistance rating (below a 1-hr rating). Yet high loads and long spans generally resulted in thick slabs with high EC, better STC ratings, and higher fire-resistance ratings. Another observation is that similar designs appear across many different design scenarios, indicating that some of the forms are high-performing in compared to other forms. A final takeaways is that although shaped slabs can have high performance for many design objectives, these floors are typically characterized by having a very thick top slab and deep ribs, potentially discouraging their implementation in buildings.

8.5 Limitations and opportunities for future studies

The main limitation of this study is that only a shaped one-way slab is evaluated for the methods and metrics derived in this dissertation. Additionally, only EC vs STC and EC vs STC* were considered in the optimization frameworks of this study. Inclusion of fire resistance rating, walking vibrations, and other acoustic transmission metrics in an optimization framework would enable holistic assessment of design trade-offs of shaped concrete components. Furthermore, the creation of design catalogs would enable building practitioners to compare and select high-performing optimized design components. Lastly, putting the performance of shaped optimized concrete components in context to the performance of conventional concrete floor systems, including one-way pan joist floors, would help determine how much better optimized concrete components are compared to existing concrete floor structures.

This chapter points to many future research opportunities. Floor layers added to the top of the bare shaped concrete floors can significantly improve the structure-borne sound insulation performance and could be coupled with the best performing shaped concrete slabs to realize high performing shaped concrete designs. The consideration of the total depth of the floor system should be considered as an additional objective in future studies. Future work could also explore how the implementation of optimized concrete components can have additional EC benefits by reducing the structural deadload in concrete girders, columns, and foundations. A broad future research direction should consider the inclusion of alternative optimization frameworks such as Bayesian Optimization (BO), generative design of shaped slabs (Bucher et al., 2023), and the implementation of machine learning models (Fang et al., 2023a). A specific variation of BO is Diversity-Guided Efficient Multi-objective Bayesian Optimization, which enables a diverse exploration of a design space while efficiently converging to the best performing designs with a limited number of required samples (Lukavocic et al., 2020). The application of this framework would be especially suitable for comprehensive multi-objective studies of optimized concrete floor components. Lastly, the incorporation of the results of a multi-objective study could be incorporated into a design tool to help building engineers and practitioners consider shaped concrete slabs to other conventional and non-traditional concrete systems with the intent of minimizing EC emissions while balancing the performance of other design objectives (Chauhan et al., 2023).

8.6 Conclusion

In conclusion, this chapter demonstrates how the methods and metrics derived in Chs. 6 and 7 can be implemented to improve how multidisciplinary design objectives, specifically acoustic insulation, can be better integrated and considered in design strategies aimed at minimizing the EC emissions of concrete floors. Although this demonstration just scratches the surface, the fact that shaped one-way concrete floors can meaningfully affect both air- and structure-borne sound insulation performance goals through shaping alone, indicates how optimized building components can enhance the performance of a building through the inclusion of secondary design objectives. Lastly, the inclusion of alternative acoustic metrics can meaningfully influence the identification and rating of a shape optimized floor design.

Part IV:

FINAL REMARKS

Chapter 9

Conclusion

In conclusion, this dissertation responds to the urgent need to reduce EC emissions in the built environment by critically evaluating existing concrete floor systems at the building system scale and by developing new methodologies to advance the design of low-carbon, optimized concrete floor components. In Ch. 3, EC equations appropriate for use in early design phases were derived based on the simulated EC and SMQ results when varying geometric and structural design parameters for ten concrete floor systems. In Ch. 4, a subset of the concrete floor systems was further evaluated for prescribed fire-resistance, air-borne sound insulation, and walking vibrations to evaluate how various secondary design requirements influenced the EC emissions of concrete floor systems. The findings of this study informed the creation of six design charts, each corresponding to a unique building case study, to better inform designers on the selection of a low-carbon concrete floor system while balancing multiple design goals.

At the component scale, Ch. 5 detailed the fabrication and experimental testing of four quarter-scaled shaped concrete slabs, which were used to validate a numerical FEA model for each slab specimen. Ch. 6 expanded on this work to assess the impact sound insulation performance of full-scale shaped concrete slabs. Because of the computational cost associated with simulating the full frequency range required to quantify IIC using existing acoustic methods, a hybrid air-hemisphere and radiated sound power method was defined and validated to adequately estimate the impact sound insulation of both flat and shaped concrete floors while minimizing computational resources. In Ch. 7, alternative acoustic transmission metrics were proposed to overcome the functional limitations of STC and IIC, especially when employed in design space exploration and optimization studies. Ch. 8 combines the IIC-Like method from Ch. 6, employs the alternative acoustic transmission metrics derived in Ch. 7, and compares the optimized shaped concrete slabs to the functionally equivalent conventional floor systems studied in Chs. 3 and 4. Because significant concrete material is needed to achieve the minimum impact sound insulation rating defined in building code, the shaped concrete slabs are optimized for air-borne sound insulation and EC to generate a design catalog of shaped concrete slabs optimized at different span lengths and structural parameters.

The expanded design knowledge, methods, and metrics developed in this dissertation are relevant to different audiences. The comprehensive evaluation of EC emissions for concrete floor systems at the building system scale is relevant to building practitioners, especially architects, structural engineers, and sustainability consultants. The derived EC equations in Ch. 3 and the design charts when considering multiple design objectives in Ch. 4 are particularly useful for practitioners comparing different floor systems in early-stage design. Acoustic practitioners and research communities can glean from the dynamic response results of shaped concrete slabs in Ch. 5, apply the IIC-Like method described in Ch. 6, and implement the alternative acoustic transmission metrics to better understand the sound insulation performance of non-traditional building elements. Lastly, building practitioners and acousticians can observe how to apply the new methods and metrics when assessing floors as demonstrated in Ch. 8.

9.1. Summary of contributions

This dissertation details six unique studies at the building system scale and component scale to help inform building designers on existing concrete floor systems that can be immediately implemented to curb EC emissions attributed to concrete structures in buildings and determine shaped concrete forms that improve upon conventional concrete floor systems while minimizing EC and improving acoustic insulation. The research questions, findings, and contributions from each chapter are summarized in Table **9-1**.

Table **9-1**: Chapter-by-chapter research questions, findings, and contributions.

Dissertation Chapter	Research Question(s)	Research Finding(s)	Contribution(s)
Ch. 3	What are the EC emissions of concrete floor systems when varying structural design parameters, such as span length, concrete compressive strength,	When assessing the EC of 41,328 / 27,552 unique design scenarios for ten different RC / PT floor systems, the composite EC emissions ranged from 50 $kgCO_2e/m^2$ at 3 m to nearly 400 $kgCO_2e/m^2$ at 15 m. Material-efficient concrete floor systems	A comprehensive assessment of ten concrete floor systems showed that the system type and the structural parameters influenced the range of EC emissions. The span length of the floor system had the largest influence on EC, regardless of the

Dissertation Chapter	Research Question(s)	Research Finding(s)	Contribution(s)
	applied loads, and deflection limits? How can building designers identify the most material-efficient (low-carbon) concrete floor system at the early design stages given the breadth of possible design scenarios, variety of concrete floor systems, and the uncertainty of carbon emissions associated with different concrete mixtures?	had smaller EC distributions while less efficient systems had larger EC distributions. Univariate polynomial regression models trained to the composite EC trendlines were found to obtain an adequate estimate of EC at the conceptual design phase (R^2 above 0.99 for all but one system). Yet a more robust model was needed to accurately estimate EC in the schematic design phase. Multivariate regression models were shown to better account for varying structural parameters, resulting in an improved EC estimate (R^2 above 0.95 for all but one system).	type of floor system. Yet varying structural parameters can also meaningfully influence EC. EC equations were derived from the univariate and multivariate polynomial regression models to simplify the estimation of EC for different concrete floor systems with the equations tailored to the design knowledge known in the conceptual and schematic design phases. The equations were deployed in a web application / design tool to better inform designers in the selection of the most material-efficient (low carbon) concrete floor system.
Ch. 4	What concrete floor system(s) is the most material-efficient (lowest EC emissions) when considering both structural performance and secondary design requirements for floors, including fire-resistance, air-borne sound insulation, and walking vibrations?	RC one-way slabs and RC two-way slabs with beams were preferred at short span while RC waffle slabs and PT voided plates were preferred at long spans, regardless of the design requirements. However, when code minimum acoustic performance was desired, no concrete floor system was sufficient at short span lengths without additional material layers.	Six design charts representative of six unique building design case studies were created to better inform designers on what concrete floor system(s) is the most material-efficient / has the lowest EC emissions when considering various structural, fire-resistance, acoustical, and vibration performance requirements.
Ch. 5	What is the experimentally-obtained dynamic response of fabricated, quarter-scaled shaped ribbed concrete slabs, and can these results be used to tune numerical models for each slab?	The mode shapes, eigenfrequencies, and mobilities were obtained for the four quarter-scaled shaped slabs. To tune the numerical models, the lowest percent error was found to be 6.75% with a modulus of elasticity of 32,064 MPa and a Poisson's ratio of 0.18.	The dynamic response for each of the four shaped slabs was determined through a modal hammer test. The tuned numerical model can be used to estimate the dynamic response of shaped concrete slab forms that were not experimentally tested.
Ch. 6	How can a numerical method adequately estimate the full	Conventional numerical methods (i.e., the air-hemisphere method) require very large computational	The IIC-Like method was developed and validated to simulate the full frequency impact

Dissertation Chapter	Research Question(s)	Research Finding(s)	Contribution(s)
	frequency (including both low and high frequencies) impact sound insulation performance of non-traditional concrete slabs while reducing the required computational resources?	models (e.g., 80 million finite elements) to simulate both low and high frequency impact sound. However, by simulating only a subset of frequencies (the 100 Hz, 125 Hz, 160 Hz, and 200 Hz OTO bands), the radiation efficiency of a concrete slab can be calculated to estimate the radiated sound power at high frequencies with significantly smaller models (e.g., 100 thousand finite elements).	sound insulation performance of concrete slabs. Unlike existing methods, the IIC-Like method reduces the granularity of the mesh by simulating a subset of frequencies above coincidence to effectively determine the radiation efficiency. The IIC-Like method can thus obtain an impact sound rating while using less computational resources.
Ch. 7	How can modifications to the existing acoustic transmission metrics correct the functional limitations of the metrics to improve the acoustic rating of floors in computational design frameworks?	Modifying the functional limitations of STC and IIC (STC* and IIC*) influenced the scalar rating by a range of -1 to +4 when compared to the conventional STC and IIC ratings. The categorical method (CM) and the composite transmission function (CTF) were defined to provide designers with more or less scalar values depending on the fidelity of acoustic information required and for various applications in computational frameworks.	Three alternative acoustic transmission metrics were proposed: STC* and IIC*, the CM, and the CTF. Different strategies to employ the three proposed metrics in computational frameworks were provided. These metrics provide a fairer acoustic rating for concrete floors in computational frameworks by removing functional limitations that can inflate or hinder the acoustic rating of a building element.
Ch. 8	How does the implementation of a computationally-efficient method to simulate impact sound insulation and the incorporation of modified acoustic transmission metrics influence the selection of a low-carbon concrete slab, and how do the best performing shaped concrete slabs compare to an equivalent conventional system?	The comprehensive assessment of shaped concrete floor slabs found that minimum building code requirements for impact sound insulation could not be satisfied without additional material layers, however, high performing designs for minimizing EC and maximizing air-borne acoustic insulation were identified. The best performing shaped slabs had an EC savings of 51% with an increased rating of +5 compared to conventional flat plates, with ~33% EC savings when compared to a structurally-equivalent conventional one-way slab.	An evaluation of both air- and structure-borne sound insulation revealed that shaping a one-way concrete floor system can improve acoustic performance while minimizing concrete material consumption and corresponding EC emissions. Shaped concrete slabs were found to outperform conventional concrete systems designed for the scenario; yet future studies are needed to assess how the inclusion of additional design objectives (e.g., fire-resistance rating) further influence these results.

9.2. Summary of limitations

9.2.1 Limitations of the studies at the building system scale

While this dissertation realizes impactful contributions at the building system and component scale, this work is not without limitations. First, only a cradle-to-gate (A1-A3 phases) life cycle assessment (LCA) was considered in the sustainable assessment (EC emissions) of the conventional concrete floor systems in Chs. 3 and 4. The concrete floors considered in these studies did not include the structural columns and foundations, potentially restricting the full knowledge of EC savings when comparing different floor systems. Also, the conventional concrete floor systems were designed as square bays, potentially missing opportunities for further EC reduction when designing rectilinear and non-traditional column grid layouts.

A specific limitation of the work in Ch. 3 is that alternative statistical models, including Bayesian regression models, may be able to consider the EC uncertainty more adequately in the structural design scenario in addition to the GWP uncertainty of concrete mixtures. Another source of uncertainty includes the life cycle inventory resources used by the U.S. EPDs in App. A which informed the GWP values used in the study (Teng et al., 2023; Warrier et al., 2024). Additionally, the polynomial regression models were all second-order models with the intent to limit the number of interaction terms needed to adequately estimate the EC of a concrete floor system in the early design phases; yet higher order models may better fit the simulated data (especially for the RC two-way waffle slab). A clear limitation in Ch. 4 is that only six building use case studies were considered, potentially limiting the utility of the design charts. Furthermore, impact sound insulation and vibrations caused by rhythmic excitations were not included in the study. Another overarching limitation of the studies at the building system scale is that no direct comparison to other floor systems (i.e., steel-composite floors and mass timber floors) was made.

9.2.2 Limitations of the studies at the component scale

The largest limitation of the studies at the component scale is that only shaped one-way concrete slabs are considered; however, a parametric model based on a different floor system (e.g., waffle slab) could reveal more design trade-offs and EC savings. As was the case for the concrete floor systems at the building system scale, only a cradle-to-gate LCA was considered. Similarly, the geometry of the shaped slabs was restricted to four different span lengths for a square bay, potentially limiting additional EC benefits that shaped concrete slabs have when designed for non-traditional and cantilever floor plans.

The experimental study in Ch. 5 could have used (or compared) alternative test methods to the tapping hammer method, such as a shaker or a tapping machine test, to ascertain (and confirm) the dynamic performance of a concrete floor. Additionally, testing of a quarter-scaled flat concrete plate and an equivalent rectilinear one-way slab could have more directly put the dynamic performance of the shaped slabs into context of conventional concrete floor systems. The study was also limited to evaluating quarter-scaled specimens due to the fabrication and transportation difficulties corresponding to full-scale slabs. Evaluation of the impact sound insulation performance of full-scale concrete slabs would have also helped validate the numerical results from the IIC-Like method presented in Ch. 6. Another important limitation of Ch. 6 is that the computational resource savings was put into context of the number of elements and nodes of the air-hemisphere, with the computational time using the air-hemisphere method estimated based on the simulation time when using the IIC-Like method. This is largely due to FEM licensing restrictions and computational resource limitations to fully simulate the full frequency range of IIC-Like.

In Ch. 7, the alternative acoustic transmission metrics were proposed based on the functional limitations well known in the building acoustics field; however, subjective testing could confirm if the ratings obtained from these new metrics are perceived differently than the existing acoustic transmission metrics. An important limitation in Chs. 7 and 8 is that not all alternative acoustic transmission metrics were demonstrated in an optimization framework. Furthermore, the current application of the alternative sound transmission metrics is limited to early-stage design exploration and optimization frameworks until subjective testing can study how well the proposed acoustic metrics compare to the perception of acoustic insulation. In Ch. 8, a multi-objective optimization framework could expand on the design insight on the relationship between maximizing both air- and structure-borne sound insulation and minimizing EC. Lastly, the design catalog of shaped concrete slabs is limited to the 16 design scenarios considered and could be improved by quantifying additional design objectives and performance goals.

9.3. Future research directions

9.3.1 Future research at the building system scale

This dissertation facilitates many future research opportunities at both the building system scale and at the component scale. At the building system scale, future research directions related to the assessment of EC emissions include:

- The inclusion of additional LCA phases beyond the A1 to A3 phases to better quantify whole life cycle EC emissions of concrete floor systems. While most of the EC emissions for concrete structures is attributed to the A1 to A3 LCA phases, the assessment of additional LCA phases (especially the A4 and A5 phases) would further reveal what conventional concrete floor systems are the most sustainable (Felicioni et al., 2023).
- The system boundary of the LCA can be expanded to include the structural columns and foundations to better assess EC emission savings when comparing different floor systems.
- The establishment of EC benchmarks for various structural systems and elements based on the design requirements (i.e., structural design parameters) could significantly encourage architects and structural engineers to design low-carbon structural solutions. Instead of setting a static EC benchmark, benchmarking a range of EC emissions could guide policymakers at the local and national levels (Belizario-Silva et al., 2023).
- The inclusion of whole-building LCA frameworks applied in early-stage design frameworks can also improve EC assessment (McCord et al., 2024). On a larger scale, the assessment of building material stock can provide useful design insight on reducing EC emissions (Sory, 2023).
- The consideration of other LCA mid-points such as freshwater consumption and acidification (see App. A for more information) could reveal more trade-offs when considering sustainable objectives in building design.

Related to the structural and secondary design considerations, future research directions include:

- A square column grid configuration was specified for all the concrete floor systems. However, rectilinear bays and non-traditional column grid layouts should be further assessed to better inform when certain concrete floor systems are preferred when minimizing EC.
- The structural analysis implemented was a modified direct design method to evenly design and fairly compare the structural performance of RC and PT floor systems; however, alternate concrete floor design methods (e.g., the equivalent frame method) and alternate concrete design codes (e.g., Eurocode 2, 2008) could result in different EC results and should be explored in future work.
- Performance-based fire-resistance and other air-borne acoustic transmission models could result in slightly different performance ratings when compared to the results obtained in Ch. 4. Additional floor vibration considerations, like rhythmic excitations, should be further studied when implementing a low-carbon concrete floor system (Gaspar et al., 2016).
- The consideration of impact sound insulation and thermal insulation performance goals, especially when material layers are applied on bare concrete floors (Arenas & Sepulveda, 2022), could influence the selection of a low-carbon concrete system when balancing many design objectives.

Future research directions on the broad topic of design tools and guidance in the identification and selection of a low-carbon concrete floor system include:

- Employment of the polynomial regression models to alternative structural systems and material types could directly aid building practitioners in identifying the structural system with the lowest EC despite the breadth of possible design scenarios.
- The trained polynomial regression models in Ch. 3 could be improved upon to include the EC from the concrete columns and footings, enabling designers the ability to quickly estimate the EC for the entire concrete structural system.
- The design charts in Ch. 4 could be expanded to other structural systems and materials, like Leonard’s (2023) work with mass timber floor structures. The design charts can also be integrated

into an interactive design tool to enable building designers to parametrically evaluate how different design parameters and secondary design objectives influence EC.

- Future tool development should incorporate additional LCA phases and secondary objectives to provide high-resolution EC estimates for different structural systems and enable comprehensive comparisons across various structural systems.

9.3.2 Future research at the concrete component scale

There are many future research directions for further improving and implementing optimized concrete components in the built environment. Opportunities to explore different types of custom structural system is an exciting research field, including:

- The exploration and optimization of shaped two-way waffle slabs and topology optimized PT voided plates could realize highly material-efficient floor forms.
- The parametric model of shaped one-way concrete slabs could be improved. Inclusion of voided areas and post-tensioning in shaped slabs could provide opportunities for further EC savings than what was found in this dissertation.
- The design for disassembly of custom concrete structures could help realize significant material and EC emission savings (Salama, 2017). The recycling and reuse of concrete elements in buildings is a burgeoning field (Byers et al., 2023; Devènes et al., 2024; DoGursel et al., 2023; Küpfer et al., 2024; Luthin et al., 2023). The reuse of concrete elements can be implemented in the design of optimized concrete components and even be used to improve the performance of structural systems composed of other materials (Estrella et al., 2024).
- Related, functionally-graded concrete components as a low-carbon solution can be coupled with shape optimization strategies to determine highly material-efficient and low-carbon systems (Ma et al., 2023; Tang et al., 2016; Torelli et al., 2020; Win et al., 2022).

- Lastly, hybrid structural systems, including the combination of optimized concrete floor forms designed with bio-based construction materials, and the integration of acoustic metamaterials have exciting implications in the built environment (Fang et al., 2024; Moutan et al., 2024).

Another broad research direction is the experimentation of shaped concrete slabs, specifically:

- Experimental testing for structural, fire-resistance, acoustical, and vibrations should be performed on shaped concrete slabs to validate numerical findings.
- Structural testing of full-scaled shaped slabs can be compared to the four quarter-scaled slabs presented in Ch. 5 to evaluate if structural size effects are equivalent regardless of the floor form.
- Full-scale shaped slabs should be validated for acoustic insulation in research facilities following ASTM standards (i.e., ASTM E90, ASTM E492) to validate the results in this dissertation.
- Additional experiments, including fire-resistance and vibration tests can be performed to evaluate the performance of shaped concrete floors to accelerate their application in the built environment.

Related to the sound transmission methods presented in this dissertation, next steps include:

- The IIC-Like method described in Ch. 6 can be applied to other concrete structural systems, including other custom concrete components. For example, the IIC-Like method can be implemented to determine the full frequency impact sound performance of optimized concrete funicular floors when assuming simple boundary conditions, as was demonstrated in the evaluation of radiated sound power by Mendez Echenagucia et al. (2016).
- The alternative acoustic transmission metrics proposed in Ch. 7 could likewise be applied to other structural elements (i.e., both floors and walls) composed of different construction materials.
- Future studies should further assess how the inclusion of the proposed acoustic transmission metrics can influence the selection and optimization of other structural systems outside of concrete floors.
- Subjective studies should be conducted to further understand the perceived performance of building elements rated by the alternative acoustic transmission metrics.

More research is needed to understand the multi-objective design trade-offs of custom concrete slabs, especially in early-stage design and optimization frameworks. Specifically, future work includes:

- The consideration of additional building and design objectives such as, cost, thermal insulation, and construction-related objectives in multi-objective optimization frameworks of optimized concrete components can deepen the understanding of interdisciplinary design trade-offs.
- Ranking the importance of different design objectives when minimizing the EC emissions of optimized concrete components. As was implied in the findings of Ch. 8, differing design scenarios would likely influence the order and magnitude of important design objectives.
- The utilization of other multidisciplinary optimization frameworks including Bayesian Optimization (BO) can improve the efficiency of the optimization method implemented in Ch. 8. Furthermore, a BO framework can act as a surrogate model and be employed in multi-disciplinary optimization problems (Lukavocic et al., 2020).

9.4. La fine

Driven by the need to reduce carbon emissions in the built environment, scientific researchers and industry practitioners will continue to rapidly explore strategies to reduce the EC emissions in structural systems. Although structural systems composed of mass timber and other bio-based construction materials provide exciting opportunities to lower carbon emissions, concrete floor systems currently and will continue to have design advantages in specific building contexts, especially when considering the additional design considerations and consequent performance goals that floors participate in. With advancing construction technologies and practices, and innovative concrete material developments, the concrete industry is on the cusp of a design renaissance where building engineers and architects will be able to explore more unique concrete floor forms, giving way to a new era of efficiency in the design of concrete structures.

This dissertation elucidates an immediate pathway to curb EC emissions of existing conventional concrete floor systems in the present and developed methods to better assess the acoustic insulation of custom concrete floors to aid their development and implementation in buildings in the near-term future.

As the building sector progresses towards net-zero carbon emission structural systems, it will be paramount to also consider the performance of additional design objectives to ensure that "sustainable buildings" are indeed sustainable for both the environment and the people using it.

References

Aalami, B. O., & Jurgens, J. D. (2003). Guidelines for the Design of Post-Tensioned Floors. *Concrete International*, 77–83.

Abbaszadeh, S., Zagreus, L., Lehrer, D., & Huizenga, C. (2006). Occupant satisfaction with indoor environmental quality in green buildings. In *HB 2006 - Healthy Buildings: Creating a Healthy Indoor Environment for People, Proceedings*, 3, 365–370, Lisbon, Portugal.

ACI 318 Committee. (2019). Building code requirements for structural concrete (ACI 318-19) and commentary. American Concrete Institute.

Agirbas, A. (2021). Multi-objective building design optimisation using acoustics and daylighting. *Indoor and Built Environment*, *31*(3), 853-867. doi: 10.1177/1420326x211040100.

Ahmad Zawawi, M., Kebangsaan Malaysia, U., Kamaruzzaman, S. N., Razali, A., & Ahmad Zawawi, E. M. (2018). Determining Significant Parameters on Health and Well-Being of Building Occupants Towards Re-Engineered Inclusive Environment. *Journal of Building Performance*, *9*(1).

Ahmed, M. S., & Mohammad, F. A. (2014). Theoretical Modal Analysis of Freely and Simply Supported RC Slabs. *International Journal of Mechanical, Aerospace, Industrial, Mechatronic and Manufacturing Engineering*, *8*(12), 2042–2046.

Ahmed, M. S., & Mohammad, F. A. (2015). Experimental modal analysis of reinforced concrete square slabs. *International Journal of Mechanical, Aerospace, Industrial, Mechatronic and Manufacturing Engineering*, *9*(3), 1–5.

Aït-Mokhtar, A., Belarbi, R., Benboudjema, F., Burlion, N., Capra, B., Carcassès, M., Colliat, J. B., Cussigh, F., Deby, F., Jacquemot, F., De Larrard, T., Lataste, J. F., Le Bescop, P., Pierre, M., Poyet, S., Rougeau, P., Rougelot, T., Sellier, A., Séménadisse, J., Torrenti, J. M., & Yanez-

Godoy, H. (2013). Experimental investigation of the variability of concrete durability properties. *Cement and Concrete Research*, *45*(1), 21–36. doi: 10.1016/j.cemconres.2012.11.002.

Ajayi, S. O., Oyedele, L. O., Jaiyeoba, B., Kadiri, K., & David, S. A. (2016). Are sustainable buildings healthy? An investigation of lifecycle relationship between building sustainability and its environmental health impacts. *World Journal of Science, Technology and Sustainable Development*, *13*(3), 190–204. doi: 10.1108/wjstsd-01-2016-0015.

Akbarnezhad, A., & Xiao, J. (2017). Estimation and minimization of embodied carbon of buildings: A review. *Buildings*, *7*(1), 1–24. doi: 10.3390/buildings7010005.

Allemang, R. J. (2003). The Modal Assurance Criterion - Twenty Years of Use and Abuse. *Sound and Vibration*, *37*(8), 14–23.

Alonso, A., Patricio, J., Suárez, R., & Escandón, R. (2020). Acoustical retrofit of existing residential buildings: Requirements and recommendations for sound insulation between dwellings in Europe and other countries worldwide. *Building and Environment*, *174*, 106771. doi: 10.1016/j.buildenv.2020.106771.

Althoey, F., Ansari, W. S., Sufian, M., & Deifalla, A. F. (2023). Advancements in low-carbon concrete as a construction material for the sustainable built environment. *Developments in the Built Environment*, *16*, 100284. doi: 10.1016/j.dibe.2023.100284.

American Society of Civil Engineers. (2016). *ASCE 7-16*.

American Society for Testing and Materials, Environmental Product Declarations. ASTM International. First accessed on February 13th, 2023. Retrieved from: https://www.astm.org/products-services/certification/environmental-product-declarations/epd-pcr.html.

American Society for Testing and Materials (ASTM). (2006). *ASTM Standard E989-06: Standard Classification for Determination of Impact Insulation Class (IIC)*. West Conshohocken, PA: ASTM International.

American Society for Testing and Materials (ASTM). (2009). *ASTM Standard E90-09: Standard Test Method for Laboratory Measurement of Airborne Sound Transmission Loss of Building Partitions and Elements*. West Conshohocken, PA: ASTM International.

American Society for Testing and Materials (ASTM). (2016). *ASTM Standard E413-16: Classification for Rating Sound Insulation*. West Conshohocken, PA: ASTM International.

American Society for Testing and Materials (ASTM). (2020). *ASTM Standard E3222-20a: Standard Classification for Determination of High-Frequency Impact Noise Ratings*. West Conshohocken, PA: ASTM International.

American Society for Testing and Materials (ASTM). (2021a). *ASTM Standard E3207-21: Standard Classification for Determination of Low-Frequency Impact Noise Ratings*. West Conshohocken, PA: ASTM International.

American Society for Testing and Materials (ASTM). (2021b). *ASTM Standard C39: Standard Test Method for Compressive Strength of Cylindrical Concrete Specimens*. West Conshohocken, PA: ASTM International.

American Society for Testing and Materials (ASTM). (2022). *ASTM Standard E492-22: Standard Test Method for Laboratory Measurement of Impact Sound Transmission Through Floor-Ceiling Assemblies Using the Tapping Machine*. West Conshohocken, PA: ASTM International.

Andargie, M. S., Touchie, M., O'Brien, W., & Müller-Trapet, M. (2023). A field study of the relationship between sound insulation and noise annoyance, activity disturbance and wellbeing in multi-unit residences. *Applied Acoustics*, *206*, 109291. doi: 10.1016/j.apacoust.2023.109291.

Anderson, J. (2023). *Reducing Embodied Carbon in the Built Environment: The Role of Environmental Product Declarations*. Doctoral dissertation, The Open University.

Anderson, J. & Moncaster A. (2020). Embodied carbon of concrete in buildings, Part 1: analysis of published EPD. *Buildings and Cities*, 1(1), 198–217. doi: 10.5334/bc.59.

Anderson, J., & Moncaster, A. (2021). Embodied carbon, embodied energy and renewable energy: A review of Environmental Product Declarations. In *Proceedings of the Institution of Civil Engineers: Structures and Buildings*, 1–12. doi: 10.1680/jstbu.21.00160.

Aouf, R. S. (2019). Plastic bubbles incorporated into high-rise to reduce concrete usage by 35 per cent. De Zeen. Available at: https://www.dezeen.com/2019/11/23/reduction-concrete-plastic-bubbles-enables-cobiax/.

Arehart, J. H., Pomponi, F., D'Amico, B., & Srubar III, W. V. (2022). Structural material demand and associated embodied carbon emissions of the United States building stock: 2020–2100. *Resources, Conservation and Recycling*, *186*, 106583. doi: 10.1016/j.resconrec.2022.106583.

Arenas, J. P., & Sepulveda, L. F. (2022). Impact sound insulation of a lightweight laminate floor resting on a thin underlayment material above a concrete slab. *Journal of Building Engineering*, 45, 103537. doi: 10.1016/j.jobe.2021.103537.

Asakura, T., Toyoda, M., & Miyajima, T. (2018). Numerical and experimental investigation on structure-borne sound transmission in multilayered concrete structures. *Journal of Sound and Vibration*, *413*, 1–25. doi: 10.1016/j.jsv.2017.09.028.

Asdrubali, F., Baldassarri, C., & Fthenakis, V. (2013). Life cycle analysis in the construction sector: Guiding the optimization of conventional Italian buildings. *Energy and Buildings*, *64*, 73–89. doi: 10.1016/j.enbuild.2013.04.018.

Attia, S., Garat, S., & Cools, M. (2019). Development and validation of a survey for well-being and interaction assessment by occupants in office buildings with adaptive facades. *Building and Environment*, *157*, 268–276. doi: 10.1016/j.buildenv.2019.04.054.

Attia, S., Gratia, E., De Herde, A., & Hensen, J. L. M. (2012). Simulation-based decision support tool for early stages of zero-energy building design. *Energy and Buildings*, *49*, 2–15. doi: 10.1016/j.enbuild.2012.01.028.

Ba, G., Miao, J., Zhang, W., & Liu, J. (2019). Influence of reinforcement corrosion on fire performance of reinforced concrete beams. *Construction and Building Materials*, *213*, 738–747. doi: 10.1016/j.conbuildmat.2019.04.065.

Babisch, W., Pershagen, G., Selander, J., Houthuijs, D., Breugelmans, O., Cadum, E., Vigna-Taglianti, F., Katsouyanni, K., Haralabidis, A. S., Dimakopoulou, K., Sourtzi, P., Floud, S., & Hansell, A. L. (2013). Noise annoyance - A modifier of the association between noise level and cardiovascular health? *Science of the Total Environment*, *452–453*, 50–57. doi: 10.1016/j.scitotenv.2013.02.034.

Babrauskas, V., & Williamson, R. B. (1978). The historical basis of fire resistance testing—Part I. *Fire Technology*, 14, 184-194.

Badiger, N. S. & Malipatil K. M. (2014). Parametric study on reinforced concrete beam using ANSYS. *Civil and Environmental Research*, 6(8), 88-94.

Balling, R. (1999). Design by shopping: A new paradigm. In *Proceedings of the Third World Congress of Structural and Multidisciplinary Optimization (WCSMO-3)*, 1, 295-297.

Barcelo, L., Kline, J., Walenta, G., & Gartner, E. (2014). Cement and carbon emissions. *Materials and Structures/Materiaux et Constructions*, *47*(6), 1055–1065. doi: 10.1617/s11527-013-0114-5.

Belizario-Silva, F., Reis, D. C., Carvalho, M., & John, V. M. (2024). Material intensity and embodied CO2 benchmark for reinforced concrete structures in Brazil. *Journal of Building Engineering*, *82*, 108234. doi: 10.1016/j.jobe.2023.108234.

Beranek, L. L. (1959). The Forty-Fifth Thomas Hawksley Lecture: The Transmission and Radiation of Acoustic Waves by Structures. *Proceedings of the Institution of Mechanical Engineers*, *173*(1), 12–35. doi: 10.1243/pime_proc_1959_173_010_02.

Bianconi, F., Filippucci, M., & Buffi, A. (2019). Automated design and modeling for mass-customized housing. A web-based design space catalog for timber structures. *Automation in Construction*, *103*, 13–25. doi: 10.1016/j.autcon.2019.03.002.

Billington, D. P., & Garlock, M. M. (2004). Thin shell concrete structures: the master builders. *Journal of the International Association for Shell and Spatial Structures*, *45*(3), 147-155.

Biswas, W. K., Alhorr, Y., Lawania, K. K., Sarker, P. K., & Elsarrag, E. (2017). Life cycle assessment for environmental product declaration of concrete in the Gulf States. *Sustainable Cities and Society*, *35*(1), 36–46. doi: 10.1016/j.scs.2017.07.011.

Blaeser, S., & Struck, C. J. (2019). A history of ASA standards. *The Journal of the Acoustical Society of America*, *145*(1), 77–109. doi: 10.1121/1.5080329.

Block, P., & Ochsendorf, J. (2007). Thrust network analysis: A new methodology for three-dimensional equilibrium. *Journal of the International Association for Shell and Spatial Structures*, *48*(155), 167–173.

Block, P., Schlueter, A., Veenendaal, D., Bakker, J., Begle, M., Hischier, I., Hofer, J., Jayathissa, P., Maxwell, I., Echenagucia, T. M., Nagy, Z., Pigram, D., Svetozarevic, B., Torsing, R., Verbeek, J., Willmann, A., & Lydon, G. P. (2017a). NEST HiLo: Investigating lightweight construction and adaptive energy systems. *Journal of Building Engineering*, *12*, 332–341. doi: 10.1016/j.jobe.2017.06.013.

Block, P., Van Mele, T., Rippmann, M., & Paulson, N. (2017b). *Beyond Bending: Reimaging Compression Shells*. Edition DETAIL.

Božiček, D., Kunič, R., & Košir, M. (2021). Interpreting environmental impacts in building design: Application of a comparative assertion method in the context of the EPD scheme for building products. *Journal of Cleaner Production*, *279*. 10.1016/j.jclepro.2020.123399.

Brandt. (1965). European Experience with Sound-Insulation Requirements subject this and the accompanying. *The Journal of the Acoustical Society of America*, *36*(4), 719-724. doi: 10.1121/1.1919051.

British Standards Institution. (2008). *Eurocode 2: Design of Concrete Structures*. British Standard.

Brown, N. C. (2019). Early Building Design Using Multi-Objective Data Approaches. PhD Dissertation. Massachusetts Institute of Technology.

Brown, N. C., Jusiega, V., & Mueller, C. T. (2020). Implementing data-driven parametric building design with a flexible toolbox. *Automation in Construction*, *118*, 103252. doi: 10.1016/j.autcon.2020.103252.

Brown, N., & Mueller, C. (2017). Designing with data: Moving beyond the design space catalog. *Disciplines and Disruption - Proceedings Catalog of the 37th Annual Conference of the Association for Computer Aided Design in Architecture, ACADIA 2017*, 154–163.

Brown, N. C., & Mueller, C. T. (2019). Design variable analysis and generation for performance-based parametric modeling in architecture. *International Journal of Architectural Computing*, *17*(1), 36–52. doi: 10.1177/1478077118799491.

Brown, N., Ochsendorf, J., Mueller, C., & de Oliveira, J. (2016). Early-stage integration of architectural and structural performance in a parametric multi-objective design tool. In *Structures and Architecture - Proceedings of the 3rd International Conference on Structures and Architecture, ICSA 2016*, *July*, 1103–1111. doi: 10.1201/b20891-152.

Broyles, J. M. (2020). Structural-acoustic optimization of shaped concrete floors in buildings. *The Pennsylvania State University*. M.S. Thesis.

Broyles, J. M. (2023a). Compiled Dataset of Concrete Mixture Environmental Product Declarations in the U.S.A., Mendeley Data, V2. doi: 10.17632/r4jgxk2mhn.2.

Broyles, J. M. (2023b). Acoustic design trade-offs when reducing the carbon footprint of buildings. *The Journal of the Acoustical Society of America*, *153*(3_supplement), A348-A348. Presentation. doi: 10.1121/10.0019111.

Broyles, J. M., Gevaudan, J. P., & Brown, N. C. (2024). A compiled dataset of ready-mix concrete Environmental Product Declarations for life cycle assessment. *Data in Brief*, *52*, 109852. doi: 10.1016/j.dib.2023.109852.

Broyles, J. M., Gevaudan, J. P., Hopper, M. W., Solnosky, R. L., & Brown, N. C. (2024). Equations for early-stage design embodied carbon estimation for concrete floors of varying loading and strength. *Engineering Structures*, *301*, 117369. doi: 10.1016/j.engstruct.2023.117369.

Broyles, J. M., Hartwell, A. J., Alvarez, E. G., Ismail, M. A., Norford, L. K., Mueller, C. T., & Brown, N. C. (2022a). Shape optimization of concrete floor systems for sustainability, acoustical, and thermal objectives. *5th International Conference on Structures and Architecture*, *2018*. doi: 10.1201/9781003023555-134.

Broyles, J. & Hopper, M. (2023). Assessment of the embodied carbon performance of post-tensioned voided concrete plates as a sustainable floor solution in multi-story buildings. *Engineering Structures*, 295, 116847. doi: 10.1016/j.engstruct.2023.116847.

Broyles, J. M., Self, I. P., & Brown, N. C. (2022b). Revisiting the Viipuri Library: Assessing performance and design trade-offs in custom ceiling geometry. In *Proceedings of the IASS 2022 Symposium Affiliated with APCS 2022 Conference*, *September*. doi: iass/piass/2022/00002022/00000010/art00012.

Broyles, J. M., Shepherd, M. R., & Brown, N. C. (2020). Evaluation of concrete floor systems for embodied carbon, air-borne, and structure-borne acoustic performance. In *Proceedings of IASS Annual Symposia 2020/21*. doi: iass/piass/2020/00002020/00000020/art00008.

Broyles, J. M., Shepherd, M. R., & Brown, N. C. (2021). Investigation of optimization techniques on structural-acoustical shaped concrete slabs in buildings. *In Proceedings of Meetings on Acoustics*, *42*, 022001. doi: 10.1121/1.5147332.

Broyles, J. M., Shepherd, M. R., & Brown, N. C. (2022c). Design Optimization of Structural – Acoustic Spanning Concrete Elements in Buildings. *Journal of Architectural Engineering*, *28*(1), 04021044-1–11. doi: 10.1061/(ASCE)AE.1943-5568.0000520.

Broyles, J. M., Shepherd, M. R., & Brown, N. C. (2022d). Modified acoustic transmission metrics for early-stage design exploration using a computational case study of heavyweight floors. *Applied Acoustics*, *196*, 108865. doi: 10.1016/j.apacoust.2022.108865.

Broyles, J. M., Shepherd, M. R., & Brown, N. C. (2023). Evaluation of the dynamic response for scaled models of shaped concrete floor slabs. *Building Acoustics*, *30*(2):143-163. doi: 10.1177/1351010X231157613.

Bucher, M. J. J., Kraus, M. A., Rust, R., & Tang, S. (2023). Performance-Based Generative Design for Parametric Modeling of Engineering Structures Using Deep Conditional Generative Models. *Automation in Construction*, *156*, 105128. doi: 10.1016/j.autcon.2023.105128.

Burger, J., Huber, T., Lloret-Fritschi, E., Mata-Falcón, J., Gramazio, F., & Kohler, M. (2022). Design and fabrication of optimised ribbed concrete floor slabs using large scale 3D printed formwork. *Automation in Construction*, *144*, 104599. doi: 10.1016/j.autcon.2022.104599.

Butko, D. (2021). A Sound Approach to Concrete: Transforming Concrete Through Shape and Porosity for Acoustical Reflection, Diffusion, and Absorption. *Technology | Architecture + Design*, *5*(1), 46-58. doi: 10.1080/24751448.2021.1863673.

Byers, B. S., Gordon, M., De Wolf, C., & Iuorio, O. (2023). Calculating embodied carbon for reused structural components with laser scanning. In *Life-Cycle of Structures and Infrastructure Systems*, 149-156. CRC Press. doi: 10.1201/9781003323020-15.

Caballero-Garatachea, O., Juarez-Luna, G., Euripides, M., & Sandoval-Hernandez, R. (2021). Methods for the vibration analysis of reinforced concrete precast one-way joist slab floor systems under human walking. *Journal of Building Engineering*, *43*, 103217. doi: 10.1016/j.jobe.2021.103217.

Cabeza, L. F., Barreneche, C., Miró, L., Morera, J. M., Bartolí, E., & Inés Fernández, A. (2013). Low carbon and low embodied energy materials in buildings: A review. *Renewable and Sustainable Energy Reviews*, *23*, 536–542. doi: 10.1016/j.rser.2013.03.017.

Cang, Y., Yang, L., Luo, Z., & Zhang, N. (2020). Prediction of embodied carbon emissions from residential buildings with different structural forms. *Sustainable Cities and Society*, *54*, 101946. doi: 10.1016/j.scs.2019.101946.

Caniato, M., Bettarello, F., Granzotto, N., Marzi, A., & Gasparella, A. (2022). A comprehensive vibroacoustic investigation of a cross laminated timber floor. *Construction and Building Materials*, *322*, 126303. doi: 10.1016/j.conbuildmat.2021.126303.

Carbon Leadership Forum, (2021). CLF Material Baselines Report. CLF. Retrieved from. https://carbonleadershipforum.org/2021-material-baseline-report/.

Cardin, M.A., De Neufville, R., Geltner, D., & Deng, Y. (2013). *Design Catalogs: A Practical Real Options Valuation Tool for Real Estate Design and Development Planning.* http://ardent.mit.edu/real_options/Common_course_materials/papers.html.

Caulfield, J. (2022). *Construction still lags other industries in use of technology*. Building Design + Production.

Carvalho, A. P. O. (2006). Reproducibility in interlaboratory impact sound insulation measurements. In *Proceedings of the ICSV 13-13th International Congress on Sound and Vibration*.

Carvalho, A. P. O., & Pereira, C. F. (2016). Sound and noise in shopping malls. In *INTER-NOISE and NOISE- CON Congress and Conference Proceedings*, *252*(2), 70-77. Institute of Noise Control Engineering.

Chauhan, D., Orme, S., Gugliotta, S., Wynne, Z., Black-Roberts, A., & Philipps, D. P. (2023). A multi-objective design tool for decarbonising buildings at the concept stage. In *Proceedings of the Institution of Civil Engineers-Engineering and Computational Mechanics*, *176*(2), 84-102. doi: 10.1680/jencm.23.00005.

Chen, Y., & Ng, S. T. (2016). Factoring in embodied GHG emissions when assessing the environmental performance of building. *Sustainable Cities and Society*, *27*, 244–252. doi: 10.1016/j.scs.2016.03.015.

Chen, S., Teng, Y., Zhang, Y., Leung, C. K., & Pan, W. (2023). Reducing embodied carbon in concrete materials: A state-of-the-art review. *Resources, Conservation and Recycling*, *188*, 106653. doi: 10.1016/j.resconrec.2022.106653.

Chmelík, V., Rychtáriková, M., Müllner, H., Jambrošić, K., Zelem, L., Benklewski, J., & Glorieux, C. (2020). Methodology for development of airborne sound insulation descriptor valid for light-weight and masonry walls. *Applied Acoustics*, *160*, 107144. doi: 10.1016/j.apacoust.2019.107144.

Chevillotte, F., & Panneton, R. (2011). Coupling transfer matrix method to finite element method for analyzing the acoustics of complex hollow body networks. *Applied Acoustics*, *72*(12), 962–968. doi: 10.1016/j.apacoust.2011.06.005.

Cho, T. (2013). Experimental and numerical analysis of floating floor resonance and its effect on impact sound transmission. *Journal of Sound and Vibration*, *332*(25), 6552–6561. doi: 10.1016/j.jsv.2013.08.011.

Christen, J. L., Ichchou, M., Troclet, B., Bareille, O., & Ouisse, M. (2016). Global sensitivity analysis of analytical vibroacoustic transmission models. *Journal of Sound and Vibration*, *368*, 121–134. doi:10.1016/j.jsv.2016.01.009.

Clark, D. M. (1970). Subjective Study of the Sound-Transmission Class System for Rating Building Partitions. *The Journal of the Acoustical Society of America*, *47*(3A), 676–682. doi: 10.1121/1.1911950.

Cobiax. (2018). *Cobiax EPD*. Cobiax International.

Cole, R. J. (1998). Energy and greenhouse gas emissions associated with the construction of alternative structural systems. *Building and Environment*, *34*(3), 335-348. doi: 10.1016/S0360-1323(98)00020-1.

Conta, S., Santoni, A., & Homb, A. (2020). Benchmarking the vibration velocity-based measurement methods to determine the radiated sound power from floor elements under impact excitation. *Applied Acoustics*, *169*, 107457. doi: 10.1016/j.apacoust.2020.107457.

Concrete Reinforcing Steel Institute (CRSI). (1998). One-way concrete joist construction: steel lap pan forming system.Engineering Data Report Number 43. Concrete Reinforcing Steel Institute.

Concrete Reinforcing Steel Institute (CRSI). (2016). *Vibration and Sound Control in Reinforced Concrete Buildings*.

Concrete Reinforcing Steel Institute. (2022). *CRSI EPD*.CRSI.

Costa, A., Keane, M. M., Torrens, J. I., & Corry, E. (2013). Building operation and energy performance: Monitoring, analysis and optimisation toolkit. *Applied Energy*, *101*, 310–316. doi: 10.1016/j.apenergy.2011.10.037.

Costa, E., Shepherd, P., Orr, J., Ibell, T., & Oval, R. (2020). Automating Concrete Construction: Digital Design of Non-prismatic Reinforced Concrete Beams. In *RILEM Bookseries*, *28*, 863–872. doi: 10.1007/978-3-030-49916-7_84.

Costa, G., & Madrazo, L. (2015). Connecting building component catalogues with BIM models using semantic technologies: An application for precast concrete components. *Automation in Construction*, *57*, 239–248. doi: 10.1016/j.autcon.2015.05.007.

Cottone, R., Shtrepi, L., Serra, V., & Pagliolico, S. L. (2023). The Recycling and Reuse of Natural Materials: Sound Absorbing Box Patterns That Use Waste from Olive Tree Pruning. *Acoustics 5*(1), 177-192. doi: 10.3390/acoustics5010011.

Cowlard, A., Bittern, A., Abecassis-Empis, C., & Torero, J. (2013). Fire safety design for tall buildings. *Procedia Engineering*, *62*, 169–181. doi: 10.1016/j.proeng.2013.08.053.

Curth, A., Hartwell, A. J., Mueller, C. T., Hartwell, A., Brodesser, T., & Mueller, C. (2022). Parametric waffle slabs: Optimal geometry materialized with additive construction. In *Proceedings of the IASS*. Accessed via: https://www.researchgate.net/publication/364152892.

D'Amico, B., & Pomponi, F. (2018). Accuracy and reliability: A computational tool to minimise steel mass and carbon emissions at early-stage structural design. *Energy and Buildings*, *168*, 236–250. doi: 10.1016/j.enbuild.2018.03.031.

D'Amico, B., & Pomponi, F. (2020). On mass quantities of gravity frames in building structures. *Journal of Building Engineering*, *31*, 101426. doi: 10.1016/j.jobe.2020.101426.

Dadabai, M. (2022). *Net Zero Carbon Concrete Facades: A catalogue on low carbon concrete strategies towards achieving net zero*. Master's Thesis. University of Southern California.

Danatzko, J. M., & Sezen, H. (2011). Sustainable Structural Design Methodologies. *Practice Periodical on Structural Design and Construction*, *16*(4), 186–190. doi: 10.1061/(asce)sc.1943-5576.0000095.

Davies, P. J., Emmitt, S., & Firth, S. K. (2015). Delivering improved initial embodied energy efficiency during construction. *Sustainable Cities and Society*, *14*, 267–279. doi: 10.1016/j.scs.2014.09.010.

De Wolf, C., Pomponi, F., & Moncaster, A. (2017). Measuring embodied carbon dioxide equivalent of buildings: A review and critique of current industry practice. *Energy and Buildings*, *140*, 68–80. doi: 10.1016/j.enbuild.2017.01.075.

Deb, K. (2011). *Multi-Objective Optimization Using Evolutionary Algorithms: An Introduction* [Indian Institute of Technology Kanpur]. http://www.iitk.ac.in/kangal/deb.htm.

Deb, K., Pratap, A., Agarwal, S., & Meyarivan, T. (2002). A Fast and Elitist Multiobjective Genetic Algorithm: NSGA-II. In IEEE TRANSACTIONS ON EVOLUTIONARY COMPUTATION (Vol. 6, Issue 2).

Deng, S., Wang, R. Z., & Dai, Y. J. (2014). How to evaluate performance of net zero energy building - A literature research. *Energy*, *71*, 1–16. doi: 10.1016/j.energy.2014.05.007.

Department of Housing and Urban Development (HUD): Office of Community Planning and Development (2009). *Sound transmission class guidance*. HUD, US.

DeRousseau, M. A., Arehart, J. H., Kasprzyk, J. R., & Srubar, W. V. (2020). Statistical variation in the embodied carbon of concrete mixtures. *Journal of Cleaner Production*, *275*, 123088. doi: 10.1016/j.jclepro.2020.123088.

DeRousseau, M. A., Kasprzyk, J. R., & Srubar, W. .V. (2018). Computational design optimization of concrete mixtures: A review. *Cement and Concrete Research*, *109*, 42–53. doi: 10.1016/j.cemconres.2018.04.007.

DeRousseau, M. A., Kasprzyk, J. R., & Srubar, W. V. (2021). Multi-Objective Optimization Methods for Designing Low-Carbon Concrete Mixtures. *Frontiers in Materials*, *8*, 1–13. doi: 10.3389/fmats.2021.680895.

Devènes, J., Bastien-Masse, M., & Fivet, C. (2024). Reusability assessment of reinforced concrete components prior to deconstruction from obsolete buildings. *Journal of Building Engineering*, *84*, 108584. doi: 10.1016/j.jobe.2024.108584.

Dijckmans, A., & Vermeir, G. (2013). Numerical investigation of the repeatability and reproducibility of laboratory sound insulation measurements. *Acta Acustica United with Acustica*, *99*(3), 421–432. doi: 10.3813/AAA.918623.

Dixit, M. K., Fernández-Solís, J. L., Lavy, S., & Culp, C. H. (2012). Need for an embodied energy measurement protocol for buildings: A review paper. *Renewable and Sustainable Energy Reviews*, *16*(6), 3730–3743. doi: 10.1016/j.rser.2012.03.021.

D'Oca, S., Hong, T., & Langevin, J. (2018). The human dimensions of energy use in buildings: A review. *Renewable and Sustainable Energy Reviews*, *81*, 731–742. doi: 10.1016/j.rser.2017.08.019.

Dong, Y. H., Jaillon, L., Chu, P., & Poon, C. S. (2015). Comparing carbon emissions of precast and cast-in-situ construction methods - A case study of high-rise private building. *Construction and Building Materials*, *99*, 39–53. doi: 10.1016/j.conbuildmat.2015.08.145.

Dong, W., LoVerde, J., & Rawlings, S. (2020). Reconsidering the '8-dB rule' in ASTM Impact and Airborne Ratings. In *INTER-NOISE and NOISE-CON Congress and Conference Proceedings 262*(1), 561-566. Institute of Noise Control Engineering.

Dong, W., Wong, D., & LoVerde, J. (2021). Gauge repeatability and reproducibility study of airborne sound isolation measurements. In *INTER-NOISE and NOISE-CON Congress and Conference Proceedings*, 263(3), 3900-3908. doi: 10.3397/IN-2021-2553.

Doraiswamy, H., Ferreira, N., Lage, M., Vo, H., Wilson, L., Werner, H., Park, M., & Silva, C. (2015). Topology-based catalogue exploration framework for identifying view-enhanced tower designs. *ACM Transactions on Graphics*, *34*(6). doi: 10.1145/2816795.2818134.

Dostart, N., Liu, Y., & Popović, M. A. (2017). Acoustic Waveguide Eigenmode Solver Based on a Staggered-Grid Finite-Difference Method. *Scientific Reports*, *7*(1). doi: 10.1038/s41598-017-17511-x.

Duan, Z. (2023). Impact of climate change on the life cycle greenhouse gas emissions of cross-laminated timber and reinforced concrete buildings in China. *Journal of Cleaner Production*, *395*, 136446. doi: 10.1016/j.jclepro.2023.136446.

Dunant, C. F., Drewniok, M. P., Orr, J. J., & Allwood, J. M. (2021). Good early stage design decisions can halve embodied CO2 and lower structural frames' cost. *Structures*, *33*, 343–354. doi: 10.1016/j.istruc.2021.04.033.

Dupree, R. B. (1980). *Catalog of STC and IIC Ratings for Wall and Floor/Ceiling Assemblies*. Office of Noise Control. Department of Health Services: California.

Ebi, K. L., Vanos, J., Baldwin, J. W., Bell, J. E., Hondula, D. M., Errett, N. A., Hayes, K., Reid, C. E., Saha, S., Spector, J., & Berry, P. (2021). Extreme Weather and Climate Change: Population Health and Health System Implications. *Annu. Rev. Public Health*, *42*, 293–315. doi: 10.1146/annurev-publhealth.

Ebrahimpour, A., & Sack, R. L. (2005). A review of vibration serviceability criteria for floor structures. *Computers & Structures*, *83*(28-20), 2488–2494. doi: 10.1016/j.compstruc.2005.03.023.

Eleftheriadis, S., Duffour, P., Greening, P., James, J., Stephenson, B., & Mumovic, D. (2018). Investigating relationships between cost and CO2 emissions in reinforced concrete structures using a BIM-based design optimisation approach. *Energy and Buildings*, *166*, 330–346. doi: 10.1016/j.enbuild.2018.01.059.

Eleftheriadis, S., Duffour, P., & Mumovic, D. (2018). BIM-embedded life cycle carbon assessment of RC buildings using optimised structural design alternatives. *Energy and Buildings*, *173*, 587–600. doi: 10.1016/j.enbuild.2018.05.042.

Erdogan, S. A., Šaparauskas, J., & Turskis, Z. (2019). A multi-criteria decision-making model to choose the best option for sustainable construction management. *Sustainability*, *11*(8). doi: 10.3390/su11082239.

Estrella, X., Muresan, A., Brütting, J., Redaelli, D., & Fivet, C. (2024). RE: SLAB—a load bearing system for open-ended component reuse in building structures. *Frontiers in Built Environment*, *10*, 1355445. doi: 10.3389/fbuil.2024.1355445.

Evans, G. W., & McCoy, J. M. (1998). When buildings don't work: The role of architecture in human health. *Journal of Environmental Psychology*, *18*(1), 85-94. doi: 10.1006/jevp.1998.0089.

Evins, R., Joyce, S. C., Pointer, P., & Williams, C. J. (2012). Multi-objective design optimisation: getting more for less. *ICE Proceedings Civil Engineering*, *165*(CE5), 5–10. doi: 10.1680/cien.11.00014.

Fanella, D. & Alsamsam, I. (2015). Professional Development Series: Design of Reinforced Concrete Floor Systems. Portland Cement Association.

Fanella, D. A., Mahamid, M., & Mota, M. (2017). Flat Plate–Voided Concrete Slab Systems: Design, Serviceability, Fire Resistance, and Construction. *Practice Periodical on Structural Design and Construction*, *22*(3), 04017004. doi: 10.1061/(asce)sc.1943-5576.0000322.

Fanella, D. A., & Mota, M. (2014). *Design Guide for Vibrations of Reinforced Concrete Floor Systems*. Concrete Reinforcing Steel Institute (CRSI), First Edition.

Fanella, D. A., Mota, M., & Trygestad, A. (2018). Fire Resistance of Flat Plate Voided Concrete Floor Systems. *Structures Magazine*.

Fang, D., Kuhn, S. V., Kaufmann, W., Kraus, M. A., & Mueller, C. (2023a). Quantifying the influence of continuous and discrete design decisions using sensitivities. In *Advances in Architectural Geometry 2023*, 411-426. De Gruyter.

Fang, D., De Wolf, C., Brown, N. C., & Mueller, C. T. (2023b). Reducing embodied carbon in structural systems: A review of early-stage design strategies. *Journal of Building Engineering*, *76*, 107054. doi: 10.1016/j.jobe.2023.107054.

Fang, B., Zhang, R., Chen, T., Wang, W., Zhu, J., & Cheng, W. (2024). Bandgap optimization and inverse design of labyrinth metamaterials for sound insulation. *Journal of Building Engineering*, *86*, 108898. doi: 10.1016/j.jobe.2024.108898.

Fediuk, R., Amran, M., Vatin, N., Vasilev, Y., Lesovik, V., & Ozbakkaloglu, T. (2021). Acoustic properties of innovative concretes: A review. *Materials*, *14*(2), 1–28. doi: 10.3390/ma14020398.

Feickert, K., & Mueller, C. T. (2023). Thin shell foundations: Quantification of embodied carbon reduction through materially efficient geometry. *Architecture, Structures and Construction*. doi: 10.1007/s44150-023-00101-z.

Felicioni, L., Gaspari, J., Veselka, J., & Malík, Z. (2023). A comparative cradle-to-grave life cycle approach for addressing construction design choices: An applicative case study for a residential tower in Aalborg, Denmark. *Energy and Buildings*, *298*, 113557. doi: 10.1016/j.enbuild.2023.113557.

Fenton, S. K., De Rycke, K., Munteanu, A., Deligiannis, N., Rufat, S., & De Laet, L. (2022). Strategies for data-driven low carbon structural design. In *Proceedings of IASS Annual Symposia*, 11, 1-11. International Association for Shell and Spatial Structures (IASS). doi: iass/piass/2022/00002022/00000011/art00004.

Ferreiro-Cabello, J., Fraile-Garcia, E., de Pison Ascacibar, E. M., & de Pison Ascacibar, F. J. M. (2016). Minimizing greenhouse gas emissions and costs for structures with flat slabs. *Journal of Cleaner Production*, *137*, 922–930. doi: 10.1016/j.jclepro.2016.07.153.

Ferreiro-Cabello, J., Fraile-Garcia, E., Martinez-Camara, E., & Perez-de-la-Parte, M. (2017). Sensitivity analysis of Life Cycle Assessment to select reinforced concrete structures with one-way slabs. *Engineering Structures*, *132*, 586–596. doi: 10.1016/j.engstruct.2016.11.059.

Foraboschi, P. (2019). Bending load-carrying capacity of reinforced concrete beams subjected to premature failure. *Materials*, 12(19), 3085. doi: 10.3390/ma12193085.

Foraboschi, P., Mercanzin, M., & Trabucco, D. (2014). Sustainable structural design of tall buildings based on embodied energy. *Energy & Buildings*, *68*, 254–269. doi: 10.1016/j.enbuild.2013.09.003.

Fraile-Garcia, E., Ferreiro-Cabello, J., Martinez-Camara, E., & Jimenez-Macias, E. (2016). Optimization based on life cycle analysis for reinforced concrete structures with one-way slabs. *Engineering Structures*, *109*, 126–138. doi: 10.1016/j.engstruct.2015.12.001.

Frederikse, T., Landerer, F., Caron, L., Adhikari, S., Parkes, D., Humphrey, V. W., Dangendorf, S., Hogarth, P., Zanna, L., Cheng, L., & Wu, Y. H. (2020). The causes of sea-level rise since 1900. *Nature*, *584*(7821), 393–397. doi: 10.1038/s41586-020-2591-3.

Frost, T. (1996). The Realities of Home Theatre. In *Audio Engineering Society Conference: UK 11th Conference: Audio for New Media (ANM)*. Audio Engineering Society.

Gagg, C. R. (2014). Cement and concrete as an engineering material: An historic appraisal and case study analysis. *Engineering Failure Analysis*, *40*, 114–140. doi: 10.1016/j.engfailanal.2014.02.004.

Gan, V. J. L., Chan, C. M., Tse, K. T., Lo, I. M. C., & Cheng, J. C. P. (2017). A comparative analysis of embodied carbon in high-rise buildings regarding different design parameters. *Journal of Cleaner Production*, *161*, 663–675. doi: 10.1016/j.jclepro.2017.05.156.

Gan, V. J. L. L., Cheng, J. C. P. P., & Lo, I. M. C. C. (2019). A comprehensive approach to mitigation of embodied carbon in reinforced concrete buildings. *Journal of Cleaner Production*, *229*, 582–597. doi: 10.1016/j.jclepro.2019.05.035.

Gardezi, S. S. S., Shafiq, N., Zawawi, N. A. W. A., Khamidi, M. F., & Farhan, S. A. (2016). A multivariable regression tool for embodied carbon footprint prediction in housing habitat. *Habitat International*, *53*, 292–300. doi: 10.1016/j.habitatint.2015.11.005.

Gascón Alvarez, E., Stamler, N., Mueller, C. T., & Norford, L. K. (2022). Shape optimization of chilled concrete ceilings – Reduced embodied carbon and enhanced operational performance. *Building and Environment*, *221*, 109330. doi: 10.1016/j.buildenv.2022.109330.

Gaspar, C. M. R., Santos Da Silva, J. G., & Costa-Neves, L. F. (2016). Multimode vibration control of building steel-concrete composite floors submitted to human rhythmic activities. *Computers and Structures*, *165*, 107–122. doi: 10.1016/j.compstruc.2015.12.010.

Gatland II, S. D. (2003). Acoustical Insulation. *Manager Building Science Technology*.

Gauch, H. L., Dunant, C. F., Hawkins, W., & Serrenho, A. C. (2023). What really matters in multi-storey building design? A simultaneous sensitivity study of embodied carbon, construction cost, and operational energy. *Applied Energy*, *333*, 120585. doi: 10.1016/j.apenergy.2022.120585.

Geyer, P. (2009). Component-oriented decomposition for multidisciplinary design optimization in building design. *Advanced Engineering Informatics*, *23*(1), 12–31. doi: 10.1016/j.aei.2008.06.008.

Gibson, B., Nguyen, T., Sinaie, S., Heath, D., & Ngo, T. (2022). The low frequency structure-borne sound problem in multi-storey timber buildings and potential of acoustic metamaterials: A review. *Building and Environment*, *224*, 109531. doi: 10.1016/j.buildenv.2022.109531.

Girdhar, S., & Barnard, A. (2020). Improved low-frequency sound measurements for impact insulation class (IIC) rating using a comparison technique. *Noise Control Engineering Journal*, *68*(1), 72–86. doi: 10.3397/1/37686.

Girdhar, S., Barnard, A. R., Blough, J. R., LoVerde, J., & Dong, W. (2023a). Evaluating proposed low-frequency measurement guidelines for impact noise in buildings with ASTM ratings. In *Proceedings of Meetings on Acoustics*, 51(1), 015005. doi: 10.1121/2.0001752.

Girdhar, S., Barnard, A. R., Blough, J. R., LoVerde, J., & Dong, W. (2023b). Guidelines to measure low-frequency floor impact performance with high reproducibility. In *Proceedings of Meetings on Acoustics*, *51*(1), 015006. doi: 10.1121/2.0001760.

Girdhar, S., Barnard, A. R., LoVerde, J., & Dong, W. (2021). Measuring the force due to standard tapping machine and floor impedance for ASTM standards. In *INTER-NOISE and NOISE-CON Congress and Conference Proceedings*, *263*(6), 767-777. doi: 10.3397/IN-2021-1644.

Grand Challenges. (2024). *Global Grand Challenges*. Bill & Melinda Gates Foundation.

Gollob, S., & Kocur, G. K. (2021). Analysis of the wave propagation paths in numerical reinforced concrete models. *Journal of Sound and Vibration*, *494*, 115861. doi: 10.1016/j.jsv.2020.115861.

Griffiths, S., Sovacool, B. K., Del Rio, D. D. F., Foley, A. M., Bazilian, M. D., Kim, J., & Uratani, J. M. (2023). Decarbonizing the cement and concrete industry: A systematic review of socio-technical systems, technological innovations, and policy options. *Renewable and Sustainable Energy Reviews*, *180*, 113291. doi: 10.1016/j.rser.2023.113291.

Grimwood, C. (1997). Complaints about poor sound insulation between dwellings in England and Wales. *Applied Acoustics*, *52*(3-4), 211-223. doi: 10.1016/S0003-682X(97)00027-3.

Gross, J. L., & Phan, L. T. (2010). Summary of best practice guidelines for structural fire resistance design of concrete and steel buildings. In *Structures Congress 2010*, 2369-2379. doi: 10.1061/41130(369)215.

Gursel, A. P., Shehabi, A., & Horvath, A. (2023). What are the energy and greenhouse gas benefits of repurposing non-residential buildings into apartments?. *Resources, Conservation and Recycling*, *198*, 107143. doi: 10.1016/j.resconrec.2023.107143.

Habert, G., Röck, M., Steininger, K., Lupisek, A., Birgisdottir, H., Desing, H., Chandrakumar, C., Pittau, F., Passer, A., Rovers, R., Slavkovic, K., Hollberg, A., Hoxha, E., Jusselme, T., Nault, E., Allacker, K., & Lützkendorf, T. (2020). Carbon budgets for buildings: harmonising temporal, spatial and sectoral dimensions. *Buildings and Cities*, *1*(S 1), 429-452. doi: https://doi.org/10.5334/bc.47.

Habert, G., & Roussel, N. (2009). Study of two concrete mix-design strategies to reach carbon mitigation objectives. *Cement and Concrete Composites*, *31*(6), 397–402. doi: 10.1016/j.cemconcomp.2009.04.001.

Hafez, H., Teirelbar, A., To, N., & Fuente, A. De. (2023). Data-driven optimization tool for the functional, economic, and environmental properties of blended cement concrete using supplementary cementitious materials. *Journal of Building Engineering*, *67*, 106022. doi: 10.1016/j.jobe.2023.106022.

Halliwell, R. E., Nightingale, T. R. T., Warnock, A. C. C., & Birta, J. A. (1998). Gypsum board walls: transmission loss data. National Research Council of Canada, Internal Report No. 761.

Halpern, A. B., Billington, D. P., & Adriaenssens, S. (2013). The ribbed floor slab systems of Pier Luigi Nervi. *Journal of the International Association for Shell and Spatial Structures*, *54*(176–177), 127–136.

Hambric, S. A., & Fahnline, J. B. (2007). Structural acoustics tutorial—part 2: sound—structure interaction. *Acoustics Today*, *3*(2), 9.

Hammond, G., & Jones, C. (2008). Inventory of carbon & energy: ICE (Vol. 5). Bath, UK: Sustainable Energy Research Team, Department of Mechanical Engineering, University of Bath.

Hanifa, M., Agarwal, R., Sharma, U., Thapliyal, P. C., & Singh, L. P. (2023). A review on CO2 capture and sequestration in the construction industry: Emerging approaches and commercialised technologies. In *Journal of CO2 Utilization 76*, 102292. doi: 10.1016/j.jcou.2022.102292.

Hart, J., D'Amico, B., & Pomponi, F. (2021). Whole-life embodied carbon in multistory buildings: Steel, concrete and timber structures. *Journal of Industrial Ecology*, *25*(2), 403–418. doi: 10.1111/jiec.13139.

Hasanbeigi, A., Price, L., & Lin, E. (2012). Emerging energy-efficiency and CO2 emission-reduction technologies for cement and concrete production: A technical review. *Renewable and Sustainable Energy Reviews*, *16*(8), 6220–6238. doi: 10.1016/j.rser.2012.07.019.

Hawkins, W. (2017). Thin-shell textile-reinforced concrete floors for sustainable buildings. *Proceedings of the IASS Annual Symposium 2017*, 7.

Hawkins, W. J., Herrmann, M., Ibell, T. J., Kromoser, B., Michaelski, A., Orr, J. J., Pedreschi, R., Pronk, A., Schipper, H. R., Shepherd, P., Veenendaal, D., Wansdronk, R., & West, M. (2016). Flexible formwork technologies – a state of the art review. *Structural Concrete*, *17*(6), 911–935. doi: 10.1002/suco.201600117.

Hawkins, W., Orr, J., Ibell, T., & Shepherd, P. (2020). A design methodology to reduce the embodied carbon of concrete buildings using thin-shell floors. *Engineering Structures*, *207*, 110195. doi: 10.1016/j.engstruct.2020.110195.

Hawkins, W., Orr, J., Shepherd, P., & Ibell, T. (2019). Design, Construction and Testing of a Low Carbon Thin-Shell Concrete Flooring System. *Structures*, *18*, 60–71. doi: 10.1016/j.istruc.2018.10.006.

Hawkins, W., Peters, A., & Mander, T. (2021). Opinion Planning application procedures Climate emergency Floor loadings. *The Structural Engineer*, *99*(5), 1–3. Available at: www.istructe.

He, L., Li, Q., Gilbert, M., Shepherd, P., Rankine, C., Pritchard, T., & Reale, V. (2022). Optimization-driven conceptual design of truss structures in a parametric modelling environment. *Structures*, *37*, 469–482. doi: 10.1016/j.istruc.2021.12.048.

Heckl, M., & Rathe, E. J. (1963). Relationship between the Transmission Loss and the Impact-Noise Isolation of Floor Structures. *Journal of the Acoustical Society of America*, *35*(11), 1825–1830. doi: 10.1121/1.1918830.

Helal, J., Stephan, A., & Crawford, R. H. (2020). The influence of structural design methods on the embodied greenhouse gas emissions of structural systems for tall buildings. *Structures*, *24*, 650–665. doi: 10.1016/j.istruc.2020.01.026.

Helal, J., Stephan, A., & Crawford, R. H. (2023). Integrating embodied greenhouse gas emissions assessment into the structural design of tall buildings: A framework and software tool for design decision-making. *Energy and Buildings*, *297*, 113462. doi: 10.1016/j.enbuild.2023.113462.

Helsel, M. A., Rangelov, M., Montanari, L., Spragg, R., & Carrion, M. (2022). Contextualizing embodied carbon emissions of concrete using mixture design parameters and performance metrics. *Structural Concrete*, *July*, 1–14. doi: 10.1002/suco.202200634.

Hens, I., Solnosky, R., & Brown, N. C. (2021). Design space exploration for comparing embodied carbon in tall timber structural systems. *Energy and Buildings*, *244*, 110983. doi: 10.1016/j.enbuild.2021.110983.

Hens, I., Solnosky, R., & Brown, N. (2023). Parametric framework for early evaluation of prescriptive fire design and structural feasibility in tall timber. *Journal of Architectural Engineering*, *29*(1), 04022040. doi: 10.1061/jaeied.aeeng-1455.

Hinkle, L. E., Wang, J., & Brown, N. C. (2022). Quantifying potential dynamic façade energy savings in early design using constrained optimization. *Building and Environment, 221*, 109265. doi: 10.1016/j.buildenv.2022.109265.

Hongisto, V., Oliva, D., & Keränen, J. (2014). Subjective and objective rating of airborne sound insulation - living sounds. *Acta Acustica United with Acustica*, *100*(5), 848–863. doi: 10.3813/AAA.918765.

Howard, C. Q., & Cazzolato, B. S. (2014). *Acoustic Analyses using MATLAB and ANSYS*. CRC press.

Huberman, N., Pearlmutter, D., Gal, E., & Meir, I. A. (2015). Optimizing structural roof form for life-cycle energy efficiency. *Energy and Buildings*, *104*, 336–349. doi: 10.1016/j.enbuild.2015.07.008.

Huijbregts, M. A. J. (1998). Application of uncertainty and variability in LCA. Part I: A general framework for the analysis of uncertainty and variability in life cycle assessment. *International Journal of Life Cycle Assessment*, *3*(5), 273–280. doi: 10.1007/BF02979835.

Idrus, N. J. B. (2002). Construction related factors influencing the choice of concrete floor systems. *Construction Management and Economics*, *20*(1), 13–19. doi: 10.1080/01446190110101218.

Imbabi, M. S., Carrigan, C., & McKenna, S. (2012). Trends and developments in green cement and concrete technology. *International Journal of Sustainable Built Environment*, *1*(2), 194–216. doi: 10.1016/j.ijsbe.2013.05.001.

International Code Council. (2021). International Building Code (IBC). Falls Church, Va.: International Code Council.

Ismail, M. (2023). *Reshaping concrete: Empowering development through low-carbon structural design*. Ph.D. Dissertation. Massachusetts Institute of Technology.

Ismail, M. (2023). Reshaping concrete: Inclusive design for low-carbon structures. *Enquiry The ARCC Journal for Architectural Research*, *20*(2), 43-59. doi: 10.17831/enqarcc.v20i2.1156.

Ismail, M. A., Mayencourt, P. L., & Mueller, C. T. (2021). Shaped beams: unlocking new geometry for efficient structures. *Architecture, Structures and Construction*, *0123456789*. doi: 10.1007/s44150-021-00003-y.

Ismail, M. A., & Mueller, C. T. (2021). Minimizing embodied energy of reinforced concrete floor systems in developing countries through shape optimization. *Engineering Structures*, *246*, 112955. doi: 10.1016/j.engstruct.2021.112955.

ISO 14040. Environmental management–Life cycle assessment–Principles and framework (ISO 14040: 2006). International Organization for Standardization, Geneva, Switzerland, 2006.

ISO 14044. Environmental management–Life cycle assessment–Requirements and management (ISO 14044: 2006). International Organization for Standardization, Geneva, Switzerland, 2006.

ISO 16283-1. Acoustics – rating of sound insulation in buildings and of building elements – Part 1: airborne sound insulation (ISO 16281-1: 2014). International Organization for Standardization Geneva, Switzerland, 2014.

ISO 16283-2. Acoustics – rating of sound insulation in buildings and of building elements – Part 1: impact sound insulation (ISO 16281-2: 2020). International Organization for Standardization Geneva, Switzerland, 2020.

ISO 21930. Sustainability in buildings and civil engineering works (ISO 21930: 2017). International Organization for Standardization, Geneva, Switzerland, 2017.

Jaramillo, A., & Ermann, M. (2010). Noise in the Classroom. In *Proceedings of Meetings on Acoustics*, *11*(1). The Acoustical Society of America. doi: 10.1121/1.4772719.

Jayasinghe, A., Orr, J., Hawkins, W., Ibell, T., & Boshoff, W. P. (2022a). Comparing different strategies of minimising embodied carbon in concrete floors. *Journal of Cleaner Production*, *345*, 131177. doi: 10.1016/j.jclepro.2022.131177.

Jayasinghe, A., Orr, J., Ibell, T., & Boshoff, W. P. (2021a). Comparing the embodied carbon and cost of concrete floor solutions. *Journal of Cleaner Production*, *324*, 129268. doi: 10.1016/j.jclepro.2021.129268.

Jayasinghe, A., Orr, J., Ibell, T., & Boshoff, W. P. (2021b). Minimising embodied carbon in reinforced concrete beams. *Engineering Structures*, *242*, 112590. doi: 10.1016/j.engstruct.2021.112590.

Jayasinghe, A., Orr, J., Ibell, T., & Boshoff, W. P. (2022b). Minimising embodied carbon in reinforced concrete flat slabs through parametric design. Journal of Building Engineering, 50, 104136. doi: 10.1016/j.jobe.2022.104136.

Jensen, A., Sehovic, Z., St, N., Knobloch, C., Klein, J., Richardson, P., & Janiski, J. (2020). *Mass Timber Solutions for Eight Story Mixed-Use Buildings : A Comparative Study of GHG emissions*. *3*, 1400–1405.

Jensen, H. A. R., Rasmussen, B., & Ekholm, O. (2018). Neighbour and traffic noise annoyance: A nationwide study of associated mental health and perceived stress. *European Journal of Public Health*, *28*(6), 1050–1055. doi: 10.1093/eurpub/cky091.

Jensen, H. A. R., Rasmussen, B., & Ekholm, O. (2019). Neighbour noise annoyance is associated with various mental and physical health symptoms: results from a nationwide study among individuals living in multi-storey housing. *BMC Public Health*, *19*(1), 1–10. doi: 10.1186/s12889-019-7893-8.

Jeon, J. Y., Jeong, J. H., Vorländer, M., & Thaden, R. (2004). Evaluation of floor impact sound insulation in reinforced concrete buildings. *Acta Acustica United with Acustica*, *90*(2), 313–318.

Jeon, J. Y., & Sato, S. (2008). Annoyance caused by heavyweight floor impact sounds in relation to the autocorrelation function and sound quality metrics. *Journal of Sound and Vibration*, *311*(3–5), 767–785. doi: 10.1016/j.jsv.2007.09.029.

Jipa, A., Bernhard, M., Meibodi, M., & Dillenburger, B. (2016). 3D-printed stay-in-place formwork for topologically optimized concrete slabs. In *Proceedings of the 2016 TxA emerging design+ technology conference*, 97-107. Texas Society of Architects.

Jusselme, T., Rey, E., & Andersen, M. (2018). An integrative approach for embodied energy: Towards an LCA-based data-driven design method. *Renewable and Sustainable Energy Reviews*, *88*, 123-132. doi: 10.1016/j.rser.2018.02.036.

Kang, G., Kim, T., Kim, Y. W., Cho, H., & Kang, K. I. (2015). Statistical analysis of embodied carbon emission for building construction. *Energy and Buildings*, *105*, 326–333. doi: 10.1016/j.enbuild.2015.07.058.

Kanyilmaz, A., Dang, V. H., & Kondratenko, A. (2023). How does conceptual design impact the cost and carbon footprint of structures? *Structures*, *58*, 105102. doi: 10.1016/j.istruc.2023.105102.

Katsiroumpas, K., Carels, P., Masoumi, H., & Salkauskis, J. (2018). Lightweight floating floor innovations in gym/sports applications. In *INTER-NOISE and NOISE-CON Congress and Conference Proceedings*, *258*(6), 1075-1084. Institute of Noise Control Engineering.

Khajeh Hesameddin, P., Irfanoglu, A., & Hacker, T. J. (2015). Effective viscous damping ratio in seismic response of reinforced concrete structures. In *6th International Conference on Advances in Experimental Structural Engineering*.

Khoury, G. A. (2000). Effect of fire on concrete and concrete structures. *Progress in Structural Engineering and Materials*, *2*(4), 429–447. doi: 10.1002/pse.51.

Kihlman, T. (1970). Sound transmission in building structures of concrete. *Journal of Sound and Vibration*, *11*(4), 435–445. doi: 10.1016/S0022-460X(70)80005-0.

Kim, H., Ryue, J., Thompson, D. J., & Müller, A. D. (2019). Application of a wavenumber domain numerical method to the prediction of the radiation efficiency and sound transmission of complex extruded panels. *Journal of Sound and Vibration*, *449*, 98–120. doi: 10.1016/j.jsv.2019.02.036.

Kirkup, S. (1994). Computational solution of the acoustic field surrounding a baffled panel by Computational solution of the acoustic field surrounding a baffled panel by the Rayleigh integral method. *Applied Mathematical Modeling*, July 1994. doi: 10.1016/0307-904X(94)90227-5.

Knight, K. A., Cunningham, P. R., & Miller, S. A. (2023). Optimizing supplementary cementitious material replacement to minimize the environmental impacts of concrete. *Cement and Concrete Composites*, 139, 105049. doi: 10.1016/j.cemconcomp.2023.105049.

Knupp, P. M. (2001). Algebraic mesh quality metrics. *SIAM journal on scientific computing*, *23*(1), 193-218. doi: 10.1137/S1064827500371499.

Kohrmann, M. (2017). Numerical methods for the vibro-acoustic assessment of timber floor constructions Doctoral dissertation. Technische Universität München.

Konakovic Lukovic, M., Tian, Y., & Matusik, W. (2020). Diversity-guided multi-objective bayesian optimization with batch evaluations. *Advances in Neural Information Processing Systems*, *33*, 17708-17720.

Kotcher, J., Maibach, E., Miller, J., Campbell, E., Alqodmani, L., Maiero, M., & Wyns, A. (2021). Views of health professionals on climate change and health: a multinational survey study. *The Lancet Planetary Health*, *5*(5), e316–e323. doi: 10.1016/S2542-5196(21)00053-X.

Kovacic, I., Reisinger, J., & Honic, M. (2018). Life Cycle Assessment of embodied and operational energy for a passive housing block in Austria. *Renewable and Sustainable Energy Reviews*, *82*, 1774–1786. doi: 10.1016/j.rser.2017.07.058.

Kovalov, A., Otrosh, Y., Ostroverkh, O., Hrushovinchuk, O., & Savchenko, O. (2018). Fire resistance evaluation of reinforced concrete floors with fire-retardant coating by calculation and experimental method. *E3S Web of Conferences*, *60*. doi: 10.1051/e3sconf/20186000003.

Küpfer, C., Bertola, N., & Fivet, C. (2024). Reuse of cut concrete slabs in new buildings for circular ultra-low-carbon floor designs. *Journal of Cleaner Production*, *448*, 141566. doi: 10.1016/j.jclepro.2024.141566.

Kuo, K. A., Verbraken, H., Degrande, G., & Lombaert, G. (2016). Hybrid predictions of railway induced ground vibration using a combination of experimental measurements and numerical modelling. *Journal of Sound and Vibration*, *373*, 263–284. doi: 10.1016/j.jsv.2016.03.007.

Kurent, B., Friedman, N., & Brank, B. (2024). Modelling of Multi-Storey Cross-Laminated Timber Buildings for Vibration Serviceability. *Buildings*, *14*(3), 689. doi: 10.3390/buildings14030689.

Kwak, H. G., & Filippou, F. C. (1990). Finite element analysis of reinforced concrete structures under monotonic loads. Berkeley, CA: Department of Civil Engineering, University of California.

Kylliäinen, M., Hongisto, V., Oliva, D., & Rekola, L. (2017). Subjective and objective rating of impact sound insulation of a concrete floor with various coverings. *Acta Acustica United with Acustica*, *103*(2), 236–251. doi: 10.3813/AAA.919053.

Langfeldt, F., Hoppen, H., & Gleine, W. (2020). Broadband low-frequency sound transmission loss improvement of double walls with Helmholtz resonators. *Journal of Sound and Vibration*, *476*, 115309. doi: 10.1016/j.jsv.2020.115309.

Lee, M. G., An, J. H., Bae, S. G., Oh, H. S., Choi, J., Yun, D. Y., Hong, T., Lee, D. E., & Park, H. S. (2020). Multi-objective sustainable design model for integrating CO2 emissions and costs for slabs in office buildings. *Structure and Infrastructure Engineering*, *16*(8), 1096–1105. doi: 10.1080/15732479.2019.1683590.

Leonard, S. J. (2023). Parametrically-informed early-design guidance for mass timber floors for embodied carbon and structural design. Ph.D. Dissertation. The Pennsylvania State University.

Leonard, S. J., Eddin, M. B., Prichard, M. K., Jonathan, M., Brown, N. C., & Ménard, S. (2023). Trade-offs in embodied carbon and acoustic insulation for mass timber floor assemblies. In *13th World Conference on Timber Engineering: Timber for a Livable Future, WCTE 2023*, 858–867. doi: 10.52202/069179-0117.

Leonard, S. J., Brown, N. C., & Solnosky, R. L. (2024). Impact of Prescriptive Fire Design Provisions on Embodied Carbon for International Building Code Type IV Construction. *Practice Periodical on Structural Design and Construction*, *29*(2), 04024012. doi: 10.1061/PPSCFX.SCENG-1418.

Leppington, F. G., Heron, K. H., Broadbent, E. G., & Mead, S. M. (1987). Resonant and Non-Resonant Acoustic Properties of Elastic Panels. Ii. the Transmission Problem. In *Proceedings of The Royal Society of London, Series A: Mathematical and Physical Sciences*, *412*(1843), 309–337. doi: 10.1098/rspa.1987.0091.

Li, X., Yang, F., Zhu, Y., & Gao, Y. (2014). An assessment framework for analyzing the embodied carbon impacts of residential buildings in China. *Energy and Buildings*, *85*, 400–409. doi: 10.1016/j.enbuild.2014.09.051.

Litvin, A., & Belliston, H. W. (1978). *Sound transmission loss through concrete and concrete masonry walls*. Portland Cement Association.

Liew, K. M., Sojobi, A. O., & Zhang, L. W. (2017). Green concrete: Prospects and challenges. *Construction and Building Materials*, *156*, 1063–1095. doi: 10.1016/j.conbuildmat.2017.09.008.

Liu, F., Battini, J. M., & Pacoste, C. (2020). Finite element modelling for the dynamic analysis of hollow-core concrete floors in buildings. *Journal of Building Engineering*, *32*, 101750. doi: 10.1016/j.jobe.2020.101750.

Liu, J. C., Hossain, M. U., Xuan, D., Ali, H. A., Ng, S. T., & Ye, H. (2023). Mechanical and durability performance of sustainable concretes containing conventional and emerging supplementary cementitious materials. *Developments in the Built Environment*, *15*, 100197. doi: 10.1016/j.dibe.2023.100197.

Ljunggren, F., Simmons, C., & Hagberg, K. (2014). Correlation between sound insulation and occupants' perception - Proposal of alternative single number rating of impact sound. *Applied Acoustics*, *85*, 57–68. doi: 10.1016/j.apacoust.2014.04.003.

Lloret, E., Shahab, A. R., Linus, M., Flatt, R. J., Gramazio, F., Kohler, M., & Langenberg, S. (2015). Complex concrete structures: Merging existing casting techniques with digital fabrication. C*AD Computer Aided Design*, *60*, 40–49. doi: 10.1016/j.cad.2014.02.011.

Long, M. (2005). *Architectural Acoustics*. Elsevier.

Longinow, A., Ph, D., & Hannen, W. R. (2009). Floor Vibrations in Buildings. *Structural Design Forum*, *14*, 143–145. doi: 10.1061/(ASCE)SC.1943-5576.0000048.

Lopez, C., & Astudillo, H. (2006). Multidimensional Catalogs for Systematic Exploration of Component-Based Design Spaces. *IFIP International Federation for Information Processing*, 32–46.

López López, D., Veenendaal, D., Akbarzadeh, M., & Block, P. (2014). Prototype of an ultra-thin, concrete vaulted floor system. In *Proceedings of IASS Annual Symposia*, 15, 1-8.

Lotteau, M., Loubet, P., & Sonnemann, G. (2017). An analysis to understand how the shape of a concrete residential building influences its embodied energy and embodied carbon. *Energy and Buildings*, *154*, 1–11. doi: 10.1016/j.enbuild.2017.08.048.

LoVerde, J., & Dong, W. (2018). The low-frequency limit of proposed ratings for quantifying low frequency impact insulation. In *176th Meeting of Acoustical Society of America 2018 Acoustics Week in Canada*, 015003. doi: 10.1121/2.0000980.

LoVerde, J. J., & Dong, D. W. (2017). A dual-rating method for evaluating impact noise isolation of floor-ceiling assemblies. *The Journal of the Acoustical Society of America*, *141*(1), 428–440. doi: 10.1121/1.4973868.

Lu, M., & Lai, J. (2020). Review on carbon emissions of commercial buildings. *Renewable and Sustainable Energy Reviews*, 119, 109545. doi: 10.1016/j.rser.2019.109545.

Lukavocic, Tian, Y., & Matusik, W. (2020). Diversity-Guided Multi-Objective Bayesian Optimization With Batch Evaluations. https://github.com/yunshengtian/DGEMO.

Lupíšek, A., Nehasilová, M., Mančík, Š., Železná, J., Ružička, J., Fiala, C., Tywoniak, J., & Hájek, P. (2017). Design strategies for buildings with low embodied energy. In *Proceedings of the Institution of Civil Engineers: Engineering Sustainability*, *170*(2), 65–80. doi: 0.1680/jensu.15.00050.

Luthin, A., Crawford, R. H., & Traverso, M. (2023). Demonstrating circular life cycle sustainability assessment–a case study of recycled carbon concrete. *Journal of Cleaner Production*, *433*, 139853. doi: 10.1016/j.jclepro.2023.139853.

Lützkendorf, T. (2020). The role of carbon metrics in supporting built-environment professionals. *Buildings and Cities*, *1*(1), 662–672. doi: 10.5334/bc.73.

Ma, J., He, Y., Zhao, Z., & Min, Y. (2023). Topology optimization of ribbed slabs and shells. *Engineering Structures*, *277*, 115454. doi: 10.1016/j.engstruct.2022.115454.

Mak, M. W. T., & Lees, J. M. (2023). Carbon reduction and strength enhancement in functionally graded reinforced concrete beams. *Engineering Structures*, *277*, 115358. doi: 10.1016/j.engstruct.2022.115358.

Mak, C. M., & Wang, Z. (2015). Recent advances in building acoustics: An overview of prediction methods and their applications. *Building and Environment*, *91*, 118–126. doi: 10.1016/j.buildenv.2015.03.017.

Malmqvist, T., Nehasilova, M., Moncaster, A., Birgisdottir, H., & Nygaard, F. (2018). Design and construction strategies for reducing embodied impacts from buildings – Case study analysis. *Energy and Buildings*, *166*, 35–47. doi: 10.1016/j.enbuild.2018.01.033.

Maluski, S. P. S., & Gibbs, B. M. (2016). Application of a finite-element model to low-frequency sound insulation in dwellings Application of a finite-element model to low-frequency sound. *Journal of the Acoustical Society of America*, *108*(4), 1741-1751. doi: 10.1121/1.1310355.

Mankiw, N. G., & Weil, D. N. (1989). The baby boom, the baby bust, and the housing market. *Regional Science and Urban Economics*, *19*(2), 235–258. doi: 10.1016/0166-0462(89)90005-7.

Maraveas, C., Wang, Y. C., & Swailes, T. (2014). Fire resistance of 19th century fireproof flooring systems: A sensitivity analysis. *Construction and Building Materials*, *55*, 69–81. doi: 10.1016/j.conbuildmat.2014.01.022.

Marburg, S. (2002). Six boundary elements per wavelength: Is that enough? *Journal of Computational Acoustics*, *10*(01), 25-51. doi: 10.1142/S0218396X02001401.

Marler, R. T., & Arora, J. S. (2004). Survey of multi-objective optimization methods for engineering. *Structural and Multidisciplinary Optimization*, *26*(6), 369-395. doi: 10.1007/s00158-003-0368-6

Marsh, E., Allen, S., & Hattam, L. (2023). Tackling uncertainty in life cycle assessments for the built environment: A review. *Building and Environment*, *231*, 109941. doi: 10.1016/j.buildenv.2022.109941.

Maschke, C. (2016). Health effects of annoyance induced by neighbor noise. *Noise Control Engineering Journal*, *55*(3), 348-356. doi: 10.3397/1.2741308.

Mata-Falcón, J., Bischof, P., Anton, A., Burger, J., Ranaudo, F., Jipa, A., Gebhard, L., Reiter, L., Huber, T., Lloret-Fritschi, E., Mele, T. Van, Block, P., Gramazio, F., Kohler, M., Dillenburger, B., & Kaufmann, W. (2022). Digitally fabricated ribbed concrete floor slabs: a sustainable solution for construction. *RILEM Technical Letters*, *7*, 68–78. doi: 10.21809/rilemtechlett.2022.161.

McCord, K. H., Dillon, H. E., Gunderson, P., Carlson, S., Phillips, A. R., Griechen, D., & Antonopoulos, C. A. (2024). Strategies for connecting whole-building LCA to the low-carbon design process. *Environmental Research: Infrastructure and Sustainability*, *4*(1), 015002. doi: 10.1088/2634-4505/ad17ce.

McKay, D. I. A., Staal, A., Abrams, J. F., Winkelmann, R., Sakschewski, B., Loriani, S., Fetzer, I., Cornell, S. E., Rockström, J., & Lenton, T. M. (2022). Exceeding 1.5°C global warming could trigger multiple climate tipping points. *Science*, *377*(6611). doi: 10.1126/science.abn7950.

Mehta, M., Johnson, J., & Rocafort, J. (1999). *Architectural acoustics: principles and design*. Prentice Hall.

Meibodi, A., Jipa, A., Giesecke, E., Shammas, D., Bernhard, M., Leschok, M., Graser, K., Dillenburger, B. (2018). Smart slab: Computational design and digital fabrication of a lightweight concrete slab. *Recalibration on Imprecision and Infidelity - Proceedings of the 38th Annual Conference of the Association for Computer Aided Design in Architecture, ACADIA 2018*, 434–443. doi: 10.3929/ethz-b-000614681.

Mendez Echenagucia, T., Roozen, N. B., & Block, P. (2016). Minimization of Sound Radiation In Doubly Curved Shallow Shells By Means of Structural Stiffness. *Proceedings of the IASS Annual Symposium 2016 "Spatial Structures in the 21st Century."*

Mendez Echenagucia, T., Sassone, M., Astolfi, A., Shtrepi, L., & Van der Harten, A. (2014). Multi-Objective Acoustic and Structural design of shell structures for concert halls. In *Proceedings of the IASS-SLTE 2014 Symposium "Shells, Membranes and Spatial Structures: Footprints."* IASS.

Menna, C., Mata-Falcón, J., Bos, F. P., Vantyghem, G., Ferrara, L., Asprone, D., Salet, T., & Kaufmann, W. (2020). Opportunities and challenges for structural engineering of digitally fabricated concrete. *Cement and Concrete Research*, *133*, 106079. doi: 10.1016/j.cemconres.2020.106079.

Miller, D., Doh, J. H., & Mulvey, M. (2015). Concrete slab comparison and embodied energy optimisation for alternate design and construction techniques. *Construction and Building Materials*, *80*, 329–338. doi: 10.1016/j.conbuildmat.2015.01.071.

Miller, S. A., John, V. M., Pacca, S. A., & Horvath, A. (2018). Carbon dioxide reduction potential in the global cement industry by 2050. *Cement and Concrete Research*, *114*, 115–124. doi: 10.1016/j.cemconres.2017.08.026.

Miller, S. A., Monteiro, P. J. M., Ostertag, C. P., & Horvath, A. (2016). Concrete mixture proportioning for desired strength and reduced global warming potential. *Construction and Building Materials*, *128*, 410–421. doi: 10.1016/j.conbuildmat.2016.10.081.

Minunno, R., O'Grady, T., Morrison, G. M., & Gruner, R. L. (2021). Investigating the embodied energy and carbon of buildings: A systematic literature review and meta-analysis of life cycle assessments. *Renewable and Sustainable Energy Reviews*, *143*, 110935. doi: 10.1016/j.rser.2021.110935.

Mohamed, A. M. O., Paleologos, E. K., & Howari, F. M. (2020). Noise pollution and its impact on human health and the environment. In *Pollution Assessment for Sustainable Practices in Applied Sciences and Engineering,* Ch. 9, 975–1026. Elsevier. doi:10.1016/B978-0-12-809582-9.00019-0.

Monteiro, C., Machimbarrena, M., De La Prida, D., & Rychtarikova, M. (2016). Subjective and objective acoustic performance ranking of heavy and light weight walls. *Applied Acoustics*, *110*, 268–279. doi: 10.1016/j.apacoust.2016.03.008.

Moncaster, A., Malmqvist, T., Forman, T., Pomponi, F., & Anderson, J. (2022). Embodied carbon of concrete in buildings, Part 2: are the messages accurate? *Buildings and Cities*, *3*(1), 334–355. doi: 10.5334/bc.199.

Mouring, S. E., & Ellingwood, B. R. (1994). Guidelines to minimize floor vibrations from building occupants. *Journal of Structural Engineering*, *120*(2), 507-526. doi: 10.1061/(ASCE)0733-9445(1994)120:2(507).

Mouton, L., Allacker, K., & Röck, M. (2023). Bio-based building material solutions for environmental benefits over conventional construction products–Life cycle assessment of regenerative design strategies (1/2). *Energy and Buildings*, *282*, 112767. doi: 10.1016/j.enbuild.2022.112767.

Mueller, C. T. (2014). Computational Exploration of the Structural Design Space. *MIT*. Available on: http://dspace.mit.edu/handle/1721.1/91293.

Mueller, C. T., & Ochsendorf, J. A. (2015). Combining structural performance and designer preferences in evolutionary design space exploration. *Automation in Construction*, *52*, 70–82. doi: 10.1016/j.autcon.2015.02.011.

Müller, H. S., Haist, M., & Vogel, M. (2014). Assessment of the sustainability potential of concrete and concrete structures considering their environmental impact, performance and lifetime. *Construction and Building Materials*, *67*(PART C), 321–337. doi: 10.1016/j.conbuildmat.2014.01.039.

Müller-Trapet, M., Möller, K., Choi, Y. J., & Zeitler, B. (2020). A subjective study of source types and rating methods for impact sounds in buildings. In *Proceedings of 2020 International Congress on Noise Control Engineering, INTER-NOISE 2020*, *261*(5), 1233-1240.

Murray, T. M., Allen, D., Ungar, E. E., & Davis, D. B. (2016). *Design Guide 11: Vibrations of steel-framed structural systems due to human activity*. American Institute of Steel Construction (AISC).

Nandy, A. K., & Jog, C. S. (2012). Optimization of vibrating structures to reduce radiated noise. *Structural and Multidisciplinary Optimization*, *45*(5), 717–728. doi: 10.1007/s00158-011-0737-5.

National Ready Mixed Concrete Association. Concrete product EPDs verified under NRMCA's EPD. NRMCA. First accessed on February 13th, 2023. Retrieved from:

https://www.nrmca.org/association-resources/sustainability/environmental-product-declarations/.

National Ready Mixed Concrete Association (NRMCA). (2022). A Cradle-to-Gate Life Cycle Assessment of Ready-Mixed Concrete Manufactured by NRMCA Members – Version 3.2. NRMCA. Retrieved from: https://www.nrmca.org/wp-content/uploads/2022/02/NRMCA_LCAReportV3-2_20220224.pdf.

National Ready Mixed Concrete Association (NRMCA). (2022). *Compilation of Acoustics Information for Concrete Construction and Other Materials.* NRMCA

Navai, M., & Veitch, J. A. (2003). Acoustic satisfaction in open-plan offices: review and recommendations. Review and Recommendations Research Report RR-151.

Nawy, E. G. (1985). Reinforced concrete. Prentice-Hall.

Nehdi, M. L., Marani, A., & Zhang, L. (2024). Is net-zero feasible: Systematic review of cement and concrete decarbonization technologies. *Renewable and Sustainable Energy Reviews*, *191*, 114169. doi: 10.1016/j.rser.2023.114169.

Neves E Sousa, A., & Gibbs, B. M. (2011). Low frequency impact sound transmission in dwellings through homogeneous concrete floors and floating floors. *Applied Acoustics*, *72*(4), 177–189. doi: 10.1016/j.apacoust.2010.11.006.

New York State. (2015). International Residential Code, 2nd Edition. Adapted from the International Code Council, 2015 International Residential Code.

Nivison, M. E., & Endresen, I. M. (1993). An analysis of relationships among environmental noise, annoyance and sensitivity to noise, and the consequences for health and sleep. *Journal of Behavioral Medicine*, *16*(3), 257–276. doi: 10.1007/BF00844759.

Northwood, T. D. (1962). Sound-Insulation Ratings and the New ASTM Sound-Transmission Class. *The Journal of the Acoustical Society of America*, *34*(4), 493–501. doi: 10.1121/1.1918155.

Northwood, T. D. (1964). Sound Insulation and the Apartment Dweller. *Journal of the Acoustical Society of America*, *36*(4), 725–728. doi: 10.1121/1.1919053.

Nukah, P. D., Abbey, S. J., Booth, C. A., & Nounu, G. (2022). Optimisation of Embodied Carbon and Compressive Strength in Low Carbon Concrete. *Materials*, *15*(23). doi: 10.3390/ma15238673.

Ochsendorf, J. (2010). *Guastavino Vaulting, The Art of Structural Tile*. Princeton Architectural Press.

Oh, B. K., Glisic, B., Lee, S. H., Cho, T., & Park, H. S. (2019). Comprehensive investigation of embodied carbon emissions, costs, design parameters, and serviceability in optimum green construction of two-way slabs in buildings. *Journal of Cleaner Production*, *222*, 111–128. doi: 10.1016/j.jclepro.2019.03.003.

Olsson, J. A., Miller, S. A., & Alexander, M. G. (2023). Near-term pathways for decarbonizing global concrete production. *Nature Communications*, *14*(1), 4574. doi: 10.1038/s41467-023-40302-0.

Orr, J., Drewniok, M. P., Walker, I., Ibell, T., Copping, A., & Emmitt, S. (2019). Minimising energy in construction: Practitioners' views on material efficiency. *Resources, Conservation and Recycling*, *140*, 125–136. doi: 10.1016/j.resconrec.2018.09.015.

Oval, R., Nuh, M., Costa, E., Abo, O., Orr, J., & Shepherd, P. (2023). A prototype low-carbon segmented concrete shell building floor system. *Structures*, *49*, 124–138. doi: 10.1016/j.istruc.2023.01.063.

Pacheco, J., de Brito, J., Chastre, C., & Evangelista, L. (2019). Experimental investigation on the variability of the main mechanical properties of concrete produced with coarse recycled concrete aggregates. *Construction and Building Materials*, *201*, 110–120. doi: 10.1016/j.conbuildmat.2018.12.200.

Pan, W., & Teng, Y. (2021). A systematic investigation into the methodological variables of embodied carbon assessment of buildings. *Renewable and Sustainable Energy Reviews*, *141*, 110840. doi: 10.1016/j.rser.2021.110840.

Park, H. K., & Bradley, J. S. (2009). Evaluating standard airborne sound insulation measures in terms of annoyance, loudness, and audibility ratings. *The Journal of the Acoustical Society of America*, *126*(1), 208-219. doi: 10.1121/1.3147499.

Park, S. H., & Lee, P. J. (2019). Reaction to floor impact noise in multi-storey residential buildings: The effects of acoustic and non-acoustic factors. *Applied Acoustics*, *150*, 268–278. doi: 10.1016/j.apacoust.2019.02.021.

Pastor, M., Binda, M., & Harčarik, T. (2012). Modal assurance criterion. *Procedia Engineering*, *48*, 543–548. doi: 10.1016/j.proeng.2012.09.551.

Paulson, B. C. (1976). *Designing to reduce construction costs. Journal of the construction division, 102*(4), 587-592. doi: 10.1061/JCCEAZ.0000639.

Pauly, J. J. (1984). The Great Chicago Fire as a National Event. In *Source: American Quarterly*, *36*(5).

Pavic, A. (2002). Vibration serviceability of long-span concrete building floors. Part 1: review of background information. *The Shock and Vibration Digest*.

Pavic, A., Reynolds, P., Waldron, P., & Bennett, K. (2001). Dynamic modelling of post-tensioned concrete floors using finite element analysis. *Finite Elements in Analysis and Design*, *37*(4), 305–323. doi: 10.1016/S0168-874X(00)00045-7.

Peeters, B., Van der Auweraer, H., Guillaume, P., & Leuridan, J. (2004). The PolyMAX frequency-domain method: a new standard for modal parameter estimation? *Shock and Vibration*, *11*(3,4), 395–409.

Pereira, A., Godinho, L., Mateus, D., Ramis, J., & Branco, F. G. (2014). Assessment of a simplified experimental procedure to evaluate impact sound reduction of floor coverings. *Applied Acoustics*, *79*, 92–103. doi: 10.1016/j.apacoust.2013.12.014.

Pérez Caldentey, A., Diego, Y. G., Ariñez Fernández, F., & Santos, A. P. (2021). Testing robustness: A full-scale experimental test on a two-storey reinforced concrete frame with solid slabs. *Engineering Structures*, *240*., 112411. doi: 10.1016/j.engstruct.2021.112411.

Pomponi, F., & Moncaster, A. (2016). Embodied carbon mitigation and reduction in the built environment – What does the evidence say? *Journal of Environmental Management*, *181*, 687–700). doi: 10.1016/j.jenvman.2016.08.036.

Pomponi, F., & Moncaster, A. (2018). Scrutinising embodied carbon in buildings: The next performance gap made manifest. In *Renewable and Sustainable Energy Reviews*, *81*, 2431–2442. doi: 10.1016/j.rser.2017.06.049.

Prakashan, L. V., George, J., Edayadiyil, J. B., & George, J. M. (2016). Experimental Study on the Flexural Behavior of Hollow Core Concrete Slabs. *Applied Mechanics and Materials*, *857*, 107–112. doi: 10.4028/www.scientific.net/amm.857.107.

Precast/Prestressed Concrete Institute. (2015). PCI Manual for the Design of Hollow Core Slabs and Walls, 8th Edition. The Donohue Group, Inc.

Portland Cement Association. (2005). An Engineers Guide to: Economical Concrete Floor Systems. Portland Cement Association.

Purnell, P., & Black, L. (2012). Embodied carbon dioxide in concrete: Variation with common mix design parameters. *Cement and Concrete Research*, *42*(6), 874–877. doi: 10.1016/j.cemconres.2012.02.005.

Rademacher, H. J. (1955). Subjective assessment of sound insulation investigated by electrically reproduced sound insulation curves. *Acustica*, *5*, 19–27.

Qian, C., Ménard, S., Bard, D., & Negreira, J. (2019). Development of a vibroacoustic stochastic finite element prediction tool for a CLT floor. *Applied Sciences, 9*(6). doi: 10.3390/app9061106.

Ranaudo, F., van Mele, T., & Block, P. (2021). A low-carbon, funicular concrete floor system: Design and engineering of the HiLo floors. In *IABSE Congress, Ghent 2021: Structural Engineering for Future Societal Needs*, 2016–2024. doi: 10.2749/ghent.2021.2016.

Rasmussen, B. (2010). Sound insulation between dwellings - Requirements in building regulations in Europe. *Applied Acoustics*, *71*, 373–385. doi: 10.1016/j.apacoust.2009.08.011.

Rasmussen, B., & Ekholm, O. (2019). Is noise annoyance from neighbours in multi-storey housing associated with fatigue and sleeping problems? *Proceedings of the International Congress on Acoustics*, *September*, 5071–5078. doi: 10.18154/RWTH-CONV-239984.

Rasmussen, B., & Ekholm, O. (2021). Neighbour noise in multi-storey housing-Annoyance and potential health effects. In *INTER-NOISE and NOISE-CON Congress and Conference Proceedings*, *263*(4), 2783-2792. doi: 10.3397/IN-2021-2228.

Ravikumar, D., Zhang, D., Keoleian, G., Miller, S., Sick, V., & Li, V. (2021). Carbon dioxide utilization in concrete curing or mixing might not produce a net climate benefit. *Nature Communications*, *12*(1). doi: 10.1038/s41467-021-21148-w.

Reinhold, S., & Hopkins, C. (2021). Sampling procedures on reception plates to quantify structure-borne sound power from machinery. *Applied Acoustics*, *172*, 107649. doi: 10.1016/j.apacoust.2020.107649.

Reyna, J. L., & Chester, M. V. (2015). The growth of urban building stock: Unintended lock-in and embedded environmental effects. *Journal of Industrial Ecology*, *19*(4), 524-537. doi: 10.1111/jiec.12211.

Reynders, E., Langley, R. S., Dijckmans, A., & Vermeir, G. (2014). A hybrid finite element - Statistical energy analysis approach to robust sound transmission modeling. *Journal of Sound and Vibration*, *333*(19), 4621–4636. doi: 10.1016/j.jsv.2014.04.051.

Rindel, J. H. (2015). *On the influence of low frequencies on the annoyance of noise from neighbours. August 2003*.

Röck, M., Saade, M. R. M., Balouktsi, M., Rasmussen, F. N., Birgisdottir, H., Frischknecht, R., Habert, G., Lützkendorf, T., & Passer, A. (2020). Embodied GHG emissions of buildings–The hidden challenge for effective climate change mitigation. *Applied Energy*, *258*, 114107. doi: 10.1016/j.apenergy.2019.114107.

Roozen, N. B., Leclère, Q., Urbán, D., Méndez Echenagucia, T., Block, P., Rychtáriková, M., & Glorieux, C. (2018). Assessment of the airborne sound insulation from mobility vibration measurements; a hybrid experimental numerical approach. *Journal of Sound and Vibration*, *432*, 680–698. doi: 10.1016/j.jsv.2018.06.058.

Roy D. M. (1999). Alkali activated cements, opportunities and challenges. *Cement and Concrete Research*, *29*, 249–254. doi: 10.1016/S0008-8846(98)00093-3.

Rychtáriková, M., Muellner, H., Chmelík, V., Roozen, N. B., Urbán, D., Garcia, D. P., & Glorieux, C. (2016). Perceived loudness of neighbour sounds heard through heavy and light-weight walls with equal R w+ C 50–5000. *Acta Acustica united with Acustica*, *102*(1), 58-66. doi: 10.3813/AAA.918924.

Ryu, J., Sato, H., Kurakata, K., Hiramitsu, A., Tanaka, M., & Hirota, T. (2010). Subjective ratings of heavy-weight floor impact sounds in wood frame construction. *Acoustical science and technology*, *31*(5), 371-375. doi: 10.1250/ast.31.371.

Sahab, M. G., Ashour, A. F., & Toropov, V. V. (2005). Cost optimisation of reinforced concrete flat slab buildings. *Engineering Structures*, *27*(3), 313-322. doi: 10.1016/j.engstruct.2004.10.002.

Salama, W. (2017). Design of concrete buildings for disassembly: An explorative review. *International Journal of Sustainable Built Environment*, 6(2), 617–635. doi: 10.1016/j.ijsbe.2017.03.005.

Salomão, Í. L., & Pinheiro, P. R. (2023). Exploring Analytical Hierarchy Process for Multicriteria Assessment of Reinforced Concrete Slabs. *Applied Sciences*, *13*(17), 9604. doi: 10.3390/app13179604.

Sandanayake, M., Lokuge, W., Zhang, G., Setunge, S., & Thushar, Q. (2018). Greenhouse gas emissions during timber and concrete building construction-A scenario based comparative case study. *Sustainable Cities and Society*, *38*, 91–97. doi: 10.1016/j.scs.2017.12.017.

Savage, K., Hoban, N., & Peters, B. (2021). Gradient Acoustic Surfaces: The Design, Simulation, Robotic Fabrication of a Prototype Wall. In *International Conference on Computer-Aided Architectural Design Futures*, 360-377. doi: 10.1007/978-981-19-1280-1_23.

Schultz, T. J. (1964). Impact-Noise Recommendations for the FHA. *Journal of the Acoustical Society of America*, *36*(4), 729–739. doi: 10.1121/1.1919055.

Schnieders, J., Eian, T. D., Filippi, M., Florez, J., Kaufmann, B., Pallantzas, S., Paulsen, M., Reyes, E., Wassouf, M., & Yeh, S. C. (2020). Design and realisation of the Passive House concept in different climate zones. *Energy Efficiency*, *13*(8), 1561-1604. doi: 10.1007/s12053-019-09819-6.

Schwarz, B. J., & Richardson, M. H. (1999). Experimental modal analysis. *CSI Reliability week*, *35*(1), 1-12.

Schweiker, M., Ampatzi, E., Andargie, M. S., Andersen, R. K., Azar, E., Barthelmes, V. M., Berger, C., Bourikas, L., Carlucci, S., Chinazzo, G., Edappilly, L. P., Favero, M., Gauthier, S., Jamrozik, A., Kane, M., Mahdavi, A., Piselli, C., Pisello, A. L., Roetzel, A., Rysanek, A., Sharma, K., Zhang S. (2020). Review of multi-domain approaches to indoor environmental perception and behaviour. *Building and Environment*, *176*, 106804. doi: 10.1016/j.buildenv.2020.106804.

Setareh, M. & Darvas, R. (2017). Concrete Structures, Second Edition. Springer International Publishing Switzerland.

Seyedabadi, M. R., Karrabi, M., Shariati, M., Karimi, S., Maghrebi, M., & Eicker, U. (2024). Global building life cycle assessment: Comparative study of steel and concrete frames across European Union, USA, Canada, and Australia building codes. *Energy and Buildings*, *304*, 113875. doi: 10.1016/j.enbuild.2023.113875.

Shafigh, P., Asadi, I., & Mahyuddin, N. B. (2018). Concrete as a thermal mass material for building applications - A review. *Journal of Building Engineering*, *19*, 14–25. doi: 10.1016/j.jobe.2018.04.021.

Shah, I. H., Miller, S. A., Jiang, D., & Myers, R. J. (2022). Cement substitution with secondary materials can reduce annual global CO2 emissions by up to 1.3 gigatons. *Nature Communications*, *13*(1), 1–11. doi: 10.1038/s41467-022-33289-7.

Sharp, B. H. (1978). Prediction Methods for the Sound Transmission of Building Elements. *Noise Control Eng*, *11*(2), 53–63. doi: 10.3397/1.2832099.

Simonen, K., Rodriguez, B. X., & De Wolf, C. (2017). Benchmarking the Embodied Carbon of Buildings. *Technology Architecture and Design*, *1*(2), 208–218. doi: 10.1080/24751448.2017.1354623.

Singer-Vine J., & Jain, S. (2023). Pdfplumber (v. 0.10.1): Pypi Python Library. First accessed on February 13th, 2023. Retried from: https://pypi.org/project/pdfplumber/#description.

Solomon, S., Plattner, G.-K., Knutti, R., & Friedlingstein, P. (2009). Irreversible climate change due to carbon dioxide emissions. *Proceedings of the National Academy of Science*. *106*(6), 1704-1709. doi: 10.1073/pnas.0812721106.

Sory, L. Y. K. (2023). *Physics-based Estimates of Structural Material Quantities for Urban-level Embodied Carbon Assessment in Buildings*. M.S. Thesis, Massachusetts Institute of Technology. Accessed on: https://hdl.handle.net/1721.1/151703.

Stefaniuk, D. (2023). Cementing CO 2 into C-S-H: A step toward concrete carbon neutrality. *PNAS Nexus*, *2*(3), 1–5. doi: 1093/pnasnexus/pgad052.

Stewart, M. A., & Craik, R. J. M. (2000). Impact sound transmission through a floating floor on a concrete slab. *Applied Acoustics*, *59*(4), 353–372. doi: 10.1016/S0003-682X(99)00030-4.

Stringer, M., & Comber, M. (2015). Differences in embodied carbon assessments of structural systems. In *SEAOC Convention Proceedings*, 131-141.

Svinkin, M. R. (2004). Minimizing construction vibration effects. *Practice periodical on structural design and construction*, *9*(2), 108-115. doi: 10.1061/(ASCE)1084-0680(2004)9:2(108).

Tahmasebinia, F., Yip, C. S., Lok, C. F., Sun, Y., Wu, J., Sepasgozar, S. M. E., & Marroquin, F. A. (2022). Dynamic Behavior of the Composite Steel–Concrete Beam Floor Systems under Free and Forced Vibration. *Buildings*, *12*(3), 320. doi: 10.3390/BUILDINGS12030320.

Tang, Y., Mak, K., & Zhao, Y. F. (2016). A framework to reduce product environmental impact through design optimization for additive manufacturing. *Journal of Cleaner Production, 137*, 1560–1572. doi: 10.1016/j.jclepro.2016.06.037.

Teng, Y., Li, C. Z., Shen, G. Q., Yang, Q., & Peng, Z. (2023). The impact of life cycle assessment database selection on embodied carbon estimation of buildings. *Building and Environment*, *243*, 110648. doi: 10.1016/j.buildenv.2023.110648.

Teng, Y., & Pan, W. (2020). Estimating and minimizing embodied carbon of prefabricated high-rise residential buildings considering parameter, scenario and model uncertainties. *Building and Environment*, *180*, 106951. doi: 10.1016/j.buildenv.2020.106951

Thilakarathna, P. S. M., Seo, S., Baduge, K. S. K., Lee, H., Mendis, P., & Foliente, G. (2020). Embodied carbon analysis and benchmarking emissions of high and ultra-high strength concrete using machine learning algorithms. *Journal of Cleaner Production*, *262*, 121281. doi: 10.1016/j.jclepro.2020.121281.

Thomas, H. R., & Rees, S. W. (1999). The thermal performance of ground floor slabs - a full scale in-situ experiment. *Building and Environment*, *34*(2), 139–164. doi: 10.1016/S0360-1323(98)00001-8.

Thormark, C. (2001). Conservation of energy and natural resources by recycling building waste. *Resources, Conservation and Recycling*, *33*(2), 113–130. doi: 10.1016/S0921-3449(01)00078-7.

Thormark, C. (2002). A low energy building in a life cycle - Its embodied energy, energy need for operation and recycling potential. *Building and Environment*, *37*(4), 429–435. doi: 10.1016/S0360-1323(01)00033-6.

Torelli, G., Fernández, M. G., & Lees, J. M. (2020). Functionally graded concrete: Design objectives, production techniques and analysis methods for layered and continuously graded elements. *Construction and Building Materials*, *242*, 118040. doi: 10.1016/j.conbuildmat.2020.118040.

Tošić, N., Marinković, S., Dašić, T., & Stanić, M. (2015). Multicriteria optimization of natural and recycled aggregate concrete for structural use. *Journal of Cleaner Production*, *87*(1), 766–776. doi: 10.1016/j.jclepro.2014.10.070.

Trinh, H. T. M. K., Chowdhury, S., Doh, J. H., & Liu, T. (2021). Environmental considerations for structural design of flat plate buildings – Significance of and interrelation between different design variables. *Journal of Cleaner Production*, *315*, 128123. doi: 10.1016/j.jclepro.2021.128123.

Turrin, M., Von Buelow, P., & Stouffs, R. (2011). Design explorations of performance driven geometry in architectural design using parametric modeling and genetic algorithms. doi: 10.1016/j.aei.2011.07.009.

United Nations. (2015). The Paris Agreement. In report of the conference of the parties to the United Nations framework convention on climate change *(21st session, 2015: Paris)*.

United Nations Environment Programme (UNEP). (2020). *The 2020 Global Status Report for Buildings and Construction*.

United Nations Environment, Scrivener, K. L., John, V. M., & Gartner, E. M. (2018). Eco-efficient cements: Potential economically viable solutions for a low-CO2 cement-based materials industry. *Cement and concrete Research*, *114*, 2-26. doi: 10.1016/j.cemconres.2018.03.015.

Valente, M., Sibai, A., & Sambucci, M. (2019). Extrusion-Based Additive Manufacturing of Concrete Products: Revolutionizing and Remodeling the Construction Industry. *Journal of Composites Science*, *3*(3), 88. doi: 10.3390/jcs3030088.

Vardaxis, N. G., & Bard, D. (2018a). Review of acoustic comfort evaluation in dwellings: part II—impact sound data associated with subjective responses in laboratory tests. *Building Acoustics*, *25*(4), 171–192. doi: 10.1177/1351010X18788685.

Vardaxis, N. G., & Bard, D. (2018b). Review of acoustic comfort evaluation in dwellings: Part III—airborne sound data associated with subjective responses in laboratory tests. *Building Acoustics* *25*(4), 289–305. doi: 10.1177/1351010X18788685.

Vardaxis, N. G., Bard, D., & Persson Waye, K. (2018c). Review of acoustic comfort evaluation in dwellings—part I: Associations of acoustic field data to subjective responses from building surveys. *Building Acoustics*, *25*(2), 151–170. doi: 10.1177/1351010X18762687.

Vardoulakis, S., & Kinney, P. (2019). Grand challenges in sustainable cities and health. *Frontiers in Sustainable Cities*, *1*, 7. doi: 10.3389/frsc.2019.00007.

Varela, W. D., & Battista, R. C. (2011). Control of vibrations induced by people walking on large span composite floor decks. *Engineering Structures*, *33*(9), 2485–2494. doi: 10.1016/j.engstruct.2011.04.021.

Venkatarama Reddy, B., & Jagadish, K. S. (2003). Embodied energy of common and alternative building materials and technologies. *Energy and Buildings*, *35*(2), 129-137. doi: 10.1016/S0378-7788(01)00141-4.

Victoria, M. F., & Perera, S. (2018). Parametric embodied carbon prediction model for early stage estimating. *Energy and Buildings*, *168*, 106–119. doi: 10.1016/j.enbuild.2018.02.044.

Wang, P., Wang, Y., Zou, C., & Guo, J. (2017). A preliminary investigation of noise impact within metro stations in the urban city of Guangzhou, China. *Environmental Science Pollutant*, 11371–11382. doi: 10.1007/s11356-017-8776-0.

Wangler, T., Lloret, E., Reiter, L., Hack, N., Gramazio, F., Kohler, M., Bernhard, M., Dillenburger, B., Buchli, J., Roussel, N., & Flatt, R. (2016). Digital Concrete: Opportunities and Challenges. *RILEM Technical Letters*, *1*, 67. doi: 10.21809/rilemtechlett.2016.16.

Wangler, T., Roussel, N., Bos, F. P., Salet, T. A. M., & Flatt, R. J. (2019). Digital Concrete: A Review. *Cement and Concrete Research*, *123*, 105780. doi: 10.1016/j.cemconres.2019.105780.

Ward, F. L., & Randall, K. E. (1966). Investigation of the sound isolation of concrete slab floors. *Journal of Sound and Vibration*, *3*(2), 205–215. doi: 10.1016/0022-460x(66)90087-3.

Warnock, A. C. C. (1985). *Factors Affecting Sound Transmission Loss*. National Research Council Canada, Institute for Research in Construction.

Warnock, A. C. C. (1990). *Sound transmission loss measurements through 190 mm and 140 mm blocks with added drywall and through cavity block walls*. National Research Council Canada, Institute for Research in Construction.

Warnock, A. C. C. (1999). Low-frequency impact sound transmission through floor systems. *The Journal of the Acoustical Society of America*, *105*(2), 1259–1259. doi: 10.1121/1.426027.

Warnock, A. C. C. (2005). *Summary report for consortium on fire resistance and sound insulation of floors: sound transmission and impact insulation data*. National Research Council Canada, Institute for Research in Construction.

Warnock, A. C. C., & Birta, J. A. (2000). *Detailed Report for Consortium on Fire Resistance and Sound Insulation of Floors: Sound Transmission and Impact Insulation Data in 1/3 Octave Bands Institute for Research in Construction IRC*. National Research Council Canada, Institute for Research in Construction.

Warrier, G. A., Palaniappan, S., & Habert, G. (2024). Classification of sources of uncertainties in building LCA. *Energy and Buildings*, *305*, 113892. doi: 10.1016/j.enbuild.2024.113892.

Waterhouse, R. V. (1957). On Standard Methods of Measurement in Architectural Acoustics. *The Journal of the Acoustical Society of America*, *29*(5), 544–547. doi: 10.1121/1.1908961.

Watari, T., Cao, Z., Serrenho, A. C., & Cullen, J. (2023). Growing role of concrete in sand and climate crises. Iscience, 26(5), 106782. doi: 10.1016/ j.isci.2023.106782.

WBCSD and ARUP. (2021). Net-zero buildings: Where do we stand? *WBCSD*, 103. Accessed on: https://www.wbcsd.org/Programs/Cities-and-Mobility/Sustainable-Cities/Transforming-the-Built-Environment/Decarbonization/Resources/Net-zero-buildings-Where-do-we-stand.

Weissenburger, J. T. (2004). Room-to-room privacy and acoustical design criteria. *Sound and Vibration*, *38*(2), 14-17.

WGBC. (2019). Bringing embodied carbon upfront: Coordinated action for the building and construction sector to tackle embodied carbon. World Green Building Council.

World Economic Forum (2023). *Scaling Low-Carbon Design and Construction with Concrete: Enabling the Path to Net-Zero for Buildings and Infrastructure*. World Economic Forum (WEF).

Wright, J. K. (2016). *Reinforced Concrete: Mechanics and Design* (Seventh). Pearson Education, Inc.

Wu, H., Liew, A., Van Mele, T., & Block, P. (2020). Analysis and optimisation of a rib-stiffened vaulted floor for dynamic performance. *Engineering Structures*, *213*, 110577. doi: 10.1016/j.engstruct.2020.110577.

Wu, T., Ng, S. T., & Chen, J. (2022). Deciphering the CO2 emissions and emission intensity of cement sector in China through decomposition analysis. *Journal of Cleaner Production*, *352*, 131627. doi: 10.1016/j.jclepro.2022.131627.

Xu, X., Yu, J., Wang, S., & Wang, J. (2014). Research and application of active hollow core slabs in building systems for utilizing low energy sources. *Applied Energy*, *116*, 424–435. doi: 10.1016/j.apenergy.2013.09.064.

Yadav, M., Cabrera, D., Love, J., Kim, J., Holmes, J., Caldwell, H., & de Dear, R. (2019). Reliability and repeatability of ISO 3382-3 metrics based on repeated acoustic measurements in open-plan offices. *Applied Acoustics*, *150*, 138–146. doi: 10.1016/j.apacoust.2019.02.010.

Yang, Y., Mace, B. R., & Kingan, M. J. (2018). Wave and finite element method for predicting sound transmission through finite multi-layered structures with fluid layers. *Computers and Structures*, *204*, 20–30. doi: 10.1016/j.compstruc.2018.04.003.

Yeo, D., & Gabbai, R. D. (2011). Sustainable design of reinforced concrete structures through embodied energy optimization. *Energy and Buildings*, *43*(8), 2028–2033. doi: 10.1016/j.enbuild.2011.04.014.

Yoo, S. Y., & Jeon, J. Y. (2014). Investigation of the effects of different types of interlayers on floor impact sound insulation in box-frame reinforced concrete structures. *Building and Environment*, *76*, 105–112. doi: 10.1016/j.buildenv.2014.03.008.

Yoro, K. O., & Daramola, M. O. (2020). CO2 emission sources, greenhouse gases, and the global warming effect. In *Advances in carbon capture* (pp. 3–28). Woodhead Publishing.

Zeitz, A., Griffin, C. T., & Dusicka, P. (2019). Comparing the embodied carbon and energy of a mass timber structure system to typical steel and concrete alternatives for parking garages. *Energy and Buildings*, *199*, 126–133. doi: 10.1016/j.enbuild.2019.06.047.

Zeitler, B., Schoenwald, S., & Gover, B. (2013). On the relevance of impact source impedance at low frequencies. *Proceedings of Meetings on Acoustics*, *19*(2013). doi: 10.1121/1.4800957.

Zelickman, Y., & Amir, O. (2022). Optimization of post-tensioned concrete slabs for minimum cost. *Engineering Structures*, *259*, 114132. doi: 10.1016/j.engstruct.2022.114132.

Zelickman, Y., & Guest, J. K. (2023). Construction aware optimization of concrete plate thicknesses. *Engineering Structures*, *296*, 116889. doi: 10.1016/j.engstruct.2023.116889.

Zhang, X., & Zhang, X. (2021). Comparison and sensitivity analysis of embodied carbon emissions and costs associated with rural house construction in China to identify sustainable structural forms. *Journal of Cleaner Production*, *293*. doi: 10.1016/j.jclepro.2021.126190.

Zwicker, E. (1961). Subdivision of the Audible Frequency Range into Critical Bands. *The Journal of the Acoustical Society of America*, *33*(2), 248–248. doi: 10.1121/1.1908630.

Zwicker, E., Flottorp, G., & Stevens, S. S. (1957). Critical Band Width in Loudness Summation. *The Journal of the Acoustical Society of America*, *29*(5), 548–557. doi: 10.1121/1.1908963.

Appendix A

A dataset of ready-mix concrete Environmental Product Declarations[1]

A.1 Motivation

The carbon footprint of a concrete structure is directly affected by the selected concrete mixture proportions. To better understand the influence of different ready-mixed concrete mixtures, data was collected from Environmental Product Declarations (EPDs). Data from 39,213 U.S.A. ready-mix concrete EPDs was obtained from public repositories provided by the American Society for Testing and Materials (ASTM) and the National Ready-Mixed Concrete Association (NRMCA). The EPDs were analyzed using a custom Python script to extract useful information for building designers, sustainability practitioners, and researchers including: life cycle assessment (LCA) midpoints (Global Warming Potential, Ozone Depletion Potential, Acidification Potential, Photochemical Ozone Creation Potential, Abiotic Depletion, Total Waste Disposed, and Consumption of Freshwater), concrete strength classes, declared unit, concrete curing time, production components, concrete manufacturers' company and plant locations, and additional LCA information. Both the dataset and an example of the Python script used to extract the information from the EPDs are provided. This dataset enables users to quickly assess the environmental impacts (including the Global Warming Potential) of different concrete mixtures without the need for extensive data collection and analysis. In summary, this dataset provides environmental information about concrete mixtures to aid civil engineering and architectural researchers, sustainability consultants, building engineering practitioners, and environmental policymakers to make sustainability-informed decisions when specifying concrete in the United States.

[1] Appendix A is adapted from the published work by Broyles et al. "A compiled dataset of ready-mix concrete Environmental Product Declarations for life cycle assessment" (2024). *Data in Brief*, 52, 109852.

A.2 Value of the dataset

The concrete mixture EPD dataset (Broyles, 2023a) allows building designers and sustainability practitioners to easily compare concrete mixtures from various ready-mix concrete plants for the primary LCA midpoints to support sustainable design decisions in the built environment. The LCA midpoints include Global Warming Potential, Ozone Depletion Potential, Acidification Potential, Eutrophication Potential, Photochemical Ozone Creation Potential, Abiotic Depletion (non-fossil fuel and fossil fuel), Total Waste Disposed (non-hazardous and hazardous), and consumption of freshwater. The LCA midpoints are provided for each individual A1, A2, and A3 LCA stage, in addition to the summation of the A1-A3 LCA stages. The dataset contains additional information extracted from the ready-mix concrete EPDs including the mixture description, concrete compressive strength, declared unit, product components, the Life Cycle Inventory products and sources, and the street locations of the ready-mix concrete plants. The locations of the ready-mix concrete producers, including each ready-mix concrete plant, are provided to help consultants identify concrete mixtures that are near their project site.

This dataset can be reused to further understand the environmental effects of the production of different concrete mixtures, which benefits building sustainability consultants, building practitioners, architects, civil and structural engineers, concrete plant manufacturers, structural concrete institutes (e.g., the American Concrete Institute, Structural Engineering Institute) and policymakers. Statistical analyses can be conducted to provide current baseline values of LCA midpoints for concrete mixtures of various compressive strength classes. Lastly, ready-mix concrete manufacturers can compare nationally the environmental footprint of their concrete mixtures to other ready-mix concrete manufacturers, encouraging the development of more sustainable concrete production.

A.3 Methodology

The information in the ready-mix concrete EPD database is obtained from EPDs made available online from ASTM (2023) and NRMCA (2023) between February and April of 2023. The internet links for each EPD are provided in the complimentary dataset (found on https://doi.org/10.1016/j.dib.2023.109852) in the column titled: "EPD Source Link." The ready-mix concrete EPDs were downloaded as PDF files and put into subfolders based on the ready-mix concrete producer. The accompanying Python script (found on https://doi.org/10.1016/j.dib.2023.109852) was written to extract the relevant information from each ready-mix concrete EPD automatically, circumventing the need for manually reading, interpreting, and reporting the information for each EPD. The Python script was run for every ready-mix concrete producer to obtain the compiled EPD dataset, as illustrated in Fig. **A-1**. The Python script was created using Anaconda Navigator 2.4.1, using Jupyter Notebook with Python v. 3.8.

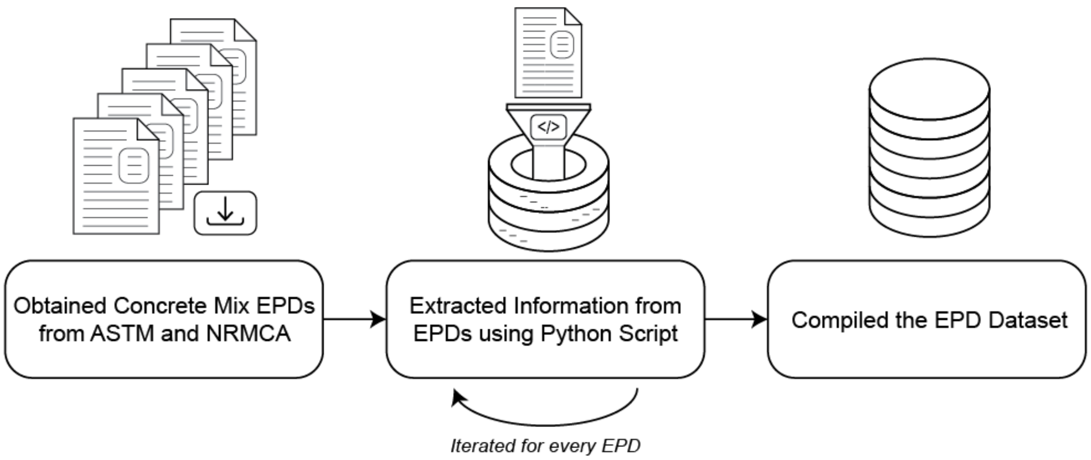

Figure **A-1**: Illustration of how the ready-mix concrete EPD dataset was generated.

The Python script employed the open-access library pdfplumber (Singer-Vine & Jain, 2023) to extract text from each EPD .pdf file. The corresponding .py file can be employed on any Python environment with Python v. 3.0 or newer. The user can define the desired information for extraction (e.g., the LCA midpoints, ready-mix concrete plant locations), and the Python script then extracts the information from the read .pdf file and saves each entry. Once the loop completes, the recorded data is written as a new .csv file which can then be assembled to the EPD dataset and cleaned to match the syntax and numerical format across all ready-mix concrete producers.

A.4 Data description

The ready-mix concrete EPDs were downloaded from public repositories provided by ASTM (2023) and NRMCA (2023), and were mined using the custom Python script (see the.py file in the supplementary materials on https://doi.org/10.1016/j.dib.2023.109852) to extract key information from the EPDs. The EPDs were followed according to ISO 14040 (2006), ISO 14044 (2006), and ISO 21930 (2017). Table **A-1** outlines the information obtained from the EPDs and presented in the dataset, including the ready-mixed concrete manufacturer, ready-mixed concrete plant location, general EPD information, engineering information regarding the concrete mixture proportions, LCA midpoints, and the Life Cycle Inventory (LCI) variability, and sources of LCI data as reported in the EPDs.

Table **A-1**: The column headers in the EPD dataset, grouped by category.

Category	Column Header
Concrete Manufacturer Information	Concrete Company
	Company Location (Street, City, State, Zip)
	Concrete Plant
	Plant Location (Street, City, State, Zip)
General EPD Information	EPD Program Operator
	EPD Date of Issue
	EPD Valid Until Date
Concrete Information	Mix Label
	Mix Description
	Concrete Compressive Strength
	Concrete Curing Time
	Declared Unit
	Product Components
Life Cycle Assessment Midpoints	Global Warming Potential (A1-A3, A1, A2, A3) in kg CO_2-eq
	Ozone Depletion Potential (A1-A3, A1, A2, A3) in kg CFC-11-eq
	Acidification Potential (A1-A3, A1, A2, A3) in kg SO_2-eq
	Eutrophication Potential (A1-A3, A1, A2, A3) in kg N-eq
	Photochemical Ozone Creation Potential (A1-A3, A1, A2, A3) in kg O_3-eq
	Abiotic Depletion, Non-fossil (A1-A3, A1, A2, A3) in kg Sb-eq
	Abiotic Depletion, Fossil (A1-A3, A1, A2, A3) in MJ
	Total Waste Disposed, Hazardous & Non-hazardous (A1-A3, A1, A2, A3) in kg

	Consumption of Freshwater (A1-A3, A1, A2, A3) in m^3
Life Cycle Inventory Variability	Percent Mixing Truck Energy
	LCI Manufacturing Variability
	LCI Cement Accounts for Percent Energy
	LCI Cement Impact Variation
Life Cycle Inventory Data Sources	Admixture (accelerating)
	Admixture (air-entraining)
	Admixture (hardening accelerator)
	Admixture (other)
	Admixture (plasticizing)
	Admixture (retarding)
	Admixture (superplasticizing)
	Admixture (waterproofing)
	Aggregate (crushed)
	Aggregate (lightweight)
	Aggregate (natural)
	Aggregate (other)
	Barge Transport
	Carbon Cure
	Cleaning Chemicals
	Diesel
	Electricity
	Fly Ash
	Municipal Water
	Natural Gas
	Non-Hazardous Solid Waste
	Oils, Lubricants and Greases
	Portland Cement
	Portland Limestone Cement
	Propane
	Rail Transport
	Ship Transport
	Silica Fume
	Slag Cement
	Truck Transport
	Other
Internet Link / Source to Access the EPD	EPD Source Link

A key aim of this dataset was to provide high fidelity information of the environmental impacts for current concrete mixtures. Existing baseline reports including the CLF (2021) and NRMCA (2022) reports exclude useful information, such as the complete list of product components in a concrete mixture and the primary sources of LCI data. Additionally, this dataset represents a broad distribution of ready-mixed concrete EPDs currently available across the U.S.A. Ready-mix concrete EPDs from 37 different ready-mixed concrete manufacturers and 389 unique ready-mixed concrete plants were collected, as detailed in Table **A-2**. Fig. **A-2** shows the geographic distribution of EPDs.

Table **A-2**: Concrete manufacturers and concrete plants (alphabetized).

Ready-Mixed Concrete Manufacturer	Ready-Mixed Concrete Plants
Altaview Concrete	American Fork Plant, Logan Plant, North Salt Lake Plant, West Haven Plant, West Jordan Plant
Argos	Armour Drive Plant, Atlanta Division Plant, Doraville Plant, Glenwood Plant, Smyrna Plant
AVR Inc. & Affiliates	Apple Valley Plant, Buffalo Plant, Burnsville Plant, Elk River Plant, Ham Lake Plant, Maple Grove Plant, Monticello Plant, South St. Paul Plant
Bayview Redi Mix Inc.	Bayview Redi Mix Plant
BURNCO Colorado	Denver Plant, Jeffco Plant, Windsor Plant
Cadman / Heidelberg Materials	Bellevue Plant, Everett-Smith Plant, Ferndale Plant, Foster Road Plant, Issaquah Plant, Orchards Plant, Port of Portland Plant, Redmond Plant, Seattle Plant, Sky River Plant, Woodinville Plant
CEMEX	19th Avenue Plant, 34th Avenue Plant, 7th Street Plant, Alabaster-Pelham Plant, Alpharetta-North Fulton Plant, Antioch Plant, Apache Junction Plant, Apex Plant, Arcola Rail Yard Plant, Baymeadows Plant, Baytown Plant, Berkeley Plant, Big Bend Plant, Bradenton Plant, Brownsville Plant, Buckeye Plant, Buford (RMUSA) Plant, Bunnell North Plant, Camp Verde Plant, Cantonment (Dual) Plant, Carroll Canyon Plant, Carson City Plant, Cemco 10 Moorsville Plant, Central South Plant, Chattanooga Jersey Plant, Chattanooga River Plant, Cocoa Plant, College Park Plant, Columbia Plant, Compton Plant, Concord Plant, Coolidge Plant, Corona RM Plant, Cullman Plant, Cutten Road Plant, Dalton Plant, Daphne Plant, Davenport RK Plant, Delray Plant, Demopolis Plant, Dothan Plant, Douglasville Plant, Downtown-Marietta Plant, Downtown SA RM Plant, East Orlando Plant, Edinburg Plant, Ehren Cut-Off Plant, Ellington Plant, Enterprise Plant, Fairfield Portable Plant, Farmersville Plant, Flagstaff Plant, Florence-Industrial Plant, Fontana RM Plant, Fort Myers Plant, French Camp Plant, Friant Plant, Ft. Pierce Plant, Ft. Walton Plant, Gainesville RK Plant, Galveston Plant, Greeneville Plant, Harlingen Plant, Harvest-Highway 53-Lafarge Plant, Higley Plant, Hockley Plant, Hollywood Plant, Holmes RM (JV) Plant, Humble RM Plant, Huntsville (Dual) Plant, Inglewood Plant, Intel Plant, Irondale Plant, Irvine Plant, Johns Creek Plant, Katy RM (JV) Plant, Kingsport Plant, Kyle Canyon Plant, Lake Park Plant, Lakeshore (Dual) (Lafarge) Plant, Lemoore Plant, Lincoln Plant, Lithonia Plant, Lockhart RK Plant, Los Angeles Plant, Los Banos Plant, Losee Plant, Lytle Creek RM Plant, Maricopa Plant, Marietta-Owenby Drive Plant, Marysville Plant, Maynardville Plant, McDuffie Rd. Plant, Melbourne RK Plant, Merced Plant, Midtown-Armour Plant, Mid-Town Miami Plant, Mission Plant, Mission Valley Plant, Missouri City RM (JV) Plant, Modesto Plant, Montgomery-Metro Plant, Montgomery-Wares Plant, Morgan's Point (La Porte) Plant, Morristown Plant, Mt. Belvieu Plant, Navarre Plant, Navigation RM Plant, Neyland Drive Plant, Niceville (Villa Tasso) Plant, North Miami Plant, North Vero Plant, Oakland Plant, Ocala Plant, Oildale Plant, Old River Plant, Opelika Plant, Orange Plant, Orlando Plant, Oxnard RM Plant, Palomar Escondido Plant, Panama City-Main Plant, Perkins Plant, Perris RM Plant, Pier 92 Amador Plant, Pima Plant, Pleasanton Plant, Pompano Plant, Portable Rexcon 1 Plant,

Ready-Mixed Concrete Manufacturer	Ready-Mixed Concrete Plants
	Prescott Plant, Prospect Avenue Plant, Redlands RM (Dual) Plant, Regency Park Plant, Reno Plant, Rockford Plant, Rosenberg Plant, Roseville Plant, Rothwell Plant, San Carlos Plant, San Jose Plant, San Juan Capistrano Plant, San Tan Plant, Santa Barbara Plant, Santa Clara Plant, Santa Puala RM Plant, Sarival Plant, Schertz RM Plant, Seagrove Plant, Sloan Plant, South Fresno Plant, South Lauderdale Plant, South Miami Plant, Spring Plant, St. Augustine Plant, St. Petersburg Plant, Stafford Plant, State Rd. 80 (WP8 FL) RM Plant, Stuart Plant, Sun City Plant, Sunrise Plant, Tomball Plant, Tracy Plant, Tric Plant, Trinity Plant, Troy Plant, TSMC Plant, Tuscaloosa (Dual) Plant, Union City Plant, Valkaria Plant, Webster Plant, West Palm Beach FL Readymix Plant, West Plant, West Sacramento Terminal Plant, Wiggings Pass (North Naples) Plant, Woodstock Plant
Central Concrete	Hayward Plant, Martinez Plant, Oakland Plant, Pleasanton (wet) Plant, Queens Lane (dry) Plant, Queens Lane (wet) Plant, Redwood City Plant, Redwood City B Plant, San Francisco Plant, South San Francisco (wet) Plant, Stockton (wet) Plant
Centre Concrete Co.	State College Plant
Corliss Resources, Inc.	Enumclaw Plant, Federal Way Plant, Puyallup Plant, Sumner Plant
CWC-WSG	Baker Flats Plant, Ephrata Plant, Othello Plant, Quincy Plant, Wenatchee Plant
Eastern Concrete	Bayonne Plant, Bogota Plant, Broadway Plant, Howell Plant, Newark Plant, North Bergen Plant, Roseland Plant, West Nyack Plant
Hawaiian Cement	Halawa Plant #1, #3
Holcim - Aggregate Industries	Bannock Plant, Belle Plaine Ready-Mix Plant, Beltsville Plant, Bladensburg Plant, Buffalo Ready-Mix – Hopkins Plant, Chantilly Plant, Costilla Plant, DFW RMX Plant, Empire Ready-Mix Plant, Everett Plant, Fargo Ready-Mix (dry) Plant, Fargo Ready-Mix (wet) Plant, Forest Lake Ready-mix Plant, Fort Totten (DC) Plant, Ft. Collins Plant, Grand Forks Ready-Mix Plant, Jessup Plant, Kirby Road Plant, Lancaster Ready-Mix – Genesee Plant, Manassas Plant, Maple Grove Ready-Mix Plant, Minneapolis Ready-Mix Plant, Newport Ready-Mix Plant, Portable LRT Ready-Mix Plant, Rexcon Plant 8, Rockville East Plant, Saugus Plant, Texas Plant, Tonawanda Ready-Mix River Rd. Plant, Waltham Plant
Hooker Creek Companies, LLC	Bend Plant, Madras Plant, Redmond Plant
Ingram Ready Mix	Pearland #35 LLC Plant
Knife River Corporation	Coffee Lake Plant, Hillsboro Plant, Linnton Plant, Prineville Plant, Sundial Plant
Liberty Ready Mix	Dixon 2 Plant, Dixon 3 Plant, Grimes 1 Plant
Martin Marietta - Smyrna Ready Mix Concrete, LLC.	Arvada Plant, Chambers Plant, Del Camino Plant, Quivas Plant, Rock Creek Plant, Valmont Plant
Nashville Ready Mix	Visco Dr. – Nashville Plant
National Ready Mix	Artesia Plant, Canoga Park Plant, Glendale Plant, Irvine Plant, Irwindale Plant, Moorpark Plant, Santa Clarita Plant, South Gate Plant, Sun Valley Plant, Van Nuys Plant, Vernon Plant
O&G Industries, Inc.	Bridgeport Plant, Danbury Plant, Harwinton Plant, Southbury Plant, Stamford Plant
Platte River Concrete	Chalco Plants 1-5, 7
Prairie Material, LLC	Yard 32 Plant, Yard 33 Plant
Ready Mix USA	Harvest Plant
Riverbend Materials	Corvallis Plant, Hilroy Plant, RBWest Plant, Wildish Plant
Robertson's Ready Mix	Anaheim Plant, Carroll Canyon Plant, El Cajon Plant, Gardena Plant, Mira Mar Plant, Otay Mesa Plant, Rialto Plant, Vernon Plant

Ready-Mixed Concrete Manufacturer	Ready-Mixed Concrete Plants
Schuster Concrete	Annapolis Junction Plant, Laurel Plant, Monument Street Plant, Portable 18 Plant, Rockville Plant
Scioto Ready Mix	Alexandria Plant, Delaware Plant, Dublin Plant, New Albany Plant, Obetz Plant
Silvi Materials	Downingtown Plant, Englishtown Plant, Kingston Plant, Limerick Plant, Logan Plant, Morrisville Plant, Mt. Holly Plant, Philadelphia Plant, South Plainfield Plant, Southampton Plant
Stoneway Concrete	Black River Plant, Houser Plant, Seattle Plant
Tec-Crete Transit Mix Corporation	Jamaica Plant, Long Island City Plant
Thomas Concrete	Airport Plant, Alpharetta Plant, Atlanta Plant, Buckhead Plant, Charleston Plant, Charlotte Graham Street Plant, Doraville Plant, Greenville Plant, Morrisville Plant, Pooler Plant, Savannah East Plant, West Street Plant
Tilcon Connecticut Inc.	East Granby Concrete Plant, Hartford Concrete Plant, New Britain Concrete Plant, Norwich Concrete Plant, Old Saybrook Concrete Plant
Titan Virginia Ready-Mix	Centerville RM Plant, Clear Brook RM Plant, Dumfries RM Plant, Front Royal RM Plant, Leesburg RM Plant, Springfield RM (Plants 1 and 2), Stafford RM Plant, Sterling RM (Plants 1 and 2)
United Companies	Crested Butte Plant, Delta Plant, Gunnison Plant, Gypsum Plant, Minturn Plant, Montrose Plant, Powers Plant, Rifle Plant, River Road Plant, Steamboat Plant, Telluride Plant, Woody Creek Plant
US Concrete Mix / Smyrna Ready Mix	Bushwick Plant, College Point Plant, Jenna Plant, Long Island City Plant, Maspeth Plant, Mt. Vernon Plant, Smith Street Plant

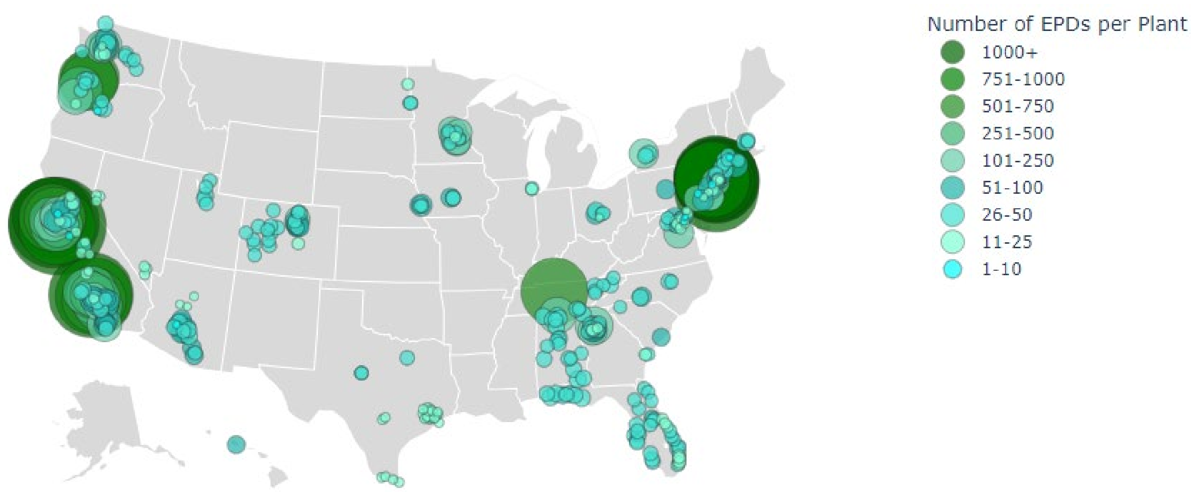

Figure **A-2**: Geographical distribution of the United States ready-mixed concrete plants in the dataset.

The dataset also represents a broad range of concrete compressive strength classes. Fig. **A-3** shows that despite over half of the concrete mixtures have a design compressive strength between 27.6 MPa (4,000 psi) to 34.5 MPa (5,000 psi), several other strength classes are represented, including those below 17.2 MPa (2,500 psi) and above 55.2 MPa (8,000 psi). Because of the breadth of compressive strengths in the dataset, holistic assessments of strength against LCA mid-points, like Global Warming Potential, can be conducted, as demonstrated by Fig. **A-4**. Note that this includes EPDs with different functional units (i.e., different curation times). Additionally, the concrete mixtures also include up to 15 different product components: portland cement, alternative cements (slag cement, type 1L cement, and hydraulic cement), aggregates (natural, crushed, and lightweight), batch water, admixtures (ASTM C494 and C260), fly ash, silica fume, fiber, glass pozzolan, and pigment. The percentage of concrete mixtures that include each component is shown in Fig. **A-5**. A single concrete mixture commonly includes several product components (for example, natural aggregate, crushed aggregate, portland cement, batch water, slag cement, and chemical admixtures). Note that the percentage of mixtures that contain any one product component is out of the entire dataset.

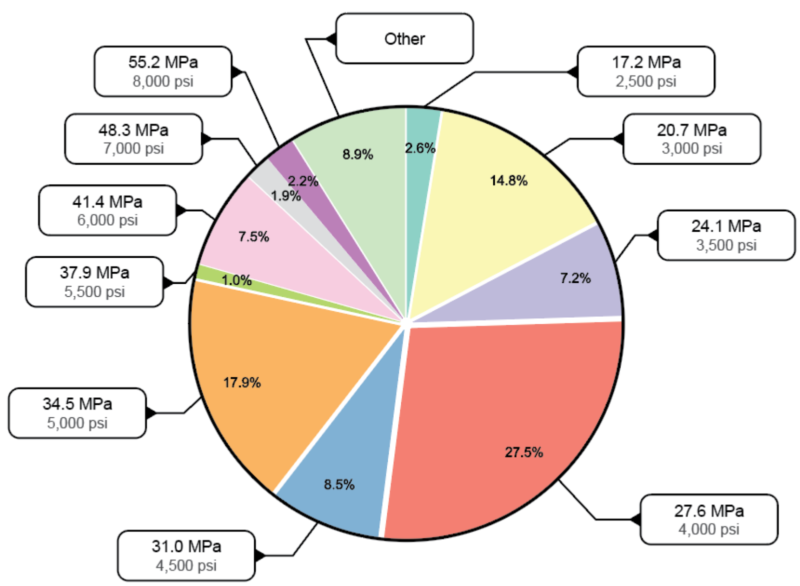

Figure **A-3**: Breakdown of concrete compressive strength classes in the EPD dataset.

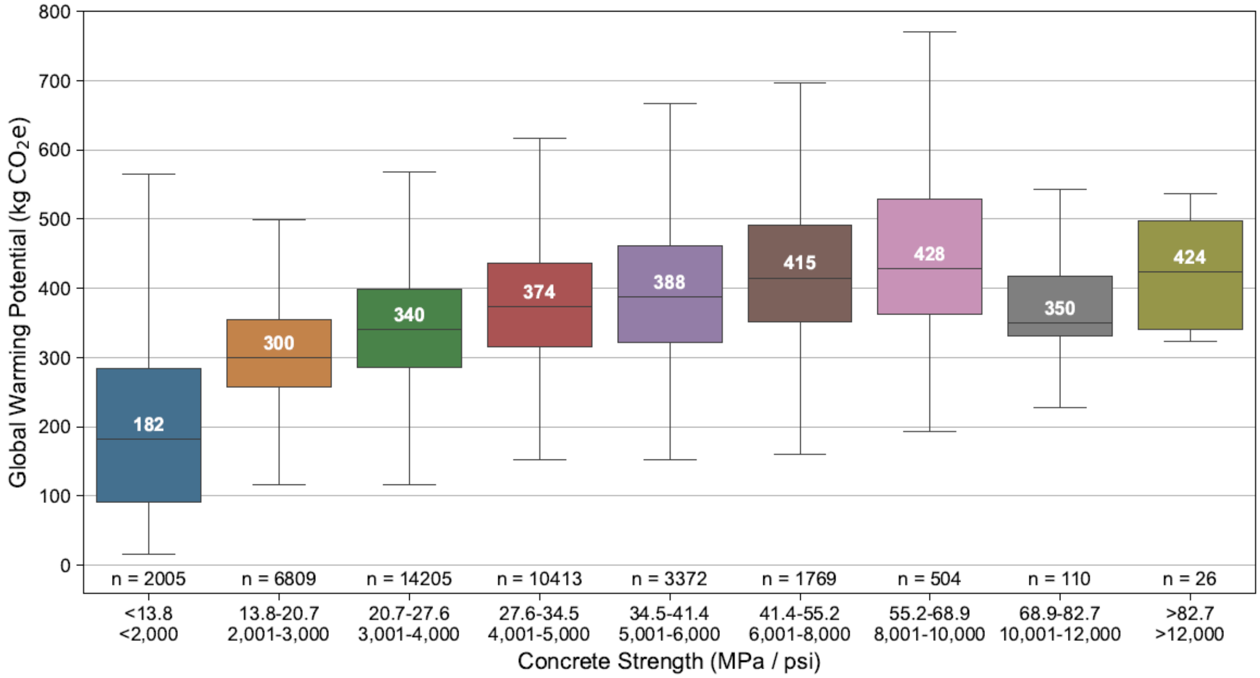

Figure **A-4**: Concrete compressive strength and A1-A3 GWP for all EPDs in the dataset.

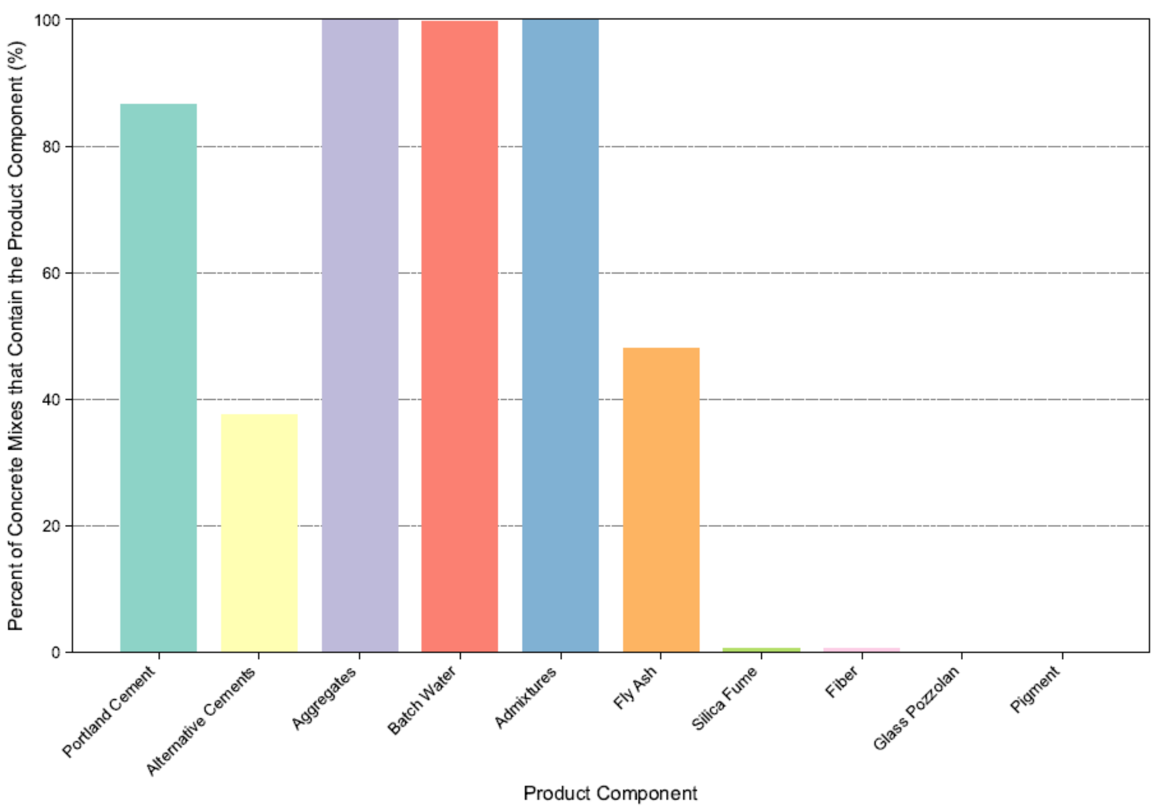

Figure **A-5**: Breakdown of concrete mixture components.

Two strategies to efficiently parse and analyze the large dataset include the filter feature in Excel and reading the dataset in Python or an equivalent coding language. In Excel or Python, users can view or filter concrete mixtures from a specific concrete plant, geographical location, concrete compressive strength class, or LCA midpoint. Python can also be used to filter the dataset and can be used to identify material components and LCI sources. Doing so can enable sustainability researchers and building practitioners to analyze the environmental performance of different concrete mixtures currently available in the United States. A study by Anderson and Moncaster (2020) is an example of what that can be done with this dataset.

A.5 Limitations

While the EPD database contains many entries, this is not an exhaustive list of concrete mixtures currently available. Second, the dataset includes ready-mix concrete produced only in the United States; no other countries are considered. Although no other countries are considered, a limitation with the analyzed EPDs is that European LCI audits are used for certain LCI items such as cleaning chemicals, indicating that the environmental performance for the items is similar within the United States, but may contribute to the LCI variability and uncertainty. Third, the quality of the data and the amount of data available differs across concrete plant / ready-mix concrete producers. However, all EPDs are externally validated by a third-party organization. Lastly, EPDs have a five-year period that they are valid. Therefore, EPDs in the dataset may not be valid depending on the time that the future analysis is conducted. The earliest date that an EPD is not valid is April 3rd, 2024. Regarding the provided Python code, it should be noted that ready-mix concrete EPDs from different plants or manufacturers can differ from one another. Therefore, the provided code may need to be modified to correctly extract all information from an EPD.

A.6 Conclusion

In conclusion, this appendix details the motivation, methodology, and value of the concrete EPD dataset. Unlike national averaged reports, this dataset provides additional information about the concrete mixtures and sustainable information, including the LCI sources, to better inform building designers, policymakers, and other stakeholders on the complex environmental footprint of concrete mixtures.

Appendix B

Methodologies and equations of conventional concrete floor structures[1]

The equations presented in this appendix are in imperial (U.S.) units unless reported otherwise. Portions of this appendix are adapted from Broyles and Hopper (2023).

B.1 RC Flat Plate

B.1.1. Initial estimate of square column width (col_{width_in}):

$$Based\ on\ Span\ Length\ (l) \begin{cases} l \le 25\ ft; col_{width_{in}} = 12\ in \\ l \le 30\ ft; col_{width_{in}} = 18\ in \\ l \le 33\ ft; col_{width_{in}} = 24\ in \\ l \le 37\ ft; col_{width_{in}} = 30\ in \\ l \le 42\ ft; col_{width_{in}} = 36\ in \\ l \le 50\ ft; col_{width_{in}} = 42\ in \end{cases}$$

B.1.2. Initial estimate of slab thickness (h), in accordance with ACI-318 Sec. 8.3.1.1 (2019):

$$l_{n_{in}} = l - col_{width_{in}}$$

$$h_{in} = max \left| \begin{matrix} \frac{l_{n_{in}}}{33} \\ 5\ in \end{matrix} \right. \quad Round\ up\ (h_{in})\ to\ nearest\ 1/2\ in$$

A minimum slab thickness of 5 inches is required to achieve a 2-hr fire rating per IBC Table 721.1(3) (International Code Council, 2021).

B.1.3. Calculate initial factored load (q_{u_in}):

$$q_{u_{in}} = max \left| \begin{matrix} 1.4\ DL \\ 1.2\ DL + 1.6\ LL \end{matrix} \right.$$

[1] Appendix B is adapted from the supplementary material labeled "Structural Methodologies and Equations" which is a companion document to the published work by Broyles et al. "Equations for early-stage design embodied carbon estimation for concrete floors of varying loading and strength" (2024).

B.1.4. Size columns and obtain final estimate for floor thickness and corresponding factored load:

$$P_n = 4q_{u_{in}}A_t$$

$$A_c = \frac{P_n}{(0.8)(0.65)[(0.85f_c'(0.98) + (f_y)(0.02)]}$$

$$col_{width_{sized}} = ceil(\sqrt{A_c})\left|\begin{matrix}12\ in\\16\ in\\18\ in\\20\ in\\24\ in\\30\ in\\36\ in\\42\ in\end{matrix}\right.$$

$$l_n = l - col_{width_{sized}}$$

$$h = max\left|\begin{matrix}\frac{l_n}{33}\\5\ in\end{matrix}\right. \quad Round\ up\ (h)\ to\ nearest\ 1/2\ in$$

$$q_u = max\left|\begin{matrix}1.4\ DL\\1.2\ DL + 1.6\ LL\end{matrix}\right.$$

B.1.5. Following a Modified Direct Design Method (M-DDM), calculate factored moment (*M_0*), as according to ACI-318 Equation 8.10.3.2 (2019)):

$$M_0 = \frac{q_u l\, l_n^2}{8}$$

B.1.6. Following the M-DDM, distribute the moments into column and middle strips (ACI-318 Table 8.10.4.2 (2019)).

Table **B-1**: Modified Direct Design Method moment distributions.

Strip	End Span			Interior Span	
Column Strip	Ext. Neg. $M_u = 0.27\ M_0$	Pos. $M_u = 0.345\ M_0$	Int. Neg. $M_u = 0.55\ M_0$	Int. Neg. $M_u = 0.535\ M_0$	Pos. $M_u = 0.186\ M_0$
Middle Strip	Ext. Neg. $M_u = 0\ M_0$	Pos. $M_u = 0.235\ M_0$	Int. Neg. $M_u = 0.18\ M_0$	Int. Neg. $M_u = 0.175\ M_0$	Pos. $M_u = 0.124\ M_0$

B.1.7. Based on the factored moment, determine the required steel reinforcement for positive and negative bending location *(which follows a similar method to* Foraboschi (2019)*)*:

$d = h - \frac{d_b}{2} - cc$; Estimate d_b as a #4 bar: 0.5 in. Clear cover (cc) = ¾ in

$b = \left(\frac{l}{2}\right)$

$R_n = \frac{M_u}{\phi b d^2}$; $\phi = 0.9$,

used in the estimation of As, as derived by Setareh and Darvas (2017) *in accordance with the strength design methods in ACI-318 Sec. 22.2* (2019).

$\beta_1 = 0.85 - 0.05(f_c' - 4)$; $f'_c \geq 4$ ksi, *in accordance with ACI-318 Sec. 22.2.2.4.3* (2019).

$A_{s,reqd} = \frac{\beta_1 f_c' b d}{f_y}\left[1 - \sqrt{1 - \frac{2R_n}{\beta_1 f_c'}}\right] \geq A_{s,min} = 0.0018bh$,

$A_{s,reqd}$ *equation, as derived by Setareh and Darvas* (2017) *in accordance with the strength design methods in ACI-318 Sec. 22.2* (2019). $A_{s,min}$ *equation in accordance with ACI-318 Sec. 8.6.1.1* (2019).

Note: *The steel reinforcement in the concrete slabs was designed according to the distributed design moments that occurred at different locations in the floor. The number of bars that satisfied the bending moment was obtained for every nominal U.S. rebar size from a #4 bar to a #10 bar at each design location. The total mass (which relates to the EC of the steel reinforcement) was obtained for each rebar size, with the lowest mass and corresponding rebar size and number of bars, selected for the given structural design and used in the EC calculation. The location of steel rebar was arranged at locations of maximum positive and negative bending moments, which follows typical U.S. design practices.*

B.1.8. Check (one-way) punching shear:

$b_0 = 4(col_{width} + d)$

$\phi V_c = 0.75\ (6)\sqrt{f_c'}\, d b_0$; $\phi = 0.75$,

In the above equation, it is assumed that punching shear reinforcement is present. This study assumed that its contribution to the total EC is negligible.

$V_u = q_u A_t$

$\phi V_c \geq V_u$

B.1.9. Check deflection:

$E_c = 57{,}000\sqrt{f_c'}$

$\eta = \dfrac{29{,}000{,}000}{E_c}$

$f_r = 7.5\sqrt{f_c'}$

$M_{cr} = \dfrac{f_r I_g}{h/2}$

$Solve\ for\ c;\ \ 0 = \frac{bc^2}{2} + \eta A_s c - \eta A_s d,$

as derived by Nawy (1985).

$I_{cr} = \dfrac{bc^3}{3} + \eta A_s (d-c)^2$

$I_{em} = \left(\frac{M_{cr}}{M_a}\right)^3 I_g + \left[1 - \left(\frac{M_{cr}}{M_a}\right)^3\right] I_{cr}$ *at midspan, as derived by Nawy* (1985).

$I_{e1} = \left(\frac{M_{cr}}{M_a}\right)^3 I_g + \left[1 - \left(\frac{M_{cr}}{M_a}\right)^3\right] I_{cr}$ *at the continuous span, as derived by Nawy* (1985).

$I_e = 0.85 I_{em} + 0.15 I_{e1}$ *Solve for each condition (DL_{conc}, DL_{conc} + SDL, DL_{conc} + SDL + LL)*

$I = min \left| \begin{matrix} I_g \\ I_{e,Load\ Case} \end{matrix} \right.$

$\Delta_{DL_{conc}} = \dfrac{0.0069 w_{DL_{conc}} l^4}{E_c I}$

$\Delta_{DL_{conc}+SDL} = \dfrac{0.0069 (w_{DL_{conc}} + w_{SDL}) l^4}{E_c I}$

$\Delta_{DL_{conc}+SDL+LL} = \dfrac{0.0069 (w_{DL_{conc}} + w_{SDL} + w_{LL}) l^4}{E_c I}$

$\Delta_{SDL} = \Delta_{DL_{conc}+SDL} - \Delta_{DL_{conc}}$

$\Delta_{LL} = \Delta_{DL_{conc}+SDL+LL} - \Delta_{DL_{conc}+SDL}$

$\lambda_{DL_{conc}} = \xi_{DL_{conc}} = 1.\ \lambda_{SDL} = \xi_{SDL} = 2.$ *Solve for both cases.*

$\Delta_{LT} = \lambda_{DL_{conc}} \Delta_{DL_{conc}} + (1 + \lambda_{SDL}) \Delta_{SDL} + (1) \Delta_{LL}$

$\Delta_{LT\,lim} = l/480$

$\Delta_{LT} \leq \Delta_{LT\,lim}$

B.1.10. Revise the design:

$IF \left| \begin{matrix} Design\ iteration\ satisfies\ all\ checks\ \rightarrow Decrease\ h\ by\ 1/2\ in \\ Design\ iteration\ fails\ any\ check\ \rightarrow Increase\ h\ by\ 1/2\ in \end{matrix} \right.$

Iterate until determining the slab design that uses the least amount of material (e.g., smallest thickness) that satisfies all design requirements.

B.2 RC Flat Slab

B.2.1. Initial estimate of square column width (col_{width_in}):

$$Based\ on\ Span\ Length\ (l) \begin{cases} l\ \leq 25\ ft; col_{width_{in}} = 12\ in \\ l\ \leq 30\ ft; col_{width_{in}} = 18\ in \\ l\ \leq 33\ ft; col_{width_{in}} = 24\ in \\ l\ \leq 37\ ft; col_{width_{in}} = 30\ in \\ l\ \leq 42\ ft; col_{width_{in}} = 36\ in \\ l\ \leq 50\ ft; col_{width_{in}} = 42\ in \end{cases}$$

B.2.2. Initial estimate of slab thickness (*h*), in accordance with ACI-318 Sec. 8.3.1.1 (2019):

$$l_{n_{in}} = l - col_{width_{in}}$$

$$h_{in} = max \left| \begin{matrix} \frac{l_{n_{in}}}{33} \\ 5\ in \end{matrix} \right. \quad Round\ up\ (h_{in})\ to\ nearest\ 1/2\ in$$

A minimum slab thickness of 5 inches is required to achieve a 2-hr fire rating per IBC Table 721.1(3) (International Code Council, 2021).

B.2.3. Calculate initial factored load (q_{u_in}):

$$q_{u_{in}} = max \left| \begin{matrix} 1.4\ DL \\ 1.2\ DL + 1.6\ LL \end{matrix} \right.$$

B.2.4. Size columns and obtain final estimate for floor thickness and corresponding factored load:

$$P_n = 4q_{u_{in}}A_t$$

$$A_c = \frac{P_n}{(0.8)(0.65)[(0.85f_c'(0.98) + (f_y)(0.02)]}$$

$$col_{width_{sized}} = ceil(\sqrt{A_c}) \left| \begin{matrix} 12\ in \\ 16\ in \\ 18\ in \\ 20\ in \\ 24\ in \\ 30\ in \\ 36\ in \\ 42\ in \end{matrix} \right.$$

$$l_n = l - col_{width_{sized}}$$

$$h = max \left| \begin{matrix} \frac{l_n}{33} \\ 5\ in \end{matrix} \right. \quad Round\ up\ (h)\ to\ nearest\ 1/2\ in$$

B.2.5. Size the drop panel around the columns:

$$depth_{Drop\ Panel} = ceil\left(\frac{h}{4}\right) \left| \begin{matrix} 2.25\ in \\ 3.25\ in \\ 4.25\ in \\ 6.25\ in \\ 8\ in \\ 10\ in \\ 12\ in \\ 16\ in \\ 20\ in \\ 24\ in \\ 32\ in \end{matrix} \right.$$

B.2.6. Following a Modified Direct Design Method (M-DDM), calculate factored moment (M_0), as according to ACI-318 Equation 8.10.3.2 (2019)):

$$q_u = max \left| \begin{matrix} 1.4\ DL \\ 1.2\ DL + 1.6\ LL \end{matrix} \right.$$

$$M_0 = \frac{q_u l\ l_n^2}{8}$$

B.2.7. Following the M-DDM, distribute the moments into column and middle strips (ACI-318 Table 8.10.4.2 (2019)) as specified in Table S-1.

B.2.8. Based on the factored moment, determine the required steel reinforcement for positive and negative bending location *(which follows a similar method to* Foraboschi (2019)*)*:

$d = h - \frac{d_b}{2} - cc$; Estimate d_b as a #4 bar: 0.5 in. Clear cover (cc) = ¾ in.

Note: d will differ depending on the location (i.e., deeper at columns with drop panels).

$$b = \left(\frac{l}{2}\right)$$

$R_n = \frac{M_u}{\phi b d^2}$; $\phi = 0.9$,

used in the estimation of As, as derived by Setareh and Darvas (2017) *in accordance with the strength design methods in ACI-318 Sec. 22.2* (2019).

$\beta_1 = 0.85 - 0.05(f_c' - 4)$; $f'_c \geq 4$ ksi*, in accordance with ACI-318 Sec. 22.2.2.4.3* (2019).

$$A_{s,reqd} = \frac{\beta_1 f_c' bd}{f_y}\left[1 - \sqrt{1 - \frac{2R_n}{\beta_1 f_c'}}\right] \geq A_{s,min} = 0.0018bh,$$

$A_{s,reqd}$ equation, as derived by Setareh and Darvas (2017) *in accordance with the strength design methods in ACI-318 Sec. 22.2* (2019). *$A_{s,min}$ equation in accordance with ACI-318 Sec. 8.6.1.1* (2019).

Refer to Note in Sec. 1.7. regarding rebar sizing and arrangement.

B.2.9. Check (one-way) punching shear:

$b_0 = 4(col_{width} + d)$

$\phi V_c = 0.75\ (6)\sqrt{f_c'}\,db_0;\ \phi = 0.75,$

In the above equation, it is assumed that punching shear reinforcement is present. This study assumed that its contribution to the total EC is negligible.

$V_u = q_u A_t$

$\phi V_c \geq V_u$

B.2.10. Check deflection:

$E_c = 57{,}000\sqrt{f_c'}$

$$\eta = \frac{29{,}000{,}000}{E_c}$$

$f_r = 7.5\sqrt{f_c'}$

$$M_{cr} = \frac{f_r I_g}{h/2}$$

$Solve\ for\ c;\ \ 0 = \frac{bc^2}{2} + \eta A_s c - \eta A_s d,$

as derived by Nawy (1985). *Note: d will be different based on location.*

$$I_{cr} = \frac{bc^3}{3} + \eta A_s (d-c)^2$$

$I_{em} = \left(\frac{M_{cr}}{M_a}\right)^3 I_g + \left[1 - \left(\frac{M_{cr}}{M_a}\right)^3\right] I_{cr}$ *at midspan, as derived by Nawy* (1985).

$I_{e1} = \left(\frac{M_{cr}}{M_a}\right)^3 I_g + \left[1 - \left(\frac{M_{cr}}{M_a}\right)^3\right] I_{cr}$ *at the continuous span, as derived by Nawy* (1985).

$I_e = 0.85 I_{em} + 0.15 I_{e1}$ *Solve for each condition (DL_{conc}, DL_{conc} + SDL, DL_{conc} + SDL + LL)*

$$I = min\left|\begin{matrix} I_g \\ I_{e,Load\ Case}\end{matrix}\right.$$

$$\Delta_{DL_{conc}} = \frac{0.0069 w_{DL_{conc}} l^4}{E_c I}$$

$$\Delta_{DL_{conc}+SDL} = \frac{0.0069 (w_{DL_{conc}} + w_{SDL}) l^4}{E_c I}$$

$$\Delta_{DL_{conc}+SDL+LL} = \frac{0.0069(w_{DL_{conc}} + w_{SDL} + w_{LL})l^4}{E_c I}$$

$$\Delta_{SDL} = \Delta_{DL_{conc}+SDL} - \Delta_{DL_{conc}}$$

$$\Delta_{LL} = \Delta_{DL_{conc}+SDL+LL} - \Delta_{DL_{conc}+SDL}$$

$\lambda_{DL_{conc}} = \xi_{DL_{conc}} = 1.\ \lambda_{SDL} = \xi_{SDL} = 2.$ *Solve for both cases.*

$$\Delta_{LT} = \lambda_{DL_{conc}} \Delta_{DL_{conc}} + (1 + \lambda_{SDL})\Delta_{SDL} + (1)\Delta_{LL}$$

$$\Delta_{LT\,lim} = l/480$$

$$\Delta_{LT} \leq \Delta_{LT\,lim}$$

B.2.11. Revise the design:

$$IF \left| \begin{array}{l} Design\ iteration\ satisfies\ all\ checks\ \rightarrow Decrease\ h\ by\ 1/2\ in \\ Design\ iteration\ fails\ any\ check\ \rightarrow Increase\ h\ by\ 1/2\ in \end{array} \right.$$

Iterate until determining the slab design that uses the least amount of material (e.g., smallest thickness) that satisfies all design requirements.

B.3 RC Modular One-Way Slab

B.3.1. Initial estimate of square column width (col_{width_in}):

$$Based\ on\ Span\ Length\ (l) \begin{cases} l \leq 25\ ft; col_{width_{in}} = 12\ in \\ l \leq 30\ ft; col_{width_{in}} = 18\ in \\ l \leq 33\ ft; col_{width_{in}} = 24\ in \\ l \leq 37\ ft; col_{width_{in}} = 30\ in \\ l \leq 42\ ft; col_{width_{in}} = 36\ in \\ l \leq 50\ ft; col_{width_{in}} = 42\ in \end{cases}$$

B.3.2. Initial estimate of required total depth (h), in accordance with ACI-318 Sec. 9.3.1.1. (2019):

$$l_{n_{in}} = l - col_{width_{in}}$$

$$h_{in} = max \left| \begin{array}{l} \frac{l_{n_{in}}}{18.5} \\ 5\ in \end{array} \right. \quad Round\ up\ (h_{in})\ to\ nearest\ 1/2\ in$$

A minimum slab thickness of 5 inches is required to achieve a 2-hr fire rating per IBC Table 721.1(3) (International Code Council, 2021).

B.3.3. Design using the appropriate wide-module pan joist system. Obtained from CRSI (1998).

Table **B-2**: Geometric properties for the wide-module pan joist systems considered in Ch. 3 and 4.

Module System (ft)	Rib Clear Spacing (in)	Rib Width (in)	Rib Depth (in)	Rib Taper (in)
2	20	4	8	2
2	20	4	10	2
2	20	4	12	2
3	30	6	8	2.5
3	30	6	10	2.5
3	30	6	12	2.5
3	30	6	14	2.5
3	30	6	16	2.5
3	30	6	20	2.5
4	40	8	12	3
4	40	8	14	3
4	40	8	16	3
4	40	8	18	3
4	40	8	20	3
4	40	8	22	3
4	40	8	24	3
5	53	7	16	3.5
5	53	7	20	3.5
6	66	6	14	4
6	66	6	16	4
6	66	6	20	4

B.3.4. Calculate initial factored load (q_{u_in}):

$$q_{u_{in}} = max \left| \begin{matrix} 1.4\ DL \\ 1.2\ DL + 1.6\ LL \end{matrix} \right.$$

B.3.5. Size columns and obtain final estimate for floor thickness and corresponding factored load:

$$P_n = 4q_{u_{in}}A_t$$

$$A_c = \frac{P_n}{(0.8)(0.65)[\left(0.85f_c'(0.98) + \left(f_y\right)(0.02)\right]}$$

$$col_{width_{sized}} = ceil\left(\sqrt{A_c}\right) \left| \begin{matrix} 12\ in \\ 16\ in \\ 18\ in \\ 20\ in \\ 24\ in \\ 30\ in \\ 36\ in \\ 42\ in \end{matrix} \right.$$

$$l_n = l - col_{width_{sized}}$$

$$h = max \left| \begin{array}{l} \frac{l_n}{18.5} \\ 5\ in \end{array} \right. \quad Round\ up\ (h)\ to\ nearest\ 1/2\ in$$

$$h_{slab} = max \left| \begin{array}{c} \frac{module\ system}{18.5} \\ 5\ in \end{array} \right. \quad Round\ up\ (h)\ to\ nearest\ 1/2\ in$$

Select a pan joist module system with a depth that exceeds $h - h_{slab}$

$$w_u = max \left|_{1.2\ DL+1.6\ LL}^{1.4\ DL} \right. in\ klf$$

Note: live load reductions may be permissible, according to ASCE 7-16. However, live load reductions were not taken in this study.

B.3.6. Following the approach using the approximate coefficients of ACI 318, distribute the moments (ACI-318 Table 6.5.2. (2019)).

Table **B-3**: Approximate moment formulas for one-way slabs from ACI-318 Table 6.5.2. (2019).

Location	**End Span**			**Interior Span**	
Location	Ext. Neg. $\frac{w_u l_n^2}{24}$	Pos. $\frac{w_u l_n^2}{14}$	Int. Neg. $\frac{w_u l_n^2}{10}$	Int. Neg. $\frac{w_u l_n^2}{11}$	Pos. $\frac{w_u l_n^2}{16}$

B.3.7. Based on the factored moment, determine the required steel reinforcement for positive and negative bending location *(which follows a similar method to* Foraboschi (2019)*)*:

$d = h - \frac{d_b}{2} - cc$; Estimate d_b as a #4 bar: 0.5 in. Clear cover (cc) = ¾ in

$$b = \left(\frac{l}{2}\right)$$

$$R_n = \frac{M_u}{\phi b d^2};\ \phi = 0.9,$$

used in the estimation of As, as derived by Setareh and Darvas (2017) *in accordance with the strength design methods in ACI-318 Sec. 22.2* (2019).

$\beta_1 = 0.85 - 0.05(f_c' - 4)$; $f'_c \geq 4$ ksi*, in accordance with ACI-318 Sec. 22.2.2.4.3* (2019).

$$A_{s,reqd} = \frac{\beta_1 f_c' bd}{f_y}\left[1 - \sqrt{1 - \frac{2R_n}{\beta_1 f_c'}}\right] \geq A_{s,min} = 0.0018bh,$$

$A_{s,reqd}$ *equation, as derived by Setareh and Darvas* (2017) *in accordance with the strength design methods in ACI-318 Sec. 22.2* (2019). $A_{s,min}$ *equation in accordance with ACI-318 Sec. 8.6.1.1* (2019).

Refer to Note in Sec. 1.7. regarding rebar sizing and arrangement.

B.3.8. Use ACI approximate shear coefficients to check shear (ACI-318 Table 6.5.4.):

Table **B-4**: Approximate shears formulas for one-way slabs from ACI-318 Table 6.5.4. (2019).

Location	V_u
End span at face of first interior support	$1.15\frac{w_u l_n}{2}$
At face of all other supports	$\frac{w_u l_n}{2}$

$$\phi V_c = 0.75\ (2)\sqrt{f_c'}db_0;\ \phi = 0.75,$$

$$\phi V_c \geq V_u$$

B.3.9. Check deflection:

$$E_c = 57{,}000\sqrt{f_c'}$$

$$\eta = \frac{29{,}000{,}000}{E_c}$$

$$f_r = 7.5\sqrt{f_c'}$$

$$M_{cr} = \frac{f_r I_g}{h/2}$$

$Solve\ for\ c;\ \ 0 = \frac{bc^2}{2} + \eta A_s c - \eta A_s d,$

as derived by Nawy (1985).

$$I_{cr} = \frac{bc^3}{3} + \eta A_s (d-c)^2$$

$I_{em} = \left(\frac{M_{cr}}{M_a}\right)^3 I_g + \left[1 - \left(\frac{M_{cr}}{M_a}\right)^3\right] I_{cr}$ *at midspan, as derived by Nawy* (1985).

$I_{e1} = \left(\frac{M_{cr}}{M_a}\right)^3 I_g + \left[1 - \left(\frac{M_{cr}}{M_a}\right)^3\right] I_{cr}$ *at the continuous span, as derived by Nawy* (1985).

$I_e = 0.85 I_{em} + 0.15 I_{e1}$ *Solve for each condition (DL_{conc}, DL_{conc} + SDL, DL_{conc} + SDL + LL)*

$$I = min \left| \begin{matrix} I_g \\ I_{e,Load\ Case} \end{matrix} \right.$$

$$\Delta_{DL_{conc}} = \frac{0.0069 w_{DL_{conc}} l^4}{E_c I}$$

$$\Delta_{DL_{conc}+SDL} = \frac{0.0069 (w_{DL_{conc}} + w_{SDL}) l^4}{E_c I}$$

$$\Delta_{DL_{conc}+SDL+LL} = \frac{0.0069(w_{DL_{conc}} + w_{SDL} + w_{LL})l^4}{E_c I}$$

$$\Delta_{SDL} = \Delta_{DL_{conc}+SDL} - \Delta_{DL_{conc}}$$

$$\Delta_{LL} = \Delta_{DL_{conc}+SDL+LL} - \Delta_{DL_{conc}+SDL}$$

$\lambda_{DL_{conc}} = \xi_{DL_{conc}} = 1.\ \lambda_{SDL} = \xi_{SDL} = 2.$ *Solve for both cases.*

$$\Delta_{LT} = \lambda_{DL_{conc}}\Delta_{DL_{conc}} + (1 + \lambda_{SDL})\Delta_{SDL} + (1)\Delta_{LL}$$

$$\Delta_{LT\,lim} = l/480$$

$$\Delta_{LT} \leq \Delta_{LT\,lim}$$

B.3.10. Revise the design:

$$IF \left| \begin{array}{l} Design\ iteration\ satisfies\ all\ checks\ \rightarrow Decrease\ h\ by\ 1/2\ in \\ \quad Design\ iteration\ fails\ any\ check\ \rightarrow Increase\ h\ by\ 1/2\ in \end{array} \right.$$

Iterate until determining the slab design that uses the least amount of material (e.g., smallest pan joist module system) that satisfies all design requirements.

B.4 RC Two-Way Slab with Beams

B.4.1. The Initial estimate of square column width (col_{width_in}):

$$Based\ on\ Span\ Length\ (l) \begin{cases} l \leq 25\ ft;\ col_{width_{in}} = 12\ in \\ l \leq 30\ ft;\ col_{width_{in}} = 18\ in \\ l \leq 33\ ft;\ col_{width_{in}} = 24\ in \\ l \leq 37\ ft;\ col_{width_{in}} = 30\ in \\ l \leq 42\ ft;\ col_{width_{in}} = 36\ in \\ l \leq 50\ ft;\ col_{width_{in}} = 42\ in \end{cases}$$

B.4.2. Initial estimate of slab thickness (h), in accordance with ACI-318 Sec. 8.3.1.1 (2019):

$$l_{n_{in}} = l - col_{width_{in}}$$

$$h_{in} = max \left| \begin{array}{l} \frac{l_{n_{in}}}{33} \\ 5\ in \end{array} \right. \quad Round\ up\ (h_{in})\ to\ nearest\ 1/2\ in$$

A minimum slab thickness of 5 inches is required to achieve a 2-hr fire rating per IBC Table 721.1(3) (International Code Council, 2021).

B.4.3. Calculate initial factored load (q_{u_in}):

$$q_{u_{in}} = max \left| \begin{array}{c} 1.4\ DL \\ 1.2\ DL + 1.6\ LL \end{array} \right.$$

B.4.4. Size columns and obtain final estimate for floor thickness and corresponding factored load:

$$P_n = 4q_{u_{in}}A_t$$

$$A_c = \frac{P_n}{(0.8)(0.65)[(0.85f_c'(0.98) + (f_y)(0.02)]}$$

$$col_{width_{sized}} = ceil(\sqrt{A_c}) \left| \begin{array}{l} 12\ in \\ 16\ in \\ 18\ in \\ 20\ in \\ 24\ in \\ 30\ in \\ 36\ in \\ 42\ in \end{array} \right.$$

$$l_n = l - col_{width_{sized}}$$

$$h = max \left| \begin{array}{l} \frac{l_n}{33} \\ 5\ in \end{array} \right. \quad Round\ up\ (h)\ to\ nearest\ 1/2\ in$$

$$q_u = max \left| \begin{array}{c} 1.4\ DL \\ 1.2\ DL + 1.6\ LL \end{array} \right.$$

B.4.5. Following a Modified Direct Design Method (M-DDM), calculate factored moment (M_0), as according to ACI-318 Equation 8.10.3.2 (2019)):

$$M_0 = \frac{q_u l\ l_n^2}{8}$$

B.4.6. Estimate initial interior and edge beam sizes:

$$width_{beam} = col_{width_{sized}}$$

$$depth_{beam} = max \left| \begin{array}{c} width_{beam} \\ \sqrt{\frac{20(0.75)M_0}{width_{beam}}}\ rounded\ up\ to\ 6\ in \end{array} \right.$$

The above equation was adapted from Fanella and Alsamsam, (2015).

Note that the coefficient for sizing the interior beam changes from 0.75 to 0.65.

B.4.7. Update the dead load and factored moment. Iterate beam sizes until convergence.

B.4.8. Following the M-DDM, distribute the moments into column and middle strips (ACI-318 Table 8.10.4.2 (2019)), as specified in Table S-1.

B.4.9. Based on the factored moment, determine the required steel reinforcement for positive and negative bending location *(which follows a similar method to* Foraboschi (2019)*)*:

$d = h - \frac{d_b}{2} - cc$; Estimate d_b as a #4 bar: 0.5 in. Clear cover (cc) = ¾ in

$b = \left(\frac{l}{2}\right)$

$R_n = \frac{M_u}{\phi b d^2}$; $\phi = 0.9$,

used in the estimation of As, as derived by Setareh and Darvas (2017) *in accordance with the strength design methods in ACI-318 Sec. 22.2* (2019).

$\beta_1 = 0.85 - 0.05(f_c' - 4)$; $f'_c \geq 4$ ksi, *in accordance with ACI-318 Sec. 22.2.2.4.3* (2019).

$A_{s,reqd} = \frac{\beta_1 f_c' b d}{f_y}\left[1 - \sqrt{1 - \frac{2R_n}{\beta_1 f_c'}}\right] \geq A_{s,min} = 0.0018bh$,

$A_{s,reqd}$ *equation, as derived by Setareh and Darvas* (2017) *in accordance with the strength design methods in ACI-318 Sec. 22.2* (2019). $A_{s,min}$ *equation in accordance with ACI-318 Sec. 8.6.1.1* (2019).

Refer to Note in Sec. 1.7. regarding rebar sizing and arrangement.

B.4.10. Check (one-way) punching shear:

$b_0 = 4(col_{width} + d)$

$\phi V_c = 0.75\,(6)\sqrt{f_c'}\,d b_0$; $\phi = 0.75$,

In the above equation, it is assumed that punching shear reinforcement is present.

This study assumed that its contribution to the total EC is negligible.

$V_u = q_u A_t$

$\phi V_c \geq V_u$

B.4.11. Check deflection:

$E_c = 57{,}000\sqrt{f_c'}$

$\eta = \frac{29{,}000{,}000}{E_c}$

$f_r = 7.5\sqrt{f_c'}$

$M_{cr} = \frac{f_r I_g}{h/2}$

$Solve\ for\ c;\ \ 0 = \frac{bc^2}{2} + \eta A_s c - \eta A_s d,$

as derived by Nawy (1985).

$$I_{cr} = \frac{bc^3}{3} + \eta A_s (d-c)^2$$

$I_{em} = \left(\frac{M_{cr}}{M_a}\right)^3 I_g + \left[1 - \left(\frac{M_{cr}}{M_a}\right)^3\right] I_{cr}$ *at midspan, as derived by Nawy* (1985).

$I_{e1} = \left(\frac{M_{cr}}{M_a}\right)^3 I_g + \left[1 - \left(\frac{M_{cr}}{M_a}\right)^3\right] I_{cr}$ *at the continuous span, as derived by Nawy* (1985).

$I_e = 0.85 I_{em} + 0.15 I_{e1}$ *Solve for each condition (DL$_{conc}$, DL$_{conc}$ + SDL, DL$_{conc}$ + SDL + LL)*

$$I = min\left|\begin{matrix} I_g \\ I_{e,Load\ Case} \end{matrix}\right.$$

$$\Delta_{DL_{conc}} = \frac{0.0069 w_{DL_{conc}} l^4}{E_c I}$$

$$\Delta_{DL_{conc}+SDL} = \frac{0.0069 (w_{DL_{conc}} + w_{SDL}) l^4}{E_c I}$$

$$\Delta_{DL_{conc}+SDL+LL} = \frac{0.0069 (w_{DL_{conc}} + w_{SDL} + w_{LL}) l^4}{E_c I}$$

$$\Delta_{SDL} = \Delta_{DL_{conc}+SDL} - \Delta_{DL_{conc}}$$

$$\Delta_{LL} = \Delta_{DL_{conc}+SDL+LL} - \Delta_{DL_{conc}+SDL}$$

$\lambda_{DL_{conc}} = \xi_{DL_{conc}} = 1.\ \lambda_{SDL} = \xi_{SDL} = 2.$ *Solve for both cases.*

$$\Delta_{LT} = \lambda_{DL_{conc}} \Delta_{DL_{conc}} + (1 + \lambda_{SDL}) \Delta_{SDL} + (1) \Delta_{LL}$$

$$\mathit{\Delta}_{LT\,lim} = l/480$$

$$\Delta_{LT} \leq \mathit{\Delta}_{LT\,lim}$$

B.4.12. Revise the design:

$$IF \left|\begin{matrix} Design\ iteration\ satisfies\ all\ checks\ \rightarrow Decrease\ h\ by\ 1/2\ in \\ Design\ iteration\ fails\ any\ check\ \rightarrow Increase\ h\ by\ 1/2\ in \end{matrix}\right.$$

Iterate until determining the slab design that uses the least amount of material (e.g., smallest thickness) that satisfies all design requirements.

B.5 RC Two-Way Modular Joist Waffle Slab

B.5.1. The Initial estimate of square column width (col_{width_in}):

$$Based\ on\ Span\ Length\ (l)\begin{cases} l\ \leq 25\ ft; col_{width_{in}} = 12\ in \\ l\ \leq 30\ ft; col_{width_{in}} = 18\ in \\ l\ \leq 33\ ft; col_{width_{in}} = 24\ in \\ l\ \leq 37\ ft; col_{width_{in}} = 30\ in \\ l\ \leq 42\ ft; col_{width_{in}} = 36\ in \\ l\ \leq 50\ ft; col_{width_{in}} = 42\ in \end{cases}$$

B.5.2. Initial estimate of slab thickness (*h*), in accordance with ACI-318 Sec. 8.3.1.1 (2019):

$$l_{n_{in}} = l - col_{width_{in}}$$

$$h_{in} = max\left|\begin{matrix} \frac{l_{n_{in}}}{33} \\ 5\ in \end{matrix}\right.\quad Round\ up\ (h_{in})\ to\ nearest\ 1/2\ in$$

A minimum slab thickness of 5 inches is required to achieve a 2-hr fire rating per IBC Table 721.1(3) (International Code Council, 2021).

B.5.3. Design using the appropriate module system. Obtained from the PCA guide (2005).

Table **B-5**: Geometric properties for the module waffle systems considered in this study.

Module System (ft)	**Rib Clear Spacing (in)**	**Rib Width (in)**	**Rib Depth (in)**
3	30	6	8
3	30	6	10
3	30	6	12
3	30	6	14
3	30	6	16
3	30	6	20
3	30	6	24
4	41	7	14
4	41	7	16
4	41	7	20
4	41	7	24
5	52	8	14
5	52	8	16
5	52	8	20
5	52	8	24
6	63	9	14
6	63	9	16
6	63	9	20
6	63	9	24

B.5.4. Calculate initial factored load (q_{u_in}):

$$q_{u_{in}} = max \left| \begin{array}{c} 1.4\ DL \\ 1.2\ DL + 1.6\ LL \end{array} \right.$$

B.5.5. Size columns and obtain final estimate for floor thickness and corresponding factored load:

$$P_n = 4 q_{u_{in}} A_t$$

$$A_c = \frac{P_n}{(0.8)(0.65)[(0.85 f_c'(0.98) + (f_y)(0.02)]}$$

$$col_{width_{sized}} = ceil\left(\sqrt{A_c}\right) \left| \begin{array}{l} 12\ in \\ 16\ in \\ 18\ in \\ 20\ in \\ 24\ in \\ 30\ in \\ 36\ in \\ 42\ in \end{array} \right.$$

$$l_n = l - col_{width_{sized}}$$

$$h = max \left| \begin{array}{l} \frac{l_n}{33} \\ 5\ in \end{array} \right. \quad Round\ up\ (h)\ to\ nearest\ 1/2\ in$$

B.5.6. Size the drop panel around the columns:

$$depth_{Drop\ Panel} = ceil\left(\frac{h}{4}\right) \left| \begin{array}{c} 2.25\ in \\ 3.25\ in \\ 4.25\ in \\ 6.25\ in \\ 8\ in \\ 10\ in \\ 12\ in \\ 16\ in \\ 20\ in \\ 24\ in \\ 32\ in \end{array} \right.$$

$$width_{Drop\ Panel} = \frac{L}{3}; \frac{L}{6}\ \textit{from centerline of column.}$$

B.5.7. Following a Modified Direct Design Method (M-DDM), calculate factored moment (M_0), as according to ACI-318 Equation 8.10.3.2 (2019)):

$$q_u = max \left| \begin{array}{c} 1.4\ DL \\ 1.2\ DL + 1.6\ LL \end{array} \right.$$

$$M_0 = \frac{q_u l\, l_n^2}{8}$$

B.5.8. Following the M-DDM, distribute the moments into column and middle strips (ACI-318 Table 8.10.4.2 (2019)), as specified in Table S-1.

B.5.9. Based on the factored moment, determine the required steel reinforcement for positive and negative bending location *(which follows a similar method to* Foraboschi (2019)*)*:

$d = h - \frac{d_b}{2} - cc$; Estimate d_b as a #4 bar: 0.5 in. Clear cover (cc) = ¾ in

$b = \left(\frac{l}{2}\right)$

$R_n = \frac{M_u}{\phi b d^2}$; $\phi = 0.9$,

used in the estimation of As, as derived by Setareh and Darvas (2017) *in accordance with the strength design methods in ACI-318 Sec. 22.2* (2019).

$\beta_1 = 0.85 - 0.05(f_c' - 4)$; $f'_c \geq 4$ ksi, *in accordance with ACI-318 Sec. 22.2.2.4.3* (2019).

$A_{s,reqd} = \frac{\beta_1 f_c' b d}{f_y}\left[1 - \sqrt{1 - \frac{2R_n}{\beta_1 f_c'}}\right] \geq A_{s,min} = 0.0018bh$,

$A_{s,reqd}$ *equation, as derived by Setareh and Darvas* (2017) *in accordance with the strength design methods in ACI-318 Sec. 22.2* (2019). $A_{s,min}$ *equation in accordance with ACI-318 Sec. 8.6.1.1* (2019).

Refer to Note in Sec. 1.7. regarding rebar sizing and arrangement.

B.5.10. Check (one-way) punching shear:

$b_0 = 4(col_{width} + d)$

$\phi V_c = 0.75\,(6)\sqrt{f_c'}\,d b_0$; $\phi = 0.75$,

In the above equation, it is assumed that punching shear reinforcement is present. This study assumed that its contribution to the total EC is negligible.

$V_u = q_u A_t$

$\phi V_c \geq V_u$

B.5.11. Check deflection:

$E_c = 57{,}000\sqrt{f_c'}$

$\eta = \frac{29{,}000{,}000}{E_c}$

$f_r = 7.5\sqrt{f_c'}$

$M_{cr} = \frac{f_r I_g}{h/2}$

$Solve\ for\ c;\ \ 0 = \frac{bc^2}{2} + \eta A_s c - \eta A_s d,$

as derived by Nawy (1985).

$$I_{cr} = \frac{bc^3}{3} + \eta A_s (d-c)^2$$

$I_{em} = \left(\frac{M_{cr}}{M_a}\right)^3 I_g + \left[1 - \left(\frac{M_{cr}}{M_a}\right)^3\right] I_{cr}$ *at midspan, as derived by Nawy* (1985).

$I_{e1} = \left(\frac{M_{cr}}{M_a}\right)^3 I_g + \left[1 - \left(\frac{M_{cr}}{M_a}\right)^3\right] I_{cr}$ *at the continuous span, as derived by Nawy* (1985).

$I_e = 0.85 I_{em} + 0.15 I_{e1}$ *Solve for each condition (*DL_{conc}*,* DL_{conc} *+ SDL,* DL_{conc} *+ SDL + LL)*

$$I = min \left| \begin{array}{c} I_g \\ I_{e,Load\ Case} \end{array} \right.$$

$$\Delta_{DL_{conc}} = \frac{0.0069 w_{DL_{conc}} l^4}{E_c I}$$

$$\Delta_{DL_{conc}+SDL} = \frac{0.0069 (w_{DL_{conc}} + w_{SDL}) l^4}{E_c I}$$

$$\Delta_{DL_{conc}+SDL+LL} = \frac{0.0069 (w_{DL_{conc}} + w_{SDL} + w_{LL}) l^4}{E_c I}$$

$$\Delta_{SDL} = \Delta_{DL_{conc}+SDL} - \Delta_{DL_{conc}}$$

$$\Delta_{LL} = \Delta_{DL_{conc}+SDL+LL} - \Delta_{DL_{conc}+SDL}$$

$\lambda_{DL_{conc}} = \xi_{DL_{conc}} = 1.\ \lambda_{SDL} = \xi_{SDL} = 2.$ *Solve for both cases.*

$$\Delta_{LT} = \lambda_{DL_{conc}} \Delta_{DL_{conc}} + (1 + \lambda_{SDL}) \Delta_{SDL} + (1) \Delta_{LL}$$

$$\Delta_{LT\,lim} = l/480$$

$$\Delta_{LT} \leq \Delta_{LT\,lim}$$

B.5.12. Revise the design:

$$IF \left| \begin{array}{c} Design\ iteration\ satisfies\ all\ checks\ \rightarrow Decrease\ h\ by\ 1/2\ in \\ Design\ iteration\ fails\ any\ check\ \rightarrow Increase\ h\ by\ 1/2\ in \end{array} \right.$$

Iterate until determining the slab design that uses the least amount of material (e.g., smallest thickness) that satisfies all design requirements.

B.6 RC Voided Plate

B.6.1. The Initial estimate of square column width (col_{width_in}):

$$Based\ on\ Span\ Length\ (l)\begin{cases} l\ \leq 25\ ft; col_{width_{in}} = 12\ in \\ l\ \leq 30\ ft; col_{width_{in}} = 18\ in \\ l\ \leq 33\ ft; col_{width_{in}} = 24\ in \\ l\ \leq 37\ ft; col_{width_{in}} = 30\ in \\ l\ \leq 42\ ft; col_{width_{in}} = 36\ in \\ l\ \leq 50\ ft; col_{width_{in}} = 42\ in \end{cases}$$

B.6.2. Initial estimate of slab thickness (*h*), in accordance with ACI-318 Sec. 8.3.1.1 (2019):

$$l_{n_{in}} = l - col_{width_{in}}$$

$$h_{in} = max \left| \begin{matrix} \frac{l_{n_{in}}}{33} \\ 7\ in \end{matrix} \right. \quad Round\ up\ (h_{in})\ to\ nearest\ 1/2\ in$$

A minimum slab thickness of 7 inches is possible using the smallest Cobiax Click-line. For additional geometric information for the voided systems, see Table B-6.

Table **B-6:** Cobiax void former material properties.

Cobiax Shell- and Click-Line	**90 - 100**	**100 - 120**	**120 - 140**	**140 - 160**	**160 - 180**	**180 - 200**	**200 - 220**	**220 - 240**	**240 - 260**	**260 - 280**
Slab Depth (mm)	175	200	213	250	275	300	313	350	375	388
Load Reduction per 2400 kg / m^3 (kN / m^2)	0.958	1.24	1.34	1.77	2.01	2.25	2.49	2.68	2.92	3.16
Volume Displacement (m^3 / m^2)	0.0414	0.0527	0.0576	0.0753	0.0856	0.0960	0.105	0.115	0.125	0.135
Shear Factor	0.5									
Stiffness Factor	0.93	0.95	0.93	0.93	0.92	0.90	0.89	0.89	0.89	0.87
Void Former Height (mm)	90	100	120	140	160	180	200	220	240	260

B.6.3. Calculate initial factored load (q_{u_in}):

$$q_{u_{in}} = max \left| \begin{matrix} 1.4\ (DL - Void\ Load\ Reduction) \\ 1.2\ (DL - Void\ Load\ Reduction) + 1.6\ LL \end{matrix} \right.$$

For void load reductions, please refer to Table S-6.

B.6.4. Size columns and obtain final estimate for floor thickness and corresponding factored load:

$$P_n = 4q_{u_{in}}A_t$$

$$A_c = \frac{P_n}{(0.8)(0.65)[\left(0.85f_c'(0.98) + \left(f_y\right)(0.02)\right]}$$

$$col_{width_{sized}} = ceil\left(\sqrt{A_c}\right)\left|\begin{array}{l} 12\ in \\ 16\ in \\ 18\ in \\ 20\ in \\ 24\ in \\ 30\ in \\ 36\ in \\ 42\ in \end{array}\right.$$

$$l_n = l - col_{width_{sized}}$$

$$h = max\left|\begin{array}{l} \frac{l_n}{33} \\ 7\ in \end{array}\right. \quad Round\ up\ (h)\ to\ nearest\ 1/2\ in$$

$$q_u = max\left|\begin{array}{c} 1.4\ (DL - Void\ Load\ Reduction) \\ 1.2\ (DL - Void\ Load\ Reduction) + 1.6\ LL \end{array}\right.$$

For void load reductions, please refer to Table S-6.

B.6.5. Using the Modified Direct Design Method (M-DDM), calculate factored moment (M_0), as according to ACI-318 Equation 8.10.3.2 (2019)):

$$M_0 = \frac{q_u l\, l_n^2}{8}$$

B.6.6. Following the M-DDM, distribute the moments into column and middle strips. See Table S-1.

B.6.7. Based on the factored moment, determine the required steel reinforcement for positive and negative bending location *(which follows a similar method to* Foraboschi (2019)*)*:

$d = h - \frac{d_b}{2} - cc$; Estimate d_b as a #4 bar: *0.5 in*

$$b = \left(\frac{L}{2}\right)$$

$$R_n = \frac{M_u}{\phi b d^2};\ \phi = 0.9$$

used in the estimation of As, as derived by Setareh and Darvas (2017) *in accordance with the strength design methods in ACI-318 Sec. 22.2* (2019).

$\beta_1 = 0.85 - 0.05(f_c' - 4)$; $f'_c \geq 4$ ksi*, in accordance with ACI-318 Sec. 22.2.2.4.3* (2019).

$A_{s,reqd} = \frac{\beta_1 f_c' bd}{f_y}\left[1 - \sqrt{1 - \frac{2R_n}{\beta_1 f_c'}}\right] \geq A_{s,min} = 0.0018bh$,

$A_{s,reqd}$ equation, as derived by Setareh and Darvas (2017) *in accordance with the strength design methods in ACI-318 Sec. 22.2* (2019). *$A_{s,min}$ equation in accordance with ACI-318 Sec. 8.6.1.1* (2019).

$c = \frac{A_s f_y}{0.85\beta_1 f_c' b} < \frac{h - h_{void}}{2}$;

check that the neutral axis depth at all critical sections is less than the solid slab depth above and below the voids.

Refer to Note in Sec. 1.7. regarding rebar sizing and arrangement.

B.6.8. Design solid area around columns:

$$b_0 = 4(col_{width} + d)$$

$$X = \left(\frac{col_{width}}{2}\right) + \left(\frac{b_0}{4} - \frac{col_{width}}{2}\right)$$

$$b_{op} = 8X$$

Round up each side to the nearest 6 inches.

B.6.9. Check (one-way) punching shear:

$$V_u = q_u(A_t - b_1 b_2^2)$$

$$\phi V_c = 0.75\ (6)\sqrt{f_c'}\, d b_0$$

In the above equation, it is assumed that punching shear reinforcement is present.

This study assumed that its contribution to the total EC is negligible.

$$\phi V_c \geq V_u$$

B.6.10. Check deflection:

$$E_c = 57{,}000\sqrt{f_c'}$$

$$\eta = \frac{29{,}000{,}000}{E_c}$$

$$f_r = 7.5\sqrt{f_c'}$$

$$M_{cr} = \frac{f_r I_g (Stiffness\ Reduction\ Factor)}{h/2}$$

$Solve\ for\ c;\ \ 0 = \frac{bc^2}{2} + \eta A_s c - \eta A_s d,$

as derived by Nawy (1985).

$$I_{cr} = \frac{bc^3}{3} + \eta A_s (d - c)^2$$

$I_{em} = \left(\frac{M_{cr}}{M_a}\right)^3 I_g(Stiffness\ Reduction\ Factor) + \left[1 - \left(\frac{M_{cr}}{M_a}\right)^3\right] I_{cr}$ *at midspan as derived by Nawy* (1985).

$I_{e1} = \left(\frac{M_{cr}}{M_a}\right)^3 I_g(Stiffness\ Reduction\ Factor) + \left[1 - \left(\frac{M_{cr}}{M_a}\right)^3\right] I_{cr}$ *at the continuous span as derived by Nawy* (1985).

$I_e = 0.85 I_{em} + 0.15 I_{e1}$ *Solve for each condition (DL_{conc}, DL_{conc} + SDL, DL_{conc} + SDL + LL)*

$$I = min \left| \begin{matrix} I_g(Stiffness\ Reduction\ Factor) \\ I_e \end{matrix} \right.$$

$$\Delta_{DL_{conc}} = \frac{0.0069 w_{DL_{conc}} l^4}{E_c I}$$

$$\Delta_{DL_{conc}+SDL} = \frac{0.0069(w_{DL_{conc}} + w_{SDL}) l^4}{E_c I}$$

$$\Delta_{DL_{conc}+SDL+LL} = \frac{0.0069(w_{DL_{conc}} + w_{SDL} + w_{LL}) l^4}{E_c I}$$

$$\Delta_{SDL} = \Delta_{DL_{conc}+SDL} - \Delta_{DL_{conc}}$$

$$\Delta_{LL} = \Delta_{DL_{conc}+SDL+LL} - \Delta_{DL_{conc}+SDL}$$

$\lambda_{DL_{conc}} = \xi_{DL_{conc}} = 1$. $\lambda_{SDL} = \xi_{SDL} = 2$. *Solve for both cases.*

$$\Delta_{LT} = \lambda_{DL_{conc}} \Delta_{DL_{conc}} + (1 + \lambda_{SDL}) \Delta_{SDL} + (1) \Delta_{LL}$$

$$\Delta_{LT_{lim}} = l/480$$

$$\Delta_{LT} \leq \Delta_{LT_{lim}}$$

B.6.11. Revise the design:

$$IF \left| \begin{matrix} Design\ iteration\ satisfies\ all\ checks\ \rightarrow Decrease\ h\ by\ 1/2\ in \\ Design\ iteration\ fails\ any\ check\ \rightarrow Increase\ h\ by\ 1/2\ in \end{matrix} \right.$$

Iterate until determining the slab design that uses the least amount of material (e.g., smallest thickness) that satisfies all design requirements.

B.7 PT Flat Plate

B.7.1. The Initial estimate of square column width (col_{width_in}):

$$Based\ on\ Span\ Length\ (l) \begin{cases} l \le 25\ ft; col_{width_{in}} = 12\ in \\ l \le 30\ ft; col_{width_{in}} = 18\ in \\ l \le 33\ ft; col_{width_{in}} = 24\ in \\ l \le 37\ ft; col_{width_{in}} = 30\ in \\ l \le 42\ ft; col_{width_{in}} = 36\ in \\ l \le 50\ ft; col_{width_{in}} = 42\ in \end{cases}$$

B.7.2. Initial estimate of slab thickness (*h*), in accordance with ACI-318 Sec. 8.3.1.1 (2019):

$$l_{n_{in}} = l - col_{width_{in}}$$

$$h_{in} = max \left| \begin{matrix} \frac{l_{n_{in}}}{33} \\ 5\ in \end{matrix} \right. \quad Round\ up\ (h_{in})\ to\ nearest\ 1/2\ in$$

A minimum slab thickness of 5 inches is required to achieve a 2-hr fire rating per IBC Table 721.1(3) (International Code Council, 2021).

B.7.3. Calculate initial factored load (q_{u_in}):

$$q_{u_{in}} = max \left| \begin{matrix} 1.4\ DL \\ 1.2\ DL + 1.6\ LL \end{matrix} \right.$$

B.7.4. Size columns and obtain final estimate for floor thickness and corresponding factored load:

$$P_n = 4 q_{u_{in}} A_t$$

$$A_c = \frac{P_n}{(0.8)(0.65)[(0.85 f_c'(0.98) + (f_y)(0.02)]}$$

$$col_{width_{sized}} = ceil(\sqrt{A_c}) \left| \begin{matrix} 12\ in \\ 16\ in \\ 18\ in \\ 20\ in \\ 24\ in \\ 30\ in \\ 36\ in \\ 42\ in \end{matrix} \right.$$

$$l_n = l - col_{width_{sized}}$$

$$h = max \left| \begin{matrix} \frac{l_n}{33} \\ 5\ in \end{matrix} \right. \quad Round\ up\ (h)\ to\ nearest\ 1/2\ in$$

$$q_u = max \left| \begin{matrix} 1.4\ DL \\ 1.2\ DL + 1.6\ LL \end{matrix} \right.$$

B.7.5. Following a Modified Direct Design Method (M-DDM), calculate factored moment (*M_0*), as according to ACI-318 Equation 8.10.3.2 (2019)):

$$M_0 = \frac{q_u l \, l_n^2}{8}$$

B.7.6. Following the M-DDM, moments can be distributed into column and middle strips for a PT system.

Table **B-7**: PT Modified Direct Design Method moment distributions.

Strip	End Span			Interior Span	
Column Strip	Ext. Neg. $M_u = 0.19\,M_0$	Pos. $M_u = 0.38\,M_0$	Int. Neg. $M_u = 0.53\,M_0$	Int. Neg. $M_u = 0.505\,M_0$	Pos. $M_u = 0.21\,M_0$
Middle Strip	Ext. Neg. $M_u = 0\,M_0$	Pos. $M_u = 0.26\,M_0$	Int. Neg. $M_u = 0.17\,M_0$	Int. Neg. $M_u = 0.165\,M_0$	Pos. $M_u = 0.14\,M_0$

B.7.7. Service design check & determine # of tendons.

Using the distributed moments from Table S-7

$M_{serv} = \max(M_u)$

$Tensile\ Stress\ Limit, U_{T_{Lim}} = 6\sqrt{f_c'}$, *in accordance with ACI-318 Table 24.5.2.1* (2019).

Compression Stress Limit, $U_{C_{Lim}} = -0.6f_c'$, *in accordance with ACI-318 Table 24.5.4.1* (2019).

$y = \frac{h}{2} - 1\ in$ *(Orthogonal tendon orientation)*

$U_{T_{Lim}} = -\frac{P_{eff}}{A_c} \pm \frac{P_{eff}\,y}{S} \pm \frac{M_{serv}}{S}$, *assuming the tensile stress limit controls.*

The above equation can be rearranged to:

$$P_{eff} = \frac{U_{T_{Lim}} - (M_{serv}/S)}{\left(-\frac{1}{A} - \frac{y}{S}\right)}$$

$$\#\ of\ Tendons = Roundup\left(\frac{P_{eff}}{27\ k/tendon}\right)$$

$$P_{eff_{prov}} = \#\ of\ Tendons\ \times 27\ k/tendon$$

B.7.8. Check minimum and maximum precompression, per ACI-318 Sec. 8.2.3 (2019):

$$125\quad psi \le \frac{P_{eff_{prov}}}{A} \le 300\ psi$$

B.7.9. Flexural design:

Using the distributed moments from Table S-7

Capacity from unbonded tendons

$$f_{se} = \frac{27\ k/tendon}{0.153\ in^2/tendon} = 176.47\ ksi$$

$$A_{ps} = \#\ of\ tendons\ \times 0.153\ in^2/tendon$$

$$\rho_p = \frac{A_{ps}}{bd_p}$$

$$f_{ps} = IF\left(\frac{l_n}{h}\right)\begin{cases}\leq 35 & min\left|\begin{array}{c} f_{py} = 0.9\ \times 270\ ksi = 243\ ksi \\ f_{se} + 60 \\ f_{se} + 10 + \dfrac{f'_c/1000}{\rho_p \times 100}\end{array}\right. \\ > 35 & min\left|\begin{array}{c} f_{py} \\ f_{se} + 30 \\ f_{se} + 10 + \dfrac{f'_c/1000}{\rho_p \times 300}\end{array}\right.\end{cases},$$

in accordance with ACI-318 Table 20.3.2.4.1 (2019).

$\beta_1 = 0.85 - 0.05(f'_c - 4\ ksi)$; $f'_c \geq 4$ ksi

$$a = \frac{A_{ps}f_{ps}}{0.85f'_c b}$$

$$c = a/\beta_1$$

$$\varepsilon_t = 0.003\left(\frac{d_p - c}{c}\right)$$

$$\phi M_{n_{pt}} = 0.9f_{ps}A_{ps}\left(d_p - \frac{a}{2}\right)$$

Design minimum bonded reinforcement:

for positive moment areas: $A_s = \frac{N_c}{0.5\ f_y}$, *where* $N_c = \frac{1}{2}(\frac{M_{Pos}}{S})\frac{h}{2}b$

for negative moment areas: $A_s = 0.00075A_{cf}$, *where* $A_{cf} = h \times L$

Capacity from non-prestressed rebar:

$$a = \frac{A_s f_y + A_{ps}f_{ps}}{0.85f'_c b}$$

$$c = a/\beta_1$$

$$\varepsilon_t = 0.003\left(\frac{d - c}{c}\right)$$

$$\phi M_{n_{Rebar}} = 0.9A_s f_y\left(d - \frac{a}{2}\right)$$

$$\phi M_n = \phi M_{n_{pt}} + \phi M_{n_{Rebar}}$$

Check:

$\phi M_n/M_{u_{Neg}} \geq 0.9$ for end spans

$\phi M_n/M_{u_{Pos}} \geq 0.9$ for mid-span

Refer to Note in Sec. 1.7. regarding rebar sizing and arrangement but note that the calculation of steel reinforcement for PT systems differs from RC systems.

B.7.10. Shear design:

$$V_u = q_u A_t$$

$$\phi V_c = 0.75\ (2)\sqrt{f'_c}\,d b_0$$

$$\phi V_c \geq V_u$$

B.7.11. Deflection check:

Assuming uncracked "U" section;

$I = I_g$

$$\Delta_{DL_{conc}} = \frac{0.0069 w_{DL_{conc}} l^4}{E_c I}$$

$$w_{pt} = -2 d_p P_{eff_{prov}} \left(\frac{1}{b}\right)\left(\frac{1}{b}\right)$$

$$\Delta_{pt} = \frac{0.0069 w_{pt} l^4}{E_c I}$$

$$\Delta_{SDL} = \frac{0.0069 w_{SDL} l^4}{E_c I}$$

$$\Delta_{LL} = \frac{0.0069 w_{LL} l^4}{E_c I}$$

$\lambda_{DL_{conc}} = \xi_{DL_{conc}} = 1.\ \lambda_{SDL} = \xi_{SDL} = 2.$ *Solve for both cases.*

$$\Delta_{LT} = \lambda_{DL_{conc}}(\Delta_{DL_{conc}} + \Delta_{pt}) + (1 + \lambda_{SDL})\Delta_{SDL} + (1)\Delta_{LL}$$

$$\Delta_{LT\,lim} = l/480$$

$$\Delta_{LT} \leq \Delta_{LT\,lim}$$

B.7.12. Revise the design:

$$IF \left| \begin{array}{c} Design\ iteration\ satisfies\ all\ checks\ \rightarrow Decrease\ h\ by\ 1/2\ in \\ Design\ iteration\ fails\ any\ check\ \rightarrow Increase\ h\ by\ 1/2\ in \end{array} \right.$$

Iterate until determining the slab design that uses the least amount of material (e.g., smallest thickness) that satisfies all design requirements.

B.8 PT Hollow Core Slab

B.8.1. Select an initial hollow core plank system:

Table **B-8**: Geometric properties of hollow core plank systems. Obtained from the PCI design manual (2015).

System	Plank Depth (in)	Plank Width (ft)	Area (in^2)	y_b (in)	Moment of Inertia (in^4)	Weight (psf)
Dynaspan *Un-topped*	4	4	133	2.00	235	35
Dynaspan *Un-topped*	6	4	165	3.02	706	43
Dynaspan *Un-topped*	8	4	233	3.93	1731	61
Dynaspan *Un-topped*	10	4	260	4.91	3145	68
Dynaspan *Un-topped*	6	8	338	3.05	1445	44
Dynaspan *Un-topped*	8	8	470	3.96	3525	61
Dynaspan *Un-topped*	10	8	532	4.96	6422	69
Dynaspan *Un-topped*	12	8	615	5.95	10505	80
Dynaspan *2 in topping*	4	4	133	3.08	689	60
Dynaspan *2 in topping*	6	4	165	4.25	1543	68
Dynaspan *2 in topping*	8	4	233	5.16	3205	86
Dynaspan *2 in topping*	10	4	260	6.26	5314	93
Dynaspan *2 in topping*	6	8	338	4.26	3106	69
Dynaspan *2 in topping*	8	8	470	5.17	6444	86
Dynaspan *2 in topping*	10	8	532	6.28	10712	94
Dynaspan *2 in topping*	12	8	615	7.32	16507	105
Flexicore *Un-topped*	6	1.33	55	3.00	243	43
Flexicore *Un-topped*	6	2	86	3.00	366	45
Flexicore *Un-topped*	8	1.33	73	4.00	560	57
Flexicore *Un-topped*	8	2	110	4.00	843	57

Flexicore *Un-topped*	10	1.67	98	5.00	1254	61
Flexicore *Un-topped*	10	2	138	5.00	1587	72
Flexicore *Un-topped*	12	2	141	6.00	2595	73
Flexicore *2 in topping*	6	1.33	55	4.23	523	68
Flexicore *2 in topping*	6	2	86	4.20	793	70
Flexicore *2 in topping*	8	1.33	73	5.26	1028	82
Flexicore *2 in topping*	8	2	110	5.26	1547	82
Flexicore *2 in topping*	10	1.67	98	6.43	2109	86
Flexicore *2 in topping*	10	2	138	6.27	2651	97
Flexicore *2 in topping*	12	2	141	7.46	4049	98
Spancrete *Un-topped*	4	4	138	2.00	238	34
Spancrete *Un-topped*	6	4	189	2.93	762	46
Spancrete *Un-topped*	8	4	258	3.98	1806	63
Spancrete *Un-topped*	10	4	312	5.16	3484	76
Spancrete *Un-topped*	12	4	355	6.28	5784	86
Spancrete *Un-topped*	15	4	417	7.45	10792	101
Spancrete *Un-topped*	16	4	401	8.14	12050	97
Spancrete *2 in topping*	4	4	138	3.14	739	59
Spancrete *2 in topping*	6	4	189	4.19	1760	71
Spancrete *2 in topping*	8	4	258	5.22	3443	88
Spancrete *2 in topping*	10	4	312	6.41	5787	101
Spancrete *2 in topping*	12	4	355	7.58	8904	111
Spancrete *2 in topping*	15	4	417	8.89	14351	126
Spancrete *2 in topping*	16	4	401	9.69	17575	122

Elematic *Un-topped*	6	4	157	3.00	694	41
Elematic *Un-topped*	8	4	196	3.97	1580	51
Elematic *Un-topped*	10	4	238	5.00	3042	62
Elematic *Un-topped*	10	4	249	5.00	3108	65
Elematic *Un-topped*	12	4	279	6.20	5104	74
Elematic *Un-topped*	12	4	274	6.00	5121	71
Elematic *Un-topped*	16	4	346	8.30	11339	91
Elematic *Un-topped*	20	4	501	10.30	24087	133
Elematic *2 in topped*	6	4	157	4.33	1557	66
Elematic *2 in topped*	8	4	196	5.41	3024	76
Elematic *2 in topped*	10	4	238	6.49	5190	87
Elematic *2 in topped*	10	4	249	6.44	5280	90
Elematic *2 in topped*	12	4	279	7.90	8406	99
Elematic *2 in topped*	12	4	274	7.56	8134	96
Elematic *2 in topped*	16	4	346	10.20	16883	116
Elematic *2 in topped*	20	4	501	12.00	33073	158

B.8.2. Determine flexural capacity:

$$\beta_1 = 0.85 - 0.05\left(\frac{f_c' - 4000}{1000}\right)$$

$$\rho_p = \frac{A_s}{bd_p}$$

$f_{ps} = f_{pu}\left(1 - \frac{\gamma_p}{\beta_1}\rho_p\frac{f_{pu}}{f_c'}\right)$; *where, γ_p is 0.28 for low-relaxation, 270 ksi strands.*

$$a = \frac{A_{ps}f_{ps}}{0.85f_c'b}$$

Check that the section is tension-controlled (ϕ = 0.9):

$$c = \frac{a}{\beta_1}$$

$$\varepsilon_t = \frac{d_p - c}{c}(0.003) > 0.005$$

$$\phi M_n = \phi A_{ps} f_{ps}\left(d_p - \frac{a}{2}\right)$$

B.8.3. Calculate initial factored load (q_{u_in}):

$$q_{u_{in}} = max \left| \begin{array}{c} 1.4\ DL \\ 1.2\ DL + 1.6\ LL \end{array} \right.$$

B.8.4. Size columns and obtain final estimate for floor thickness and corresponding factored load:

$$P_n = 4q_{u_{in}}A_t$$

$$A_c = \frac{P_n}{(0.8)(0.65)[(0.85f_c'(0.98) + (f_y)(0.02)]}$$

$$col_{width_{sized}} = ceil(\sqrt{A_c}) \left| \begin{array}{l} 12\ in \\ 16\ in \\ 18\ in \\ 20\ in \\ 24\ in \\ 30\ in \\ 36\ in \\ 42\ in \end{array} \right.$$

$$l_n = l - col_{width_{sized}}$$

$$h = max \left| \begin{array}{l} \frac{l_n}{33} \\ 5\ in \end{array} \right. \quad Round\ up\ (h)\ to\ nearest\ 1/2\ in$$

$$q_u = max \left| \begin{array}{c} 1.4\ DL \\ 1.2\ DL + 1.6\ LL \end{array} \right.$$

B.8.5. Following a Modified Direct Design Method (M-DDM), calculate factored moment (M_0), as according to ACI-318 Equation 8.10.3.2 (2019)):

$$M_0 = \frac{q_u l\ l_n^2}{8}$$

B.8.6. Check minimum reinforcement:

$$\phi M_n \geq 1.2M_{cr}$$

$$Assume\ a\ loss\ of\ 15\%$$

$$P_{eff} = A_{ps}f_{pi}(1 - loss)$$

Bottom compression:

$$f_{bot} = \frac{P_{eff}}{A} + \frac{P_{eff}e}{S}$$

$$M_{cr} = \frac{I}{y_b}\left(f_{bot} + 7.5\sqrt{f_c'}\right)$$

Note: the above check is necessary only at the critical section (2015).

Design minimum bonded reinforcement:

for positive moment areas: $A_s = \frac{N_c}{0.5\, f_y}$, *where* $N_c = \frac{1}{2}(\frac{M_{Pos}}{S})\frac{h}{2}b$

for negative moment areas: $A_s = 0.00075A_{cf}$, *where* $A_{cf} = h \times L$

Refer to Note in Sec. 1.7. regarding rebar sizing and arrangement but note that the calculation of steel reinforcement for PT systems differs from RC systems.

B.8.7. Check minimum and maximum precompression, per ACI-318 Sec. 8.2.3 (2019):

$$125\, psi \leq \frac{P_{eff_{prov}}}{A} \leq 300\, psi$$

Iterate to determine the number of tendons needed to satisfy minimum reinforcement, minimum, and maximum precompression checks.

B.8.8. Shear check:

$$V_u = q_u A_t$$

$$\phi V_c = 0.75\left(0.6(2)\sqrt{f_c'} + 700\frac{V_u d_p}{M_u}\right) d b_0$$

$$\phi V_c \geq V_u$$

B.8.9. Deflection check:

Assuming uncracked "U" section;

$$I = I_g$$

$$\Delta_{DL_{conc}} = \frac{0.0069 w_{DL_{conc}} l^4}{E_c I}$$

$$w_{pt} = -2 d_p P_{eff_{prov}}\left(\frac{1}{b}\right)\left(\frac{1}{b}\right)$$

$$\Delta_{pt} = \frac{0.0069 w_{pt} l^4}{E_c I}$$

$$\Delta_{SDL} = \frac{0.0069 w_{SDL} l^4}{E_c I}$$

$$\Delta_{LL} = \frac{0.0069 w_{LL} l^4}{E_c I}$$

$\lambda_{DL_{conc}} = \xi_{DL_{conc}} = 1$. $\lambda_{SDL} = \xi_{SDL} = 2$. *Solve for both cases.*

$$\Delta_{LT} = \lambda_{DL_{conc}}(\Delta_{DL_{conc}} + \Delta_{pt}) + (1 + \lambda_{SDL})\Delta_{SDL} + (1)\Delta_{LL}$$

$$\mathit{\Delta}_{LT\,lim} = l/480$$

$$\Delta_{LT} \leq \mathit{\Delta}_{LT\,lim}$$

B.8.10. Revise the design:

$$IF \left| \begin{array}{l} Design\ iteration\ satisfies\ all\ checks\ \rightarrow Decrease\ h\ by\ 1/2\ in \\ Design\ iteration\ fails\ any\ check\ \rightarrow Increase\ h\ by\ 1/2\ in \end{array} \right.$$

Iterate until determining the slab design that uses the least amount of material (e.g., smallest thickness) that satisfies all design requirements.

Assumptions when designing the PT Hollow Core Slab:

- The hollow core slab systems were designed to sit on RC beams as one-way planks.
- The width of the RC beams was designed to match the width of the column.
- The depth of the RC beams was taken as half of the beam width.
- Hollow core slabs can also be designed to sit on steel beams, which may be both an economical and low-carbon solution. However, the inclusion of structural steel members (outside of steel rebar and PT tendons) was considered out of the scope of this work.

B.9 PT Voided Plate (Orthogonal Tendon Layout)

B.9.1. The Initial estimate of square column width (col_{width_in}):

$$Based\ on\ Span\ Length\ (l) \begin{cases} l\ \leq 25\ ft; col_{width_{in}} = 12\ in \\ l\ \leq 30\ ft; col_{width_{in}} = 18\ in \\ l\ \leq 33\ ft; col_{width_{in}} = 24\ in \\ l\ \leq 37\ ft; col_{width_{in}} = 30\ in \\ l\ \leq 42\ ft; col_{width_{in}} = 36\ in \\ l\ \leq 50\ ft; col_{width_{in}} = 42\ in \end{cases}$$

B.9.2. Initial estimate of slab thickness (*h*), in accordance with ACI-318 Sec. 8.3.1.1 (2019):

$$l_{n_{in}} = l - col_{width_{in}}$$

$$h_{in} = max \left| \begin{array}{l} \frac{l_{n_{in}}}{33} \\ 7\ in \end{array} \right. \quad Round\ up\ (h_{in})\ to\ nearest\ 1/2\ in$$

B.9.3. Calculate initial factored load (q_{u_in}):

$$q_{u_{in}} = max \left| \begin{array}{c} 1.4\ (DL - Void\ Load\ Reduction) \\ 1.2\ (DL - Void\ Load\ Reduction) + 1.6\ LL \end{array} \right.$$

For void load reductions, please refer to Table S-6.

B.9.4. Size columns and obtain final estimate for floor thickness and corresponding factored load:

$$P_n = 4q_{u_{in}}A_t$$

$$A_c = \frac{P_n}{(0.8)(0.65)[(0.85f_c'(0.98) + (f_y)(0.02)]}$$

$$col_{width_{sized}} = ceil(\sqrt{A_c}) \left| \begin{array}{l} 12\ in \\ 16\ in \\ 18\ in \\ 20\ in \\ 24\ in \\ 30\ in \\ 36\ in \\ 42\ in \end{array} \right.$$

$$l_n = l - col_{width_{sized}}$$

$$h = max \left| \begin{array}{l} \frac{l_n}{33} \\ 7\ in \end{array} \right. \quad Round\ up\ (h)\ to\ nearest\ 1/2\ in$$

$$q_u = max \left| \begin{array}{c} 1.4\ (DL - Void\ Load\ Reduction) \\ 1.2\ (DL - Void\ Load\ Reduction) + 1.6\ LL \end{array} \right.$$

For void load reductions, please refer to Table S-6.

B.9.5. Using a Modified Direct Design Method (M-DDM), calculate factored moment (M_0), as according to ACI-318 Equation 8.10.3.2 (2019)):

$$M_0 = \frac{q_u l\, l_n^2}{8}$$

B.9.6. Calculate the solid area around the columns:

$$b_0 = 4(col_{width} + d)$$

$$X = \left(\frac{col_{width}}{2}\right) + \left(\frac{b_0}{4} - \frac{col_{width}}{2}\right)$$

$$b_{op} = 8X$$

Round up each side to the nearest 6 inches.

B.9.7. Service design check & determine # of tendons:

Using the distributed moments from Table S-7.

$M_{serv} = max(M_u)$

$Tensile\ Stress\ Limit, U_{T_{Lim}} = 6\sqrt{f_c'}$, *in accordance with ACI-318 Table 24.5.2.1* (2019).

Compression Stress Limit, $U_{C_{Lim}} = -0.6f_c'$, *in accordance with ACI-318 Table 24.5.4.1* (2019).

$y = \frac{h}{2} - 1\ in$ *(Orthogonal tendon orientation)*

$U_{T_{Lim}} = -\frac{P_{eff}}{A_{Mod}} \pm \frac{P_{eff}\, y}{S_{Mod}} \pm \frac{M_{serv}}{S_{Mod}}$, *assuming the tensile stress limit controls.*

The above equation can be rearranged to:

$$P_{eff} = \frac{U_{T_{Lim}} - (M_{serv}/S_{Mod})}{\left(-\frac{1}{A_{Mod}} - \frac{y}{S_{Mod}}\right)}$$

$$\#\ of\ Tendons = Roundup\left(\frac{P_{eff}}{27\ k/tendon}\right)$$

$$P_{eff_{prov}} = \#\ of\ Tendons\ \times 27\ k/tendon$$

B.9.8. Check minimum and maximum precompression, per ACI-318 Sec. 8.2.3 (2019):

$$125\quad psi \leq \frac{P_{eff_{prov}}}{A} \leq 300\ psi$$

B.9.9. Flexural design:

Using the distributed moments from Table S-7.

Capacity from unbonded tendons:

$$f_{se} = \frac{27\ k/tendon}{0.153\ in^2/tendon} = 176.47\ ksi$$

$$A_{ps} = \#\ of\ tendons\ \times 0.153\ in^2/tendon$$

$$\rho_p = \frac{A_{ps}}{bd_p}$$

$$f_{ps} = IF\ \left(\frac{l_n}{h}\right) \begin{cases} \leq 35 & min \left| \begin{array}{c} f_{py} = 0.9\ \times 270\ ksi = 243\ ksi \\ f_{se} + 60 \\ f_{se} + 10 + \dfrac{f'_c/1000}{\rho_p \times 100} \end{array} \right. \\ > 35 & min \left| \begin{array}{c} f_{py} \\ f_{se} + 30 \\ f_{se} + 10 + \dfrac{f'_c/1000}{\rho_p \times 300} \end{array} \right. \end{cases}$$

in accordance with ACI-318 Table 20.3.2.4.1 (2019).

$\beta_1 = 0.85 - 0.05(f'_c - 4\ ksi)$; $f'_c \geq 4$ ksi

$$a = \frac{A_{ps} f_{ps}}{0.85 f'_c b}$$

$$c = a/\beta_1$$

$$\varepsilon_t = 0.003\left(\frac{d_p - c}{c}\right)$$

$$\phi M_{n_{pt}} = 0.9 f_{ps} A_{ps}\left(d_p - \frac{a}{2}\right)$$

Design minimum bonded reinforcement:

for positive moment areas: $A_s = \frac{N_c}{0.5\ f_y}$, *where* $N_c = \frac{1}{2}\left(\frac{M_{Pos}}{S}\right)\frac{h}{2}b$

for negative moment areas: $A_s = 0.00075 A_{cf}$, *where* $A_{cf} = h \times L$

Capacity from non-prestressed rebar:

$$a = \frac{A_s f_y + A_{ps} f_{ps}}{0.85 f'_c b}$$

$c = a/\beta_1$

$\varepsilon_t = 0.003\left(\frac{d-c}{c}\right)$

$\phi M_{n_{Rebar}} = 0.9A_s f_y\left(d - \frac{a}{2}\right)$

$\phi M_n = \phi M_{n_{pt}} + \phi M_{n_{Rebar}}$

Check:

$\phi M_n/M_{u_{Neg}} \geq 0.9$ for end spans

$\phi M_n/M_{u_{Pos}} \geq 0.9$ for mid-span

Refer to Note in Sec. 1.7. regarding rebar sizing and arrangement but note that the calculation of steel reinforcement for PT systems differs from RC systems.

B.9.10. Shear design:

$V_u = q_u A_t$

$\phi V_c = 0.75\,(2)\sqrt{f_c'}\,d b_0$

$\phi V_c \geq V_u$

B.9.11. Deflection check:

Assuming uncracked "U" section;

$I = I_g$

$\Delta_{DL_{conc}} = \frac{0.0069 w_{DL_{conc}} l^4}{E_c I}$

$w_{pt} = -2d_p P_{eff_{prov}}\left(\frac{1}{b}\right)\left(\frac{1}{b}\right)$

$\Delta_{pt} = \frac{0.0069 w_{pt} l^4}{E_c I}$

$\Delta_{SDL} = \frac{0.0069 w_{SDL} l^4}{E_c I}$

$\Delta_{LL} = \frac{0.0069 w_{LL} l^4}{E_c I}$

$\lambda_{DL_{conc}} = \xi_{DL_{conc}} = 1.$ $\lambda_{SDL} = \xi_{SDL} = 2.$ *Solve for both cases.*

$\Delta_{LT} = \lambda_{DL_{conc}}(\Delta_{DL_{conc}} + \Delta_{pt}) + (1 + \lambda_{SDL})\Delta_{SDL} + (1)\Delta_{LL}$

$\Delta_{LT_{lim}} = l/480$

$\Delta_{LT} \leq \Delta_{LT_{lim}}$

B.9.12. Revise the design:

$$IF \left| \begin{array}{l} Design\ iteration\ satisfies\ all\ checks\ \rightarrow Decrease\ h\ by\ 1/2\ in \\ \quad Design\ iteration\ fails\ any\ check\ \rightarrow Increase\ h\ by\ 1/2\ in \end{array} \right.$$

Iterate until determining the slab design that uses the least amount of material (e.g., smallest thickness) that satisfies all design requirements.

B.10 PT Voided Plate (Diagonal Tendon Layout)

B.10.1. Initial estimate of square column width (col_{width_in}):

$$Based\ on\ Span\ Length\ (l) \begin{cases} l \le 25\ ft; col_{width_{in}} = 12\ in \\ l \le 30\ ft; col_{width_{in}} = 18\ in \\ l \le 33\ ft; col_{width_{in}} = 24\ in \\ l \le 37\ ft; col_{width_{in}} = 30\ in \\ l \le 42\ ft; col_{width_{in}} = 36\ in \\ l \le 50\ ft; col_{width_{in}} = 42\ in \end{cases}$$

B.10.2. Initial estimate of slab thickness (h), in accordance with ACI-318 Sec. 8.3.1.1 (2019):

$$l_{n_{in}} = l - col_{width_{in}}$$

$$h_{in} = max \left| \begin{array}{l} \frac{l_{n_{in}}}{33} \\ 7\ in \end{array} \right. \quad Round\ up\ (h_{in})\ to\ nearest\ 1/2\ in$$

B.10.3. Calculate initial factored load (q_{u_in}):

$$q_{u_{in}} = max \left| \begin{array}{c} 1.4\ (DL - Void\ Load\ Reduction) \\ 1.2\ (DL - Void\ Load\ Reduction) + 1.6\ LL \end{array} \right.$$

For void load reductions, please refer to Table S-6.

B.10.4. Size columns and obtain final estimate for floor thickness and corresponding factored load:

$$P_n = 4q_{u_{in}}A_t$$

$$A_c = \frac{P_n}{(0.8)(0.65)[(0.85f_c'(0.98) + (f_y)(0.02)]}$$

$$col_{width_{sized}} = ceil(\sqrt{A_c}) \left| \begin{array}{l} 12\ in \\ 16\ in \\ 18\ in \\ 20\ in \\ 24\ in \\ 30\ in \\ 36\ in \\ 42\ in \end{array} \right.$$

$$l_n = l - col_{width_{sized}}$$

$$h = max \begin{vmatrix} \frac{l_n}{33} \\ 7\ in \end{vmatrix} \quad Round\ up\ (h)\ to\ nearest\ 1/2\ in$$

$$q_u = max \begin{vmatrix} 1.4\ (DL - Void\ Load\ Reduction) \\ 1.2\ (DL - Void\ Load\ Reduction) + 1.6\ LL \end{vmatrix}$$

For void load reductions, please refer to Table S-6 in the manuscript.

B.10.5. Using a Modified Direct Design Method (M-DDM), calculate factored moment (M_0), as according to ACI-318 Equation 8.10.3.2 (2019)):

$$M_0 = \frac{q_u l\, l_n^2}{8}$$

B.10.6. Calculate the solid area around the columns:

$$b_0 = 4(col_{width} + d)$$

$$X = \left(\frac{col_{width}}{2}\right) + \left(\frac{b_0}{4} - \frac{col_{width}}{2}\right)$$

$$b_{op} = 8X$$

Round up each side to the nearest 6 inches.

B.10.7. Service design check & determine # of tendons:

Using the distributed moments from Table S-7.

$M_{serv} = max(M_u)$

$Tensile\ Stress\ Limit, U_{T_{Lim}} = 6\sqrt{f_c'}$, *in accordance with ACI-318 Table 24.5.2.1* (2019).

Compression Stress Limit, $U_{C_{Lim}} = -0.6 f_c'$, *in accordance with ACI-318 Table 24.5.4.1* (2019).

$y = \frac{h}{2} - 1.5\ in$ *(Diagonal tendon orientation)*

$U_{T_{Lim}} = -\frac{P_{eff}}{A_{Mod}} \pm \frac{P_{eff}\, y}{S_{Mod}} \pm \frac{M_{serv}}{S_{Mod}}$, *assuming the tensile stress limit controls.*

The above equation can be rearranged to:

$$P_{eff} = \frac{U_{T_{Lim}} - (M_{serv}/S_{Mod})}{\left(-\frac{1}{A_{Mod}} - \frac{y}{S_{Mod}}\right)}$$

$$\#\ of\ Tendons = Roundup\left(\frac{P_{eff}}{27\ k/tendon}\right)$$

$$\#\ of\ Diagonal\ Tendons = Roundup\left(\frac{\#\ of\ Tendons}{1.414}\right)$$

$$P_{eff_{prov}} = \#\ of\ Diagonal\ Tendons\ \times 27\ k/tendon$$

B.10.8. Check minimum and maximum precompression, per ACI-318 Sec. 8.2.3 (2019):

$$125 \quad psi \le \frac{P_{eff_{prov}}}{A} \le 300\ psi$$

B.10.9. Flexural design:

Using the distributed moments from Table S-7.

Capacity from unbonded tendons:

$$f_{se} = \frac{27\ k/tendon}{0.153\ in^2/tendon} = 176.47\ ksi$$

$$A_{ps} = \#\ of\ tendons\ \times 0.153\ in^2/tendon$$

$$\rho_p = \frac{A_{ps}}{bd_p}$$

$$f_{ps} = IF\left(\frac{l_n}{h}\right) \begin{cases} \leq 35 & min \left| \begin{array}{c} f_{py} = 0.9\ \times 270\ ksi = 243\ ksi \\ f_{se} + 60 \\ f_{se} + 10 + \dfrac{f_c'/1000}{\rho_p \times 100} \end{array} \right. \\ > 35 & min \left| \begin{array}{c} f_{py} \\ f_{se} + 30 \\ f_{se} + 10 + \dfrac{f_c'/1000}{\rho_p \times 300} \end{array} \right. \end{cases}$$

$\beta_1 = 0.85 - 0.05(f_c' - 4\ ksi)$; $f'_c \geq 4$ ksi

$$a = \frac{A_{ps} f_{ps}}{0.85 f_c' b}$$

$$c = a/\beta_1$$

$$\varepsilon_t = 0.003\left(\frac{d_p - c}{c}\right)$$

$$\phi M_{n_{pt}} = 0.9 f_{ps} A_{ps}\left(d_p - \frac{a}{2}\right)$$

Design minimum bonded reinforcement:

for positive moment areas: $A_s = \frac{N_c}{0.5\ f_y}$, *where* $N_c = \frac{1}{2}\left(\frac{M_{Pos}}{S}\right)\frac{h}{2}b$

for negative moment areas: $A_s = 0.00075 A_{cf}$, *where* $A_{cf} = h \times L$

Capacity from non-prestressed rebar:

$$a = \frac{A_s f_y + A_{ps} f_{ps}}{0.85 f_c' b}$$

$$c = a/\beta_1$$

$$\varepsilon_t = 0.003\left(\frac{d - c}{c}\right)$$

$$\phi M_{n_{Rebar}} = 0.9 A_s f_y\left(d - \frac{a}{2}\right)$$

$$\phi M_n = \phi M_{n_{pt}} + \phi M_{n_{Rebar}}$$

Check:

$\phi M_n / M_{u_{Neg}} \geq 0.9$ for end spans

$\phi M_n / M_{u_{Pos}} \geq 0.9$ for mid-span

Refer to Note in Sec. 1.7. regarding rebar sizing and arrangement but note that the calculation of steel reinforcement for PT systems differs from RC systems.

B.10.10. Shear design:

$V_u = q_u A_{trib}$

$\phi V_c = 0.75\ (2)\sqrt{f_c'}db_0$

$\phi V_c \geq V_u$

B.10.11. Deflection check:

Assuming uncracked "U" section;

$I = I_g$

$$\Delta_{DL_{conc}} = \frac{0.0069 w_{DL_{conc}} l^4}{E_c I}$$

$$w_{pt} = -2 d_p P_{eff_{prov}} \left(\frac{1}{b}\right)\left(\frac{1}{b}\right)$$

$$\Delta_{pt} = \frac{0.0069 w_{pt} l^4}{E_c I}$$

$$\Delta_{SDL} = \frac{0.0069 w_{SDL} l^4}{E_c I}$$

$$\Delta_{LL} = \frac{0.0069 w_{LL} l^4}{E_c I}$$

$\lambda_{DL_{conc}} = \xi_{DL_{conc}} = 1$. $\lambda_{SDL} = \xi_{SDL} = 2$. *Solve for both cases.*

$\Delta_{LT} = \lambda_{DL_{conc}}(\Delta_{DL_{conc}} + \Delta_{pt}) + (1 + \lambda_{SDL})\Delta_{SDL} + (1)\Delta_{LL}$

$\Delta_{LT_{lim}} = l/480$

$\Delta_{LT} \leq \Delta_{LT_{lim}}$

B.10.12. Revise the design:

$$IF \left| \begin{array}{l} Design\ iteration\ satisfies\ all\ checks\ \rightarrow Decrease\ h\ by\ 1/2\ in \\ Design\ iteration\ fails\ any\ check\ \rightarrow Increase\ h\ by\ 1/2\ in \end{array} \right.$$

Iterate until determining the slab design that uses the least amount of material (e.g., smallest thickness) that satisfies all design requirements.

Appendix C

Embodied carbon equation coefficients and statistical metrics

C.1 Coefficients, R^2, and RMSEs for the Conceptual Design Phase Equations

The following tables provide the β coefficient magnitudes and statistical parameters that quantify how well the single variate polynomial regression models fit the composite embodied carbon (EC) trendlines for the conceptual design phases (see Sec. **4.4.1** in the dissertation). Table **C-1** provides the imperial (U.S.) equivalent to the EC_{est} equations (refer to Eq. **4-2** in Ch. 4 in the dissertation) for the conceptual design phase (Table **4-7** in Ch. 4 of the dissertation provides the EC_{est} equations in the metric unit system). Table **C-2** gives the R^2 and RMSE values for the fitted EC_{est} curves.

Table **C-1**: The analytically derived EC_{est} equations (see Eq. **4-2** in Ch. 4 of the dissertation) for use in the conceptual design phase. Imperial (U.S.) equations are provided in parentheses.

Concrete System	Full Span Length Range	Economical Span Length Range
RC Flat Plate	$EC_{est} = 0.076\ L^2 + 4.14\ L - 1.1$	$EC_{est} = 0.10\ L^2 + 2.97\ L + 9.8$
RC Flat Slab	$EC_{est} = 0.075\ L^2 + 4.15\ L + 0.49$	$EC_{est} = 0.069\ L^2 + 4.63\ L - 7.7$
RC One-Way Pan Joist Slab	$EC_{est} = 0.16\ L^2 - 5.73\ L + 126$	$EC_{est} = 0.12\ L^2 - 3.32\ L + 100$
RC Two-Way Slab with Beams	$EC_{est} = 0.056\ L^2 - 0.30\ L + 73$	$EC_{est} = 0.070\ L^2 - 1.01\ L + 81$
RC Two-Way Waffle Slab	$EC_{est} = 0.015\ L^2 + 0.70\ L + 63$	$EC_{est} = -0.13\ L^2 + 11.3\ L - 128$
RC Voided Plate	$EC_{est} = 0.11\ L^2 + 0.066\ L + 48$	$EC_{est} = 0.12\ L^2 - 0.68\ L + 54$
PT Flat Plate	$EC_{est} = 0.074\ L^2 + 1.01\ L + 31$	$EC_{est} = 0.080\ L^2 + 0.57\ L + 39$
PT Hollow Core Slab	$EC_{est} = 0.075\ L^2 - 0.12\ L + 49$	$EC_{est} = 0.057\ L^2 + 1.17\ L + 29$
PT Voided Plate – Orthogonal Layout	$EC_{est} = 0.10\ L^2 - 2.34\ L + 77$	$EC_{est} = 0.091\ L^2 - 1.65\ L + 65$
PT Voided Plate – Diagonal Layout	$EC_{est} = 0.11\ L^2 - 2.91\ L + 85$	$EC_{est} = 0.10\ L^2 - 2.26\ L + 74$

Note. L: Length in feet. EC_{est}: Embodied carbon in $kgCO_2e/m^2$.

Table **C-2**: The R^2 values and RMSEs for the EC_{est} equations (see Eq. **4-2** in Ch. 4 of the dissertation) described in Table **4-7** in Ch. 4 of the dissertation and Table **C-1**. Note that the R^2 and RMSEs are the same regardless of metric or imperial units.

Concrete System	Full Span Length Range		Economical Span Length Range	
	R^2	RMSE	R^2	RMSE
RC Flat Plate	> 0.999	0.937	> 0.999	0.597
RC Flat Slab	> 0.999	0.950	> 0.999	0.123
RC One-Way Pan Joist Slab	0.991	5.002	0.977	1.438
RC Two-Way Slab with Beams	0.998	1.736	> 0.999	0.509
RC Two-Way Waffle Slab	0.880	7.066	0.827	3.942
RC Voided Plate	> 0.999	2.207	> 0.999	0.785
PT Flat Plate	> 0.999	1.545	> 0.999	0.771
PT Hollow Core Slab	0.999	1.807	> 0.999	1.071
PT Voided Plate – Orthogonal Layout	0.999	1.600	0.999	1.396
PT Voided Plate – Diagonal Layout	0.998	1.776	0.998	1.786

C.2 Coefficients for the Schematic Design Phase Equations

Tables **C-3** and **C-4** provide the coefficients obtained from the multi-variate polynomial regression models that derived the MQ^* equations (refer to Eq. **4-3** in Ch. 4 of the dissertation) in both metric and imperial units for the schematic design phase (see Sec. 4.4.2 in Ch. 4 of the dissertation) when considering the **full** span range. These coefficients can be implemented in the general form of the polynomial equation (refer to Eq. **4-3** in Ch. 4 of the dissertation) to predict the concrete slab volume per area (m^3/m^2) for each concrete floor system given the span length and structural parameters. Similarly, Tables **C-5** and **C-6** provide the coefficients for the MQ^* equations when considering the **economic** span length range. The R^2 values and RMSEs for the derived MQ^* equations can be found in Section C-3. Tables **C-7** to **C-14** provide the coefficients for predicting the EC contribution from the steel rebar, void formers, and PT tendons, for both the full and economic span ranges. Readers are encouraged to download the corresponding .csv files that provide the coefficients presented in the tables below (available at: https://www.sciencedirect.com/science/article/pii/S0141029623017844).

Table **C-3**: The coefficients derived for the MQ^{*} equations (see Eq. **4-3** in Ch. 4 of the dissertation) for the six RC floor systems when considering the full span length range. Span length (L), concrete compressive strength ($f'c$), live load (LL), and dead load (DL) are in metric units when using the top coefficients; the bottom coefficients are compatible with imperial units.

Coefficient	Flat Plate	Flat Slab	One-Way Slab	Two-Way Slab with Beams	Waffle Slab	Voided Plate
β_0	-4.48×10^{-2}	-4.47×10^{-2}	0.424	0.114	0.157	0.111
	-4.48×10^{-2}	-4.47×10^{-2}	0.424	0.114	0.157	0.111
β_1	2.42×10^{-2}	2.48×10^{-2}	-6.83×10^{-2}	-4.28×10^{-3}	8.22×10^{-3}	-1.18×10^{-2}
	7.28×10^{-3}	7.45×10^{-3}	-2.05×10^{-2}	-1.28×10^{-3}	2.47×10^{-3}	-3.54×10^{-3}
β_2	-1.18×10^{-3}	-1.17×10^{-3}	1.99×10^{-3}	8.27×10^{-4}	-3.74×10^{-4}	4.58×10^{-4}
	-7.74×10^{-6}	-7.68×10^{-6}	1.40×10^{-5}	5.76×10^{-6}	-2.54×10^{-6}	3.44×10^{-6}
β_3	6.79×10^{-3}	6.63×10^{-3}	-2.30×10^{-2}	2.22×10^{-2}	-2.18×10^{-3}	1.48×10^{-3}
	3.25×10^{-4}	3.18×10^{-4}	-1.10×10^{-3}	1.06×10^{-3}	-1.04×10^{-4}	7.07×10^{-5}
β_4	1.91×10^{-2}	2.02×10^{-2}	-2.83×10^{-2}	1.56×10^{-3}	3.78×10^{-3}	5.14×10^{-3}

Coefficient	Flat Plate	Flat Slab	One-Way Slab	Two-Way Slab with Beams	Waffle Slab	Voided Plate
	9.19×10^{-4}	9.71×10^{-4}	-1.35×10^{-3}	7.52×10^{-5}	1.81×10^{-4}	2.48×10^{-4}
β_5	2.75×10^{-4}	2.91×10^{-4}	-1.22×10^{-4}	3.16×10^{-5}	3.76×10^{-6}	1.16×10^{-4}
	2.75×10^{-4}	2.91×10^{-4}	-1.22×10^{-4}	3.16×10^{-5}	3.80×10^{-6}	1.16×10^{-4}
β_6	2.11×10^{-3}	2.09×10^{-3}	4.08×10^{-3}	9.72×10^{-4}	2.18×10^{-4}	2.85×10^{-3}
	1.90×10^{-4}	1.88×10^{-4}	3.67×10^{-4}	8.75×10^{-5}	1.96×10^{-5}	2.57×10^{-4}
β_7	-6.67×10^{-4}	-6.76×10^{-4}	-5.30×10^{-4}	-8.19×10^{-5}	-6.32×10^{-5}	-5.56×10^{-4}
	-1.38×10^{-6}	-1.40×10^{-6}	-1.10×10^{-6}	-1.70×10^{-7}	-1.31×10^{-7}	-1.15×10^{-6}
β_8	9.21×10^{-4}	9.10×10^{-4}	4.80×10^{-3}	6.80×10^{-4}	2.63×10^{-4}	1.10×10^{-3}
	1.32×10^{-5}	1.31×10^{-5}	6.89×10^{-5}	9.77×10^{-6}	3.78×10^{-6}	1.58×10^{-5}
β_9	4.18×10^{-3}	4.29×10^{-3}	6.31×10^{-3}	5.07×10^{-4}	2.52×10^{-4}	3.83×10^{-3}
	6.01×10^{-5}	6.16×10^{-5}	9.06×10^{-5}	7.28×10^{-6}	3.62×10^{-6}	5.51×10^{-5}
β_{10}	6.48×10^{-5}	6.70×10^{-5}	4.28×10^{-5}	7.07×10^{-6}	1.41×10^{-6}	5.21×10^{-5}

Coefficient	Flat Plate	Flat Slab	One-Way Slab	Two-Way Slab with Beams	Waffle Slab	Voided Plate
	1.94×10^{-5}	2.01×10^{-5}	1.28×10^{-5}	2.12×10^{-6}	4.24×10^{-7}	1.56×10^{-5}
β_{11}	7.82×10^{-5}	7.95×10^{-5}	4.83×10^{-5}	6.53×10^{-6}	1.65×10^{-5}	5.49×10^{-5}
	3.68×10^{-9}	3.74×10^{-9}	2.28×10^{-9}	3.07×10^{-10}	7.84×10^{-10}	2.59×10^{-9}
β_{12}	-4.95×10^{-5}	-5.13×10^{-5}	-2.25×10^{-4}	-4.33×10^{-4}	-3.95×10^{-5}	-3.68×10^{-5}
	-1.64×10^{-8}	-1.70×10^{-8}	-7.45×10^{-8}	-1.43×10^{-7}	-1.31×10^{-8}	-1.22×10^{-8}
β_{13}	-2.40×10^{-4}	-2.50×10^{-4}	-4.11×10^{-4}	-5.38×10^{-5}	-8.77×10^{-5}	-2.13×10^{-4}
	-7.94×10^{-8}	-8.27×10^{-8}	-1.36×10^{-7}	-1.78×10^{-8}	-2.90×10^{-8}	-7.05×10^{-8}
β_{14}	-4.84×10^{-6}	-4.98×10^{-6}	-3.23×10^{-6}	-2.95×10^{-8}	-7.82×10^{-7}	-4.43×10^{-6}
	-3.34×10^{-8}	-3.44×10^{-8}	-2.23×10^{-8}	-2.04×10^{-10}	-5.40×10^{-9}	-3.06×10^{-8}
β_{15}	-3.35×10^{-4}	-3.50×10^{-4}	-3.17×10^{-4}	-3.48×10^{-4}	8.31×10^{-5}	-2.05×10^{-4}
	-7.69×10^{-7}	-8.02×10^{-7}	-7.27×10^{-7}	-7.97×10^{-7}	1.90×10^{-7}	-4.69×10^{-7}
β_{16}	-2.30×10^{-3}	-2.34×10^{-3}	-8.24×10^{-4}	-5.21×10^{-6}	-1.15×10^{-4}	-1.71×10^{-3}

Coefficient	Flat Plate	Flat Slab	One-Way Slab	Two-Way Slab with Beams	Waffle Slab	Voided Plate
	-5.28×10^{-6}	-5.37×10^{-6}	-1.89×10^{-6}	-1.19×10^{-8}	-2.64×10^{-7}	-3.91×10^{-6}
β_{17}	1.25×10^{-5}	1.37×10^{-5}	2.73×10^{-5}	2.04×10^{-7}	5.69×10^{-6}	7.79×10^{-6}
	5.98×10^{-7}	6.56×10^{-7}	1.31×10^{-6}	9.77×10^{-9}	2.73×10^{-7}	3.73×10^{-7}
β_{18}	-3.06×10^{-3}	-3.32×10^{-3}	5.97×10^{-4}	1.82×10^{-4}	-1.36×10^{-4}	-2.07×10^{-3}
	-7.05×10^{-6}	-7.65×10^{-6}	1.35×10^{-6}	4.12×10^{-7}	-3.15×10^{-7}	-4.77×10^{-6}
β_{19}	-1.49×10^{-6}	-2.39×10^{-6}	2.69×10^{-5}	4.77×10^{-7}	1.14×10^{-6}	4.73×10^{-6}
	-7.13×10^{-8}	-1.14×10^{-7}	1.29×10^{-6}	2.28×10^{-8}	5.48×10^{-8}	2.27×10^{-7}
β_{20}	-5.62×10^{-7}	-5.95×10^{-7}	-2.16×10^{-7}	-4.09×10^{-9}	1.01×10^{-8}	-3.34×10^{-7}
	-5.62×10^{-7}	-5.95×10^{-7}	-2.16×10^{-7}	-4.09×10^{-9}	1.01×10^{-8}	-3.34×10^{-7}

Notes: For the coefficients using the metric unit system, *L* is in meters, *f'c* is in MPa, *LL* is in kN/m^2, and *DL* is in kN/m^2. For the coefficients using the imperial unit system, *L* is in feet, *f'c* is in psi, *LL* is in psf, and *DL* is in psf.
MQ^*: Estimated material quantity (i.e., volume) of the concrete slab normalized by the floor area, m^3/m^2. Both sets of coefficients obtain MQ^* in m^3/m^2.

Table **C-4**: The coefficients derived for the MQ^* equations (see Eq. **4-3** in Ch. 4 of the dissertation) for the four PT floor systems when considering the full span length range. Span length (L), concrete compressive strength ($f'c$), live load (LL), and dead load (DL) are in metric units when using the top coefficients; the bottom coefficients are compatible with imperial units.

Coefficient	**Flat Plate**	**Hollow Core Slab**	**Voided Plate (Orthogonal Layout)**	**Voided Plate (Diagonal Layout)**
β_0	0.118	0.102	0.277	0.253
	0.116	0.101	0.276	0.252
β_1	7.82×10^{-3}	-9.97×10^{-3}	-2.78×10^{-2}	-2.51×10^{-2}
	2.35×10^{-3}	-2.98×10^{-3}	-8.33×10^{-3}	-7.52×10^{-3}
β_2	-2.62×10^{-3}	-6.58×10^{-4}	-5.55×10^{-4}	-4.60×10^{-4}
	-1.76×10^{-5}	-3.99×10^{-6}	-3.46×10^{-6}	-2.70×10^{-6}
β_3	-2.46×10^{-3}	1.63×10^{-3}	-8.94×10^{-3}	-9.97×10^{-3}
	-1.15×10^{-4}	7.82×10^{-5}	-4.26×10^{-4}	-4.74×10^{-4}
β_4	-4.35×10^{-3}	3.80×10^{-3}	-3.12×10^{-2}	-2.33×10^{-2}
	-2.06×10^{-4}	1.83×10^{-4}	-1.49×10^{-3}	-1.11×10^{-3}
β_5	-3.49×10^{-5}	4.30×10^{-5}	-1.97×10^{-4}	-1.19×10^{-4}
	-3.49×10^{-5}	4.30×10^{-5}	-1.98×10^{-4}	-1.19×10^{-4}
β_6	1.94×10^{-3}	2.10×10^{-3}	2.66×10^{-3}	2.57×10^{-3}
	1.74×10^{-4}	1.89×10^{-4}	2.39×10^{-4}	2.31×10^{-4}
β_7	-4.20×10^{-4}	-5.19×10^{-4}	-3.87×10^{-4}	-4.90×10^{-4}

Coefficient	Flat Plate	Hollow Core Slab	Voided Plate (Orthogonal Layout)	Voided Plate (Diagonal Layout)
	-8.71×10^{-7}	-1.08×10^{-6}	-8.02×10^{-7}	-1.02×10^{-6}
β_8	2.73×10^{-3}	2.58×10^{-3}	2.83×10^{-3}	3.04×10^{-3}
	3.92×10^{-5}	3.70×10^{-5}	4.06×10^{-5}	4.37×10^{-5}
β_9	2.59×10^{-3}	2.86×10^{-3}	3.38×10^{-3}	3.17×10^{-3}
	3.72×10^{-5}	4.11×10^{-5}	4.86×10^{-5}	4.56×10^{-5}
β_{10}	-1.26×10^{-6}	1.24×10^{-5}	9.34×10^{-6}	1.09×10^{-5}
	-3.78×10^{-7}	3.72×10^{-6}	2.80×10^{-6}	3.27×10^{-6}
β_{11}	1.13×10^{-4}	5.29×10^{-5}	7.95×10^{-5}	1.08×10^{-4}
	5.33×10^{-9}	2.47×10^{-9}	3.75×10^{-9}	5.10×10^{-9}
β_{12}	-5.61×10^{-4}	-1.42×10^{-4}	-5.89×10^{-4}	-9.12×10^{-4}
	-1.86×10^{-7}	-4.68×10^{-7}	-1.95×10^{-7}	-3.02×10^{-7}
β_{13}	-4.97×10^{-4}	-1.42×10^{-4}	-4.33×10^{-4}	-5.90×10^{-4}
	-1.64×10^{-7}	-4.70×10^{-8}	-1.43×10^{-7}	-1.95×10^{-7}
β_{14}	-5.24×10^{-7}	-4.36×10^{-7}	3.55×10^{-7}	5.13×10^{-7}
	-3.62×10^{-9}	-3.01×10^{-9}	2.46×10^{-9}	3.54×10^{-9}
β_{15}	1.28×10^{-3}	-4.14×10^{-4}	1.93×10^{-3}	2.62×10^{-3}

Coefficient	Flat Plate	Hollow Core Slab	Voided Plate (Orthogonal Layout)	Voided Plate (Diagonal Layout)
	$2.93\ \times 10^{-6}$	$-9.48\ \times 10^{-7}$	$4.43\ \times 10^{-6}$	$6.00\ \times 10^{-6}$
β_{16}	$7.60\ \times 10^{-4}$	$-1.62\ \times 10^{-3}$	$1.88\ \times 10^{-3}$	$3.00\ \times 10^{-3}$
	$1.74\ \times 10^{-6}$	-3.72×10^{-6}	$4.31\ \times 10^{-6}$	$6.88\ \times 10^{-6}$
β_{17}	$-5.08\ \times 10^{-6}$	3.71×10^{-6}	$-1.72\ \times 10^{-5}$	$-9.49\ \times 10^{-6}$
	$-2.43\ \times 10^{-7}$	1.78×10^{-7}	$-8.26\ \times 10^{-7}$	$-4.54\ \times 10^{-7}$
β_{18}	$1.25\ \times 10^{-3}$	-2.85×10^{-4}	$1.14\ \times 10^{-3}$	$6.98\ \times 10^{-4}$
	$2.85\ \times 10^{-6}$	-6.73×10^{-7}	$2.61\ \times 10^{-6}$	$1.59\ \times 10^{-6}$
β_{19}	$1.94\ \times 10^{-5}$	$3.73\ \times 10^{-6}$	$5.29\ \times 10^{-2}$	$3.64\ \times 10^{-5}$
	$9.30\ \times 10^{-7}$	$1.79\ \times 10^{-7}$	$2.53\ \times 10^{-6}$	$1.74\ \times 10^{-6}$
β_{20}	$1.07\ \times 10^{-7}$	$-9.71\ \times 10^{-8}$	$2.36\ \times 10^{-7}$	$8.72\ \times 10^{-8}$
	$1.07\ \times 10^{-7}$	$-9.71\ \times 10^{-8}$	$2.36\ \times 10^{-7}$	$8.72\ \times 10^{-8}$

Table **C-5**: The coefficients derived for the *MQ** equations for the six RC floor systems when considering the economic span length range. Span length (*L*), concrete compressive strength (*f'c*), live load (*LL*), and dead load (*DL*) are in metric units when using the top coefficients; the bottom coefficients are compatible with imperial units.

Coefficient	Flat Plate	Flat Slab	One-Way Slab	Two-Way Slab with Beams	Waffle Slab	Voided Plate
β_0	$-2.16\ \times 10^{-3}$	$-5.40\ \times 10^{-2}$	0.243	$7.83\ \times 10^{-2}$	-0.296	0.151
	$-2.72\ \times 10^{-3}$	$-5.49\ \times 10^{-2}$	0.243	$7.80\ \times 10^{-2}$	-0.296	0.150

Coefficient	Flat Plate	Flat Slab	One-Way Slab	Two-Way Slab with Beams	Waffle Slab	Voided Plate
β_1	1.79×10^{-2}	2.91×10^{-2}	-2.59×10^{-2}	-2.63×10^{-3}	8.89×10^{-2}	-1.95×10^{-2}
	5.38×10^{-3}	8.73×10^{-3}	-7.78×10^{-3}	-7.86×10^{-4}	2.67×10^{-2}	-5.83×10^{-3}
β_2	-4.61×10^{-4}	-1.38×10^{-3}	5.11×10^{-4}	1.06×10^{-3}	-3.61×10^{-3}	1.02×10^{-3}
	-2.96×10^{-6}	-9.11×10^{-6}	3.59×10^{-6}	7.38×10^{-6}	-2.48×10^{-5}	7.30×10^{-6}
β_3	4.75×10^{-3}	8.71×10^{-3}	-3.65×10^{-3}	2.62×10^{-2}	4.31×10^{-3}	1.47×10^{-3}
	2.28×10^{-4}	4.17×10^{-4}	-1.74×10^{-4}	1.26×10^{-3}	-2.06×10^{-4}	7.04×10^{-5}
β_4	1.07×10^{-2}	2.53×10^{-2}	-5.10×10^{-3}	4.60×10^{-3}	3.90×10^{-2}	1.77×10^{-3}
	5.12×10^{-4}	1.21×10^{-3}	-2.44×10^{-4}	2.21×10^{-4}	1.87×10^{-3}	8.67×10^{-5}
β_5	1.04×10^{-4}	2.15×10^{-4}	-1.33×10^{-5}	1.02×10^{-4}	2.55×10^{-4}	-2.95×10^{-6}
	1.05×10^{-4}	2.16×10^{-4}	-1.33×10^{-5}	1.02×10^{-4}	2.55×10^{-4}	-2.72×10^{-6}
β_6	2.94×10^{-3}	1.84×10^{-3}	2.61×10^{-3}	1.21×10^{-3}	-3.18×10^{-3}	3.29×10^{-3}
	2.65×10^{-4}	1.66×10^{-4}	2.35×10^{-4}	1.09×10^{-4}	-2.87×10^{-4}	2.96×10^{-4}

Coefficient	Flat Plate	Flat Slab	One-Way Slab	Two-Way Slab with Beams	Waffle Slab	Voided Plate
β_7	-6.30×10^{-4}	-6.54×10^{-4}	-2.63×10^{-4}	-2.03×10^{-4}	1.63×10^{-4}	-6.34×10^{-4}
	-1.31×10^{-6}	-1.36×10^{-6}	-5.46×10^{-7}	-4.22×10^{-7}	3.37×10^{-7}	-1.31×10^{-6}
β_8	1.23×10^{-3}	9.49×10^{-4}	1.84×10^{-3}	6.12×10^{-4}	-2.91×10^{-4}	1.28×10^{-3}
	1.77×10^{-5}	1.36×10^{-5}	2.64×10^{-5}	8.79×10^{-6}	-4.18×10^{-6}	1.84×10^{-5}
β_9	4.83×10^{-3}	4.39×10^{-3}	2.05×10^{-3}	5.59×10^{-4}	-2.36×10^{-3}	4.88×10^{-3}
	6.94×10^{-5}	6.30×10^{-5}	2.95×10^{-5}	8.03×10^{-6}	-3.40×10^{-5}	7.01×10^{-5}
β_{10}	4.49×10^{-5}	6.75×10^{-5}	8.95×10^{-6}	8.20×10^{-7}	-2.01×10^{-5}	5.97×10^{-5}
	1.35×10^{-5}	2.03×10^{-5}	2.68×10^{-6}	2.46×10^{-7}	-6.02×10^{-6}	1.79×10^{-5}
β_{11}	4.92×10^{-5}	8.09×10^{-5}	1.88×10^{-5}	2.50×10^{-5}	2.38×10^{-5}	5.93×10^{-5}
	2.32×10^{-9}	3.81×10^{-9}	8.89×10^{-10}	1.19×10^{-9}	1.13×10^{-9}	2.80×10^{-9}
β_{12}	-5.38×10^{-5}	-6.26×10^{-5}	-1.06×10^{-4}	-5.33×10^{-4}	-4.37×10^{-5}	-4.16×10^{-5}
	-1.78×10^{-8}	-2.07×10^{-8}	-3.51×10^{-8}	-1.76×10^{-7}	-1.45×10^{-8}	-1.38×10^{-8}

Coefficient	Flat Plate	Flat Slab	One-Way Slab	Two-Way Slab with Beams	Waffle Slab	Voided Plate
β_{13}	-2.48×10^{-4}	-2.93×10^{-4}	-1.41×10^{-4}	-1.21×10^{-4}	-8.63×10^{-5}	-2.91×10^{-4}
	-8.22×10^{-8}	-9.69×10^{-8}	-4.66×10^{-8}	-4.02×10^{-8}	-2.85×10^{-8}	-9.63×10^{-8}
β_{14}	-2.39×10^{-6}	-4.70×10^{-6}	-5.33×10^{-7}	-6.82×10^{-9}	-7.53×10^{-7}	-4.38×10^{-6}
	-1.65×10^{-8}	-3.24×10^{-8}	-3.68×10^{-9}	-4.73×10^{-11}	-5.20×10^{-9}	-3.02×10^{-8}
β_{15}	-2.17×10^{-4}	-3.88×10^{-4}	-4.12×10^{-5}	-2.72×10^{-4}	1.07×10^{-4}	-2.41×10^{-4}
	-4.98×10^{-7}	-8.89×10^{-7}	-9.45×10^{-8}	-6.24×10^{-7}	2.44×10^{-7}	-5.52×10^{-7}
β_{16}	-1.97×10^{-3}	-2.77×10^{-3}	-1.11×10^{-4}	4.13×10^{-5}	-3.38×10^{-4}	-2.19×10^{-3}
	-4.53×10^{-6}	-6.36×10^{-6}	-2.54×10^{-7}	9.49×10^{-8}	-7.76×10^{-7}	-5.01×10^{-6}
β_{17}	9.43×10^{-6}	1.14×10^{-5}	3.06×10^{-6}	1.95×10^{-7}	6.80×10^{-6}	7.99×10^{-6}
	4.52×10^{-7}	5.45×10^{-7}	1.47×10^{-7}	9.35×10^{-9}	3.26×10^{-7}	3.83×10^{-7}
β_{18}	-1.78×10^{-3}	-3.98×10^{-3}	2.32×10^{-4}	-1.83×10^{-4}	-4.89×10^{-4}	-2.39×10^{-3}
	-4.11×10^{-6}	-9.16×10^{-6}	5.28×10^{-7}	-4.27×10^{-7}	-1.13×10^{-6}	-5.51×10^{-6}

Coefficient	Flat Plate	Flat Slab	One-Way Slab	Two-Way Slab with Beams	Waffle Slab	Voided Plate
β_{19}	4.36×10^{-7}	-3.27×10^{-6}	5.45×10^{-6}	4.74×10^{-7}	-2.13×10^{-6}	4.58×10^{-6}
	2.09×10^{-8}	-1.56×10^{-7}	2.61×10^{-7}	2.27×10^{-8}	-1.02×10^{-7}	2.19×10^{-7}
β_{20}	-2.47×10^{-7}	-5.43×10^{-7}	-2.80×10^{-8}	-3.63×10^{-9}	2.52×10^{-8}	-3.04×10^{-7}
	-2.47×10^{-7}	-5.43×10^{-7}	-2.80×10^{-8}	-3.63×10^{-9}	2.52×10^{-8}	-3.04×10^{-7}

Notes: For the coefficients using the metric unit system, *L* is in meters, *f'c* is in MPa, *LL* is in kN/m^2, and *DL* is in kN/m^2. For the coefficients using the imperial unit system, *L* is in feet, *f'c* is in psi, *LL* is in psf, and *DL* is in psf.
MQ^*: Estimated material quantity (i.e., volume) of the concrete slab normalized by the floor area, m^3/m^2. Both sets of coefficients obtain MQ^* in m^3/m^2.

Table **C-6**: The coefficients derived for the MQ^* equations for the four PT floor systems when considering the economic span length range. Span length (*L*), concrete compressive strength (*f'c*), live load (*LL*), and dead load (*DL*) are in metric units when using the top coefficients; the bottom coefficients are compatible with imperial units.

Coefficient	Flat Plate	Hollow Core Slab	Voided Plate (Orthogonal Layout)	Voided Plate (Diagonal Layout)
β_0	0.115	9.13×10^{-2}	0.255	0.225
	0.113	8.94×10^{-2}	0.254	0.223
β_1	6.53×10^{-3}	-8.41×10^{-3}	-2.11×10^{-2}	-1.84×10^{-2}
	1.97×10^{-3}	-3.28×10^{-3}	-6.33×10^{-3}	-5.51×10^{-3}
β_2	-2.19×10^{-3}	-1.02×10^{-3}	5.97×10^{-4}	1.16×10^{-3}
	-1.45×10^{-5}	4.50×10^{-6}	4.64×10^{-6}	8.64×10^{-6}
β_3	-5.46×10^{-3}	4.08×10^{-3}	-2.02×10^{-2}	-2.40×10^{-3}

Coefficient	Flat Plate	Hollow Core Slab	Voided Plate (Orthogonal Layout)	Voided Plate (Diagonal Layout)
	-2.58×10^{-4}	-5.78×10^{-5}	-9.63×10^{-4}	-1.15×10^{-3}
β_4	-2.33×10^{-3}	7.22×10^{-3}	-4.42×10^{-2}	-3.54×10^{-2}
	-1.09×10^{-4}	9.72×10^{-5}	-2.11×10^{-3}	-1.69×10^{-3}
β_5	-1.57×10^{-5}	5.89×10^{-5}	-2.19×10^{-4}	-1.16×10^{-4}
	-1.55×10^{-6}	4.40×10^{-5}	-2.19×10^{-4}	-1.16×10^{-4}
β_6	2.21×10^{-3}	2.10×10^{-3}	2.42×10^{-3}	2.35×10^{-3}
	1.99×10^{-4}	1.84×10^{-4}	2.18×10^{-4}	2.11×10^{-4}
β_7	-6.05×10^{-4}	-5.79×10^{-4}	-5.72×10^{-4}	-7.30×10^{-4}
	-1.25×10^{-6}	-9.77×10^{-7}	-1.19×10^{-6}	-1.51×10^{-6}
β_8	3.28×10^{-3}	2.57×10^{-3}	4.01×10^{-3}	4.49×10^{-3}
	4.72×10^{-5}	3.93×10^{-5}	5.76×10^{-5}	6.45×10^{-5}
β_9	2.70×10^{-3}	3.04×10^{-3}	4.10×10^{-3}	4.03×10^{-3}
	3.88×10^{-5}	3.75×10^{-5}	5.89×10^{-5}	5.79×10^{-5}
β_{10}	-4.38×10^{-6}	1.30×10^{-5}	6.27×10^{-6}	8.42×10^{-6}
	-1.31×10^{-6}	3.48×10^{-6}	1.88×10^{-6}	2.52×10^{-6}
β_{11}	1.50×10^{-4}	6.98×10^{-5}	1.08×10^{-4}	1.47×10^{-4}

Coefficient	Flat Plate	Hollow Core Slab	Voided Plate (Orthogonal Layout)	Voided Plate (Diagonal Layout)
	7.11×10^{-9}	1.87×10^{-9}	5.09×10^{-9}	6.93×10^{-9}
β_{12}	-7.44×10^{-4}	-1.51×10^{-4}	-7.96×10^{-4}	-1.24×10^{-3}
	-2.46×10^{-7}	-8.43×10^{-8}	-2.64×10^{-7}	-410×10^{-7}
β_{13}	-6.23×10^{-4}	-1.84×10^{-4}	-5.81×10^{-4}	-7.96×10^{-4}
	-2.06×10^{-7}	-6.99×10^{-8}	-1.92×10^{-7}	-2.63×10^{-7}
β_{14}	-4.83×10^{-7}	-5.55×10^{-7}	5.28×10^{-7}	7.25×10^{-7}
	-3.34×10^{-9}	-4.88×10^{-9}	3.66×10^{-9}	5.01×10^{-9}
β_{15}	1.60×10^{-3}	-6.14×10^{-4}	2.61×10^{-3}	3.55×10^{-3}
	3.66×10^{-6}	-8.34×10^{-9}	5.99×10^{-6}	8.13×10^{-6}
β_{16}	9.39×10^{-4}	-2.17×10^{-3}	2.50×10^{-3}	4.03×10^{-3}
	2.15×10^{-6}	-1.14×10^{-6}	5.73×10^{-6}	9.23×10^{-6}
β_{17}	-6.17×10^{-6}	4.51×10^{-6}	-2.37×10^{-5}	-1.31×10^{-5}
	-2.96×10^{-7}	2.47×10^{-7}	-1.14×10^{-6}	-6.26×10^{-7}
β_{18}	1.24×10^{-3}	-5.29×10^{-4}	1.44×10^{-3}	8.73×10^{-4}
	2.82×10^{-6}	-3.92×10^{-7}	3.27×10^{-6}	1.99×10^{-6}
β_{19}	1.99×10^{-5}	-2.69×10^{-7}	7.11×10^{-5}	4.90×10^{-5}

Coefficient	Flat Plate	Hollow Core Slab	Voided Plate (Orthogonal Layout)	Voided Plate (Diagonal Layout)
	9.52×10^{-7}	2.67×10^{-7}	3.40×10^{-6}	2.35×10^{-6}
β_{20}	1.15×10^{-7}	-1.23×10^{-7}	3.17×10^{-7}	1.16×10^{-7}
	1.15×10^{-7}	-9.11×10^{-8}	3.17×10^{-7}	1.16×10^{-7}

Table **C-7**: The coefficients derived for the EC_{est} equations for the steel rebar (EC_{Rebar}) for the six RC floor systems when considering the full span length range. Span length (*L*), concrete compressive strength (*f'c*), live load (*LL*), and dead load (*DL*) are in metric units when using the top coefficients; the bottom coefficients are compatible with imperial units.

Coefficient	Flat Plate	Flat Slab	One-Way Slab	Two-Way Slab with Beams	Waffle Slab	Voided Plate
β_0	-0.836	3.409	23.62	21.09	11.59	2.242
	-0.861	3.410	23.57	21.07	11.60	2.212
β_1	0.753	2.95×10^{-2}	-3.920	-0.431	-1.054	-3.62×10^{-2}
	0.226	8.87×10^{-3}	-1.175	-0.129	-0.316	-1.06×10^{-2}
β_2	-3.85×10^{-2}	-2.10×10^{-2}	-0.3270	-1.024	-4.25×10^{-2}	-7.81×10^{-3}
	-2.56×10^{-4}	-1.46×10^{-4}	-2.24×10^{-3}	-7.06×10^{-3}	-2.95×10^{-4}	-4.21×10^{-5}
β_3	0.2968	-0.3481	6.41×10^{-2}	-1.428	-0.5059	0.2046
	1.42×10^{-2}	-1.67×10^{-2}	3.14×10^{-3}	-6.85×10^{-2}	-2.42×10^{-2}	9.79×10^{-3}

Coefficient	Flat Plate	Flat Slab	One-Way Slab	Two-Way Slab with Beams	Waffle Slab	Voided Plate
β_4	0.660	-0.267	-0.402	0.356	-0.285	0.493
	3.17×10^{-2}	-1.27×10^{-2}	-1.91×10^{-2}	1.72×10^{-2}	-1.36×10^{-2}	2.37×10^{-2}
β_5	9.03×10^{-3}	1.92×10^{-4}	-3.54×10^{-3}	4.57×10^{-3}	1.57×10^{-3}	6.80×10^{-3}
	9.04×10^{-3}	1.94×10^{-4}	-3.55×10^{-3}	4.56×10^{-3}	1.57×10^{-3}	6.81×10^{-3}
β_6	0.1042	9.71×10^{-2}	0.3946	0.2729	8.84×10^{-2}	0.1459
	9.38×10^{-3}	8.74×10^{-3}	3.55×10^{-2}	2.46×10^{-2}	7.96×10^{-3}	1.31×10^{-2}
β_7	-1.75×10^{-2}	2.99×10^{-4}	-6.85×10^{-2}	-1.43×10^{-2}	5.24×10^{-3}	-2.33×10^{-2}
	-3.62×10^{-5}	6.17×10^{-7}	-1.42×10^{-4}	-2.96×10^{-5}	1.09×10^{-5}	-4.83×10^{-5}
β_8	4.31×10^{-2}	0.1577	0.3872	0.3183	0.1033	5.69×10^{-2}
	6.19×10^{-4}	2.27×10^{-3}	5.56×10^{-3}	4.57×10^{-3}	1.48×10^{-3}	8.17×10^{-4}
β_9	0.1361	0.1276	0.2926	0.4360	6.32×10^{-2}	0.1838
	1.95×10^{-3}	1.83×10^{-3}	4.20×10^{-3}	6.26×10^{-3}	9.07×10^{-4}	2.64×10^{-3}
β_{10}	1.85×10^{-3}	7.27×10^{-5}	-4.57×10^{-4}	-4.15×10^{-3}	-2.56×10^{-4}	2.40×10^{-3}

Coefficient	Flat Plate	Flat Slab	One-Way Slab	Two-Way Slab with Beams	Waffle Slab	Voided Plate
	5.55×10^{-4}	2.18×10^{-5}	-1.37×10^{-4}	-1.25×10^{-3}	-7.68×10^{-5}	7.21×10^{-4}
β_{11}	3.02×10^{-3}	6.05×10^{-4}	1.38×10^{-2}	1.33×10^{-2}	-5.37×10^{-5}	2.82×10^{-3}
	1.43×10^{-7}	2.89×10^{-8}	6.57×10^{-7}	6.34×10^{-7}	-2.36×10^{-9}	1.33×10^{-7}
β_{12}	4.97×10^{-3}	3.06×10^{-4}	-2.68×10^{-2}	5.69×10^{-2}	4.17×10^{-3}	3.27×10^{-3}
	1.64×10^{-6}	1.01×10^{-7}	-8.86×10^{-6}	1.88×10^{-5}	1.38×10^{-6}	1.08×10^{-6}
β_{13}	-1.12×10^{-2}	-1.20×10^{-3}	-1.25×10^{-2}	-1.46×10^{-2}	3.14×10^{-3}	-1.08×10^{-2}
	-3.69×10^{-6}	-3.97×10^{-7}	-4.15×10^{-6}	-4.84×10^{-6}	1.04×10^{-6}	-3.57×10^{-6}
β_{14}	-3.04×10^{-4}	-2.35×10^{-5}	1.61×10^{-4}	1.98×10^{-4}	-5.52×10^{-6}	-2.54×10^{-4}
	-2.10×10^{-6}	-1.63×10^{-7}	1.12×10^{-6}	1.37×10^{-6}	-3.82×10^{-8}	-1.75×10^{-6}
β_{15}	-7.15×10^{-3}	2.55×10^{-2}	-4.93×10^{-2}	-7.08×10^{-2}	3.02×10^{-3}	-1.01×10^{-2}
	-1.64×10^{-5}	5.85×10^{-5}	-1.13×10^{-4}	-1.62×10^{-4}	6.92×10^{-6}	-2.30×10^{-5}
β_{16}	-9.91×10^{-2}	2.09×10^{-2}	-0.1272	-0.1305	-5.39×10^{-3}	-0.1103
	-2.27×10^{-4}	4.79×10^{-5}	-2.92×10^{-4}	-2.99×10^{-4}	-1.23×10^{-5}	-2.53×10^{-4}

Coefficient	Flat Plate	Flat Slab	One-Way Slab	Two-Way Slab with Beams	Waffle Slab	Voided Plate
β_{17}	-1.44×10^{-4}	-1.60×10^{-4}	-9.06×10^{-4}	-1.37×10^{-3}	-2.35×10^{-4}	7.05×10^{-5}
	-6.92×10^{-6}	-7.65×10^{-6}	-4.34×10^{-5}	-6.54×10^{-5}	-1.12×10^{-5}	3.38×10^{-6}
β_{18}	-8.30×10^{-2}	3.77×10^{-3}	-3.00×10^{-2}	-2.87×10^{-2}	-5.67×10^{-3}	-0.1043
	-1.91×10^{-4}	7.73×10^{-6}	-7.01×10^{-5}	-6.79×10^{-5}	-1.33×10^{-5}	-2.40×10^{-4}
β_{19}	4.06×10^{-4}	3.92×10^{-5}	5.20×10^{-4}	-3.19×10^{-3}	-4.27×10^{-5}	3.07×10^{-4}
	-1.94×10^{-5}	1.88×10^{-6}	2.49×10^{-5}	-1.53×10^{-4}	-2.05×10^{-6}	1.47×10^{-5}
β_{20}	-9.28×10^{-6}	7.95×10^{-7}	8.32×10^{-6}	2.74×10^{-5}	1.73×10^{-6}	-1.37×10^{-5}
	-9.28×10^{-6}	7.95×10^{-7}	8.32×10^{-6}	2.74×10^{-5}	1.73×10^{-6}	-1.37×10^{-5}

Table **C-8**: The coefficients derived for the EC_{est} equations for the steel rebar (EC_{Rebar}) for the four PT floor systems when considering the full span length range. Span length (*L*), concrete compressive strength (*f'c*), live load (*LL*), and dead load (*DL*) are in metric units when using the top coefficients; the bottom coefficients are compatible with imperial units.

Coefficient	Flat Plate	Hollow Core Slab	Voided Plate (Orthogonal Layout)	Voided Plate (Diagonal Layout)
β_0	2.226	-6.498	1.801	11.13
	2.226	-6.498	1.825	11.13
β_1	1.14×10^{-2}	3.578	-0.2570	-1.744

Coefficient	Flat Plate	Hollow Core Slab	Voided Plate (Orthogonal Layout)	Voided Plate (Diagonal Layout)
	3.44×10^{-3}	1.073	-7.72×10^{-2}	-0.5225
β_2	-1.45×10^{-2}	-0.2573	6.01×10^{-3}	2.58×10^{-2}
	-1.01×10^{-4}	-1.75×10^{-3}	3.30×10^{-5}	2.05×10^{-4}
β_3	2.93×10^{-2}	1.971	6.77×10^{-3}	-0.9156
	1.41×10^{-3}	9.44×10^{-2}	2.80×10^{-4}	-4.36×10^{-2}
β_4	4.66×10^{-2}	2.393	0.4302	-1.752
	2.26×10^{-3}	0.1146	2.06×10^{-2}	-8.37×10^{-2}
β_5	3.17×10^{-4}	1.91×10^{-2}	6.54×10^{-4}	-8.31×10^{-3}
	3.17×10^{-4}	1.91×10^{-2}	6.55×10^{-4}	-8.31×10^{-3}
β_6	7.86×10^{-2}	-1.26×10^{-2}	5.78×10^{-2}	0.1435
	7.07×10^{-3}	-1.13×10^{-3}	5.20×10^{-3}	1.29×10^{-2}
β_7	-6.05×10^{-4}	-1.43×10^{-2}	6.36×10^{-3}	-2.86×10^{-2}
	-1.26×10^{-6}	-2.96×10^{-5}	1.32×10^{-5}	-5.93×10^{-5}
β_8	9.83×10^{-2}	2.37×10^{-2}	0.1112	0.2734
	1.41×10^{-3}	3.41×10^{-4}	1.60×10^{-3}	3.93×10^{-3}
β_9	7.89×10^{-2}	1.94×10^{-2}	7.70×10^{-2}	0.2506
	1.13×10^{-3}	2.78×10^{-4}	1.11×10^{-3}	3.60×10^{-3}

Coefficient	Flat Plate	Hollow Core Slab	Voided Plate (Orthogonal Layout)	Voided Plate (Diagonal Layout)
β_{10}	-4.09×10^{-6}	8.65×10^{-5}	-8.61×10^{-5}	6.63×10^{-4}
	-1.23×10^{-6}	2.59×10^{-5}	-2.58×10^{-5}	1.99×10^{-4}
β_{11}	4.56×10^{-4}	2.13×10^{-3}	-1.57×10^{-3}	6.05×10^{-3}
	2.19×10^{-8}	9.89×10^{-8}	-7.40×10^{-8}	2.86×10^{-7}
β_{12}	-8.39×10^{-4}	7.69×10^{-3}	1.46×10^{-2}	-6.09×10^{-2}
	-2.79×10^{-7}	2.54×10^{-6}	4.82×10^{-6}	-2.01×10^{-5}
β_{13}	-4.43×10^{-4}	2.22×10^{-2}	8.65×10^{-3}	-3.47×10^{-2}
	-1.47×10^{-7}	-7.33×10^{-6}	2.86×10^{-6}	-1.15×10^{-5}
β_{14}	3.47×10^{-7}	1.12×10^{-4}	1.11×10^{-5}	5.04×10^{-5}
	2.39×10^{-9}	7.70×10^{-7}	7.67×10^{-8}	3.48×10^{-7}
β_{15}	-1.24×10^{-2}	-7.84×10^{-2}	-5.27×10^{-2}	0.1879
	-2.85×10^{-5}	-1.80×10^{-4}	-1.21×10^{-4}	4.31×10^{-4}
β_{16}	-2.73×10^{-2}	-0.3109	-9.84×10^{-2}	0.229
	-6.26×10^{-5}	-7.13×10^{-4}	-2.26×10^{-4}	5.27×10^{-4}
β_{17}	-1.70×10^{-5}	-8.90×10^{-4}	-6.66×10^{-6}	-4.73×10^{-4}
	-8.13×10^{-7}	-4.26×10^{-5}	-3.19×10^{-7}	-2.26×10^{-5}
β_{18}	-1.95×10^{-2}	-0.1590	-3.55×10^{-2}	5.97×10^{-2}

Coefficient	Flat Plate	Hollow Core Slab	Voided Plate (Orthogonal Layout)	Voided Plate (Diagonal Layout)
	-4.53×10^{-5}	-3.66×10^{-4}	-8.19×10^{-5}	1.36×10^{-4}
β_{19}	-5.51×10^{-5}	-1.36×10^{-3}	-1.01×10^{-3}	2.22×10^{-3}
	-2.64×10^{-6}	-6.54×10^{-6}	-4.83×10^{-5}	1.06×10^{-4}
β_{20}	-2.11×10^{-7}	-1.39×10^{-5}	-1.25×10^{-6}	5.11×10^{-6}
	-2.11×10^{-7}	-1.39×10^{-5}	-1.25×10^{-6}	5.11×10^{-6}

Table **C-9**: The coefficients derived for the EC_{est} equations for the steel rebar (EC_{Rebar}) for the six RC floor systems when considering the economic span length range. Span length (L), concrete compressive strength ($f'c$), live load (LL), and dead load (DL) are in metric units when using the top coefficients; the bottom coefficients are compatible with imperial units.

Coefficient	Flat Plate	Flat Slab	One-Way Slab	Two-Way Slab with Beams	Waffle Slab	Voided Plate
β_0	0.3072	4.562	25.55	19.69	12.94	0.8376
	0.2944	4.566	25.54	19.69	12.96	0.8081
β_1	0.6897	-0.2534	-4.207	-1.632	-0.9446	0.2208
	0.2071	7.61×10^{-2}	-1.262	-0.4894	-0.2835	6.65×10^{-2}
β_2	-3.64×10^{-2}	-2.30×10^{-2}	-0.2460	-0.8339	-0.1245	-3.88×10^{-2}
	-2.46×10^{-4}	-1.61×10^{-4}	-1.70×10^{-3}	-5.75×10^{-3}	-8.63×10^{-4}	-2.56×10^{-4}

Coefficient	Flat Plate	Flat Slab	One-Way Slab	Two-Way Slab with Beams	Waffle Slab	Voided Plate
β_3	0.2978	-0.2305	-0.6602	-2.651	-0.9752	0.5121
	1.42×10^{-2}	-1.10×10^{-2}	-3.16×10^{-2}	-0.1271	-4.67×10^{-2}	2.45×10^{-2}
β_4	0.4514	-0.2810	-1.177	-1.378	-0.1897	0.8134
	2.17×10^{-2}	-1.34×10^{-2}	-5.63×10^{-2}	-6.59×10^{-2}	-9.07×10^{-3}	3.90×10^{-2}
β_5	3.76×10^{-3}	-1.93×10^{-4}	-1.07×10^{-2}	2.55×10^{-2}	7.57×10^{-3}	3.73×10^{-3}
	3.77×10^{-3}	-1.91×10^{-4}	-1.07×10^{-2}	2.55×10^{-2}	7.57×10^{-3}	3.74×10^{-3}
β_6	0.1176	0.1106	0.3971	0.3587	7.31×10^{-2}	0.1377
	1.06×10^{-2}	9.96×10^{-3}	3.57×10^{-2}	3.23×10^{-2}	6.58×10^{-3}	1.24×10^{-2}
β_7	-1.36×10^{-2}	2.66×10^{-3}	-3.09×10^{-2}	-9.35×10^{-3}	1.10×10^{-2}	-2.19×10^{-2}
	-2.82×10^{-5}	5.52×10^{-6}	-6.41×10^{-5}	-1.94×10^{-5}	2.27×10^{-5}	-4.54×10^{-5}
β_8	4.52×10^{-2}	0.1449	0.2409	0.3966	0.1433	3.84×10^{-2}
	6.50×10^{-4}	2.08×10^{-3}	3.46×10^{-3}	5.70×10^{-3}	2.06×10^{-3}	5.52×10^{-4}

Coefficient	Flat Plate	Flat Slab	One-Way Slab	Two-Way Slab with Beams	Waffle Slab	Voided Plate
β_9	0.1418	0.1218	0.2157	0.5526	5.51×10^{-2}	0.1919
	2.04×10^{-3}	1.75×10^{-3}	3.10×10^{-3}	7.94×10^{-3}	7.91×10^{-4}	2.76×10^{-3}
β_{10}	1.22×10^{-3}	8.19×10^{-5}	6.29×10^{-4}	-5.50×10^{-3}	-7.76×10^{-4}	2.53×10^{-3}
	3.66×10^{-4}	2.46×10^{-5}	1.89×10^{-4}	-1.65×10^{-3}	-2.33×10^{-4}	7.59×10^{-4}
β_{11}	1.77×10^{-3}	1.78×10^{-4}	7.73×10^{-3}	1.08×10^{-2}	-1.37×10^{-4}	2.95×10^{-3}
	8.36×10^{-8}	8.68×10^{-9}	3.68×10^{-7}	5.15×10^{-7}	-6.17×10^{-9}	1.39×10^{-7}
β_{12}	4.08×10^{-3}	3.40×10^{-3}	-4.19×10^{-3}	6.13×10^{-2}	6.30×10^{-3}	5.27×10^{-3}
	1.35×10^{-6}	1.12×10^{-6}	-1.39×10^{-6}	2.03×10^{-5}	2.08×10^{-6}	1.74×10^{-6}
β_{13}	-8.58×10^{-3}	5.54×10^{-4}	-2.24×10^{-3}	-5.23×10^{-3}	3.14×10^{-3}	-1.30×10^{-2}
	-2.84×10^{-6}	1.83×10^{-7}	-7.43×10^{-7}	-1.73×10^{-6}	1.85×10^{-6}	-4.29×10^{-6}
β_{14}	-1.58×10^{-4}	-2.54×10^{-5}	-1.19×10^{-5}	4.57×10^{-5}	7.56×10^{-6}	-2.40×10^{-4}
	-1.09×10^{-6}	-1.76×10^{-7}	-8.24×10^{-8}	3.17×10^{-7}	5.21×10^{-8}	-1.66×10^{-6}

Coefficient	Flat Plate	Flat Slab	One-Way Slab	Two-Way Slab with Beams	Waffle Slab	Voided Plate
β_{15}	-1.28×10^{-2}	1.51×10^{-2}	9.78×10^{-3}	-4.51×10^{-2}	-2.14×10^{-4}	-2.07×10^{-2}
	-2.94×10^{-5}	3.46×10^{-5}	-2.24×10^{-5}	-1.03×10^{-4}	-4.78×10^{-7}	-4.57×10^{-5}
β_{16}	-7.60×10^{-2}	1.33×10^{-2}	2.94×10^{-3}	-8.91×10^{-2}	-1.55×10^{-2}	-0.1468
	-1.74×10^{-4}	3.04×10^{-5}	6.75×10^{-6}	-2.04×10^{-4}	-3.56×10^{-5}	-3.37×10^{-4}
β_{17}	-3.08×10^{-5}	-1.48×10^{-4}	5.13×10^{-4}	-1.31×10^{-3}	-4.07×10^{-4}	2.95×10^{-5}
	-1.47×10^{-6}	-7.06×10^{-6}	2.45×10^{-5}	-6.25×10^{-5}	-1.95×10^{-5}	1.41×10^{-6}
β_{18}	-5.06×10^{-2}	1.39×10^{-2}	2.42×10^{-2}	1.47×10^{-2}	-1.02×10^{-2}	-0.1319
	-1.17×10^{-4}	3.09×10^{-5}	5.50×10^{-5}	3.19×10^{-5}	-2.40×10^{-5}	-3.04×10^{-4}
β_{19}	2.13×10^{-4}	6.56×10^{-5}	1.43×10^{-3}	-3.18×10^{-3}	-1.14×10^{-4}	1.85×10^{-4}
	1.02×10^{-5}	3.14×10^{-6}	6.83×10^{-5}	-1.52×10^{-4}	-5.47×10^{-6}	8.84×10^{-6}
β_{20}	-3.30×10^{-6}	1.04×10^{-6}	6.56×10^{-6}	2.44×10^{-5}	2.89×10^{-6}	-1.28×10^{-5}
	-3.30×10^{-6}	1.04×10^{-6}	6.56×10^{-6}	2.44×10^{-5}	2.89×10^{-6}	-1.28×10^{-5}

Table **C-10**: The coefficients derived for the EC_{est} equations for the steel rebar (EC_{Rebar}) for the four PT floor systems when considering the economic span length range. Span length (L), concrete compressive strength ($f'c$), live load (LL), and dead load (DL) are in metric units when using the top coefficients; the bottom coefficients are compatible with imperial units.

Coefficient	Flat Plate	Hollow Core Slab	Voided Plate (Orthogonal Layout)	Voided Plate (Diagonal Layout)
β_0	1.457	−32.52	3.266	11.80
	1.456	−32.59	3.299	11.68
β_1	6.01×10^{-2}	7.750	−0.6356	−1.823
	1.81×10^{-3}	2.325	−0.1908	−0.5462
β_2	-3.24×10^{-3}	−0.4642	1.55×10^{-3}	0.1646
	-2.30×10^{-5}	-3.17×10^{-3}	-6.52×10^{-7}	1.17×10^{-3}
β_3	0.2124	3.818	0.6677	−1.999
	1.02×10^{-2}	0.1828	3.19×10^{-2}	-9.55×10^{-2}
β_4	0.1581	4.881	0.8037	−2.629
	7.60×10^{-3}	0.2337	3.85×10^{-2}	−0.1257
β_5	2.73×10^{-5}	3.42×10^{-2}	-4.06×10^{-3}	-8.91×10^{-3}
	2.75×10^{-5}	3.42×10^{-2}	-4.06×10^{-3}	-8.91×10^{-3}
β_6	8.04×10^{-2}	−0.1756	7.51×10^{-2}	0.1517
	7.24×10^{-3}	-1.58×10^{-2}	6.76×10^{-3}	1.37×10^{-2}
β_7	-2.58×10^{-3}	4.16×10^{-4}	7.82×10^{-3}	-4.51×10^{-2}

Coefficient	Flat Plate	Hollow Core Slab	Voided Plate (Orthogonal Layout)	Voided Plate (Diagonal Layout)
	-5.36×10^{-6}	8.76×10^{-7}	1.62×10^{-5}	-9.36×10^{-5}
β_8	9.03×10^{-2}	-0.1204	6.11×10^{-2}	0.3805
	1.30×10^{-3}	-1.73×10^{-3}	8.78×10^{-4}	5.47×10^{-3}
β_9	7.23×10^{-2}	-0.1503	6.30×10^{-2}	0.3111
	1.04×10^{-3}	-2.16×10^{-3}	9.05×10^{-4}	4.47×10^{-3}
β_{10}	3.89×10^{-6}	-8.94×10^{-4}	3.54×10^{-4}	5.52×10^{-4}
	1.17×10^{-6}	-2.68×10^{-4}	1.06×10^{-4}	1.66×10^{-4}
β_{11}	6.59×10^{-4}	2.18×10^{-3}	-2.10×10^{-3}	8.26×10^{-3}
	3.15×10^{-8}	1.00×10^{-7}	-9.89×10^{-8}	3.90×10^{-7}
β_{12}	-1.12×10^{-3}	1.27×10^{-2}	1.94×10^{-2}	-8.34×10^{-2}
	-3.72×10^{-7}	4.21×10^{-6}	6.42×10^{-6}	-2.76×10^{-5}
β_{13}	-7.73×10^{-4}	2.52×10^{-2}	1.15×10^{-2}	-4.72×10^{-2}
	-2.56×10^{-7}	8.43×10^{-6}	3.79×10^{-6}	-1.56×10^{-5}
β_{14}	-1.26×10^{-6}	1.30×10^{-4}	1.44×10^{-5}	7.00×10^{-5}
	-8.73×10^{-9}	9.00×10^{-7}	9.93×10^{-8}	4.84×10^{-7}
β_{15}	-2.11×10^{-2}	-0.1008	-7.49×10^{-2}	0.2519

Coefficient	Flat Plate	Hollow Core Slab	Voided Plate (Orthogonal Layout)	Voided Plate (Diagonal Layout)
	-4.83×10^{-5}	-2.31×10^{-4}	-1.72×10^{-4}	5.78×10^{-4}
β_{16}	-3.97×10^{-2}	-0.3594	-0.1385	0.3014
	-9.10×10^{-5}	-8.24×10^{-4}	-3.17×10^{-4}	6.91×10^{-4}
β_{17}	-5.92×10^{-6}	-1.12×10^{-3}	-5.13×10^{-6}	-6.53×10^{-4}
	-2.83×10^{-7}	-5.35×10^{-5}	-2.46×10^{-7}	-3.13×10^{-5}
β_{18}	-1.76×10^{-2}	-0.2106	-4.60×10^{-2}	6.96×10^{-2}
	-4.09×10^{-5}	-4.85×10^{-4}	-1.06×10^{-4}	1.58×10^{-4}
β_{19}	-1.08×10^{-6}	-1.03×10^{-3}	-1.34×10^{-3}	2.99×10^{-3}
	-5.20×10^{-8}	-4.91×10^{-5}	-6.43×10^{-5}	1.43×10^{-4}
β_{20}	-7.23×10^{-10}	-1.74×10^{-5}	-1.53×10^{-6}	6.76×10^{-6}
	-7.23×10^{-10}	-1.74×10^{-5}	-1.53×10^{-6}	6.76×10^{-6}

Table **C-11**: The coefficients derived for the EC_{est} equations for the void formers (EC_{Voids}) for the three voided systems when considering the full span length range. Span length (*L*), concrete compressive strength (*f'c*), live load (*LL*), and dead load (*DL*) are in metric units when using the top coefficients; the bottom coefficients are compatible with imperial units.

Coefficient	RC Voided Plate	PT Voided Plate (Orthogonal Layout)	PT Voided Plate (Diagonal Layout)
β_0	0.2166	0.9940	0.1931

Coefficient	RC Voided Plate	PT Voided Plate (Orthogonal Layout)	PT Voided Plate (Diagonal Layout)
	0.2089	0.9907	0.1926
β_1	2.45×10^{-2}	0.1921	0.2818
	7.41×10^{-3}	5.77×10^{-2}	8.45×10^{-2}
β_2	-3.80×10^{-4}	-8.31×10^{-4}	-4.56×10^{-3}
	4.62×10^{-7}	-4.87×10^{-6}	-3.15×10^{-5}
β_3	3.45×10^{-2}	-1.93×10^{-2}	7.20×10^{-2}
	1.65×10^{-3}	-9.08×10^{-4}	3.46×10^{-3}
β_4	0.1006	-0.2815	1.39×10^{-2}
	4.83×10^{-3}	-1.35×10^{-2}	6.70×10^{-4}
β_5	1.59×10^{-3}	-2.04×10^{-3}	-2.26×10^{-4}
	1.60×10^{-3}	-2.04×10^{-3}	-2.26×10^{-4}
β_6	2.46×10^{-2}	-4.77×10^{-3}	-6.94×10^{-3}
	2.21×10^{-3}	-4.30×10^{-4}	-6.25×10^{-4}

Coefficient	RC Voided Plate	PT Voided Plate (Orthogonal Layout)	PT Voided Plate (Diagonal Layout)
β_7	-5.66×10^{-3}	-1.10×10^{-3}	1.66×10^{-4}
	-1.17×10^{-5}	-2.28×10^{-6}	3.43×10^{-7}
β_8	1.05×10^{-2}	1.76×10^{-4}	-1.14×10^{-2}
	1.50×10^{-4}	2.53×10^{-6}	-1.63×10^{-4}
β_9	3.87×10^{-2}	4.39×10^{-3}	-1.14×10^{-2}
	5.56×10^{-4}	6.31×10^{-5}	-1.64×10^{-4}
β_{10}	5.39×10^{-4}	9.57×10^{-5}	3.44×10^{-5}
	1.62×10^{-4}	2.87×10^{-5}	1.03×10^{-5}
β_{11}	6.01×10^{-4}	4.64×10^{-4}	2.64×10^{-4}
	2.83×10^{-8}	2.21×10^{-8}	1.26×10^{-8}
β_{12}	-3.28×10^{-4}	-5.13×10^{-3}	-2.80×10^{-3}
	-1.08×10^{-7}	-1.70×10^{-6}	-9.26×10^{-7}
β_{13}	-2.21×10^{-3}	-2.61×10^{-3}	-1.56×10^{-3}

Coefficient	RC Voided Plate	PT Voided Plate (Orthogonal Layout)	PT Voided Plate (Diagonal Layout)
	-7.30×10^{-7}	-8.62×10^{-7}	-5.15×10^{-7}
β_{14}	-4.68×10^{-5}	7.54×10^{-6}	1.80×10^{-6}
	-3.23×10^{-7}	5.22×10^{-8}	1.24×10^{-8}
β_{15}	-2.39×10^{-3}	2.08×10^{-2}	7.20×10^{-3}
	5.48×10^{-6}	4.78×10^{-5}	1.65×10^{-5}
β_{16}	-2.01×10^{-2}	2.37×10^{-2}	7.32×10^{-3}
	-4.60×10^{-5}	5.44×10^{-5}	1.68×10^{-5}
β_{17}	8.53×10^{-5}	-1.81×10^{-4}	-4.95×10^{-5}
	4.08×10^{-6}	-8.64×10^{-6}	-2.37×10^{-6}
β_{18}	-2.41×10^{-2}	9.79×10^{-3}	-2.22×10^{-3}
	-5.55×10^{-5}	2.24×10^{-5}	-5.05×10^{-6}
β_{19}	3.75×10^{-5}	6.31×10^{-4}	2.16×10^{-4}
	1.80×10^{-6}	3.02×10^{-5}	1.03×10^{-5}

Coefficient	RC Voided Plate	PT Voided Plate (Orthogonal Layout)	PT Voided Plate (Diagonal Layout)
β_{20}	-3.73×10^{-6}	2.33×10^{-6}	2.65×10^{-7}
	-3.73×10^{-6}	2.33×10^{-6}	2.65×10^{-7}

Table **C-12**: The coefficients derived for the EC_{est} equations for the void formers (EC_{Voids}) for the three voided systems when considering the economical span length range. Span length (*L*), concrete compressive strength (*f'c*), live load (*LL*), and dead load (*DL*) are in metric units when using the top coefficients; the bottom coefficients are compatible with imperial units.

Coefficient	RC Voided Plate	PT Voided Plate (Orthogonal Layout)	PT Voided Plate (Diagonal Layout)
β_0	-0.4451	3.76×10^{-2}	-1.344
	-0.4529	3.19×10^{-2}	-1.345
β_1	0.1625	0.3732	0.5369
	4.88×10^{-2}	0.1120	0.1611
β_2	-7.95×10^{-3}	1.11×10^{-2}	-3.41×10^{-3}
	-5.17×10^{-5}	7.84×10^{-5}	-2.34×10^{-5}
β_3	8.84×10^{-2}	-0.1287	7.47×10^{-2}
	4.23×10^{-3}	-6.14×10^{-3}	3.59×10^{-3}

Coefficient	RC Voided Plate	PT Voided Plate (Orthogonal Layout)	PT Voided Plate (Diagonal Layout)
β_4	0.1785	-0.3687	7.69×10^{-2}
	8.57×10^{-3}	-1.76×10^{-2}	3.69×10^{-4}
β_5	1.16×10^{-3}	-1.80×10^{-3}	4.61×10^{-4}
	1.16×10^{-3}	-1.80×10^{-3}	4.61×10^{-4}
β_6	1.83×10^{-2}	-1.16×10^{-2}	-1.69×10^{-2}
	1.65×10^{-3}	-1.05×10^{-3}	-1.52×10^{-3}
β_7	-5.28×10^{-3}	-2.49×10^{-3}	-1.03×10^{-4}
	-1.09×10^{-5}	-5.17×10^{-6}	-2.14×10^{-7}
β_8	7.38×10^{-3}	1.03×10^{-2}	-1.08×10^{-2}
	1.06×10^{-4}	1.48×10^{-4}	-1.55×10^{-4}
β_9	4.00×10^{-2}	4.49×10^{-3}	-1.85×10^{-2}
	5.75×10^{-4}	6.45×10^{-5}	-2.65×10^{-4}
β_{10}	5.47×10^{-4}	2.46×10^{-5}	-2.87×10^{-5}

Coefficient	RC Voided Plate	PT Voided Plate (Orthogonal Layout)	PT Voided Plate (Diagonal Layout)
	1.64×10^{-4}	7.39×10^{-6}	-8.61×10^{-6}
β_{11}	6.41×10^{-4}	6.49×10^{-4}	3.72×10^{-4}
	3.02×10^{-8}	3.08×10^{-8}	1.77×10^{-8}
β_{12}	-1.78×10^{-4}	-7.24×10^{-3}	-4.06×10^{-3}
	-5.87×10^{-8}	-2.40×10^{-6}	-1.34×10^{-6}
β_{13}	-2.77×10^{-3}	-3.58×10^{-3}	-2.16×10^{-3}
	-9.17×10^{-7}	-1.19×10^{-6}	-7.16×10^{-7}
β_{14}	-4.41×10^{-5}	1.10×10^{-5}	2.75×10^{-6}
	-3.05×10^{-7}	7.61×10^{-8}	1.90×10^{-8}
β_{15}	-3.26×10^{-3}	2.94×10^{-2}	1.12×10^{-2}
	-7.47×10^{-6}	6.74×10^{-5}	2.56×10^{-5}
β_{16}	-2.76×10^{-2}	3.30×10^{-2}	1.17×10^{-2}
	-6.32×10^{-5}	7.57×10^{-5}	2.68×10^{-5}

Coefficient	RC Voided Plate	PT Voided Plate (Orthogonal Layout)	PT Voided Plate (Diagonal Layout)
β_{17}	7.69×10^{-5}	-2.49×10^{-4}	-6.86×10^{-5}
	3.68×10^{-6}	-1.19×10^{-5}	-3.29×10^{-6}
β_{18}	-2.99×10^{-2}	1.26×10^{-2}	-3.18×10^{-3}
	-6.88×10^{-5}	2.88×10^{-5}	-7.25×10^{-6}
β_{19}	1.03×10^{-5}	8.39×10^{-4}	2.83×10^{-4}
	4.96×10^{-7}	4.02×10^{-5}	1.36×10^{-5}
β_{20}	-3.59×10^{-6}	3.08×10^{-6}	3.05×10^{-7}
	-3.59×10^{-6}	3.08×10^{-6}	3.05×10^{-7}

Table **C-13**: The coefficients derived for the EC_{est} equations for the PT tendons (EC_{PT}) for the four PT systems when considering the full span length range. Span length (*L*), concrete compressive strength (*f'c*), live load (*LL*), and dead load (*DL*) are in metric units when using the top coefficients; the bottom coefficients are compatible with imperial units.

Coefficient	Flat Plate	Hollow Core Slab	Voided Plate (Orthogonal Layout)	Voided Plate (Diagonal Layout)
β_0	-0.9309	-12.34	0.9338	8.107
	-0.9453	-12.32	0.9322	8.069
β_1	8.16×10^{-2}	0.8834	-0.4709	-1.385

Coefficient	Flat Plate	Hollow Core Slab	Voided Plate (Orthogonal Layout)	Voided Plate (Diagonal Layout)
	2.45×10^{-2}	0.2650	-0.1413	-0.4152
β_2	3.11×10^{-2}	0.6186	-9.19×10^{-4}	2.60×10^{-2}
	2.22×10^{-4}	4.26×10^{-3}	-4.32×10^{-6}	1.93×10^{-4}
β_3	0.2279	-0.4166	7.68×10^{-2}	-0.7419
	1.09×10^{-2}	-2.00×10^{-2}	3.61×10^{-3}	-3.55×10^{-2}
β_4	0.1812	-1.356	1.235	-1.007
	8.66×10^{-3}	-6.50×10^{-2}	-5.91×10^{-2}	-4.82×10^{-2}
β_5	5.67×10^{-4}	9.35×10^{-3}	9.48×10^{-3}	-8.23×10^{-4}
	5.67×10^{-4}	9.36×10^{-3}	9.48×10^{-3}	-8.23×10^{-4}
β_6	3.06×10^{-2}	7.09×10^{-3}	7.31×10^{-2}	0.1061
	2.75×10^{-3}	6.38×10^{-4}	6.58×10^{-3}	9.55×10^{-3}
β_7	-4.98×10^{-3}	-2.81×10^{-4}	-1.71×10^{-3}	-1.44×10^{-2}
	-1.03×10^{-5}	-5.76×10^{-7}	-3.54×10^{-6}	-2.98×10^{-5}
β_8	2.54×10^{-2}	1.43×10^{-2}	7.59×10^{-2}	0.1732
	3.66×10^{-4}	2.05×10^{-4}	1.09×10^{-3}	2.49×10^{-3}
β_9	2.91×10^{-2}	1.33×10^{-2}	6.96×10^{-2}	0.1907
	4.17×10^{-4}	1.90×10^{-4}	1.00×10^{-3}	2.74×10^{-3}

Coefficient	Flat Plate	Hollow Core Slab	Voided Plate (Orthogonal Layout)	Voided Plate (Diagonal Layout)
β_{10}	1.69×10^{-5}	8.20×10^{-5}	-3.80×10^{-4}	1.95×10^{-4}
	5.07×10^{-6}	2.46×10^{-5}	-1.14×10^{-4}	5.86×10^{-5}
β_{11}	-1.04×10^{-3}	-9.89×10^{-3}	-1.41×10^{-3}	1.24×10^{-3}
	-5.02×10^{-8}	-4.70×10^{-7}	-6.75×10^{-8}	5.78×10^{-8}
β_{12}	7.34×10^{-3}	-1.51×10^{-5}	2.15×10^{-2}	-9.59×10^{-3}
	-2.43×10^{-6}	-3.57×10^{-9}	7.12×10^{-6}	-3.17×10^{-6}
β_{13}	5.22×10^{-3}	-6.88×10^{-4}	7.41×10^{-3}	-8.85×10^{-3}
	-1.73×10^{-6}	-2.29×10^{-7}	-2.45×10^{-6}	-2.93×10^{-6}
β_{14}	8.20×10^{-6}	-3.15×10^{-5}	-3.15×10^{-5}	7.48×10^{-6}
	5.67×10^{-8}	-2.18×10^{-7}	-2.18×10^{-7}	5.18×10^{-8}
β_{15}	-3.69×10^{-2}	7.78×10^{-2}	-8.71×10^{-2}	6.04×10^{-2}
	-8.45×10^{-5}	1.78×10^{-4}	-2.00×10^{-4}	1.38×10^{-4}
β_{16}	-4.23×10^{-2}	1.04×10^{-2}	-0.1430	6.45×10^{-2}
	-9.70×10^{-5}	2.37×10^{-5}	-3.27×10^{-4}	1.48×10^{-4}
β_{17}	7.38×10^{-5}	2.90×10^{-6}	4.84×10^{-4}	-2.89×10^{-4}
	3.53×10^{-6}	1.39×10^{-7}	2.32×10^{-5}	-1.38×10^{-5}
β_{18}	-2.60×10^{-2}	0.8746	-3.25×10^{-2}	4.02×10^{-2}

Coefficient	Flat Plate	Hollow Core Slab	Voided Plate (Orthogonal Layout)	Voided Plate (Diagonal Layout)
	-5.99×10^{-5}	2.00×10^{-3}	-7.49×10^{-5}	9.13×10^{-5}
β_{19}	-3.15 $\times 10^{-4}$	-7.31×10^{-5}	-2.81×10^{-3}	3.90×10^{-4}
	-1.51×10^{-5}	-3.50×10^{-6}	-1.34×10^{-4}	1.87×10^{-5}
β_{20}	-1.60×10^{-6}	-3.98×10^{-7}	-9.43×10^{-6}	7.03×10^{-7}
	-1.60×10^{-6}	-3.98×10^{-7}	-9.43×10^{-6}	7.03×10^{-7}

Table **C-14**: The coefficients derived for the EC_{est} equations for the PT tendons (EC_{PT}) for the four PT systems when considering the economic span length range. Span length (L), concrete compressive strength ($f'c$), live load (LL), and dead load (DL) are in metric units when using the top coefficients; the bottom coefficients are compatible with imperial units.

Coefficient	Flat Plate	Hollow Core Slab	Voided Plate (Orthogonal Layout)	Voided Plate (Diagonal Layout)
β_0	-2.176	-13.05	-1.050	7.922
	-2.190	-13.05	-1.048	7.871
β_1	0.2846	0.7119	-0.3435	-1.438
	8.53×10^{-2}	0.2137	-0.1032	-0.4312
β_2	1.15×10^{-2}	0.7313	-6.01×10^{-2}	4.96×10^{-2}
	8.75×10^{-5}	5.04×10^{-3}	-4.13×10^{-4}	3.60×10^{-4}
β_3	0.5189	-0.4401	1.148	-0.6543
	2.48×10^{-2}	-2.11×10^{-2}	5.49×10^{-2}	-3.13×10^{-2}

Coefficient	Flat Plate	Hollow Core Slab	Voided Plate (Orthogonal Layout)	Voided Plate (Diagonal Layout)
β_4	0.3131	-1.477	1.998	-1.301
	1.50×10^{-2}	-7.07×10^{-2}	-9.56×10^{-2}	-6.22×10^{-2}
β_5	5.66×10^{-4}	8.10×10^{-3}	8.65×10^{-3}	-7.68×10^{-4}
	5.60×10^{-4}	8.10×10^{-3}	8.65×10^{-3}	-7.69×10^{-4}
β_6	2.12×10^{-2}	1.71×10^{-2}	7.04×10^{-2}	0.1122
	1.91×10^{-3}	1.54×10^{-3}	6.34×10^{-3}	1.01×10^{-2}
β_7	-2.09×10^{-3}	-4.68×10^{-3}	3.53×10^{-3}	-1.79×10^{-2}
	-4.32×10^{-6}	-9.71×10^{-6}	-7.32×10^{-6}	-3.71×10^{-5}
β_8	4.54×10^{-4}	2.32×10^{-2}	-8.17×10^{-3}	0.1748
	6.52×10^{-6}	3.33×10^{-4}	-1.17×10^{-4}	2.51×10^{-3}
β_9	1.80×10^{-2}	3.00×10^{-2}	4.87×10^{-2}	0.2204
	2.58×10^{-4}	4.32×10^{-4}	6.99×10^{-4}	3.17×10^{-3}
β_{10}	6.31×10^{-5}	2.10×10^{-4}	-7.35×10^{-5}	1.90×10^{-4}
	1.89×10^{-5}	6.31×10^{-5}	-2.21×10^{-5}	5.69×10^{-5}
β_{11}	-1.52×10^{-3}	-1.06×10^{-2}	-1.95×10^{-3}	1.60×10^{-3}
	-7.34×10^{-8}	-5.03×10^{-7}	-9.33×10^{-8}	7.45×10^{-8}
β_{12}	1.14×10^{-2}	-2.50×10^{-3}	3.05×10^{-2}	-1.09×10^{-2}

Coefficient	Flat Plate	Hollow Core Slab	Voided Plate (Orthogonal Layout)	Voided Plate (Diagonal Layout)
	3.77×10^{-6}	-8.28×10^{-7}	1.01×10^{-5}	-3.61×10^{-6}
β_{13}	7.78×10^{-3}	-1.96×10^{-3}	1.05×10^{-2}	-1.17×10^{-2}
	2.57×10^{-6}	-6.50×10^{-7}	3.48×10^{-6}	-3.86×10^{-6}
β_{14}	8.47×10^{-6}	-3.48×10^{-5}	-4.56×10^{-5}	1.03×10^{-5}
	5.85×10^{-8}	-2.41×10^{-7}	-3.15×10^{-7}	7.11×10^{-8}
β_{15}	-5.12×10^{-2}	7.86×10^{-2}	-0.1313	5.85×10^{-2}
	-1.17×10^{-5}	1.80×10^{-4}	-3.01×10^{-4}	1.34×10^{-4}
β_{16}	-5.80×10^{-2}	1.08×10^{-2}	-0.2055	5.62×10^{-2}
	-1.33×10^{-4}	2.48×10^{-5}	-4.71×10^{-4}	1.29×10^{-4}
β_{17}	9.56×10^{-5}	-1.04×10^{-5}	6.85×10^{-4}	-3.92×10^{-4}
	4.58×10^{-6}	-5.00×10^{-7}	3.28×10^{-5}	-1.88×10^{-5}
β_{18}	-3.48×10^{-2}	0.8677	-4.58×10^{-2}	5.27×10^{-2}
	-8.02×10^{-5}	1.99×10^{-3}	-1.06×10^{-4}	1.20×10^{-4}
β_{19}	-3.36×10^{-4}	-1.26×10^{-4}	-3.73×10^{-3}	5.35×10^{-4}
	-1.61×10^{-5}	-6.05×10^{-6}	-1.79×10^{-4}	2.56×10^{-5}
β_{20}	-1.75×10^{-6}	-4.31×10^{-7}	-1.24×10^{-5}	9.86×10^{-7}
	-1.75×10^{-6}	-4.31×10^{-7}	-1.24×10^{-5}	9.86×10^{-7}

C.3 R^2 and RMSEs for the Schematic Design Phase Equations

Table **C-15**: The R^2 values and RMSEs for the *MQ** equations with the coefficients described in Tables **C-3** to **C-6**.

Concrete System	**Full Span Length Range**		**Appropriate Span Length Range**	
	R^2	**RMSE**	**R^2**	**RMSE**
RC Flat Plate	> 0.999	7.443×10^{-3}	0.998	5.077×10^{-3}
RC Flat Slab	> 0.999	7.864×10^{-3}	0.999	4.633×10^{-3}
RC One-Way Pan Joist Slab	0.979	1.939×10^{-2}	0.948	5.689×10^{-3}
RC Two-Way Slab with Beams	0.966	1.243×10^{-2}	0.936	1.094×10^{-2}
RC Two-Way Waffle Slab	0.744	2.555×10^{-2}	0.283	2.490×10^{-2}
RC Voided Plate	0.998	8.192×10^{-3}	0.998	4.847×10^{-3}
PT Flat Plate	0.989	1.646×10^{-2}	0.983	1.751×10^{-2}
PT Hollow Core Slab	0.982	1.512×10^{-2}	0.974	1.705×10^{-2}
PT Voided Plate – Orthogonal Layout	0.963	1.984×10^{-2}	0.958	2.059×10^{-2}
PT Voided Plate – Diagonal Layout	0.950	2.258×10^{-2}	0.947	2.286×10^{-2}

Note that the R^2 and RMSEs are the same regardless of metric or imperial units.

Table **C-16**: The R^2 values and RMSEs for the *MQ** equations described in Tables **C-7** through **C-14**.

Concrete System *Structural Material*	**Full Span Length Range**		**Economic Span Length Range**	
	R^2	**RMSE**	**R^2**	**RMSE**
RC Flat Plate *Rebar*	0.999	0.367	0.996	0.308
RC Flat Slab *Rebar*	> 0.999	0.297	0.997	0.261
RC One-Way Pan Joist Slab *Rebar*	0.960	2.482	0.901	0.955
RC Two-Way Slab with Beams *Rebar*	0.968	2.975	0.972	1.620

Concrete System *Structural Material*	Full Span Length Range		Economic Span Length Range	
	R^2	RMSE	R^2	RMSE
RC Two-Way Waffle Slab *Rebar*	0.988	0.463	0.983	0.411
RC Voided Plate *Rebar*	0.998	0.521	0.997	0.319
RC Voided Plate *Void Formers*	0.998	9.71×10^{-2}	0.999	3.70×10^{-2}
PT Flat Plate *Rebar*	0.998	0.280	0.999	0.189
PT Flat Plate *PT Tendons*	0.970	0.403	0.964	0.391
PT Hollow Core Slab *Rebar*	0.942	2.727	0.919	2.532
PT Hollow Core Slab *PT Tendons*	0.966	0.775	0.951	0.725
PT Voided Plate – Orthogonal Layout *Rebar*	0.972	0.975	0.956	1.047
PT Voided Plate – Orthogonal Layout *Void Formers*	0.818	0.196	0.732	0.198
PT Voided Plate – Orthogonal Layout *PT Tendons*	0.950	0.932	0.952	0.854
PT Voided Plate – Diagonal Layout *Rebar*	0.940	1.639	0.939	1.662
PT Voided Plate – Diagonal Layout *Void Formers*	0.949	0.103	0.944	8.12×10^{-2}
PT Voided Plate – Diagonal Layout *PT Tendons*	0.992	0.395	0.994	0.356

Note that the R^2 and RMSEs are the same regardless of metric or imperial units.

VITA

Jonathan M. Broyles

EDUCATION

Ph.D. in Architectural Engineering
Discipline: Structural
The Pennsylvania State University, University Park, PA
Dissertation Adviser: Dr. Nathan C. Brown — Expected May 2024

M.S. in Architectural Engineering
Discipline: Structural | Minor: Acoustics
Minor in Acoustics
The Pennsylvania State University, University Park, PA
Adviser: Dr. Nathan C. Brown — August 2020

B.S. in Civil Engineering
Emphasis: Structural | Minor in Music Performance (Percussion)
Clemson University, Clemson, SC — May 2018

JOURNAL PUBLICATIONS

[6] **Broyles, J. M.**, Gevaudan, J. P., Hopper, M. W., Solnosky, R. L., & Brown, N. C. (2024). Equations for early-stage design embodied carbon estimation for concrete floors of varying loading and strength. *Engineering Structures*, **301**, 117369. doi: 10.1016/j.engstruct.2023.117369.

[5] **Broyles, J. M.** Gevaudan, J. P., & Brown, N. C. (2024). A compiled dataset of concrete mix Environmental Product Declarations for life cycle assessment. *Data in Brief*, **52**, 109852. doi: 10.1016/j.dib.2023.109852.

[4] **Broyles, J. M.** & Hopper, M. W. (2023). Assessment of the embodied carbon performance of post-tensioned voided concrete plates as a sustainable floor solution in multi-story buildings. *Engineering Structures*, **295**, 116847. doi: 10.1016/j.engstruct.2023.116847.

[3] **Broyles, J. M.**, Shepherd, M. R., & Brown, N. C. (2023). Evaluation of the dynamic response for scaled models of shaped concrete floor slabs. *Building Acoustics*, **30**(2), 143-163. doi: 10.1177/1351010X231157613.

[2] **Broyles, J. M.**, Shepherd, M. R., & Brown, N. C. (2022). Modified acoustic transmission metrics for early-stage design exploration using a computational case study of heavyweight floors. *Applied Acoustics*, **196**, 108865. doi: 10.1016/j.apacoust.2022.108865.

[1] **Broyles, J. M.**, Shepherd, M. R., & Brown, N. C. (2022). Design optimization of structural-acoustic spanning concrete elements in buildings. *Journal of Architectural Engineering*, **28**(1), 04021044. doi: 10.1061/(ASCE)AE.1943-5568.0000520.

PROFESSIONAL EXPERIENCE

Cora Structural | Boston, MA | Sept. – Nov. 2023
Part-Time Software Developer

LERA Consulting Structural Engineers | New York City, NY | Dec. 2021 – Dec. 2022
Part-Time Researcher

Kimley Horn | Atlanta, GA | May – Aug. 2018
Structural Engineer Intern